Jing Zhang · Yeon-Gil Jung *Editors*

Advanced Ceramic and Metallic Coating and Thin Film Materials for Energy and Environmental Applications

Springer

Advanced Ceramic and Metallic Coating and Thin Film Materials for Energy and Environmental Applications

Jing Zhang • Yeon-Gil Jung
Editors

Advanced Ceramic and Metallic Coating and Thin Film Materials for Energy and Environmental Applications

Springer

Editors
Jing Zhang
Department of Mechanical Engineering
Indiana University-Purdue
University Indianapolis
Indianapolis, IN, USA

Yeon-Gil Jung
School of Materials Science and Engineering
Changwon National University
Changwon, Gyeongnam, Republic of Korea

ISBN 978-3-319-59905-2 ISBN 978-3-319-59906-9 (eBook)
DOI 10.1007/978-3-319-59906-9

Library of Congress Control Number: 2017946164

Printed on acid-free paper

This Springer imprint is published by Springer Nature
The registered company is Springer International Publishing AG
The registered company address is: Gewerbestrasse 11, 6330 Cham, Switzerland

Preface

The field of research into advanced metallic and ceramic thin film materials for energy and environmental applications has been rapidly moving forward. This book provides the latest information of the developments in the field. It also gives the perspective of future research. This book collects the contributions by several established worldwide researchers from academia, industry, and a government research laboratory. The book covers the fundamental mechanisms, processing, and applications of advanced thin film and coating materials.

The book covers a broad range of topics related to thin film and coating materials, including overview of advanced ceramic and metallic coatings, surface modification, magnetic materials, thermoelectric materials, solar energy materials, solid oxide fuel cells, coatings in solid-phase microextraction process, and modeling and simulation of thin film materials.

This book is primarily aimed at researchers in thin film and coating fields in both academia and industry. It can be used as a reference book for graduate and undergraduate students in materials science and mechanical engineering.

Indianapolis, IN, USA — Jing Zhang
Changwon, Gyeongnam Republic of Korea — Yeon-Gil Jung

Acknowledgements

Prof. Jing Zhang acknowledges support from Indiana University–Purdue University Indianapolis and the many graduate students who contributed technically to the relevant content in this book. Particularly, he thanks Dr. Xingye Guo, Yi Zhang, Linmin Wu, and Michael Golub. He would like to thank Dr. James Knapp and Dr. Li Li at Praxair Surface Technologies in Indianapolis, who provided valuable scientific guidance in developing novel lanthanum zirconate-based thermal barrier coatings, a project sponsored by the U.S. Department of Energy (Grant No. - DE-FE0008868, program manager: Richard Dunst). He also dedicates this book to his dear mother and hopes she would be proud of this wonderful achievement.

Prof. Yeon-Gil Jung thanks support from Changwon National University. The work of the following students or postdocs is acknowledged: Dr. Zhe Lu, Dr. Sang-Won Myoung, Sung-Hoon Jung, Soo-Hyeok Jeon, and Guanlin Lyu. He would like to thank a project sponsored by the National Research Foundation of Korea (NRF-2011-0030058). A special dedication goes to his dear father for his unconditional support.

Finally, Prof. Jing Zhang and Prof. Yeon-Gil Jung would like to thank Marta Moldvai and Prasad Gurunadham at Springer for their support and encouragement of developing this book project.

Contents

Contributors

Ana M. Afonso Departamento de Química, Unidad Departamental de Química Analítica, Universidad de La Laguna (ULL), La Laguna, Tenerife, Spain

David Alique Department of Chemical and Energy Technology, Rey Juan Carlos University, Móstoles, Madrid, Spain

Tapas K. Chaudhuri Department of Applied Physics, S.V. National Institute of Technology, Surat, India

Ruihua Cheng Department of Physics, Indiana University–Purdue University Indianapolis, Indianapolis, IN, USA

Jong-Jin Choi Functional Ceramics Department, Korea Institute of Materials Science, Changwon, South Korea

Maykel Courel Instituto de Energías Renovables, Universidad Nacional Autónoma de México, Temixco, Morelos, Mexico

Prashant R. Ghediya Department of Physics, Faculty of Sciences, Marwadi University, Rajkot, Gujarat, India

Adrián Gutiérrez-Serpa Departamento de Química, Unidad Departamental de Química Analítica, Universidad de La Laguna (ULL), La Laguna, Tenerife, Spain

Yeon-Gil Jung School of Materials Science and Engineering, Changwon National University, Changwon, Gyeongnam, Republic of Korea

Andrei V. Kovalevsky Department of Materials and Ceramic Engineering, CICECO—Aveiro Institute of Materials, University of Aveiro, Aveiro, Portugal

Hyung-Tae Lim School of Materials Science and Engineering, Changwon National University, Changwon, South Korea

Zhe Lu School of Materials and Metallurgical Engineering, University of Science and Technology Liaoning, Anshan, Liaoning Province, China

Idaira Pacheco-Fernández Departamento de Química, Unidad Departamental de Química Analítica, Universidad de La Laguna (ULL), La Laguna, Tenerife, Spain

Verónica Pino Departamento de Química, Unidad Departamental de Química Analítica, Universidad de La Laguna (ULL), La Laguna, Tenerife, Spain

Tae Ho Shin Energy Materials Center, Korea Institute of Ceramic Engineering and Technology, Jinju, South Korea

Osvaldo Vigil-Galán Escuela Superior de Física y Matemáticas-Instituto Politécnico Nacional (IPN), México DF, Mexico

Jing Zhang Department of Mechanical Engineering, Indiana University-Purdue University Indianapolis, Indinapolis, Indiana, USA

Chapter 1
Overview of Advanced Ceramic and Metallic Coating for Energy and Environmental Applications

Zhe Lu, Yeon-Gil Jung, and Jing Zhang

1.1 Introduction

Advanced ceramics have gradually become an important part as the new and key materials in developing modern technologies, affecting the advancement and progress in industries. A series of excellent properties in advanced ceramics, specifically fine structure, such as superior strength and hardness, wear-resisting, corrosion resistance, high temperature resistant, conductive, insulation, magnetic, pervious to light, piezoelectric, ferroelectric, acousto-optic, semiconductor and superconductor, and biological compatibility are widely used in national defense, chemical industry, metallurgy, electronics, machinery, aviation, spaceflight, biomedicine, etc. Also, the development of advanced ceramics is a new growth point of national economy, and its status—research, application, and development, embodies a country as an important symbol of comprehensive strength of national economy. At present, the worldwide advanced ceramic technology is rapidly progressing, its application area is expanding, and the stable growth trend in market is obvious.

The United States and Japan are leading the development and application of advanced ceramics. The United States National Aeronautics and Space Agency (NASA) is in the development of structural ceramics and a processing technology is

Z. Lu
School of Materials and Metallurgical Engineering, University of Science and Technology Liaoning, Anshan, Liaoning Province, China

Y.-G. Jung (✉)
School of Materials Science and Engineering, Changwon National University, Changwon, Gyeongnam 641-773, Republic of Korea
e-mail: jungyg@changwon.ac.kr

J. Zhang
Department of Mechanical Engineering, Indiana University-Purdue University Indianapolis, Indinapolis 46202, Indiana, USA

J. Zhang, Y.-G. Jung (eds.), *Advanced Ceramic and Metallic Coating and Thin Film Materials for Energy and Environmental Applications*,
DOI 10.1007/978-3-319-59906-9_1

to implement a massive research and development program, focusing on the key closed-loop implementation of aircraft engine, engine ceramic replacement, at the same time of nanostructured ceramic coatings, biological medicine, and photoelectric ceramic research and industrialization on funding [1]. There are ten big plans, like America's "brittle material design" and so on. One of federal plans is "the advanced material and equipment," with cost up to $2–$2.5 billion in a year for materials research and the construction, in order to improve its international competitiveness. The advanced ceramics in Japan, related to the advanced manufacturing equipment and excellent product stability, are also gradually becoming the leader of the international market, especially in functional ceramics areas including thermal, pressure sensitive, magnetic susceptibility, gas sensor, photosensitive monopoly in the international market gradually [2]. One of Nippon Provincial fine ceramics production research and development plans is "moonlight"; one of items is the development of 300 MW gas turbine [3]. In addition, the EU countries, especially Germany and France, have carried on the key researches in the field of structural ceramics, mainly concentrated in the power generation equipment, new energy materials and ceramic components of engine, etc. The European Union, including Germany, France, Britain, and other countries, are adopting some corresponding measures to the development of new materials, such as "eureka program" [4]. The United States department of ceramic industry statistics shows that average annual growth rate in advanced ceramics market is about 12% in the United States, Japan, and the European Union—Annual average growth rates of EU, United States, and Japan are 15–18%, about 9.9%, and about 7.2%, respectively [5].

This chapter is aimed at providing a comprehensive review of two major coating materials, i.e., thermal barrier coating and environmental barrier coating. The historical evolution and latest advancement of the materials are presented. Suggested future development is also provided.

1.2 Thermal Barrier Coating (TBC)

1.2.1 Overview of TBC

The gas turbine cycle usually describes the relationship between air volume (V) and pressure (P) in the system. The Brayton cycle (1876) called as a simple cycle of gas turbine is a representation of the properties of a fixed amount of air as it passed through a gas turbine in operation (Fig. 1.1a). These same points are also marked in the engine schematic in Fig. 1.1b. The useful work (from 3′ to 4 in Fig. 1.1a) is the energy available to cause output shaft power for a land-based gas turbine (for power generation), or thrust for jet aircraft. Unlike the aircraft engine, land-based gas turbine added other equipments to increase efficiency and/or the output of a unit such as regeneration, intercooling, and reheating. The regeneration involves in the installation of heat exchanger to heat the exhaust gas before entering combustor. Thus, this regenerated process increases the efficiency by 5–6%. The intercooler is a heat exchanger that cools compressed gas during the compressing process.

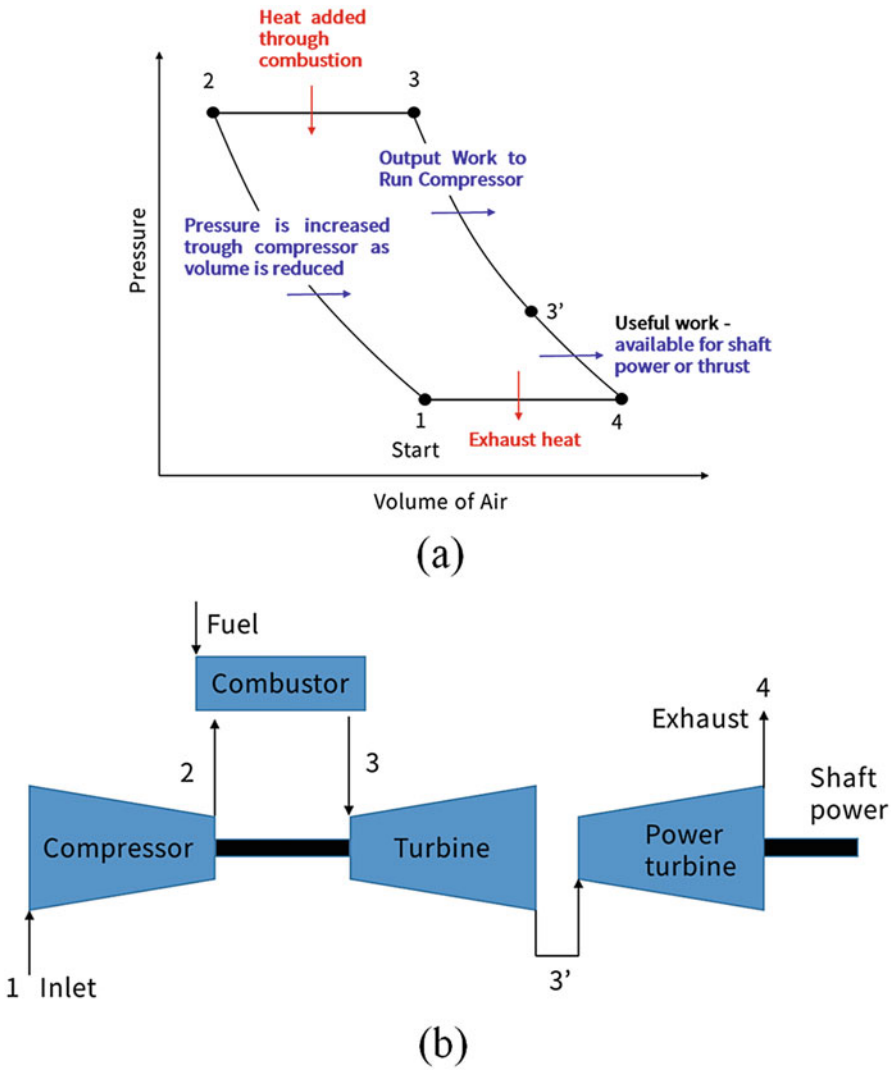

Fig. 1.1 Brayton cycle diagram: (**a**) pressure–volume diagram for a unit mass of working fluid and (**b**) gas turbine schematic showing relative points

In the system consisting of a high and low pressure unit, the intercooler is mounted between them and reduces the necessary work for compressing in the high pressure compressor. The reheating located between high pressure turbine and low pressure turbine can be used to "reheat" the flow. The combined cycle gas turbine (CCGT) power plant combined with gas turbine and steam turbine achieves greater efficiency with using the exhaust gas of gas turbine to stream turbine heat resource. Actually efficiency values have obtained as high as 52–58% with CCGT [6]—now days the

efficiency is increasing to 62%. As gas turbine engine is designed to meet demands for higher power or lower specific fuel consumption, the engine must accommodate: (1) increased mass airflow, (2) increased pressure ratio, (3) increased maximum allowable turbine inlet and outlet temperature, and (4) improved efficiency of the compressor and turbine sections [7]. Several technical progresses have been achieved to satisfy these demands, and one of them is thermal barrier coating (TBC).

Numerous types of coating are applying to protect structural engineering materials from corrosion, erosion, wear, etc., providing more hardness, lubricant and thermal insulation. Especially, TBCs are the most complexity structure due to high operating temperature and high rotating speed of aircraft and industrial gas turbine engines. TBCs have been used since 1970s (jet engine for aircraft) and 1980s (gas turbine for power generation) to protect the metallic parts in hot section components of gas turbine engine. TBCs comprise (1) a substrate, (2) a metallic bond coat, (3) a TGO (thermally grown oxide), and (4) a ceramic top coat, which can improve durability and efficiency in the gas turbine as insulating turbine and combustor engine components from the hot gas stream (Fig. 1.2). Demands for advanced TBC systems for enhanced performance and longer lifetime have continuously been emerging at higher operating temperature [8, 9].

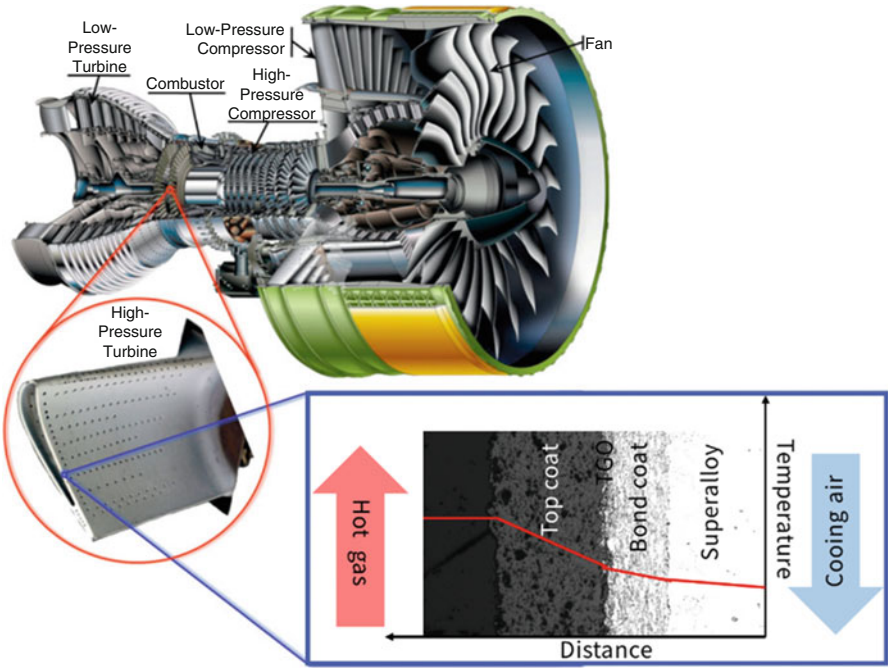

Fig. 1.2 Cutaway view of Engine Alliance GP7200 aircraft engine and photograph of a turbine blade with TBC from the high-pressure hot section of an engine, and microstructure image of TBCs (Engine image courtesy of Engine Alliance, turbine blade photograph courtesy of YXLON) [10]

Over the past 60 years, the development of high temperature engineering alloys has been a primary driver of increased operating temperatures in gas turbine engines [11]. The temperatures that turbine blades are exposed to can be close to the melting point of superalloys. Therefore, TBCs are extensively employed in high temperature components of gas turbine engines, such as turbine blade, turbine vane, and combustion, to increase the turbine inlet temperature, hence increasing the efficiency and performance of gas turbine engines [12]. TBCs can be considered a four-layered material system as mentioned above, consisting of the following aspects: (1) a substrate of the nickel- or cobalt-based superalloy, (2) an oxidation-resistant metallic bond coat of MCrAlY formed by the air plasma spray (APS), vacuum plasma spray (VPS), low-pressure plasma spray (LPPS), and high velocity oxy-fuel (HVOF) methods, (3) TGO layer, typically α-Al_2O_3 or spinel structure oxide, formed during heat treatment or in service, and (4) a ceramic top coat of 6–8% (mass %) yttria (Y_2O_3)-stabilized zirconia (ZrO_2: 6–8 YSZ) deposited by either APS or electron beam-physical vapor deposition (EB–PVD) processes [13, 14]. APS, twin wire-arc spraying, and HVOF spraying are the most popular deposition processes from an economic point of view and involve many small particles being accelerated by the high-power plasma or combustion flow to form a coating layer. It is well known that many new techniques, such as solution-precursor plasma spraying (SPPS) and EB–PVD, have exhibited an increasing potential in improving the thermal durability of TBC systems [15–17].

The common processes used to deposit the ceramic top coat are APS and EB–PVD. The EB–PVD method has been developed to enhance adhesive strength and improve strain resistance. The APS method with its economic benefits is still preferred commercially, in contrast to the use of the complex and expensive EB–PVD [8, 18, 19], although it has a relatively low strain tolerance compared with coatings prepared by more advanced coating methods. The bond coat plays an important role in ensuring structural effectiveness and affording extra adhesion of the top coat to the substrate. Many techniques, such as LPPS, APS, high-frequency pulse detonation, and HVOF, have been applied to form the bond coat [20–23]. The APS process is widely used to create the bond coat in a TBC system because of its economic benefits. However, to meet the requirement in increasing working temperature and improving fuel efficiency in gas turbines and diesel engines, the HVOF process is employed for the bond coat. Unfortunately, the oxidation environment required for the HVOF process may affect the subsequent oxidation properties of the top coat, which are important in the applied high-temperature working environments. A dense bond coat without oxide formation during spraying can be deposited by LPPS or VPS [24, 25]. Therefore, the bond coat prepared by LPPS or VPS has been employed in the most advanced TBCs [26–29], although their wide application is limited because of their high costs.

Numerous factors have to be considered in practical applications of TBCs, including high melting point, thermal stability, low thermal conductivity, chemical inertness, thermal expansion match and good adhesion with the metallic substrate, low sintering rate, and thermo-mechanical properties [30, 31]. Among them, the thermal stability or durability in high-temperature environments, especially in

cyclic thermal exposure, is essential factor to improve the reliability and lifetime performance of TBC system, and the thermal durability of TBC system is closely related with its microstructure. There are three ways to enhance TBC performance, specially focused on the lowering of thermal conductivity of TBC system: (1) studying about coating materials with a low thermal conductivity, (2) controlling the porosity in TBC, and (3) increasing the thickness of TBC. The effects of porosity and material on thermal conductivity of TBC have been reported, indicating that thermal conductivity is strongly dependent on the porosity and material composition [32]. When the thicknesses of TBCs using APS are greater than 1.5 mm, the TBCs spontaneously fail during preparation or service [27, 28, 33–35], which makes other coatings or processes preferable, such as a dense vertical crack (DVC) TBC, gradient or high-porosity coatings, and SPPS process [15, 35, 36].

1.2.2 Current Research Status of TBC

1.2.2.1 Research Background

The industrial development of TBCs started in the 1950s with the manufacture of the first enamel coatings for military engine components [37]. In the 1960s the first flame sprayed ceramic layers with NiAl bond coats were used in commercial aero engines [38]. The science and technology of TBCs have advanced considerably since reports of the first test on turbine blades in a research engine in 1976. Today, TBCs are flying in revenue service in a low risk location within the turbine section of certain gas turbine engines [39]. To improve combustion efficiency and reduce fuel consumption, the operation temperature of gas turbine engines is increased as high as 1600 °C. A high operation temperature requires the use of many advanced structural materials, extensive cooling of components, and adoption of various coatings. Currently, single crystal Ni-based superalloys have been employed to the environment with a maximum temperature of approximately 1100 °C. Therefore, more temperature gain can be obtained by developing TBCs [40, 41].

1.2.2.2 TBC Materials

Demands for higher operating temperature and more efficiency in gas turbines were originally met with the development of superalloys. However, the addition demand to increase the operating temperature has been continuously requesting and it has been achieving with evolution of cooling technology and TBCs that are used to protect hot section components, especially in blade and vane. The hot section components in a gas turbine engine are subjected to serve mechanical, chemical, and thermal stresses. Hence, requirements demanded in TBC materials are (1) high

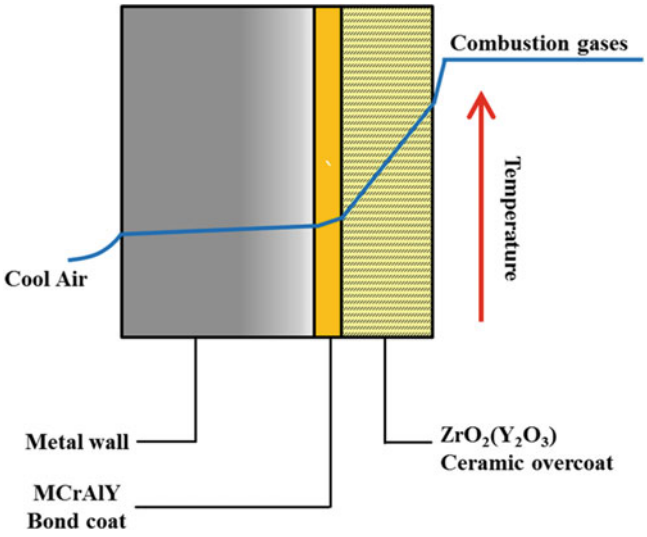

Fig. 1.3 A schematic diagram showing the temperature reduction provided by TBC

melting point, (2) no phase transformation under temperature changes, (3) low thermal conductivity, (4) chemical inertness, (5) high coefficient of thermal expansion (CTE), (6) bonding strength, and (7) high sintering resistance [41].

1.2.2.3 Structure of TBC

The typical TBC system can be considered as a four-layered material system as mentioned above [13, 14]. The insulation top coat of usually 6–8YSZ is deposited either using APS or EB–PVD process. The bond coat protects the substrates from oxidative and corrosive attacks and improves the bonding between the top coat and the substrate. The top coat has a significantly lower thermal conductivity than the metallic substrate and it is possible to establish a large temperature drop (general reduce of 100–150 °C) across the top coat by applying an internal cooling inside the components as shown in Fig. 1.3.

1.2.3 Material Selection for TBC

Material selection guidelines are desirable in identifying and developing alternative materials for higher temperature capability of TBCs in protective and insulative coatings on hot section components of gas turbines and their applications, like blade, vane, and combustion chamber, resulting in improving turbine efficiency and increasing service temperature [42, 43]. Some relate to candidate materials that

exhibit particularly low values of thermal conductivity at high temperatures and others relate to thermodynamic stability in contact with the TGO formed between the bond and top coats [44, 45]. First, a thermally protective TBC with a low thermal conductivity is required to maximize the thermal drop across the top coat. Also, the top coat is likely to have a CTE that differs from the component (substrate or bond coat) to which it is applied. Therefore, the top coat should have a high in-plane compliance to accommodate the thermal expansion mismatch between the bond and top coats, and/or between the coating layer and the underlying superalloy-based substrate. In addition, it must be able to retain the thermal and mechanical properties and its low thermal conductivity during prolonged environmental exposure [46, 47].

1.2.3.1 Ceramic Material for Top Coat

The selection of TBC materials for top coat is restricted by some basic requirements as mentioned above: (1) high melting point, (2) no phase transformation between room temperature and operation temperature, (3) low thermal conductivity, (4) chemical inertness, (5) thermal expansion match with metallic substrate, (6) good adherence to metallic substrate, and (7) sintering resistance at operation temperature [37, 41, 48–51]. The number of materials that can be used as TBCs is very limited. So far, only a few materials have been found to basically satisfy these requirements [31, 52].

The applications of pure ZrO_2 are restricted because it shows polymorphism. It is monoclinic (*m*) at room temperature and changes to tetragonal phase (*t*) from above 1100 °C, as shown in Fig. 1.4 [53]. This involves a large change in the volume (4–5%) and causes extensive cracking. Hence ZrO_2 has a low thermal shock resistivity. The addition of some oxides results in stabilizing the cubic phase and the creation of one oxygen vacancy, as shown in Fig. 1.5. However, YSZ is a mixture of ZrO_2 polymorphs, a cubic phase (*c*) and a metastable tetragonal ZrO_2 phase (*t'*) obtained with specific amount of stabilizer. Hence YSZ is also called tetragonal zirconia polycrystal (TZP). This has one of the lowest thermal conductivity (~2.3 W m^{-1} K^{-1} at 1000 °C for fully dense material) due to its high concentration of point defects (oxygen vacancies and substitutional solute atoms), which scatter heat-conducting phonons (lattice wave) [54]. YSZ also has a high CTE (~11 × 10^{-6} °C^{-1}), which helps to alleviate arising stress between the top coat and the bond coat (~14 × 10^{-6} °C^{-1}). YSZ has relatively the low density (~6.4 kg m^{-3}), which is critical for parasitic weight consideration in high speed rotating engine component [55]. The hardness (~14 GPa) of YSZ can also have the resistance to erosion and foreign material impact [8].

The amount of yttrium is an important parameter since it has an influence on the grain size, the temperature of the martensitic transformation, strength, and degradation behavior, especially in humid environment [7]. In practice, a Y_2O_3 concentration in the range of 6–8 wt.% is generally used since this composition maximizes spallation life due to the formation of the "non-transformable" metastable tetragonal YSZ phase (*t'*), which is remarkably resistant and does not undergo the

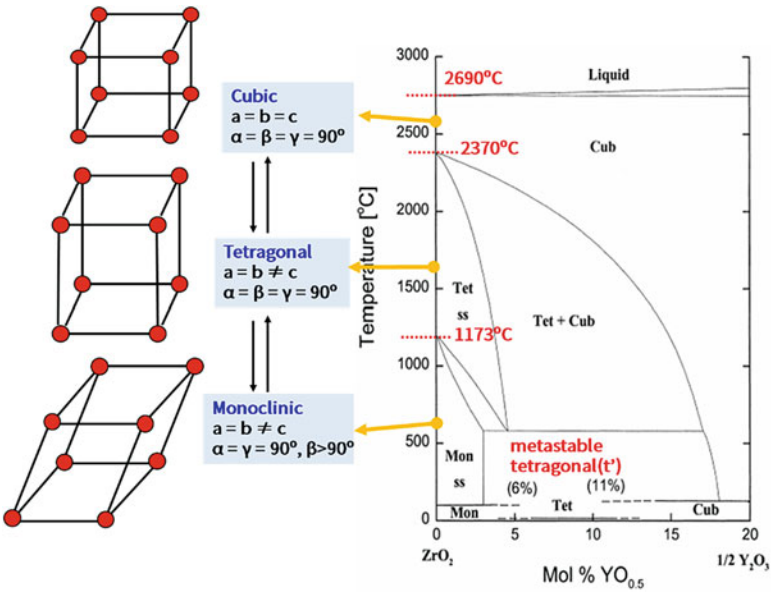

Fig. 1.4 Phase diagram of yttria-stabilized zirconia (YSZ) [53]

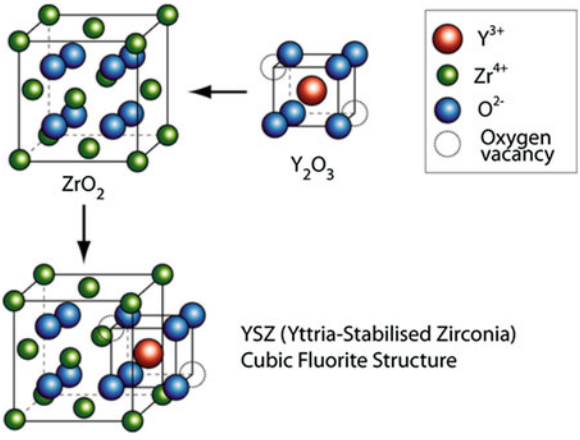

Fig. 1.5 YSZ crystal structure with oxygen vacancy

transformation to the monoclinic phase under stresses [56, 57]. However, the metastable tetragonal YSZ phase (t') undergoes a phase separation by diffusion when aged at temperatures greater than 1200 °C, which can allow the $t \rightarrow m$ transformation upon cooling. From a crystallographic point of view, the ratio of the cell parameters can be used to distinguish between the two tetragonal phases, t and t': the ratio $c/a\sqrt{2}$ tends to 1.010 for the t' cell parameters while it is superior to 1.010 for the t phase [58]. The 7–8 YSZ is the most widely studied and used as TBC material in high-temperature applications such as diesel engines and gas turbines,

and reports about this material are numerous [59]. The TBCs prepared with by 7–8 YSZ have been proved to be more resistant against the corrosion of Na_2SO_4 and V_2O_5 than the ZrO_2 coating stabilized by CaO or MgO [31, 60].

1.2.3.2 Intermetallic Material for Bond Coat

The bond coat provides environmental resistance, oxidation and corrosion protection, adherence, and chemical and mechanical stability between the top coat and the superalloy substrate. Due to the high oxygen penetrability of the external top coat, the oxidation protection of substrate is imposed to the bond coat. This metallic coating is engineered to ideally ensure the formation of a slow-growing, uniform, and defect-free α-Al_2O_3 scale (TGO) that acts as an oxygen diffusion barrier for the substrate. Thus, a sufficient aluminum reservoir is a necessary constituent of the coating chemical composition. Therefore, the bond coat is one of the most important components of the TBC system, and that is very decisive in determining TBC's durability [61, 62].

The bond coat provides a rough surface for the mechanical bonding of top coat, protects the underlying substrate against the high-temperature oxidation corrosion, and reduces the CTE mismatch between the substrate and the top coat. The bond coat is an oxidation resistant metallic layer, 75–300 μm in thickness, and it essentially dictates the spallation failure of the TBC. The bond coat is typically made of intermetallic alloys and deposited by using the APS or HVOF process. Other types of bond coat are made of aluminides of Ni and/or Pt, which are deposited electroplating in conjunction with diffusion aluminizing or chemical vapor deposition. In a minority of cases, the bond coat consists of more than one layer, having a different chemical/phase composition [63–65]. But due to their lack of oxidation and corrosion resistances, these materials are protected by nickel aluminides or MCrAlY (where M = Co, Ni or Co/Ni) coatings. NiCoCrAlYTa presents a very good corrosion resistance and is used as a standalone coating or as a bond coat in TBC systems [65–67]. The usual ways of coating preparation are physical vapor deposition (PVD), LPPS, VPS, APS, or HVOF spraying, and finally electrolytic deposition methods are also applied [68–70].

The high temperature microstructure of MCrAlY coating is mainly composed of two phases: γ-Ni provides ductility and β-NiAl provides Al-reservoir for the oxidation resistance. The proper contents of Cr and Al in the metallic bond coat are adjusted to provide an adjustment between oxidation and corrosion resistance. The concentrations of Cr and Al typically vary between 15–25 wt.% and 10–15 wt.%, respectively. The quantities of Cr in the alloy reduce the necessary amount of Al for exclusive alumina formation scale [71]. Co improves the ductility and the corrosion resistance because of increasing solubility of Cr in the γ-matrix phase, reducing the tendency to form brittle phase such as γ′-Ni_3Al and α-Cr. Furthermore Co reduces the stacking fault energy (SFE, a measure of the mobility of dislocations inside the material), since SFEs for Ni and Co are 300 mJ/m^2 and 25 mJ/m^2, respectively, and thus improves the creep resistance of the MCrAlY [72]. Some

commercial MCrAlY coatings could include Re, amount of 1–3 wt.%, for improving the oxide scale adherence, thermomechanical fatigue resistance, and retardation of inter diffusion with substrate [73, 74]. Ta reacts with the upward diffusing carbon and titanium from the substrate, and thus, prevents their inclusion in the oxide scale. Ta-contained MCrAlY coating improves creep resistance and yield strength [75]. Ti diffusion from the substrate causes TGO to degrade the adherence of alumina oxide by forming TiO_2 [76]. The reactive elements are usually added to the bond coat to mainly improve the oxide scale adherence. Comparing with the oxides of other main elements (Ni, Co, Cr.), the oxide of Al, alumina (α-Al_2O_3, TGO) has a lower formation energy, and is always the chosen oxide to form a continuous and dense scale against high-temperature oxidation in MCrAlY coatings.

1.2.4 Fabrication Method of TBC

The widely used TBCs for various applications can be classified into two categories as diffusion coating and overlay coating [77, 78]. The diffusion coating process is a thermally activated high temperature oxidation/corrosion/wear resistance coating for iron-, nickel-, cobalt-based metals in severe operating conditions. It provides a chemically bonded, tenacious coating which acts as a diffusion barrier against oxygen and other elements into the substrate [79, 80]. Diffusion coating has the superior oxidation, corrosion, and erosion resistance for the base metal up to 1150 °C without spallation, providing highly reliable substrate for critical components. It is commonly used for gas turbine engine components, such as blades, vanes, cases, seals in power generation, pump impellers, and valve gates in diesel applications. The overlay coatings are mostly deposited by using PVD and APS techniques [81–83]. The PVD describes a variety of vacuum deposition methods used to deposit thin films by the condensation of a vaporized form of the desired film material onto the surfaces of various work pieces [84, 85]. The PVD coatings show sometimes harder and more corrosion resistant than coatings applied by the electroplating process. Most coatings have high temperature and good impact strength, excellent abrasion resistance and are so durable that protective top coats are almost never necessary [86, 87].

The thermal spraying techniques are a kind of coating process in which melted (or heated) materials are sprayed onto a surface. The thermal spraying techniques are widely used for coating the materials such as metallic, ceramic, polymeric, and cermet. Thermal spraying can provide thick coatings (approx. thickness range is 20 μm to several mm, depending on the process and feedstock), over a large area at high deposition rate as compared to other coating processes such as electroplating and vapor deposition. They are fed in powder or wire form, heated to a molten or semi-molten state, and then accelerated toward substrates in the form of micrometer-size particles. Combustion or electrical arc discharge is usually used as the source of energy for thermal spraying. Resulting coatings are made by the

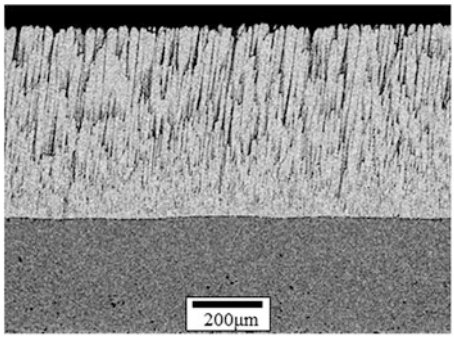

Fig. 1.6 Typical microstructure of top coat prepared by EB–PVD

accumulation of numerous sprayed particles. The surface may not heat up significantly, allowing the coating of flammable substances.

1.2.4.1 EB–PVD Process

The EB–PVD method has been developed to obtain a good microstructure, enhance adhesive strength, and improve strain resistance. The EB–PVD TBCs have been used in production since 1989. The TBCs produced by EB–PVD have a columnar microstructure with elongated inter-columnar pores that become predominantly aligned perpendicular to the plane of the coating as its thickness increases [54]. A typical microstructure for an EB–PVD is shown in Fig. 1.6, exhibiting a columnar structure with a gap between the columns that extend from the interface between the bond and top coats to the surface. The columnar structure, with a certain space between the individual columns, can improve the strain tolerance, resulting in good thermal durability under service conditions. Usually, the fine intra-columnar pores contribute a moderate reduction in thermal conductivity as they are generally inclined to the heat flow. Even though the EB–PVD TBC (which are currently being used in jet aircraft engines) usually exhibits higher durability, extending its lifetime performance, the lower deposition rate and higher cost of the EB–PVD process limits its application [88]. In addition, when the material composition is complicated, the process is more difficult due to the element's vapor pressure. The performance of EB–PVD TBC has been studied extensively for several decades and a new technology and an advanced TBC are still proposed [89, 90].

1.2.4.2 APS Process

Plasma spraying is the most commonly used method for depositing TBCs and has been used since 1950s to protect hot section components of gas turbine engines [91–93]. In plasma spraying process, the material to be deposited (feedstock)—typically as a powder, sometimes as a liquid, suspension or wire—is introduced into the plasma jet, emanating from a plasma torch. In the jet, where the temperature is on

the order of 15,000 °C, the material is melted and propelled toward a substrate. The molten droplets flatten, rapidly solidify, and form a deposit. Commonly, the deposits remain adherent to the substrate as coatings; free-standing parts can also be produced by removing the substrate. There are a large number of technological parameters that influence the interaction of the particles with the plasma jet and the substrate, and therefore the deposit properties. These parameters include feedstock type, plasma gas composition and flow rate, energy input, torch offset distance, substrate cooling, etc. [94–96].

In recent decades, the development of advanced coatings and processing methods has been a field of active research in TBCs. Many new techniques, such as SPPS, electrostatic spray assisted vapor deposition, electron beam-directed vapor deposition (EB–DVD), and EB–PVD, have been used to create advanced TBCs [97, 98]. Economical coating methodologies that enable a high degree of control over the coating morphology are desired in land-based gas turbines. The APS process, with its economic benefits, is still preferred commercially, because of the relatively low cost and simple process compared with advanced coating methods, such as EB–PVD and EB–DVD [99–101]. The APS process also has its own advantages in producing the large and complex-shaped TBCs. Numerous factors have to be considered in practical applications of TBCs, such as thermal durability, thermal conductivity, chemical inertness, CTEs, and thermomechanical properties. Among them, the thermal durability in cyclic thermal exposure is an essential factor for the reliability and lifetime performance of APS–TBC system, which is closely related to its microstructure. In addition, there are many ways to enhance TBC performance, such as controlling the porosity of TBC, employing materials with a low thermal conductivity, and increasing the thickness of TBC [102, 103]. The TBCs prepared by APS method present a strong damage tolerance under the most severe operating conditions, even when a high number of defects are present, such as pores and microcracks. The typical microstructure (cross-sectional microstructure) with horizontal "splat" boundaries/cracks, pores, and unmelted powders in the top coat is shown in Fig. 1.7, in which both coats, the bond and top coats, are prepared by using APS process. The bond coat indicates a general microstructure prepared by using APS process with oxide layer, and some pores and unmelted powders.

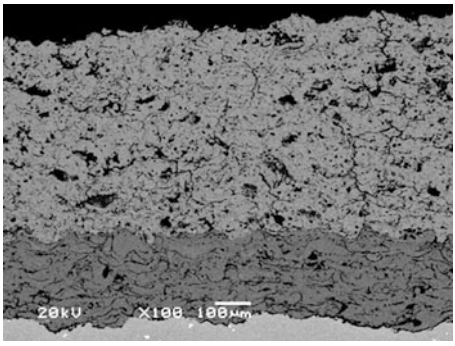

Fig. 1.7 Typical microstructure of TBC system prepared by APS

1.2.4.3 HVOF Process

A thermal spray process utilizing the combustion of gases such as hydrogen or a liquid fuel such as kerosene has been developed in 1980s, which is HVOF process. The HVOF spraying is commonly used for its versatility to deposit dense metallic/alloy and cermet coatings. By these HVOF process features the coating generally near bulk density and low residual tensile stress, in most case, compressive stress, which enable to product thicker coating than other processes (e.g., cold spray, arc coating, flame coating, plasma spray). Fuel and oxygen mix and atomize within the combustion area under conditions that monitor the correct combustion mode and pressure. There are two distinct differences between conventional flame spray and HVOF. HVOF utilizes a confined combustion and an extended nozzle to heat and accelerate the powdered coating material [104, 105]. Typical HVOF devices operate at hypersonic gas velocities, i.e., greater than MACH 5. The extreme velocities provide kinetic energy which help to produce coatings that are very dense and very well adhered in the as-sprayed condition (some of which exceed 83 MPa, or 12,000 psi). The HVOF process efficiently combusts oxygen and a gaseous or liquid fuel to produce high kinetic energy with controlled heat input. Depending on user requirements, both gas fuel (propylene, propane, hydrogen, or natural gas) and liquid fuel (kerosene) can be used. The coating material, in powder form, is introduced into and uniformly heated by the hot gas stream to a molten or semi-molten condition [106–108]. The flame and powder are accelerated by a converging and diverging nozzle (air cap) to produce supersonic gas and particle velocities, which propel the powder particles toward the substrate to be coated.

As a result, the injected particles flatten plastically and they impact on the surface of substrate. For this reason, coating microstructure shows homogeneous and fine granular structure. Coating formed by high velocity particle impact of spray particles on the substrate in solid state provides the compressive residual stress state. This is very beneficial about lifetime of coated components under dynamical load. Additionally, the actual flame temperature can be affected by the ratio between combustible and oxygen flow rate. And the choice of the combustible must also be taken under consideration of the required supply pressure that should be higher than the combustion chamber pressure (modern guns can exceed 1 MPa). More recently, HVOF coatings due to its low cost and high quality deposits have a similar oxidation rates with VPS coatings at high temperature, being sometimes even lower than this one [105, 108]. The bond coat prepared by HVOF process has outstanding characteristics, even above other thermal spray processes, that include high density, high bonding strength, optimum hardness, improved toughness, thicker coating thickness, beneficial residual stress, and superior corrosion resistance [109, 110]. A typical microstructure of the bond coat prepared by HVOF process is shown in Fig. 1.8.

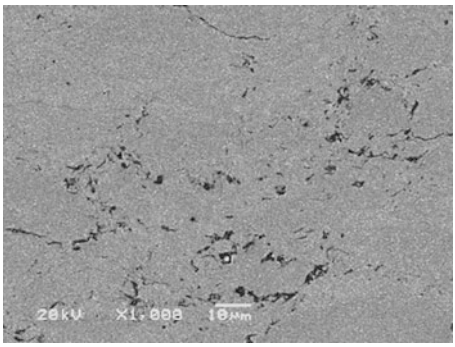

Fig. 1.8 Typical microstructure of bond coat prepared by HVOF

1.2.4.4 LPPS Process

The LPPS process, also known as VPS, has been employed at higher chamber pressure than 2 kPa during the coating operation. However the chamber is usually evacuated to nearly 1 Pa before it is flooded with an inert gas to the required working pressure. The LPPS process is a low velocity and high temperature spraying process that is performed in a near-vacuum argon atmosphere. The LPPS and VPS processes are two different designations for the same process. The "flame" (no fire is actually involved in the process) is high temperature plasma and the spraying is performed in a low-pressure argon atmosphere. This process enables materials, so-called MCrAlYs, which are sensitive to oxidation to be sprayed [111, 112]. The coating features high density (porosities of coatings are less than 1 or 2%), homogeneous and oxide-free microstructure on the bond coat. The surface roughness is strongly dependent on the particle size used for the spraying. Normally, a relatively high degree of roughness is created and the surface will be smoothened by a shot peening and/or polishing process after coating production. The LPPS process is the preferred metallic coating technology for single airfoil components. It is also used for the production of metallic anti-corrosion coatings [20, 113, 114].

The bond coats of TBCs are typically manufactured using the APS and HVOF processes. The predominant drawback of these techniques is that their inherent high temperatures inevitably lead to changes in the coating microstructure, namely oxide inclusions. The MCrAlY bond coats prepared using the APS and HVOF processes show oxide contents of 1.8 and 0.94 wt.%, respectively, which are attributed to the oxidation during spraying [96, 115–117]. A dense bond coat without oxide formation during spraying can be deposited by VPS process. Significantly, the oxide content in the bond coat prepared by LPPS process is about 0.16%, which is lower than bond coats prepared by the APS and HVOF processes [118]. A typical microstructure of the bond coat prepared by LPPS process is shown in Fig. 1.9, indicating that there is less oxide content compared with those of the APS and HVOF processes shown in Figs 1.7 and 1.8, respectively.

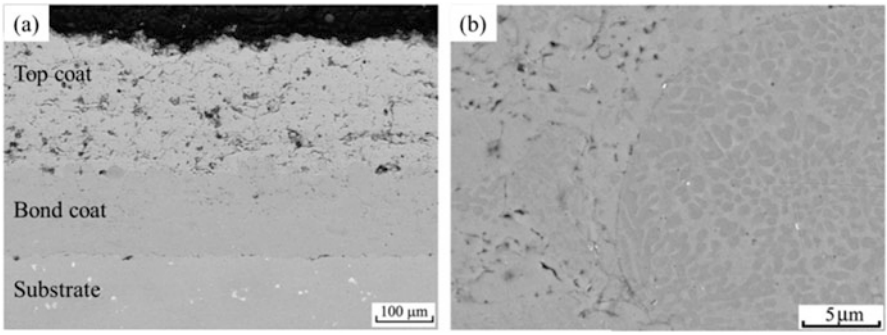

Fig. 1.9 Typical microstructure of TBC with bond coat prepared by LPPS: (**a**) overall microstructure and (**b**) bond coat microstructure

1.2.5 Advanced Thermal Barrier Coatings

1.2.5.1 Rare-Earth Oxides

Advanced TBCs with low conductivity and high thermal stability have been developed using a multi-component oxide defect-clustering approach. The advanced coatings are designed by incorporating multi-component, paired-cluster rare-earth oxide dopants into conventional ZrO_2 and hafnia–Y_2O_3 oxide systems [119]. As the atomic radius of rare-earth oxide dopants is increased with a certain range, the thermal diffusivity can be reduced due to the addition of expansion distorted. TBCs with advanced multi-component and low conductivity oxide have been developed based on an oxide defect-clustering design approach and using a laser high-heat-flux thermal conductivity technique. The laser test approach emphasizes real-time monitoring of the coating conductivity at high temperatures in order to assess the overall coating thermal conductivity performance under engine-like heat-flux and thermal gradient conditions. Although the advanced coatings with oxide cluster follow a similar trend as the pseudo-binary ZrO_2–Y_2O_3 coatings in the furnace cyclic behavior where the cyclic lifetime of coating generally decreases with increasing the total dopant concentration, the oxide cluster coatings show a promise to have significantly better cyclic durability (comparable to that of zirconia–4.55 mol% Y_2O_3) than the binary ZrO_2–Y_2O_3 coatings with equivalent dopant concentrations [118]. Under the NASA Ultra-Efficient Engine Technology (UEET) program, the durability of the advanced low conductivity coatings was evaluated using cyclic furnace tests. In terms of performance the rare-earth oxide dopants into conventional ZrO_2 and hafnia–Y_2O_3 oxide systems provide superior low conductivity, longer cycling lifetime performance and higher stability compared to the current YSZ coatings at high temperature. Through advanced coating system design, optimized dopant and composition, and improved processing technology, it can be expected in the future that the cycling lifetime performance of the coating will be more extended.

1.2.5.2 Lanthanum Hexaaluminate (LHA)

Lanthanum hexaaluminate (LHA) with a magnetoplumbite structure is a promising competitor to Y-PSZ as a TBC, since most ZrO_2 coating's lifetime performance significantly decreases, including undesired densification at temperatures exceeding 1100 °C. The microstructure of calcined lanthanum hexaaluminate powders and thermally sprayed coatings show a platelet structure [120]. Due to its high melting point, high thermal expansion, low thermal conductivity, excellent longtime sintering resistance, and structural stability up to 1800 °C, these materials have also been found advantageous for TBC applications. The nominal composition is (La, Nd) $MAl_{11}O_{19}$ where M could be Mg, Mn to Zn, Cr, Sm [121]. Also the addition of Li has been proven to be advantageous [122]. Among these, the most interesting one is $LaMgAl_{11}O_{19}$ which has been extensively investigated in terms of its thermophysical properties and processing issues during air plasma spraying [123–126]. The plasma sprayed coating is partly amorphous in the as-sprayed condition due to the rapid quenching from the molten state. Upon an initial heat treatment recrystallization occurs over the temperature range from 800 to 1200 °C which is marked by a large decrease in the volume of the free-standing coatings [125].

It characterizes that the magnetic structure is highly charged lanthanum cation located in an oxygen position of a hexagonal close-packed oxygen ions. Ion diffusion strongly inhibits perpendicular to the crystallographic c-axis, thereby obstructs the densification by sintering. Compared to Y-PSZ, the LHA shows similar thermophysical properties, outstanding structural and thermochemical stability. LHA crystallizes in the magnetoplumbite structure, a super lattice of the spinel structure as shown in Fig. 1.10. In contrast to the oxygen ion conducting ZrO_2, LHA permits operating temperatures above 1300 °C because of its thermal stability and electrically insulating properties.

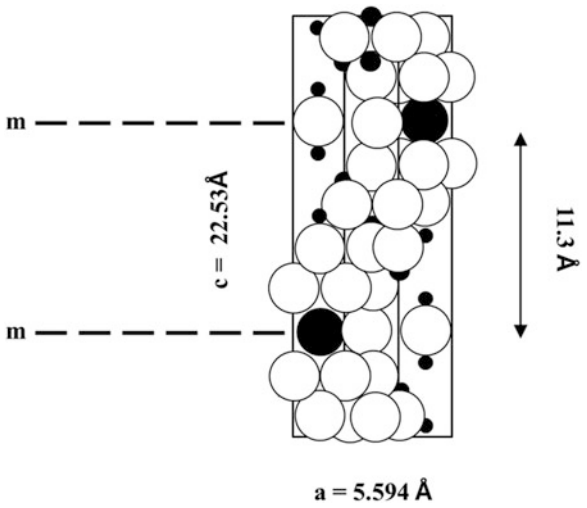

Fig. 1.10 Crystallographic unit cell of lanthanum hexaaluminate (LHA)

1.2.5.3 $La_2Ce_2O_7$ (LC)

$La_2Ce_2O_7$ (LC) is proposed as a promising TBC material which is the solid solution. CeO_2 has higher CTE and lower thermal conductivity than YSZ, and the addition of CeO_2 into YSZ coating is supposed to be effective for the improvement of thermal cycling lifetime performance. Remarkable improvement of thermal shock tolerability could be attained by the addition of CeO_2 into YSZ [127–129]. The CeO_2-doped coating has a better thermal shock resistance because mainly: (1) there is little phase transformation between the monoclinic and tetragonal phase in the CeO_2 + YSZ coating [130], (2) stress generated by bond coat oxidation is smaller in the CeO_2 + YSZ coating due to better thermal insulation, and (3) the CTE of CeO_2 + YSZ coating is larger than that of YSZ coating. However, the addition of CeO_2 has some negative effects, such as the decrease of hardness and stoichiometry change of the coating due to the vaporization of CeO_2 [127], reduction of CeO_2 into Ce_2O_3, and accelerated sintering rate of the coating [131, 132]. Some previous investigations declare that the LC solid solutions with more CeO_2 content than LC have higher CTEs below 400 °C—it should be effective to reduce the stress induced by the CTE mismatch between the substrate and the top coat in the low temperature range. Obviously the LC is used as an outer layer due to its lower thermal conductivity and good phase stability at high temperatures compared to YSZ. However, the CTE of LZ suddenly reduces at low temperature range (200–350°C).

1.2.5.4 Graded TBC

Commonly TBCs include a metal layer (substrate) and a ceramic layer (top coat)—the substrate has a high thermal conductivity, toughness, and ductility properties, and the top coat has high hardness, wear resistance, corrosion, and high temperature resistance performance. However, the CTE, the elastic modulus, and other properties between the top coat and the substrate provide with a great diversity, and there exists an obvious interface. Therefore, the bond layer (coat) alleviates the thermal expansion mismatch between the top coat and the substrate, and improves high temperature oxidation resistance performance. TBC structure is divided into three types: (a) double layer system, (b) multilayer system, and (c) graded system, which are shown in Fig. 1.11. Among them, the double layer system mainly composed of the top coat and the bond coat has a simple structure and mature technology advantages. However, the CTE and elastic modulus of the top coat and the bond coat have the deviation in temperature during thermal cycling easy to delaminate.

Therefore, in order to release the physical properties mismatch at the interface, the multilayer system has been developed which is mainly composed of substrate, heat insulation multilayer, Al_2O_3 anti-oxidation layer, and the top coat. Compared with the double layer system, the multilayer system can reduce the growth rate of the oxide (TGO) layer and improve the oxidation resistance of the coating, but the

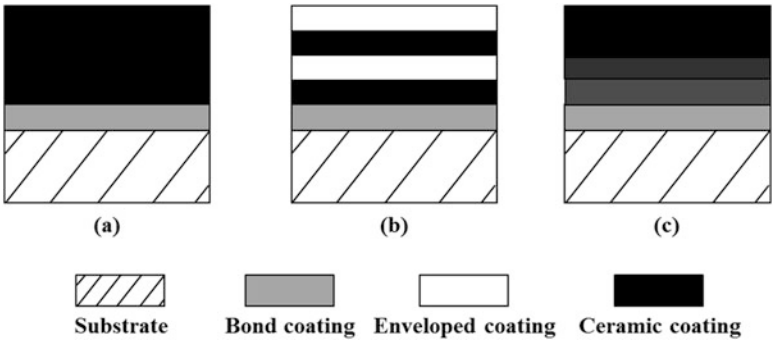

Fig. 1.11 Three kinds of TBC structure: (**a**) normal structure, (**b**) layered structure, and (**c**) graded structure

sophisticated technological process and performance poorly in thermal shock resistance restrict application in the field of aero engine areas. As a consequence, the graded system design in order to further improve the mechanical properties and high temperature oxidation resistance of TBCs can reduce the residual stress and effectively prevent delamination of the coating by changing chemical composition, organization structure, and mechanical properties with coating thickness along the direction of the gradient changes.

1.3 Environmental Barrier Coating (EBC)

1.3.1 Overview of EBC

One key barrier to the application of advanced silicon-based ceramics and composites for hot section structural components in gas turbines is their lack of environmental durability. A new class of coating, environmental barrier coating (EBC), has been developed in the 90s to protect Si-based ceramics and ceramic composites from the degradation by water vapor, even though silicon-based ceramics exhibit excellent oxidation resistance in clean and dry oxygen environments, by forming a slow-growing and dense silica scale [133, 134]. Oxide coatings are a promising approach to provide environmental protection for advanced heat engine components because oxides are in general more resistant than silicon-based ceramics to corrosive environments [135].

There are several key issues that must be considered in selecting coating materials [136, 137]. Figure 1.12 schematically shows the key issues. Firstly, the coating must possess the ability to resist reaction with aggressive environments, as well as low oxygen permeability to limit the transport of oxygen. Secondly, the coating must possess CTE close to that of the substrate material to prevent delamination or racking due to CTE mismatch. Thirdly, the coating must maintain a stable

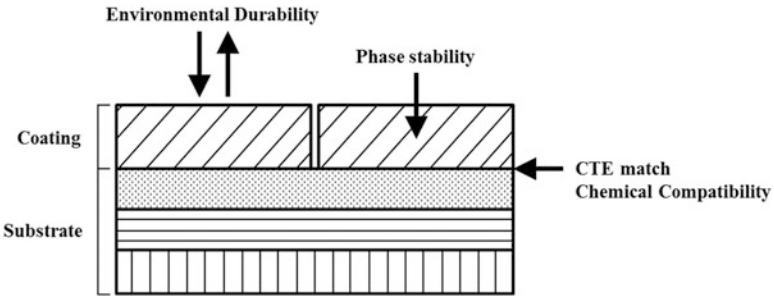

Fig. 1.12 Key issues in selecting coating materials for EBCs

phase under thermal exposure. Phase transformation typically accompanies a volumetric change, disrupting the integrity of the coating. Fourthly, the coating must be chemically compatible with the substrate to avoid detrimental chemical interaction [138]. Early coatings work focused on protecting Si-based ceramics from molten salt corrosion. Mullite has attracted interest as a coating for Si-based ceramics mainly because of its close CTE match with SiC.

1.3.2 Development of EBC

The first generation water vapor-resistant EBC was developed by combining the crystalline mullite coating with an Y_2O_3-stabilized ZrO_2 (YSZ, ZrO_2–8 wt.% Y_2O_3) top coat [139, 140]. In the first generation EBC, the mullite bond coat provided adherence, while the YSZ top coat provided protection from water vapor. The relatively high silica activity in mullite and the resulting selective volatilization of silica cause rapid recession of mullite in water vapor, necessitating the top coat for a water vapor resistant. YSZ was a logical candidate for the top coat because it had been successfully used as the TBC for metallic components in gas turbine engines, indicating its durability in water vapor. The first generation EBC could provide protection from water vapor for several 100 h at 1300°C. In longer exposures, however, water vapor eventually penetrated through cracks in the EBC and attacked the Si-based substrate, leading to coating delamination [141].

The second generation EBC, with substantially improved performance compared with the first generation EBC, was developed in the NASA High Speed Research–Enabling Propulsion Materials (HSR-EPM) program in joint research by NASA, General Electric, and Pratt and Whitney [142]. The new EBC consists of three layers: a silicon bond coat, a mullite or a mullite + BSAS ($(1–x)$ $BaO{\cdot}xSrO{\cdot}Al_2O_3{\cdot}2SiO_2$, $0 \leq x \leq 1$) intermediate coat, and a BSAS top coat [143]. The second generation EBC has some durability issues that limit their use temperature and lifetime performance. One key issue is the volatilization of the BSAS top coat in high velocity combustion environments. A projection based on a silica volatility model in conjunction with BSAS volatility data from high steam

low velocity environments indicates a BSAS recession of 70 μm after 1000 h at 1400 °C, 6 atm total pressure, and 24 m/s gas velocity [141]. Actual gas turbines operate at significantly higher pressures and gas velocities, increasing the projected recession to much higher levels. In fact the EBC on solar turbine engines suffered significant BSAS recession in some areas after the 14,000 h test [144]. Another key durability issue is the chemical reaction between BSAS and SiO_2 formed on the Si bond coat by oxidation. The reaction between BSAS and SiO_2 generates a low-melting (1300 °C) glass that causes EBC degradation and premature failure at temperatures above 1300 °C [141]. Therefore, under the gas turbines working environments, the corrosion resistance in water vapor of the top coat becomes particularly important.

Owing to the existed deficiencies of the second generation EBC, hence the NASA research center concentrated on a new top coat that can be substituted for the BSAS. Research has been undertaken at the NASA Glenn Research Center under the support of the Ultra Efficient Engine Technology (UEET) program to develop EBCs that can withstand a 1482 °C (2700 °F) surface temperature and sustain 1316 °C (2400 °F) EBC/substrate temperature over thousands of hours. Figure 1.13 shows plasma-sprayed Si/mullite +20 wt.% BSAS/BSAS on SiC/SiC composite after 1000 h at 1316 °C (1 h cycles) in 90% H_2O-balance O_2 [138]. The purpose of the third-generation EBC was substituted for original BSAS, showing a multilayer system. It has the key attributes for a successful EBC, such as a low silica activity, a low CTE, and a low modulus (~100 GPa for dense BSAS). The low silica activity provides stability in water vapor, while the low CTE and low modulus provide low thermal stresses. The EPM (Enabling Propulsions Materials) EBCs exhibit dramatically improved durability compared to the mullite/YSZ EBC [145]. The EBC maintains excellent adherence and crack resistance. New coating system preserves favorable thermal stability at 1500 °C which have been required. In addition, which have remarkable chemical and mechanical with the mullite/mullite + BSAS inter-layer.

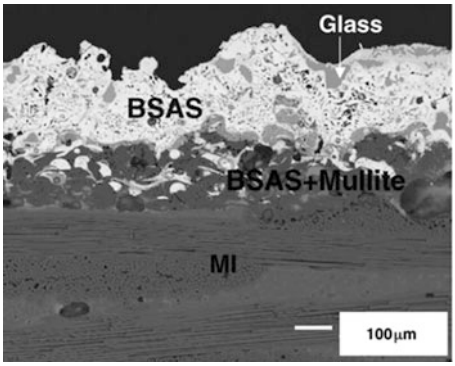

Fig. 1.13 Plasma-sprayed Si/mullite +20 wt.% BSAS/BSAS on a SiC/SiC composite coupon after 1000 h at 1316 °C (1-h cycles) in 90% H_2O-balance O_2 [138]

1.3.3 EBC Materials

Plasma-sprayed RE_2SiO_5 [146] and Ta_2O_5-based [147] EBCs showed good adherence on Si-based ceramics under thermal exposures in air. However, these coatings on SiC/SiC composite did not maintain the adherence in water vapor environments [148]. Consequently, the substrate suffered rapid oxidation, forming thick and porous scale. A premature EBC spallation occurred along the scale since the thick scale constituted a weak mechanical link. Possible explanations for the rapid oxidation include lack of chemical bonding and EBC cracking under thermal cycling. Both can provide an easy access for water vapor into the interface. Although mullite develops similar cracks, the fact that the Si/mullite EBC shows far superior oxidation resistance and longer lifetime performance suggests that inadequate chemical bonding may be responsible for the lack of oxidation resistance. Other low CTE rare earth monosilicates, such as Y_2SiO_5, Er_2SiO_5, Sc_2SiO_5, and Lu_2SiO_5, exhibited similar poor oxidation resistance [138]. CVD Ta_2O_5 was unstable in an environment containing Na_2SO_4, rapidly reacting to form $NaTaO_3$ which subsequently interacted destructively with the underlying Si_3N_4 substrate to form a molten phase [134]. Rare earth disilicates ($RE_2Si_2O_7$) were applied on Si_3N_4 ceramics by a slurry process followed by sintering [148]. Short-term exposures at relatively low temperatures showed promising results, indicating their merits for further research.

Acknowledgments This work was supported by a National Research Foundation of Korea (NRF) grant funded by the Korean Government (2011–0030058), by the Ministry of Science, ICT and Future Planning (234-4413.C), by the Power Generation & Electricity Delivery of the Korea Institute of Energy Technology Evaluation and Planning (KETEP) grants funded by the Korean Government Ministry of Trade, Industry and Energy (2013-101010-170C), and by the United States Department of Energy (Grant No. DE-FE0008868, program manager: Richard Dunst).

References

1. Y.J. Zhao, J. Adv, Mater. Industry **8**, 55–62 (2006)
2. J.F. Wu, J. Chin. Ceram. Industry (2011)
3. C. Watanabe, Res. Policy **28**(7), 719–749 (1999)
4. C. Bayona-Saez, T. Gatcia-Marco, Res. Policy **39**(10), 1375–1386 (2010)
5. A.M. Li, J. Cerm. Eng. **5**, 44–47 (1999)
6. Introduction to Gas Turbines for Non-Engineers (Published in the Global Gas Turbine News, 37, 1997)
7. Rolls-Royce plc, The Jet Engine, 4th, (Derby, UK: The Technical Publications Department, Rolls-Royce plc, 1992)
8. N.P. Padture, M. Gell, E.H. Jordan, Science **296**(5566), 280–284 (2002)
9. M.-P. Bacos, J.-M. Dorvaux, S. Landais, O. Lavigne, R. Mévrel, M. Poulain, C. Rio, M.-H. Vidal-Sétif, J. Aero, Laboratory **3**, 1–14 (2011)
10. D.R. Clarke, M. Oechsner, N.P. Padture, MRS Bull. **37**, 891–897 (2012)
11. X.L. Jiang, C.B. Liu, F. Lin, J. Mater. Sci. Technol. **23**(4), 449–456 (2007)

12. S.A. Tsipasand, I.O. Golosnoy, J. Eur, Ceram. Soc. **31**(15), 2923–2929 (2011)
13. M. Madhwal, E.H. Jordan, M. Gell, Mater. Sci. and Eng. A. **384**(1), 151–161 (2004)
14. Y.N. Wu, P.L. Ke, Q.M. Wang, et al., Corros. Sci. **46**(12), 2925–2935 (2004)
15. Y. Itoh, M. Saitoh, M. Tamura, J. Eng. Gas Turbine Power **122**, 43–49 (2000)
16. Y.N. Wu, G. Zhang, Z.C. Feng, et al., Surf. Coat. Technol. **136**, 56–60 (2001)
17. N.P. Padture, K.W. Schlichting, T. Bhatia, et al., Acta Mater. **49**, 2251–2257 (2001)
18. D.R. Clarke, C.G. Levi, Annu. Rev. Mater. Res. **33**, 383–417 (2003)
19. D.R. Clarke, S.R. Phillport, Mater. Today **8**, 22–29 (2005)
20. Y. Li, C.J. Li, G.J. Yang, et al., Surf. Coat. Technol. **205**(7), 2225–2233 (2010)
21. J.A. Haynes, M.K. Ferber, W.D. Porter, Mater. High Temp. **16**, 49–69 (1999)
22. N.J. Simms, P.J. Kilgallon, C. Roach, et al., Mater. High Temp. **20**, 519–526 (2003)
23. A. Peichl, T. Beck, O. Vöhringer, Surf. Coat. Technol. **162**, 113–118 (2003)
24. S.J. Bull, R.I. Davidson, E.H. Fisher, et al., Surf. Coat. Technol. **130**, 257–265 (2000)
25. X.Q. Ma, M. Takemoto, Mater. Sci. Eng. A **308**, 101–110 (2001)
26. B.K. Pant, V. Arya, B.S. Mann, J. Therm, Spray Technol. **16**, 275–280 (2007)
27. K.W. Schlichting, N.P. Padture, E.H. Jordan, et al., J. Therm. Spray Technol. **342**, 120–130 (2003)
28. A. Rabiei, A.G. Evans, Acta Mater. **48**, 3963–3976 (2000)
29. A. Feuerstein, J. Knapp, T. Taylor, et al., J. Therm. Spray Technol. **17**, 199–213 (2008)
30. K. Richardt, K. Bobzin, D. Sporer, et al., J. Therm. Spray Technol. **17**, 612–616 (2008)
31. X.Q. Cao, R. Vassen, D. Stoeverb, J. Eur. Ceram. Soc. **24**, 1–10 (2004)
32. R. Dutton, R. Wheeler, K.S. Ravichandran, et al., J. Therm. Spray Technol. **9**, 204–209 (2000)
33. T. Bhatia, A. Ozturk, L. Xie, et al., J. Mater. Res. **17**, 2363–2372 (2002)
34. A.D. Jadhav, N.P. Padture, F. Wu, et al., Mater. Sci. and Eng. A. **405**, 313–320 (2005)
35. T.A. Taylor, D.L. Appleby, A.E. Weatherill, et al., Surf. Coat. Technol. **43–44**, 470–480 (1990)
36. Y.H. Sohn, E.Y. Lee, B.A. Nagaraj, et al., Surf. Coat. Technol. **146–147**, 132–139 (2001)
37. R.A. Miller, J. Therm, Spray Technol. **6**, 35–42 (1997)
38. S. Bose, J. DeMasi-Marcin, J. Therm, Spray Technol. **6**, 99–104 (1997)
39. R.A. Miler, Surf. Coat. Technol. **30–1**, 1–11 (1987)
40. G.W. Goward, Surf. Coat. Technol. **108–119**, 73–79 (1998)
41. F. Cernushci, P. Bianchi, M. Leoni, P. Scardi, J. Therm. Spray Technol. **8**(1), 102–109 (1999)
42. S. Rangaraj, K. Kokini, Surf. Coat. Technol. **20**(4), 201–212 (2003)
43. R. Taylor, J.R. Brandon, P. Morrel, Surf. Coat. Technol. **50**, 141–149 (1992)
44. D.R. Clarke, Surf. Coat. Technol. **163**, 67–74 (2003)
45. J. Gupta, G. Singh, L. Divan, et al., Adv. Sci. Focus. **2**(2), 159–164 (2014)
46. A.M. Limarga, S. Shian, R.M. Leckie, J. Eur. Ceram. Soc. **34**(12), 2085–3094 (2014)
47. M. Han, G. Zhou, J. Huang, et al., Surf. Coat. Technol. **240**, 320–326 (2014)
48. F. Cernuschi, P. Bianchi, M. Leoni, et al., J. Therm. Spray Technol. **8**(1), 102–109 (1999)
49. X. Zhou, Z. Xu, X. Fan, et al., Mater. Lett. **134**, 146–148 (2014)
50. R. Vaßen, M.O. Jarligo, T. Steinke, Surf. Coat. Technol. **205**(4), 938–942 (2010)
51. S. Das, S. Datta, D. Basu, Ceram. Int. **35**(4), 1403–1406 (2009)
52. W. Ma, H. Dong, H. Guo, et al., Surf. Coat. Technol. **204**(21), 3366–3370 (2010)
53. H.G. Scott, J. Mater. Sci. **10**(9), 1527–1535 (1975)
54. J.R. Nicholls et al., Surf. Coat. Technol. **151**, 383–391 (2002)
55. M. Peters, U. Schulz, in *Proc. First CEAS European Air and Space Conference Deutscher Luft- und Raumfahrtkongress*, (2017), pp. 1–9
56. C.R.C. Lima, R. da Exalltacao Trevisan, J. Therm, Spray Technol. **8**(2), 323–327 (1999)
57. M. Tamura, M. Takahashi, J. Ishii, et al., J. Therm. Spray Technol. **8**(1), 68–72 (1999)
58. C. Viazzi, J.P. Bonino, F. Ansart, A. Barnabé, J. Alloys Compd. **452**, 377–383 (2008)
59. J.S. Wallace, J. Ilavsky, J. Therm. Spray Technol. **7**(4), 521–526 (1999)

60. P. Ramaswamy, S. Seetharamu, K.B.R. Varma, J. Therm. Spray Technol. **7**(4), 497–504 (1999)
61. E.A.G. Shillington, D.R. Clarke, Acta Mater. **47**(4), 1297–1305 (1999)
62. B.A. Pint, I.G. Wright, W.Y. Lee, et al., Mater. Sci. and Eng. A. **254**(2), 201–211 (1998)
63. D. Mercier, B.D. Gauntt, M. Brochu, Surf. Coat. Technol. **205**(17), 4162–4168 (2011)
64. P.F. Zhao, X.D. Li, F.L. Shang, et al., Mater. Sci. Eng. A **528**(25), 7641–7647 (2011)
65. Y. Li, C.J. Li, Q. Zhang, et al., J. Therm. Spray Technol. **19**(1–2), 168–177 (2010)
66. J. Benoista, K.F. Badawi, A. Malie, et al., Surf. Coat. Technol. **182**(1), 14–23 (2004)
67. H.M. Tawancy, N.M. Abbas, A. Bennett, Surf. Coat. Technol. **68**, 10–16 (1994)
68. M. Li, X. Sun, W. Hu, H. Guan, Surf. Coat. Technol. **201**(16), 7387–7391 (2007)
69. H.J. Rätzer-Scheibe, U. Schulz, T. Krell, Surf. Coat. Technol. **200**, 5636–5644 (2006)
70. D.B. Lee, J.H. Ko, J.H. Yi, J. Therm, Spray Technol. **14**(3), 315–320 (2005)
71. B. Gleeson, J. Propul, Power **22**, 375–383 (2006)
72. U. Täck, Ph.D. Thesis, Tech. Univ. Freiberg, 2004, p. 25, p. 151, p. 169
73. W. Beele, N. Czech, W.J. Quadakkers, W. Stamm, Surf. Coat. Technol. **94–95**, 41–45 (1997)
74. N. Czech, F. Schmitz, W. Stamm, Surf. Coat. Technol. **68**, 17–21 (1994)
75. P. Fox, G.J. Tatlock, Mater. Sci. Technol. **5**(8), 816–827 (1989)
76. H.M. Tawancy, L.M. Al-Hadhrami, Turbo Expo (2010)
77. D. Renusch, M. Schütze, Surf. Coat. Technol. **202**(4), 740–744 (2007)
78. R. Sivakumar, B.L. Mordike, Surf. Coat. Technol. **37**(2), 139–160 (1989)
79. M.J. Pomeroy, Mater. Des. **26**(3), 223–231 (2005)
80. H. Echsler, D. Renusch, M. Schütze, Mater. Sci. Eng. **20**(3), 307–318 (2004)
81. W.R. Chen, X. Wu, B.R. Marple, P.C. Patnaik, Surf. Coat. Technol. **201**(3), 1074–1079 (2006)
82. J. Zhang, V. Desai, Surf. Coat. Technol. **190**(1), 98–109 (2005)
83. W.R. Chen, X. Wu, B.R. Marple, et al., Surf. Coat. Technol. **202**(16), 3787–3796 (2008)
84. S. Sridharan, L. Xie, E.H. Jordan, et al., Mater. Sci. Eng. A **393**(1), 51–62 (2005)
85. T. Tomimatsu, S. Zhu, Y. Kagawa, Acta Mater. **51**(8), 2397–2405 (2003)
86. K.M. Carling, E.A. Carter, Acta Mater. **55**(8), 2791–2803 (2007)
87. U. Schulz, M. Menzebach, C. Leyens, Y.Q. Yang, Surf. Coat. Technol. **146**, 117–123 (2001)
88. A. Weisenburger, G. Rizzi, A. Scrivani, Surf. Coat. Technol. **202**(4), 704–708 (2007)
89. Y. Zhao, A. Shinmi, X. Zhao, et al., Surf. Coat. Technol. **206**(23), 4922–4929 (2012)
90. G. Mauer, M.O. Jarligo, D.E. Mack, R. Vaßen, J. Therm. Spray Technol. **22**(5), 646–658 (2013)
91. Y. Zhang, D.E. Mack, M.O. Jarligo, J. Therm. Spray Technol. **18**(4), 694–701 (2009)
92. S. Paulussen, R. Rego, O. Goossens, et al., Surf. Coat. Technol. **200**(1), 672–675 (2005)
93. F. Leroux, C. Campagne, A. Perwuelz, L. Gengembre, Appl. Surf. Sci. **254**(13), 3902–3908 (2008)
94. S. Kuroda, J. Kawakita, M. Watanabe, H. Katanoda, Sci. Technol. Adv. Mater. **9**, 1–17 (2008)
95. P. Scardi, M. Leoni, L. Bertini, L. Bertamini, Surf. Coat. Technol. **94**, 82–88 (1997)
96. E. Lugscheider, K. Bobzin, S. Bärwulf, A. Etzkorn, Surf. Coat. Technol. **138**(1), 9–13 (2001)
97. U. Schulz, J. Amer. Cer. Soc. **83**(4), 904–910 (2000)
98. B. Saruhan, P. Francois, K. Fritscher, U. Schulz, Surf. Coat. Technol. **182**(2), 175–183 (2004)
99. D.E. Wolfe, J. Singh, R.A. Miller, et al., Surf. Coat. Technol. **190**(1), 132–149 (2005)
100. S.M. Meier, D.M. Nissley, K.D. Sheffler, T.A. Cruse, J. Eng. Gas Turbines Power **114**(2), 258–263 (1992)
101. J. Singh, D.E. Wolfe, J. Mater. Sci. **40**(1), 1–26 (2005)
102. G. Wahl, W. Nemetz, M. Giannozzi, et al., J. Eng. Gas Turbines Power **123**(3), 520–524 (2001)
103. W.R. Chen, X. Wu, B.R. Marple, et al., Surf. Coat. Technol. **202**(12), 2677–2683 (2008)
104. P. Richer, M. Yandouzi, L. Beauvais, B. Jodoin, Surf. Coat. Technol. **204**, 3962–3974 (2010)
105. C.R.C. Lima, J. Nin, J.M. Guilemany, Surf. Coat. Technol. **200**, 5963–5972 (2006)

106. F.H. Yuan, Z.X. Chen, Z.W. Huang, et al., Corros. Sci. **50**(6), 1608–1617 (2008)
107. A.C. Karaoglanli, E. Altuncu, I. Ozdemir, et al., Surf. Coat. Technol. **205**, 369–373 (2011)
108. J.Y. Kwon, J.H. Lee, H.C. Kim, et al., Mater. Sci. Eng. A **429**(1), 173–180 (2006)
109. Y. Itoh, M. Saitoh, M. Tamura, J. Eng. Gas Turbines Power **122**, 43–49 (2000)
110. J. Pina, A. Dias, J.L. Lebrun, Mater. Sci. Eng. A **347**(1), 21–31 (2003)
111. K. Ogawa, K. Ito, T. Shoji, et al., J. Therm. Spray Technol. **15**(4), 640–651 (2006)
112. M. Tanno, K. Ogawa, T. Shoji, Surf. Coat. Technol. **204**(15), 2504–2509 (2010)
113. D. Seo, K. Ogawa, Y. Nakao, et al., Surf. Coat. Technol. **203**(14), 1979–1983 (2009)
114. R.G. Wellman, A. Scrivani, G. Rizzi, et al., Surf. Coat. Technol. **202**(4), 709–713 (2007)
115. L. Ajdelsztajn, B. Jodoin, J.M. Schoenung, Surf. Coat. Technol. **201**, 1166–1172 (2006)
116. T.H. Van Steenkiste, J.R. Smith, R.E. Teets, Surf. Coat. Technol. **154**, 237–252 (2002)
117. S. Saeidi, K.T. Voisey, D.G. McCartney, J. Therm. Spray Technol. **18**(2), 209–216 (2009)
118. Q. Zhang, C.-J. Li, C.-X. Li, et al., Surf. Coat. Technol. **202**(14), 3378–3384 (2008)
119. D.M. Zhu, R.A. Miller, Int. J. Am. Ceram. Technol. **1**, 86–94 (2004)
120. R. Gadow, M. Lischka, Surf. Coat. Technol. **151**, 392–399 (2002)
121. R. Gadow, G. W. Schäfer, Patent 99-EP982 9942630, WO (1999)
122. G. Pracht, R. Vassen, D. Stöver, Ger. Pat. App. **10**(11), 225 (2005)
123. G.W. Schäfer, R. Gadow, Ceram. Eng. Sci. Proc. **20**(4), 291–297 (1999)
124. C.J. Friedrich, R. Gadow, M.H. Lischka, Ceram. Eng. Sci. Proc. **22**(4), 375 (2001)
125. C. Friedrich, R. Gadow, T. Schirmer, J. Therm. Spray Technol. **10**, 592 (2001)
126. R. Gadow, M. Lischka, Surf. Coat. Technol. **151**, 392 (2002)
127. S. Sodeoka, M. Suzuki, T. Inoue, K. Ueno, and S. Oki, ASM Inter. (1996), pp. 295–302
128. J.W. Holmes and B.H. Pilsner, ASM Inter. (1987), pp. 259–270
129. G.N. Heintze, R. McPherson, ASM Inter. (1987), pp. 271–275
130. H.K. Kim, H.S. Choi, C.H. Lee, Proc. Un. Therm. Spray Conf., 740–746 (1999)
131. J. Thornton, A. Majumdar, G. McAdam, Surf. Coat. Technol. **94**(/95), 112–117 (1997)
132. A. Rouanet et al., Thermal Spraying-Current Status and Future Trends **1**, 507–512 (1995)
133. K.N. Lee, H. Fritze, Y. Ogura, ASME PRESS (2003), pp. 641–664
134. N.S. Jacobson, J. Am. Ceram. Soc. **76**(1), 3–28 (1993)
135. W.J. Lackey, D.P. Stinton, G.A. Cerny, A.C. Schaffhauser, L.L. Fehrenbacher, Adv. Ceram. Mater. **2**(1), 24–30 (1987)
136. D.W. Graham, D.P. Stinton, in *Proc. Coat. Adv. Heat Eng. Workshop. IV65-IV71* (1992)
137. K.N. Lee, R.A. Miller, D. Surf. Coat. Technol. **86**(/87), 142–148 (1996)
138. K.N. Lee, D.S. Fox, N.P. Bansal, J. Eur. Ceram. Soc. **25**(10), 1705–1715 (2005)
139. K.N. Lee, Sur. Coat, Technol. **133**, 1–7 (2000)
140. K.N. Lee, R.A. Miller, N.S. Jacobson, J. Am. Ceram. Soc. **78**(3), 705–710 (1995)
141. K.N. Lee et al., J. Am. Ceram. Soc. **86**(8), 1299–1306 (2003)
142. K.N. Lee, Surf. Coat. Technol. **1–7**, 133–134 (2000)
143. K.N. Lee, Trans. ASME. **122**, 632–636 (2000)
144. K.L. More, P.F. Tortorelli, L.R. Walker, J.B. Kimmel, N. Miriyala, J.R. Price, et al., ASME. **4**, 155–162 (2002)
145. Y. Tamarin, *ASM Inter.* (2002)
146. K.N. Lee, Unpublished Research, NASA Glenn Research Center
147. C.M. Weyant, K.T. Faber, J.D. Almer, J.V. Guibeen, J. Am. Ceram. Soc. **88**(8), 2169–2176 (2005)
148. T. Ohji, H. Klemm, M. Fritsch, et al., in *The 28th Int. Conf. & Exp. On Adv. Ceram. & Comp.,* FL (2004)

Chapter 2
Processing and Characterization of Coating and Thin Film Materials

David Alique

2.1 Introduction

Coatings and thin film materials are employed in many different industrial fields for decades, mainly for protective purposes. This large experience provokes that, currently, a wide variety of technologies for both preparation and characterization are available. Particularly, focusing on energy and environmental applications, three main film types can be distinguished: (1) materials with catalytic activity for hydrogen production, (2) membranes for hydrogen separation or CO_2 capture, and (3) coatings for some specific fuel cell components. Membranes are especially relevant for hydrogen separation from other gases after the production unit or combining both production and separation steps in a unique equipment, the membrane reactor. The last case represents a significant advance in terms of process intensification, increasing the hydrogen production rate with a high purity and saving costs. In the last years, the relevance of these membrane materials has significantly increased, as can be denoted by the large number of published manuscripts in indexed scientific journals of high impact. In this context, this chapter summarizes the main advances in thin film membranes towards energy and environmental applications, including both preparation strategies and the most common characterization techniques. The production of all these thin films, independently of the particular application, can be carried out by different physical-chemical alternatives such as Sol–Gel methods, Electrodeposition, Electroless Plating, Physical Vapor Deposition, Chemical Vapor Deposition, Atomic Layer Deposition, or Molecular Beam Epitaxy, achieving thicknesses ranged from the nanometer scale

D. Alique (✉)
Department of Chemical and Energy Technology, Rey Juan Carlos University,
C/Tulipán s/n, 28933 Móstoles, Madrid, Spain
e-mail: david.alique@urjc.es

J. Zhang, Y.-G. Jung (eds.), *Advanced Ceramic and Metallic Coating and Thin Film Materials for Energy and Environmental Applications*,
DOI 10.1007/978-3-319-59906-9_2

to some microns. Each technique presents advantages and disadvantages that have to be taken into account for final applications. Moreover, the structure of the film should also be considered, being possible to distinguish amorphous or crystalline materials. All these films, independently of the composition, structure, or production technique, are usually prepared over a substrate material. Thus, the original coating surface properties can affect in a significant grade to the final properties of the film and many researchers focus their efforts on studying these effects and developing new strategies to improve the final quality of films in terms of homogeneity, thickness reduction, thermal and mechanical resistance, and adherence.

Considering all these facts, this chapter is structured in three differentiated sections: (1) Common coating surface materials and main modifications to make the later incorporation of the thin film easer, including chemical or mechanical treatments and incorporation of intermediate layers; (2) Recent advances for preparation of thin films employed as hydrogen-selective membranes; and (3) The most relevant characterization techniques for determining critical properties of these films and developing innovative products.

2.2 Coating Surface and Interface Modifications

Thin film materials for energy applications are usually incorporated onto a support surface to provide specific properties in terms of protection, catalytic activity, or selectivity to a target compound [1]. Only few applications employ directly unsupported thin films with an enough thickness to ensure both thermal and mechanical resistances under operation conditions. An example of these unsupported materials can be found at ENEA laboratories for hydrogen purification [2] and separation of isotopes from nuclear fusion processes [3]. In particular, palladium-based films with thicknesses in the range 50–200 μm are used for these purposes [4, 5].

However, researchers prefer to incorporate a thin film onto a porous substrate in order to decrease the minimum thickness required, saving money but maintaining good properties and mechanical resistance of the system [6, 7]. A wide variety of materials have been proposed as support for the preparation of these composite materials, including Vycor glass [8], metals [9, 10], or ceramics [11, 12]. The selection of an appropriate substrate is crucial, although up to now an ideal solution is not found. Diverse surface characteristics, such as material compatibility, adhesion, mechanical strength, roughness, or porosity need to be considered prior to taking a decision. In fact, metallic supports present an exceptional mechanical resistance that makes the integration in current facilities, usually made in stainless steel, easier. However, they also present a very rough surface with a large pore distribution, which makes the generation of an ultrathin layer without defects really difficult [13]. On the other hand, ceramic supports present a very smooth surface with a narrow pore size distribution that could overcome this problem [14]. Unfortunately, these supports

present a lower mechanical resistance than metallic ones and the thermal expansion coefficient can be significantly different from that of metallic coatings, i.e., palladium or alloys. This fact could represent a relevant inconvenience for an adequate lifespan of the composite membranes [15].

In this context, it is usual to find materials in which the original interface between the support and the thin film has been modified in order to overcome some of these drawbacks, trying to take advantage of other original features [16–18]. Diverse alternatives can be carried out, including chemical or mechanical treatments and incorporation of additional intermediate layers.

2.2.1 Chemical Treatments

The use of chemicals can provoke the modification of original coating surfaces. This technique, very often for modification of polymeric layers, can also be employed for inorganic materials such as metals or ceramics. The treatment is usually known as etching, and it consists of immersing the sample into a corrosive solution, traditionally a strong acid, at controlled temperature to remove part of the material. The effect of the treatment is determined by different factors, emphasizing acid concentration, support composition, temperature, and duration of the process. Mardilovich et al. [19] indicated a double effect of 5 min treating stainless steel surface in hydrochloric acid, increasing the original roughness of the support and providing a preactivated surface for a later deposition. Li et al. [20] used a similar etching treatment at room temperature but with a mixture of hydrochloric and nitric acids. Later, Kim et al. [21] followed this procedure to prepare a composite Pd membrane over a porous nickel support.

In general, it can be affirmed that actually an etching pretreatment on the support is a conventional step in commercial processes for incorporating thin layers on composite materials, independently of using any additional treatment for surface modification [22].

2.2.2 Mechanical Treatments

Other researchers employ physical treatments to modify the original properties of support materials, mainly with the aim of decreasing both pore size and external roughness. Jemaa et al. [23] modified the porous stainless steel surface by high velocity shot peening with ion particles, producing rounded depressions in the surface, stretching it radially and causing plastic flow of surface metal at the instant of contact. As a result, they obtained a smaller average pore size over the modified surface. Jayaraman et al. [24] prepared the supports for a later Pd film incorporation by successive polishing with sandpapers #320, #500, and #800 to smooth the original surface. Mardilovich et al. [19] used a similar mechanical polishing process

with sandpaper over porous stainless steel supports, decreasing both average pore size diameter and roughness. However, a significant porosity loss was evidenced by decreasing the permeation capacity up to 20% of the original one. Li et al. [20] polished the surface of a stainless steel disc using commercial sandpapers with increasing grits step by step, finishing with a #1200 grit sandpaper for about 1 min. Ryi et al. [25] employed similar mechanical polishing treatments over a porous nickel support by using commercial sandpapers followed by wet polishing with alumina powder. The results evidenced a reduction in both roughness and average pore size of the original material, facilitating the later incorporation of a thin selective coating. Pinacci et al. [26] used a similar procedure to reduce the original roughness of stainless steel supports. They modified the materials in a polishing machine with a diamond paste for 8 h, reducing the original roughness from 3.4 to 0.65 μm. Alique [27] presented a complete study of the morphology modification achieved on porous stainless steel supports (PSS) by using commercial silica carbide sandpapers with diverse grits. Figure 2.1 collects the images of the external surface after each treatment. As it can be seen, rougher sandpapers provoke the generation of large defects and grooves due to a plastic deformation of the original material. Moreover, the size of the original small pores is reduced, even disappearing in some samples, while the biggest ones are maintained. In contrast, smoother sandpapers have a finer effect.

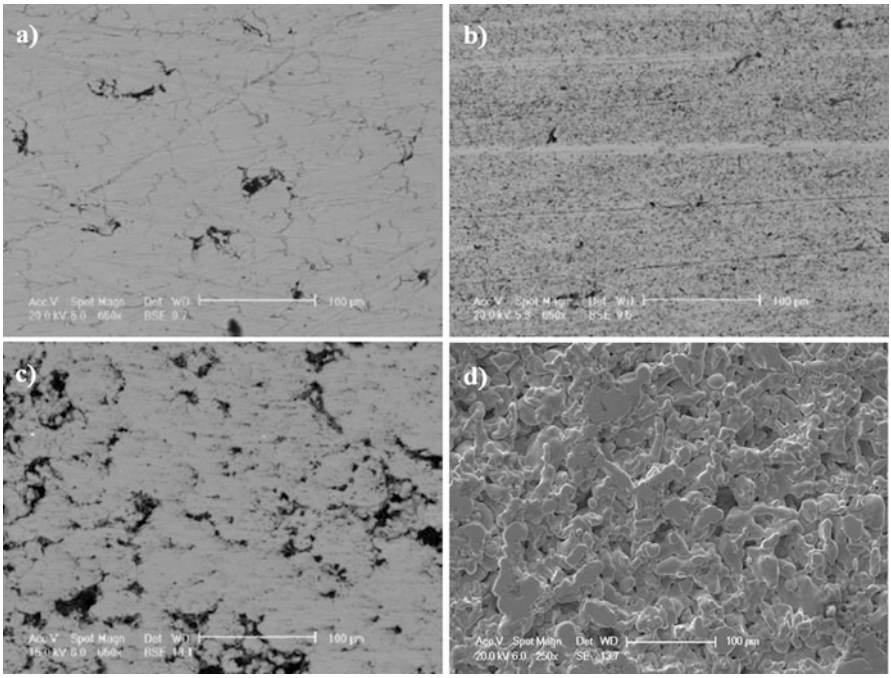

Fig. 2.1 SEM images of PSS supports after polishing with commercial sandpapers: (**a**) #100, (**b**) #400, (**c**) #800, and (**d**) #1200

The polishing technique not only has been proposed for modifying the surface properties of supports. The reparation of palladium thin films in composite membranes can also be carried out by mechanical treatments, drastically decreasing the remained pinholes on the selective palladium layer [28].

On the contrary, this technique also has detractors due to the negative effect on the permeation capability of the materials. Moreover, several studies also affirm that very smooth surfaces may cause poor adhesion and poor physical strength of the composite membrane, which spoils the long-term stability during temperature and pressure cycling [29]. It is accepted that, in general, the adhesion between a thin film and a support surface depends on the mechanical binding and anchoring effects, thus a minimum roughness of the support it is necessary for a suitable adhesion of the incorporated coatings [30]. Diverse works, as published by Collins and Way [31] and Huang et al. [32], indicate that larger pore sizes and surface roughness of supports results in better adhesion of the thin coating layer. In this manner, it is necessary to achieve a compromise solution between smoothing the original surface and decreasing the average pore size of supports and maintaining minimum values to guarantee a suitable adherence for the incorporated thin film.

2.2.3 Incorporation of Additional Intermediate Layer

The incorporation of additional intermediate layers is one of the most popular alternatives for preparing free-defect thin films on porous supports. Material, thickness, and properties of this interlayer can be adjusted for different purposes, including modification of original morphology, improvement of adhesion capacity, prevention of corrosion, surface pre-activation, or impediment of direct contact between the support and the thin film. Usually, a unique intermediate layer can be employed simultaneously for some of these purposes. The prevention of possible interactions between both support and thin film, mainly in case of metallic materials, is especially relevant for high temperature applications. It is well known that interdiffusion processes appear when metals are maintained in contact at high temperatures, provoking a modification of their original properties [33]. In this manner, many researchers prefer to incorporate an interlayer between the support and the thin selective coating, independently of using any previous additional treatment (i.e., chemical treatment or polishing) to guarantee a suitable behavior of the final composite material. At this point, the selection of the material and thickness of this intermediate layer, as well as the preparation technique, are critical issues to obtain a system with enough mechanical strength and moderate cost [34].

As mentioned in previous sections, ceramic and metallic porous materials are widely used as support for different coatings on the field of environmental and energy applications. Ceramic supports usually are prepared with an asymmetric structure as stacked layers with graduated particle sizes, achieving a very smooth surface with very narrow pore size distribution up to 3 nm [35, 36]. In this case, the use of an intermediate layer is not essential in terms of roughness and pore size

modification and it is really scarce in literature. However, the preparation of asymmetric ceramic supports is relatively costly and the use of macroporous ceramic substrates with symmetric configuration and a very simple intermediate layer could represent an attractive alternative. In this context, Zheng et al. [37] modified a sol–gel method to incorporate an intermediate γ-Al_2O_3 layer over a macroporous α-Al_2O_3 support, showing superiority in smoothening out defects and bumps compared to conventional methods and improving both adhesion between layers and dispersal uniformity of small alumina particles. Over this modified supports, they incorporated a very thin palladium layer of about 4.5 μm without remarkable defects. Hu et al. [38] proposed the modification of a low-cost macroporous Al_2O_3 substrate surface with a conventional 2B pencil composed of graphite and clay, obtaining a free-defect membrane with an external palladium thin film of about 5 μm. Nevertheless, the incorporation of intermediate layers for improving the activation of the ceramic supports prior to incorporating the final thin coating is more usual. One example is the research published by Zhao et al. [39], based on the activation of a ceramic substrate by the sol–gel process of a Pd(II)-modified boehmite sol for the preparation of a composite Pd-membrane with a thickness of about 1 μm. A very particular application is the synthesis of pore-filled type membranes, in which YSZ particles are used to modify the original surface of ceramic supports in a double layer, helping to achieve a good adhesion and uniform coating of the membrane film onto the support and protecting the selective layer [40, 41]. More details about this alternative can be found in the next section, talking of advanced metallic and ceramic composite laminate coatings.

On the other hand, the use of additional intermediate layers is a widespread alternative when metallic supports are used for the incorporation of thin films. As mentioned before, the use of this type of supports for incorporating thin coatings, mainly those composed by other metals such as palladium or alloys, is very attractive due to the excellent mechanical resistance and the facility for integration in conventional equipments [9, 10]. However, the surface properties (high roughness and average pore size) and the migration of components at high temperatures (interdiffusion process), independently of the support grade, represent the main drawbacks that the use of additional intermediate layers tries to resolve [42]. At this point, a wide variety of materials can be found in the literature for obtaining these interlayers and a unique solution is not achieved up to now.

One of the easiest solutions consists of oxidizing the metallic support at high temperatures in air atmosphere in order to generate a mixed Fe_2O_3-Cr_2O_3 coating as effective interlayer to prevent the interdiffusion process [43]. Ma et al. [44] employed this controlled in situ oxidation method for preparing Pd and Pd/alloy porous stainless steel composite membranes. They found that oxidation temperatures higher than 600 °C generated oxide layers as effective barriers for avoiding the undesirable intermetallic diffusion. At lower oxidation temperatures, there might still be an oxide layer at the membrane-substrate interface, although it was too thin to be detected. This process was patented as an effective solution for preventing the intermetallic diffusion [45]. Following this patent, Guazzone et al. used oxidized supports in stagnant air at 400–500 °C to produce an oxide layer as

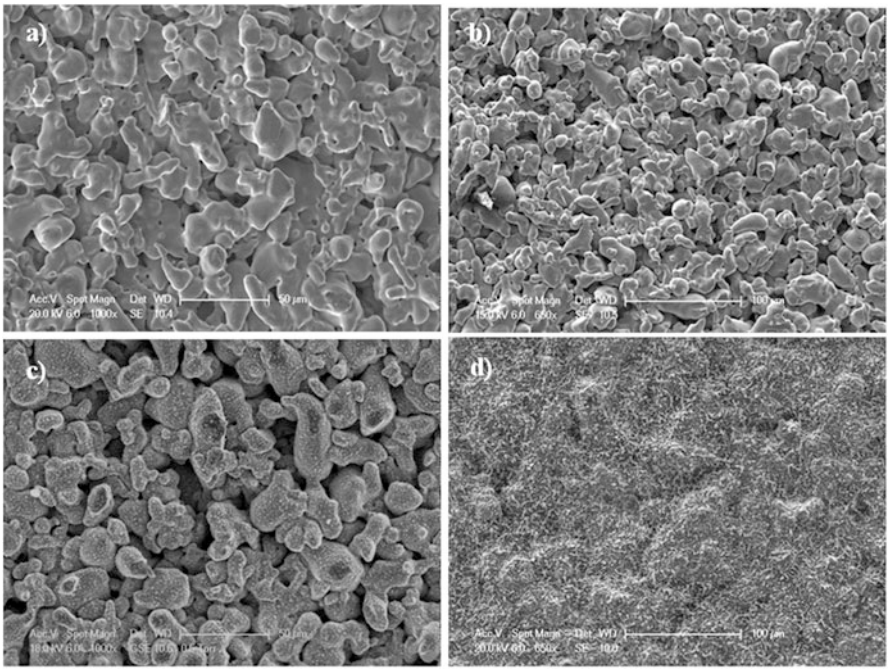

Fig. 2.2 SEM images of oxidized PSS supports at diverse temperatures: (**a**) 400 °C, (**b**) 500 °C, (**c**) 600 °C, and (**d**) 700 °C

intermetallic diffusion barrier for analyzing the effects of surface activity, defects and mass transfer on hydrogen permeance, and *n*-value in composite palladium-porous stainless steel membranes [46]. In the same line, Mateos-Pedrero et al. [47] carried out an oxidation treatment at diverse temperatures (600, 700, and 800 °C with heating ramp rate of 2 °C/min) in air atmosphere for 12 h, detecting a decrease in the permeate flux as the temperature increase. Moreover, they indicated that the achieved surface modifications after the treatments were not enough to significantly decrease the Pd coating thickness in comparison to other alternatives. As an example, Fig. 2.2 shows the results obtained after oxidizing commercial 0.2 μm grade PSS supports at different temperatures. In terms of surface properties (roughness and average external pore size), only slight modifications can be observed after the thermal treatments, except for higher temperatures. For this reason, despite the simplicity of this alternative, many authors choose other kind of materials as intermediate layer for achieving additional surface modifications.

Siliceous materials are the next group of intermediate layers that can be found in the specialized literature. They are considered an interesting alternative due to additional selectivity or catalytic activity in either amorphous or crystalline structures. In fact, microporous silica layers have been applied on porous stainless steel supports to separate H_2 from CO_2 or N_2 without any other additional layer [48] or even combined with palladium in a mixed-matrix structure [49]. As intermediate

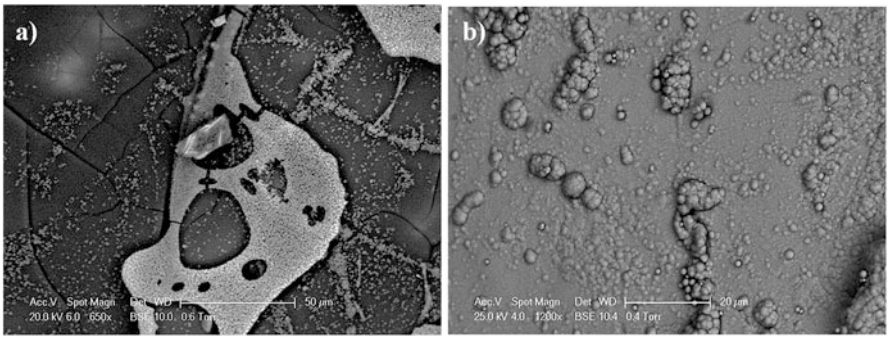

Fig. 2.3 SEM micrograph of silicalite-1 modified PSS support before (**a**) and after palladium deposition by electroless plating (**b**) [51]

layer, Nam et al. [50] introduced a thin film of silica by sol–gel method between a selective Pd-Cu layer and a 316L stainless steel substrate to improve the structural stability of the composite material. The membrane, with a 2 μm thickness for the selective layer, exhibited excellent separation performance with hydrogen permeance of $2.5 \cdot 10^{-2}$ $cm^3/cm^2 \cdot cmHg \cdot s$ and H_2/N_2 ideal separation factor up to 70,000 at 450 °C. Similar amorphous silica particles have also been employed by Mateos-Pedrero et al. [46], comparing the results obtained in terms of support modification and permeation capacity with other alternatives, such as direct oxidation of the substrate. Calles et al. [51] analyzed the influence of three different siliceous materials used as intermediate layers for composite Pd-PSS membranes: amorphous disordered silica, amorphous ordered silica (HMS), and crystalline silica (silicalite-1). In all cases, both roughness and pore size of the original supports were reduced, allowing to decrease the thickness of the H_2-selective Pd layer. Among these three diverse materials, silicalite-1 provided the best results with a completely defect-free Pd layer of 5 μm, permeance of $1.423 \cdot 10^{-4}$ $mol\ m^{-2}\ s^{-1}\ Pa^{-0.5}$, and a complete ideal selectivity for hydrogen. Figure 2.3 shows the changes on the morphology of the PSS support after modification with silicalite-1 as intermediate layer and palladium deposition.

One additional step is not only using these silica materials as intermediate layer but applying high temperature resistant silicate gel/ceramic particles for defect repairing of Pd composite membranes as a simply, effective and low-cost method [52].

Considering the relatively good properties of alumina materials as support in terms of roughness and porosity, the use of intermediate layers based on Al_2O_3 have also been proposed by several authors. Thus, Yepes et al. [25] compared the use of γ-Al_2O_3 and α-Fe_2O_3 oxides as diffusion barriers in composite PSS-Pd hydrogen permeable membranes. Moreover, presented the possibility of using an additional Pd doped thin alumina layer as activated surface. Li et al. [20] employed an alumina coating after other treatments for further smoothening the surface, decreasing the original pore size of the substrate and preventing interdiffusion processes at

elevated temperatures. Broglia et al. [53] incorporated a double layer of γ-Al_2O_3 on a PSS support by dip-coating, followed by drying and calcination, activation of the modified support, and deposition of crack-free Pd layer about 11 μm thick. Chi et al. [54] employed alumina particles of two different sizes to modify the nonuniform pore distribution and the surface roughness of the PSS tubes. Large particles (~10 μm) filled larger pores on the surface and left the smaller ones intact, while small particles (~1 μm) were then used to further decrease the surface roughness, achieving a continuous dense Pd membrane with a minimum thickness of 4.4 μm and good thermal stability. Lee et al. [55] compared the effect of Al_2O_3 and ZrO_2 materials as 200 nm thick intermediate layer for the preparation of a composite PdAu membrane over a porous nickel support. The selective metal incorporation was successful for both intermetallic diffusion barriers although the ZrO_2 interlayer provided 1.5 times higher permeate flux than that achieved by the Al_2O_3 material. Recently, Bottino et al. [56] have determined that the quality of alumina intermediate layers was related to the original surface characteristics of the supports, sol composition (aluminum and additive content), and viscosity of the gel.

Combining silicates and alumina materials is possible to obtain zeolites, with additional benefits on the control of pore structure for molecular sieve applications and catalytic activity. Mabande et al. [57] prepared, with good reproducibility, silicalite-1 and Al-ZSM-5 membranes by combining one-step in situ seeding with one secondary membrane growth step onto PSS substrates. In spite of not using these materials as intermediate layer, they observed comparable hydrogen permeation rates but higher perm-selectivities than obtained for silicalite-1 in case of using the zeolite Al-ZSM-5, despite the lower thickness of the layer. This fact indicates that the use of an adequate zeolite can provide significant advantages for gas separation applications. Bosko et al. [58] presented the synthesis of NaA zeolite by vacuum-assisted secondary growth for modifying the pore size of a PSS substrate and forming a diffusion barrier between the support and a 19 μm thick palladium film. The resulting Pd membrane showed high H_2/N_2 ideal selectivity in the entire working temperature range (400–450 °C). Recently, Dehghani Mobarake et al. [59] have proposed the use of NaX nanozeolites synthesized by microwave heating method for coating the PSS surface to prepare hydrogen-selective Pd-composite membranes. After optimizing diverse synthesis parameters, they have achieved a hydrogen permeation flux of 0.245 mol/m^2·s and ideal selectivity upper than 1,000. Similar works have also been carried out for incorporating zeolites as intermediate layer not only onto metallic supports but also in macroporous ceramic ones [60–62]. The particular properties of zeolites materials additionally can be used for creating a protective coating on the thin selective palladium layer, mainly when these membranes are employed in membrane reactors for hydrogenation or de-hydrogenation processes. Yu et al. [63] proposed the use of a hydroxysodalite, NaA, and Z-21 mixture for this purpose, while Sato et al. [64] employed an FAU-type zeolite and Abate et al. [65] worked with a TS-1 material. In all cases, an increased stability was observed and deactivation effects of the Pd layer by certain compounds were minimized. However, the permeation

properties of the composite material were modified due to the partial coverage of the metal surface with the zeolite material [65].

Many other researchers prefer to employ other types of metal oxides in order to guarantee a similar thermal expansion coefficient between each layer of the composite structure. In this context, the use of ceria (CeO_2), zirconia (ZrO_2), or yttria-stabilized zirconia (YSZ) are the predominant alternatives. Tong et al. [66] obtained a thin Pd layer with 13 μm in thickness on a macroporous stainless steel tube modified with CeO_2 with almost equal hydrogen permeability to the theoretical value for a pure Pd membrane. The stability of the composite was evidenced by the absence of changes after long-term experiments at diverse conditions in morphology, permeation behavior, and hydrogen selectivity. Qiao et al. [67] introduced successfully sol–gel-derived CeO_2 to prevent intermetallic diffusion between a Pd-Cu/PSS at temperatures in the range 300–400 °C and to enhance the affinity between both layers, support and membrane. Wang et al. [33] incorporated ZrO_2 particles inside the pores of a PSS support to make the preparation of a defect-free palladium film easy, achieving a metal thickness of ca. 10 μm by electroless plating. However, they found that hydrogen permeability for these composite membranes was partly governed by gas diffusion in the pores of intermediate layer. Gao et al. [68] modified PSS disks with a mesoporous palladium impregnated zirconia intermediate layer for preparing thin Pd-Cu membranes near 10 μm thick. This intermediate layer provided seeds for the Pd-Cu film growth and improved the membrane stability avoiding intermetallic diffusion processes and improving the adherence between layers. Lee et al. [55] employed a 200 nm thick ZrO_2 intermediate layer onto a porous nickel support for preparing a Pd-Au selective layer of ca. 3.5 μm, and the results evidenced a better permeation capacity than other membranes prepared with alumina as intermediate layer. Tarditi et al. [69] proposed a vacuum-assisted ZrO_2 incorporation on the top of porous stainless steel disks to enable the formation of defect-free Pd-Au films. In this manner, they obtained a 10 μm thick Pd-Au membrane that exhibits a hydrogen permeation flux of 0.14 $mol \cdot s^{-1} \cdot m^{-2}$ and ideal selectivity higher than 10,000 at 400 °C and 100 kPa. Ryi et al. [70] modified planar porous stainless steel supports with ZrO_2 in order to prepare thermally stable palladium composite membranes. Other researchers, such as Huang et al. [29] and Pacheco Tanaka et al. [40], decided to add small amounts of yttria to improve the intrinsic properties of zirconia material, using this yttria-stabilized zirconia (YSZ) as intermediate layer. Following these pioneer works, Zhang et al. [71] incorporated a sol–gel-derived mesoporous YSZ on PSS disks, forming a thin gastight Pd layer with highly stability in the temperature range of 500–600 °C. Sanz et al. [72] prepared a composite material formed by stacked layers of YSZ and palladium onto a stainless steel support and analyzed the permeation properties at different operating conditions for applying a rigorous mathematical model focused on the resistance contribution for each layer. The YSZ intermediate barrier with a thickness of ca. 50 μm was achieved by atmospheric plasma spraying and it let to obtain a completely defect-free 27.7 μm thick Pd film with a permeability of $1.1 \cdot 10^{-8}$ $mol \cdot s^{-1} \cdot m^{-1} \cdot Pa^{-0.5}$ and complete selectivity to hydrogen. This study was completed by Calles et al. [73] and the permeation

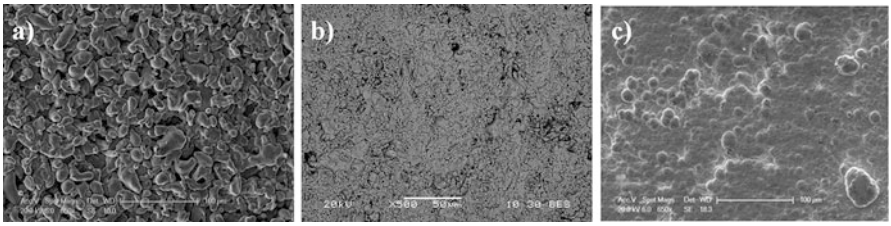

Fig. 2.4 SEM images of: (**a**) raw PSS support (grade 0.1 μm) (**b**) YSZ-modified support by Atmospheric Plasma Spraying and (**c**) composite Pd-YSZ-PSS membrane [73]

behavior of a Pd/YSZ/PSS membrane composite for WGS typical mixtures containing H_2, N_2, CO, and CO_2 was published. The membrane was prepared following a similar experimental procedure in both cases, although in the last case YSZ thickness was increased up to 100 μm in order to reduce the selective Pd film up to 13.8 μm. The morphology of the external surface of raw PSS support and its modification after the incorporation of YSZ and Pd layers are collected in Fig. 2.4. As it can be seen, the original PSS surface is practically covered after the incorporation of the YSZ intermediate barrier, decreasing significantly the surface roughness and achieving a very uniform and flat surface with negligible porosity.

Fernandez et al. [9] studied two deposition techniques, atmospheric plasma spraying, and dip-coating of a powder suspension, for preparing ceramic intermediate layers, comparing also the results obtained for zirconia and alumina raw materials. Following these strategies, the most promising membranes required only a Pd-Ag thickness of ca. 4–5 μm with extremely high hydrogen selectivity up to 200,000.

Other alternatives include the use of a wide variety of materials that have demonstrated good effectiveness for preventing the interdiffusion between the Pd-based selective layer and the support. As an example, Nam et al. [9] used a thin layer of TiN obtained by sputtering as diffusion barrier between a Pd-Ni-selective film and stainless steel substrates. Tong et al. [74] prepared a pinhole-free Pd-Ag membrane with a thickness of 3 μm on the surface of a PSS substrate coated with a thin silver layer as a diffusion barrier and aluminum hydroxide gel for filling in the big pores of the support. Ayturk et al. [75] presented a novel bi-metal multilayer (BMML) deposition technique for preparing Pd-Ag composite membranes on PSS supports. The BMML, formed by consecutive deposition of Pd and Ag porous layers with no intermediate surface activation and a final gas tight Pd layer, presented an extremely high efficiency as intermetallic diffusion barrier for over 500 h at temperatures exceeding 500 °C. Similar results have been published by Lee et al. [76] with multilayered Pd-Ag introduced in order to prevent Ag segregation to block the intermetallic diffusion from the porous stainless steel and to improve the stability of the membrane. Experimental results showed an extremely efficiency as diffusion barrier and excellent thermal stability for a period of 2,000 h. Chi et al. [77] used a layered double hydroxide (LDH) on a PSS surface to reduce the pore opening of the support and to be a middle layer retarding Pd/Fe

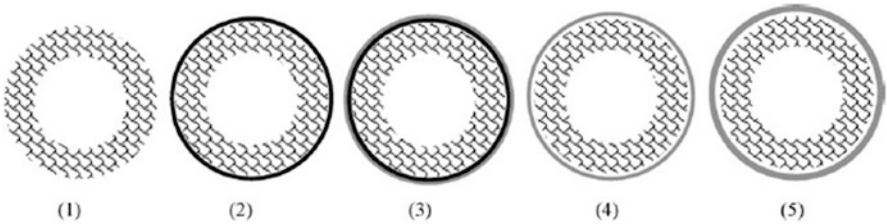

Fig. 2.5 Schematic diagram of cross-sections at different stages in the preparation of defect-free Pd-PSS membranes by using temporary intermediate layer: (1) fresh substrate, (2) polymer layer + substrate, (3) Pd layer + polymer layer + substrate, (4) Pd layer + small gap + substrate, and (5) defect-free Pd layer + small gap + substrate [83]

interdiffusion. With this material, a completely defect-free thin Pd film of around 7.85 μm thick was plated by electroless plating. Pujari et al. [78] proposed the use of nickel as interdiffusion barrier between Pd and PSS, but it was inferred that this route is not fruitful to reduce the critical thickness of dense Pd film without jeopardizing upon the pore densification. Recently, Nayebossadri et al. [79] have modified the surface pores of PSS substrates by impregnation of varying amounts of tungsten powder that also inhibit the iron interdiffusion between the PSS substrate and the deposited Pd-Cu film at temperature as high as 800 °C. Nozaki et al. also included hafnium nitride (HfN) as suitable material for non-porous intermediate layer to improve the high temperature stability of Pd-Ta composite membranes for hydrogen separation [80, 81].

One original alternative, only for adjusting the surface properties of supporting materials, but not for avoiding the possible metal interdiffusion, consists of using a temporary intermediate layer. Tong et al. followed this alternative for depositing thin Pd membranes on PSS tubular supports. First, the pores of the substrate are filled in with aluminum hydroxide gel and/or Pd/aluminum hydroxide gel. After that, the selective Pd film is deposited and, finally, the original pores of the support are recovered [82]. Same authors published other similar work in which a polymer was employed as temporary intermediate layer in order to make the incorporation of Pd easy [83]. In Fig. 2.5, a schematic diagram of this interesting process is represented, depicting the composite membrane cross-sections at different stages during the synthesis process.

2.3 Processing of Advanced Metallic and Ceramic Composite Laminate Coatings

In the last few years, a large number of methods have been developed for processing advanced laminate coatings based on metallic and ceramic materials. Pd-based membranes are one of the most representative metallic films for energy and environmental applications due to their really high hydrogen selectivity that

can be applied for purification and CO_2 capture purposes or intensification of hydrogen production processes in membrane reactors [84]. However, palladium availability at reasonable cost for covering all possible industrial uses in the future can be a key factor for real implementation [85]. In this context, the proposed solutions are aimed to develop more efficient preparation processes for obtaining free defects and ultrathin layers or to replace the palladium by an economical ceramic material of similar properties, i.e., cermets [86]. Up to now, the best solution is still under discussion and researchers are divided between different options. In spite of the high cost of palladium, the mechanical properties of the metallic materials and its compatibility with the majority of current devices in the industry, usually made of stainless steel, are propitious and many authors opt for this alternative [85, 87–90]. Considering this fact, this section includes the most relevant advances of common techniques for composite thin film processing, mainly focused on composite Pd-based membranes. At the end, some considerations for preparing other alternative materials have also been included.

2.3.1 Advances in Pd-Based Composite Film Preparation

As previously mentioned, palladium film deposition over a porous support involves a wide variety of techniques, such as Physical Vapor Deposition (PVD), Chemical Vapor Deposition (CVD), Atomic Layer Deposition (ALD), Molecular Beam Epitaxy (MBE), Electrodeposition (ED), or Electroless Plating (ELP). Among all of them, PVD and ELP alternatives have prevailed in the last years and most of published works in this field include any of them. In these cases, recent advances are directed to reduce the thickness of the palladium layer while maintaining good resistance and mechanical properties [91–93], improve the reproducibility of the preparation method and minimize the number of rejected membranes [94, 95], and combine the unique properties of pure palladium with other metals in alloys to increase the permeability and/or resistance to poisons such as carbon monoxide or sulfur [96–98].

The Physical Vapor Deposition technique (PVD) consists of incorporating metal particles onto a substrate from a vapor phase without any chemical reaction [24]. This metal vapor phase is generated by thermal evaporation at vacuum conditions [99] or, more usually, magnetron sputtering, in which a metal target is bombed with ions of high energy, generating a plasma [100]. The main advantages of this technology are the high control on thickness, being possible to prepare films with only some nanometers, and film composition, especially relevant for the preparation of alloys [101]. This technique is employed by SINTEF for manufacturing ultrathin Pd-alloy membranes of multiple compositions in a patented two-stage technology [102–104]. In a first step, metal films of palladium or palladium alloys are deposited onto a silicon single crystal substrate by magnetron sputtering. Later, the membrane film is removed manually from the silicon substrate, and it is incorporated to an adequate support, usually made of stainless steel. This research

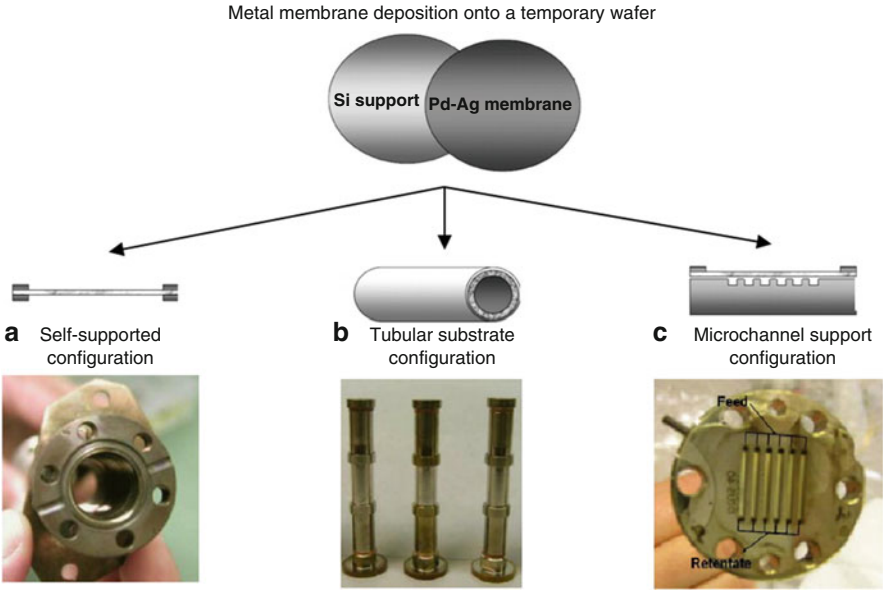

Fig. 2.6 Different configurations for H_2-selective Pd-based membranes proposed by SINTEF: (**a**) self-supported membrane fixed in the housing; (**b**) tubular, mid-section having the active membrane area and (**c**) microchannel housing membrane. Figure adapted from original published in [104]

group, headed by R. Bredesen, employs the selective film as unsupported membrane or deposited onto conventional supports with tubular geometry or a novel microchannel configuration based on a stainless steel feed channel plate with parallel small channels [104]. In the last case, the thin membrane was placed between the channel housing and a stainless steel plate with apertures corresponding to the channel geometry, obtaining a very compact system with relative high permeation surface. In Fig. 2.6, all these configurations are summarized, including an easy diagram of the support-membrane coupling and a real photo for each particular case.

Anyway, the SINTEF manufacturing technique offers multiple possibilities for investigating tailor-made multicomponent Pd-based alloy membranes with controlled composition, homogeneity, and thickness [105]. In this context, Peter et al. published diverse studies of around 2 μm thick Pd binary and ternary alloys with Ag, Au, Ru, Mo, Ta, Nb, and Y by using this technology [106, 107]. Pd-Au and Pd-Y binary alloys provided the highest H_2 permeability, while in case of preparing ternary alloys is found that the permeability increases with greater fcc lattice constant of the alloy. The addition of small amounts of Ta or Y (1 at.%) over a Pd-Cu increase in H_2 permeability of roughly 10 and 45%, respectively, while the permeability increased in a 65% preparing a ternary Pd-Ag-Cu alloy, compared to the binary Pd-Cu counterpart with equivalent Pd content [106]. They also analyzed the sulfur resistance of these membranes, observing that pure Pd and Pd-Ag films showed instant failures,

while binary Pd-Cu and Pd-Au alloys survived sour atmospheres, although the permeate flux decreased drastically. Moreover, they evidenced that the addition of a third element in some alloys can improve not only the permeability, but also the sulfur tolerance [107]. A similar procedure based on PVD technique is published by Dunbar in order to prepare novel hydrogen-selective thin films [90]. He employed a silicon wafer to incorporate a palladium thin film by thermal evaporation under high vacuum. First, a 20 nm layer of chrome is deposited to act as an adhesion layer of the palladium film, with a thickness of around 1 μm. This method allows the preparation of dense, highly precise and reproducible palladium films with less than 1% variability palladium thickness across the surface. After the metal incorporation, the wafer is treated with a photo-resistant layer and UV light to add a contact mask containing a grid pattern that acts as a mold for a nickel electroplating which builds the mechanical support grid for the palladium film. The complete removal of the mold is critical to a well-functioning membrane. The palladium/nickel composite membrane is released from the silicon starting substrate by dissolving in a hot basic solution and the chrome adhesion layer is selectively etched. The resulting membrane is completely metallic, planar in geometry and contains less than 1.2 $mg \cdot cm^{-2}$ palladium metal loading. The membrane exhibited a good performance with hydrogen to helium selectivity of over 5,000:1 and permeance of approximately $3 \cdot 10^{-6}$ $mol \cdot m^{-2} \cdot s^{-1} \cdot Pa^{-1}$.

On the other hand, the Electroless Plating technique (ELP) is presented as a very simple method for the synthesis of Pd-based membranes, which does not require any expensive equipment and neither high operational cost due to the absence of electrodes and external sources of electricity [108–112]. This method is based on the deposition of a metal from aqueous solutions onto both conducting and nonconducting surfaces of porous supports with different geometries. Basically, the solution contains a metal-complex that reacts with some reducing agent by a controlled autocatalytic chemical reaction, and it is deposited onto the target surface of the support. For example, most of the Pd-based membranes presented in scientific manuscripts are prepared from $Pd(NH_3)_4{}^{2+}$ and N_2H_4 (hydrazine) as the most common metal-complex and reducing agent, respectively [113, 114]. Next, the main chemical reactions involved in the process, including the hydrazine oxidation, the metal reduction, and the global reaction, are described as:

$$N_2H_4 + 4OH^- \rightarrow N_2 + 4H_2O + 4e^- \qquad E^0 = 1.12\ V$$
$$2Pd(NH_3)_4^{2+} + 4e^- \rightarrow 2Pd^0 + 8NH_3 \qquad E^0 = 0.95\ V$$
$$2Pd(NH_3)_4^{2+} + N_2H_4 + 4OH^- \rightarrow 2Pd^0 + 8NH_3 + N_2 + 4H_2O \qquad E^0 = 2.07\ V$$

In general, prior to carrying out the metal incorporation, it is necessary to activate the surface of the support in order to decrease the activation time for the film generation and improve the homogeneity of the coating [115]. Traditionally, the activation process of different types of support has been carried out by using successive immersions in acidic solutions of tin and palladium in the so-called sensibilization-activation method [116]. However, recent studies have analyzed the influence of Sn residues on the stability of composite palladium membranes. It was

found that the higher concentration of tin solution, as well as the number of sensibilization-activation cycles, enlarged the Sn residue amount and led to a lower initial selectivity but a better membrane stability [117]. Considering the possible negative effects of tin residues, some authors have presented alternative methods for generating the first Pd nuclei avoiding the use of tin solutions. In this context, as it is already described in previous sections, some authors used the incorporation of an intermediate layer between the porous support and the selective coating to include homogeneously distributed nuclei [68, 71, 75–77]. Touyeras et al. [118] carried out the activation step in an ultrasonic bath to increase the nuclei deposition rate and avoid the generation of conglomerates on the support surface. Sanz et al. [95, 119] employed a direct reduction method of a diluted palladium solution to activate the surface of porous stainless steel supports and Seshimo et al. [120] investigated the use of catalyzed anodic alumina surfaces to facilitate the Pd electroless plating.

However, in spite of the substrate selection and a correct surface activation are key factors on the quality of the final coating, most researchers concentrate their efforts on reducing the metal thickness and improving the membrane properties by modifying the conventional electroless plating method. Thus, Uemiya et al. [121] proposed to increase the metal incorporation rate by immersing previously the porous substrate in a hydrazine solution. Yeung et al. [122], Souleimanova et al. [123] and Li et al. [124] combined the ELP technique with osmosis to facilitate the incorporation of the metal in the pore areas. Zhao et al. [39] and Zhang et al. [125] employed a vacuum-assisted ELP with similar purposes, obtaining Pd composite membranes with finer and more uniform microstructure. On the other hand, some authors are focused on modifying the composition of solutions employed in the ELP process in order to improve the properties of the deposited film. Most of them propose the use of free-EDTA baths to avoid the presence of carbon deposits on the selective metal film that can react at particular conditions for generating CO_2 and, consequently, defects in the coating [126–128]. Finally, the influence that supports rotation during the ELP process has also been studied, considering this alternative simple and easily scalable for mass production. Chi et al. [129] determined that the rate of Pd deposition increased as the support rotation rate does. Compared with conventional ELP in static, the proposed modification using support rotation yielded Pd membranes with more uniform and smooth surface morphology, which substantially enhanced the membrane stability. These membranes exhibited a permeance of $3.0 \cdot 10^{-3}$ $mol \cdot m^{-2} \cdot s^{-1} \cdot Pa^{-0.5}$ with ideal hydrogen separation factor upper than 400 with only 5 μm thick.

In addition to all developments above collected, it is important to emphasize that many membranes are usually rejected during their manufacturing process due to the presence of defects, increasing the overall cost of the ELP process that makes the industrial scale-up difficult. In this mean, it is crucial to improve the current procedures and develop new routes for the generation of low-cost thin films by ELP with high reproducibility. Recently, some authors have developed novel alternatives to repair defects produced during the fabrication of composite Pd-based membranes. From this angle, Li et al. [124] reported the combination of

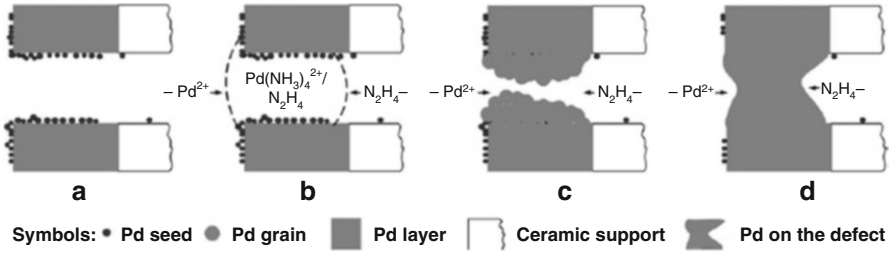

Fig. 2.7 Stages of defect sealing during the Pd pore-plating [94]

conventional ELP and osmosis for repairing defects in Pd/α-Al_2O_3 composite membranes. They affirm the complete disappearance of defects, evidenced by a significant increase of hydrogen perm-selectivity without any reduction of the permeation flux or increase in the selective film thickness. Following this pioneer work, Zeng et al. [94] presented the so-called point plating as an attractive alternative for repairing small defects and cracks in palladium membranes. The point plating method is based on the conventional chemical reactions of electroless plating, but feeding the palladium salt and the reducing agent from opposite sides of the composite membrane. In this manner, the selective deposition of palladium is forced to be place just over the palladium layer defect. Figure 2.7 shows a scheme of the progressive defect sealing following the proposed technique:

Based on both pioneer methods, the Chemical and Environmental Engineering Research Group of the University Rey Juan Carlos has developed a new route to prepare very reproducible defect-free palladium composite membranes by incorporation of palladium directly over tubular commercial porous stainless steel supports by modified electroless plating [43, 95, 119]. This new method is called Electroless Pore-Plating (ELP-PP) and consists on feeding the solution that contains the Pd source and the reducing agent (hydrazine) from opposite sides of the support from the first stages of the membrane conformation. In this manner, the chemical reaction between Pd^{2+} ions and the reducing agent is initiated in the internal porosity of the support, in a similar way to the method proposed by Zeng et al. [94] for defect sealing. However, there is no any previous palladium layer in this case and the palladium incorporation is performed directly over both commercial and modified PSS supports. The main advantage of this method is that a minimum palladium thickness for a complete coating is guaranteed due to the palladium incorporation turns difficult the encounter of reactants until all pores become completely filled and the process ends. Figure 2.8 reproduces simple schemes for both conventional ELP and the novel ELP-PP in order to evidence the benefits of the last one. At this point, it is important to emphasize the noticeable reduction of preparation costs for these composite membranes.

The membranes obtained by the novel ELP-PP method evidenced that palladium was not only incorporated on the pore areas, and an external film was generated on both commercial and modified PSS supports. The authors explain this fact is produced by the presence of a wide variety of pore diameters in the PSS supports.

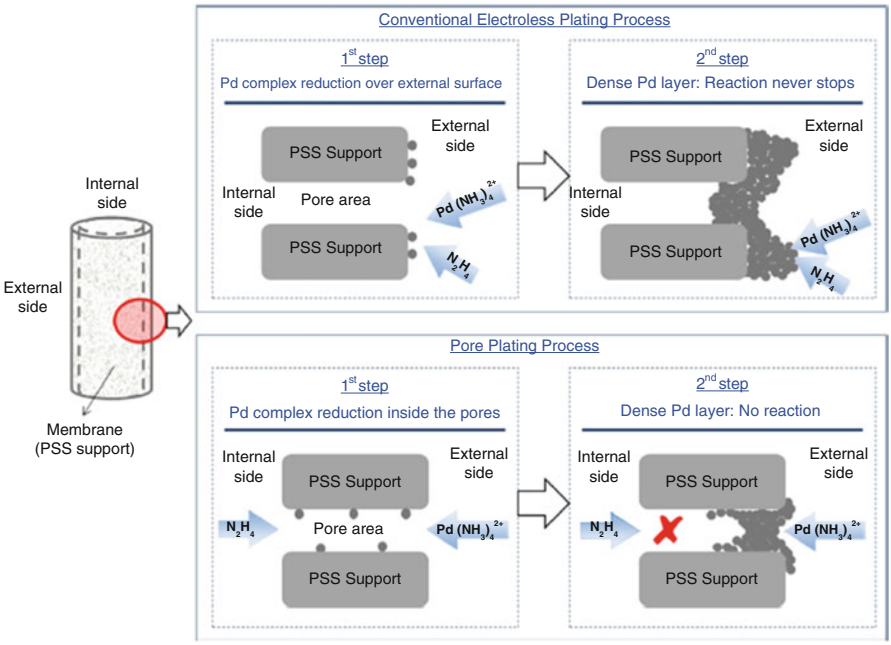

Fig. 2.8 Comparison of conventional Electroless Plating and novel Pore-Plating techniques [95]

The smallest pores can be fully closed by palladium incorporation in a relative short time, but the hydrazine can diffuse from the internal to the external side of the support through the biggest ones, partially covered, where reacts with the Pd solution and generates an external layer. Thus, support characteristics, concentration of solutions, and the ratio membrane length/solution volume during the process define the palladium distribution in the composite membrane. As an example, the use of calcined supports for reducing the original average pore diameter of pores provokes a significant reduction in the final thickness for the composite Pd membranes from 20 to 11 μm (estimated value from gravimetric analysis). In both cases, the real external thickness is around 2–6 μm lower than the previous estimated value due to the partially infiltration in the pores close to the external surface of the support. The palladium distribution for each membrane is showed in cross-sectional SEM images reproduced in Fig. 2.9. This research group also demonstrates the quality and high stability of the membranes prepared following this method through both permeation experiments and tests in a real membrane reactor for the water gas shift (WGS) process [43, 95, 119]. In all cases, the membranes maintained a good integrity, complete hydrogen selectivity and permeances in the range $1–6 \cdot 10^{-4}$ $mol \cdot m^{-2} \cdot s^{-1} \cdot Pa^{-0.5}$.

Recently, the ELP-PP technique is also applied onto ceramic substrates, evidencing the possibility to generate an ultrathin selective layer by this technique over a support with vary small pores and a narrow pore size distribution, although the presence of palladium in both internal pores and external surface is still presented [130].

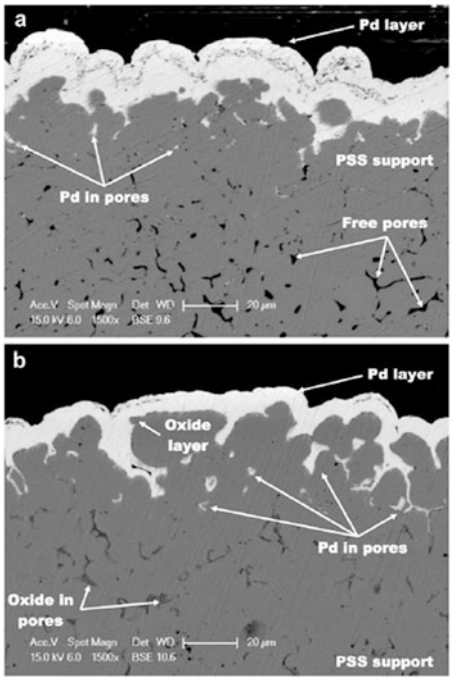

Fig. 2.9 SEM micrographs depicting cross-sections of: (**a**) PSS-Pd and (**b**) PSS-OXI-Pd composite membranes [95]

Other interesting alternative is proposed by Pacheco Tanaka et al. [40, 131, 132] that consists on the preparation of pore-filled membranes by the incorporation of the selective metal between two ceramic layers in a sandwich-type structure. Following this procedure, the palladium nanoparticles are deposited through vacuum-assisted electroless plating, taking up the free spaces leaving between the ceramic particles of a first interlayer, which is covered later by a new ceramic layer. In this way, the advanced composite membranes are able to work below the critical temperature and maintain a high stability, instead of conventional membranes based on an external coating, where fatal damages usually occur. Recently, a clear scheme of the conformation process following this procedure has been published by Arratibel et al. [41], and it has been reproduced here with permission in Fig. 2.10.

Independently of using a conventional or a improved electroless plating technique, most researchers combine the palladium with other metals for improving permeate flux, mechanical stability, and poison tolerance of the composite membrane in a similar way that works previously presented for PVD methods. In this context, the research group headed by J.D. Way has so many years of experience preparing diverse binary and ternary alloys with copper [133–136], gold [16, 96, 137–140], silver [16, 138, 141], and ruthenium [142]. Braun et al. [143] prepared a ternary Pd-Ag-Au layer over a porous stainless steel support by sequential electroless deposition and studied the morphology and microstructure of the membrane before and after permeation tests in the presence of sulfur. Miller et al. [144] collected the physics and chemistry of H_2 transport through dense Pd-alloy layers in

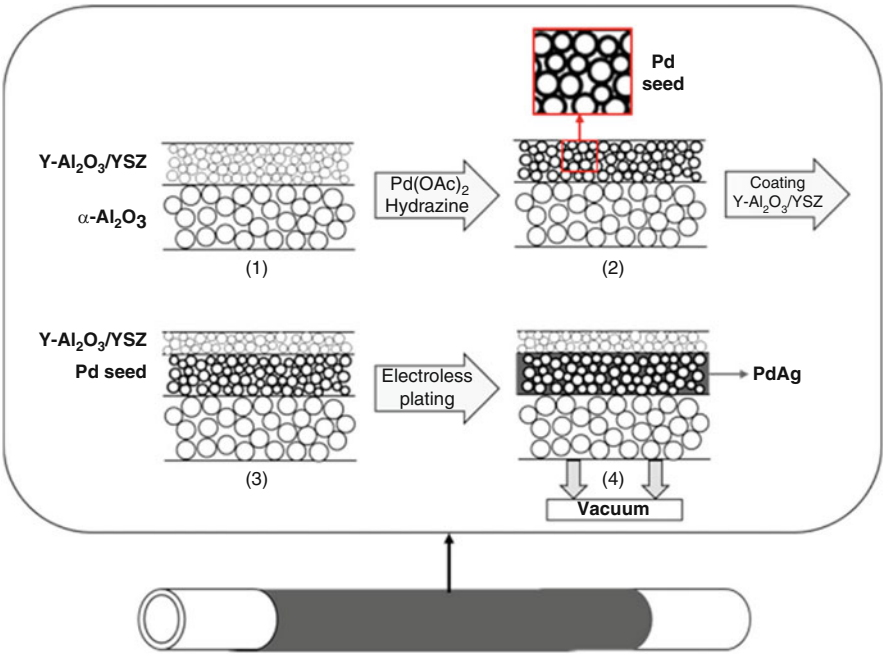

Fig. 2.10 Schematic description of the preparation of Pd pore-filled membranes [41]

a book chapter, as well as the permeation behavior modification in the presence of pollutants typically present in stream from fossil energy. The list of published works is very long, but the main objective in all cases is to increase the permeance of the membrane in unfavorable operational conditions.

As a general conclusion, it can be pointed that a wide variety of strategies are being followed to develop new Pd-based composite coatings, achieving free-defect thin films with good reproducibility and resistance at reasonable cost. In fact, after the last advances, the cost of the selective coating is within the average cost of the support materials, in spite of being composed by noble metals.

2.3.2 Alternative Materials to Metallic Thin Films

In order to avoid the use of large amounts of noble metals for preparing hydrogen-selective films, some researchers have proposed the fabrication of membranes based on alternative materials. In this context, non-Pd BBC alloys and proton conducting membranes stand out as attractive option for reducing the cost of materials while a significant hydrogen permeability is maintained [145]. Dolan presented a review of diverse body-centered-cubic (BCC) alloys comprising Group IV and V metals as suitable materials for high temperature hydrogen separation

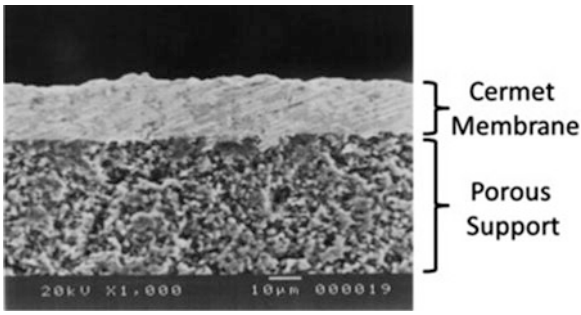

Fig. 2.11 Cross-sectional SEM image of a supported cermet membrane [86]

applications, overcoming the traditional embrittlement problem and enhancing the permeation capability [146]. On the other hand, Tao et al. [147] recently published a complete overview of last developments with dense proton-electron conducting ceramic materials and their associated membranes. These materials have been classified into categories by typical composition formulation. As a conclusion, these researchers showed that proton-electron conducting ceramic membranes are not yet ready for industrial requirements. In order to overcome the current limitations of these materials, the authors proposed some recommendations to address the future necessary challenges, mainly including the analysis of new formulation to enhance the conductivity and mechanical properties and developing of mathematical models for better understanding the behavior of these materials. The use of cermet materials combines the properties of ceramic with metallic components in a composite structure with enhanced permeance. In general, for the preparation of these materials, both ceramic and metallic powders are mechanically mixed, pressed and sintered at high temperature (upper than 1,200 °C). After that, for the film preparation, the cermet powders are dispersed in an alcohol solution and mixer with other compounds as binder and plasticizer to obtain a malleable paste that is incorporated onto a porous substrate by a painting method. Balachandran et al. [86, 148, 149] employed this type of materials as a thin film with thicknesses in the range of 22–200 μm for hydrogen separation processes with acceptable permeance and high selectivity. Figure 2.11 shows a cross-sectional micrograph of a typical cermet membrane prepared by this research group by using a porous ceramic support.

2.4 Characterization Techniques

After processing any coating or thin film material for energy and environmental applications, an exhaustive and complete characterization is a critical issue necessary to ensure the correct operational behavior for the complete lifespan of membranes. A large variety of techniques can be used for this purpose, being usually classified as morphological analyses, determination of mechanical properties, and

permeation tests. The first group includes all techniques aimed to determine the main structural properties of the materials, i.e., continuity, porosity, roughness, thickness, composition, or crystallinity. The second one is focused on the analysis of critical mechanical properties, such as hardness or adherence of coatings. All these properties can be used for predicting the future behavior of the membrane and define the most appropriate applications for each material. However, it is necessary to demonstrate the capability of the material through permeation tests at diverse conditions as real as possible in both laboratory and pilot-plant scales.

This section tries to gather the most common characterization techniques, describing the basic principles and usual applications for each one.

2.4.1 Optical Microscopy and Profilometry

One of the oldest techniques to analyze the morphology of coatings and thin films materials is the optical microscopy (OM), which is usually capable of achieving a resolution up to 300 nm, around 200 times upper the human eye limitation. In the last years, this technique has been developed to offer better possibilities. Particularly, confocal microscopy offers several advantages over conventional optical microscopy, including controllable depth of field, the elimination of image degrading out-of-focus information, and the ability to collect serial optical sections from thick specimens. The key to the confocal approach is the use of spatial filtering to eliminate out-of-focus light or flare in specimens that are thicker than the plane of focus. The relatively low cost of optical microscopies has been favored their diffusion and many researchers use this technique to analyze the morphology of thin films. Usually, the images obtained from optical microscopy are used to observe changes or damages in the coatings after thermal treatments or mechanical stresses, as well as for detecting cracks and pinholes. In Fig. 2.12, a Pd membrane surface is analyzed by this technique in order to observe the progressive defect sealing by the point-plating method developed by Zeng et al. [94].

Associated to the optical microscopy, it is possible to find a profilometer integrated in a computerized system for roughness determination and recreating the real surface in a 3D image. In general, these systems scan the surface of the sample and record all areas in focus, repeating the process for different values of the Z axis. An example of the surface recreation for two commercial PSS supports with diverse characteristics (porosity grade 0.1 and 0.2 μm) can be seen in Fig. 2.13.

2.4.2 Scanning Electron Microscopy

The scanning electron microcopy (SEM) is a very useful tool for morphology and structural characterization of solid film surfaces with high resolution at micron scale. Surfaces with dimensions ranged from 1 cm to 5 μm can be usually analyzed

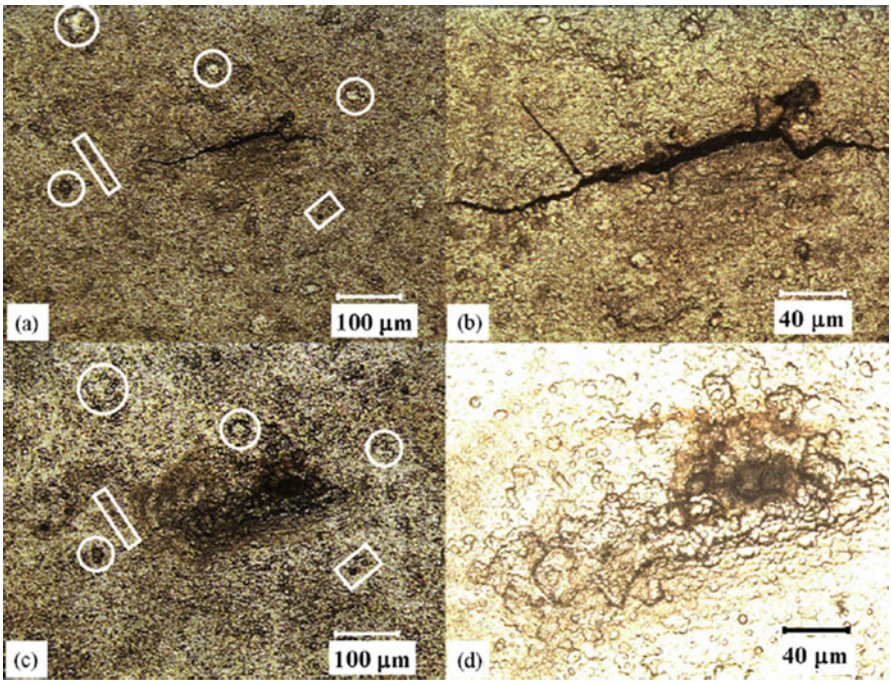

Fig. 2.12 Surface images of a Pd membrane surface by optical microscopy at different magnification: (**a**, **b**) crack detection and (**c**, **d**) repaired area after point plating [94]

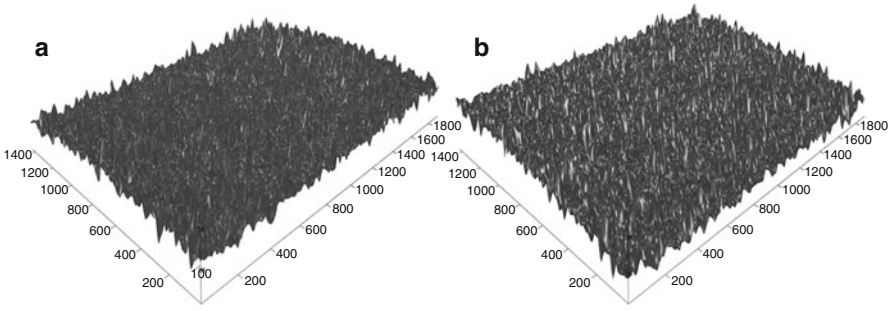

Fig. 2.13 Surface 3D reconstruction of commercial PSS supports with porosity grade: (**a**) 0.1 µm and (**b**) 0.2 µm

varying the magnification. This technique is based on the scanning of a target surface by focusing a beam of high energy electrons to generate multiple signals from electron-sample interactions such as secondary (SE), backscattered (BSE), or diffracted backscattered electrons (EBSD). SE and BSE are the most common signals used for imaging thin films and coatings of composite membranes. The amount of detected SE is function to the topography of the sample, decreasing

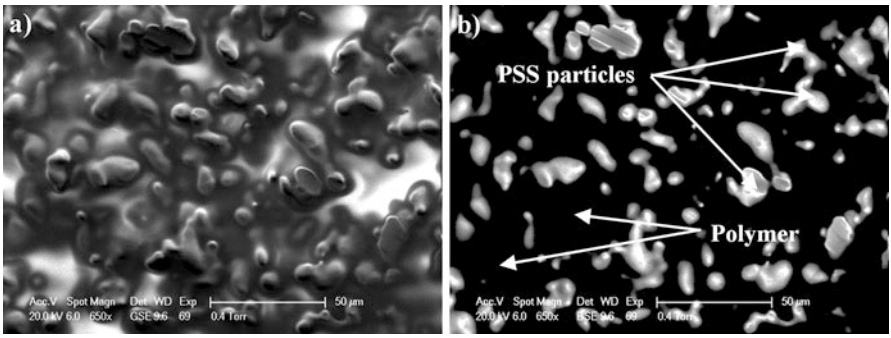

Fig. 2.14 Conventional SEM images of a membrane surface obtained by: (**a**) SE and (**b**) BSE

the signal for deepest areas and increasing for raised ones. On the other hand, the amount of BSE can be directly related to the composition of the sample, obtaining bright areas when heavy atoms are dominant and a dark color for areas where light atoms, i.e., carbon, are the larger part.

Figure 2.14 shows the surface of a porous stainless steel support modified by the incorporation of a polymer material with both detectors, SE and BSE. The external morphology of the sample can be clearly analyzed from the SE mode image (Fig. 2.14a), obtaining an apparent good continuity, absence of pores, and a certain roughness. On contrast, the image obtained from BSE evidences the presence of different tones due to composition changes on the sample (Fig. 2.14b). In this manner, the brightest areas correspond to the highest stainless steel particles, not affected by the incorporation of the polymer, which appears dark due to the low molecular weight of the carbon mainly present in the structure.

At this point, it is important to emphasize that it is possible to complete the characterization obtained from these SEM images with help of diverse commercial processing tools, such as Scanning Probe Image Processor® (SPIP®) or Digital Micrograp™ [51, 72, 73]. Basically, they allow determining quantitatively relevant parameters of the studied surface. In fact, SPIP® software calculates an apparent external roughness from the SE mode image and offers the possibility to reconstruct a 3D image in a similar way to the previously described optical profilometers. On the contrary, Digital Micrograp™ software uses the micrograph obtained from BSE mode and segments the images for distinguishing the solid areas in some grey scale from the dark pores. In this manner, considering the total size of the analyzed area, the external porosity can be determined.

Other conventional application of SEM pictures is to determine the thickness of intermediate layers and selective coatings by visualizing the sample cross-section. As an example, Fig. 2.15 shows an SEM photograph of a composite membrane cross-section formed by stacked layers of stainless steel (main support), silicalite-1 (intermediate layer), and palladium (selective layer for hydrogen permeation).

Moreover, it is also possible to analyze the generation of X-rays produced by inelastic collisions of the incident beam with other electrons of atoms present in the

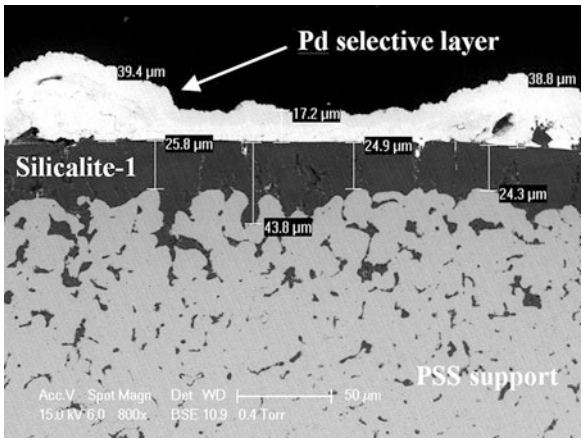

Fig. 2.15 Micrograph of a composite membrane cross-section with thickness measurements

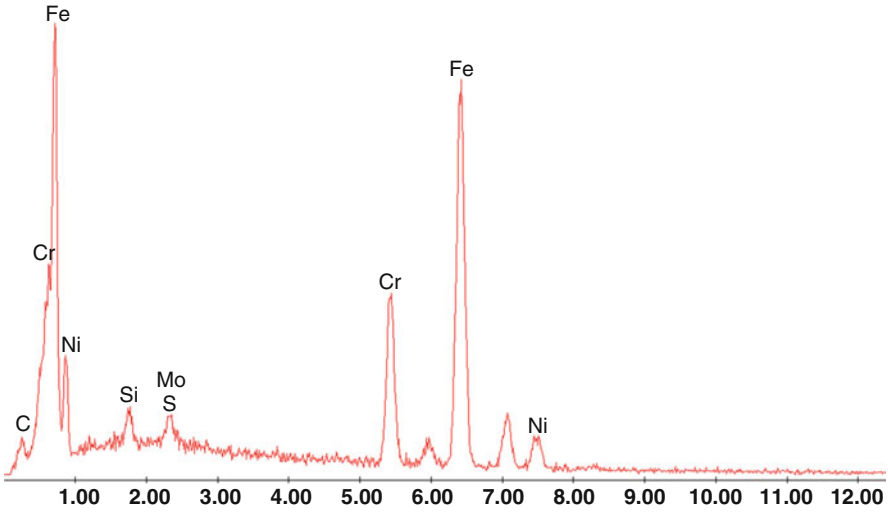

Fig. 2.16 EDX spectra for a porous stainless steel membrane

sample by an EDX detector. Currently, most scanning electron microscopes are equipped with this accessory. The excited electrons of the sample by the incident beam return to lower energy states yielding X-rays of fixed wavelength characteristic for each element. In general, for the analysis of inorganic materials, SEM analysis is considered to be nondestructive and X-rays generated by electron interactions do not lead to volume loss of the sample, so it is possible to analyze the same materials repeatedly. Figure 2.16 shows the X-ray spectra obtained for a 316 L stainless steel material, being possible to distinguish iron, chromium, nickel, silica, molybdenum, and carbon as main components.

One popular application for the in situ composition analysis inside an SEM is the characterization of alloys. Combining both surface visualization and EDX analyses,

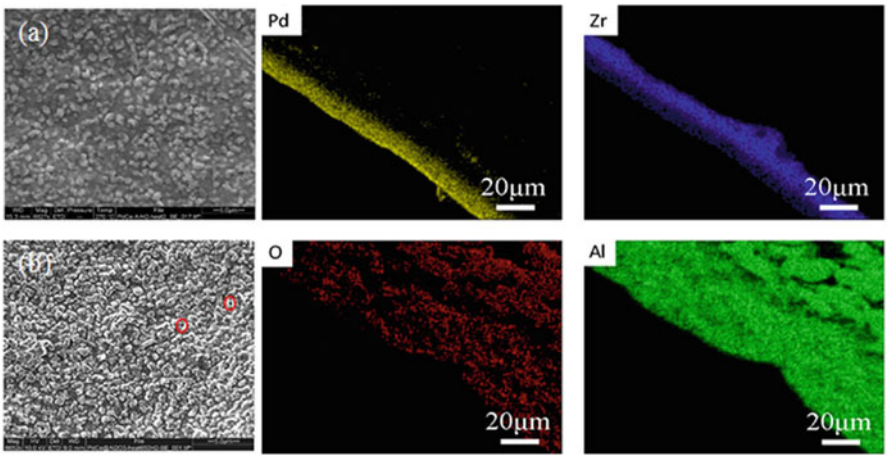

Fig. 2.17 SEM images of a composite Pd membrane at diverse conditions: (**a**) after heating to 250 °C under H_2 gas (1 Torr, for 20 min) and (**b**) heated to 650 °C in succession (pinholes are highlighted in red cycles). (**c**) Element mapping of Pd, Zr, Al, and O from the cross-section of sample [150]

it is possible to study the distribution of each metal that form the alloy. This is very useful for ensuring the preparation of homogeneous alloys and analyzing the intermetallic diffusion process when diverse metal layers are in contact for long time at high temperatures. As an example, Zhu et al. [150] carried out element mappings of a composite membrane formed by stacked layers of ZrO_2 (15 μm thick) and Pd (4 μm thick) onto a ceramic support in order to study both microstructure and composition of the composite system under diverse gas-thermal treatments. Figure 2.17 contains the SEM surface images of the membrane at two different thermal conditions, as well as the elemental mapping obtained from EDX analyses for each case.

2.4.3 Auger Electron Spectroscopy

The auger electron spectroscopy (AES) is a widely used technique to investigate the composition of surfaces, and it is certainly similar to the previously described EDX technique. The AES technique is based also on the ionization of a core atomic state by an incident electron beam. In general, the excited atom can relax through two different competitive effects: emission of photons (X-ray) or electrons (Auger effect). The first case is favored in case of heavy elements are predominant in the thin film, while the Auger effect appears clearly for light elements. Thus, characterization by EDX is usually the dominant technique for determination of composition in most inorganic films, while AES is less extended and only few works employ this technique for the analysis of impurities on the surface of inorganic thin

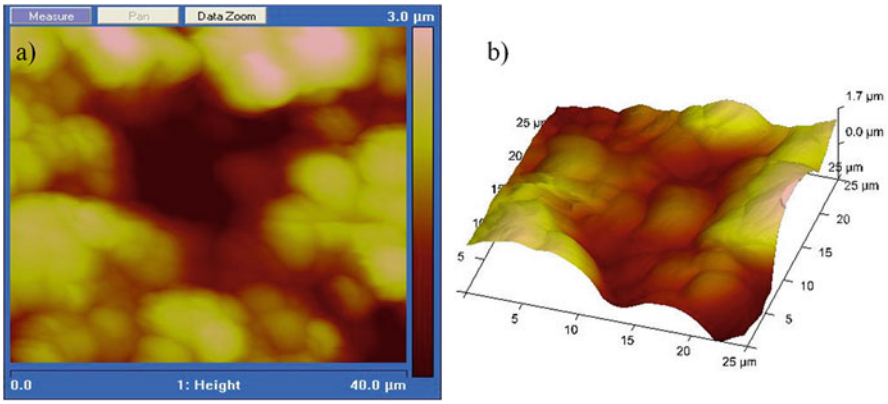

Fig. 2.18 (**a**) Image of a Pd-composite membrane directly obtained by AFM and (**b**) 3D recreation

films and coatings. For instance, Antoniazzi et al. [151] studied the effect of carbon surface impurities on the hydrogen permeation rates of a dense palladium membrane by in situ monitoring of the membrane and Auger analysis.

2.4.4 Atomic Force Microscopy

This type of microscopy employs a mechanic-optical instrument able to detect forces in the range of piconewtons. The microscope is usually equipped with a sharp tip with conic or pyramidal geometry that scans the sample. The tip is connected to a cantilever spring to let free movements onto the surface topography. Each variation of the tip position is detected by a laser diode, and the information is used to recreate accurately the analyzed surface. In this manner, the atomic force microscopy can be used for studying the morphology of diverse materials with even higher resolution of traditional scanning electron microscopes, achieving extremely high magnifications up to 1,000,000x.

Figure 2.18 shows the image obtained directly with an AFM for a Pd-composite membrane and the three-dimensional recreation of the surface in order to visualize clearly the morphology and roughness of the sample.

2.4.5 Mercury Porosimetry

The mercury porosimetry is an indirect technique for the characterization of the porous structure of a sample, mainly the pore volume, porosity, average pore size, and tortuosity of the pores. It is based on the capillarity properties of pore internal

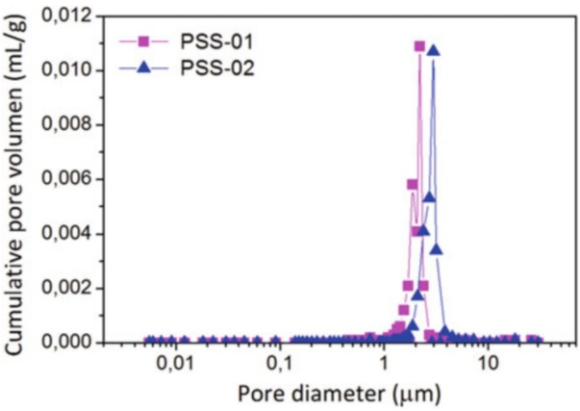

Fig. 2.19 Pore size distribution of porous stainless steel filters determined by mercury porosimetry

channels and the low capacity of mercury to wet the surface of solids. In this manner, it is necessary to apply some pressure to introduce the mercury inside the pores so much as the pore is narrower. The conventional procedure consists of immersing the sample in a mercury bath and progressively increases the pressure. For each value of pressure, the equipment determines the volume of the metal that penetrates into the pores. This volume provides information about the porosity of the sample, and the pressure can be related to the pore size. Typically, pore sizes ranged from $3.0 \cdot 10^{-3}$ to $1.0 \cdot 10^{3}$ can be measured. Figure 2.19 shows a typical pore size distribution of two different porous stainless steel tubes with grade 0.1 and 0.2 μm obtained by mercury porosimetry.

2.4.6 X-Ray Diffraction

X-ray diffraction (XRD) is an analytic technique employed for identifying crystalline structures of solid samples, being possible to distinguish diverse allotropic or isomorphic phases. A crystalline material can be considered a periodic and ordered group of atoms. When the material is reached by an electromagnetic radiation with wavelength near to the interatomic distance, constructive interactions in particular directions appear. In this way, the diffracted beam will rely on the type of atoms in the sample and their geometric positions, generating a unique diffraction spectrum for each crystalline material, like a finger print.

The analysis of a sample by this technique is based on the Bragg's law that connects the wavelength of the incident X-ray (λ), the distance between crystalline planes (d), and the angle between both (θ).

$$n \cdot \lambda = 2 \cdot d \cdot \text{sen}(\theta)$$

When this equation is reached, the reflected rays by the crystal generate constructive interferences. Otherwise, destructive interferences are produced and no signal can be observed. In this manner, a typical XRD pattern represents the angular positions of each signal, and the identification of each crystalline phase is carried out by comparison with other patterns. The intensity for each signal can be related with the amount of that crystalline phase in the sample.

Traditionally, the use of XRD analyses is very attractive for studying the synthesis or ordered materials or following the alloying processes for the preparation of advanced materials. As an example of this technique application, Fig. 2.20 presents high temperature X-ray diffraction measurements carried out by Pati et al. [152] for pure palladium and palladium-rich alloys. The lattice parameters, coefficient of thermal expansion, and X-ray Debye temperature of these materials were calculated as a function of temperature from the XRD data.

2.4.7 X-Ray Photoelectron Spectroscopy

X-ray Photoelectron Spectroscopy (XPS) is also one of the most widely used techniques for the surface analysis of thin films and coatings. This characterization technique can be applied to a wide variety of materials and provides valuable quantitative information about both elemental composition and chemical state of the species. The technique is based on the irradiation of a surface with an X-ray beam at high vacuum and measurement of both kinetic energy and number of electrons that escape from the top of the sample. The obtained results usually are related to an average depth of around 5–10 nm. Combining these measurements with some milling treatment, it is also possible to analyze accurately both elemental identity and chemical state of the sample at entire thin film thickness. In general, the XPS results of a thin film structures are very useful for many industrial and research applications where the composition plays a critical role in performance.

As an example, Fig. 2.21 shows the XPS spectra obtained for two different Pd coatings onto an alumina substrate presented by Elam et al. [153]. A typical signal of pure palladium metal can be distinguished at a binding energy of around 335 eV for the sample with 51 Å thick (pick identified as Pd3d). The lightly increase of the energy for this signal in the thinner sample (13 Å thick) indicate oxidation of the palladium, suggesting that much of the Pd is bound to oxygen atoms of the alumina support.

Other examples of using XPS analysis for characterization of thin films can be found in the works presented by Leiro et al. [154] for the analysis of surface segregation and core-level shift of a Pd-Rh alloy film, Tang et al. [155], focused on the study of composition and corrosion resistance of palladium film on 316 L stainless steel by brush plating, and Skoryna et al. [156] for valence band studies of nanocrystalline Pd-Zr alloy thin films.

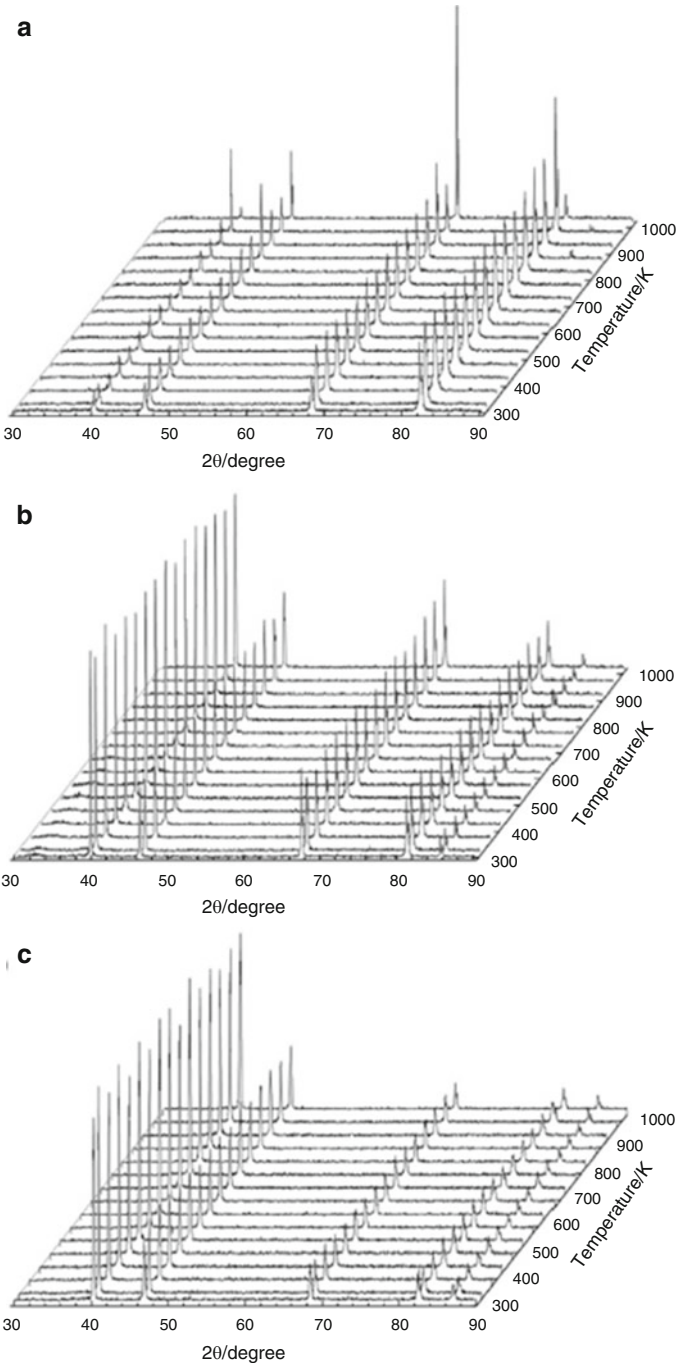

Fig. 2.20 High temperature XRD patterns of: (**a**) Pd, (**b**) $Pd_{77}Ag_{23}$, and (**c**) $Pd_{77}Ag_{10}Cu_{13}$ [152]

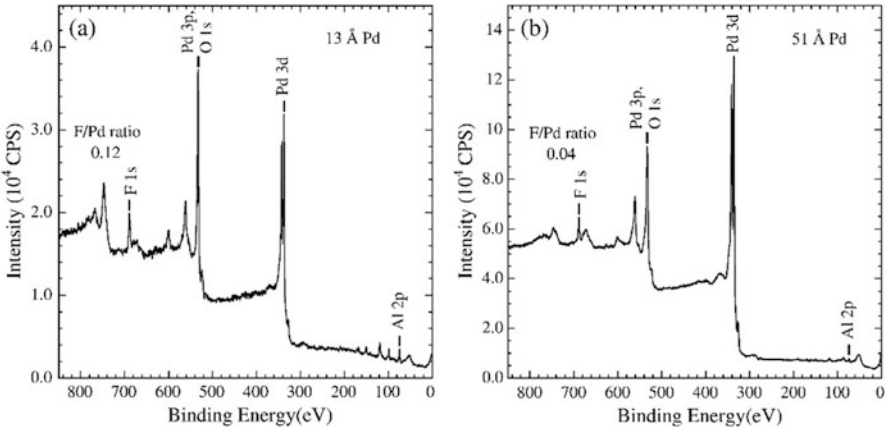

Fig. 2.21 XPS spectra for two different Pd coatings on Al_2O_3. Film thickness: (**a**) 13 and (**b**) 51 Å [153]

2.4.8 Gravimetric Analysis

The gravimetric analysis is a quantitative method for determining the weight variation of a sample after certain processes. This simple method is very common for the thickness estimation of selective film coatings, considering the geometry of the surface, the composition of the film, the density of each component, and a homogeneous deposition process. In this manner, an average thickness value for the coating is usually obtained in good agreement with the real value, determined necessary by SEM. Main deviations are usually attributed to a heterogeneous incorporation or the partial penetration of the coating into the porous structure of the support [95].

2.4.9 Mechanical Resistance and Adherence

Mechanical properties of coatings and thin films are critical issues for ensuring a suitable behavior of composite materials in real applications. In this context, the main concerns that it is necessary to take into account are adherence to the substrate, stresses present in the composite material, thermal resistance, hardness and wear resistance [157]. It is clear that a composite membrane formed by stacked layers of a porous substrate and a thin selective film is exposed to a wide variety of factors that can be compromise its integrity. Firstly, the operation mode in terms of permeate flux direction strongly affects to the resistance of the films. Stresses and delamination can be produced when the permeate flows from one side of the support to the other side where the selective film is deposited [158]. Thermal resistance is one of the most important aspects that it is necessary to take into

account, especially in case of using cycles of temperatures during the membrane operation, i.e., for a noncontinuous operation and adsorbent or catalyst regeneration varying the temperature in membrane reactor applications [54, 159]. For Pd-based membranes, hydrogen embrittlement can also be considered if temperature drops under 297 °C [160–162]. Moreover, the intrinsic thermal expansion coefficient of each material that compose the composite membrane also represents a critical parameter that it is necessary to analyze, mainly in case of using a multilayer structure, i.e., including an intermediate layer between the support and the selective thin film or a final protective coating [163]. Adherence between substrate and coatings is other fundamental parameter from the first preparation stages. Surface properties of substrate, composition, and deposition techniques are the main responsible of the film adherence. As mentioned in previous sections, smooth surfaces of supports make the adherence of the thin film weak, while a certain roughness improves the anchoring between both layers, in spite of hindering the generation of a free-defect low thickness [29, 30]. Finally, hardness and wear resistance of the incorporated thin film is also essential, especially in case of working in fluidized-bed membrane reactors, in which catalyst particles are in constant movement, hitting with the thin film [164, 165].

Although electrical properties are usually showed in specialized literature as a separated category from mechanical properties, they can also be relevant for some particular applications in case of using metal thin films. As an example, Tosti et al. [166] studied the electrical resistivity of a Pd-Ag permeator tube under different hydrogenation conditions for heating the membrane system. From this perspective, the electrical resistance of the membrane film when a voltage difference is applied provokes an ohmic effect and the consequent heating. They found that, in general, the electrical resistivity increases with both temperature and hydrogen partial pressure, although in a major grade for the first one, evidencing that the hydrogenation process should not significantly affect the design of the proposed heating system.

In spite of the importance of these critical issues, as mentioned before, and the availability of a wide variety of techniques for the determination of these parameters, only a few manuscripts address in detail these concepts for composite-based Pd membranes, comparing the effects of using diverse supports (i.e., ceramic or metallic ones), surface modification treatments (i.e., incorporation of diverse materials as intermediate layer), or the most recent advances for the palladium thin layer incorporation. The research group headed by Tosti analyzed the strain of unsupported Pd-Ag membranes at diverse temperatures and pressures under thermal and hydrogenation cycling, observing that an increase in temperature provokes an expected material elongation, but under hydrogen presence an equivalent variation of temperature involves a contraction effect. In this manner, below 200 °C the hydrogen presence prevails over the conventional temperature effect [166]. On the other hand, one of the most complete studies about adherences of thin films for Pd-based membranes was carried out by Huang et al. [32]. They addressed the adhesion of palladium thin films prepared by conventional electroless plating over tubular ceramic supports modified with an intermediate layer of Al_2O_3 or ZrO_2. The

membranes were prepared in different laboratories from Germany and China. The characterization of the Pd film adhesion was carried out through five different methods: cross-cut, thermal-shock, hydrogen embrittlement, pull-off, and pressure-tolerating tests. They affirmed that the use of a single method for adhesion determination may give weakness or wrong results, being necessary to confirm the experimental data through diverse techniques. After the complete study, they indicated that roughness in porous supports determines the adherence of the films, being the presence of larger pores more favorable for increasing the adhesion of the palladium coating and, consequently, the mechanical resistance of the composite membrane. In Fig. 2.22, adapted from the images presented in the original work, the results obtained after using each technique for three different membranes are summarized: A, B, and C (from the left to the right). As it can be seen, the membrane C, prepared over a rough surface, exhibited the better adherence for the palladium layer, while the other ones presented delamination and weak mechanical resistance. More recently, Wald et al. [167] studied the strength, hardness, and ductility variations after successive hydrogen absorption/desorption cycles of Pd-Ag alloys. They observed the main changes to the mechanical properties occur just after the first hydrogen exposure treatment and the magnitude of the change is function of the silver content in the alloy, decreasing as it increases.

2.4.10 Gas Permeation Measurements

The coatings prepared as thin film membranes always need to be evaluated in terms of permeation capacity, independently of previous characterization carried out. This crucial property will determine the real behavior of the membrane through gas permeation experiments, the most suitable applications for the obtained material, and the recommended limits for operating conditions.

Usually, a first experiment called bubble point test can be employed in order to evaluate rapidly the homogeneity of the film and the presence of defects, cracks, and pinholes at room temperature. This test consists of dipping the membrane into a solution (tipically, water or isopropanol solution) and feeding an inert gas (i.e., helium, argon, or nitrogen) from one side of the film at a constant pressure, detecting the formation of bubbles on the contrary membrane surface. In case of preparing dense palladium or ceramic films, the nonappearance of bubbles indicates a good continuity in the metal films and, consequently, the absence of defects, cracks, or pinholes [43, 51, 72, 73]. On the other hand, in case of considering porous ceramic films, this test provides a qualitative useful information about porosity homogeneity, being possible to detect defects from areas where a great amount of big bubbles are generated. Jakobs and Koros presented the use of this technique in the 1990s as an easy, fast, and inexpensive method to determine both maximum pore size and pore size distribution of diverse ceramic membranes [168], while Reichelt extends the application of this techniques on large membrane areas up to 1 m^2 [169]. From these first applications, many authors include similar experiments

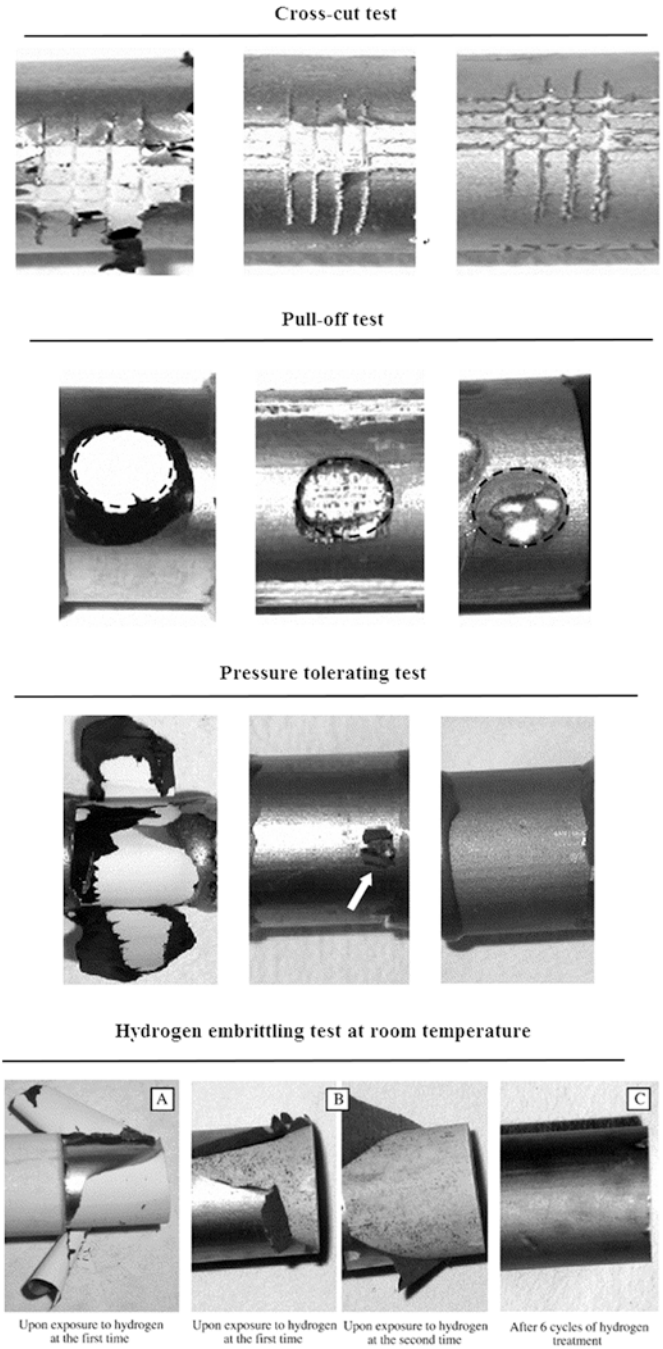

Fig. 2.22 Mechanical experiments over three different composite Pd-ceramic membranes (A, B, and C) prepared by ELP: cross-cut, pull-off, pressure tolerance, and H_2 embrittlement tests. Adapted from [32]

prior to analyzing the permeation behavior at operating conditions, i.e., high temperature or gas mixtures in feed stream.

After these preliminary experiments, real gas permeation measurements are usually carried out at operating conditions in order to determine the real behavior of the membrane in terms of permeated flux, selectivity, and resistance of the material. The effect of pressure, temperature, and feed composition are the most common parameters analyzed in these cases.

The influence of pressure on the membrane behavior is determined by representing the permeate flux versus the pressure, which represents the driving force of the permeation process and it is expressed as partial pressure difference between retentate and permeate sides. In case of using palladium-based membranes, all values are referred to the hydrogen content and the experimental data is fitted to the following general expression:

$$J_{H_2} = \frac{p_{H_2}\left(P^n_{H_2,ret} - P^n_{H_2,perm}\right)}{t} \tag{2.1}$$

where J_{H_2} represents the hydrogen permeate flux through the membrane film, p_{H_2} the hydrogen permeability, t the film thickness, P_{H_2} the hydrogen partial pressure in the retentate (subscript *"ret"*) or the permeate side (subscript *"ret"*), and n an exponential factor ranged from 0.5 to 1 that represents the rate-controlling step for the permeation process. For completely free-defect palladium films with thickness upper than 1 μm, hydrogen diffusion though bulk metal is the limiting step of the global permeation mechanism and a good fitting can be achieved considering $n = 0.5$, named the expression as the Sieverts' law [170, 171]. On the contrary, deviations from this general expression are quantified by varying the coefficient between $n = 0.5$–1 and they can be caused by the presence of defects or additional resistances to the hydrogen permeation process (i.e., problems in the gas phase diffusion or hydrogen dissociation steps) [172].

It is clear that the hydrogen permeation flux can be maximized by increasing the pressure driving force or decreasing the film thickness, but also depends on the membrane permeability (p_{H_2}). This parameter only relays on the film composition and usually is affected by the temperature through an Arrhenius-type dependence [173].

$$p_{H_2} = p^0_{H_2} \mathrm{e}^{\left(-\frac{E_a}{RT}\right)} \tag{2.2}$$

Besides pressure, temperature, presence of defects, membrane composition, and film thickness, the permeation flux can also be affected by the gas feed composition. All these effects are typically analyzed from experimental data representation as depicted in Fig. 2.23, reproduced from the original work presented by Sanz et al. [43]. Figure 2.23a shows a reasonable good fitting of permeation data to the Sieverts' law ($n = 0.5$) and the temperature effect on the hydrogen permeability (obtained from the diverse slopes in fitting equations). Figure 2.23b represents the

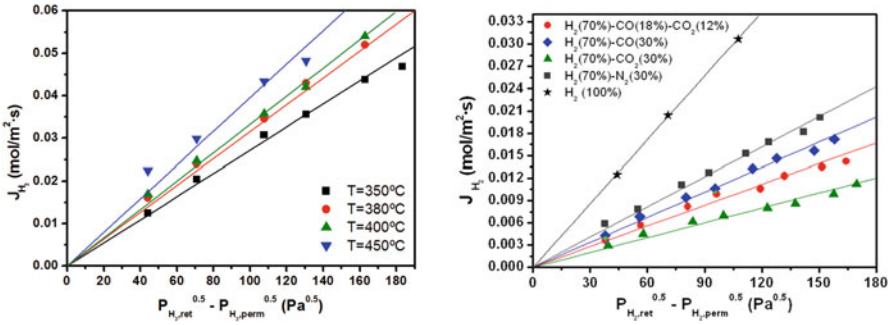

Fig. 2.23 Conventional representation of H_2 flux vs. pressure difference accordingly the Sieverts' law for determination of permeation behavior of Pd membranes: (**a**) temperature effect and (**b**) influence of feed composition. Adapted from [43]

influence of carrying out the permeation experiments with diverse feed gas composition on the obtained hydrogen permeability. As it can be observed in the last case, the presence of carbon dioxide and carbon monoxide in the feed stream clearly affect to the permeation process, reducing the hydrogen flux through the thin palladium film at analogous operating conditions.

Finally, selectivity needs to be also determined to evaluate the quality of the membrane films. As an example, only hydrogen can permeate through dense palladium or palladium alloys coatings, although it is usual to find some residual amounts of other gases from the feed stream in the permeate, mainly due to intrinsic defects or membrane deterioration with time. In order to determine the hydrogen selectivity, researchers usually differentiate between ideal separation factor and "real" selectivity.

The first parameter, ideal separation factor, is calculated from total permeate fluxes when hydrogen and other inert compounds, typically helium or nitrogen, are fed to the membrane module separately, being denoted as:

$$\alpha_{\text{ideal}} = \frac{J_{H_2}^{perm}}{J_i^{perm}} \tag{2.3}$$

This ideal separation factor is usually defined as the maximum capability of the membrane for separating compounds, and it is widely accepted to present this value for comparison of diverse membranes.

On the other hand, real selectivity is expressed as the ratio between the hydrogen (y_{H_2}) and the inert gas (y_i) molar fractions in permeate and retentate streams. This parameter determines the separation efficiency of a membrane at real operation conditions when diverse compounds are fed simultaneously.

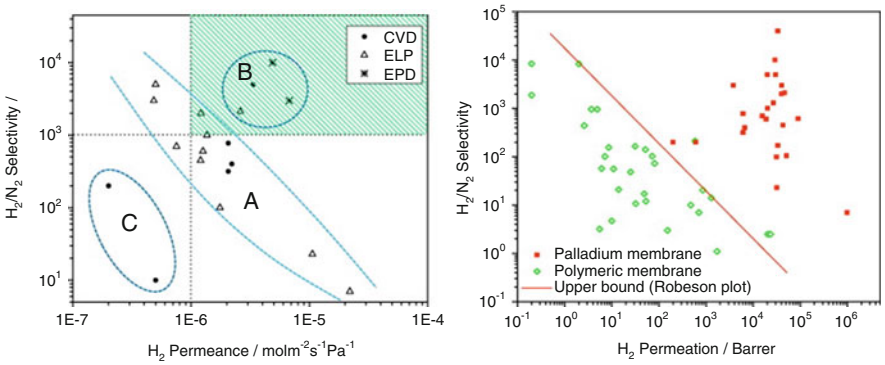

Fig. 2.24 Relationship between ideal H_2/N_2 selectivity and H_2 permeance for diverse membranes: (**a**) Pd-based membranes prepared by different techniques and (**b**) comparison of metallic and polymeric membranes. Adapted from original figures in [17]

$$\alpha_{\text{real}} = \frac{y_{H_2}^{perm} / y_i^{perm}}{y_{H_2}^{ret} / y_i^{ret}} \tag{2.4}$$

In this manner, the selection of a membrane must be carried out attending simultaneously both permeate flux (permeation capability) and selectivity to the compound of interest (separation potential). Figure 2.24 shows different representations for comparing diverse membranes through these permeation properties, permeance and H_2 selectivity. Figure 2.24a compares similar Pd-based membranes prepared by diverse techniques, while Fig. 2.24b compares the permeation behavior of palladium and polymeric membranes.

Acknowledgements First of all, I want to acknowledge prof. Jing Zhang the opportunity to contribute in the preparation of this book. Also, it has been very important the support of prof. José Antonio Calles and prof. Raúl Sanz for developing my research career during the last years in the field of palladium membranes for hydrogen production in a membrane reactor, as well as the support of my host institution, the University Rey Juan Carlos, where I am currently working as associate professor. Lastly, I am grateful to the publishers of cited figures for allowing the reproduction of the images in the present chapter.

References

1. S.N. Paglieri, J.D. Way, Innovations in palladium membrane research. Sep Purif Methods **31** (1), 1–169 (2002)
2. S. Tosti, Overview of Pd-based membranes for producing pure hydrogen and state of art at ENEA laboratories. Int. J. Hydrog. Energy **35**, 12650–12659 (2010)

3. S. Tosti, C. Rizzello, Membranes for Nuclear Power Applications, in *Advanced Membrane Science and Technology for Sustainable Energy and Environmental Applications*, ed. by A. Basile, S. Nunes (Eds), (Woodhead Publishing Series in Energy, Cambridge, 2011), pp. 769–791
4. S. Tosti, A. Basile, L. Bettinali, F. Borgognoni, F. Gallucci, C. Rizzello, Design and process study of Pd membrane reactors. Int. J. Hydrog. Energy **33**(19), 5098–5105 (2008)
5. A. Santucci, F. Borgognoni, M. Vadrucci, S. Tosti, Testing of dense Pd-Ag tubes: effect of pressure and membrane thickness on the hydrogen permeability. J. Membr. Sci. **444**, 378–383 (2013)
6. S. Tosti, Supported and laminated Pd-based metallic membranes. Int. J. Hydrog. Energy **28** (12), 1445–1454 (2003)
7. A. Basile, F. Gallucci, S. Tosti, Synthesis, characterization, and applications of palladium membranes. Membr. Sci. Technol. **13**, 255–323 (2008)
8. Y.S. Cheng, K.L. Yeung, Palladium-silver composite membranes by electroless plating technique. J. Membr. Sci. **158**(1), 127–141 (1999)
9. E. Fernandez, J.A. Medrano, J. Melendez, M. Parco, J.L. Viviente, M. van Sint Annaland, D.A. Pacheco Tanaka, Preparation and characterization of metallic supported thin Pd-Ag membranes for hydrogen separation. Chem. Eng. J. **305**, 182–190 (2016)
10. J.A. Medrano, E. Fernandez, J. Melendez, M. Parco, D.A.P. Tanaka, M. van Sint Annaland, F. Gallucci, Pd-based metallic supported membranes: high-temperature stability and fluidized bed reactor testing. Int. J. Hydrog. Energy **41**(20), 8706–8718 (2016)
11. T. Nakajima, T. Kume, Y. Ikeda, M. Shiraki, H. Kurokawa, T. Iseki, M. Ito, Effect of concentration polarization on hydrogen production performance of ceramic-supported Pd membrane module. Int. J. Hydrog. Energy **40**(35), 11451–11456 (2015)
12. H. Richter, Large-Scale Ceramic Support Fabrication for Palladium Membranes, in *Palladium Membrane Technology for Hydrogen Production, Carbon Capture and Other Applications*, ed. by A. Doukelis, K. Panopoulos, A. Koumanakos, E. Kakaras (Eds), (Woodhead Publishing, Cambridge, 2015), pp. 69–82
13. I. Pinnau, Membrane Separations: Membrane Preparation, in *Encyclopedia of Separation Science*, ed. by C. Poole, M. Cooke (Eds), (Elsevier, Oxford, 2007), pp. 1755–1764
14. D. Pizzi, R. Worth, B.M. Giacinti, G.C. Sarti, K. Noda, Hydrogen permeability of 2.5μm palladium-silver membranes deposited on ceramic supports. J. Membr. Sci. **325**(1), 446–453 (2008)
15. J. Catalano, B.M. Giacinti, G.C. Sarti, Influence of the gas phase resistance on hydrogen flux through thin palladium-silver membranes. J. Membr. Sci. **339**(1), 57–67 (2009)
16. Ø. Hatlevik, S.K. Gade, M.K. Keeling, P.M. Thoen, A.P. Davidson, J.D. Way, Palladium and palladium alloy membranes for hydrogen separation and production: history, fabrication strategies, and current performance. Sep. Purif. Technol. **73**(1), 59–64 (2010)
17. S. Yun, O.S. Ted, Correlations in palladium membranes for hydrogen separation: a review. J. Membr. Sci. **375**(1–2), 28–45 (2011)
18. P. Pinacci, A. Basile, Palladium-Based Composite Membranes for Hydrogen Separation in Membrane Reactors, in *Handbook of Membrane Reactors*, Fundamental Materials Science, Design and Optimisation, ed. by A. Basile (Ed), vol. 1, (Woodhead Publishing Series in Energy, 2013), pp. 149–182
19. P.P. Mardilovich, Y. She, Y.H. Ma, Defect-free palladium membranes on porous stainless-steel support. AIChE J. **44**(2), 310–322 (1998)
20. A. Li, J.R. Grace, C.J. Lim, Preparation of thin Pd-based composite membrane on planar metallic substrate: part I: pre-treatment of porous stainless steel substrate. J. Membr. Sci. **298** (1), 175–181 (2007)
21. S.S. Kim, N. Xu, A. Li, J.R. Grace, C.J. Lim, S.-K. Ryi, Development of a new porous metal support based on nickel and its application for Pd based composite membranes. Int. J. Hydrog. Energy **40**(8), 3520–3527 (2015)
22. C. Lee, A. Kim, J. Kim, Electrochemically etched porous stainless steel for enhanced oil retention. Surf. Coat. Technol. **264**(25), 127–131 (2015). https://doi.org/10.1016/j.surfcoat.2015.01.004

23. N. Jemaa, J. Shu, S. Kaliaguine, P.A. Grandjean, Thin palladium film formation on shot peening modified porous stainless steel substrates. Ind. Eng. Chem. Res. **35**, 973–977 (1996)
24. V. Jayaraman, Y.S. Lin, M. Pakala, R.Y. Lin, Fabrication of ultrathin metallic membranes on ceramic supports by sputter deposition. J. Membr. Sci. **99**(1), 89–100 (1995)
25. S.-K. Ryi, J.-S. Park, S.-H. Kim, D.-W. Kim, K.-I. Cho, Formation of a defect-free Pd-Cu-Ni ternary alloy membrane on a polished porous nickel support (PNS). J. Membr. Sci. **318**(1), 346–354 (2008)
26. P. Pinacci, F. Drago, Influence of the support on permeation of palladium composite membranes in presence of sweep gas. Catal. Today **193**(1), 186–193 (2012)
27. D. Alique, Modification of porous stainless-steel support for the preparation of Pd membrane. Network Young MemBrains 8th Meeting. Rende, Italy, 2006, pp. 81–82
28. S.-K. Ryi, J.-S. Park, K.-R. Hwang, C.-B. Lee, S.-W. Lee, Repair of Pd-based composite membrane by polishing treatment. Int. J. Hydrog. Energy **36**(21), 13776–13780 (2011)
29. Y. Huang, R. Dittmeyer, Preparation of thin palladium membranes on a porous support with rough surface. J. Membr. Sci. **302**(1), 160–170 (2007)
30. Y. Huang, X. Li, Y. Fan, N. Xu, Palladium-based composite membranes: Principle, preparation and characterization. Prog. Chem. **18**, 230–238 (2006)
31. J.P. Collins, J.D. Way, Catalytic decomposition of ammonia in a membrane reactor. J. Membr. Sci. **96**(3), 259–274 (1994)
32. Y. Huang, S. Shu, Z. Lu, Y. Fan, Characterization of the adhesion of thin palladium membranes supported on tubular porous ceramics. Thin Solid Films **515**(13), 5233–5240 (2007)
33. D. Wang, J. Tong, H. Xu, Y. Matsumura, Preparation of palladium membrane over porous stainless steel tube modified with zirconium oxide. Catal. Today **93–95**, 689–693 (2004)
34. S.-E. Nam, K.-H. Lee, Preparation and characterization of palladium alloy composite membranes with a diffusion barrier for hydrogen separation. Ind. Eng. Chem. Res. **44**(1), 100–105 (2005)
35. J. Coronas, Santamarıa J. Catalytic reactors based on porous ceramic membranes. Catal. Today **51**(3), 377–389 (1999)
36. H. Lim, S.T. Oyama, Hydrogen selective thin palladium-copper composite membranes on alumina supports. J. Membr. Sci. **378**(1), 179–185 (2011)
37. L. Zheng, H. Li, H. Xu, "Defect-free" interlayer with a smooth surface and controlled pore-mouth size for thin and thermally stable Pd composite membranes. Int. J. Hydrog. Energy **41** (2), 1002–1009 (2016)
38. X. Hu, W. Chen, Y. Huang, Fabrication of Pd/ceramic membranes for hydrogen separation based on low-cost macroporous ceramics with pencil coating. Int. J. Hydrog. Energy **35**(15), 7803–7808 (2010)
39. H.-B. Zhao, K. Pflanz, J.-H. Gu, A.-W. Li, N. Stroh, H. Brunner, G.-X. Xiong, Preparation of palladium composite membranes by modified electroless plating procedure. J. Membr. Sci. **142**(2), 147–157 (1998)
40. D.A. Pacheco Tanaka, M.A.L. Tanco, J. Okazaki, Y. Wakui, F. Mizukami, T.M. Suzuki, Preparation of "pore-fill" type Pd-YSZ-γ-Al_2O_3 composite membrane supported on α-Al_2O_3 tube for hydrogen separation. J. Membr. Sci. **320**(1–2), 436–441 (2008)
41. A. Arratibel, U. Astobieta, D.A. Pacheco Tanaka, M. Van Sint Annaland, F. Gallucci, N_2, He and CO_2 diffusion mechanism through nanoporous YSZ/γ-Al_2O_3 layers and their use in a pore-filled membrane for hydrogen membrane reactors. Int. J. Hydrog. Energy **41**(20), 8732–8744 (2016)
42. D. Yepes, L.M. Cornaglia, S. Irusta, E.A. Lombardo, Different oxides used as diffusion barriers in composite hydrogen permeable membranes. J. Membr. Sci. **274**(1–2), 92–101 (2006)
43. R. Sanz, J.A. Calles, D. Alique, L. Furones, H_2 production via water gas shift in a composite Pd membrane reactor prepared by the pore-plating method. Int. J. Hydrog. Energy **39**(9), 4739–4748 (2014)

44. Y.H. Ma, B.C. Akis, M.E. Ayturk, F. Guazzone, E.E. Engwall, I.P. Mardilovich, Characterization of intermetallic diffusion barrier and alloy formation for Pd/Cu and Pd/Ag porous stainless steel composite membranes. Ind. Eng. Chem. Res. **43**(12), 2936–2945 (2004)
45. Y.H. Ma, P.P. Mardilovich, Y. She, U.S. Patent 6,152,987
46. F. Guazzone, E.E. Engwall, Y.H. Ma, Effects of surface activity, defects and mass transfer on hydrogen permeance and n-value in composite palladium-porous stainless steel membranes. Catal. Today **118**(1–2), 24–31 (2006)
47. C. Mateos-Pedrero, M.A. Soria, I. Rodríguez-Ramos, A. Guerrero-Ruiz, Modifications of porous stainless steel previous to the synthesis of Pd membranes. Stud. Surf. Sci. Catal. **175**, 779–783 (2010)
48. G.T. Van, F. Hauler, M. Bram, W.A. Meulenberg, H.P. Buchkremer, Synthesis and characterization of hydrogen-selective sol-gel SiO_2 membranes supported on ceramic and stainless steel supports. Sep. Purif. Technol. **121**, 20–29 (2014)
49. M. Kanezashi, D. Fuchigami, T. Yoshioka, T. Tsuru, Control of Pd dispersion in sol-gel-derived amorphous silica membranes for hydrogen separation at high temperatures. J. Membr. Sci. **439**, 78–86 (2013)
50. S.-E. Nam, K.-H. Lee, Hydrogen separation by Pd alloy composite membranes: introduction of diffusion barrier. J. Membr. Sci. **192**(1), 177–185 (2001)
51. J.A. Calles, R. Sanz, D. Alique, Influence of the type of siliceous material used as intermediate layer in the preparation of hydrogen selective palladium composite membranes over a porous stainless steel support. Int. J. Hydrog. Energy **37**(7), 6030–6042 (2012)
52. L. Zheng, H. Li, T. Xu, F. Bao, H. Xu, Defect size analysis approach combined with silicate gel/ceramic particles for defect repair of Pd composite membranes. Int. J. Hydrog. Energy **41** (41), 18522–18532 (2016)
53. M. Broglia, P. Pinacci, M. Radaelli, A. Bottino, G. Capannelli, A. Comite, G. Vanacore, M. Zani, Synthesis and characterization of Pd membranes on alumina-modified porous stainless steel supports. Desalination **245**(1–3), 508–515 (2009)
54. Y.-H. Chi, P.-S. Yen, M.-S. Jeng, S.-T. Ko, T.-C. Lee, Preparation of thin Pd membrane on porous stainless steel tubes modified by a two-step method. Int. J. Hydrog. Energy **35**(12), 6303–6310 (2010)
55. C.-B. Lee, S.-W. Lee, J.-S. Park, S.-K. Ryi, D.-W. Lee, K.-R. Hwang, S.-H. Kim, Ceramics used as intermetallic diffusion barriers in Pd-based composite membranes sputtered on porous nickel supports. J. Alloys Compd. **578**, 425–430 (2013)
56. A. Bottino, M. Broglia, G. Capannelli, A. Comite, P. Pinacci, M. Scrignari, F. Azzurri, Sol-gel synthesis of thin alumina layers on porous stainless steel supports for high temperature palladium membranes. Int. J. Hydrog. Energy **39**(9), 4717–4724 (2014)
57. G.T.P. Mabande, G. Pradhan, W. Schwieger, M. Hanebuth, R. Dittmeyer, T. Selvam, A. Zampieri, H. Baser, R. Herrmann, A study of Silicalite-1 and Al-ZSM-5 membrane synthesis on stainless steel supports. Microporous Mesoporous Mater. **75**(3), 209–220 (2004)
58. M.L. Bosko, F. Ojeda, E.A. Lombardo, L.M. Cornaglia, NaA zeolite as an effective diffusion barrier in composite Pd/PSS membranes. J. Membr. Sci. **331**(1), 57–65 (2009)
59. M.M. Dehghani, P. Jafari, M. Irani, Preparation of Pd-based membranes on Pd/TiO_2 modified NaX/PSS substrate for hydrogen separation: design and optimization. Microporous Mesoporous Mater. **226**, 369–377 (2016)
60. Y. Guo, Y. Jin, H. Wu, L. Zhou, Q. Chen, X. Zhang, X. Li, Preparation of palladium membrane on Pd/silicalite-1 zeolite particles modified macroporous alumina substrate for hydrogen separation. Int. J. Hydrog. Energy **39**(36), 21044–21052 (2014)
61. Y. Guo, Y.J. Jin, H.M. Wu, D.X. Li, L.D. Zhou, Q.Q. Chen, X.F. Zhang, Preparation of Pd composite membrane and its surface morphological changes after elevating temperature in different Atmoshphere. Mater Process Technol **941**, 1602–1605 (2014)
62. X. Wang, X. Tan, B. Meng, X. Zhang, Q. Liang, H. Pan, S. Liu, TS-1 zeolite as an effective diffusion barrier for highly stable Pd membrane supported on macroporous α-Al_2O_3 tube. RSC Adv. **3**(14), 4821–4834 (2013)

63. J. Yu, C. Qi, J. Zhang, C. Bao, H. Xu, Synthesis of a zeolite membrane as a protective layer on a metallic Pd composite membrane for hydrogen purification. J. Mater. Chem. A **3**(9), 5000–5006 (2015)
64. K. Sato, M. Natsui, Y. Hasegawa, Preparation of double layer membrane combined with palladium metal and FAU zeolite for catalytic membrane reactor. Mater. Trans. JIM **56**(4), 473–478 (2015)
65. S. Abate, U. Díaz, A. Prieto, S. Gentiluomo, M. Palomino, S. Perathoner, A. Corma, G. Centi, Influence of zeolite protective overlayer on the performances of Pd thin film membrane on tubular asymmetric alumina supports. Ind. Eng. Chem. Res. **55**(17), 4948–4959 (2016)
66. J. Tong, Y. Matsumura, H. Suda, K. Haraya, Thin and dense Pd/CeO_2/MPSS composite membrane for hydrogen separation and steam reforming of methane. Sep. Purif. Technol. **46** (1), 1–10 (2005)
67. A. Qiao, K. Zhang, Y. Tian, L. Xie, H. Luo, Y.S. Lin, Y. Li, Hydrogen separation through palladium-copper membranes on porous stainless steel with sol-gel derived ceria as diffusion barrier. Fuel **89**(6), 1274–1279 (2010)
68. H.S. Gao, J.Y. Lin, Y. Li, B. Zhang, Electroless plating synthesis, characterization and permeation properties of Pd-Cu membranes supported on ZrO_2 modified porous stainless steel. J. Membr. Sci. **265**(1), 142–152 (2005)
69. A. Tarditi, C. Gerboni, L. Cornaglia, PdAu membranes supported on top of vacuum-assisted ZrO_2-modified porous stainless steel substrates. J. Membr. Sci. **428**, 1–10 (2013)
70. S.-K. Ryi, S.-W. Lee, D.-K. Oh, B.-S. Seo, J.-W. Park, J.-S. Park, D.-W. Lee, S.S. Kim, Electroless plating of Pd after shielding the bottom of planar porous stainless steel for a highly stable hydrogen selective membrane. J. Membr. Sci. **467**, 93–99 (2014)
71. K. Zhang, H. Gao, Z. Rui, P. Liu, Y. Li, Y.S. Lin, High-temperature stability of palladium membranes on porous metal supports with different intermediate layers. Ind. Eng. Chem. Res. **48**(4), 1880–1886 (2009)
72. R. Sanz, J.A. Calles, D. Alique, L. Furones, S. Ordóñez, P. Marín, P. Corengia, E. Fernandez, Preparation, testing and modelling of a hydrogen selective Pd/YSZ/SS composite membrane. Int. J. Hydrog. Energy **36**(24), 15783–15793 (2011)
73. J.A. Calles, R. Sanz, D. Alique, L. Furones, Thermal stability and effect of typical water gas shift reactant composition on H_2 permeability through a Pd-YSZ-PSS composite membrane. Int. J. Hydrog. Energy **39**(3), 1398–1409 (2014)
74. J. Tong, R. Shirai, Y. Kashima, Y. Matsumura, Preparation of a pinhole-free Pd-Ag membrane on a porous metal support for pure hydrogen separation. J. Membr. Sci. **260**(1), 84–89 (2005)
75. M.E. Ayturk, I.P. Mardilovich, E.E. Engwall, Y.H. Ma, Synthesis of composite Pd-porous stainless steel (PSS) membranes with a Pd/Ag intermetallic diffusion barrier. J. Membr. Sci. **285**(1), 385–394 (2006)
76. J.-H. Lee, J.-Y. Han, K.-M. Kim, S.-K. Ryi, D.-W. Kim, Development of homogeneous Pd-Ag alloy membrane formed on porous stainless steel by multi-layered films and Ag-upfilling heat treatment. J. Membr. Sci. **492**, 242–248 (2015)
77. Y.-H. Chi, J.-Y. Uan, M.-C. Lin, Y.-L. Lin, J.-H. Huang, Preparation of a novel Pd/layered double hydroxide composite membrane for hydrogen filtration and characterization by thermal cycling. Int. J. Hydrog. Energy **38**(31), 13734–13741 (2013)
78. M. Pujari, A. Agarwal, R. Uppaluri, A. Verma, Role of electroless nickel diffusion barrier on the combinatorial plating characteristics of dense Pd/Ni/PSS composite membranes. Appl. Surf. Sci. **305**, 658–664 (2014)
79. S. Nayebossadri, S. Fletcher, J.D. Speight, D. Book, Hydrogen permeation through porous stainless steel for palladium-based composite porous membranes. J. Membr. Sci. **515**, 22–28 (2016)
80. T. Nozaki, Y. Hatano, E. Yamakawa, A. Hachikawa, K. Ichinose, Improvement of high temperature stability of Pd coating on Ta by HfN intermediate layer. Int. J. Hydrog. Energy **35**(22), 12454–12460 (2010)

81. T. Nozaki, Y. Hatano, Hydrogen permeation through a Pd/Ta composite membrane with a HfN intermediate layer. Int. J. Hydrog. Energy **38**(27), 11983–11987 (2013)
82. J. Tong, H. Suda, K. Haraya, Y. Matsumura, A novel method for the preparation of thin dense Pd membrane on macroporous stainless steel tube filter. J. Membr. Sci. **260**(1), 10–18 (2005)
83. J. Tong, L. Su, K. Haraya, H. Suda, Thin Pd membrane on α-Al_2O_3 hollow fiber substrate without any interlayer by electroless plating combined with embedding Pd catalyst in polymer template. J. Membr. Sci. **310**(1–2), 93–101 (2008)
84. B.D. Adams, A. Chen, The role of palladium in a hydrogen economy. Mater. Today **14**(6), 282–289 (2001)
85. N.A. Al-Mufachi, N.V. Rees, R. Steinberger-Wilkens, Hydrogen selective membranes: a review of palladium-based dense metal membranes. Renew. Sust. Energ. Rev. **47**, 540–551 (2015)
86. U. Balachandran, T.H. Lee, C.Y. Park, J.E. Emerson, J.J. Picciolo, S.E. Dorris, Dense cermet membranes for hydrogen separation. Sep. Purif. Technol. **121**, 54–59 (2014)
87. J. Boon, J.A.Z. Pieterse, F.P.F. van Berkel, Y.C. van Delft, M. van Sint Annaland, Hydrogen permeation through palladium membranes and inhibition by carbon monoxide, carbon dioxide, and steam. J. Membr. Sci. **496**, 344–358 (2015)
88. J. Catalano, M.G. Baschetti, G.C. Sarti, Hydrogen permeation in palladium-based membranes in the presence of carbon monoxide. J. Membr. Sci. **362**(1–2), 221–233 (2010)
89. L. Cornaglia, J. Múnera, E. Lombardo, Recent advances in catalysts, palladium alloys and high temperature WGS membrane reactors: a review. Int. J. Hydrog. Energy **40**(8), 3423–3437 (2015)
90. Z.W. Dunbar, Hydrogen purification of synthetic water gas shift gases using microstructured palladium membranes. J. Power Sources **297**, 525–533 (2015)
91. G.Q. Lu, J.C.D. da Costa, M. Duke, S. Giessler, R. Socolow, R.H. Williams, T. Kreutz, Inorganic membranes for hydrogen production and purification: a critical review and perspective. J. Colloid Interface Sci. **314**(2), 589–603 (2007)
92. F.R. García-García, L. Torrente-Murciano, D. Chadwick, K. Li, Hollow fibre membrane reactors for high H_2 yields in the WGS reaction. J. Membr. Sci. **405–406**, 30–37 (2012)
93. J. Melendez, E. Fernandez, F. Gallucci, M. van Sint Annaland, P.L. Arias, D.A.P. Tanaka, Preparation and characterization of ceramic supported ultra-thin (~1 μm) Pd-Ag membranes. J. Membr. Sci. **528**, 12–23 (2017)
94. G. Zeng, A. Goldbach, H. Xu, Defect sealing in Pd membranes via point plating. J. Membr. Sci. **328**(1–2), 6–10 (2009)
95. R. Sanz, J.A. Calles, D. Alique, L. Furones, New synthesis method of Pd membranes over tubular PSS supports via "pore-plating" for hydrogen separation processes. Int. J. Hydrog. Energy **37**(23), 18476–18485 (2012)
96. S.K. Gade, S.J. DeVoss, K.E. Coulter, S.N. Paglieri, G.O. Alptekin, J.D. Way, Palladium-gold membranes in mixed gas streams with hydrogen sulfide: effect of alloy content and fabrication technique. J. Membr. Sci. **378**(1–2), 35–41 (2011)
97. A.E. Lewis, H. Zhao, H. Syed, C.A. Wolden, J.D. Way, PdAu and PdAuAg composite membranes for hydrogen separation from synthetic water-gas shift streams containing hydrogen sulfide. J. Membr. Sci. **465**, 167–176 (2014)
98. M. Voldsund, K. Jordal, R. Anantharaman, Hydrogen production with CO_2 capture. Int. J. Hydrog. Energy **41**(9), 4969–4992 (2016)
99. D.M. Mattox, Vacuum Evaporation and Vacuum Deposition, in *Handbook of Physical Vapor Deposition (PVD) Processing*, (Elsevier, Oxford, 2010), pp. 195–235
100. R. Checchetto, N. Bazzanella, B. Patton, A. Miotello, Palladium membranes prepared by r.f. magnetron sputtering for hydrogen purification. Surf. Coat. Technol. **177**, 73–79 (2004)
101. B. Navinšek, P. Panjan, I. Milošev, PVD coatings as an environmentally clean alternative to electroplating and electroless processes. Surf. Coat. Technol. **116**, 476–487 (1999)
102. T.A. Peters, M. Stange, R. Bredesen, Fabrication of palladium-based membranes by magnetron sputtering, in *Palladium Membrane Technology for Hydrogen Production, Carbon*

Capture and Other Applications, ed. by A. Doukelis, K. Panopoulos, A. Koumanakos, E. Kakara (Eds), (Woodhead Publishing, 2015), pp. 25–41
103. W.M. Tucho, H.J. Venvik, M. Stange, J.C. Walmsley, R. Holmestad, R. Bredesen, Effects of thermal activation on hydrogen permeation properties of thin, self-supported Pd/Ag membranes. Sep. Purif. Technol. **68**(3), 403–410 (2009)
104. A.L. Mejdell, T.A. Peters, M. Stange, H.J. Venvik, R. Bredesen, Performance and application of thin Pd-alloy hydrogen separation membranes in different configurations. J. Taiwan Inst. Chem. Eng. **40**(3), 253–259 (2009)
105. T.A. Peters, M. Stange, R. Bredesen, On the high pressure performance of thin supported Pd-23%Ag membranes—evidence of ultrahigh hydrogen flux after air treatment. J. Membr. Sci. **378**(1–2), 28–34 (2011)
106. T.A. Peters, T. Kaleta, M. Stange, R. Bredesen, Hydrogen transport through a selection of thin Pd-alloy membranes: membrane stability, H_2S inhibition, and flux recovery in hydrogen and simulated WGS mixtures. Catal. Today **193**(1), 8–19 (2012)
107. T.A. Peters, T. Kaleta, M. Stange, R. Bredesen, Development of ternary Pd-Ag-TM alloy membranes with improved sulphur tolerance. J. Membr. Sci. **429**, 448–458 (2013)
108. A. Li, J.R. Grace, C.J. Lim, Preparation of thin Pd-based composite membrane on planar metallic substrate: part II. Preparation of membranes by electroless plating and characterization. J. Membr. Sci. **306**(1–2), 159–165 (2007)
109. B. Zornoza, C. Casado, A. Navajas, Advances in Hydrogen Separation and Purification with Membrane Technology, in *Renewable Hydrogen Technologies*, ed. by L. M. Gandía, G. Arzamendi, P. M. Diéguez (Eds), (Elsevier, Amsterdam, 2013), pp. 245–268
110. M. De Falco, G. Iaquaniello, E. Palo, B. Cucchiella, V. Palma, P. Ciambelli, Palladium-Based Membranes for Hydrogen Separation: Preparation, Economic Analysis and Coupling with a Water Gas Shift Reactor, in *Handbook of Membrane Reactors*, ed. by A. Basile (Ed), (Woodhead Publishing, 2013), pp. 456–486
111. M.J. den Exter, The Use of Electroless Plating as a Deposition Technology in the Fabrication of Palladium-Based Membranes, in *Palladium Membrane Technology for Hydrogen Production, Carbon Capture and Other Applications*, Woodhead Publishing, ed. by A. Doukelis, K. Panopoulos, A. Koumanakos, E. Kakaras (Eds), vol. 2015, (2015), pp. 43–67
112. D.A.P. Tanaka, J. Okazaki, M.A.L. Tanco, T.M. Suzuki, Fabrication of Supported Palladium Alloy Membranes Using Electroless Plating Techniques, in *Palladium Membrane Technology for Hydrogen Production, Carbon Capture and Other Applications*, Woodhead Publishing, ed. by A. Doukelis, K. Panopoulos, A. Koumanakos, E. Kakaras (Eds), vol. 2015, (2015), pp. 83–99
113. A. Basile, J. Tong, P. Millet, Inorganic Membrane Reactors for Hydrogen Production: An Overview with Particular Emphasis on Dense Metallic Membrane Materials, in *Handbook of Membrane Reactors*, Woodhead Publishing, ed. by A. Basile (Ed), vol. 2013, (2013), pp. 42–148
114. Y.S. Cheng, K.L. Yeung, Effects of electroless plating chemistry on the synthesis of palladium membranes. J. Membr. Sci. **182**(1–2), 195–203 (2001)
115. J. Shu, B.P.A. Grandjean, E. Ghali, S. Kaliaguine, Simultaneous deposition of Pd and Ag on porous stainless steel by electroless plating. J. Membr. Sci. **77**(2–3), 181–195 (1993)
116. K.S. Rothenberger, A.V. Cugini, B.H. Howard, R.P. Killmeyer, M.V. Ciocco, B.D. Morreale, R.M. Enick, F. Bustamante, I.P. Mardilovich, Y.H. Ma, High pressure hydrogen permeance of porous stainless steel coated with a thin palladium film via electroless plating. J. Membr. Sci. **244**(1–2), 55–68 (2004)
117. L. Wei, J. Yu, X. Hu, R. Wang, Y. Huang, Effects of Sn residue on the high temperature stability of the H_2-permeable palladium membranes prepared by electroless plating on Al_2O_3 substrate after $SnCl_2$-$PdCl_2$ process: a case study. Chin. J. Chem. Eng. **24**(9), 1154–1160 (2016)
118. F. Touyeras, J.Y. Hihn, S. Delalande, R. Viennet, M.L. Doche, Ultrasound influence on the activation step before electroless coating. Ultrason. Sonochem. **10**(6), 363–368 (2003)

119. R. Sanz, J.A. Calles, S. Ordóñez, P. Marín, D. Alique, L. Furones, Modelling and simulation of permeation behaviour on Pd/PSS composite membranes prepared by "pore-plating" method. J. Membr. Sci. **446**, 410–421 (2013)
120. M. Seshimo, M. Ozawa, M. Sone, M. Sakurai, H. Kameyama, Fabrication of a novel Pd/γ-alumina graded membrane by electroless plating on nanoporous γ-alumina. J. Membr. Sci. **324**(1–2), 181–187 (2008)
121. S. Uemiya, N. Sato, H. Ando, E. Kikuchi, The water gas shift reaction assisted by a palladium membrane reactor. Ind. Eng. Chem. Res. **30**(3), 585–589 (1991)
122. K.L. Yeung, J.M. Sebastian, A. Varma, Novel preparation of Pd/Vycor composite membranes. Catal. Today **25**(3–4), 231–236 (1995)
123. R.S. Souleimanova, A.S. Mukasyan, A. Varma, Effects of osmosis on microstructure of Pd-composite membranes synthesized by electroless plating technique. J. Membr. Sci. **166** (2), 249–257 (2000)
124. A. Li, W. Liang, R. Hughes, Characterisation and permeation of palladium/stainless steel composite membranes. J. Membr. Sci. **149**(2), 259–268 (1998)
125. X. Zhang, G. Xiong, W. Yang, A modified electroless plating technique for thin dense palladium composite membranes with enhanced stability. J. Membr. Sci. **314**(1–2), 226–237 (2008)
126. P.M. Thoen, F. Roa, J.D. Way, High flux palladium-copper composite membranes for hydrogen separations. Desalination **193**(1–3), 224–229 (2006)
127. S.K. Gade, P.M. Thoen, J.D. Way, Unsupported palladium alloy foil membranes fabricated by electroless plating. J. Membr. Sci. **316**(1–2), 112–118 (2008)
128. S.-K. Ryi, N. Xu, A. Li, C.J. Lim, J.R. Grace, Electroless Pd membrane deposition on alumina modified porous Hastelloy substrate with EDTA-free bath. Int. J. Hydrog. Energy **35**(6), 2328–2335 (2010)
129. Y.-H. Chi, J.-J. Lin, Y.-L. Lin, C.-C. Yang, J.-H. Huang, Influence of the rotation rate of porous stainless steel tubes on electroless palladium deposition. J. Membr. Sci. **475**, 259–265 (2015)
130. D. Alique, M. Imperatore, R. Sanz, J.A. Calles, M.G. Baschetti, Hydrogen permeation in composite Pd-membranes prepared by conventional electroless plating and electroless pore-plating alternatives over ceramic and metallic supports. Int. J. Hydrog. Energy **41**(42), 19430–19438 (2016)
131. D.A. Pacheco Tanaka, M.A. Llosa Tanco, T. Nagase, J. Okazaki, Y. Wakui, F. Mizukami, T.M. Suzuki, Fabrication of hydrogen-permeable composite membranes packed with palladium nanoparticles. Adv. Mater. **18**(5), 630–632 (2006)
132. D.A.P. Tanaka, M.A.L. Tanco, J. Okazaki, Y. Wakui, F. Mizukami, T.M. Suzuki, Preparation of "pore-fill" type Pd-YSZ-γ-Al_2O_3 composite membrane supported on α-Al_2O_3 tube for hydrogen separation. J. Membr. Sci. **320**(1–2), 436–441 (2008)
133. F. Roa, M.J. Block, J.D. Way, The influence of alloy composition on the H_2 flux of composite Pd-Cu membranes. Desalination **147**(1), 411–416 (2002)
134. F. Roa, J.D. Way, The effect of air exposure on palladium-copper composite membranes. Appl. Surf. Sci. **240**(1–4), 85–104 (2005)
135. F. Roa, J.D. Way, R.L. McCormick, S.N. Paglieri, Preparation and characterization of Pd-Cu composite membranes for hydrogen separation. Chem. Eng. J. **93**(1), 11–22 (2003)
136. A. Kulprathipanja, G.O. Alptekin, J.L. Falconer, J.D. Way, Pd and Pd-Cu membranes: inhibition of H_2 permeation by H_2S. J. Membr. Sci. **254**(1–2), 49–62 (2005)
137. S.K. Gade, E.A. Payzant, H.J. Park, P.M. Thoen, J.D. Way, The effects of fabrication and annealing on the structure and hydrogen permeation of Pd-Au binary alloy membranes. J. Membr. Sci. **340**(1–2), 227–233 (2009)
138. K. Zhang, S.K. Gade, J.D. Way, Effects of heat treatment in air on hydrogen sorption over Pd-Ag and Pd-Au membrane surfaces. J. Membr. Sci. **403–404**, 78–83 (2012)
139. N.S. Patki, S.-T. Lundin, J.D. Way, Rapid annealing of sequentially plated Pd-Au composite membranes using high pressure hydrogen. J. Membr. Sci. **513**, 197–205 (2016)

140. H.W.A. El Hawa, S.-T.B. Lundin, N.S. Patki, J.D. Way, Steam methane reforming in a PdAu membrane reactor: long-term assessment. Int. J. Hydrog. Energy **41**(24), 10193–10201 (2016)
141. K. Zhang, S.K. Gade, Ø. Hatlevik, J.D. Way, A sorption rate hypothesis for the increase in H_2 permeability of palladium-silver (Pd-Ag) membranes caused by air oxidation. Int. J. Hydrog. Energy **37**(1), 583–593 (2012)
142. S.K. Gade, M.K. Keeling, A.P. Davidson, Ø. Hatlevik, J.D. Way, Palladium-ruthenium membranes for hydrogen separation fabricated by electroless co-deposition. Int. J. Hydrog. Energy **34**(15), 6484–6491 (2009)
143. F. Braun, J.B. Miller, A.J. Gellman, A.M. Tarditi, B. Fleutot, P. Kondratyuk, L.M. Cornaglia, PdAgAu alloy with high resistance to corrosion by H_2S. Int. J. Hydrog. Energy **37**(23), 18547–18555 (2012)
144. J.B. Miller, B.D. Morreale, M.W. Smith, Pd-Alloy Membranes for Hydrogen Separation, in *Reactor and Process Design in Sustainable Energy Technology*, ed. by F. Shi (Ed), (Elsevier, Amsterdam, 2014), pp. 135–161
145. F. Gallucci, E. Fernandez, P. Corengia, M. van Sint Annaland, Recent advances on membranes and membrane reactors for hydrogen production. Chem. Eng. Sci. **92**, 40–66 (2013)
146. M.D. Dolan, Non-Pd BCC alloy membranes for industrial hydrogen separation. J. Membr. Sci. **362**(1–2), 12–28 (2013)
147. Z. Tao, L. Yan, J. Qiao, B. Wang, L. Zhang, J. Zhang, A review of advanced proton-conducting materials for hydrogen separation. Prog. Mater. Sci. **74**, 1–50 (2015)
148. U. Balachandran, T.H. Lee, G. Zhang, S.E. Dorris, K.S. Rothenberger, B.H. Howard, B. Morreale, A.V. Cugini, R.V. Siriwardane, J.A. Poston Jr., E.P. Fisher, Development of Dense Ceramic Membranes for Hydrogen Separation, in *Studies in Surface Science and Catalysis*, ed. by E. Iglesia, J. J. Spivey, T. H. Fleisch (Eds), (Elsevier, 2001), pp. 465–470
149. U. Balachandran, T.H. Lee, L. Chen, S.J. Song, J.J. Picciolo, S.E. Dorris, Hydrogen separation by dense cermet membranes. Fuel **85**(2), 150–155 (2006)
150. B. Zhu, C.H. Tang, H.Y. Xu, D.S. Su, J. Zhang, H. Li, Surface activation inspires high performance of ultra-thin Pd membrane for hydrogen separation. J. Membr. Sci. **526**, 138–146 (2017)
151. A.B. Antoniazzi, A.A. Haasz, O. Auciello, P.C. Stangeby, Atomic, ionic and molecular hydrogen permeation facility with in situ auger surface analysis. J. Nucl. Mater. **128–129**, 670–675 (1984)
152. S. Pati, R.A. Jat, S.K. Mukerjee, S.C. Parida, X-ray diffraction study of thermal parameters of Pd, Pd-Ag and Pd-Ag-Cu alloys as hydrogen purification membrane materials. Phys. B Condens. Matter **484**, 42–47 (2016)
153. J.W. Elam, A. Zinovev, C.Y. Han, H.H. Wang, U. Welp, J.N. Hryn, M.J. Pellin, Atomic layer deposition of palladium films on Al_2O_3 surfaces. Thin Solid Films **515**(4), 1664–1673 (2006)
154. J.A. Leiro, M.H. Heinonen, I.G. Batirev, Surface segregation and core-level shift of a Pd-Rh alloy studied by XPS. Appl. Surf. Sci. **90**(4), 515–521 (1995)
155. J. Tang, Y. Zuo, Y. Tang, J. Xiong, Composition and corrosion resistance of palladium film on 316L stainless steel by brush plating. Trans. Nonferrous Metals Soc. China **22**(1), 97–103 (2012)
156. J. Skoryna, S. Pacanowski, A. Marczyńska, M. Werwiński, A. Rogowska, M. Wachowiak, Ł. Majchrzyckic, R. Czajkac, L. Smardz, XPS valence band studies of nanocrystalline ZrPd alloy thin films. Surf. Coat. Technol. **303**, 125–130 (2016)
157. M. Ohring, Mechanical Properties of Thin Films, in *The Materials Science of Thin Films*, (Academic Press, London, 1992), pp. 403–450
158. W. Liang, R. Hughes, The effect of diffusion direction on the permeation rate of hydrogen in palladium composite membranes. Chem. Eng. J. **112**(1), 81–86 (2005)
159. T. Maneerung, K. Hidajat, S. Kawi, Ultra-thin (<1 μm) internally-coated Pd–Ag alloy hollow fiber membrane with superior thermal stability and durability for high temperature H_2 separation. J. Membr. Sci. **452**, 127–142 (2014)

160. J. Dahlmeyer, T. Garrison, T. Garrison, S. Darkey, F. Massicotte, K. Rebeiz, S. Nesbit, A. Craft, Effects of hydrogen exposure temperature on the tensile strength, microhardness and ductility of Pd/Ag (25wt.%) alloy. Scr. Mater. **64**(8), 789–792 (2011)
161. S.P. Lynch, *Hydrogen Embrittlement (HE) Phenomena and Mechanisms. In Stress Corrosion Cracking* (Woodhead Publishing Series in Metals and Surface Engineering, 2011), pp. 90–130
162. A. Suzuki, H. Yukawa, T. Nambu, Y. Matsumoto, Y. Murata, Analysis of pressure–composition–isotherms for design of non-Pd-based alloy membranes with high hydrogen permeability and strong resistance to hydrogen embrittlement. J. Membr. Sci. **503**, 110–115 (2016)
163. A.F. Jankowski, Metallic multilayers at the nanoscale. Nanostruct. Mater. **6**(1–4), 179–190 (1995)
164. M.M. Mardanpour, R. Sadeghi, M.R. Ehsani, E.M. Nasr, Enhancement of dimethyl ether production with application of hydrogen-permselective Pd-based membrane in fluidized bed reactor. J. Ind. Eng. Chem. **18**(3), 1157–1165 (2012)
165. C. Ruocco, E. Meloni, V. Palma, M. van Sint Annaland, V. Spallina, F. Gallucci, Pt–Ni based catalyst for ethanol reforming in a fluidized bed membrane reactor. Int. J. Hydrog. Energy **41** (44), 20122–20136 (2016)
166. S. Tosti, F. Borgognoni, A. Santucci, Electrical resistivity, strain and permeability of Pd-Ag membrane tubes. Int. J. Hydrog. Energy **35**(15), 7796–7802 (2010)
167. K. Wald, J. Kubik, D. Paciulli, M. Talukder, J. Nott, F. Massicotte, K. Kebeiz, S. Nesbit, A. Craft, Effects of multiple hydrogen absorption/desorption cycles on the mechanical properties of the alloy system palladium/silver (wt% = 10–25). Scr. Mater. **117**, 6–10 (2016)
168. E. Jakobs, W.J. Koros, Ceramic membrane characterization via the bubble point technique. J. Membr. Sci. **124**(2), 149–159 (1997)
169. G. Reichelt, Bubble point measurements on large areas of microporous membranes. J. Membr. Sci. **60**(2), 253–259 (1991)
170. M. Vadrucci, F. Borgognoni, A. Moriani, A. Santucci, S. Tosti, Hydrogen permeation through Pd–Ag membranes: surface effects and Sieverts' law. Int. J. Hydrog. Energy **38** (10), 4144–4152 (2013)
171. N.D. Deveau, Y.H. Ma, R. Datta, Beyond Sieverts' law: a comprehensive microkinetic model of hydrogen permeation in dense metal membranes. J. Membr. Sci. **437**, 298–311 (2013)
172. A. Caravella, S. Hara, Y. Sun, E. Drioli, G. Barbieri, Coupled influence of non-ideal diffusion and multilayer asymmetric porous supports on Sieverts law pressure exponent for hydrogen permeation in composite Pd-based membranes. Int. J. Hydrog. Energy **39**(5), 2201–2214 (2014)
173. F. Gallucci, M. De Falco, S. Tosti, L. Marrelli, A. Basile, The effect of the hydrogen flux pressure and temperature dependence factors on the membrane reactor performances. Int. J. Hydrog. Energy **32**(16), 4052–4058 (2007)

Chapter 3
Magnetic Thin Film Materials: Magnetic Particles Synthesized by Thin Film Dewetting for Energy Applications

Ruihua Cheng

3.1 Introduction

Metallic nanoparticle arrays which exhibit magnetic moments are a promising platform for the electrically and thermally conductive micro- and nanoscale structures. Real-world application fields include biomedical engineering, data storage, and nonlinear optics. In order to capitalize on major natural energy sources, such as solar and wind energies, efficient methods of energy storage must be developed. Recently, attention has been given to Latent Heat Storage (LHS) devices which utilize Phase Change Materials (PCMs) due to their low cost, low toxicity, and high engineering versatility, as candidates for efficient, cost-effective methods of thermal energy storage [1, 2]. One promising work to develop a LHS device utilizes parafin as a PCM and incorporates a matrix of magnetically susceptible, thermally conductive nanorod frameworks which are self-assembled under an externally applied magnetic field. The assembly process to create the matrix is well documented; however, the prohibitive cost of the magnetic pads, fabricated by lithography processes makes large-scale production impractical [3–6].

Planar thin films are susceptible to a dewetting instability in which a continuous film spontaneously decomposes into an equilibrium morphology of discrete shapes having characteristic size [7]. This process, known as agglomeration, is primarily a surface energy-driven phenomenon and is best understood through the thermodynamics of energy minimization [7–10]. During the agglomeration process, void nucleation occurs at various sites throughout the thin film as a result of stress, strains, defects, and structures which protrude up into the thin film from the

R. Cheng (✉)
Department of Physics, Indiana University—Purdue University Indianapolis, 402 N Blackford St., Indianapolis, IN 46202, USA
e-mail: rucheng@iupui.edu

J. Zhang, Y.-G. Jung (eds.), *Advanced Ceramic and Metallic Coating and Thin Film Materials for Energy and Environmental Applications*,
DOI 10.1007/978-3-319-59906-9_3

substrate, or at preexisting voids which exceed a critical radius. As nucleation proceeds, laminar flow of mass away from the void edges will cause fingers of the material to form. Eventually, Rayleigh instabilities cause breakup of these fingers into discreet islands of a hemispherical or near-spherical equilibrium shapes will complete the thermodynamic transition. Here, we examine the self-assembly of a nanoarray of cobalt nanospheres synthesized by thermodynamically driven solid state dewetting on a low surface energy carbon nanotube substrate with nontrivial local geometry. Solid state dewetting by Intense Pulsed Light (IPL) annealing is an easily repeatable morphological process, driven by thermodynamic and hydrodynamic principles, which utilizes a simple experimental setup, providing a navigable roadmap to create tunable magnetic nanoparticle arrays [7]. We found that the dimensions of end state equilibrium shapes after agglomeration in our thin film-substrate system are highly parameter dependent.

The main process parameters studied in this work are initial thin film thickness h°, excitation energy, application of an external magnetic field, and density of the underlying carbon nanotube substrate. The related study can be applied to different applications. One such application falls in the realm of energy storage devices as we mentioned. The high latent heat of PCMs is promising, but a major issue in their realization as energy storage devices is their inherent low thermal conductivity. A possible solution to this problem is to embed PCMs with highly conductive nanoparticles. While this has been somewhat successful, the techniques developed so far have lack of robust repeatability after phase change cycles. Significant settling occurs once the PCM undergoes a few melting/solidification cycles [11, 12].

One of the promising work to develop a latent heat storage device utilizing paraffin as a PCM incorporates a matrix of magnetically susceptible, thermally conductive nanorods which are self-assembled and then soldered together using a micro-scaled array of magnetic pads. The self-assembly process to create the matrix is well documented; however, the prohibitive cost of the magnetic nickle pads fabricated by lithography makes large-scale production of the devices impractical [6].

Solid state dewetting by xenon lamp flash annealing is an easily repeatable morphological process, which utilizes a simple experimental setup providing a navigable roadmap to the creation of tunable nanoparticles [10, 13]. However, the application of solid state dewetting on magnetic materials has not been reported. In particular to this research, a patterned nanoarray that exhibits a net local magnetic moment can be used to position, align, and orient magnetic nanostructures forming large-scale ordered structures that may be used in thermal transport or other continuous network applications.

3.1.1 Solid State Dewetting

Planar solid thin films are susceptible to a dewetting instability in which a continuous film spontaneously decomposes into an equilibrium morphology of discrete shapes having characteristic size [7]. This process, known as agglomeration, is primarily a surface energy-driven phenomenon and is best understood through the thermodynamics of energy minimization [9, 14, 15].

Agglomeration typically occurs when an initially flat thin film is subject to an annealing process, thereby transitioning from a local thermodynamic minimum to an equilibrium minimum. A stress-free planar thin film remains stable to agglomeration provided there are no perturbations in its surface which exceed the thin film thickness [16, 17].

This means that agglomeration must initiate from the edges of the thin film or from regions, where the substrate is exposed such as preexisting voids or new voids of a critical diameter must be formed [7]. Due to local high aspect ratio geometry, mass is driven away from the edges. The voids then evolve through a capillary action until they begin to impinge leaving an equilibrium shape, typically hemispherical or bead-like in nature. This "boundary-induced behavior" is a result of high aspect ratio geometry around the edge of the thin film [14].

Consider a vapor-thin film-substrate system such as the one illustrated in Fig. 3.1. Given

γi = interface energy of thin film-substrate interface

γf = surface energy of thin film

γs = surface energy of substrate

A critical radius, shown in Fig. 3.2, for which surface energy would be minimized, thus initiating void growth, can be calculated by considering the total free energy of the system [7, 14, 15, 18]. This would include the increase in substrate exposure $\gamma s \pi R_2$, increase in film-vapor area along the inner diameter edge of the hole $\gamma f\ 2\pi Rh$, decrease of interface energy—$\gamma i \pi R_2$, and decrease of film-vapor energy—$\gamma f\, R_2$. Putting these together, we have

$$\gamma s \pi R_2 - \gamma i \pi R_2 - \gamma f \pi R_2 + \gamma f 2\pi Rh = 0 \tag{3.1}$$

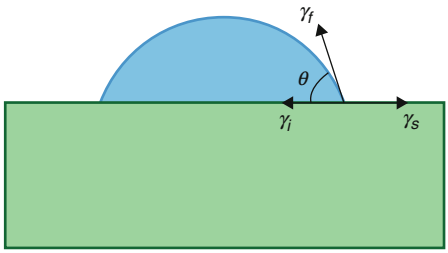

Fig. 3.1 Thin film-vapor-substrate

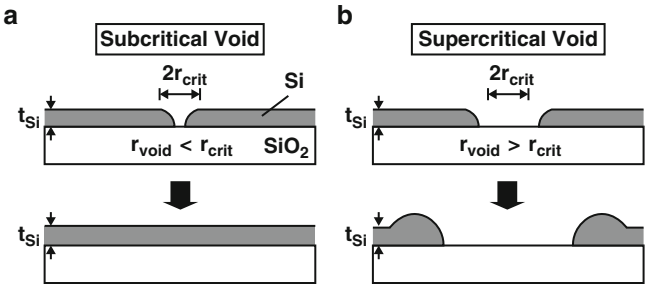

Fig. 3.2 Diagram of the critical void scenario modeled for Si by Danielson [7]

$$\gamma sR - \gamma iR - \gamma fR + \gamma f2h = 0 \tag{3.2}$$

$$\gamma f2h = (\gamma i + \gamma f - \gamma s)R \tag{3.3}$$

Using the Young-Laplace equation

$$\gamma s = \gamma i + \gamma f \ \cos\theta \tag{3.4}$$

and rearranging gives $R = \dfrac{2\gamma_f h}{\gamma_i + \gamma_f - (\gamma_i + \gamma_f \cos\theta)} = \dfrac{2h}{1 - \cos\theta}$.

In the ultrathin regime for $h < 20$ nm, grooving at grain boundaries can play a role for void formation during annealing of crystalline film [15]. If an energetic process such as magnetron sputtering deposition is used to form the thin film the microstructure of as-deposited cobalt thin film on this scale can show definite grain boundaries and exhibit characteristic strain [19]. Other sites for void nucleation include defects, or structures from the substrate that protrude up into the thin film. It can be shown that void nucleation is a heterogeneously distributed occurrence and that energy minimization would exclude homogeneous distribution of nucleation sites.

The model proposed by Danielson [7], shown in Fig. 3.3, best describes the behavior of a system undergoing agglomeration including five clear steps, each using the instability mechanisms. It is a nice combination of theory backed up by experimental observation and able to explain the surface energy-driven nature of solid state dewetting. Danielson's model is as follows: (1) critical void formation, (2) void edge thickening, (3) void edge breakdown, (4) void finger formation and growth, and (5) island formation.

Step **I** dictates the heterogeneously distributed regions where agglomeration begins, from both critical voids and thin film edges which are unstable regions susceptible to capillary action. Mass transport away from unstable edge regions proceeds in step **II**, causing rims to form around voids and film edges. As the radius of curvature and thin film thickness changes in these regions, the growth velocity will decrease. Brandon and Bradshaw showed that if this were to continue mass

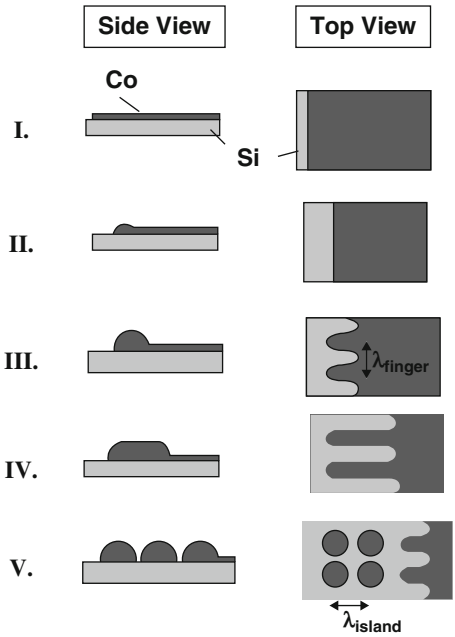

Fig. 3.3 Evolution of the agglomeration process following Danielson's five steps [7]

flow would eventually cease [20]. However, as the void propagates through continuous regions of the thin film, mass is deposited to the side of the receding void front, and the thickness of the front is comparable or equal to the initial thin film thickness [7, 21].

The edges of the propagating void are in fact unstable and subject to the well-known Rayleigh-Plateau instability. This instability describes an energetically isotropic liquid cylinder subject to a critical perturbation across its surface and will evolve into a periodic array of spheres in order to lower its total surface energy. In fact, it has been shown that this also holds for solid cylinders as well. Using a Monte Carlo simulation, Kan and Wong's theoretical work shows strong support for this theory as well (Fig. 3.4) [9].

The Rayleigh perturbation wavelength is proportional to initial thin film thickness. This film instability has a time scale proportional to both temperature and initial film thickness. Now void and film growth occur in step **IV**. As the void penetrates into the film, it creates regions with thickened edges contrasting against regions around thinner edges, which still have a very high radius of curvature. These regions transport mass back away from the thinner edges causing a regular pattern of void fingers to appear with characteristic, uniform spacing as predicted by Kan and Wong [9] and verified by Jiran and Thompson's experimental observations [18].

Clearly, a thinner film should undergo agglomeration at a higher rate than a thicker one, due to the inverse dependence on thickness, making a thinner film more susceptible to dewetting. The final step **V** of the model denotes the appearance of

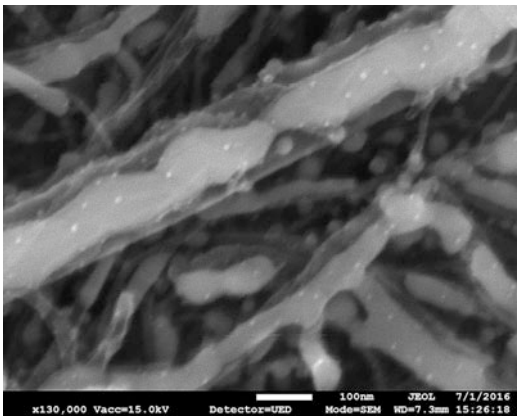

Fig. 3.4 Partially agglomerated cobalt thin film on carbon nanotubes by our work showing receding front and evidence of capillary Rayleigh instabilities

discrete islands of material. Void finger evolution leaves regularly spaced lines of material again subject to Rayleigh instability. It is here that we begin to see the equilibrium shapes of the system, typically in the form of hemispheres as the system has now lowered its surface energy by exposing as much of the underlying substrate as possible. A line of material in this state can be modeled by treatment such as McCallum and Voorhees examination of the morphological instability of a line of material on a substrate [22]. Their work shows that the Rayleigh wavelength for such a line is proportional to its circular arc cross sectional dimensions, which is in agreement to the original work by Rayleigh [23, 24]. Time scale of evolution is also in agreement with Rayleigh which means that it increases proportionally with the fourth power of the finger cross section and is inversely proportional to the surface diffusion constant.

Another process that accounts for agglomeration is surface Ostwald Ripening. In this process, mass transport of ions and adatoms occurs. The mass transport of the adatoms is characterized by the surface diffusion coefficient and surface diffusion length. Beke and Kaganovskii make the condition that given some islands of mass (thin film) their surface diffusion fields must overlap for Ostwald ripening to occur. In other words, their average nearest neighbor spacing should be less than twice the diffusion length. In effect, this causes particles that are in the vicinity of each other to be subsumed, thereby creating a single larger mass particle [25–27].

3.2 Experimental Approach

Our goal is to synthesize a discrete array of magnetic nanostructures using the solid state flash annealing technique. A variety of approaches were used to achieve this, utilizing different substrates and changing parameters of thin film thickness, excitation energy, and the presence of an external magnetic field. The proper choice of a substrate to facilitate the agglomeration process was very important to this work.

The early solid state dewetting work published by other groups are focused on silicon substrates. An ideal substrate should readily dewet and remain thermally robust after flash annealing treatment. Substrates with low surface energy and good thermal conductivity such as Highly Ordered Pyrolytic Graphite (HOPG) and Carbon Nanotubes (CNTs) were ideal choices. We studied planar substrate such as HOPG being a natural starting point, then moved to high aspect ratio of carbon nanotube (CNT) surfaces. The method of thin film deposition used was magnetron sputtering. Characterization was done using a JEOL 7800F Field Emission Scanning Electron Microscope (FESEM).

Highly Ordered Pyrolytic Graphite is one of the purest forms of graphite, exhibiting highly ordered crystallographic orientation perpendicular to the surface and a near defect-free lattice structure [28, 29]. In fact, it can be thought of as stacked sheets of graphene, and its surface properties are very close to those of graphene, even mimicking graphene's wettability the same as, or better than some epitaxially grown graphene. When exfoliated graphene was first synthesized in the lab, it was "pulled" from a piece of HOPG with scotch tape. This characteristic makes it a reusable substrate, when an experiment is finished, a fresh surface can easily be created using Scotch tape to pull the old surface away.

Essentially, a carbon nanotube CNT is a rolled up sheet of graphite with two hemispherical caps on either end, whose characteristics such as electron transport, etc. are dependent upon in what manner the lattice lines up upon rolling. For the present work, we are mainly concerned with two features of the nanotube: surface geometry and surface energy.

The nanotubes used for our experiments, shown in Fig. 3.5, were from Nano-Tech Labs in Yadkinville, North Carolina. They are M-grade multiwall carbon nanotubes with an average diameter of 70–80 nm giving a radius of curvature 38 nm. The large aspect ratio, a low surface energy, and thermal stability yields an optimal substrate for dewetting by xenon flash lamp annealing. These nanotubes were prepared in suspension form by adding 5 mg of nanotubes to 20 mL acetone and 180 min of sonication. The suspension was then drawn into a syringe and

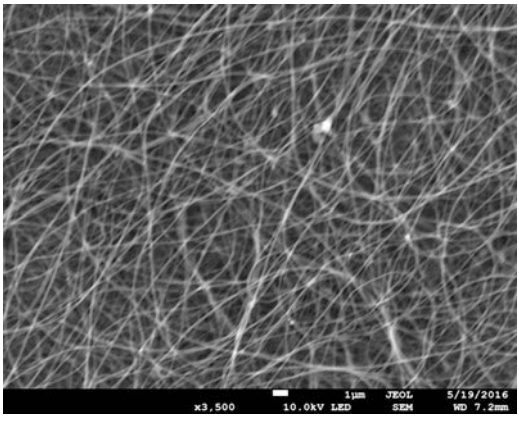

Fig. 3.5 SEM image of drop-cast CNT substrate. CNTs were provided by NanoTech Labs, Inc.

deposited onto a clean silicon substrate. Several methods where tested to achieve somewhat uniform distribution of the nanotubes onto the silicon with varying results, including spin casting and mixing of nanotubes with wetting agents. In the end, the best method was the most straightforward, simply drop-casting the acetone-nanotube suspension onto the silicon. This did not achieve regular coverage of the silicone base however. We also work on 60 gsm buckypaper from Nanotech Labs, a dense mesh of pure multiwall carbon nanotubes. Several pieces of buckypaper were cut and glued to silicon wafers with colloidal silver paste to create an electrically conductive sample that would accommodate imaging by scanning electron microscopy (SEM).

During agglomeration, the thin film substrate system moves from metastable local thermodynamic minima to an equilibrium state. Traditional dewetting processes include thermal annealing using an oven, which works on a large time scale, laser irradiation, which can damage the underlying substrate and introduce impurities into the nanoparticles, and UV radiation. Solid state dewetting by flash lamp annealing utilizes a xenon flash lamp as an energy source. This facilitates dewetting on a short time scale, and thermal conditions do not destroy the underlying substrate. Due to these properties, its relatively inexpensive construction cost as well as small footprint, flash lamp annealing lends itself well to industrial sector mass production applications.

The flash lamp used for this study consists of a bank of computer-controlled capacitors which store electrical potential energy that is then released on demand into a xenon gas filled bulb. A large potential difference is created across a cathode in the form of a sharp electron emitting tip. As they travel to the adjacent cathode, electrons thermally transition the xenon atoms to an excited state. About 80% of the initial electrical potential energy stored in the capacitor bank is converted to radiation [30]. Convection and thermal conduction makes up the difference. Upon decay they release a large amount of photons in the visible and UV wavelength range. These photons travel to the surface of our samples causing the thermal excitation necessary to drive the agglomeration process. Pulse energy density is dependent upon the controllable applied voltage and varies up to 50 J/cm^2. Pulse duration may be set from 1 to 10 ms and multiple pulses can be delivered with a variable step time frame.

3.3 Experimental Data and Discussion

We notice that dimension of end state equilibrium shapes are highly parameter dependent. The main parameters studied are initial film thickness, flash annealing excitation energy, and the strength of applied external magnetic fields. A general outline of our process is shown as Fig. 3.6. Substrates are prepared either by the aforementioned method of drop-casting a suspension from a syringe, or affixing as-purchased CNT matrix to a silicon wafer with conductive paste. High vacuum magnetron sputtering was used to deposit cobalt thin films onto the Si-CNT

Fig. 3.6 General graphical outline of experimental process

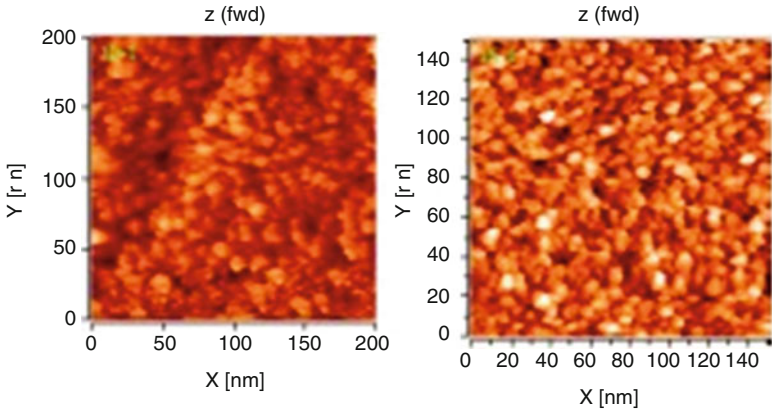

Fig. 3.7 Two STM micrographs of planar regions of HOPG deposited with 5 nm Co (*left*) and 15 nm Co (*right*). Both samples were exposed

substrates. Samples of different thickness of 10 nm, 15 nm, and 20 nm were prepared in a low base pressure chamber. Samples were flash annealed at a specified energy with pulse time of 20 ms held at a working distance (WD) of 3 mm.

3.3.1 Experiments on HOPG

Our first set of experiments focused on growing nanoparticles on an HOPG substrate due to the reason that HOPG substrates can be easily cleaned by scotch tape peeling. Primary tests were carried out by depositing cobalt on the surface of HOPG with the maximum exposure energy of 50 J/cm^2. The topological image of particles are shown as Fig. 3.7.

Some nanoscale structures were observed on flat HOPG substrates. This indicates that graphite-like carbon surface is promising to facilitate solid state dewetting as we expected. High curvature of CNT substrates would be ideal to laterally resolve those particles.

3.3.2 *Experiments on Drop-Cast CNT*

Several silicon wafers were cleaned with a series of acetone, methanol, isopropyl alcohol, and deionized (DI) water rinsing. Wafers were then dried with nitrogen. Five milligrams of M-grade MWCNTs from NanoTech Labs Inc. were placed into 20 mL of acetone and sonicated for 180 min following previous works to disperse the nanotubes somewhat evenly in a suspension form [31–33]. A syringe was used to draw the suspension out of the Erlenmeyer flask and then deposit it onto the silicon wafers. Surface tension held a hemispherically shaped drop of the suspension on the silicon wafer. The acetone quickly evaporated leaving behind a film of nanotubes.

We investigated the energy variation parameter for Co on CNTs by processing a series of samples with increasing excitation energy. A systematic relationship between particle diameter and excitation energy was noted wherein an increase in energy correlated to an increase in diameter up to some threshold energy after which mass loss occurred through evaporation. After exposure to excitation energy, and upon imaging with the SEM, we noticed a boundary which separates the area populated with nanoparticles from an area without dewetting, as shown in Figs. 3.8 and 3.9.

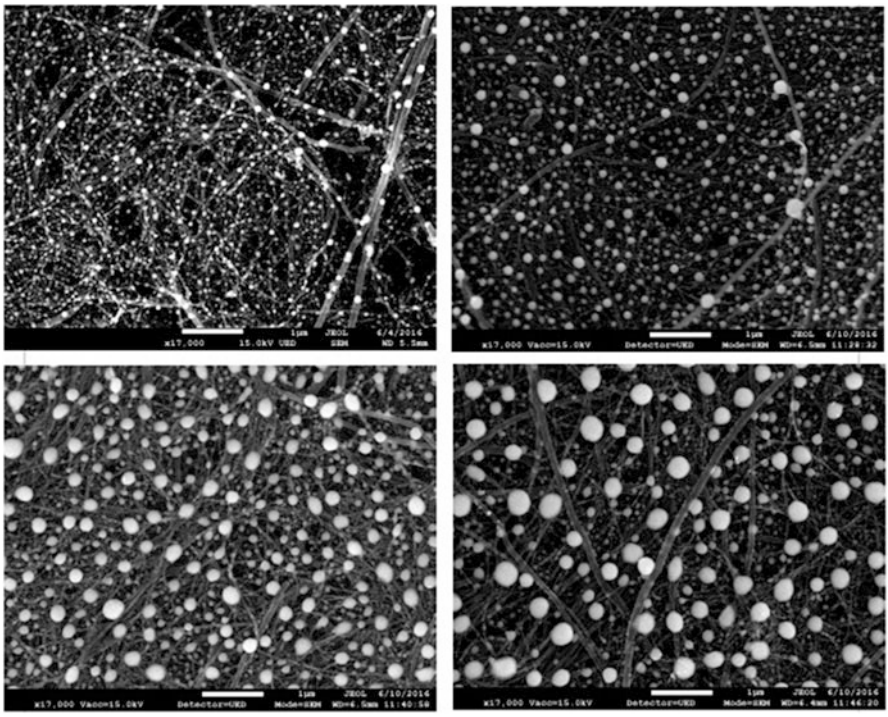

Fig. 3.8 Clockwise from *top left*, 5 nm, 10 nm, 15 nm, 20 nm Co on Buckypaper. The excitation energy is 40 J/cm^2 for all sample

All of these samples were produced using the drop-cast method, and the consistency of nanotube coverage was not as regular as on the nanoparticle producing samples. It has been noted in the literature that reflectivity of base substrates plays a major role in producing the thermal conditions necessary for agglomeration [8]. It is believed that the base silicon substrate is reflecting enough energy that threshold conditions at the thin film surface were never met, thus explaining the absence of end state discreet particles.

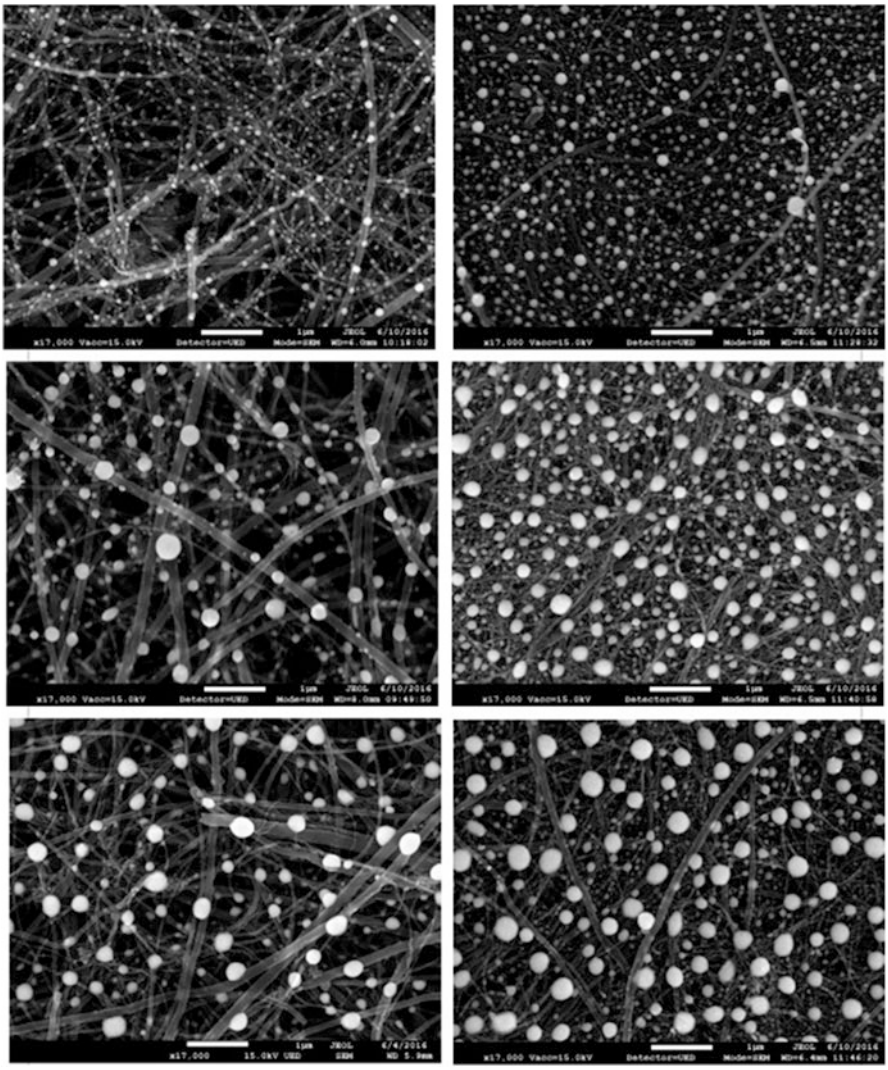

Fig. 3.9 Substrate Comparison. *Left row*, Co on drop-cast CNT. *Right row*, Co on 60 gsm Buckpaper. Initial film depth from top to bottom $h^{\circ} = 10$ nm, 15 nm, 20 nm

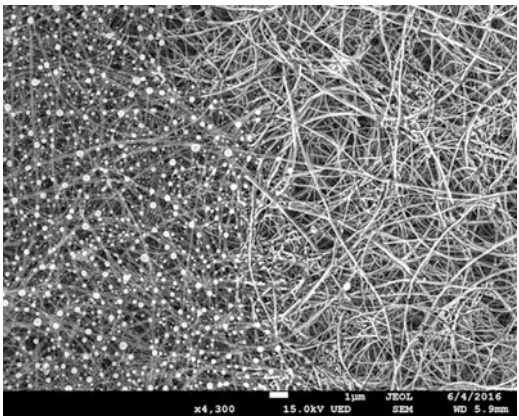

Fig. 3.10 Clear line of demarcation between continuous thin film and agglomerated nanoparticles indicates a threshold energy. Initial cobalt thin film of nominal thickness $h = 20$ nm and excitation energy of 50 J/cm^2, scale bar indicates 1 μm

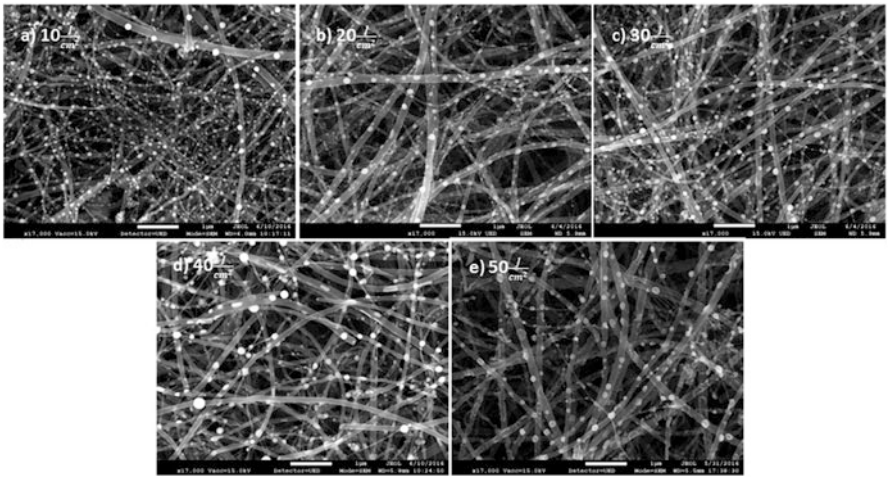

Fig. 3.11 Cobalt nanoparticles fabricated from thin film of nominal thickness 20 nm, by flash annealing on CNT substrates using excitation energy. Scale bar is 1 μm for all SEM images

Another interesting observation was that of "transition areas" in which partial dewetting can be observed. The nature of our experimental setup is such that the excitation source cannot fully cover the total surface of the substrate, therefore leaving a "strip" of nanoparticles bordered by a transition area separating a nanoparticle region from a region where the thin film is still continuous and in an agglomerated state. This can provide insight into a proper developed theory for solid state dewetting on cylindrical surfaces of high aspect ratio (Fig. 3.10).

In order to determine the relationship between excitation energy and the end state particle size, two series of samples were studied. One set with film thickness of 5 nm with energy progressing from 10 to 50 J/cm^2 and another set with thickness of 20 nm. As shown in Fig. 3.11 and Table 3.1, a systematic change in particle size

Table 3.1 General statistics for excitation energy tests, Co on drop-cast CNT

Varied excitation energies, Co on CNT					
Excitation energy (J/cm^2)	10	20	30	40	50
Mean diameter (nm)	46.231	44.795	54.752	63.71	74.69
Median (nm)	43.70	33.37	45.90	46.70	56.95
Max (nm)	140.83	175.4	194.44	280.00	204.00
Standard deviation	26.938	35.82	39.85	52.78	45.20

was observed in both series with progressively larger particles forming for higher energies up through 40 J/cm^2 at which point a reduction in size is noted for 50 J/cm^2 samples. This drop off in size is explained by the evaporation of material at higher energy. The progressively larger size is a result of accelerated process as a result of absorbed energy resulting in Ostwald ripening of the particles. These observations agree with theoretical models and other experiments. Visual inspection of the micrographs show a consistent correspondence between excitation energy and particle size. This agrees with the theory outlined earlier, in that higher excitation energies correspond to higher surface temperatures. Diffusivity is a temperature-dependent quantity, increased diffusivity would mean increased flux, and increased flux would allow for the evolution of the agglomeration process to proceed into the Ostwald ripening stage. In the 40 and 50 J/cm^2 regime, the data shows that although the mean diameter continue to increase, but some mass may have evaporated. Ostwald ripening could account for the shift to larger particles and hence the absence of smaller ones, as the smaller particles are subsumed by their larger neighbors.

3.3.3 Variation of Initial Thin Film Thickness

To investigate the film thickness dependence, we prepared a series of samples with increasing thickness ranging from 5 to 20 nm in 5 nm increments, and all samples were exposed to the same energy of 40 J/cm^2. Here, we did comparison study on both drop-cast CNT and 60 gsm Buckypaper CNT substrates.

It has been noticed by other studies that for a planar thin film on both continuous and patterned substrates, initial film thickness plays a significant role in susceptibility to agglomeration, as well as end state particle size. Therefore, for our surface, comprised mainly a high aspect ratio geometry landscape, we observe similar results. In the samples made on drop-cast CNTs, the results shown in Fig. 3.12 and Table 3.2, indicating a steady progression of mean particle size with increasing thickness. This can be explained by the generalized Rayleigh instability, which says that the wavelength of the perturbation across a cylinder is proportional to the equilibrium end state shapes. Applied to a thin film system, this means that the wavelength of perturbation cross a retracting finger or line of thin film is

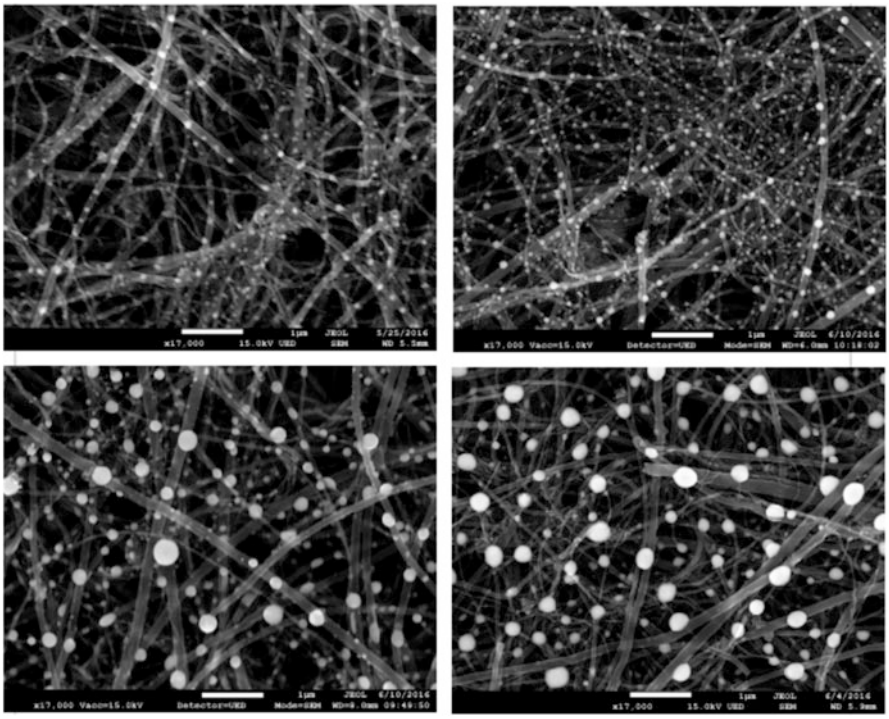

Fig. 3.12 Clockwise from *top left*, 5 nm, 10 nm, 15 nm, 20 nm Co on drop-cast CNT. Excitation energy of 40 J/cm^2

Table 3.2 General statistics for initial thin film thickness dependence, Co on drop-cast CNT

Varied initial thin film depth, Co on CNT				
Initial thin film depth (nm)	5	10	15	20
Mean diameter (nm)	74.69	57.186	94.188	107.84
Median (nm)	56.95	52.40	74.15	75.95
Max (nm)	204.00	163.18	432.38	413.23
Standard deviation	45.20	25.09	69.09	90.2

proportional to its initial cross sectional area, which is related to the film thickness, in the meanwhile it is independent of temperature [22].

These results also agree with Danielson's model, which predicts that agglomerated structures size during void edge breakdown (**III**) and void finger growth (**IV**) [7]. Danielson's model predicts that end state size as well as nearest neighbor spacing is proportional to original thin film thickness.

The results of nanoparticles grown on the 60 gsm Buckypaper CNTs showing relatively uniform particles due to higher CNT density on Buckypaper. As shown in Fig. 3.13 and Table 3.3, the Buckypaper samples showed a clear progression of

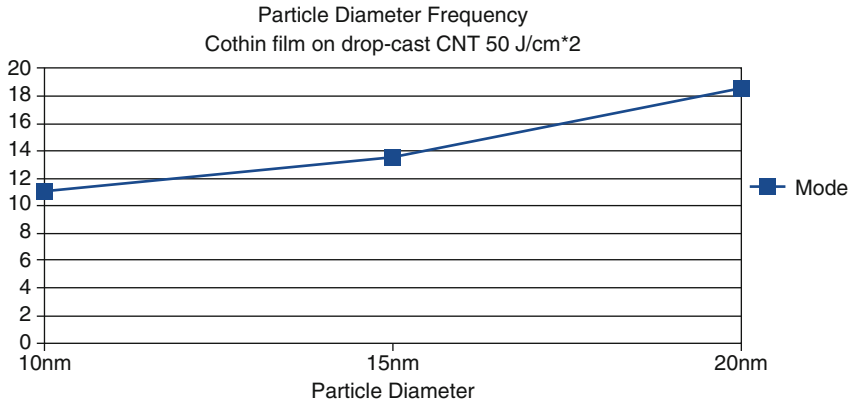

Fig. 3.13 Graph of increasing mode with increasing initial film thickness

Table 3.3 General statistics for initial thin film depth tests, Co on 60 gsm Buckypaper

Varied initial thin film depth, Co 60 gsm Buckypaper			
Initial thin film depth (nm)	10	15	20
Mean diameter (nm)	69.03	91.65	95.5
Median (nm)	64.928	65.87	57.76
Max (nm)	249.51	340.25	415.57
Standard deviation	41.93	75.07	92.76

particle size with increasing h°. They also showed a very uniform distribution of nanoparticles. Due to the density of the buckypaper as compared to drop-cast CNT, the surface better resembles a continuum, a more isotropic environment for growth.

As seen in the following page, comparing the two experiments it becomes apparent that for a regular array of magnetic Co nanoparticles, that could be tunable by variation in h°, Buckypaper would be the substrate of choice.

3.3.4 Application of External Magnetic Field

Considering the magnetization of nanoparticles, we tried applied magnetic field during the flash annealing process. It could yield other avenues for further scientific exploration of the agglomeration process, or prove useful during production for industrial sector applications. The introduction of an external magnetic film during annealing was tested by initial thickness variations on both the Buckypaper substrates. Series of 5 nm, 10 nm, 15 nm, and 20 nm were prepared in the routine way and the flash annealed with 40 J/cm^2 excitation energy for 20 ms.

The first noticeable feature when contrasting images shown in Fig. 3.14 was that for same initial thicknesses particles with larger diameter were grown in the presence of a magnetic field. One possible explanation for this behavior could be

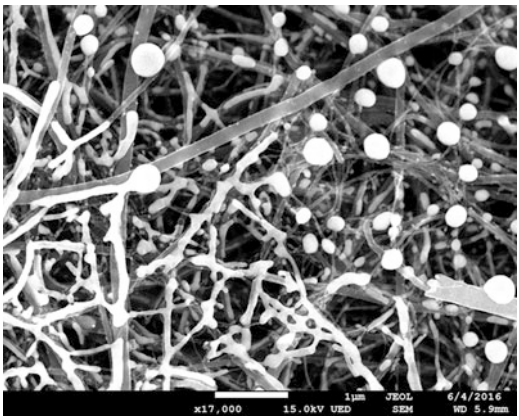

Fig. 3.14 A zoom in picture of Co thin film to nanoparticles on CNTs shows a "transition area"

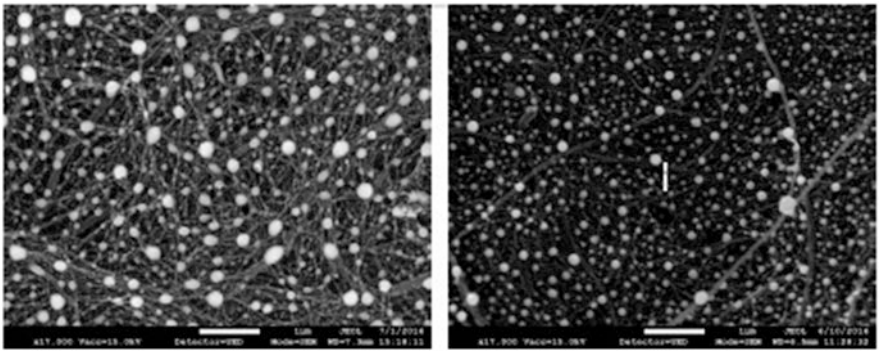

Fig. 3.15 Comparison of initial film thickness of 10 nm Co on 60gsm Buckypaper. *Left*, with external applied magnetic field. *Right*, without magnetic field. Excitation energy of 40 J/cm^2. Scale bars indicate 1 μm size

an accelerated Ostwald-like ripening process due to the anisotropic environment. The magnetic field may cause the particles to behave like magnetic dipoles. Smaller particles may experience an attraction to larger particles during the later stages of agglomeration and become subsumed (Figs. 3.15 and 3.16).

As we increased the initial film thickness to 15 nm and applied variable magnetic field, we notice that the spacing between particles shows strong magnetic field dependence. These results are very promising for nearest neighbor spacing tunability. Previously, nearest neighbor spacing has only been tunable initial film thickness and thus related to end particle diameter. It may be possible to tune the spacing regardless of initial thickness and independent of particle size. Further experiments may reveal the feasibility of this parameter.

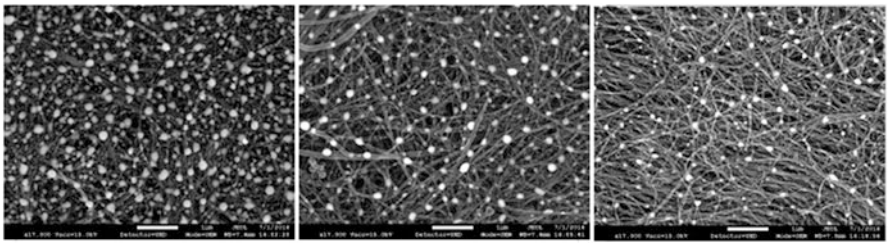

Fig. 3.16 Comparison of initial film thickness of 15 nm Co on 60 gsm Buckypaper. *Left*, with external applied magnetic field. *Right*, without magnetic field. Excitation energy of 40 J/cm^2. Scale bars indicate 1 μm size

3.4 Future Works and Conclusion

We have demonstrated that the solid state dewetting of cobalt thin films on CNT substrate is a highly tunable, easily repeatable process to fabricate nanoparticle arrays. The short time scale and relatively low energetics involved make this method a suitable candidate for roll-to-roll production or as an in expensive platform for research. It was shown that density of the underlying CNT foundation, initial thin film thickness, excitation energy, and the application of an external magnetic field are all parameters that can be used to adjust end state structure. Transition areas indicating a threshold energy or temperature present in solid state dewetting. These observations fell in line with expectations upon the consideration of models designed for a planar geometry agglomeration processes.

This work also opens the door to other possibilities. Utilizing the thermal properties of CNTs, it may be possible to drive an agglomeration of metallic thin film by microwave irradiation. This would require a simple setup and small investment. Further investigation of particle size and nearest neighbor tunability by an improved setup with a variable magnetic field.

The magnetic nanoparticles matrix could be used as templates to incorporate magnetic metal frames in latent heat storage devices for energy applications. Previously electron beam lithography and other time-consuming expensive techniques have been used to create magnetic arrays for the self-assembly of nanowires in phase change materials. Solid state dewetted arrays of magnetic nanoparticles, especially on a substrate like buckypaper, are inexpensive, easy to make, and versatile and most important it is highly thermally conductive. This will greatly improving the performance of current latent heat-based energy storage media.

References

1. M. Kenisarin, K. Mahkamov, Renew Sust Energ Rev **11**, 1913 (2007)
2. A. Sharma, V.V. Tyagi, C.R. Chen, D. Buddhi, Renew Sust Energ Rev **13**, 318 (2009)

3. F. Gao, Z. Gu, Nanotechnology **21**, 115604 (2010)
4. M. Tanase, D.M. Silevitch, A. Hultgren, L.A. Bauer, P.C. Searson, G.J. Meyer, D.H. Reich, J Appl Phys **91**, 8549 (2002)
5. Y. Rheem, B.Y. Yoo, W.P. Beyermann, N.V. Myung, Phys Status Solidi Appl Mater Sci **204**, 4004 (2007)
6. J. Su, I. Mirzaee, F. Gao, X. Liu, M. Charmchi, Z. Gu, H. Sun, J Nanotechnol Eng Med **5**, 031005 (2014)
7. D.T. Danielson, D.K. Sparacin, J. Michel, L.C. Kimerling, J Appl Phys **100**, 083507 (2006)
8. J. Bischof, D. Scherer, S. Herminghaus, P. Leiderer, Phys Rev Lett **77**, 1536 (1996)
9. W. Kan, H. Wong, J Appl Phys **97**(4), 043515 (2005)
10. J.D. Fowlkes, L. Kondic, J. Diez, Y. Wu, P.D. Rack, Nano Lett **11**, 2478 (2011)
11. J. Fukai, M. Kanou, Y. Kodama, O. Miyatake, Energy Convers Manag **41**, 1543 (2000)
12. R. Ehid, R.D. Weinstein, A.S. Fleischer, Energy Convers Manag **57**, 60 (2012)
13. A.B. Tesler, B.M. Maoz, Y. Feldman, A. Vaskevich, I. Rubinstein, J Phys Chem C **117**, 11337 (2013)
14. D.J. Srolovitz, S.A. Safran, J Appl Phys **247**, 255 (1986)
15. D.J. Srolovitz, M.G. Goldiner, J. Minerals, Met Mater **47**, 31 (1995)
16. F.A. Nichols, W.W. Mullins, J Appl Phys **36**, 1826 (1965)
17. T. Vilmin, E. Raphael, Eur Phys J E **21**, 161 (2006)
18. C.V. Thompson, Annu Rev Mater Res **42**, 399 (2012)
19. V. Chawla, R. Jayaganthan, A.K. Chawla, R. Chandra, J Mater Process Technol **209**, 3444 (2009)
20. F.J. Bradshaw, R.H. Brandon, C. Wheeler, Acta Metall **12**, 1057 (1964)
21. D.J. Srolovitz, S.A. Safran, MRS Proc **47**, 23 (1985)
22. M.S. McCallum, P.W. Voorhees, M.J. Miksis, S.H. Davis, H. Wong, J Appl Phys **79**, 7604 (1996)
23. L. Rayleigh, Proc Lond Math Soc **4**, s1–10 (1978)
24. J.W. Cahn, Scr Metall **13**, 1069 (1979)
25. D.L. Beke, Y.S. Kaganoxskii, Mater Sci Eng **32**, 18 (1995)
26. A. Imre, D.L. Beke, Appl Phys A Mater Sci Process **72**, 357 (2001)
27. I. Beszeda, E.G. Gontier-Moya, W. Imre, Appl Phys A Mater Sci Process **81**, 673 (2005)
28. D.R. Cooper, B. D'Anjou, N. Ghattamaneni, B. Harack, M. Hilke, A. Horth, N. Majlis, M. Massicotte, L. Vandsburger, E. Whiteway, V. Yu, Experimental review of graphene. ISRN Condens Matter Phys **2012**, 56 (2012)
29. A. Ashraf, Y. Wu, M.C. Wang, N.R. Aluru, S.A. Dastgheib, S.W. Nam, Langmuir **30**, 12827 (2014)
30. W.S. Han, J.M. Hong, H.S. Kim, Y.W. Song, Nanotechnology **22**, 395705 (2011)
31. N. Salaets, M. Ervin, ARL-TR-4854, 2009
32. R. Rastogi, R. Kaushal, S.K. Tripathi, A.L. Sharma, I. Kaur, L.M. Bharadwaj, J Colloid Interface Sci **328**, 421 (2008)
33. R. Cheng, J. Carvell, F.Y. Fradin, J Appl Phys **108**, 53720 (2010)

Chapter 4
Defects Engineering for Performing $SrTiO_3$-Based Thermoelectric Thin Films: Principles and Selected Approaches

Andrei V. Kovalevsky

4.1 Introduction

4.1.1 Background: Thermoelectric Materials and Applications

A challenging task for the energy sector worldwide is represented by the development of environmentally friendly sources of the electrical power. "Green" energy sources are rapidly becoming more and more important to meet the increasing energy demand, limited availability of the fossil fuels and various environmental issues, including CO_2 emissions, global warming, and impacts of other emissions on human health. One of the promising solutions is the thermoelectric conversion of waste heat or solar heat into electricity by reliable, sustainable, and scalable devices, with self-sufficiency to enable mobile or remote applications [1–3]. Significant impact for the future sustainable technologies is also supported by the fact that most of the energy (60–70%) used in the world is discharged as waste heat [3]. Theoretically, thermoelectric generation provides one of the most reliable ways for conversion, irrespectively of the source size and without using turbines, moving parts or producing CO_2, with potential applications in power plants, various industrial processes, incinerators, geothermal sources, and for automotive waste heat recovery. Recent research results have convincingly demonstrated good prospects of thermoelectric technology for power generation from concentrated solar irradiation, in the systems involving salinity gradient solar ponds, evacuated tube heat pipe solar collectors, and biomass powered stoves [2, 4].

A.V. Kovalevsky (✉)
Department of Materials and Ceramic Engineering, CICECO—Aveiro Institute of Materials, University of Aveiro, 3810-193 Aveiro, Portugal
e-mail: akavaleuski@ua.pt

J. Zhang, Y.-G. Jung (eds.), *Advanced Ceramic and Metallic Coating and Thin Film Materials for Energy and Environmental Applications*,
DOI 10.1007/978-3-319-59906-9_4

The efficiency of thermoelectric conversion is limited by the Carnot efficiency and is described by the figure of merit (ZT) of a candidate material,

$$\mathrm{ZT} = \sigma \times \alpha^2 \times T/\kappa \tag{4.1}$$

which includes the electrical conductivity (σ), Seebeck coefficient (α), and thermal conductivity (κ). The product $\sigma \times \alpha^2$ defines the power factor (PF), which relates to the electronic properties. Operation at higher temperature is desirable, as it correspondingly yields higher Carnot efficiency of the conversion. However, in this case the thermoelectric materials with high thermal and chemical stability are required. Additional economic and safety issues are imposed by natural abundance of the constituent elements and their minimal toxicity towards "greener" operation.

One of the major challenges in developing highly efficient TE materials is to achieve a delicate balance between the functional properties, namely, σ, α, and κ [5]. For many years, development of new thermoelectrics was slowed down basically for all types of materials, due to coupling between electrical and thermal properties. As an example, an increase in electrical conductivity is usually accompanied with a decrease of the Seebeck coefficient and higher thermal conductivity, without noticeable benefits for the final performance. The progress in creating low-dimensional structures and structural engineering in complex materials broke this coupling, with emphasis on enhanced phonon interface scattering, efficiently lowering the thermal conductivity, and modification of the electronic band structure, band convergence, and quantum-confinement effects, leading to an enhanced power factor [5–7]. A promising approach for advanced bulk thermoelectrics targets those materials demonstrating the so-called phonon-glass/electron-crystal (PGEC) behaviour, namely, low thermal conductivity as in a glass, and a high electrical conductivity of crystals [8]. This can be accomplished through introducing heavy-ion species with large vibrational amplitude (rattlers) at partially filled structural sites, as in skutterudites [6, 9].

Modern challenges in thermoelectric research thus include both search for new advanced materials and efficient fabrication concepts, allowing to maintain appropriate level of the relevant properties, being at the same time cheap and environmentally friendly. The demand for performing TE materials having ZT around unity ($\mathrm{ZT} \geq 1$) for low- and intermediate temperature applications is covered by "traditional" Bi_2Te_3, Bi_2Se_3, and PbTe-based thermoelectrics, based, however, on toxic and low-abundant constituents [3, 5]. Existing alternatives with promising peak ZTs of 0.7–1.2 (skutterudites, Half-Heusler, etc.) still lack the thermal and chemical stability at ~500–600 °C or require a protection/vacuum packing to operate at high temperatures [10, 11]. Some of these best-performing materials need expensive and time-consuming production methods like high-energy milling, arc-melting, vacuum processing, etc. Oxide materials represent a promising alternative, especially for high-temperature thermoelectric applications, provided by their thermal and chemical stability, high natural abundance, and less toxic composition.

4.1.2 Oxide Thermoelectrics and Strontium Titanate

Oxide-based electroceramics already became indispensable for many key technologies, including energy storage and conversion. Triggered by the discovery of high thermoelectric performance in layered $NaCo_2O_4$ and some other Co-containing materials [12–14], particular research efforts have been focused on the TE properties of various transition metal-based oxides [15]. Appropriate high-temperature stability enables several specific applications, such as direct conversion of concentrated solar radiation to electricity, waste heat recovery from exhaust gases, produced by ceramics, concrete and glass industry, and automobiles. Additional functionalities can be provided by unique redox flexibility of oxides, which can be precisely set-up by controlled heat treatments combined with oxygen partial pressure changes. Representative examples of thermoelectric oxide systems include $Ca_3Co_4O_9$-, ZnO-, $CaMnO_3$-, and $SrTiO_3$-based materials [15–19]. Yet, ZT values obtained for the best-known oxide thermoelectrics are lower than those required by most of the potential applications.

An important family of oxide thermoelectrics is represented by donor-substituted strontium titanate [15, 18, 20], with the highest ZTs in bulk ceramics reached up to now of about 0.4 at 970–1200 K [21–23]. Versatile perovskite-type structure provides an array of functional properties, including excellent thermal and phase stability, under both oxidizing and reducing conditions. The $SrTiO_3$-based perovskite unit cell is flexible to sustain significant stresses, imposed by various substitutions and defects. An appropriate power factor of $SrTiO_3$-based thermoelectrics can be achieved after sintering under very reducing conditions, ensuring the formation of electronic defects. Potential applications of strontium titanate-based thermoelectrics are, however, limited by large thermal conductivity and relatively low charge carrier mobilities ($\kappa \sim 12$ W m^{-1} K^{-1} and $\mu \sim 6$–8 cm^2 V^{-1} s^{-1} at 300 K for single crystals) [24]. Known approaches to promote the thermoelectric performance in strontium titanate include A- and/or B-site donor substitutions with rare-earth and/or transition metal cations to generate *n*-type charge carriers and supress the thermal conductivity by impurity scattering [15, 17, 18, 20–23]. Introducing the micro-/nanoinclusions and formation of core-shell structures are also being used to increase the phonon scattering and charge carrier mobility [25–27].

$SrTiO_3$-based materials possess complex defect chemistry, which is determined by the oxygen chemical potential in atmosphere, substitution level and A:B site ratio in the perovskite lattice [28, 29]. Largely due to this fact, the literature data regarding the substitution mechanisms and related effects on the thermoelectric performance are often inconsistent and contradictory. The complexity of the defect reactions imposes certain difficulties for accounting various defect types and their simultaneous effects. As an example, presence of A-site deficiency under reducing conditions may promote the formation of oxygen vacancies, while oxygen deficiency in perovskite layers may be still accompanied by Ruddlesden-Popper (RP) type planar faults and other "oxygen-excessive" defects [21]. In the work [30], based on comparative analysis of the thermal conductivities of reduced and

oxidized lanthanum-substituted strontium titanate, the oxygen vacancies were mentioned as efficient phonon scatterers. On the other hand, low thermal conductivity of A-site-deficient donor-substituted strontium titanate and its unusual "glass-like" behaviour were attributed exclusively to the presence of cation vacancies [31]. However, possible effects due to the formation/annihilation of other defects during reduction/oxidation were not assessed. In RP-type titanates, phonon scattering at $SrO/SrTiO_3$ interfaces was claimed as a reason for reduced thermal conductivity [32, 33], while the effects provided by oxygen vacancies in the perovskite layers are not considered. Thus, understanding the particular role of various defect types in thermoelectric properties of $SrTiO_3$-based materials and tuning their contribution towards enhanced performance still remain a big challenge.

4.1.3 $SrTiO_3$-Based Thermoelectric Thin Films

Oxide-based thin films concept is an efficient platform to access the fundamental transport properties and mechanisms, taking into account both easier control of the defect chemistry as compared to the bulk materials and additional possibilities for creating unique structures and defects clusters. Thin-film thermoelectrics are also expected to play an increasing role in applications towards waste heat recovery and simple cooling ([34] and references therein). Strontium titanate is quite commonly used as a substrate for thin film growth and as a model system for studying defects in the perovskites, in particular, due to a wide range of relevant properties from insulating to superconducting ([34] and references therein). The discovery of large Seebeck coefficient in lanthanum-substituted $SrTiO_3$ [35] has boosted the exploration of thin-film-thermoelectrics concept for these materials, mostly using pulsed laser deposition. In particular, one of the first studies of thermoelectric properties in Nb-substituted $CaTiO_3$-$SrTiO_3$-$BaTiO_3$ system was performed on the samples, deposited by this method [36]. Other techniques including molecular beam epitaxy and sputtering were also successfully applied for growth of substituted $SrTiO_3$-based films [34, 37, 38]. Several in-depth investigations were performed to access the effects of various substitutions, simultaneous co-substitutions, and RP planar faults on the thermoelectric properties of such films [34, 37–41]. One of the highest performances ever reached in thermoelectric titanates ($ZT \sim 0.37$ at 1000 K) was observed for heavily Nb-substituted $SrTiO_3$ epitaxial films, grown on insulating (100)-oriented $LaAlO_3$ single-crystalline substrates by pulsed laser deposition method [39]. A promising pathway to design performing thermoelectric thin films, based on simultaneous donor co-substitution in Sr- and Ti-sites of $SrTiO_3$, which results in well-distributed phononic scattering centres and suppressed lattice thermal conductivity, was demonstrated in [41].

Due to non-optimized charge carrier concentration and film fabrication procedure, yet the ZT values obtained for films are often below those attained in the bulk materials of the same composition. However, some specific and elegant solutions are facilitated in thin films. As an example, an unique crystal engineering

approaches by deliberate introduction of strontium vacancy clusters and altering the strain in Nb-substituted $SrTiO_3$ films resulted in exceptionally high charge carrier mobility above 53,000 $cm^2\ V^{-1}\ s^{-1}$ [42]. Thermoelectric properties are known to be influenced by low dimensionality, as predicted by Hicks and Dresselhaus [6, 43]; the conceptual solutions can be realized in ultrathin films and superlattices. Large Seebeck coefficients were reported in the so-called two-dimensional electron gas systems, based on dimensionally confined Nb-substituted $SrTiO_3$ layers in $SrTiO_3$/$SrTi_{0.8}Nb_{0.2}O_3$ superlattices and TiO_2/$SrTiO_3$ heterointerfaces [44], leading to a maximum estimated ZT of 2.4 at room temperature. Today, many research efforts are focused on fabricating thermally robust $SrTiO_3$-based superlattices, where both high power factor and low thermal conductivity are provided by introducing alternating layers of various compositions. Recently, novel superlattice structures based on epitaxial nanoscale layers of NbO_x and $SrTi_{0.8}Nb_{0.2}O_3$ layers on $LaAlO_3$ support were successfully fabricated by pulsed laser deposition, and relevant effects of layers thickness ratio on the thermoelectric properties were investigated [45]. High ZT value of 0.46 at 1000 K was observed in epitaxial superlattices composed from alternating layers of $Sr_{0.95}Pr_{0.05}TiO_3$ and $SrTi_{0.8}Nb_{0.2}O_3$ grown on an $LaAlO_3$ support [46] (Fig. 4.1).

These superlattices also possess an excellent thermal stability and show reproducible thermoelectric properties after thermal cycling, what is of special importance for potential applications. Although these studies highlight great prospects for thin film technology towards advanced thermoelectrics, the question how such superlattices can be implemented in scalable thermoelectric devices still remains. In this chapter, some recent research results are reviewed to show how, by altering

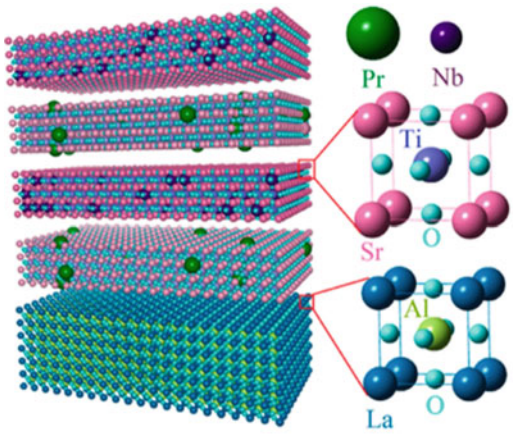

Fig. 4.1 Schematic diagram of epitaxial perovskite $[(Sr_{0.95}Pr_{0.05}TiO_3)_a/(SrTi_{0.8}Nb_{0.2}O_3)_b]_{20}$ superlattices on an $LaAlO_3$ substrate. The unit cells of $LaAlO_3$ substrate, $SrTiO_3$, and the extrinsic dopants (Pr^{3+} and Nb^{5+}) in each layer are shown with arbitrary atomic sizes (for illustration purpose). Adapted with permission from [46]. Copyright (2015) American Chemical Society

the defect chemistry mechanisms is donor-substituted $SrTiO_3$, one can significantly improve the thermoelectric performance, with particular prospects for implementation in thin films.

4.2 Methods

4.2.1 Processing of the Samples

A series of various (Sr,Pr)$TiO_{3\pm\delta}$, Sr(Ti,Ta)$O_{3\pm\delta}$, and Sr(Ti,Nb)$O_{3\pm\delta}$-based ceramic materials were synthesized via a conventional solid-state route, using carbonate or oxide precursors, as described in [47–49]. To enhance densification, which is essential for the correct comparison of the thermoelectric properties for the different samples, in several cases the ceramics was sintered through two-step approach [47]. In this case, the main densification step was conducted in air at 1973 K for 10 h. Pre-sintered ceramics were further reduced in 10%H_2–90%N_2 atmosphere at 1773 K for 10 h. Otherwise, the compacted samples were sintered directly in reducing atmosphere at 1773 K for 10 h. The oxidized samples in $Sr_{1-y}Ti_{0.9}Nb_{0.1}O_{3\pm\delta}$ series after the first processing step were also considered for structural and thermal transport studies to obtain additional information on the role of A-site and oxygen vacancies on the lattice thermal conductivity. Subsequently, the prepared ceramic samples were ground into the fine powders for X-ray diffraction (XRD), thermogravimetric (TG), transmission electron microscopy (TEM), and differential scanning calorimetry (DSC) studies. The total conductivity and Seebeck coefficient were measured on freshly cut ceramic rectangular bars (~2 × 3 × 12 mm^3). The sintered disc-shaped ceramics, polished down to ~1.00 mm thickness for removing possible surface contamination and providing uniform geometry, were used for the thermal diffusivity studies. For further assessment by SEM/EDS, the ceramic samples were polished and thermally etched. The experimental densities (ρ) of disc-shaped ceramics were calculated from geometrical measurements and weighing. X-ray photoelectron spectroscopy (XPS) was performed on the as-fractured sample surfaces. More processing details for the discussed materials are given in [47–49].

4.2.2 Structural and Microstructural Characterization

The room-temperature XRD patterns were recorded using Rigaku D/Max-B and PANalytical X'Pert Pro diffractometers (Cu K_α, $2\Theta = 10–80°$, step 0.02°, exposition 3–5 s). The patterns were used for analysis of the phase composition of prepared samples and calculation of the unit cell parameters. Additional assessment of the phase purity and presence of any compositional inhomogeneities, which may

be crucial for the thermoelectric performance, was performed by complementary SEM (Hitachi SU-70 instrument) and EDS (Bruker Quantax 400 detector) studies on fractured and polished ceramics. Deeper studies of the crystal structure, morphology, and composition were carried out using TEM techniques at University of Zaragoza, including scanning transmission electron microscopy with a high annular angular dark field (STEM-HAADF) coupled with energy dispersive X-ray (EDX) measurements and electron energy loss spectroscopy (EELS) [48].

The total oxygen content of the studied materials was evaluated by TG; a detailed description of the corresponding procedure can be found in [47]. The temperature dependence of the relative weight changes was measured in flowing 10%H_2-N_2 mixture at 298–1373 K. The total oxygen content in reduced materials was estimated on complete oxidation in air at 1273 K, assuming 2+, 3+, 4+, and 5+ oxidation states for strontium, praseodymium, titanium, and tantalum/niobium, correspondingly.

The electronic structure and cationic composition were further evaluated using X-ray photoelectron spectroscopy (XPS), performed at CEMUP (Porto, Portugal) in a Kratos AXIS Ultra HSA spectrometer equipped with monochromatic Al K_α radiation (1486.7 eV). More experimental details can be found elsewhere [48, 49]. Atomic contents were determined with a standard accuracy of ±10% from the corresponding peak areas and normalized by the sensitivity factors provided by the manufacturer. To avoid possible oxidation and maintain the same conditions for all studied compositions, the ceramic samples were broken immediately prior to being placed to the measurement chamber; further XPS studies were performed on those fresh fractures.

4.2.3 Evaluation of the Electrical Properties

The total electrical conductivity and Seebeck coefficient were measured simultaneously using bar-shaped samples placed in specially developed alumina holder system described in [50]. The measurements were performed in 10%H_2–90%N_2 mixture after equilibration at 473–1173 K, decreasing the temperature by steps of 50–80 K. While Seebeck coefficient measurements were performed at typical temperature gradients of 15–30 K, after each 2–3 steps the dependence of thermal voltage on the temperature gradient was verified in order to reveal and eliminate the effect of any voltage offset. For all measured compositions, the contribution of the offset voltage into the measured thermal voltage was found to be less than 3%. For the total conductivity, four-probe DC technique was used. The criteria for equilibration of a sample after change in temperature included the relaxation rates of the conductivity and Seebeck coefficient less than 0.1%/min and 0.002 mV/(K × min), respectively.

4.2.4 Studies of the Thermal Transport

The thermal conductivity ($\kappa = D\rho c_p$) was determined indirectly by measurements of thermal diffusivity (D) (Netzsch LFA 457 Microflash), specific heat capacity (c_p) (Netzsch DSC 404 C), and density. The detailed measurement procedure can be found elsewhere [47–49]. The measurements were performed in flowing 5%H_2–95%Ar mixture at 423–1273 K; the experimental route included stepwise (50 K) change in temperature, followed by dwell of 15–30 min for thermal equilibration of the sample. The estimated error in obtained values of thermal conductivity was less than 10% for all measured samples. In the case of $Sr_{1-y}Ti_{0.9}Nb_{0.1}O_{3\pm\delta}$ system, thermal conductivity studies were also performed for oxidized materials in air atmosphere under identical temperature conditions, aiming on comparative analysis of the thermal transport in oxidized and reduced samples. The lattice contribution to the thermal transport was calculated from the data on electrical and thermal conductivities, using Wiedemann-Franz law:

$$\kappa_{ph} = \kappa - LT\sigma \tag{4.2}$$

where L is the Sommerfeld value (2.45×10^{-8} W Ω K^{-2}) of the Lorenz number.

4.3 Results and Discussion

4.3.1 Guidelines for Defects Engineering Strategies

General idea behind the defect chemistry engineering for enhanced thermoelectric performance approach is based on the strategy to shift prevailing defect types by controlling the nominal chemical composition of donor-substituted strontium titanate-based materials, while corresponding changes in the relevant properties can be followed and linked to the actual defect structure. A reasonable pathway, naturally provided by exceptional stability of the SrTiO3-based perovskite unit cell against imposed lattice stresses, is based on gradual transition from structures, containing significant amounts of extended oxygen-rich defects to oxygen nonstoichiometry on introducing the A-site deficiency in the perovskite layers. The compositions range, discussed in this chapter, covers strontium titanates, donor-substituted either in A-sites by praseodymium, or in B-sites by niobium or tantalum. This allows to compare the impacts coming from the defect chemistry in various systems for conclusive interpretations of the obtained results. The series of studied ceramic materials thus included those containing A-site cation excess, stoichiometric A:B = 1:1 perovskites and A-site deficient compositions, the complete list of the compositions is given in Table 4.1.

Total oxygen content in perovskite-type titanates represents an excellent in situ indicator for predominant charge compensation and defect formation mechanisms.

Table 4.1 Chemical and phase composition of the studied donor-substituted strontium titanates

System	A-site composition	Prepared materials	Phase composition	Lattice parameters, Å
$(Sr,Pr)TiO_{3\pm\delta}$ [47]	Stoichiometric	$Sr_{0.95}Pr_{0.05}TiO_{3\pm\delta}$	CP[a]	a = 3.9086(3)
		$Sr_{0.90}Pr_{0.10}TiO_{3\pm\delta}$	TP	a = 5.5294(5) c = 7.8124(6)
		$Sr_{0.80}Pr_{0.20}TiO_{3\pm\delta}$	TP	a = 5.5190(3) c = 7.8363(4)
		$Sr_{0.70}Pr_{0.30}TiO_{3\pm\delta}$	OP	a = 5.5378(2) b = 7.7971(3) c = 5.5217(2)
	Deficient	$Sr_{0.925}Pr_{0.05}TiO_{3\pm\delta}$	CP	a = 3.9056(2)
		$Sr_{0.85}Pr_{0.10}TiO_{3\pm\delta}$	TP	a = 5.5266(6) c = 7.8061(9)
		$Sr_{0.70}Pr_{0.20}TiO_{3\pm\delta}$	TP	a = 5.5108(3) c = 7.8250(4)
		$Sr_{0.55}Pr_{0.30}TiO_{3\pm\delta}$	TP	a = 5.5002(2) c = 7.8122(3)
$Sr(Ti,Nb)O_{3\pm\delta}$ [47, 48]	Excess	$Sr_{1.05}Ti_{0.90}Nb_{0.10}O_{3\pm\delta}$	CP	a = 3.9212(2)
	Stoichiometric	$SrTi_{0.90}Nb_{0.10}O_{3\pm\delta}$	CP	a = 3.9206(2)
		$SrTi_{0.80}Nb_{0.20}O_{3\pm\delta}$	CP	a = 3.9357(2)
	Deficient	$Sr_{0.97}Ti_{0.90}Nb_{0.10}O_{3\pm\delta}$	CP	a = 0.39223(1)
		$Sr_{0.95}Ti_{0.90}Nb_{0.10}O_{3\pm\delta}$	CP	a = 3.9209(2)
		$Sr_{0.93}Ti_{0.90}Nb_{0.10}O_{3\pm\delta}$	CP + minor TiO_2	a = 3.9200(2)
		$Sr_{0.97}Ti_{0.8}Nb_{0.2}O_{3\pm\delta}$	CP	a = 3.9281(1)
		$Sr_{0.94}Ti_{0.8}Nb_{0.2}O_{3\pm\delta}$	CP	a = 3.9287(1)
		$Sr_{0.90}Ti_{0.8}Nb_{0.2}O_{3\pm\delta}$	CP	a = 3.9316(1)
$Sr(Ti,Ta)O_{3\pm\delta}$ [49]	Stoichiometric	$SrTi_{0.95}Ta_{0.05}O_{3\pm\delta}$	CP	a = 3.9131(2)
		$SrTi_{0.90}Ta_{0.10}O_{3\pm\delta}$	CP	a = 3.9201(2)
		$SrTi_{0.80}Ta_{0.20}O_{3\pm\delta}$	CP	a = 3.9323(3)
		$SrTi_{0.70}Ta_{0.30}O_{3\pm\delta}$	CP	a = 3.9428(2)
	Deficient	$Sr_{0.975}Ti_{0.95}Ta_{0.05}O_{3\pm\delta}$	CP	a = 3.9128(3)
		$Sr_{0.95}Ti_{0.90}Ta_{0.10}O_{3\pm\delta}$	CP	a = 3.9197(2)
		$Sr_{0.90}Ti_{0.80}Ta_{0.20}O_{3\pm\delta}$	CP	a = 3.9318(2)
		$Sr_{0.85}Ti_{0.70}Ta_{0.30}O_{3\pm\delta}$	CP + minor TiO_2	a = 3.9361(2)

[a]CP, TP, and OP correspond to cubic, tetragonal, and orthorhombic perovskites, accordingly

Fig. 4.2 shows the estimates of the total oxygen content for several representative materials [47–49], obtained from the TG data. According to the current state of knowledge on the defect reactions in substituted strontium titanate, at temperatures below 1350–1470 K the diffusion of cations is slow [51]. Thus, any impacts from re-equilibration of the cation sublattices at temperatures of thermoelectric studies on the relevant properties can be neglected. At the same time, oxygen ions and vacancies are several orders of magnitude more mobile, suggesting that oxygen

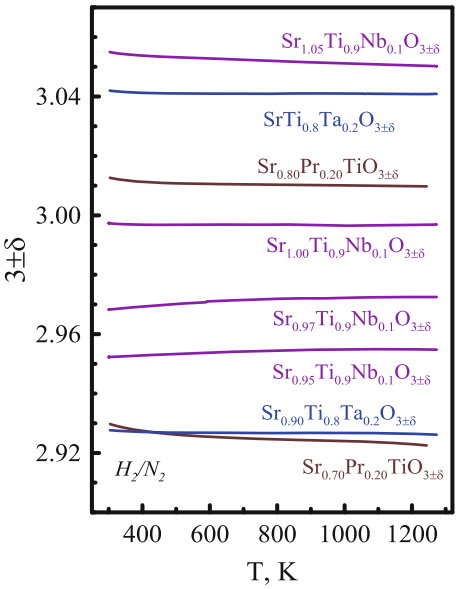

Fig. 4.2 Temperature dependence of the total oxygen content estimated from TG data [47–49]

nonstoichiometry can be considered as a reasonable prediction tool to evaluate the predominant defect types. The changes in total oxygen content $3 \pm \delta$, measured in relevant conditions of the thermoelectric characterization (300–1273 K, 10%H_2–90%N_2 atmosphere), are rather minor (Fig. 4.2). This also implies that the results of structural studies (XRD/XPS/HRTEM) performed at room temperature are relevant for the whole studied temperature range.

The $Sr_{1.05}Ti_{0.90}Nb_{0.10}O_{3\pm\delta}$ is the only intentionally A-site excess composition between those studied (Table 4.1) and also demonstrates the highest oxygen overstoichiometry (Fig. 4.2). In closely packed perovskite structure, the formation of truly interstitial oxygen ions as point defects is unlikely to take place [52, 53]. Known alternative way to compensate oxygen excess refers to the formation of SrO shear layers, similar to Ruddlesden-Popper (RP) phases [28, 29]. In this case, the formation of $(SrO)^{RP}$ is also guided by intentional nominal excess of strontium. Thus, using a standard Kröger-Vink notation, one may assume the following defect reaction for $Sr_{1.05}Ti_{0.90}Nb_{0.10}O_{3\pm\delta}$:

$$\begin{aligned}(1+\beta)\ \mathrm{SrO} + 0.05\,\mathrm{Nb_2O_5} + 0.9\,\mathrm{TiO_2} \\ \rightarrow \mathrm{Sr}_{\mathrm{Sr}}^{x} + \beta(\mathrm{SrO})^{\mathrm{RP}} + 0.8\mathrm{Ti}_{\mathrm{Ti}}^{x} + 0.1\,\mathrm{Ti}'_{\mathrm{Ti}} + 0.1\,\mathrm{Nb}_{\mathrm{Ti}}^{\bullet} + 3\,\mathrm{O}_{\mathrm{O}}^{x} \\ + 0.25\,\mathrm{O_2\,(g)}\end{aligned} \tag{4.3}$$

Several nominal A-site stoichiometric compositions also demonstrate an oxygen content above three, as shown for $SrTi_{0.80}Ta_{0.20}O_{3\pm\delta}$ and $Sr_{0.80}Pr_{0.20}TiO_{3\pm\delta}$ (Fig. 4.2). In addition to the formation of $(SrO)^{RP}$ planar faults, excessive oxygen in $SrTi_{0.80}Ta_{0.20}O_{3\pm\delta}$, $SrTi_{0.80}Nb_{0.20}O_{3\pm\delta}$, and other tantalum-containing A-site

stoichiometric samples can be accommodated through the formation of $Sr_2Ta_2O_7$- and $Sr_2Nb_2O_7$-like layers (O''_{layer}) [54, 55]. This can be represented by the following defect reaction (Me = Nb or Ta in $SrTi_{1-z}Me_zO_{3\pm\delta}$):

$$\begin{aligned} SrO + (z/2)Me_2O_5 + (1-z)TiO_2 \rightarrow (1-(1-\phi)z/2)Sr_{Sr}^{\times} + ((1-\phi)z/2)V''_{Sr} + \\ ((1-\phi)z/2)SrO^{RP} + + (1-z)Ti_{Ti}^{\times} + zMe_{Ti}^{\bullet} + \\ (\phi z/2)O''_{layer} + 3O_O^{\times} \end{aligned} \tag{4.4}$$

where ϕ denotes the contribution of the above layers, which can be viewed as a result of cutting the cubic perovskite lattice along the (110) direction and insertion of additional oxygen [54]. The value of ϕ is expected to increase for higher content of the B-site donor additive.

Quite similar defect reaction is expected for A-site stoichiometric Pr-substituted samples $Sr_{1-x}Pr_xTiO_{3\pm\delta}$, where accommodation of excessive oxygen can also be viewed as a combined result of the formation of rock-salt $(SrO)^{RP}$ layers and structures similar to those described for $(La,Sr)TiO_3$ system [56] as members of $A_nB_nO_{3n+2-\delta}$ series:

$$\begin{aligned} (1-x)SrO + (x/2)Pr_2O_3 + TiO_2 \rightarrow (1-x-(1-\varphi)x/2)Sr_{Sr}^{\times} + ((1-\varphi)x/2)V''_{Sr} + \\ + ((1-\varphi)x/2)SrO^{RP} + xPr_{Sr}^{\bullet} + Ti_{Ti}^{\times} \\ + (\varphi x/2)O''_{layer} + 3O_O^{\times} \end{aligned} \tag{4.5}$$

The contribution of these series, which can be described as perovskite slabs joined by crystallographic shears with excess oxygen (O''_{layer}), is denoted by φ and may increase for high praseodymium content.

On the contrary, the total oxygen content in A-site deficient compositions is notable below three (Fig. 4.2), indicating progressive formation of the oxygen vacancies as a predominant type of oxygen defects under reducing conditions. Corresponding defect chemistry mechanism involves the formation of cation vacancies ($V_O^{\bullet\bullet}$) and electronic defects (Ti'_{Ti}) to compensate for donor substitution:

$$\begin{aligned} (1-z/2)SrO + (z/2)Me_2O_5 + (1-z)TiO_2 \rightarrow (1-z/2)Sr_{Sr}^{\times} + (z/2)V''_{Sr} + zMe_{Ti}^{\bullet} + \\ (2\delta)Ti'_{Ti} + + (1-z-2\delta)Ti_{Ti}^{\times} \\ + \delta V_O^{\bullet\bullet} + (3-\delta)O_O^{\times} + (\delta/2)O_2(g) \end{aligned} \tag{4.6}$$

In the case of A-site Pr-substituted titanates corresponding defect reaction can be represented as:

$$(1-1.5x)\mathrm{SrO}+(x/2)\mathrm{Pr_2O_3}+\mathrm{TiO_2}\rightarrow(1-1.5x)\mathrm{Sr_{Sr}^{\times}}+(0.5x)\mathrm{V_{Sr}''}+x\mathrm{Pr_{Sr}^{\bullet}}+(2\delta)\mathrm{Ti'_{Ti}}++(1-2\delta)\mathrm{Ti_{Ti}^{\times}}+\delta\mathrm{V_O^{\bullet\bullet}}+(3-\delta)\mathrm{O_O^{\times}}+(\delta/2)\mathrm{O_2(g)} \quad (4.7)$$

Additional significant contribution to the formation of oxygen vacancies is expected due to direct reduction of the titanium cations:

$$2\mathrm{Ti_{Ti}^{x}}+\mathrm{O_O^{x}}\rightarrow 2\mathrm{Ti'_{Ti}}+\mathrm{V_O^{\bullet\bullet}}+(\delta/2)\mathrm{O_2(g)} \quad (4.8)$$

While the reactions (Eqs. 4.3–4.5) and (Eqs. 4.6 and 4.7) describe the defects formation in Sr-excessive and stoichiometric, and A-site deficient compositions, correspondingly, the reaction (Eq. 4.8) will contribute for all materials, prepared under reducing conditions. It should be noticed that the A-site deficiency level in Sr(Ti,Ta)$O_{3\pm\delta}$ and (Sr,Pr)$TiO_{3\pm\delta}$ systems was selected based on nominal compensation for the excessive charge of the donor additive. In the compositions with gradual changes of the strontium concentration, namely, $Sr_{0.97}Ti_{0.90}Nb_{0.10}O_{3\pm\delta}$, $Sr_{0.97}Ti_{0.8}Nb_{0.2}O_{3\pm\delta}$, and $Sr_{0.94}Ti_{0.8}Nb_{0.2}O_{3\pm\delta}$, one may expect a combined contribution of the reactions (Eqs. 4.4, 4.6, and 4.8). In this way, the prevailing defect types are gradually shifted from oxygen-rich Ruddlesden-Popper type for A-site excessive and, most probably, stoichiometric compositions to oxygen and cation vacancies on introducing the strontium deficiency. This compositional design, allowing fine-tuning of the defect chemistry, should be, however, complemented by the structural studies to prove the proposed mechanisms and prevailing defect types.

4.3.2 Structural and Microstructural Features

The objective to elucidate the impact of structural features on thermoelectric properties implies that possible contributions of the compositional inhomogeneities, phase impurities, and microstructural differences should be minimized. Thus, all studied materials were firstly subjected to combined preliminary XRD/SEM/EDS studies, as described in [47–49]; some representative results are shown in Figs. 4.3 and 4.4, corresponding phase composition and lattice parameters are listed in Table 4.1. All prepared materials were found single-phase and have perovskite-type lattice, either cubic, tetragonal, or orthorhombic (e.g., Fig. 4.3a, b), except for $Sr_{0.85}Ti_{0.7}Ta_{0.3}O_{3\pm\delta}$ (Fig. 4.3c) and $Sr_{0.93}Ti_{0.9}Nb_{0.1}O_{3\pm\delta}$ (Fig. 4.3d) compositions. More detailed information can be found elsewhere [47–49]. The observed trends for the changes in lattice parameters (Table 4.1) with A-site composition are not completely clear, in particular, indicating that the defects formation and charge compensation mechanisms may be complex. Separation of minor secondary rutile phase for $Sr_{0.85}Ti_{0.7}Ta_{0.3}O_{3\pm\delta}$ (Fig. 4.3c), confirmed by EDS results (Fig. 4.4), is attributed to the compensation for significant deviation in the A/B perovskite sites

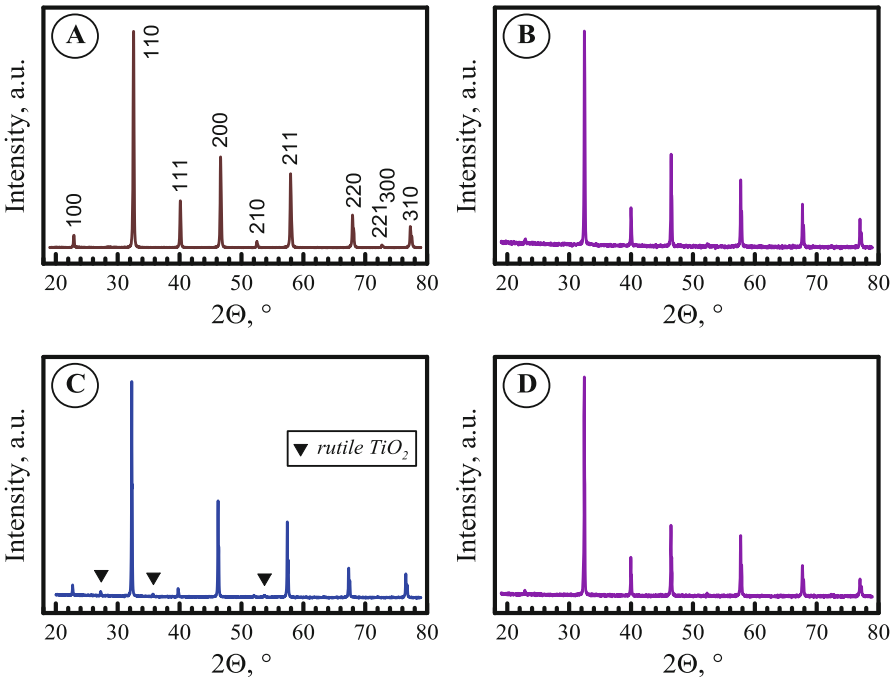

Fig. 4.3 Typical room-temperature XRD patterns of reduced $Sr_{0.95}Pr_{0.05}TiO_{3\pm\delta}$ (**a**), $Sr_{0.97}Ti_{0.9}Nb_{0.1}O_{3\pm\delta}$ (**b**), $Sr_{0.85}Ti_{0.7}Ta_{0.3}O_{3\pm\delta}$ (**c**), and $Sr_{0.93}Ti_{0.9}Nb_{0.1}O_{3\pm\delta}$ (**d**) [47–49]

ratio from stoichiometric [49]. Interestingly, the XRD results for $Sr_{0.93}Ti_{0.9}Nb_{0.1}O_{3\pm\delta}$ (Fig. 4.3d) suggest single-phase perovskite, while minor TiO_2 impurities were clearly identified by the EDS mapping (Fig. 4.4). In this case, the phase segregation is promoted by excessive A-site deficiency, exceeding the level of nominal donor charge compensation. The mapping results for other compositions suggest a homogeneous cations distribution at micron- and submicron scale.

The results of microstructural characterization, performed in [47–49], clearly indicated that the variations of A-site composition have a noticeable effect on the microstructure of prepared ceramic materials. Corresponding SEM results for selected representative samples are shown in Fig. 4.4. Even minor introduction of cation deficiency results in significant grain growth and better densification. According to some literature data, A-site deficiency promotes the grain growth in titanates, as the presence of strontium vacancies is crucial for solid-state diffusion step [57]. However, at the discussed size scale any specific contributions of the grain boundaries to the thermal and electronic transport can be neglected. The variations of grain dimensions correspond to the range of 2–15 μm, while one may expect significant effects rather for a large difference in grain size between the samples (at least, two orders of magnitude) or for submicron- and nanosized grain structures. Thus, for the discussed single-phase materials the changes in

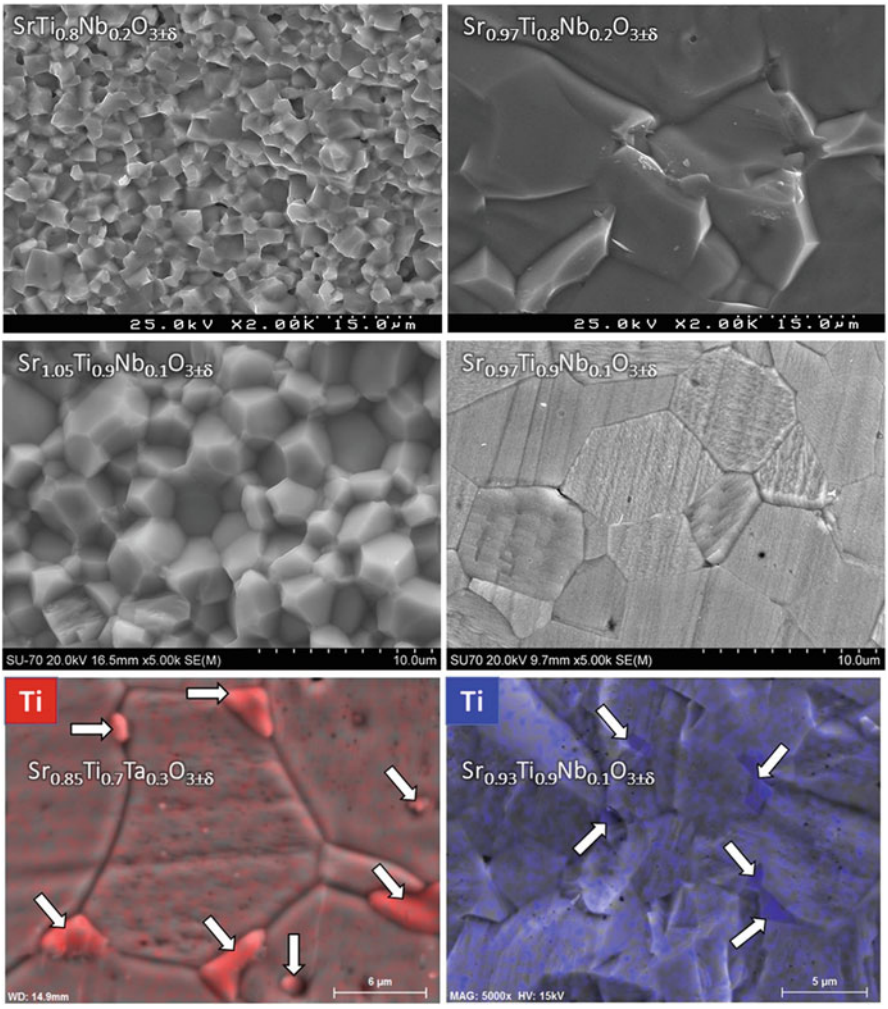

Fig. 4.4 SEM micrographs of reduced fractured and polished $Sr_{1-y}Ti_{0.8}Nb_{0.2}O_{3\pm\delta}$ and $Sr_{1-z}Ti_{0.9}Nb_{0.1}O_{3\pm\delta}$ samples. SEM mapping results are shown to illustrate TiO_2 exsolution (marked by *arrows*) for $Sr_{0.85}Ti_{0.7}Ta_{0.3}O_{3\pm\delta}$ (*left*) and $Sr_{0.93}Ti_{0.9}Nb_{0.1}O_{3\pm\delta}$ (*right*) materials. Adapted from [47–49] with permissions from the American Chemical Society (Copyright 2014 and 2015) and The Royal Society of Chemistry

thermoelectric properties can be mainly attributed to the structural differences and defect chemistry features, introduced by A-site composition design and donor substitution.

Detailed HRTEM studies to prove the proposed defect chemistry, mostly for oxygen-excessive compositions, were performed for $Sr_{1-y}Ti_{0.9}Nb_{0.1}O_{3\pm\delta}$ series [48]. The results clearly confirmed the formation of $(SrO)^{RP}$ in the case of $Sr_{1.05}Ti_{0.9}Nb_{0.1}O_{3\pm\delta}$ sample (Fig. 4.5). However, at the same time the studies

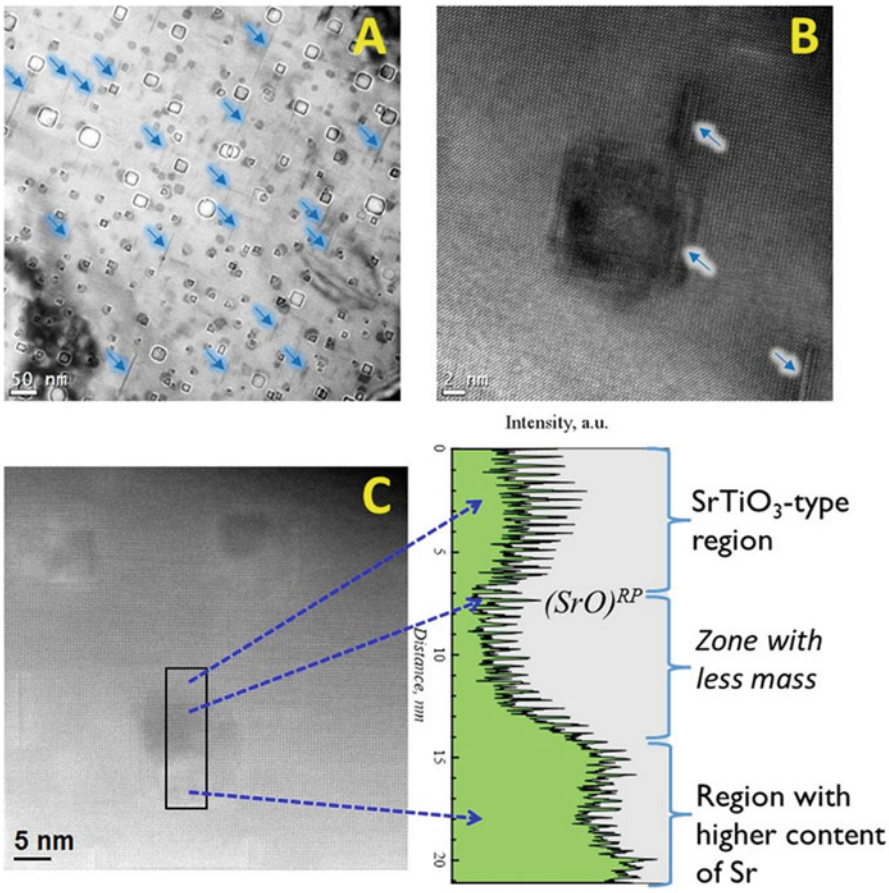

Fig. 4.5 TEM general view image showing RP faults and bubbles in a lamella prepared from sintered $Sr_{1.05}Ti_{0.90}Nb_{0.10}O_{3\pm\delta}$ ceramics (**a**); HRTEM image obtained for powdered reduced $Sr_{1.05}Ti_{0.90}Nb_{0.10}O_{3\pm\delta}$ sample (**b**). Arrows in (**a**) and (**b**) show $(SrO)^{RP}$ layers. STEM-HAADF image of the bubble-like region with RP defects (**c**). Analysis of the intensity contrast for image (**c**), where different regions including stoichiometric ideal $SrTiO_3$, RP-fault, empty zone, and zone with high strontium concentration can be detected (**d**). Reproduced from [48] with permission from The Royal Society of Chemistry

revealed a complex arrangement of the defect structures, described by the reaction (Eq. 4.3). A bright-field image (Fig. 4.5a) shows an area of a typical $Sr_{1.05}Ti_{0.9}Nb_{0.1}O_{3\pm\delta}$ grain, incorporating RP defects (marked by arrows), and some darker and bright spots with bubble-like shape, apparently having a high defect concentration. Figure 4.6 shows more details for the rock-salt shifts in RP planar faults, demonstrating the formation of SrO layers embedded parallel to (100) planes of the perovskite slabs. This represents a mechanism for accommodation of excess SrO in nominal $Sr_{1.05}Ti_{0.9}Nb_{0.1}O_{3\pm\delta}$ composition, which also shows the highest total oxygen content between studied materials (Fig. 4.2). The average

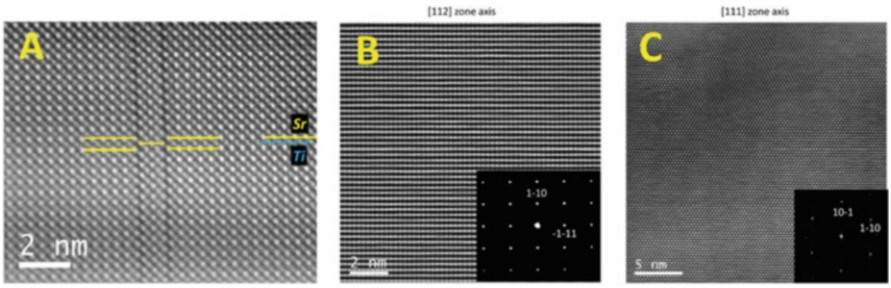

Fig. 4.6 (**a**) STEM-HAADF image of $Sr_{1.05}Ti_{0.90}Nb_{0.10}O_{3\pm\delta}$, showing a RP defect slab; (**b**, **c**) show HRTEM images of—$Sr_{0.97}Ti_{0.90}Nb_{0.10}O_{3\pm\delta}$ with a corresponding diffraction pattern of [112] and [111] zone axis. Reproduced from [48] with permission from The Royal Society of Chemistry

thickness of around 20 perovskite slabs per one rock-salt layer may be expected if to assume the site occupancy $(SrO)^{RP}_{0.05}\left(Sr\,Ti^{4+}_{0.8}Ti^{3+}_{0.1}Nb^{5+}_{0.1}O_3\right)^{perovskite}_{1.00}$.

Another possible pathway for donor compensation through the formation of cation vacancies implies that actual concentration of the RP defects may be even higher.

General TEM view of the $Sr_{1.05}Ti_{0.90}Nb_{0.10}O_{3\pm\delta}$ sample (Fig. 4.5a) reveals that the RP planar defects can be organized at least in two ways, including homogeneous distribution as isolated defects and concentration in the vicinity of bubble-like spots. The internal highly defective structure of the spot is shown in Fig. 4.5b. The analysis of the intensities, performed for high-resolution STEM-HAADF image (Fig. 4.5c), clearly indicates the mass contrast in the spot area and, thus, outlines the topography of these defect clusters, including surrounding perovskite-type layers, RP faults, hollow core, and a region with strontium excess. Most probably, the apparent topography is a result of releasing the lattice stresses, imposed by the excess of relatively large Sr^{2+} cations, which is likely to result in the formation of localized defect clusters with hollow cores. The size of these clusters vary in the range of 5–20 nm, where potential benefits for the enhanced phonon scattering can be foreseen.

Although in the case of $Sr_{0.97}Ti_{0.90}Nb_{0.10}O_{3\pm\delta}$ sample with intermediate level of the cation deficiency the partial compensation of Nb^{5+} by the formation of $(SrO)^{RP}$ is still possible, no evidences of presence for such defects were found by TEM studies, indicating that their concentration is relatively low or negligible. Corresponding HRTEM images and [112] and [111] SAED patterns (Fig. 4.6b, c) resemble the ideal $SrTiO_3$ perovskite structure. The same observations were obtained for the reduced $Sr_{1.00}Ti_{0.90}Nb_{0.10}O_{3\pm\delta}$.

In general, the results of structural studies support the defect structure, proposed for the A-site excessive and stoichiometric compositions, which also possess oxygen excess. Additional studies may be necessary to confirm the presence and organization of cation and oxygen vacancies, especially in the case where their defect clusters can be expected, as discussed below. However, for the discussed

materials the nominal A-site composition and total oxygen content, determined from TG data, appear to be enough reliable tools to assess the changes in concentration of those defects, also supported by existing knowledge on the defect chemistry of reduced donor-substituted strontium titanates.

4.3.3 *Structural Defects vs. Electrical Performance: The Case Studies*

Electronic conduction in donor-substituted strontium titanates is associated with Ti^{3+}/Ti^{4+} redox couple and is strongly affected by the concentration of donor additive (Eqs. 4.6 and 4.7) and extent of reduction (Eq. 4.8). Substitution of either strontium or titanium by higher valence cations promotes the formation of Ti^{3+} (Ti'_{Ti}) and filling of the n-type conduction band, also confirmed by a negative sign of the Seebeck coefficient for all studied materials in the whole temperature range [47–49]. Electrical conductivity of all A-site deficient samples decreases with increasing the temperature, indicating metallic-type conduction [47–49]. The same behaviour was observed for the majority of A-site stoichiometric compositions, except for $Sr_{0.80}Pr_{0.20}TiO_{3\pm\delta}$, $Sr_{0.70}Pr_{0.30}TiO_{3\pm\delta}$ [47], $SrTi_{0.80}Nb_{0.20}O_{3\pm\delta}$, and $SrTi_{0.70}Ta_{0.30}O_{3\pm\delta}$ [49]. The latter compositions and Sr-excess $Sr_{1.05}Ti_{0.90}Nb_{0.10}O_{3\pm\delta}$ [48] show rather thermally activated electronic transport with significantly lower conductivity values; a mixed case of metallic-semiconducting regime was observed for the $Sr_{0.55}Pr_{0.30}TiO_{3\pm\delta}$. An obvious preliminary conclusion is that, although conductivity is boosted by the introduction of electronic defects on substitution, the dependence on the donor concentration is not straightforward. This can be understood as a fingerprint of contributions from various structural defects, affecting the electronic transport.

In order to provide some visual guidelines on the effects of structural defects on the electrical performance, Fig. 4.7 shows a compositional dependence of various electrical properties in $(Sr,Pr)TiO_{3\pm\delta}$, $Sr(Ti,Ta)O_{3\pm\delta}$, and $Sr(Ti,Nb)O_{3\pm\delta}$ series, including conductivity, Seebeck coefficient, and power factor, at a fixed temperature. Interestingly, in both $(Sr,Pr)TiO_{3\pm\delta}$ (Fig. 4.7a–c) and $Sr(Ti,Ta)O_{3\pm\delta}$ (Fig. 4.7d–f) the difference in electrical properties between A-site stoichiometric and deficient compositions is relatively small at low and moderate substitution level (up to 10%), suggesting that the mechanisms for donor compensation are similar in these systems, while the concentration of generated defects is too small to exert any significant effects on the charge carriers. Relatively moderate increase of the electrical conductivity in $Sr_{1-y}Ti_{0.90}Nb_{0.10}O_{3\pm\delta}$ with A-site deficiency (Fig. 4.7g) also corroborates this assumption: corresponding changes in σ do not exceed ~20%. Heavily substituted samples (x, $z \geq 0.20$) show completely distinct behaviour, depending on the composition of A-site. Both electrical conductivity and, in several cases, Seebeck coefficient are improved by nominal A-site deficiency (Fig. 4.7a, b, d, e), whereas one can expect a decrease in α along with the σ increase. The changes

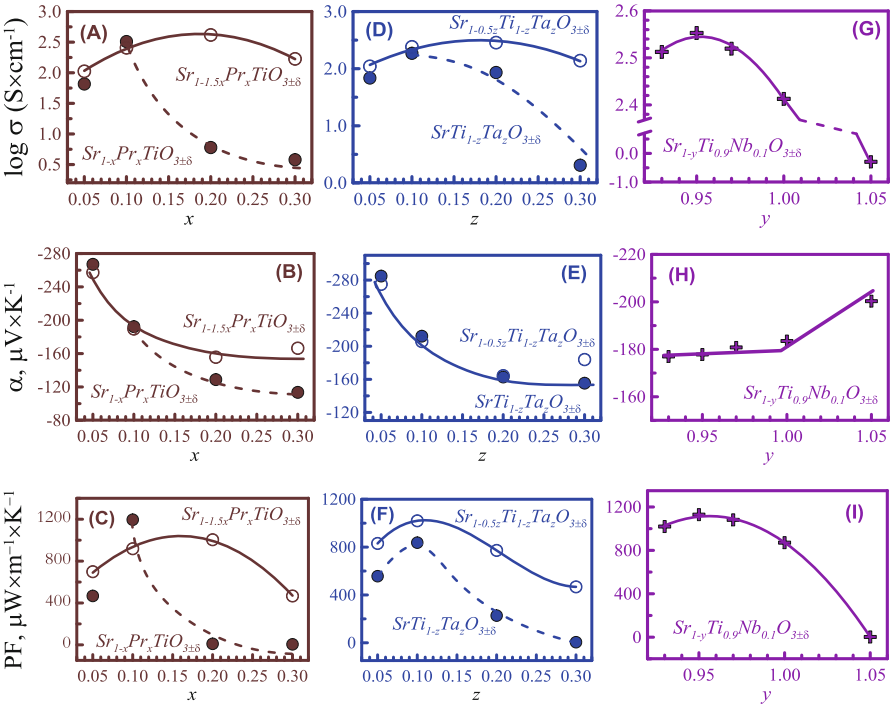

Fig. 4.7 Electrical properties of selected materials series at 800 K: electrical conductivity (**a**, **d**, **g**), Seebeck coefficient (**d**, **e**, **f**) and power factor (**g**, **h**, **i**). Closed and open circles correspond to nominally stoichiometric and A-site deficient compositions, respectively (**a**–**f**). Shown results were obtained by interpolation of the data presented in [47–49]

in Seebeck coefficient of $Sr_{1-y}Ti_{0.90}Nb_{0.10}O_{3\pm\delta}$ ($0.0 \leq y \leq 0.07$) are rather smooth (Fig. 4.7h), most likely due to relatively low donor substitution level.

Further insights regarding the mechanisms of such behaviour can be obtained from the results of XPS. Fig. 4.8 shows an example of deconvoluted Ti 2*p* and Ta 4*f* high-resolution spectra for $SrTi_{0.95}Ta_{0.05}O_{3\pm\delta}$ and $SrTi_{0.90}Ta_{0.10}O_{3\pm\delta}$ ceramic samples [49]; similar studies were performed in $Sr_{1-y}Ti_{0.90}Nb_{0.10}O_{3\pm\delta}$ system [48]. The binding energies and peak separation values, obtained from fitting, allowed to confirm the oxidation states of transition metal cations and quantify the cationic composition. As expected, in $Sr(Ti,Ta)O_{3\pm\delta}$ series titanium cations possess predominantly 4+ oxidation state, while the amount of Ti^{3+} was significantly lower and showed a tendency to increase with Ta substitution [49]. Although it is typically assumed that niobium substitutes titanium in 5+ oxidation state, the results revealed that at least a part of the niobium cations act as isovalent substituting species [48].

However, as a most important outcome, the results of the XPS studies, together with the electrical conductivity and Seebeck coefficient data, were used to calculate the charge carriers concentration (n) and to estimate the charge carrier mobility (μ)

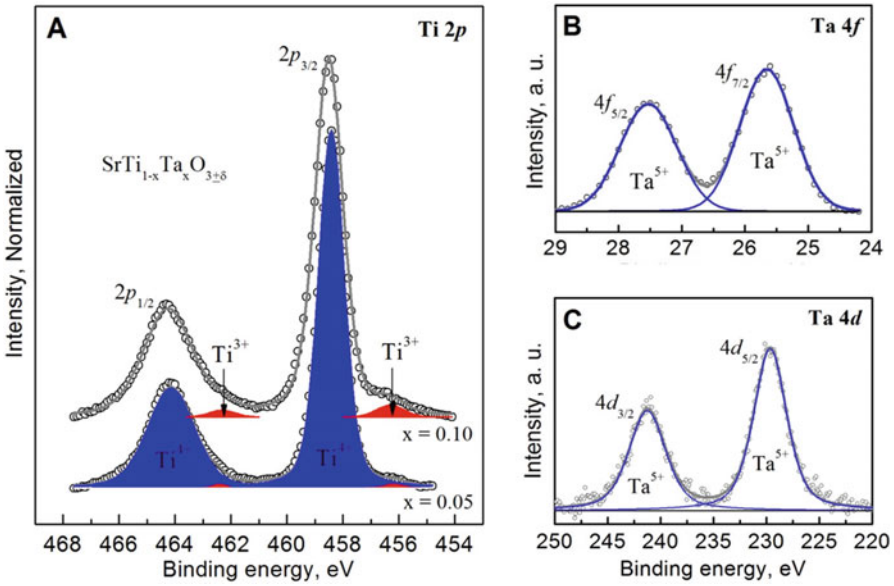

Fig. 4.8 Deconvoluted high-resolution XPS spectra of $Sr(Ti,Ta)O_{3\pm\delta}$ ceramics in (**a**) Ti 2*p*, (**b**) Ta 4*f*, and (**c**) Ta 4*d* core-level regions, respectively. Experimental points and the overall simulated spectra are represented by *open* symbols and *grey* lines, respectively. Spectra of Ti 2*p* were normalized by the Ti $2p_{3/2}$ peak intensity for easier comparison. Reprinted with permission from [49]. Copyright (2015) American Chemical Society

and effective mass (m^*/m_0, assuming a parabolic band model in the energy independent scattering approximation [25, 58]) using the equations below:

$$n = \left[\mathrm{Ti}^{3+}\right]/[\mathrm{Ti}]_{\mathrm{tot}} \times (1-z) \times N_{\mathrm{fu}}/V_{\mathrm{uc}} \tag{4.9}$$

$$\mu = \sigma/ne \tag{4.10}$$

$$m^*/m_0 = \frac{3\alpha e h^2}{8\pi^2 k_{\mathrm{B}}^2 \mathrm{Tm}_0 (\pi/3n)^{2/3}} \tag{4.11}$$

where $[\mathrm{Ti}]_{\mathrm{tot}}$ is the total concentration of titanium sites, z is the substitution level, N_{fu} is the number of formula units per unit cell, V_{uc} is the unit cell volume, e is the elementary charge, m_0 is the free electron mass, h is the Planck's constant and k_{B} is the Boltzmann constant.

The obtained results of the calculations, shown in Fig. 4.9, strongly suggest that introducing the A-site deficiency is favourable for enhancing the mobility of the charge carriers. The tendencies are clear for both $Sr(Ti,Ta)O_{3\pm\delta}$ (Fig. 4.9a) and $Sr_{1-y}Ti_{0.90}Nb_{0.10}O_{3\pm\delta}$ (Fig. 4.9b) series. A very likely explanation for this behaviour is the formation of extended defects (RP and other oxygen-excess) when strontium content approaches the stoichiometric and above, as described by Eq. 4.4. These defects promote scattering of the charge carriers and induce their localization, also

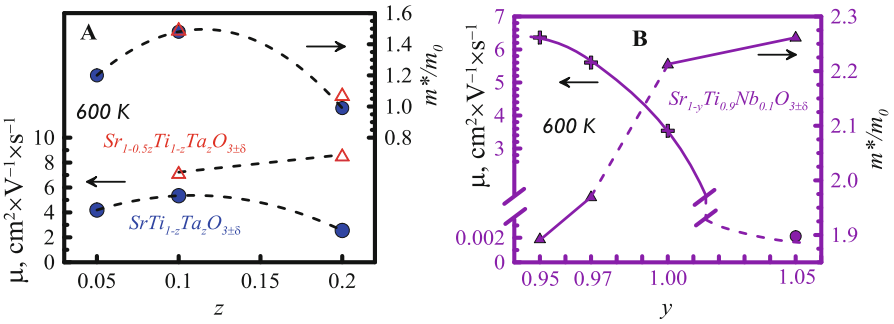

Fig. 4.9 Charge carrier mobility and effective mass at 600 K, calculated using Eqs. (4.10)–(4.12) based on the data published in [48, 49]. A-site stoichiometric and deficient compositions are represented by closed and opened symbols, respectively (**a**)

supported by the changes from metallic to semiconducting regime of the conduction as observed in [49]. Thus, extremely low mobilities were obtained for Sr-excess $Sr_{1.05}Ti_{0.90}Nb_{0.10}O_{3\pm\delta}$ (Fig. 4.9b), where high concentration of the RP planar faults and their clusters was confirmed by TEM (Figs. 4.5 and 4.6), while corresponding charge carrier concentration for this composition, obtained from XPS data, is similar to that for the other $Sr_{1-y}Ti_{0.90}Nb_{0.10}O_{3\pm\delta}$ samples.

It is also reasonable to state that both RP and highly deficient core-shell clusters have electrically insulating nature. A gradual increase in the mobility on decreasing the Sr content in $Sr_{1-y}Ti_{0.90}Nb_{0.10}O_{3\pm\delta}$ ($0.0 \leq y \leq 0.05$) suggests some additional guidelines on the effect of A-site deficiency on the electronic transport. Firstly, nominal cation deficiency avoids the formation of insulating defects, accommodating excessive oxygen. Secondly, progressive formation of strontium vacancies observed in Nb-substituted $SrTiO_3$ films facilitates high electron mobility by altering the local strains in the crystal lattice [42]; this might also be the case for the discussed $Sr_{1-y}Ti_{0.90}Nb_{0.10}O_{3\pm\delta}$ materials. Rather generic explanation may be based on the electronic structure, which is composed of a conduction band formed by Ti 3*d* orbitals and a valence band formed by an O 2*p* orbital, while strontium cations act rather as blocking species for the electronic transport. Thus, a lowest possible fraction of A-site cations may be favourable for the high conductivity, so long as it is within the stability limits of flexible perovskite lattice, providing an excellent 3D framework for the charge transport.

The results shown in Fig. 4.7b suggest some increase of the Seebeck coefficient due to A-site deficiency in (Sr,Pr)$TiO_{3\pm\delta}$ system. However, in general, the presence of structural defects accommodating excess oxygen is only slightly affecting the Seebeck coefficient (Fig. 4.7e,h), which is rather determined by the concentration of the charge carriers and the electronic structure of the perovskite matrix. Another important parameter, responsible for the changes in α, is the charge carrier effective mass. The results of estimation of m^*/m_0 values for Sr(Ti, Ta)$O_{3\pm\delta}$ system (Fig. 4.9a) indicate negligible variations of this parameter in response to A-site composition, corresponding changes obtained for $Sr_{1-y}Ti_{0.90}Nb_{0.10}O_{3\pm\delta}$ materials

are rather moderate (Fig. 4.9b). In quasi-classical approach of the semiconductor theory, the charge carrier mobility can also be represented as:

$$\mu = \frac{e\tau}{m^*} \tag{4.12}$$

where τ is a phenomenological scattering time to account for the scattering of the electrons by impurities and phonons. Thus, the data shown in Fig. 4.9b illustrates the relevant effects of the A-site composition on the electronic band structure, resulting in mobility increase for cation-deficient compositions.

The coupling between electrical properties is a known obstacle for boosting the power factor in materials with similar crystal structures. A striking feature is that designing the A-site composition in donor-substituted titanates allows to tune the electrical conductivity and Seebeck coefficient quasi-independently. This obviously can be considered as a particular benefit for seeking highly performing $SrTiO_3$-based thermoelectrics. In all studied series (Fig. 4.7c, f, i), the power factor was significantly higher for A-site deficient compositions, especially at high donor substitution level. A slight decrease in PF observed for $Sr_{0.93}Ti_{0.90}Nb_{0.10}O_{3\pm\delta}$ is attributed to the presence of phase impurities, confirmed by SEM/EDS (Fig. 4.4). It is generally accepted that the thermoelectric power factor increases with the carrier effective mass, as the gain in squared Seebeck coefficient is normally larger than decrease in mobility. When comparing the data shown in Fig. 4.9, one may conclude that high power factors in the discussed compositions are promoted by A-site deficiency rather through a substantial increase of the mobility, while the corresponding variations of the effective mass are less significant.

4.3.4 Lattice Thermal Conductivity and Overall Performance

In many oxide materials, including titanates, the lattice thermal conductivity prevails over the electronic counterpart, what is advantageous in terms of tuning the κ towards higher thermoelectric performance without affecting the power factor. The electronic contribution κ_{el} for the discussed materials, estimated using Wiedemann-Franz law (Eq. 4.2), was below 25% for the majority of compositions, reaching 30–35% only for heavily substituted $Sr_{1-a}Ti_{0.8}Nb_{0.2}O_{3\pm\delta}$ ($0.03 \leq a \leq 0.10$) series at 500–800 K. The effects imposed by the defect chemistry and chemical composition on the κ_{el} are similar to those discussed above for the electrical conductivity. Thus, the relevant effects on the lattice counterpart deserve special attention.

The lattice contribution to the thermal conductivity, which originates from lattice vibrations (phonons), can be represented as follows, using the simplified case of the Callaway model [59, 60]:

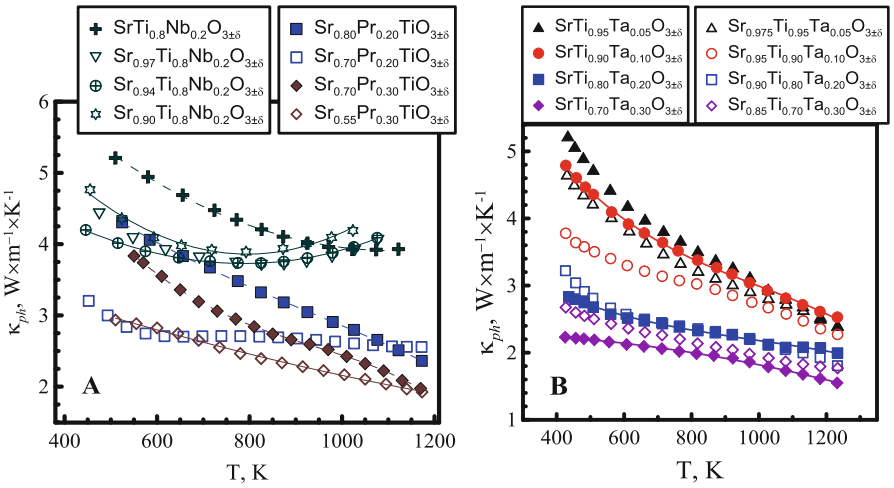

Fig. 4.10 Temperature dependence of the lattice thermal conductivity in (Sr,Pr)$TiO_{3\pm\delta}$, Sr(Ti, Nb)$O_{3\pm\delta}$, and Sr(Ti,Ta)$O_{3\pm\delta}$ series. Adapted with permission from [47, 49]. Copyright (2014–2015) American Chemical Society

$$\kappa_{\text{ph}} = \frac{1}{3}\int_0^{\omega_{\max}} C_s(\omega) v_g(\omega)^2 \tau(\omega) d\omega \tag{4.13}$$

where C_s is the spectral heat capacity, ν_g is the phonon group velocity, τ is the phonon relaxation time, and ω is the phonon frequency. In accordance with Matthiessen's rule, the κ_{ph} is contributed by the point defects scattering (τ_{PD}), grain boundary scattering (τ_{GB}), and Umklapp phonon–phonon interactions (τ_{U}) as:

$$1/\tau = 1/\tau_{\text{PD}} + 1/\tau_{\text{U}} + 1/\tau_{\text{GB}} \tag{4.14}$$

The Umklapp scattering usually dominates at high temperatures and, presumably, is less affected by the defect chemistry. Indeed, the results shown in Fig. 4.10a, b suggest a general tendency of the lattice thermal conductivity to converge at high T for the materials having different composition and defect structure. One can roughly account for the grain boundary scattering as [60]:

$$\tau_{\text{GB}} = \frac{d}{v_g} \tag{4.15}$$

where d is the average grain size, v_g is the phonon group velocity.

However, in the case of studied materials this contribution, which normally becomes noticeable in nanostructured ceramics [60], can be neglected due to microscale grain size (Fig. 4.4). The point defects and impurities represent effective

phonon scatterers when inducing significant local variations of density and interatomic forces. The point defect scattering is particularly effective at relatively low temperatures, where the phonon mean free path is larger. In the simplified case, the relaxation time for point defects scattering can be presented as [60]:

$$\tau_{PD}^{-1} = \frac{V\omega^4}{4\pi {v_p}^2 v_g}\left(\sum_i f_i\left(1-\frac{m_i}{\bar{m}}\right)^2 + \sum_i f_i\left(1-\frac{r_i}{\bar{r}}\right)^2\right) \tag{4.16}$$

where V is the volume per atom, v_p phonon phase velocity, f_i the fraction of atoms with mass m_i, and radius r_i, residing on a site with average mass and radius $\bar{m}$ and $\bar{r}$, respectively. As an example, praseodymium and tantalum are 1.6 and 3.5 times heavier than strontium and titanium, correspondingly, this results in general thermal conductivity decrease on donor substitution being more pronounced for Ta-substituted $SrTiO_3$ (Fig. 4.10). Efficient scattering of significant part of the phonon spectrum, however, requires the defects having various sizes, being present in reasonable amounts. In simplified way, this interrelation can be accounted from kinetic theory as [61]:

$$\tau_{PD}^{-1} = K\pi\eta\frac{\omega^4 R^6/v^3}{(\omega R/v)^4 + 1} \tag{4.17}$$

where K, η, R, and v are a constant of the order of unity, number of scattering sites per unit volume, radius of the point defect or lattice imperfection and speed of sound, respectively. Thus, the oxygen and A-site vacancies are expected to contribute significantly to the deviations of the mass and size of the crystallographic sites from the average, with corresponding impact on the thermal transport. This is well illustrated by the difference in lattice thermal conductivity of A-site stoichiometric and deficient compositions of the $(Sr,Pr)TiO_{3\pm\delta}$, $Sr(Ti,Nb)O_{3\pm\delta}$ series (Fig. 4.10a). Additional contributions to the κ_{ph} reduction may also be provided by local distortions of the crystal lattice due to the presence of $V_O^{\bullet\bullet}$ and V_{Sr}'', and, probably, different phonon scattering mechanism of vacancies as compared to atoms [31, 62].

A particularly interesting feature is the specific "glass-like" $\kappa_{ph}(T)$ behaviour of heavily substituted A-site deficient compositions, observed for $Sr_{1-a}Ti_{0.8}Nb_{0.2}O_{3\pm\delta}$ ($0.03 \le a \le 0.10$) and $Sr_{1-1.5x}Pr_xTiO_{3\pm\delta}$ ($0.20 \le x \le 0.30$), in contrast with stoichiometric $SrTi_{0.8}Nb_{0.2}O_{3\pm\delta}$ and $Sr_{1-x}Pr_xTiO_{3\pm\delta}$ ($0.20 \le x \le 0.30$) (Fig. 4.10a). On introducing cation deficiency, the temperature dependence of the lattice thermal conductivity becomes much weaker, while corresponding κ_{ph} values significantly decrease, similar to that observed in [31]. It is assumed that a simple atomic substitution could not result in appearance of glass-like lattice vibrations [62]; hence, high donor concentration does not appear to be a main reason for this behaviour. Moreover, stoichiometric compositions with the same substitution level show "usual" temperature dependence of the thermal conductivity, typical for titanates. On the other hand, in a disordered crystal the "glass-like" thermal

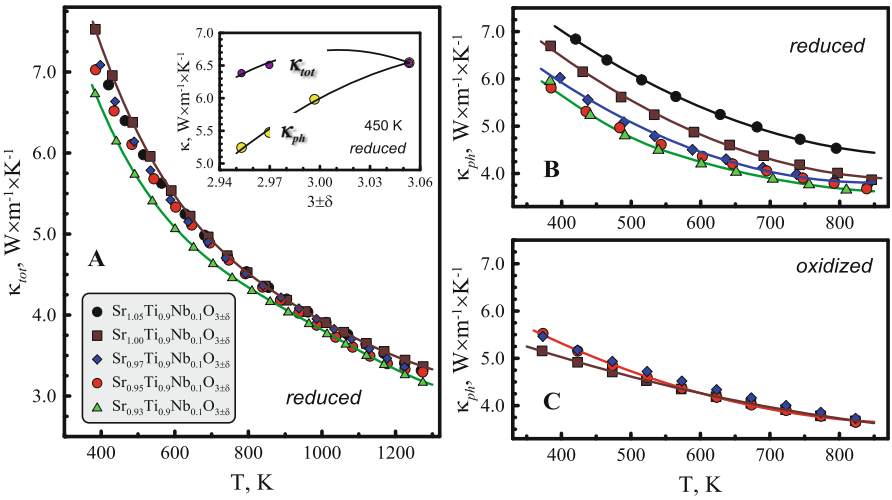

Fig. 4.11 Temperature dependence of total (**a**) and lattice thermal conductivity (**b**, **c**) for reduced (**a**, **b**) and oxidized $Sr_{1-y}Ti_{0.9}Nb_{0.1}O_{3\pm\delta}$ (**c**) samples. The inset shows the effect of total oxygen content on the total and lattice thermal conductivity for reduced samples. Reproduced from [48] with permission from The Royal Society of Chemistry

transport may originate from random, noncentral distortions of the lattice [62], which are very likely to be promoted by vacant sites. Thus, one may view the significant decrease in the lattice thermal conductivity for heavily substituted compositions with cation deficiency as a combined results of phonon scattering at donor sites, cation and oxygen vacancies, with possible synergistic effects from the defects clustering. Relative contribution of RP and other oxygen-excess defects to the lattice thermal conductivity in $(Sr,Pr)TiO_{3\pm\delta}$, $Sr_{1-a}Ti_{0.8}Nb_{0.2}O_{3\pm\delta}$, and Sr(Ti, Ta)$O_{3\pm\delta}$ is less clear although their dimensional scale should be appropriate for phonon scattering in $SrTiO_3$-based materials.

More guidelines on particular role of various defects in the lattice thermal transport can be obtained by comparing the thermal conductivity changes in both reduced and oxidized $Sr_{1-y}Ti_{0.9}Nb_{0.1}O_{3\pm\delta}$, where the alterations in the defect chemistry mechanisms from the formation of RP layers to A-site and oxygen deficiency are provided by gradual change of the nominal composition. The data on the total thermal conductivity for these materials (Fig. 4.11) suggest quite moderate differences between the samples with various A-site composition, being, however, significantly above the experimental error. Gradual decrease in κ on introducing the nominal cation deficiency is better visible at temperatures below 800 K; the tendency for the lattice counterpart κ_{ph} is much clearer (inset in Fig. 4.11a). The clues to understand the underlying mechanisms again can be provided by the Eq. 4.16, taking into account expected contribution of the oxygen and cation vacancies to the mass and size terms. The results demonstrate that shifting the predominant defect types to $V_O^{\bullet\bullet}$ and V''_{Sr} is more efficient towards

supressing the lattice thermal conductivity than deliberate formation of $(SrO)^{RP}$ planar faults, putting the doubts on the prospects of pure and substituted RP-type $SrO(SrTiO_3)_n$ as thermoelectric materials [32, 33]. Firstly, the expected contribution of $(SrO)^{RP}$ to the mass and size terms (Eq. 4.16) is lower than for $V_O^{\bullet\bullet}$ and V_{Sr}'', provided by similarities in chemical composition with the perovskite matrix. Secondly, one can assume that strong Sr-O bonding in RP layers is less likely to promote anharmonic lattice vibrations, which is essential for the low lattice thermal conductivity.

A straightforward assessment of the separate contributions, provided by oxygen and cation vacancies towards κ_{ph} reduction, represents certain difficulties in the samples, prepared under reducing conditions since all cation-deficient compositions also possess the oxygen deficiency. However, conclusive information can be obtained by analysing the composition dependence of the κ_{ph} for oxidized samples, where the $[V_O^{\bullet\bullet}]$ is relatively low or negligible. In particular, minor observed difference between oxidized A-site deficient compositions and nominal A-site stoichiometric $Sr_{1.00}Ti_{0.90}Nb_{0.10}O_{3\pm\delta}$ (Fig. 4.11c) strongly suggest that cation vacancies provide rather smaller specific contribution to the phonon scattering. Still, potential contribution from various defect clusters should also be considered. As an example, the formation of $V_{Sr}^{\bullet\bullet} - nV_O''$ clusters in $SrTiO_3$ was confirmed by high-resolution XPS, positron annihilation, and first-principles calculations, as a possible origin of ferroelectric and bipolar resistance switching effects [61, 63, 64]. Such structures are likely to be present in sufficient amounts, when both strontium and oxygen content are decreasing, to provide the observed reduction of the lattice thermal conductivity from $Sr_{1.05}Ti_{0.90}Nb_{0.10}O_{3\pm\delta}$ to $Sr_{0.93}Ti_{0.90}Nb_{0.10}O_{3\pm\delta}$. (Fig. 4.11b). Similar effects are expected in $(Sr,Pr)TiO_{3\pm\delta}$ and $Sr(Ti,Ta)O_{3\pm\delta}$ series. Still, the size scale and the structure of the defects, accommodating excess oxygen in these system, can differ from that of RP planar faults and their clusters in $Sr_{1.05}Ti_{0.90}Nb_{0.10}O_{3\pm\delta}$. Therefore, one should not underestimate possible contribution of oxygen-rich defects to the enhanced phonon scattering. The main problem for elucidating the exact role of these extended defects is represented by the fact that their composition, structural organization, and spatial distribution may depend strongly on the nature of donor-substituting cation and processing conditions of the sample, in contrast with rather predictable properties and arrangements of point defects such as oxygen and cation vacancies.

Cumulative impact of the electrical and thermal transport properties on the thermoelectric performance is illustrated by the dimensionless figure-of-merit ZT (Fig. 4.12). A significant improvement (marked by green) of the thermoelectric performance due to A-site deficiency was achieved in $(Sr,Pr)TiO_{3\pm\delta}$ (Fig. 4.12a) and $Sr(Ti,Ta)O_{3\pm\delta}$ (Fig. 4.12b) series, especially for the compositions with high donor content, leading to attractive ZT values of about ~0.35 reached for Ta-substituted titanates. This was mainly provided by high power factors due to enhanced charge carriers mobility in A-site deficient compositions although the contribution of "glass-like" thermal conductivity in corresponding samples is also

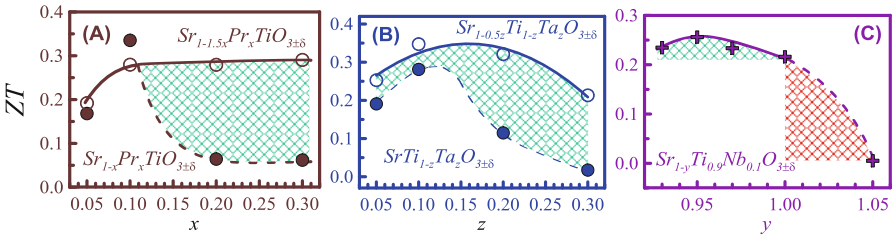

Fig. 4.12 Compositional dependence of the dimensionless figure-of-merit ZT, calculated at 1150 K from the data [47–49]. *Green* and *red* diagonal-cross areas illustrate ZT enhancement due to the presence of oxygen and cation vacancies, and dramatic reduction of the thermoelectric performance promoted by RP-type defects, correspondingly

significant. The observed gains in $Sr_{1-y}Ti_{0.90}Nb_{0.10}O_{3\pm\delta}$ series, where high donor substitution was avoided, are rather moderate, as shown in Fig. 4.12c.

A drastic ZT decrease (marked by red) from $Sr_{1.00}Ti_{0.90}Nb_{0.10}O_{3\pm\delta}$ to $Sr_{1.05}Ti_{0.90}Nb_{0.10}O_{3\pm\delta}$ is promoted by the formation of RP layers, impairing the electronic transport in this composition. The results unambiguously show that oxygen and cation vacancies are essential ingredients towards high mobility of the charge carriers and efficient phonon scattering, resulting in enhanced thermoelectric performance.

4.4 Summary and Outlook

This chapter provided an overview of recently developed approaches aimed on boosting thermoelectric performance of donor-substituted strontium titanates through controlled tuning of the predominant defects type, including oxygen-excess and RP defects, donor cations, cation- and oxygen vacancies. Conclusively, the introduction of A-site and oxygen vacancies led to a significant enhancement of the thermoelectric performance by providing a synergistic effect of combining fast charge transport in the perovskite lattice and suppressing the lattice thermal conductivity. At the same time, the prospects of RP-type titanates as thermoelectrics look less optimistic, mainly due to the low charge carrier's mobility. The discussion clearly evidenced that significant suppression of the thermal transport still requires all-scale phonon scattering, as an essential tool combined with the structural defects engineering approach. In addition to A-site and oxygen deficiency, promising "glass-like" thermal conductivity behaviour, observed for several samples, apparently requires high donor substitution level, which is relatively easy to attain in flexible $SrTiO_3$ perovskite lattice.

The discussed results also demonstrated that inherent complexity of the defect chemistry of $SrTiO_3$-based materials provides a number of opportunities for designing functional electrical and thermal properties. In this respect, thin films approach represents a very promising pathway to implement the above discoveries for

seeking highly performing thermoelectric systems. As an example, conventional introducing the oxygen vacancies in bulk titanates is performed through reduction at high temperatures and in hydrogen-containing atmospheres, in other words, requires highly reducing conditions. Another issue is that uniform distribution of the oxygen vacancies is hardly achieved by direct bulk reduction, resulting in non-optimized charge carrier's concentration in the volume and lower thermoelectric performance. Using epitaxial thin film growth, one can introduce oxygen vacancies in easier and more controllable manner. Alternative ways, already explored for $SrTiO_3$-based materials, may include sputtering and pulsed laser deposition. The specificity of the thin film processing technologies combined with appropriate redox conditions also allow unique defect structures and defects clustering, which are hardly achievable or not possible to reach by conventional processing of the bulk materials. Modern developments in oxide thin film growth methods enable the fabrication of stable atomically precise low-dimensional heterostructures and superlattices incorporating layers with various defects, where nanoscale electrical and thermal transport may result in significant improvement of the thermoelectric properties. These factors point out particular prospects of the thin film technology for designing the defect chemistry towards highly performing strontium titanate-based thermoelectrics.

Acknowledgements This work was supported by the FCT Investigator program (grant IF/00302/2012) and project CICECO-Aveiro Institute of Materials (ref. UID/CTM/50011/2013), financed by COMPETE 2020 Programme and National Funds through the FCT/MEC and when applicable co-financed by FEDER under the PT2020 Partnership Agreement. AK would like also to acknowledge the contributions of the following researchers to the previously published results, used as an experimental support for the discussion, namely, Dr. A. A. Yaremchenko, Dr. S. G. Patrício, Dr. J. Macías, Dr. N. M. Ferreira, Dr. S. M. Mikhalev, Dr. D. P. Fagg, Prof. J. R. Frade (University of Aveiro), Dr. S. Populoh, Dr. Ph. Thiel (Empa), Prof. A. Weidenkaff (University of Stuttgart), and Dr. M. H. Aguirre (University of Zaragoza).

References

1. T.M. Tritt, M.A. Subramanian, Thermoelectric materials, phenomena, and applications: a bird's eye view. MRS Bull. **31**, 188–198 (2006)
2. A. Date, A. Date, C. Dixon, A. Akbarzadeh, Progress of thermoelectric power generation systems: prospect for small to medium scale power generation. Renew. Sust. Energ. Rev. **33**, 371–381 (2014)
3. X. Zhang, L.-D. Zhao, Thermoelectric materials: energy conversion between heat and electricity. J. Mater. **1**, 92–105 (2015)
4. C. Suter, P. Tomeš, A. Weidenkaff, A. Steinfeld, A solar cavity-receiver packed with an array of thermoelectric converter modules. Sol. Energy **85**, 1511–1518 (2011)
5. G.J. Snyder, E.S. Toberer, Complex thermoelectric materials. Nat. Mater. **7**, 105–114 (2008)
6. M.S. Dresselhaus, G. Chen, M.Y. Tang, R. Yang, H. Lee, D. Wang, Z. Ren, J.P. Fleurial, P. Gogna, New directions for low-dimensional thermoelectric materials. Adv. Mater. **19**, 1043–1053 (2007)

7. K. Biswas, J. He, I.D. Blum, C.-I. Wu, T.P. Hogan, D.N. Seidman, V.P. Dravid, M.G. Kanatzidis, High-performance bulk thermoelectrics with all-scale hierarchical architectures. Nature **489**, 414–418 (2012)
8. G.A. Slack, New materials and performance limits for thermoelectric cooling, in *Thermoelectrics Handbook*, ed. by D. M. Rowe (Ed), (CRC Press, 1995). doi:10.1201/9781420049718.ch34
9. C. Uher, Skutterudite-Based Thermoelectrics, in *Thermoelectrics Handbook*, (CRC Press, 2005), pp. 17–34
10. J. Leszczynski, K.T. Wojciechowski, A.L. Malecki, Studies on thermal decomposition and oxidation of $CoSb_3$. J. Therm. Anal. Calorim. **105**, 211–222 (2011)
11. K. Gałązka, S. Populoh, L. Sagarna, L. Karvonen, W. Xie, A. Beni, P. Schmutz, J. Hulliger, A. Weidenkaff, Phase formation, stability, and oxidation in (Ti, Zr, Hf)NiSn half-Heusler compounds. Phys Status Solidi Appl Mater Sci **211**, 1259–1266 (2014)
12. T. Fujii, I. Terasaki, Block-Layer Concept for the Layered Co Oxide: A Design for Thermoelectric Oxides, in *Chemistry, Physics, and Materials Science of Thermoelectric Materials*, ed. by M. G. Kanatzidis, S. D. Mahanti, T. P. Hogan (Eds), (Springer, 2003), pp. 71–87
13. I. Terasaki, Y. Sasago, K. Uchinokura, Large thermoelectric power in $NaCo_2O_4$ single crystals. Phys. Rev. B **56**, R12685–R12687 (1997)
14. K. Koumoto, I. Terasaki, R. Funahashi, Complex oxide materials for potential thermoelectric applications. MRS Bull. **31**, 206–210 (2006)
15. M. Backhaus-Ricoult, J. Rustad, L. Moore, C. Smith, J. Brown, Semiconducting large bandgap oxides as potential thermoelectric materials for high-temperature power generation. Appl. Phys. A Mater. Sci. Process. **116**, 433–470 (2014)
16. G. Xu, R. Funahashi, M. Shikano, I. Matsubara, Y. Zhou, Thermoelectric properties of the Bi- and Na-substituted $Ca_3Co_4O_9$ system. Appl. Phys. Lett. **80**, 3760 (2002)
17. M. Ohtaki, Oxide Thermoelectric Materials for Heat-to-Electricity Direct Energy Conversion. Kyushu University Global COE Program Novel Carbon Resources Sciences Newsletter 3, 2010
18. K. Koumoto, R. Funahashi, E. Guilmeau, Y. Miyazaki, A. Weidenkaff, Y. Wang, C. Wan, Thermoelectric ceramics for energy harvesting. J. Am. Ceram. Soc. **96**, 1–23 (2013)
19. L. Bocher, M.H. Aguirre, D. Logvinovich, A. Shkabko, R. Robert, M. Trottmann, A. Weidenkaff, $CaMn_{1-x}Nb_xO_3$ ($x \leq 0.08$) perovskite-type phases as promising new high-temperature n-type thermoelectric materials. Inorg. Chem. **47**, 8077–8085 (2008)
20. H. Ohta, Thermoelectrics based on strontium titanate. Mater. Today **10**, 44–49 (2007)
21. A.V. Kovalevsky, A.A. Yaremchenko, S. Populoh, P. Thiel, D.P. Fagg, A. Weidenkaff, J.R. Frade, Towards a high thermoelectric performance in rare-earth substituted SrTiO3: effects provided by strongly-reducing sintering conditions. Phys. Chem. Chem. Phys. **16**, 26946–26954 (2014)
22. Z. Lu, H. Zhang, W. Lei, D.C. Sinclair, I.M. Reaney, High-Figure-of-merit thermoelectric LA-doped A-site-deficient $SrTiO_3$ ceramics. Chem. Mater. **28**, 925–935 (2016)
23. B. Zhang, J. Wang, T. Zou, S. Zhang, X. Yaer, N. Ding, C. Liu, L. Miao, Y. Li, Y. Wu, High thermoelectric performance of Nb-doped $SrTiO_3$ bulk materials with different doping levels. J. Mater. Chem. C **3**, 11406–11411 (2015)
24. S. Ohta, T. Nomura, H. Ohta, K. Koumoto, High-temperature carrier transport and thermoelectric properties of heavily La- or Nb-doped $SrTiO_3$ single crystals. J. Appl. Phys. **97**, 18–21 (2005)
25. N. Wang, H. Chen, H. He, W. Norimatsu, M. Kusunoki, K. Koumoto, Enhanced thermoelectric performance of Nb-doped $SrTiO_3$ by nano-inclusion with low thermal conductivity. Sci. Rep. **3**, 3449 (2013)
26. Y. Lin, C. Norman, D. Srivastava, F. Azough, L. Wang, M. Robbins, K. Simpson, R. Freer, I.A. Kinloch, Thermoelectric power generation from lanthanum strontium titanium oxide at room temperature through the addition of graphene. ACS Appl. Mater. Interfaces **7**, 15898–15908 (2015)

27. A.V. Kovalevsky, S. Populoh, S.G. Patrício, P. Thiel, M.C. Ferro, D.P. Fagg, J.R. Frade, A. Weidenkaff, Design of $SrTiO_3$-based thermoelectrics by tungsten substitution. J. Phys. Chem. C **119**, 4466–4478 (2015)
28. P. Blennow, A. Hagen, K.K. Hansen, L.R. Wallenberg, M. Mogensen, Defect and electrical transport properties of Nb-doped $SrTiO_3$. Solid State Ionics **179**, 2047–2058 (2008)
29. R. Moos, K.H. Hardtl, Defect chemistry of donor-doped and undoped strontium titanate ceramics between 1000 degrees and 1400 degrees C. J. Am. Ceram. Soc. **80**, 2549–2562 (1997)
30. C. Yu, M.L. Scullin, M. Huijben, R. Ramesh, A. Majumdar, Thermal conductivity reduction in oxygen-deficient strontium titanates. Appl. Phys. Lett. **92**, 23–25 (2008)
31. S.R. Popuri, A.J.M. Scott, R.A. Downie, M.A. Hall, E. Suard, R. Decourt, M. Pollet, J.-W.G. Bos, Glass-like thermal conductivity in $SrTiO_3$ thermoelectrics induced by A-site vacancies. RSC Adv. **4**, 33720–33723 (2014)
32. Y. Wang, C. Wan, X. Zhang, L. Shen, K. Koumoto, A. Gupta, N. Bao, Influence of excess SrO on the thermoelectric properties of heavily doped $SrTiO_3$ ceramics. Appl. Phys. Lett. **102**, 183905 (2013)
33. Y. Wang, K.H. Lee, H. Ohta, K. Koumoto, Thermoelectric properties of electron doped SrO $(SrTiO_3)$ n (n=1,2) ceramics. J. Appl. Phys. **105**, 103701 (2009)
34. J. Ravichandran, Thermoelectric and thermal transport properties of complex oxide thin films, heterostructures and superlattices. J. Mater. Res. **32**, 1–21 (2016)
35. T. Okuda, K. Nakanishi, S. Miyasaka, Y. Tokura, Large thermoelectric response of metallic perovskites: $Sr_{1-x}La_xTiO_3$ ($0<\sim x<\sim 0.1$). Phys. Rev. B **63**, 113104 (2001)
36. M. Yamamoto, H. Ohta, K. Koumoto, Thermoelectric phase diagram in a $CaTiO_3$-$SrTiO_3$-$BaTiO_3$ system. Appl. Phys. Lett. **90**, 8–10 (2007)
37. B. Jalan, S. Stemmer, Large Seebeck coefficients and thermoelectric power factor of La-doped $SrTiO_3$ thin films. Appl. Phys. Lett. **97**, 42106 (2010)
38. J.D. Baniecki, M. Ishii, H. Aso, K. Kobayashi, K. Kurihara, K. Yamanaka, A. Vailionis, R. Schafranek, Electronic transport behavior of off-stoichiometric La and Nb doped $Sr_xTi_yO_{3-\delta}$ epitaxial thin films and donor doped single-crystalline $SrTiO_3$. Appl. Phys. Lett. **99**, 232111 (2011)
39. S. Ohta, T. Nomura, H. Ohta, M. Hirano, H. Hosono, K. Koumoto, Large thermoelectric performance of heavily Nb-doped $SrTiO_3$ epitaxial film at high temperature. Appl. Phys. Lett. **87**, 3–5 (2005)
40. S. Kumar, A. Barasheed, H.N. Alshareef, High temperature thermoelectric properties of strontium titanate thin films with oxygen vacancy and niobium doping. ACS Appl. Mater. Interfaces **5**, 7268–7273 (2013)
41. A.I. Abutaha, S.R. Sarath Kumar, A. Mehdizadeh Dehkordi, T.M. Tritt, H.N. Alshareef, Doping site dependent thermoelectric properties of epitaxial strontium titanate thin films. J. Mater. Chem. C **2**, 9712–9719 (2014)
42. S. Kobayashi, Y. Mizumukai, T. Ohnishi, N. Shibata, Y. Ikuhara, T. Yamamoto, High electron mobility of Nb-doped $SrTiO_3$ films stemming from rod-type Sr vacancy clusters. ACS Nano **9**, 10769–10777 (2015)
43. L.D. Hicks, M.S. Dresselhaus, Effect of quantum-well structures on the thermoelectric figure of merit. Phys. Rev. B **47**, 12727–12731 (1993)
44. H. Ohta, S. Kim, Y. Mune, et al., Giant thermoelectric Seebeck coefficient of a two-dimensional electron gas in $SrTiO_3$. Nat. Mater. **6**, 129–134 (2007)
45. S.R.S. Kumar, M.N. Hedhili, D. Cha, T.M. Tritt, H.N. Alshareef, Thermoelectric properties of strontium titanate superlattices incorporating niobium oxide nanolayers. Chem. Mater. **26**, 2726–2732 (2014)
46. A.I. Abutaha, S.R.S. Kumar, K. Li, A.M. Dehkordi, T.M. Tritt, H.N. Alshareef, Enhanced thermoelectric figure-of-merit in thermally robust, nanostructured superlattices based on $SrTiO_3$. Chem. Mater. **27**, 2165–2171 (2015)

47. A.V. Kovalevsky, A.A. Yaremchenko, S. Populoh, A. Weidenkaff, J.R. Frade, Effect of A-site cation deficiency on the thermoelectric performance of donor-substituted strontium titanate. J. Phys. Chem. C **118**, 4596–4606 (2014)
48. A. Kovalevsky, M.H. Aguirre, S. Populoh, S.G. Patrício, N.M. Ferreira, S.M. Mikhalev, D.P. Fagg, A. Weidenkaff, J. Frade, Designing strontium titanate-based thermoelectrics: insight into defect chemistry mechanisms. J. Mater. Chem. A (2017). doi:10.1039/C6TA09860F
49. A.A. Yaremchenko, S. Populoh, S.G. Patrício, J. Macías, P. Thiel, D.P. Fagg, A. Weidenkaff, J.R. Frade, A.V. Kovalevsky, Boosting thermoelectric performance by controlled defect chemistry engineering in Ta-substituted strontium titanate. Chem. Mater. **27**, 4995–5006 (2015)
50. A.V. Kovalevsky, A.A. Yaremchenko, S. Populoh, A. Weidenkaff, J.R. Frade, Enhancement of thermoelectric performance in strontium titanate by praseodymium substitution. J. Appl. Phys. **113**, 53704 (2013)
51. K. Gömann, G. Borchardt, M. Schulz, A. Gömann, W. Maus-Friedrichs, B. Lesage, O. Kaïtasov, S. Hoffmann-Eifert, T. Schneller, Sr diffusion in undoped and La-doped SrTiO3 single crystals under oxidizing conditions. Phys. Chem. Chem. Phys. **7**, 2053–2060 (2005)
52. N.G. Eror, U. Balachandran, Self-compensation in lanthanum-doped strontium titanate. J. Solid State Chem. **40**, 85–91 (1981)
53. M.C. Verbraeken, T. Ramos, K. Agersted, Q. Ma, C.D. Savaniu, B.R. Sudireddy, J.T.S. Irvine, P. Holtappels, F. Tietz, Modified strontium titanates: from defect chemistry to SOFC anodes. RSC Adv. **5**, 1168–1180 (2015)
54. F. Lichtenberg, A. Herrnberger, K. Wiedenmann, Synthesis, structural, magnetic and transport properties of layered perovskite-related titanates, niobates and tantalates of the type $A_nB_nO_{3n+2}$, $A'A_{k-1}B_kO_{3k+1}$ and $A_mB_{m-1}O_{3m}$. Prog. Solid State Chem. **36**, 253–387 (2008)
55. I. Levin, L.A. Bendersky, T.A. Vanderah, A structural study of the layered perovskite-derived $Sr_n(Ti,Nb)_nO_{3n+2}$ compounds by transmission electron microscopy. Philos Mag A **80**, 411–445 (2000)
56. J. Canales-Vázquez, M.J. Smith, J.T.S. Irvine, W. Zhou, Studies on the reorganization of extended defects with increasing n in the perovskite-based $La_4Sr_{n-4}Ti_nO_{3n+2}$ series. Adv. Funct. Mater. **15**, 1000–1008 (2005)
57. L. Amaral, A.M.R. Senos, P.M. Vilarinho, Sintering kinetic studies in nonstoichiometric strontium titanate ceramics. Mater. Res. Bull. **44**, 263–270 (2009)
58. Y. Liu, P. Sahoo, J.P.A. Makongo, X. Zhou, S.J. Kim, H. Chi, C. Uher, X. Pan, P.F.P. Poudeu, Large enhancements of thermopower and carrier mobility in quantum dot engineered bulk semiconductors. J. Am. Chem. Soc. **135**, 7486–7495 (2013)
59. J. Callaway, Model for lattice thermal conductivity at low temperatures. Phys. Rev. **113**, 1046–1051 (1959)
60. E.S. Toberer, A. Zevalkink, G.J. Snyder, Phonon engineering through crystal chemistry. J. Mater. Chem. **21**, 15843 (2011)
61. S. McGuire, D.J. Keeble, R.E. Mason, P.G. Coleman, Y. Koutsonas, T.J. Jackson, Variable energy positron beam analysis of vacancy defects in laser ablated $SrTiO_3$ thin films on $SrTiO_3$. J. Appl. Phys. **100**, 44109 (2006)
62. D.G. Cahill, S.K. Watson, R.O. Pohl, Lower limit to the termal conductivity of disordered crystals. Phys. Rev. B **46**, 6131–6140 (1992)
63. Y. Su Kim, J. Kim, M. Jee Yoon, et al., Impact of vacancy clusters on characteristic resistance change of nonstoichiometric strontium titanate nano-film. Appl. Phys. Lett. **104**, 13501 (2014)
64. Y.S. Kim, J. Kim, S.J. Moon, W.S. Choi, Y.J. Chang, J.G. Yoon, J. Yu, J.S. Chung, T.W. Noh, Localized electronic states induced by defects and possible origin of ferroelectricity in strontium titanate thin films. Appl. Phys. Lett. **94**, 202906 (2009)

Chapter 5
Microwave-Processed Copper Zinc Tin Sulphide (CZTS) Inks for Coatings in Solar Cells

Prashant R. Ghediya and Tapas K. Chaudhuri

5.1 Introduction

Solar electricity, generated from sunlight by solar cells, is environmentally clean, carbon-free and renewable. It has the potential to meet the terawatt energy demand of the world, provided it is available at par with grid electricity. The prevalent solar cells made from silicon (Si) or cadmium telluride (CdTe) or copper indium gallium selenide (CIGS) generate electricity that are still too expensive. Hence, there is a frantic search for new materials for solar cells which will generate cost-competitive electricity [1]. One such promising candidate is earth-abundant, low-cost and non-toxic kesterite copper zinc tin sulphide/selenide. Copper zinc tin sulphide (CZTS) is a *p*-type semiconductor with a direct band gap of about 1.5 eV and absorption coefficient of above 10^4 cm^{-1} in the solar spectrum [2]. CZTS exists in tetragonal kesterite structure with lattice constants: $a = 0.5435$ nm, $c = 1.0843$ nm. The absorber layer is the heart of TFSCs. The CZTS film in a thin film solar cell (photovoltaic device) acts as the *p*-type photoactive absorber layer. The absorber layer is the most critical part of a cell because major processes required for photovoltaic effect occur here. The processes of absorption of solar radiation, generation of electron-hole pairs and separation of charges take place in this layer. Hence, effect of light on conductivity (photoconductivity) of CZTS films is as important as the dark conductivity itself. In other words, understanding of electrical and photoelectrical properties of CZTS is essential for development of

P.R. Ghediya (✉)
Department of Physics, Faculty of Sciences, Marwadi University, Rajkot-Morbi Highway, Rajkot, Gujarat 360003, India
e-mail: prashantghediya@gmail.com

T.K. Chaudhuri
Department of Applied Physics, S. V. National Institute of Technology, Surat 395007, India

J. Zhang, Y.-G. Jung (eds.), *Advanced Ceramic and Metallic Coating and Thin Film Materials for Energy and Environmental Applications*,
DOI 10.1007/978-3-319-59906-9_5

Table 5.1 Suitability of CZTS as an absorber layer for solar cells [3]

Properties of absorber	Desirable	CZTS
Band gap	1–1.7 eV, direct transition	1.4–1.5 eV
Absorption coefficient	10^4–10^5 cm^{-1}	$>10^4$
Conduction type	*p*-type (10^{16}–10^{17} cm^{-3})	*p*-type(10^{15}–10^{18} cm^{-3})
Mobility	High	High
Diffusion length of minority carriers	$>$ 1 μm	–
Availability	Abundant at affordable price	Earth-abundant
Toxicity	Non-toxic	Environmental benign
Deposition	Simple and amenable to large scale	Solution-processed

efficient solar cells. Table 5.1 confirms that properties of CZTS match quite well with the desired one.

Band gap of the absorber should be small enough to allow absorption of a significant portion of solar spectrum and at the same time large enough to minimize the reverse saturation current density. Direct band gap semiconductors (1–1.7 eV) with high absorption coefficient are preferred for this purpose [3]. Further, the diffusion length of the minority carriers must be large enough so that the generated carriers can reach the contacts without much loss. Therefore, in general, *p*-type semiconductors are used as absorber layers.

The intrinsic *p*-type conductivity, due to Cu-on-Zn antisites (Cu_{Zn}), also makes it an ideal absorber material in solar cells due to the fast transfer of photo-generated holes at the front of illuminated side [4]. However, due to the formation of different binary and ternary secondary phases along with CZTS and various types of defects, achieving pure CZTS is rather difficult. Hence, different properties of CZTS including structural, compositional, optical, electrical and photovoltaic have been extensively studied. Varity of vacuum and non-vacuum deposition methods have been developed to fabricate efficient CZTS solar cells. However, CZTS solar cells fabricated from *direct ink coating* (*DIC*) technique have yielded, so far, efficiencies between 10 and 12.7% [5–7]. A numbers of reasons why we restrict to such technique have been elaborated below:

- Ink can be directly deposited on any types of substrate under any mild conditions.
- The present approach allows all advantages of non-vacuum deposition, like the possibility to use low-cost and high-throughput equipment, low wastage of raw materials and high uniformity of coated layer.
- Inks can be sprayed, screen-printed, ink-jet printed or doctor bladed via single deposition step which is ultimately implemented in a roll-to-roll industrial process.

Figure 5.1 shows the methodology to prepare different types of CZTS ink along with the deposition methods to prepare films. It may be noted here that efficiency of

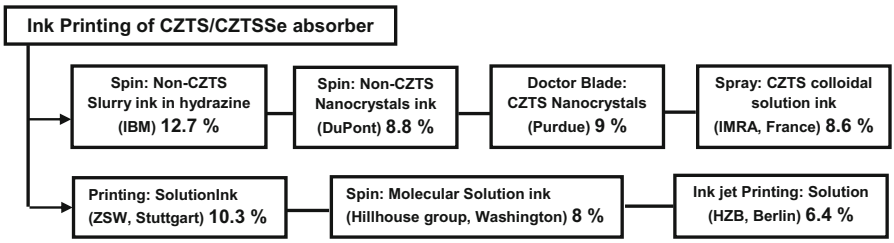

Fig. 5.1 Different types of CZTS ink and printing methods to prepare films

12.7% was reported in August 2014 using hydrazine and there has been no improvement so far, even after 2 years! However, hydrazine is highly toxic and very unstable that requires extreme caution during handling. Hence, there is a need to replace these solvents by non-toxic solvents for preparation of CZTS inks. The synthesis of CZTS inks has been quite complex with time-consuming cumbersome procedures. Hence, there is a need for simple rapid process for making CZTS nanoparticle ink. Microwave-assisted [8] preparation methods have those capabilities.

5.2 Inks for Coatings

Figure 5.2 shows the various types of CZTS inks with their respective preparation methods. CZTS ink may be either a pure solution, i.e. metal salts dissolved in precursor solution, or suspension. The suspended particles can be synthesized with high purity, but the synthetic processes involve multiple stapes, hence found tedious. On the other hand, molecular solution inks are stable. However, the later approach is less suited for the removal of excess organic solvents and precursors, mainly carbon.

On the other hand, CZTS inks can be synthesized either by mixing binary and ternary compounds such as Cu_2S, ZnS and SnS in some solvents/capping or by dissolving pure metal salts directly in solvents. However, CZTS nanoparticle ink via suspension route seems to be more promising since it involves only a single step. For large-scale ink-based deposition of CZTS films, it is imperative that formulation of ink should be simple and straight forward preferably containing CZTS only. CZTS ink with suspended particles can be synthesized by hot-injection [9, 10], sonochemical [11], solvothermal [12] and microwave-assisted (MA) [8] methods. It was previously showed that the slurry-ink containing of molecular solution and non-CZTS NPs in toxic hydrazine yields best CZTSSe solar cells till date [6]. Figure 5.3 shows the cross-sectional scanning electron microscopy view and J-V characteristics of a champion CZTSSe device with the absorber layer produced by a non-vacuum solution/ink approach that uses hydrazine [7]. Hydrazine is a powerful reducing agent that, in presence of excess chalcogen

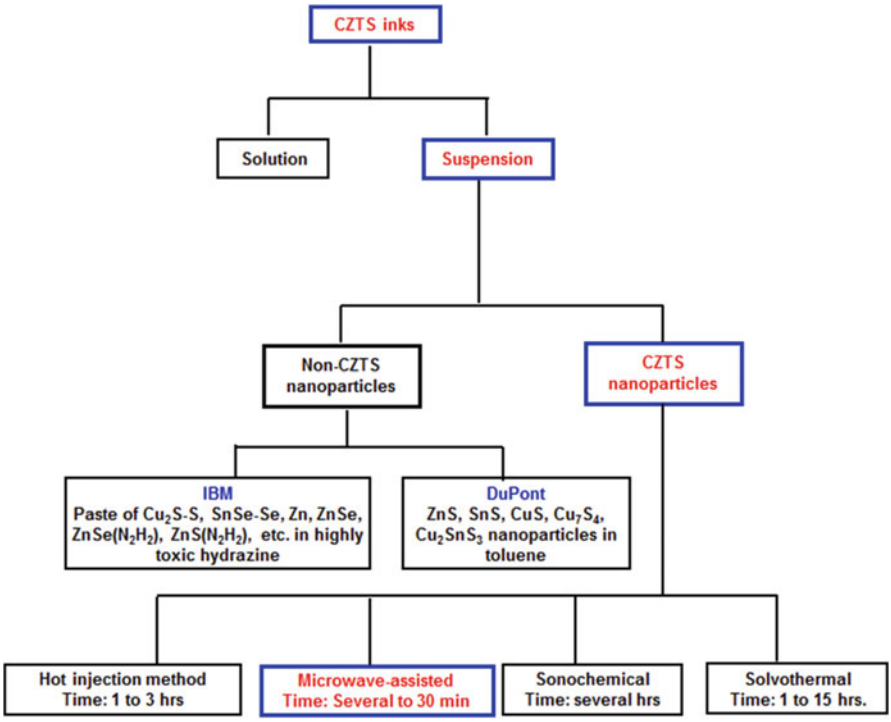

Fig. 5.2 Methodology for the preparation of CZTS inks

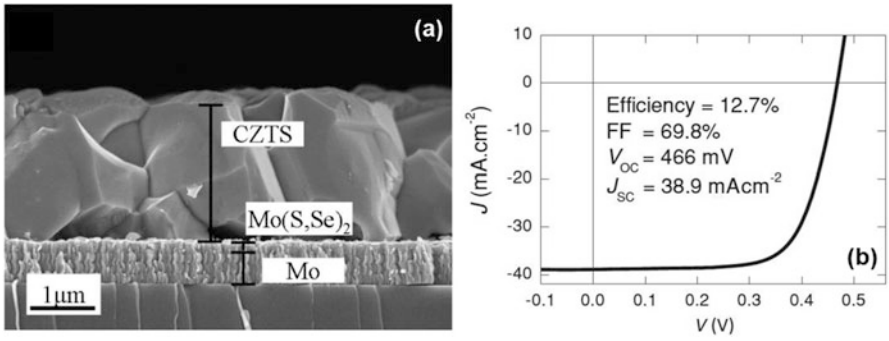

Fig. 5.3 (**a**) Cross-sectional SEM of the most efficient CZTSSe absorber and (**b**) J-V characteristics of the champion device [7]

(S, Se, Te), can solvate different metal chalcogenides as hydrazinium-based complexes at room temperature. Its controlled degradation produces N_2 and H_2 only, which are gaseous products that are released during thermal treatment and thus should not leave any contaminant in the CZTSSe film [13]. Because of its high toxicity and flammability, finding alternatives with a high solvating power,

reducing capability and 'clean' products upon degradation is highly desirable. Hence, there is a need to replace these solvents by non-toxic solvents for preparation of CZTS inks.

5.2.1 CZTS Nanoparticles Ink

CZTS nanoparticles (NPs) through hot-injection method were synthesized by Riha et al. [9] for the first time in 2009 and recently there has been significant interest both in CZTS and CZTSe NPs [14, 15]. The CZTS NPs have primarily been synthesized by hot-injection and solvothermal methods, where oleylamine (OLA) is often used as a solvent/surfactant/capping agent. Hot-injection method, in general, involves injecting a cold solution of precursors into a hot surfactant solution, thus leading to the instant nucleation and growth of nanocrystals. Table 5.2 presents the summary of CZTS NPs ink prepared by different methods.

At the same time, Guo et al. [10] investigated CZTS nano ink for solar cells by the same method. For making thin films, the CZTS inks were directly deposited on Mo-coated glass substrates by drop casting. The films were first annealed at 632 K for 1 h in argon atmosphere to remove the organic ligands. Finally, these films were selenized at 673–773 K under Se vapour in a graphite box to form CZTSSe absorber layer. The solar cells based on CZTSSe absorber yield efficiency of 0.80%. Similarly, Steinhagen et al. [16] also developed CZTS NPs ink for solar cells using OLA. However, the process varies from the others in the way that all precursors are mixed at room temperature (RT) in OLA and then heated to 553 K. It can be seen that all the above three groups have used OLA as a capping.

The NPs were generally synthesized using organic capping ligands for controlling the formation and growth. It provides good dispersibility in solvents enabling the formation of nanocrystal inks that can be deposited on substrates under mild conditions using direct ink coating methods. However, major problem with capping ligands is that they can hinder the charge transport in the nanocrystalline films. Complete removal of the ligands also leads to surface defects that trap electrons and holes which ultimately degrade the performance of solar photovoltaic devices [17].

Following these three groups [9, 10, 16], various researchers synthesized CZTS inks for low-cost solar cells by either changing the compositions of the metal salts or capping agents or source of sulphur. However, this process is not only complex but also time-consuming. It should be noted that OLA is hydrophobic and can only be dispersed into toluene which is also harmful.

Alternatively, CZTS NPs have been synthesized by solvothermal process [12, 18, 19]. Cao et al. [12] reported kesterite quaternary CZTS NPs by solvothermal process. In a typical process, appropriate amounts of copper chloride, zinc acetate, tin chloride and sulphur were added into a stainless steel autoclave with a Teflon liner, which was filled with ethylenediamine (EDA) up to 85% of the total volume (20 mL). The autoclave was sealed and maintained at 453 K for 15 h and then allowed to cool to RT naturally. The precipitates were filtered off, washed

Table 5.2 Summary of CZTS nanoparticle ink prepared by different methods

Sr. No.	Author	Precursors	Preparation method	Solvents/capping	Temperature	Total time	Results
1	Riha et al. [9]	$Cu(OAc)_2$+ $Zn(OAc)_2$+ $SnCl_4$ + S	**Hot injection**	OLA + TOPO	423 K in vacuum for 30 min	3 h	Particle size = 12.8 ± 1.8 nm E_g = 1.5 eV
2	Guo et al. [10]	All acetates+ S	Hot injection	OLA + toluene+ isopropanol	403 K in vacuum and degassed for 30 min	1 h	Particle size = 15–25- nm E_g = 1.5 eV Efficiency(η) = 0.80%
3	Steinhagen et al. [16]	$Cu(OAc)_2$ + $Zn(OAc)_2$ + $SnCl_4$ + S	Hot injection	OLA	553 K in inert atm. for 1 h	1 h	Particle size = 10.6 ± 2.9 nm E_g = 1.3 eV Efficiency(η) = 0.23%
4	Kameyama et al. [17]	All acetates + S	Hot injection	OLA	393–573 K in N_2 atm. for 60 min	1 h	Particle size = 5–6 nm E_g = 1.5 eV
5	Cao et al. [12]	$CuCl_2$ + $Zn(OAc)_2$ + $SnCl_4$ + S	**Solvothermal**	EDA	453 K for 15 h	15 h	Particle size = 5–10 nm E_g = 1.5 eV
6	Zhou et al. [18]	All chlorides + TU	Solvothermal	EG + PVP	503 K for 24 h	24 h	Particle size = 100–150 nm E_g = 1.48 eV
7	Zaberca et al. [19]	All chlorides + TU	Solvothermal	EG + ethanol + tetra methyl ammo-nium hydroxide	473 K for 16 h	16 h	XRD: Secondary phase
8	Flynn et al. [8]	All chlorides + TAA	**Microwave**	EG	463 K for 30 min	30 min	Particle size = 7.6 ± 2.1 nm E_g = 1.5 eV Efficiency(η) = 0.25%

9	Yang et al. [20]	$Cu(NO_3)_2$ + $Zn(NO_3)_2$ + $SnCl_4$ + S	Microwave	OLA + chloroform + hexane	533 K for 30 minand annealed at 623 K for several hours in N_2 gas	30 min	Particle size = 10–15 nm E_g = 1.6 eV
10	Kumar et al. [21]	All chlorides + TU	Microwave	EG	–	3 h	Particle size = 7 nm E_g = 1.76 eV
11	Shin et al. [22]	$Cu(OAc)_2$ + $Zn(OAc)_2$ + $SnCl_2$ + C_2H_5NS + NH_4OH	Microwave	Water	Sulphurized in N_2(95%) + H_2S (5%) at 823 K for 1 h	10 min	Particle size = 42.1 ± 23.7 nm E_g = 1.5 eV
12	Wang et al. [23]	All acetates + TU + PVP	Microwave	EG	–	Several min	Particle size = 250–350 nm E_g = 1.5 eV
13	Sarswat et al. [24]	All acetates + dodecanethiol	Microwave	OLA/EG	–	20 min	Particle size = 8–16 nm E_g = 1.7 eV
14	Wang et al. [25]	All acetate +S	Microwave	OLA	538 K for 15 min	15 min	Particle size = 38.9 ± 5.8 nm E_g = 1.5 eV Carrier concentration (n) = 1.56×101^6 cm^{-3} Mobility (μ_h) = 4.86 cm^2/Vs
15	Knuston et al. [26]	$Cu(OAc)_2$ + $Zn(OAc)_2$ + $SnCl_2$ + TU	Microwave	EG + thioglycolic acid + octadecene	433 K for 10 min		CZTS thin films directly into ITO Film thickness = 1–3 μm
16	Zhao et al. [27]	All chlorides + TU	Microwave	EG + PVP	473 K for 10 min	1 h	Films directly on FTO Particle size = 200–300 nm

(continued)

Table 5.2 (continued)

Sr. No.	Author	Precursors	Preparation method	Solvents/capping	Temperature	Total time	Results
17	W. Wang et al. [28]	$Cu(NO_3)_2$ + $Zn(OAc)_2$ + $SnCl_2$ + TAA	Ultrasound-assisted microwave	PEG	403–453 K for 10 min	8 h	XRD: CuS Raman: CTS E_g = 1.58–2.24 eV
18	Lin et al. [29]	All acetates + TU	Microwave-Assisted solvothermal	EDA + water	433–513 K for 1 h	7 h	Particle size = 200–500 nm XRD and Raman: Cu_2S
19	Martini et al. [30]	$Cu(OAc)_2$ + $SnCl_4$ + $Zn(OAc)_2$ + Na_2S	Microwave	Water + HCl + 3-mercaptoacetic acid + NH_4OH + dodecanthiol + methyl-ethyl-ketone	–		Particle size = 3–5 nm E_g = 1.4 eV

Bold part separates the individual techniques used to synthesised CZTS nanoparticle ink

with absolute ethanol. The CZTS thin films were fabricated by dip coating technique on silicon substrate. Finally, the nanocrystalline thin films were annealed in H_2S (5%)/Ar mixed gasses. The band gap of the CZTS NPs was 1.5 eV.

Zaberca et al. [19] also prepared CZTS NPs by solvothermal method for low-cost solar cells without any surfactant. For making ink, the appropriate metal chloride salts with TU were dissolved in mixture of ethylene glycol (EG) and methyl ammonium hydroxide (TMaOH). The resulting solution is loaded into a 1000 mL Teflon-lined steel autoclave and transferred into an oven preheated to the desired temperature. The autoclave is maintained at 473 K for 16 h and then cooled to RT. The CZTS thin films were deposited by dip coating method which was finally selenized at 823 K for 1 h. The films synthesized by this route shows good electronic properties and low-defect concentrations. Similarly, sphere-like kesterite CZTS NPs synthesized by a facile solvothermal method has also been reported by Zhou et al. [18]. The CZTS NPs were synthesized using EG and polyvinylpyrrolidone (PVP). In general, this technique allows for the precise control over the size, shape distribution and crystallinity of NPs. However, total processing time to synthesize CZTS NPs is too high (hours/days), and hence an additional improvement for reduction in time will be certainly required.

The use of microwave heating, in the place of conventional heating, is an alternative approach to synthesizing CZTS NPs. Microwave-assisted (MA) method for preparing CZTS ink seems to be promising since it is rapid. Microwave-based method has been employed in synthesizing NPs such as TiO_2, ZnO and many other inorganic materials including chalcopyrite NPs. Recently, MA synthesis of CZTS absorber material was carried out by various authors [8, 20–30]. Synthesis of CZTS NPs using microwave-assisted approach was first reported by Flynn et al. [8] in 2012 with total processing time of 30 min. The authors utilized metal chloride salt and TAA as precursors in EG to synthesize CZTS NPs ink in one pot. The CZTS ink is directly spin coated into Mo-coated glass substrates. The film was annealed at 673 K for 20 min in the presence of tin(II) sulphide and sulphur under nitrogen flow to avoid sulphur loss and phase separation. The solar cell fabricated using CZTS NPs delivered photo conversion efficiency of 0.25%.

Subsequently, there have been reports [20–30] on MA synthesis of CZTS NPs using either different solvents or salts or sulphur sources. Kumar et al. [21] have used chloride salts while metal acetates have been used by Shin et al. [22] and Sarswat and Free [24]. Alternatively, Wang et al. [25] have used salts of acetylacetonate. A combination of copper nitrate, zinc acetate and tin chloride was also utilized [23]. For microwave heating, choice of appropriate solvent is vital since solvent itself acquires heat. Solvents such as EG [8, 21, 24], water [22] and OLA [25] have been used. Different sulphur sources, such as TAA [8, 22], elemental sulphur [25] and TU [21, 23, 24], were used for synthesis of CZTS. In general, after synthesis, NPs were first centrifuged, filtered, washed and then dispersed in some other solvent to prepare CZTS ink. The sizes of NPs were typically in the range 7–8 nm [8, 21, 24]. Flynn et al. [8] and Sarswat and Free [24] also deposited CZTS films from their inks. Further, there have been some reports on MA synthesis of CZTS inks and films. CZTS films were directly

deposited on ITO by Knutson [26]. Recently, mass production of CZTS NPs by microwave heating was also reported by Martini et al. [30]. The microwave ink was prepared by dissolving copper acetate, zinc acetate, tin chloride and sodium sulphide in mixture of acetic acid and water.

A critical assessment of earlier work on MACZTS NPs revealed that most of the authors [21–23, 25, 31–33] have synthesized CZTS NPs from solutions that are similar in composition. However, only very few [8, 24] have ultimately formulated ink from CZTS NPs. Further, solvents used for preparation of CZTS inks were completely different from those used for synthesis of CZTS NPs. In general, CZTS NPs were separated from the microwave solvent, cleaned, dried and dispersed in another solvent [8, 21–25]. That is, preparation of CZTS ink by microwave heating is rather complicated because of multiple cumbersome steps. However, it should be straightforward for mass scale.

5.3 Microwave Processing of Inks

A microwave is a rapid one-step process which is nowadays used to synthesize almost all types of materials, including sulphides, metals, phosphates, oxides and halides. Microwave irradiation is a form of electromagnetic energy which falls at the lower frequency end within electromagnetic spectrum and it is defined in the frequency range of 0.3–300 GHz (wavelengths range from 0.01 to 1 m). The frequency 2.45 GHz is preferred out of four available frequencies for industrial, scientific or medical applications since it has the suitable penetration depth to deal with laboratory scale samples, and there are power sources available to produce microwaves at this particular frequency. Microwave heating is often considered as *'microwave dielectric heating'*. This process is depending on the ability of a specific material to absorb microwaves and exchange it into heat. The mechanisms of microwave heating could be classified broadly into two different categories, i.e. dipolar polarization and ionic conduction [34].

Presently, chemical mechanisms take place by one of the two ways: conventional heating or microwave heating. In conventional heating, solvents and reactants are slowly activated by a conventional external heat source such as oil bath or hot plates. Heat is driven into the substance, passing first through the walls of the vessel in order to reach the solvent and reactants. However, this process is very slow.

In contrast, microwave heating generates efficient internal heating (in-core volumetric heating) by direct coupling of microwave energy with the molecules (solvents, reagents, catalysts) that are present in the reaction mixture, resulting in rapid rise in temperature. Since this process is not depending upon thermal conductivity of the vessel materials, the result is an instantaneous localized superheating of anything that will react to either dipole polarization or ionic conduction. The main benefit of using microwave-processed organic as well as

inorganic synthesis is the shorter reaction time. The reaction rate is determined by the Arrhenius equation as follow:

$$k = \mathrm{Ae}^{-\mathrm{Ea/RT}} \tag{5.1}$$

where T is the absolute temperature that controls the kinetics of the reaction and E_a is the activation energy. Further, the ability of a substance to convert electromagnetic energy into heat at a given frequency and temperature is determined by its tan delta loss which is given by Eq. (5.2) as,

$$\tan\delta = \varepsilon''/\varepsilon' \tag{5.2}$$

Tangent delta or tan delta loss is the dissipation factor of the sample. The dielectric constant or relative permittivity (ε') describes the ability of a dielectric material to store electrical potential energy under the effect of an electric field. Dielectric loss (ε'') represents the amount of input microwave energy that is lost to the sample by being dissipated as heat. Three main dialectic parameter, tan delta loss, dielectric constant and dielectric loss are all related to the ability of a solvent to absorb microwave energy. The loss factor (tan delta loss) for some common solvents along with its boiling point and viscosity is summarized in Table 5.3. The solvents should be such that it absorbs the microwave energy very quickly and converts it into heat. Depending upon dielectric loss of solvents, it is divided into three categories, i.e. high, low and medium absorber solvents. The high absorbing solvents are one that has dielectric losses greater than 14 [35].

The aim of the present investigation is to coat CZTS films by doctor blading from ink. Hence, synthesis of appropriate CZTS ink is critical and imperative. Inks for deposition of semiconductor are of two types, i.e. suspension and solution. Suspension type of ink consists of micro or nano particles of material (CZTS) suspended in a solvent. However, in case of solution ink, the precursor chemicals are dissolved in the solvent. After doctor blading, the film is obtained by evaporating the solvent and heating at higher temperatures to obtain the final film. In case of solution ink, CZTS precursor is dissolved in a solvent. After deposition of films, the wet layer is preheated to evaporate the solvent. The dry films which are the precursor layer is then heated at thermolysis temperature (473 K for CZTS) to thermochemically convert it to CZTS. The CZTS film is finally annealed at higher temperature to achieve large grains. However, the present investigation is only restricted to suspension inks. For preparation of suspension ink, microwave process has been used for rapid in situ synthesis of CZTS particles.

Table 5.3 Different properties of most common solvents

Solvent	Boiling point (K)	Viscosity (cP)	Dielectric loss	Tan δ loss
Ethylene glycol	470	16.1	49.95	1.350
DMSO	462	1.99	37.12	0.825
Nitrobenzene	483	1.80	20.49	0.589

5.3.1 Basis for Development of CZTS Ink

One of the major objectives of this investigation is to prepare CZTS nanoparticle ink by microwave processing. The desired suspension ink essentially consists of nanoparticles of kesterite CZTS homogeneously dispersed in a solvent. Microwave processing as described above is not only simple and rapid but also does not require complicated experimental arrangement. The idea is to prepare CZTS suspension ink by microwave heating of a solution consisting of CZTS precursor dissolved in an appropriate solvent without any capping agent. Hence, the choice of CZTS precursor and solvent is important.

It has been observed by Chaudhuri and Tiwari [36] of our group that a complex of Cu^{+}, Zn^{++}, Sn^{++} and thiourea (CZTTU) is an excellent CZTS precursor and thermolyze to kesterite CZTS at around 473 K as depicted by the reaction:

$$\left[\mathrm{CuZnSn}\left(\mathrm{CS}\left(\mathrm{NH_2}\right)_n\right)\right]^{m+} \underset{\text{Heat}}{\rightarrow} \text{CZTS} + \text{Volatile Matter}$$

The thermogravimetric analysis (TGA) of the dry complex powder is shown in Fig. 5.4. The graph reveals that the CZTTU complex starts decomposing at around 473 K. The CZTTU solution was prepared by dissolving copper (II) acetate (0.1 mol/L), zinc acetate (0.05 mol/L), tin (II) chloride (0.05 mol/L) and thiourea (0.5 mol/L) in methanol acidified by a few drops of HCl.

In the compound Cu_2ZnSnS_4, copper is in $Cu(I)^{+}$ state while tin is in $Sn(II)^{++}$ state. Although the starting salt of copper in solution is $Cu(II)^{++}$, under acidic condition TU reduces $Cu(II)^{++}$ to $Cu(I)^{+}$ by forming stable $[Cu(TU)_3]^{+}$ complex

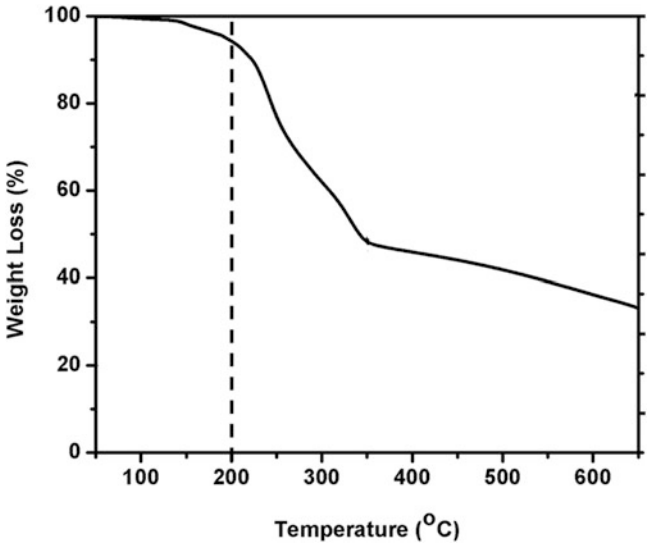

Fig. 5.4 Thermogravimetric analysis of metal-thiourea complex precursor

[37]. TU also readily forms soluble complexes with Zn^{++} and Sn^{++} as $[Zn(TU)_2]^{++}$ and $[Sn(TU)]^{++}$, respectively. When all these TU complexes are mixed in methanol, the CZTS precursor (CZTTU) is produced, given by the reaction:

$$\left[Cu(TU)_3\right]^{+} + \left[Zn(TU)_2\right]^{++} + [Sn(TU)]^{++} \rightarrow \left[CuZnSn(TU)_n\right]^{m+}$$

Hence CZTTU complex, suggested by Chaudhuri and Tiwari [36], was used as a CZTS precursor for synthesis of ink by microwave heating. The selection of appropriate solvent for ink was very vital. The ultimate solvent had to meet the following criteria:

- Precursor chemicals should dissolve easily
- Boiling point should be around 473 K
- Should be favourable to microwave heating, that is, high tanδ loss
- Should have moderate viscosity for doctor blading

Some of the common solvents with boiling point ~473 K are listed in Table 5.3.

It can be seen that ethylene glycol (EG) qualifies as appropriate solvent for preparing ink since it has boiling point of 470 K, moderate viscosity of 16 cP and high tanδ loss of 1.35. Further, all the chemicals required for synthesis of CZTS precursor (CZTTU complex) are dissolved easily in EG. The basic concept of microwave synthesis of CZTS ink is as follows:

First, CZTS precursor (CZTTU) is dissolved in EG to form a clear solution. The solution is then heated with microwave radiation. During heating, EG rapidly attains temperature of 470 K and starts boiling. At this temperature (~473 K) CZTTU molecules present in EG also thermolyzes to CZTS, thus producing CZTS particles in situ EG.

To prove the above concept, CZTS powders were first synthesized in EG by microwave processing. This was followed by making of CZTS inks with micro and nano particles dispersed in EG. Molecular ink with CZTTU in EG and methanol was also prepared for comparison [38, 39].

Figure 5.5 reveals that a high microwave absorbing solvent EG (tan delta = 1.350) can be rapidly superheated to temperatures >473 K above its boiling point when irradiated under suitable microwave conditions. Generally, this is difficult to achieve using standard thermal heating. During microwaving, the temperature of PS is rapidly ramped from 303 to 433 K in about 90 s at a heating rate of about 5°/s. There is no hold time. In short, the microwave is a type of rapid thermal processing.

5.3.2 *Synthesis of Micropowder*

CZTS powder was made from microparticle ink synthesized by microwave irradiation of precursor solution (PS) consisting of copper (II) acetate (0.1 M), zinc acetate (0.05 M), tin (II) chloride (0.05) and thiourea (0.5 M) in EG. All the

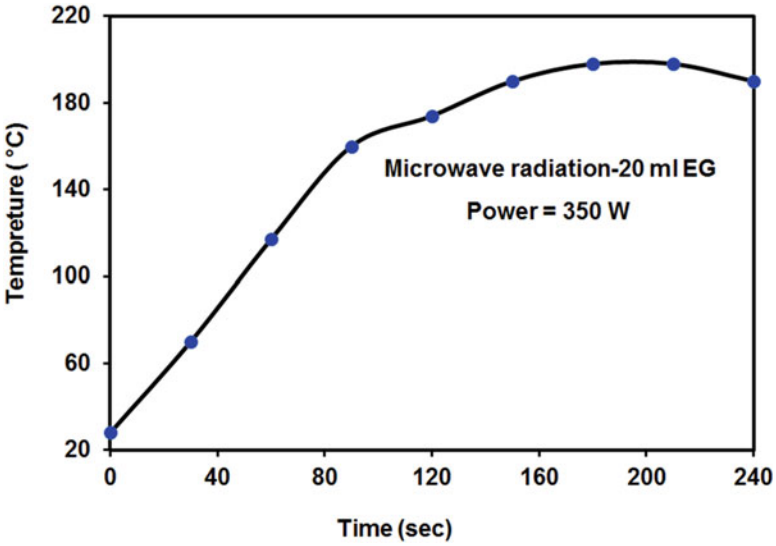

Fig. 5.5 The temperature increases of ethylene glycol (20 mL) at 350 W microwave power

chemicals and solvents used in the present work are of analytical grade supplied by Merck limited, India. Typically 100 mL of PS was heated in a domestic microwave oven for 5 min operated at 350 W. The temperature of the PS was instantly rose to 473 K, converting clear solution into black micro particles. The particles were separated from the ink by centrifugation at 8000 rpm for 10 min. The particles were cleaned and washed with methanol several times. Finally, the products were dried at 373 K in vacuum for several hours. The particles were then heated in a furnace at 473 K in air to remove any residual EG for few minutes. Upon heating, the particles are converted into black powders as shown in Fig. 5.6. The powder was then converted into pellet using steel dye and punch. For making pellets, the pressure of 10 ton was applied using hydraulic press. The diameter and height of the pellet was ~10 mm and 3 mm, respectively.

5.3.3 Microparticle Ink

Earlier section reveals that CZTTU precursor yields pure kesterite CZTS phase. However, to further explore the sulphur source, CZTS ink has been synthesized using six different sulphur sources. These are: thioglycolic acid (TA), sodium thiosulphate (ST), thiourea (TU), sodium sulphide (SS), sulphur (S) and thioacetamide (TAA). The precursor solution (PS) was prepared by dissolving copper (II) acetate (0.1 mol/L), zinc acetate (0.05 mol/L), tin (II) chloride (0.05 mol/L) and above sulphur sources (0.5 mol/L) step by step in separate beaker

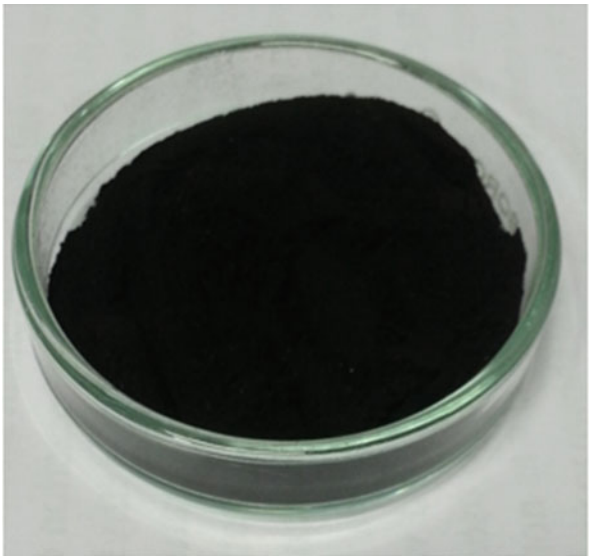

Fig. 5.6 CZTS micropowder after heating at 473 K in air

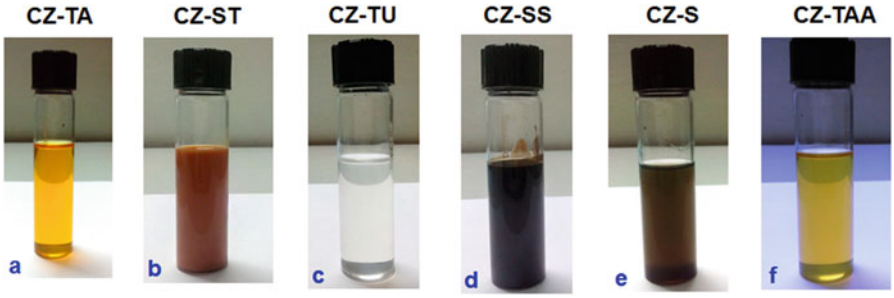

Fig. 5.7 CZTS precursor solution synthesized in different sulphur sources: (**a**) thioglycolic acid (TA), (**b**) sodium thiosulphate (ST), (**c**) thiourea (TU), (**d**) sodium sulphide (SS), (**e**) sulphur (S) and (**f**) thioacetamide (TAA)

in 20 mL of EG. Figure 5.7 shows the CZTS precursor solution prepared using different sulphur sources.

It is also clear that TA-, TU- and TAA-based PS is clear. Further, only TU-based PS is clear and stable. Hence, it is confirmed that TU is suitable for making clear homogeneous solution. Further, CZTS ink was prepared using entire sulphur sources using microwave heating.

For the synthesis of ink, 20 mL of PS was placed in a domestic microwave oven operated at 350 W. In about 3 min, the temperature of the PS increased to 463 K and consequently the clear PS was converted into black opaque ink. The microwave production of CZTS ink in TU is depicted in Fig. 5.8. The similar procedure was done for all the sulphur sources. It is interesting to note that the ink was synthesized without adding any capping or legends unlike to those reported by Riha et al. [9] and Saraswat et al. [24].

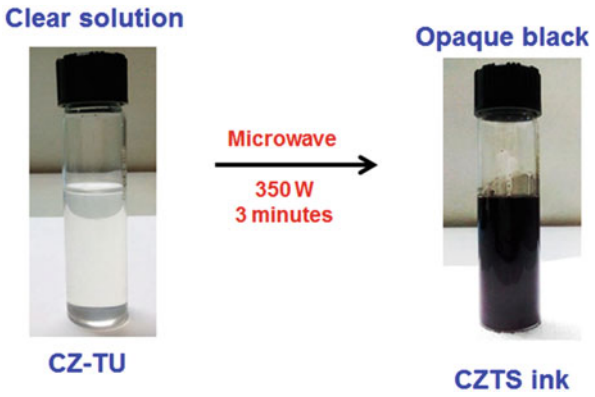

Fig. 5.8 Synthesis of microwave-processed microparticle CZTS ink

5.3.4 Nanoparticle Ink

CZTS microparticle ink has been synthesized by a one-step method involving the microwave heating of a glycolic solution of copper (II) acetate, zinc acetate, tin (II) chloride and thiourea. However, similar precursor solution of lower concentration, when irradiated with lower microwave power and longer duration, yielded CZTS nanoparticles (NPs).

In typical process, precursor solution was prepared by dissolving copper acetate (0.01 mol/L), zinc acetate (0.005 mol/L), tin chloride (0.005 mol/L) and thiourea (TU, 0.05 mol/L) as copper, zinc, tin and sulphur sources, respectively, in acidic EG. First, 20 mL of clear glycolic solution was microwaved at 250 W for 10 min. Within 10 min, a temperature of the solution was rose to 463 K, converting a clear solution into brown transparent stable ink. The ink was then allowed to cool naturally to the room temperature in air. The process of making CZTS NPs is shown in Fig. 5.9. This ink was used directly without any further treatments for the deposition of films.

Figure 5.9 shows that the clear colourless glycolic solution coating of meta-TU complex turned rapidly into clear brown CZTS ink upon microwave heating. During microwaving the temperature of the solution was rapidly increased to ~463 K, which is actually a boiling point of EG (460 K). It was showed in the earlier section that Cu^{+2}, Zn^{+2}, Sn^{+2} and TU form a complex which thermally decomposes to CZTS at ~463 K. Some volatile products were formed during thermolyses which escape into the air leaving only CZTS as a final product. In the present investigation Cu^{+2}, Zn^{+2}, Sn^{+2} and TU also form a complex in EG. During microwave irradiation, the complex thermolyzes to CZTS in situ the solvent EG. The other volatile products are expelled into the air. It was observed that during microwave heating, the precursor solution not only boiled but also copious bubbles were generated throughout the volume of the solution.

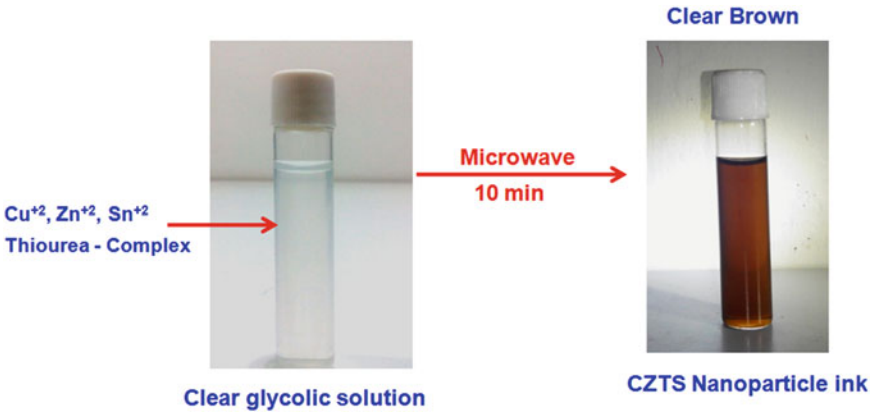

Fig. 5.9 Microwave-processed nanoparticle CZTS ink [40]

5.3.5 *Characterizations*

The synthesized products (inks/powder/films) have been characterized for structural, optical, morphological and electrical properties. The shapes and sizes of the CZTS nanoparticles were observed by a transmission electron microscope (TEM, Philips, Tecnai 20). A drop of ink was placed on a carbon-coated TEM grid and dried for observation under TEM. The transmittance spectrum of the nano inks was measured using an UV-VIS-NIR spectrophotometer (Shimadzu, UV-3600) in the wavelength range of 200–1500 nm. Band gap of CZTS powder has been measured in diffuse reflectance mode using integrating sphere. An X-ray diffractometer (Bruker, D2 PHASER) was used to identify CZTS with Ni-filtered CuKα radiation ($\lambda = 1.5418$ Å) operated in the 2θ range from 10 to 80°. The elemental composition of the films was analysed by energy dispersive X-ray spectroscopy (EDS Philips XL 30). Cross-sectional views of films were analysed by a field-emission scanning electron microscope (FE-SEM, Carl Zeiss 55). The thickness of the samples was also estimated from the cross-sectional SEM view. The vibrational modes of CZTS were analysed by a Laser Raman Spectrometer (LRS Jobin–Yvon, HR800) with an excitation wavelength of 514 nm in the range of 200–500 nm to identify the proper phase of the CZTS. The Raman spectra were calibrated by standard Si wafer (Raman shift of 520 cm^{-1}). A linearly polarized Ar-ion laser beam with a power of 10 mW was focused into a spot size 1 μm in diameter.

For the electrical measurements gap cells (~2 mm) were fabricated with graphite paint (Ted Pella) as ohmic contacts. The films were dried under IR lamp at room temperature for few minutes. The electrical conductivity of the CZTS films in the temperature range of 77–500 K in the dark and under light were measured using cryostat (Janis VPF-100). The dark and photocurrent was measured with a source/meter unit (Keithly 2611) and a data acquisition system.

5.4 Issues in CZTS

A slight deviation from the optimal growth conditions (1–2%) will result in the formation of secondary phases, including ZnS, Cu_2SnS_3 (CTS), SnS, SnS2 and CuS. The growth of these materials induced many problems in quaternary CZTS which ultimately affects the overall efficiencies. Chemical potential μSn–μZn diagram reveals only about 0.1 eV wide stability regions for Cu-rich CZTS compositions. The following sections describe the effect of some detrimental phases on final device and defects associated with it.

5.4.1 Detrimental Phases

Due to the complexity of the material and quaternary nature, the numbers of secondary phases are likely to form within CZTS. The most common ones are Cu_2SnS_3 (CTS) and ZnS. A wide list of secondary compounds along with CZTS is reported in the literature. The secondary phases are detrimental for photovoltaic devices. Cu-S and Cu-Sn-S compounds are unfavourable for CZTS, being highly conductive phases [41], which can create shunting paths in the final devices. Table 5.4 shows the formation of possible secondary phases with their common properties.

CTS can form a solid solution with CZTS which lowers the E_g and ultimately increasing the conductivity of the final compound. On the other hand, copper sulphide phases appear in Cu-rich or Sn-poor conditions. They are low band gap semiconductors. Thus, they have a metallic behaviour, it means they can shunt the solar cells if their grains are big or in such a quantity that connects the front to the back electrode in the device. Small CuS/Cu_2S crystals act as traps for electrons and holes and enhance recombination. As far as transport properties are concerned, these phases are responsible for lowering the mobility and hence increase the carrier concentrations [43]. The effect of this phase on the final devices is still unclear as presence of ZnS was also observed in the best solar cells [44]. In general, these phases are responsible to suppress the overall efficiencies in CZTS thin films solar cells (TFSCs). Copper-poor, Zinc-rich compositions are therefore beneficial to suppress Cu-S phase and are generally taken in the literature for realization of high-efficiency CZTS devices [45].

Copper sulphide phases such as Cu_2S, CuS and unwanted phases based on tin (SnS, SnS_2 and Sn_2S_3) are easily detected by XRD as diffraction peaks of these phases and CZTS are completely different. However, due to the similarity in crystal structure and lattice constant of ZnS and CTS, these phases cannot be identified by XRD alone. Figure 5.10 shows the comparison of XRD patterns of kesterite CZTS along with CTS and ZnS. It is seen that the primary peaks of CZTS, CTS and ZnS are overlapping on each other and hence impossible to distinguish from XRD. Further, it has been shown that only 0.1% energy is required to phase separate

Table 5.4 List of probable secondary phases observed in CZTS [42]

Materials	Crystal structure	Band gap	JCPDS	Type of semiconductor
Cu_2ZnSnS_4	Kesterite tetragonal	1.5	26-0575	P
Cu_2SnS_3[a]	Cubic	0.96	89-2877	P
Cu_2SnS_3[a]	Tetragonal	1.12	89-4714	P
Cu_3SnS_4	Orthorhombic	1.60	36-0218	P
Cu_4SnS_6	Rhombohedral	–	36-0053	P
ZnS[a]	Sphalerite-Cubic	3.54	05-0566	Insulator
2H-ZnS[a]	Wurtzite-Hexagonal	3.91	79-2204	Insulator
CuS	Covellite-Hexagonal	1.7	06-0464 75-2233	P
Cu_2S[a]	Low-Chalcocite Orthorhombic	1.18	23-0961 73-1138	P
Cu_2S[a]	High-Chalcocite Hexagonal	–	84-0206	P
Cu_9S_5	Digenite-rhombohedral	1.8	47-1748 84-1770	P
Cu_7S_4	Anilite-orthorhombic	–	72-0617	P
α-SnS	Herzenbergite-orthorhombic	1.3	83-1758 (Amnm)	P
β-SnS	–	1.3	73-1859 (Pbnm)	P
SnS_2	Berndtite-Rhombohedral	2.2	23-0677 83-1705	N
Sn_2S_3	Orthorhombic	1.09	75-2183	N

[a]Most common observed phases in CZTS

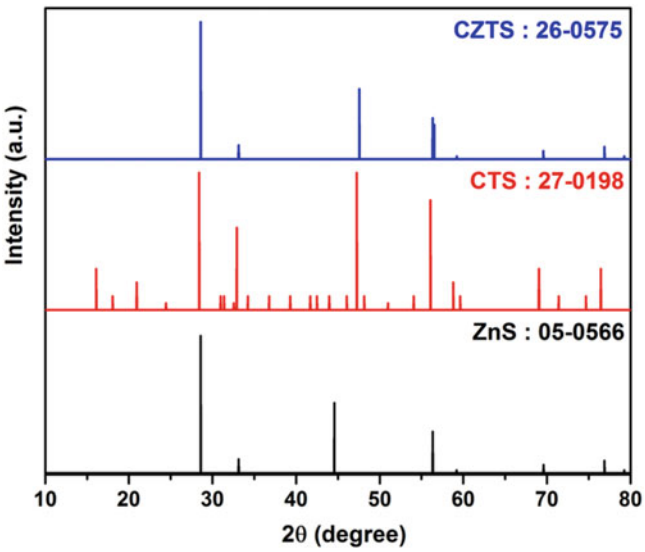

Fig. 5.10 Powder X-ray diffraction patterns showing overlapping of kesterite CZTS with related secondary phases

Table 5.5 Raman peaks of different binary and ternary compounds [49]

CZTS	Cu_2SnS_3	Cu_3SnS_4	Cu_2S	ZnS	SnS_2	SnS
266	–	295	264	278	–	164
288	295–303	318	–	–	–	192
338	355	348	–	351	315	218
368–374	–	–	475	–	–	–

stoichiometric CZTS into ZnS and CTS [46]. Experimentally, both ZnS and CTS have been scrutinized within CZTS, which can only be confirmed by Raman spectroscopy.

Raman spectroscopy is the precise technique used to studying the presence and spatial distribution of various chalcogenide and kesterite phases. Slight differences in the phonon densities of states between these phases can be easily distinguished from the shifts in Raman scattering peaks. Table 5.5 illustrates the peak position (Raman shift) of different binary and ternary sulphides along with CZTS. Further, Fernandes et al. [47], Fontane et al. [48] and Cheng et al. [49] used a 514 nm laser source in Raman spectroscopy to successfully identify and distinguish the presence of CTS, Cu_3SnS_4, Cu_2S, ZnS and SnS_2 in CZTS. Hence, in the present work, the same source has been utilized to examine the CZTS samples.

Table 5.5 reveals that the Raman peaks of CZTS, CTS and ZnS are completely different. Himmrich and Haeuseler [50] studied the Raman spectra of CZTS and other stannite and wurtzstannite compounds. They identified a primary peak at 336 cm^{-1} and two weaker peaks at 285 and 362 cm^{-1}, for CZTS. Recently, a most intense peak of CZTS thin films has been found at 336–338 cm^{-1} and the weaker peaks at 287–288 cm^{-1} and 368–374 cm^{-1} [14, 51, 52]. The primary peak of CZTS has been found to vary from 339 to 330 cm^{-1} depending upon growth conditions [53, 54]. The distribution of Raman peaks in CZTS is explained by selection rules which can only be identified using polarization Raman study. The irreducible representation of the zone centre phonon mode in kesterite structure is given as [55].

$$\Gamma = 3A \oplus 6B \oplus 6E \tag{5.3}$$

The main peak in CZTS is dominated by the A1 vibrational mode. The weaker peak at 287 cm^{-1} is due to the B symmetry mode corresponding to movements of the Cu/Zn and Cu/Sn atomic planes [55]. However, minor peak appearing in the range 350–380 cm^{-1} is assigned to B and E symmetry mode of CZTS.

5.4.2 Defects

Crystal defects are inevitable in chalcopyrite and quaternary kesterite semiconductors and always associated with their photovoltaic properties. One of the major factors limiting the efficiency of TFSCs is the occurrence of different types of

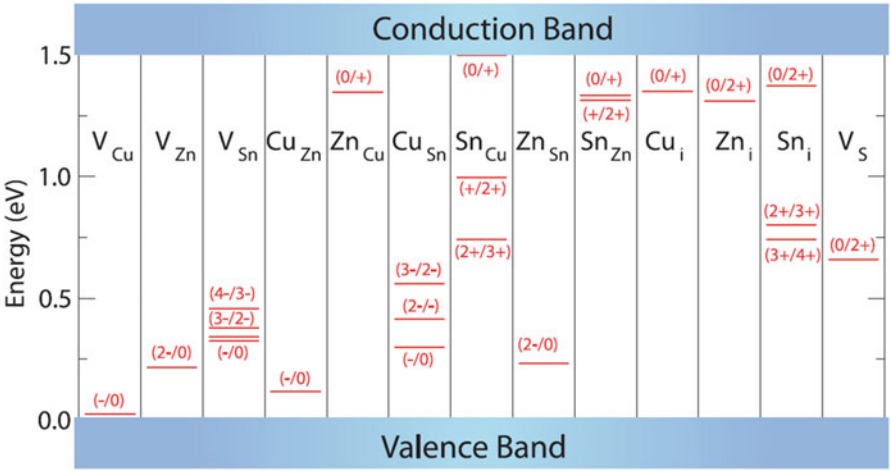

Fig. 5.11 The ionization levels of intrinsic defects in the band gap of CZTS [46]

defects, like vacancies, antisites, interstitials and clusters, which affect the charge transport mechanisms in the solar cells. Further, higher number of constituent atoms makes the properties of the intrinsic defects more intricated. Theoretical studies have predicted various intrinsic point defects including vacancies (V_{Cu}, V_{Zn}, V_{Sn} and V_S), antisites (Cu_{Zn}, Zn_{Cu}, Cu_{Sn}, Sn_{Cu}, Zn_{Sn} and Sn_{Zn}), interstitials (Cu_i, Zn_i and Sn_i) and several defect complexes may play crucial part in CZTS depending on its composition [56].

Crystal structural, electronic state and point defect formation of kesterites and chalcopyrites have been investigated using density functional theory (DFT) [56]. These examinations have revealed both similarities and differences between kesterites and chalcopyrites. Antisite defects can form either acceptor or donor levels in CZTS, subjected to their formation energies or transition levels. The ionization levels of various point defects were predicted by Chen et al. [56] as summarized in Fig. 5.11. The dominant *p*-type acceptor in kesterite CZTS is the Cu_{Zn} antisite defect.

According to Chen et al. [56], the V_{Cu} results in a shallow acceptor level just above the valence band, while the Cu_{Zn} antisite results in a level 0.12 eV higher in energy. Lowest formation energy is reported in Cu_{Zn} antisite by Chen et al. [57] whereas a negative value is also reported by Nagoya et al. [58]. However, calculations reported in [57] predict that the Cu_{Zn} formation energy becomes negative for Fermi level higher than 0.12 eV. In general, these investigations prevent the possibility of an *n*-type doping. Apart from the Cu_{Zn} antisites, other four dominant defects are expected, showing relatively low formation energy for Cu-poor CZTS compositions. These defects, in terms of increasing formation energy: V_{Cu}, Zn_{Sn}, V_{Zn} and Cu_{Sn}.

Formation of donor defects is rather unlikely due to the high formation energies or the facile formation of compensating acceptors [59].The lowest formation energy was reported for the defect complex [Cu_{Zn} + Zn_{Cu}] [60] which give rise to the possibility of Cu and Zn disorder. This disorder in the cation sublattice is reported to reduce the band gap [61]. Due to the manifold possibility of the formation of defect complexes, CZTS is assumed to possess an electrically benign character.

5.5 Properties of Inks

Two different types of inks including micro and nano were synthesized without any capping agent. For comparison, pellets from micropowder were also synthesized. In this section, structural, optical and morphological properties of such inks and powder have been studied.

5.5.1 Structural, Morphological and Optical Properties of Micropowder

A typical X-ray diffractograph of powder is shown in Fig. 5.12. The X-ray diffraction (XRD) comprises sharp peaks at 2θ values of 28.6°, 47.3°, 56.2° and minute peak at 76.4°; these peaks are found to match well with standard data for kesterite

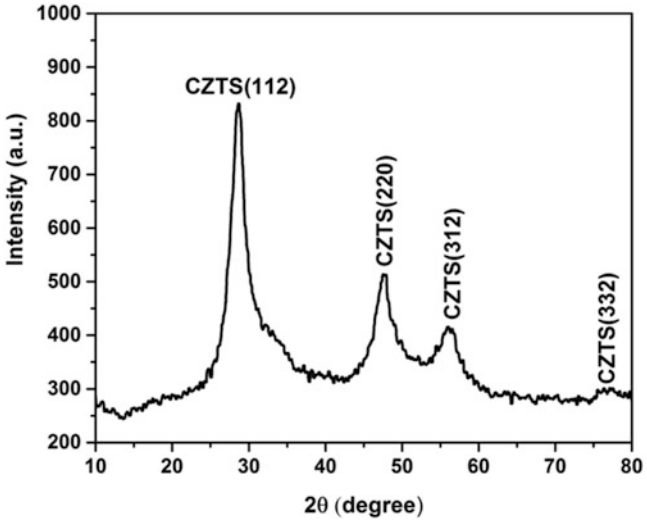

Fig. 5.12 X-ray pattern of CZTS powder heated at 473 K

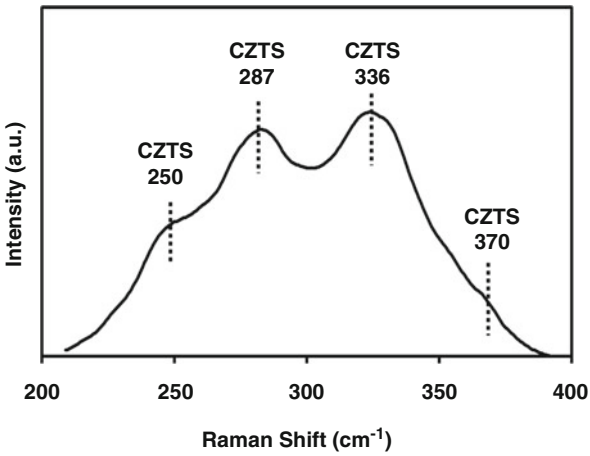

Fig. 5.13 Raman spectrum of CZTS powder

CZTS (JCPDS 26-0575) and are identified to be due to reflections from (112), (220), (312) and (332) planes, respectively. The sharpness of the (112) peaks suggests a good crystallinity. No other peaks such as Cu_xS or SnS_y were assigned which shows the powder is possibly CZTS.

The Raman spectrum of CZTS powder taken at room temperature is shown in Fig. 5.13. In general, the spectrum shows peaks at 250, 287, 336 and 370 cm^{-1}. These peaks are characteristics of kesterite CZTS [49]. The main peak at 336 cm^{-1} is due to the A1 vibrational mode, arising from the vibrations of the sulphur atoms in the CZTS lattice while the rest of the atoms remains stationary [50]. The peaks at 250 and 287 cm^{-1} were allied to B symmetry mode while the peak at 370 cm^{-1} has been assigned to B and E symmetry modes of CZTS [55]. Thus, it is confirmed that 473 K is sufficient for the formation of crystalline CZTS phase. Further, this vibrational feature is supported by theoretical calculations as well [62].

The surface morphology of the CZTS powder is observed using scanning electron microscopy (SEM) as shown in Fig. 5.14. The particles are agglomerate and form relatively large microparticles clusters. The powder is made of spherical particles of diameters about 0.6–0.8 μm. Thus, the microwave-processed synthesis displays good homogeneity and compositional control.

The diffuse reflectance spectrum of CZTS microparticles (powder) is measured in the wavelength range of 300–2000 nm as shown in Fig. 5.15. The spectrum has a strong absorption below 900 nm due to absorption by the CZTS microparticles confirms its suitability of maximal solar photons absorption.

The optical band gap of CZTS powder has been estimated from diffuse reflectance spectrum using Kubelka–Munk function, $F(R_\infty)$ [63]. Kubelka–Munk function can be expressed as:

$$F(R_\infty)h\upsilon = \left(h\upsilon - \mathrm{E_g}\right)^{1/2} \tag{5.4}$$

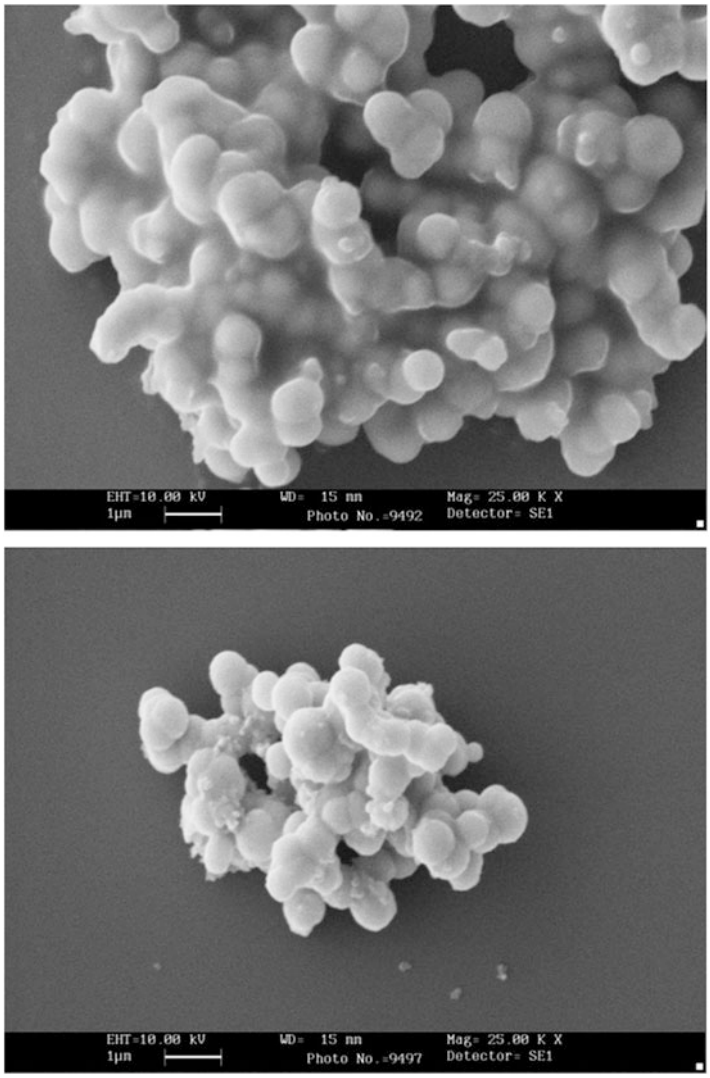

Fig. 5.14 Scanning electron microscopy of CZTS powder

where $F(R_\infty)$ is Kubelka–Munk function, h is Planck's constant, ϑ wave number. The $F(R_\infty)$ is obtained from diffuse reflectance

$$[F(R_\infty)] = \frac{(1 - R_\infty)^2}{(2R_\infty)} \tag{5.5}$$

$R_\infty = R(\%)/R_{\text{ref}}(\%)$, R_{ref}: diffuse reflectance of reference (in the present study, we use $BaSO_4$ as a reference)]. Tauc plot of $[F(R_\infty)h\nu]^2$ vs. $h\upsilon$ is shown in Fig. 5.16. The band gap of CZTS powder as determined from the plot is found to be ~1.5 eV.

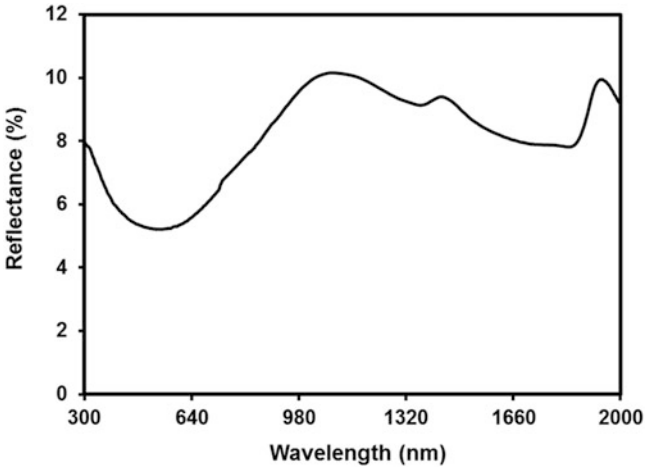

Fig. 5.15 Diffuse reflectance spectrum of CZTS powder

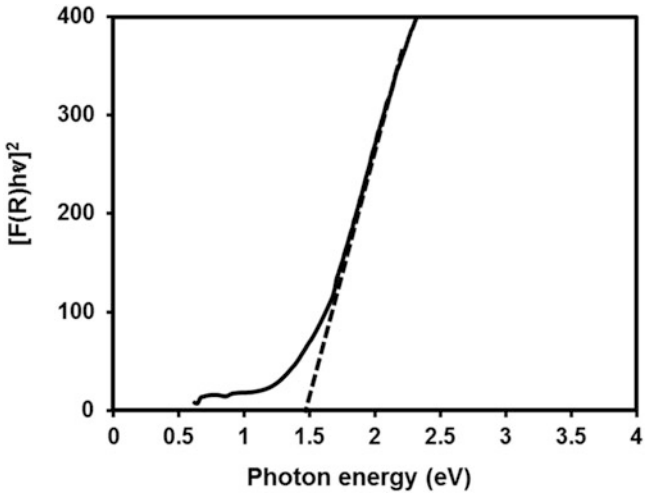

Fig. 5.16 Optical band gap using Kubelka–Munk function

5.5.2 Structural and Morphological Properties of Microparticles Ink

To analyse the crystalline structure and phase, X-ray diffraction of all the inks synthesized using different sulphur sources were performed. Figure 5.17 shows the XRD plots of inks drop cast into glass followed by vacuum dried at 373 K.

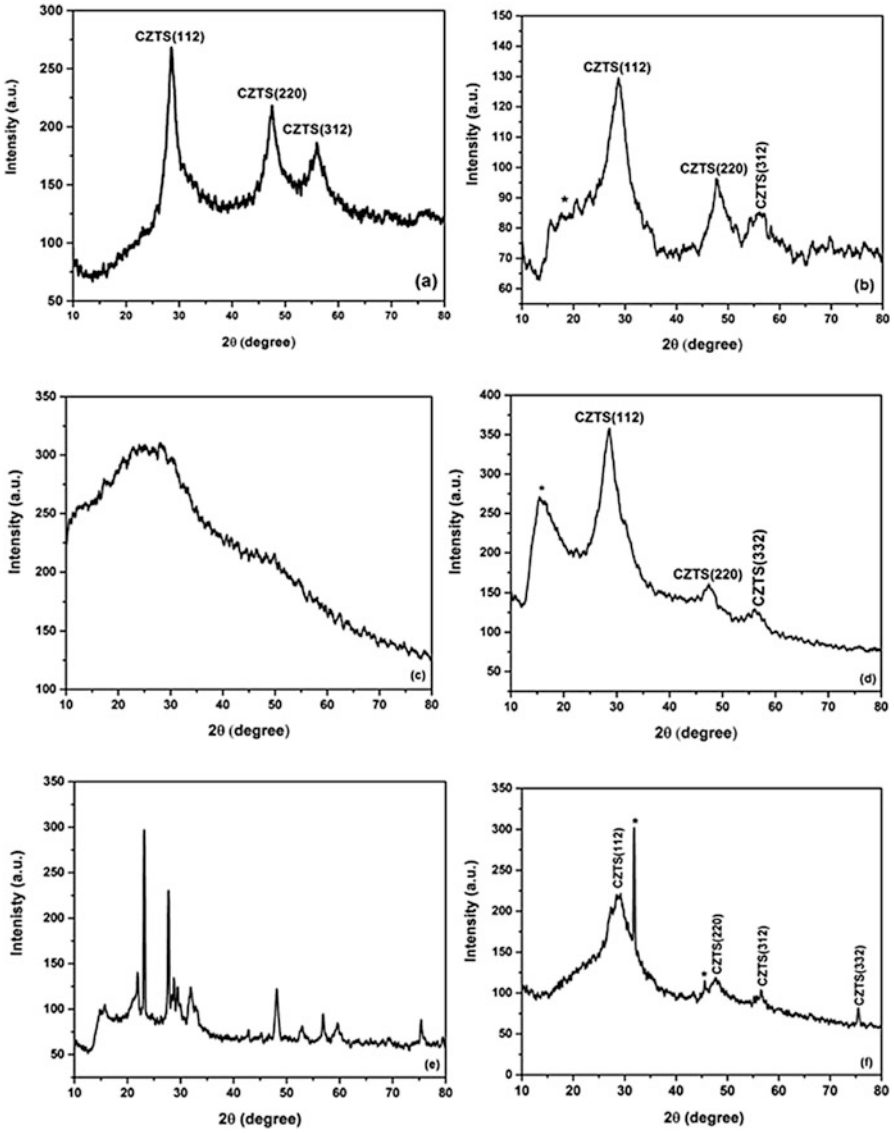

Fig. 5.17 XRD plots of CZTS ink prepared using different sulphur sources: (**a**) thiourea, (**b**) thioacetamide, (**c**) sodium thiosulphate, (**d**) thioglycolic acid, (**e**) sulphur and (**f**) sodium sulphide

The XRD of all the samples (expect for the sample prepared using thiourea) shows impurity (indicated as *). Surprisingly, XRD of CZ (ST) shows no intense peak indicating amorphous nature of the particles (5.17 c) whereas those for CZ (SS) (5.17 e), peaks due to Na source along with CZTS phase has been found. The crystalline structure of the CZ (S) is unidentified. However, XRD plot of CZ

(TU) shows peaks due to tetragonal CZTS only and no other extra peaks are present inferring formation of pure CZTS. Three broad and intense peaks ascribed to the (112), (220) and (312) planes are detected (JCPDS-26-0575) for the CZTS ink prepared using TU. This result shows that microwave-processed CZTS ink in TU yields pure CZTS phase. Hence, further study is on CZTS-TU only (hereafter mentioned as CZTS).

Figure 5.18 shows the SEM images of the CZTS microparticles synthesized using TU as a sulphur source. Low and high magnification images reveal that prepared particles consist of large amount of sphere-like grains ranging from 0.8 to 1 μm. Further CZTS microparticles are linked with adjacent ones to from chain-like network. The synthesis of sphere-like CZTS microparticles by microwave irradiation was also investigated by Kumar et al. [21].

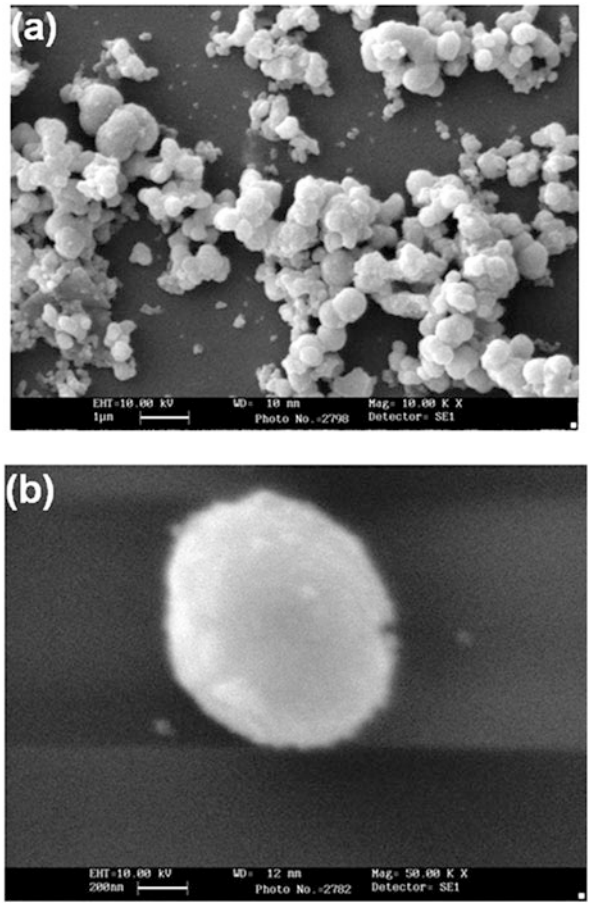

Fig. 5.18 (**a**) Low and (**b**) high magnification SEM images of CZTS microparticles

5.5.3 *Characterizations of Nanoparticles Ink*

The clarity of CZTS ink (Fig. 5.9) suggested that the CZTS particles are of nanoscale dimension. The shape and size of the NPs were determined by transmission electron microscopy (TEM). A typical TEM image of CZTS NPs is shown in Fig. 5.19. Nanoparticles are homogeneously distributed in the ink as revealed from the figure. The CZTS NPs are in general irregular with average diameters of 25–30 nm.

The transmittance spectrum of the CZTS NPs ink is measured in the wavelength range of 200–1200 nm as shown in Fig. 5.20. The spectrum reveals that ink has

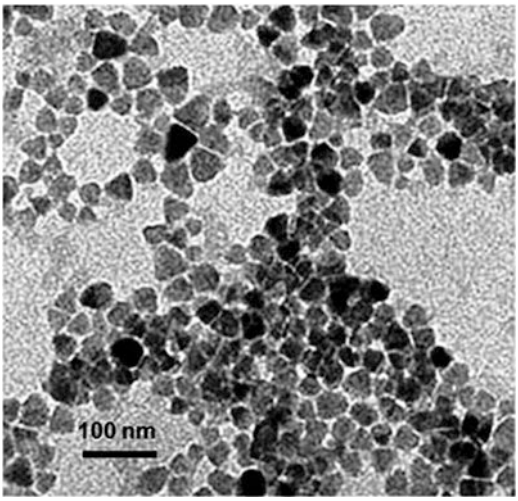

Fig. 5.19 Transmission electron microscopy of CZTS nanoparticles presented in ink [40]

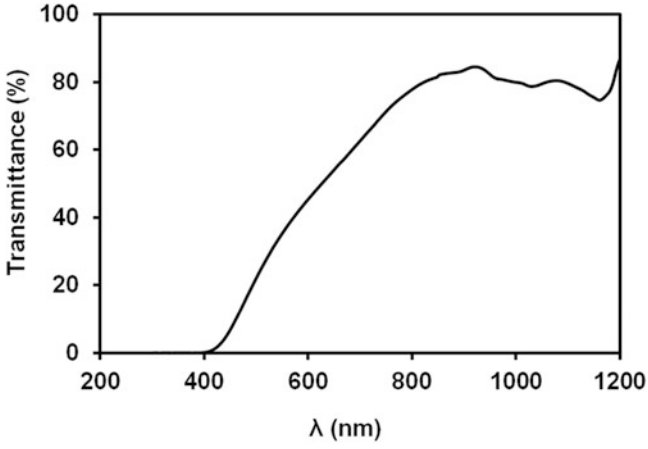

Fig. 5.20 Transmittance spectrum of CZTS nanoparticle ink

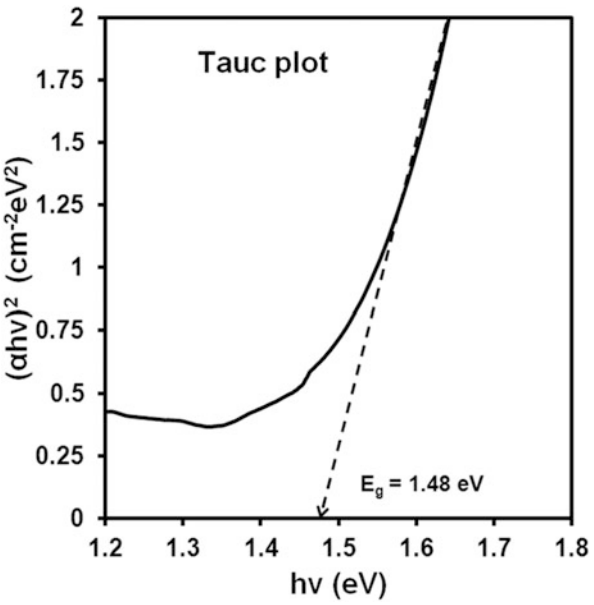

Fig. 5.21 Tauc plot of CZTS nanoparticle ink revealing band gap of 1.48 eV [40]

strong absorption below about 850 nm due to absorption by the CZTS particles showing its potential for solar cell application.

The band gap of the CZTS nanoparticles was estimated from the transmittance spectrum using Tauc plot for direct band gap semiconductors

$$\alpha h\nu = \mathrm{A}\left(h\nu - \mathrm{E_g}\right)^{1/2} \tag{5.6}$$

where
α is the absorption coefficient (cm^{-1}),
h is Plank's constant (J-s),
ν is the frequency of radiation (Hz),
A is an appropriate constant and
$\mathrm{E_g}$ is the band gap (eV).

The Tauc plot of hν versus $(\alpha h\nu)^2$ is shown in Fig. 5.21. The band gap of the CZTS NPs determined by extrapolating the linear part of the plot is found to be 1.48 eV, which is in good agreement with 1.49 eV reported for the CZTS [2].

To check the reproducibility of inks, transmittance spectrum of two more samples have been measured in the wavelength range of 300–1500 nm (synthesized at different time duration) as shown in Fig. 5.22. However, the results were similar. Both the samples show absorption edge near 850 nm which is due to the CZTS nanoparticles.

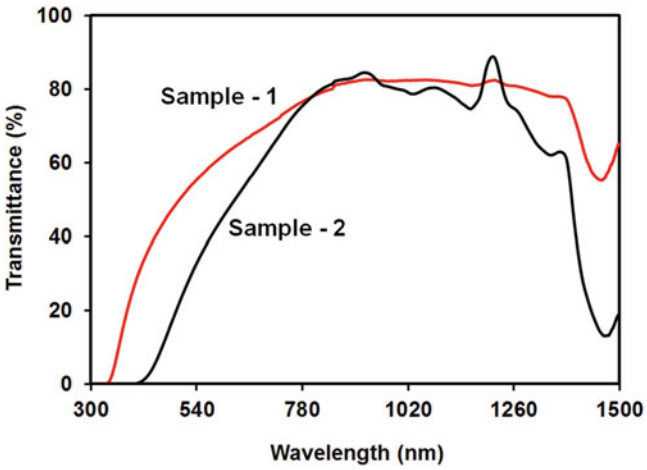

Fig. 5.22 Transmission spectrum of CZTS ink

5.6 Doctor Blade Coating of Films

The solution/inks were first deposited on prepared substrates. Surface preparation generally involves appropriate cleaning and drying in order to reduce the surface contamination and improve film adhesion and coating quality. The substrates used in this work for the deposition of the samples were 1.5 mm thick soda-lime glasses. The glass substrates were first cleaned in ultrasonic bath in mixture of water–chromic acid solutions followed by washed two times in bi-distilled water. The substrates were then cleaned with methanol two times. Finally, the substrates were dried in oven for 323–343 K for few minutes to avoid any contaminations.

Most of the groups working on kesterite use a two-step process in general, i.e. a low-temperature deposition combined with a high-temperature annealing step in S or Se [64]. The steps and critical parameters involved in ink printing of CZTS films are illustrated in Fig. 5.23. These methods work by coating a layer of precursor-containing solution on the surface of a substrate followed by appropriate thermal processing to yield the desired kesterite phase.

5.6.1 Doctor Blade Coating

Doctor blade is a simple, economical and direct-write printing technique which can deposit films on any type of substrate. It is amenable to large area deposition and suitable for roll-to-roll processing. It offers an advantage over conventional spin coating, dip coating and drop casting in terms of low materials consumption, surface roughness and control of films thickness. Doctor blading nowadays is

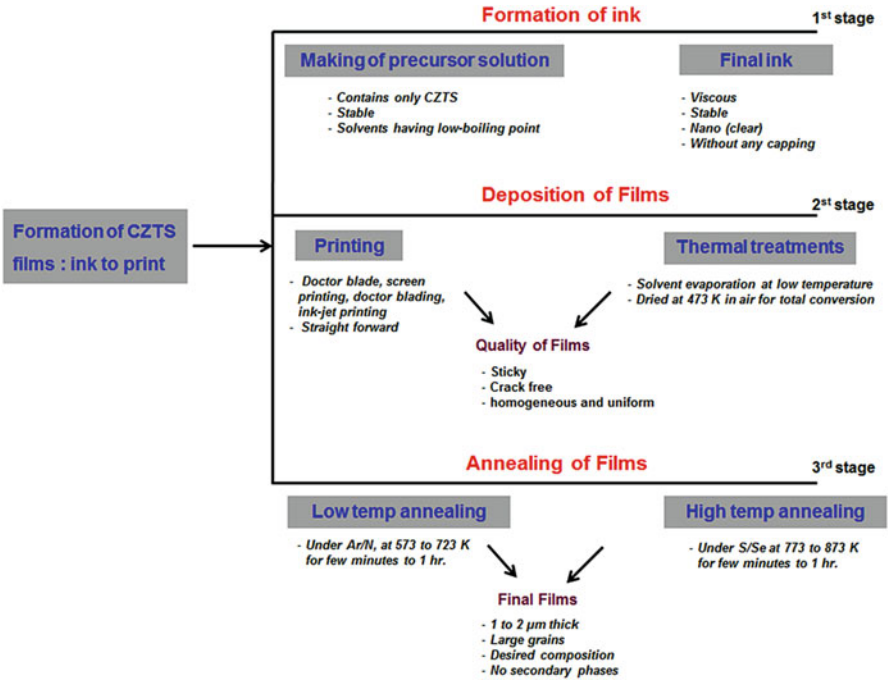

Fig. 5.23 A general scheme for the coating of CZTS films: ink to print

widely used in fabrication of organic and dye-sensitized solar cells. Doctor blading-based processes are well-established techniques for the large-scale fabrication of ceramic substrates and related multilayered structures.

In principal, it uses a sharp blade at a fixed distance under which the coating liquid is deposited. The latter is then spread over the substrate by moving the blade at a constant rate. Figure 5.24 depicts the main stages involved in doctor blade technique. Compared to spin coating, doctor blading is relatively slow and it may happen that the dissolved material aggregates or crystallizes during processing. On the other hand, doctor blading is easily transferable and integrable into R-2-R fabrication concept, which is then often called knife-over-edge coating [64]. The Doctor Blade printer used in the present work is depicted in Fig. 5.25. It comprises two independent systems, i.e. blading part and applicator.

The finalized system was fabricated in our laboratory to combined blading and applicator. The blading part was provided by Royal Enterprises, Chennai, India. However, the applicator was delivered by Darteno Industries, Gujarat, India. For printing of films, the inks are directly deposited on glass substrate (75×25 mm^2). The coating was done by sharp blade with a drawdown speed of 5 mm/s. The blade-to-substrate distance was 20 μm. No temperature and/or vacuum were applied while depositing films. The technical specifications of the doctor blading are presented in Table 5.6.

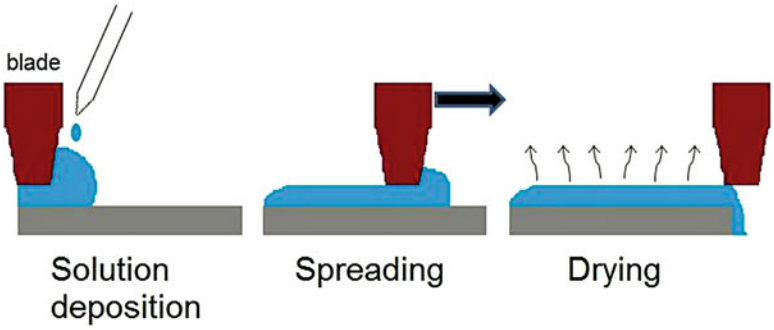

Fig. 5.24 Main stages involved in doctor blade technique [65]

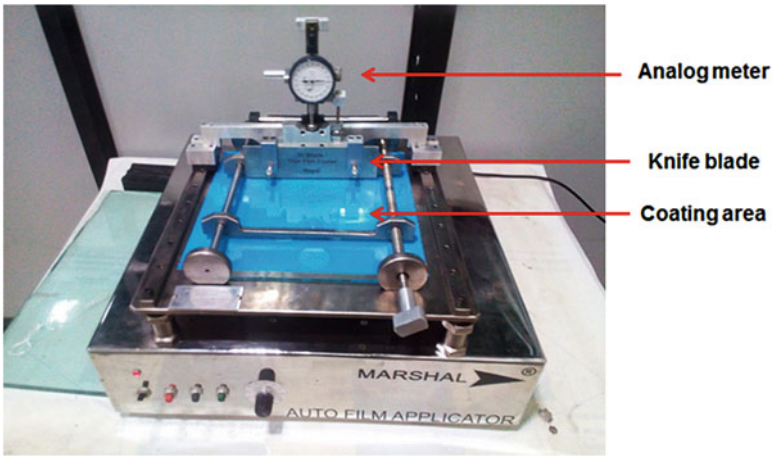

Fig. 5.25 Auto film applicator/Doctor Blading consisting of (1) Blading and (2) Applicator part

Table 5.6 Technical specifications of the thin film coater (Doctor Blade)

Mark and model	'Marshal' AP-E (basic)
Blade adjustable height	0–100 nm (from base to knife edge)
Coating area	200 × 200 nm
Wet film coating thickness	0–100 μm
Draw down speed	4.1–49 mm/s
Power supply	Single phase 220 V, 50 Hz
Weight	50 Kg
System	Automatic

5.7 CZTS Coating with Microwave-Processed Inks and Properties

Coating of CZTS films from different types of inks is one of the objective of this investigation. Two different types of inks were developed in preceding section. These inks are: (1) Microparticle ink (MPI) and (2) Nanoparticle ink (NPI). In this section, films deposited and characterized from these inks were studied.

5.7.1 Films Coated from Micro Ink

The XRD patterns of different heat-treated CZTS films are shown in Fig. 5.26. Diffractogram of the sample CZMP (Fig. 5.26a) shows broadlines at 2Θ values of 28.51°, 47.31° and 56.11°, which is identified to be due to reflections from (112), (220) and (312) planes of kesterite CZTS (Joint Committee on Powder Diffraction Standards, JCPDS 26-0575). No other XRD lines were found suggesting that pure CZTS has been synthesized. In case of CZMP350 sample (Fig. 5.26b), a hump at 32.97° along with all the diffraction peaks of sample CZMP is analysed. This peak is also found to be due to kesterite CZTS(200) (JCPDS 26-0575). However, two more peaks at 26.9° and 51.2° in addition to the standard kesterite CZTS lines were found in CZMP400 film. These additional peaks are probably because of the

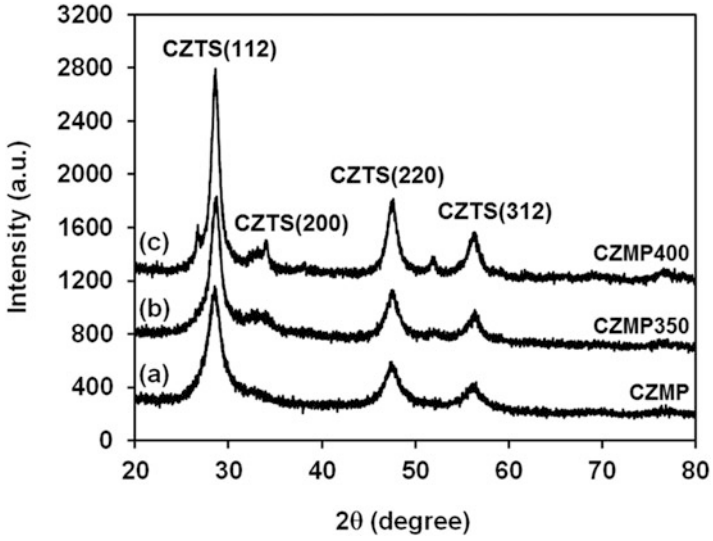

Fig. 5.26 X-ray diffraction of CZTS films prepared from microparticle ink: (**a**) CZMP, (**b**) CZMP350 and (**c**) CZMP400 [66]

Table 5.7 Average crystallite size of the CZTS films

Sample	Crystallite size (nm)
CZMP	5
CZMP350	7
CZMP400	10

presence of wurtzite CZTS (JCPDS 36-1450). Intensities of these peaks are very low with respect to the strongest peak of kesterite (112) at 28.51°.

In general, XRD lines of (112), (220) and (312) of CZMP400 films were more intense and sharper as compared to those of CZMP film (Fig. 5.26a). This result reveals that there is some enhancement in the crystallinity due to annealing effect. The average crystallite size of the CZTS film has been estimated according to full width at half maximum (FWHM) of diffraction peaks using Scherrer's formula,

$$\beta = \frac{k\lambda}{\mathrm{Lcos}\theta} \tag{5.7}$$

where β is the broadening of diffraction line measured at half maximum intensity (radians) and $\lambda = 1.5418$ Å is the wavelength of CuKα X-ray radiation. The average crystallite size of the films obtained by measuring the broadening of most intense diffraction peak (112) is presented in Table 5.7. It is seen from Table 5.7 that crystallinity is considerably increased by increasing annealing temperatures. The temperature used in the preparation greatly affected the composition and crystallinity of the resulting samples.

Raman spectra of different types of CZTS films (CZMP, CZMP350 and CZMP400) are shown in Fig. 5.27. All the films, in general, show a strong peak at 336 cm^{-1} and accomplished by minute peaks at 250, 266 and 287 cm^{-1}. These peaks are due to kesterite CZTS and are in good agreement with previously reported Raman data [49, 66, 67] for CZTS.

The main peak at 336 cm^{-1} is due to the A1 vibrational mode, arising from the vibration of sulphur atoms in CZTS lattice while rest of the atoms remains stationary [49]. However, a small peak was found at 298 cm^{-1} in sample CZMP, which may be due to tetragonal CTS [68]. This peak is disappeared when annealed at 632 K (CZMP350) and 673 K (CZMP400) in Ar as shown in Fig. 5.27b, c. Further, intensity of the main peak increased slightly with increasing annealing temperatures which further shows crystallinity of the films improves with increasing annealing temperatures. This is consistent with results obtained from XRD. Hence, it is confirmed that CZTS films deposited from microwave-processed ink yield pure kesterite CZTS phase.

Scanning electron microscopy (SEM) is used to scrutinize the surface morphologies and cross sections of the CZTS films in order to define how the annealing temperature affected the surface morphology of the films. Figure 5.28 depicts the SEM top-view and cross-sectional images of three different types of CZTS films.

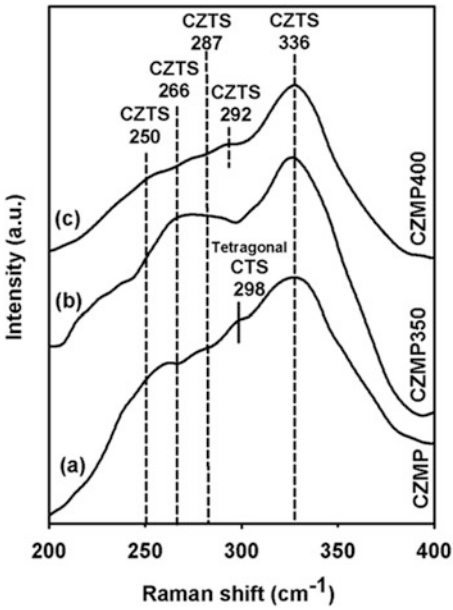

Fig. 5.27 Raman spectra of CZTS films: (**a**) CZMP, (**b**) CZMP350 and (**c**) CZMP400 [66]

In general, the films are spongy comprising interconnected spherical grains. The film thickness is irregular since the films were deposited by a doctor blade technique using bar applicator with the thickness of 20 μm. Further, the interface between the film and glass substrate is clearly distinct. From morphology of CZMP film (Fig. 5.28a), it is clearly seen that CZTS particles are agglomerated which can reduce the electrical transport properties of the films. The grains in CZMP film (Fig. 5.28b) are not fully formed and seem to be connected with ink which might be related with removing the TU and metal salts during heat treatments. Heat activates the loss of TU and metal salts which results in the formation of more holes in the precursor films. However, SEM images of the surface morphologies of the CZMP350 sample shows that the grains are well formed as smooth spheres. The CZTS films uniformly covered the substrates and the films are few microns thick, as shown in the cross-sectional SEM images (Fig. 5.28c). In case of sample CZMP400, the surface of the grains becomes rough and uneven. The spherical grains have diameters between 1.5 and 2 μm. The cross-sectional SEM of the films shows that the surface of the CZMP350 film is smoother than that of CZMP or CZMP400. CZMP400 films have developed some overgrowths. It is clear from above discussion that the grain size increases with increasing annealing temperatures. This is also consistent with the results of XRD and Raman spectroscopy discussed above. In general, structurally and morphologically CZMP350 films showed better results.

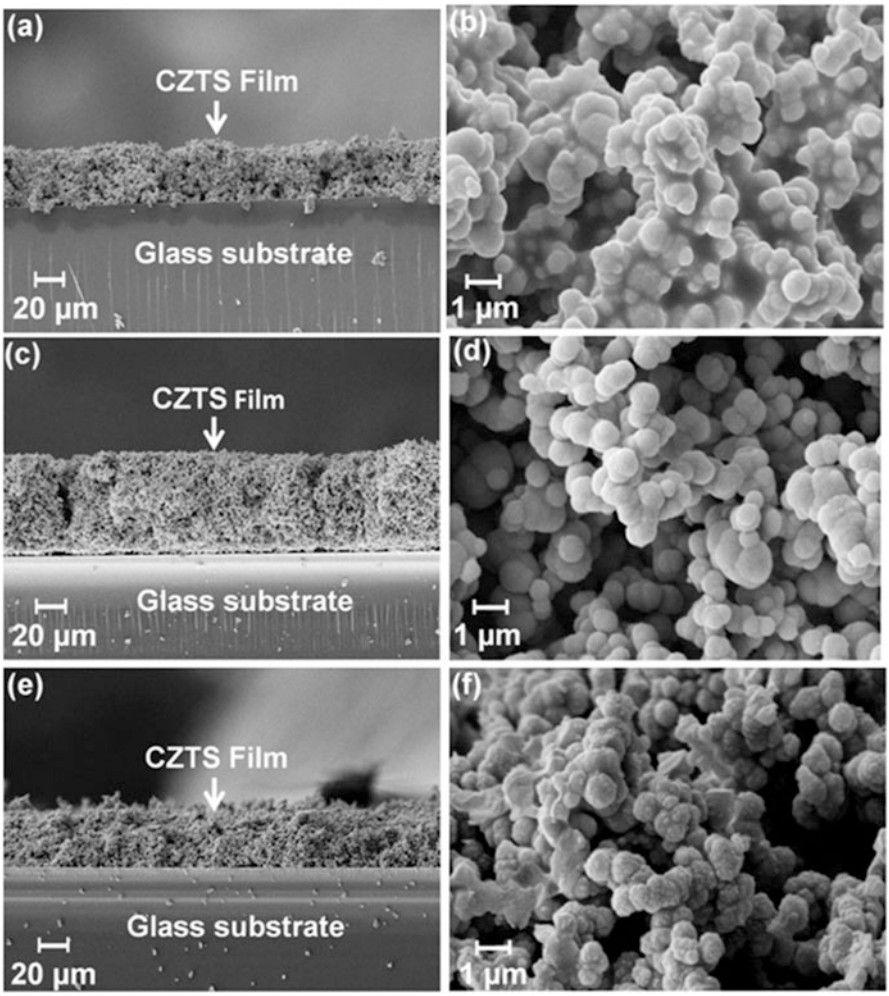

Fig. 5.28 SEM images of cross-sectional and top view of: (**a**, **b**) CZMP; (**c**, **d**) CZMP350; (**e**, **f**) CZMP400 films [66]

5.7.2 Films from Nano Ink

It was shown in the earlier section that the CZTS films coated from MPI yielded micro grains which in general were pores. The films coated by these inks were granular with average grain size of 1.5–2 μm. However, similar methods when employed with lower microwave power and lower concentrations, small grains with nanoparticles were achieved. The nanoparticle inks were used as it is for coating of films.

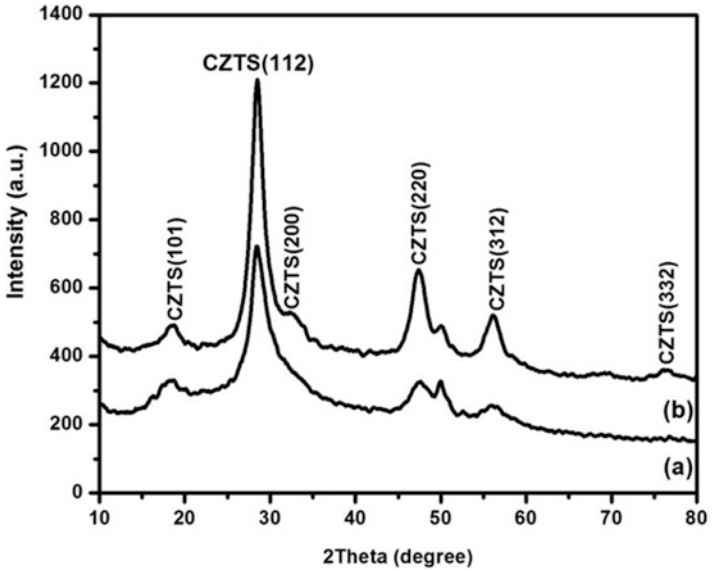

Fig. 5.29 X-ray diffractograms of doctor bladed CZTS films on glass: (**a**) CZNP and (**b**) CZNP350 [40]

Figure 5.29 shows the XRD of CZNP and CZNP350 films. XRD plot reveals that printed CZTS films are polycrystalline. Diffraction peaks of both the films show the kesterite CZTS [JCPDS: 26-0575] with the peaks examined at 2Θ values of 18.29°, 28.55°, 47.58° and 56.39° corresponding to the crystal planes of (101), (112), (220) and (312), respectively. However, upon annealing (Fig. 5.29b), two additional peaks at 2Θ = 32.98° and 76.42° have been observed. These peaks were also found to be due to kesterite CZTS(200) and CZTS(332) planes, respectively.

Table 5.8 compares the observed d-values of both the samples with standard JCPDS: 26-0575 data card. It can be seen from the table that all the XRD peaks of both the samples are matched exactly with JCPDS card revealing the formation of pure kesterite CZTS phase. The diffraction lines in annealed samples were sharper and stronger as compared to as-deposited which infers that annealing imparted improvement in crystallinity of the films. Further, a minute peak at 49.93° shrouded on CZTS (220) line (47.58°) was detected in as-deposited and annealed samples. To categorize this line, JCPDS files of probable compounds, such as Cu_3SnS_4 (033-0501), tetragonal CTS (089-4714), ZnS (097-2204), SnS (039-0354), SnS_2 (023-0677), CuS (06-0464) and Cu_2S (026-116), were examined.

However, it was found that none of them were exactly matched with this XRD line. The only (110) line of hexagonal SnS_2 (JCPDS 023-0677) coincided with the unidentified line at 49.93°. But, the other intense XRD lines of SnS_2, such as (001) at 15.029°, (100) at 28.2° or (101) at 32.125°, were absent in the CZTS diffractograms as depicted in Fig. 5.29. Therefore, it is unclear whether this

Table 5.8 Identification of observed XRD lines with standard CZTS (JCPDS)

Experimental					
CZNP		CZNP350		Standard JCPDS: 26-0575	
2Θ (degree)	*d* (nm)	2Θ (degree)	*d* (nm)	*d* (nm)	Indexing
18.29	0.48	18.29	0.48	0.48	CZTS(101)
28.55	0.31	28.55	0.31	0.31	CZTS(112)
–	–	32.98	0.27	0.27	CZTS(200)
47.58	0.19	47.58	0.19	0.19	CZTS(220)
56.39	0.16	56.39	0.16	0.16	CZTS(312)
–	–	76.42	0.12	0.12	CZTS(332)

particular XRD line is due to SnS_2 or not. The presence or absence of SnS_2 can be fixed by analysing Raman spectroscopy. Further, it has been found by earlier authors [22, 29] that microwave-processed CZTS nanoparticles also give rise to secondary phases. Hence, even though XRD studies of the present CZTS films did not reveal any unwanted phases, the conformational characterization technique would be Raman spectroscopy.

The Raman shift spectra along with deconvolution of peaks of two different types of CZTS films (CZNP and CZNP350) are shown in Fig. 5.30. Deconvolution of each spectrum was done using Gaussian and Lorentzian functions. The spectra, in general, show three peaks: a strong one at 332 cm^{-1} and weaker ones at ~250 and 287 cm^{-1}. These peaks are due to the kesterite CZTS and are in good agreement with formerly reported data for CZTS [49, 67]. The main peak at 332 cm^{-1} is due to the A1 vibrational mode, arising from the vibrations of sulphur atoms in CZTS lattice while rest of the atoms remains stationary [50]. Here it should be noted that peak position of the A1 mode of CZTS varies from 338 to 330 cm^{-1} according to the Raman excitation wavelength, synthesis process and film deposition parameters [49, 67]. The weaker peak at 252 cm^{-1} is due to the B(TO LO)/E(TO LO) modes that can be detected only by polarization Raman measurements using selection rules [69].

For CZNP sample (Fig. 5.30a), the peaks are broad and the weaker peaks of 252 and 287 cm^{-1} convolute the main strong peak of 332 cm^{-1} to create a significant shoulder. However, after annealing (Fig. 5.30b), the peaks become sharper due to improvement in crystallinity. The main peak of 332 cm^{-1} is significantly stronger than the other two peaks due to the enhancement of crystallinity. Raman peaks due to tetragonal CTS (297, 337 and 352 cm^{-1}), cubic CTS (295-303 and 355 cm^{-1}), orthorhombic CTS (318 cm^{-1}), cubic ZnS (267, 303 and 356 cm^{-1}), $Cu_{2-x}S$ (264 and 475 cm^{-1}) and SnS_2 (215 and 315 cm^{-1}) are absent revealing formation of kesterite CZTS. Hence, it is confirmed that CZTS films printed from microwave-processed nanoparticle ink yields pure kesterite CZTS phase.

The preceding section reveals that both the type of films was pure kesterite CZTS. Hence, optical properties of only as-deposited samples (CZNP) were measured. Transmittance spectra of number of as-deposited CZTS films were measured

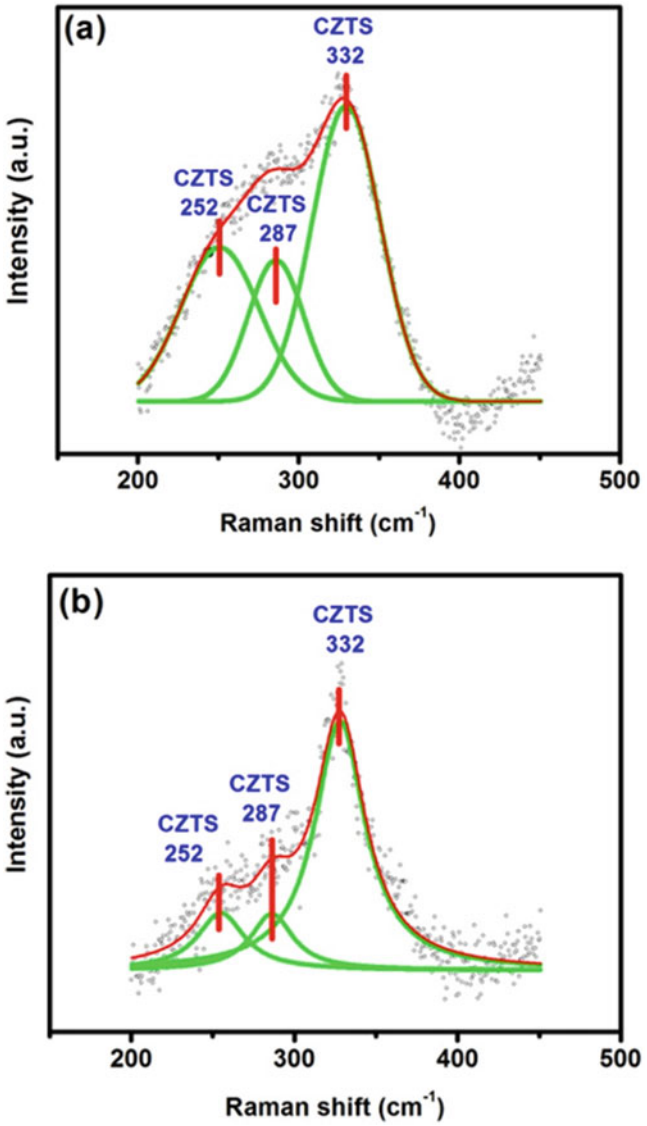

Fig. 5.30 Raman shift spectra of typical (**a**) CZNP and (**b**) CZNP350 films

in the wavelength range of 300–2400 nm as shown in Fig. 5.31. Almost all the samples show a similar trend. The spectra reveal that the films have strong absorption below about 850 nm due to absorption by the CZTS. The transmittance data is used to calculate the absorption coefficient (α) using following Eq. (5.8):

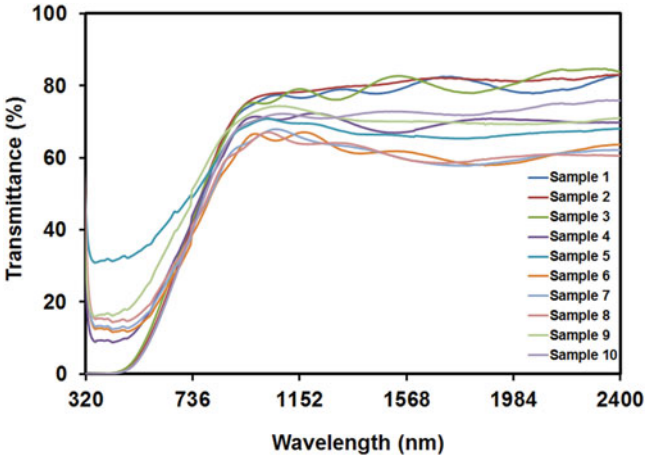

Fig. 5.31 Transmission spectra of as-deposited CZTS films

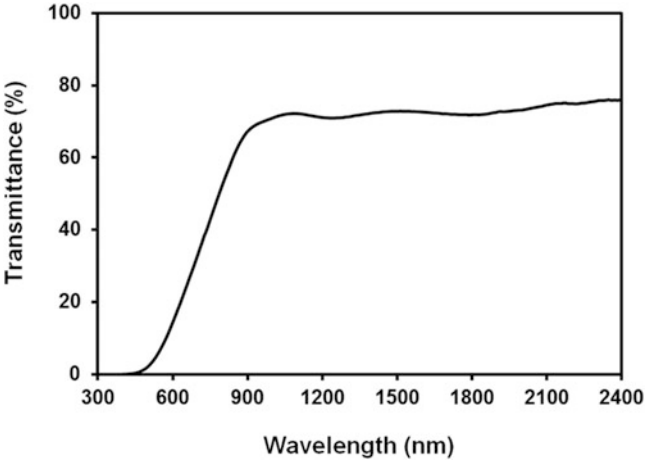

Fig. 5.32 Transmission spectrum of best CZTS films

$$\alpha = 1/d\,[\ln(1/T)] \tag{5.8}$$

where

d is the thickness and

T is the transmittance of the film.

The absorption coefficient of the CZTS films, in general, is determined to be $>10^4$ cm^{-1} at the onset of the absorption edge. Transmittance spectrum of best CZTS films is shown in Fig. 5.32. Further, the transmittance data is also used to determine the band gap of the CZTS film using Tauc relation [70] for direct band gap semiconductors:

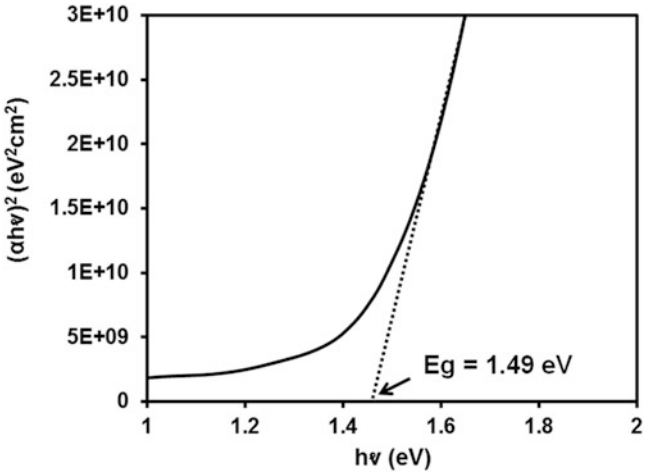

Fig. 5.33 Tauc plot of CZTS films showing band gap of 1.48 eV

$$\alpha h\nu = \mathrm{A}\left(h\nu - \mathrm{E_g}\right)^{1/2} \tag{5.9}$$

where
α is the absorption coefficient (cm^{-1}),
h is Plank's constant (J-s),
υ is the frequency of radiation (Hz),
A is an appropriate constant and
E_g is the band gap (eV).

Figure 5.33 plots the band gap estimation from the curves of $(\alpha h^2(\upsilon$ versus $h\upsilon$. Band gap values were given by extrapolating the straight line portion of the graph in the high absorption regime. The band gap of the films is found to be 1.49 eV which is in good agreement with earlier reported values of CZTS [2].

The microstructure of the CZTS films was studied by scanning electron microscopy. Figure 5.34 shows the typical cross-sectional view of both CZNP (Fig. 5.34a) and CZNP350 (Fig. 5.34b) films. The thickness of films is about 10 μm. In general, the films consist of closely packed interconnected grains. This is completely different from micro grains as observed in the case of the films deposited from microparticle ink. In a word, microstructural properties are hugely affected by grain size. Nanoparticle reduces the diffusion between two particles joined together by boundaries in case of polycrystalline semiconductors which leads to increases in the packing fraction. The CZNP films contain irregular shaped grains of sizes from 0.2 to 0.4 μm while CZNP350 films comprise spherical grains of sizes ranging from 0.6 to 0.8 μm.

Further, the CZNP films had some voids between the grains which reduce on annealing as the film become smoother and compact. However, the CZNP350 films are still not as well-densified as those useful for solar cells [6].

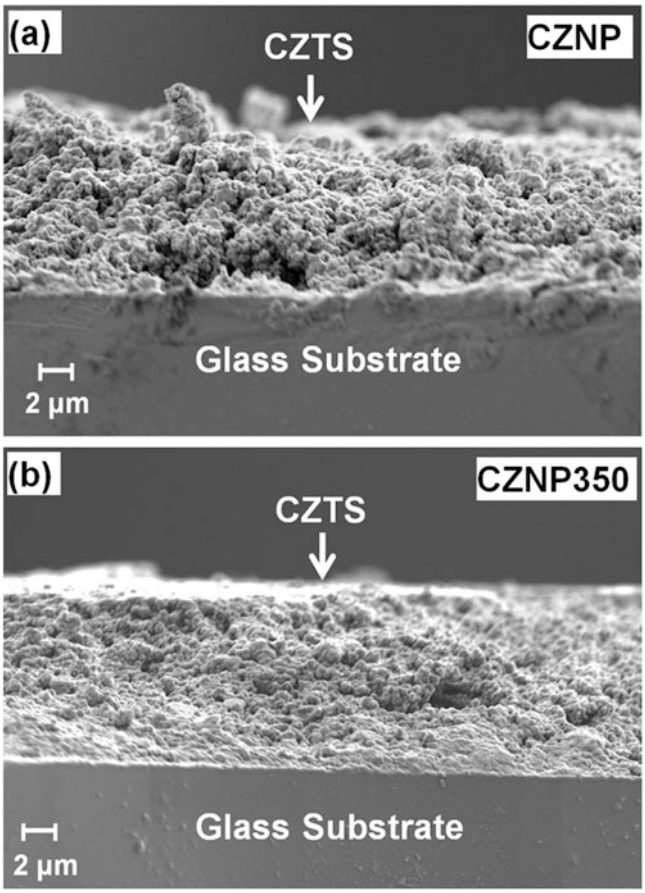

Fig. 5.34 Scanning electron micrograph of the cross section of CZTS films: (**a**) CZNP and (**b**) CZNP350 [40]

The chemical composition of both the types of CZTS films examined from the Energy Dispersive X-ray Spectrum (EDS) revealed that the films to be CZTS exhibits the existence of only copper, zinc, tin and sulphur. The composition of the CZNP and CZNP350 films is Cu:Zn:Sn:S = 2.06:1.13:0.93:3.83 and 2.12:1.10:1.06:3.69, respectively, which is close to the theoretical value of 2:1:1:4. Both the samples were zinc-rich and tin poor.

Some interesting results from structural, optical and morphological properties may be summed up as follows:

- XRD and Raman spectroscopy confirms the formation of only kesterite CZTS phase.
- Band gap of the CZTS films was 1.49 eV.

- The grains are relatively compact and small compared to those obtained from microparticle ink.
- Grain size increases with increasing annealing temperatures.
- The thickness of the films is ~10 μm which is 4 times lower than that obtained from microparticle inks.
- Hence, the effect of microwave power and time on structural and morphological properties of CZTS films is clearly observed.

5.8 Electrical Properties

Preceding section described CZTS films deposited from two different types of inks, such as microparticle ink (MPI) and nanoparticle ink (NPI). This section reports the electrical properties from 77 to 500 K in dark and under illumination. Temperature variation of dark and conductivity under illumination of films from NPI was measured at different temperatures. Thermoelectric power (TEP) was also ascertained at room temperature (~300 K) to determine the carrier concentration. The films deposited from MPI were not suitable for electrical investigation since there were considerable voids between the grains (Sect. 5.7, Fig. 5.28). However, the microparticle pellets were examined in lieu of the MPI films [71].

5.8.1 Electrical Properties in Dark (~300 K)

Electrical conductivity (σ) and thermoelectric power (TEP, α_{th}) of different types of CZTS films and micropowder pellets were measured in dark at room temperature (~300 K). The thermoelectric voltages generated by all the samples were positive indicating that they are *p*-type with holes as majority carriers.

Electrical conductivity (σ) of a sample is given by the relation;

$$\sigma = p\, e \mu_p \tag{5.10}$$

where
p is the hole concentration
e is the charge of electron
μ_p is the mobility of holes
TEP (α_{th}) of a sample is given by

$$\alpha_{th} = k/e\ [A + \ln (N_v/p)] \tag{5.11}$$

where
p is the concentration of holes (cm^{-3}),
N_v is the effective density of state in valance band ($6.91 \times 10^{17}\ cm^{-3}$ for CZTS),
A is a scattering constant (4 for impurity scattering),

Table 5.9 Electrical properties of different types of CZTS films in dark (~300 K)

Sample	TEP(μV/K)	σ (S/cm)	n (cm^{-3})	μ ($cm^2\ V^{-1}\ s^{-1}$)
Films from NPI				
CZNP	+350	3.5×10^{-4}	1.3×10^{18}	0.003
CZNP350	+130	4×10^{-2}	1.2×10^{19}	0.35
Films from MPI				
CZMP	+640	0.007	3.32×10^{16}	0.14
CZMP350	+326	0.086	1.18×10^{18}	0.001
CZMP400	+130	0.22	1.25×10^{19}	0.004

k is the Boltzmann constant (86.7 μV/K) and
e is the electronic charge.

For each sample, Eq. (5.11) was used to derive p from the measured value of TEP. Further, Eq. (5.10) was then utilized to calculate μ_p from measured value of σ and p. The electrical properties of different types of CZTS films and pellets are presented in Table 5.9.

Table 5.9 reveals that,

- Both types of films and pellets show p-type conduction with holes as majority carriers.
- The concentration of holes in as-deposited films is ~10^{18} cm^{-3}; however, it increases to ~10^{19} cm^{-3} upon annealing (in case of NPI).
- In general, electrical conductivity and mobility of samples increases with increasing annealing temperatures.
- Mobility of as-deposited film increases to 10 times upon annealing.
- The films show photoconductivity.

5.8.2 *Temperature Variation Electrical Conductivity of NPI Coated CZTS Films: 77–500 K*

Temperature variation of electrical conductivity (TVEC) of a semiconductor sample elucidates how charge carriers move in the sample. The conductivities of CZTS films (NPI) have been measured in dark and under illumination at different temperatures varying from 77 to 500 K. The TVEC (σ) of typical as-coated films was investigated in two parts: (1) Low temperatures region: 77–300 K and (2) High temperatures region: 300–500 K in dark and under different light intensities (100 and 190 mW/cm^2). Figure 5.35 shows the TVEC of CZTS films in dark (σ_D) and under illumination (σ_L) (intensity: 100 and 190 mW/cm^2) in the temperature range of 77–300 K. Figure 5.36 shows the TVEC of a typical CZTS film in the temperature range 300–500 K.

At lower temperature, the conductivity was found to be due to Mott-variable range hopping (M-VRH) which was not only confirmed by the starlight line of plot

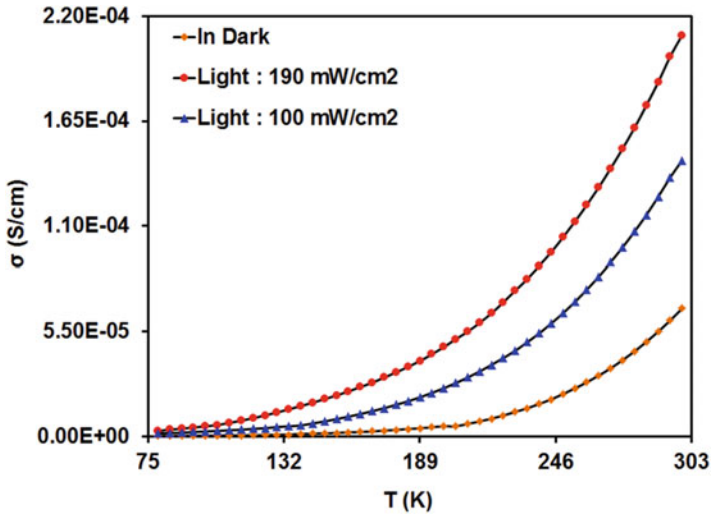

Fig. 5.35 Temperature variation of conductivity of typical CZNP film in dark and under light from 77 to 300 K

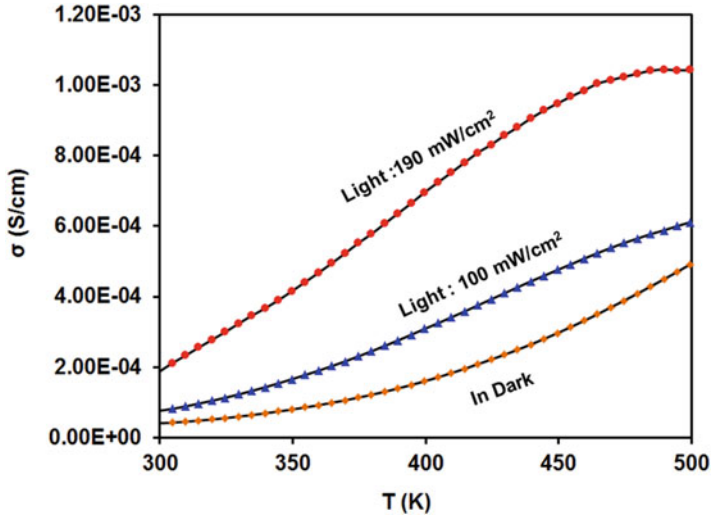

Fig. 5.36 Temperature variation of conductivity of typical CZNP film in dark and under light from 300 to 500 K

$ln\sigma T^{0.5}$ vs. $T^{-0.25}$ (Fig. 5.37) but also from the low hopping energy between 10 and 15 meV (Table 5.10) [39]. The basic mode of light remains unchanged even under different illumination intensities. However, hopping energy reduces linearly with increasing light intensities.

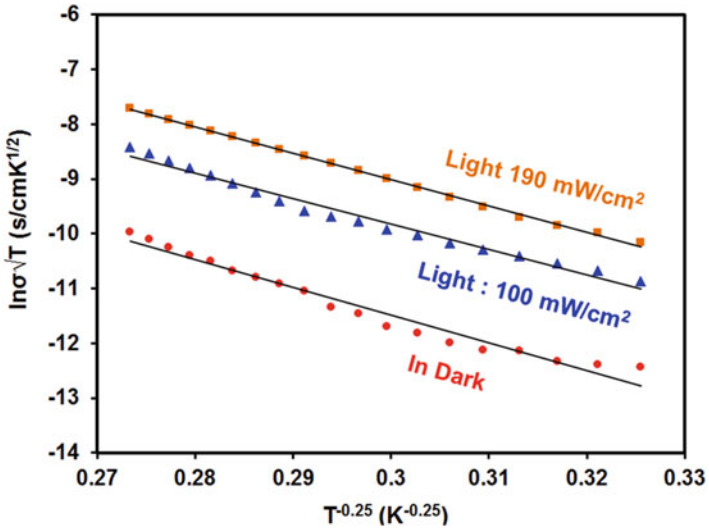

Fig. 5.37 Plot of $ln\sigma\sqrt{T}$ vs. $T^{-0.25}$ for CZNP films in dark and under light revealing M-VRH from 77 to 180 K

Table 5.10 Hopping parameters of CZNP films in dark and under illumination

Light conditions	σ_{oM} (S/cmK$^{1/2}$)	$T_M \times 10^5$ (K)	$N_o(E_F) \times 10^{25}$ (cm^{-3} eV^{-1})	$\bar{R}_{hop,\ Mott} \times 10^{-8}$ (cm)	$\bar{W}_{hop,\ Mott}$ (meV)
Dark	41.67	5	1.5	1	15
100 mW/cm^2	64	4.6	1.6	0.9	14
190 mW/cm^2	228	4.8	1.62	0.95	15

At intermediate temperatures (>50 to <300 K) Thermally Activated Conduction (TAC) is very possible, which can play crucial role in the conduction process of semiconductor thin films, as has been reported for polycrystalline CZTS films [72, 73]. For the TAC conduction mechanism, the temperature variation of dark conductivity can be written as:

$$\sigma = \sigma_0 \exp\left(-\frac{E_A}{k_b T}\right) \tag{5.12}$$

where
σ_o is a constant,
E_A is the activation energy in dark and
k_b is the Boltzmann constant

The linear plot of $ln\sigma$ Vs. T^{-1} in dark and under light confirms TAC in the range of 200–300 K (Fig. 5.38). The activation energy is high compared to M-VRH and it decreases under light. The activation energies are indication of defects [40].

The CZTS films are polycrystalline and shows interconnected grains. Hence, it is expected that Grain Boundary Barriers (GBBs) will be formed at the interfaces of

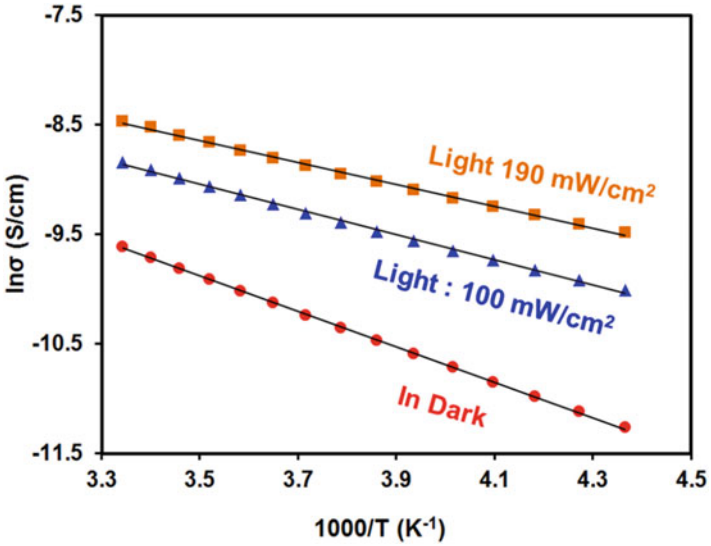

Fig. 5.38 Electrical conduction due to activated band conduction of CZNP films in dark and under illumination from 200 to 300 K

the GBs [71, 72, 73]. The mode of transport will be found due to thermionic emission (TE) over GBBs [73]. Following Seto, the expression for the dark conductivity (σ_D) of the CZTS films can be written as:

$$\sigma = \frac{\sigma_0}{T^{\frac{1}{2}}\exp\left(-\frac{E_B}{k_b T}\right)} \tag{5.13}$$

where
σ_0 is an appropriate constant
T is the temperature
E_B is grain boundary barrier height in dark

Hence, in the temperature region of 300–500 K, dominant mode of transport of holes is because of thermal emission over grain boundaries (Seto) and the activation energies denotes grain boundary barrier heights which is 180 meV in dark. The barrier height decreases due to illumination (Table 5.11). The straight line of $ln\sigma T^{1/2}$ vs. 1000/T as shown in Fig. 5.39 confirms the validation of Seto's model in CZTS films.

In general, the transport of holes in dark in these films is sum of M-VRH, TAC and TE over GB as:

$$\sigma_D = \sigma_{01MD}\exp\left(\left(-\frac{T_{MD}}{T}\right)^{\frac{1}{4}}\right) + \sigma_{02D}\exp\left(-\frac{E_{TACD}}{k_b T}\right) + \frac{\sigma_{03D}}{T^{\frac{1}{2}}\exp\left(-\frac{E_{BD}}{k_b T}\right)} \tag{5.14}$$

Table 5.11 Activation energy of CZNP films in dark and under light

	Activation energy (meV)		
Temperature range (K)	In dark	Light: 100 mW/cm^2	Light: 190 mW/cm^2
200–300: TAC	140	99	86
300–500: TE over GB	180	160	130

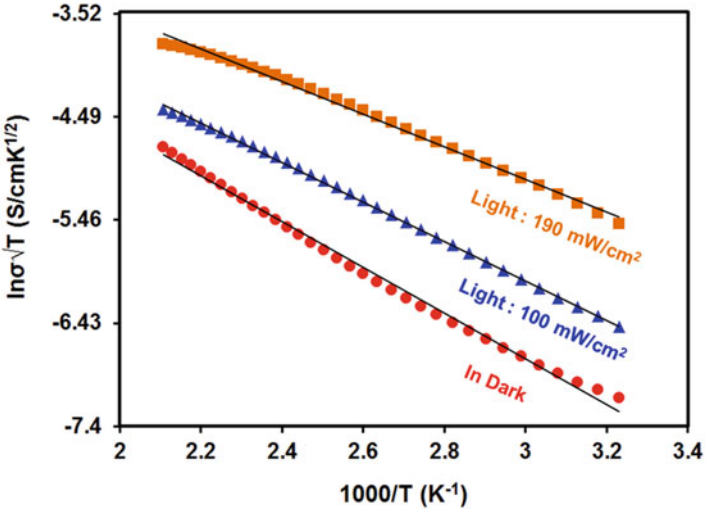

Fig. 5.39 Plot of $ln\sigma\sqrt{T}$ vs. 1000/T for CZNP films in dark and under different light intensities: 300–500 K

However, under illumination the above equation is modified as:

$$\sigma_{\mathrm{L}} = \sigma_{01\mathrm{ML}}\exp\left(\left(-\frac{T_{\mathrm{ML}}}{T}\right)^{\frac{1}{4}}\right) + \sigma_{02\mathrm{L}}\exp\left(-\frac{E_{\mathrm{TACL}}}{k_{\mathrm{b}}T}\right) + \frac{\sigma_{03\mathrm{L}}}{T^{\frac{1}{2}}\exp\left(-\frac{E_{\mathrm{BL}}}{k_{\mathrm{b}}T}\right)} \tag{5.15}$$

5.9 Solar Cells with CZTS Coatings

Apart from the physical properties of the absorber layer, understanding of solar cell structure is also required to further increase the device efficiency. One benefit of studying CZTS is that much of the knowledge regarding CIGS can be directly extended to kesterite CZTS simply by replacing CIGS absorber layer with *p*-type CZTS thin films.

5.9.1 Basic Structure

A typical structure (substrate) of solar cells based on kesterite CZTS absorber is depicted in Fig. 5.40. In general, the structure consists of 4–5 layer stacked on each other. Generally, CZTS solar cells are grown in a *'substrate'* configuration (Fig. 5.40).

Highest efficiencies of 12.7% and 8.9% have been reported for CZTSSe and CZTS solar cells, respectively, on glass by IBM. Glass is a most commonly used substrate; however, efforts have been made to develop flexible solar cells on polyimide and metal foils. It consists of a substrate that acts as a support for the electrode layer, which is a few hundred nm thick molybdenum (Mo) films, usually deposited on the glass by sputtering. Mo is generally used as a back contact. On top of back contact, the *p*-type CZTS absorber layer with thickness ranging from 1 to 2.0 μm is deposited. A variety of vacuum and non-vacuum techniques have been employed for the deposition of *p*-type absorber layer. At the interface, a thin 50–70 nm layer of CdS (*n*-type), typically referred to as buffer layer, has been deposited on absorber layer by conventional chemical bath deposition technique, thus formatting *p*-*n* junction, which allows charge separation. The finalization of the cell proceeds then with the sputtering of a bilayer of ZnO-based transparent conducting oxides (TCOs): intrinsic zinc oxide (i-ZnO) and aluminium doped ZnO (AZO) are the most common. The solar cell is then completed with a metal contact grid and an MgF_2 anti-reflection coating, used to enhance the charge collection and to reduce the reflected light loss, respectively.

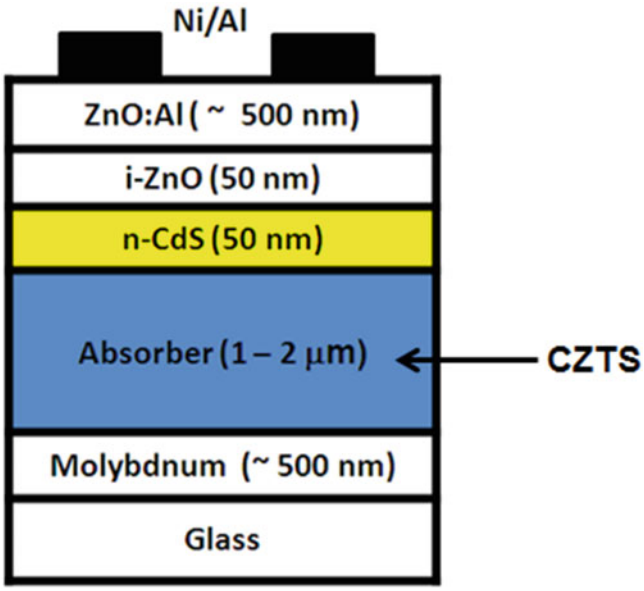

Fig. 5.40 Typical substrate structure of CZTS solar cell

5.9.2 Device Efficiency

CZTS/CZTSe/CZTSSe solar cells have been fabricated by vacuum and non-vacuum solution-based processes. The highest efficiency of 12.7% has been obtained for CZTSSe solar cells fabricated from ink-based deposition technique. Table 5.12 presents the properties of CZTS solar cells produced by different techniques.

Table 5.12 Photovoltaic properties of CZTS/Se/SSe solar cells

Group/authors	Absorber deposition method	V_{OC} (mV)	J_{SC} (mA/cm^2)	Fill factor (%)	Efficiency (%)
HZB (2015) Lin et al. [74]	Solution: Inkjet printing	428	31.3	65.9	8.8
IBM (2014) Kim et al. [7][a]	**Ink (Slurry): Spin coating**	**466**	**38.9**	**69.8**	**12.7**
CHARUSAT (2014) Tiwari et al. [72]	Solution based: Ion-exchange	521	19.13	62	6.17
Osaka Univ. (2014) Jiang et al. [75]	Electrodeposition: Cu/Zn/Sn stack	719	17.7	62.9	8
SUNY-Binghamton (2014) Dhakal et al. [76]	Vacuum: Co sputtering sulphurization	603	19	55	6.2
UNSW (2014) Su et al. [77]	Solution: Sol-gel	610	14.82	58	5.1
Dupont (2014) Wu et al. [78]	Solution: Spin coating	428	31.3	65.9	8.8
Washington Univ. (2014) Xin et al. [79]	Solution: Spin coating	443	31.2	60.2	8.32
IMRA Europe (2014) Larramona et al. [80]	Solution: water-ethanol spray coating	460	30.9	60	8.6
Purdue (2014) Miskin et al. [81]	Solution: Doctor blade	404	35.1	63.7	9
IMEC, Solliance (2013) [82]	Vacuum: sputtering/ selenization	410	38.9	61	9.7
ZSW (2013) Schnabel et al. [5]	Solution: Doctor blade	–	–	–	10.3
IBM (2012) Shin et al. [83][a]	**Vacuum: co-evaporation**	**661**	**19.5**	**65.8**	**8.9**
NREL (2012) Repins et al. [84]	Vacuum: co-evaporation	377	37.4	64.9	9.15
UCLA (2012) Yang et al. [85]	Solution: Spin coating	409	32.25	61	8.1

[a]Highest efficient solar cells based on selenides and pure sulphide CZTS absorber layer, respectively in Reference [7] and [83]

Table 5.12 reveals that:

- Efficient CZTS TFSCs can be fabricated by diverse deposition techniques, such as co-evaporation, sputtering, electrodeposition, ion-exchange and direct ink coating techniques.
- The highest efficiency of 12.7% has been achieved by IBM (USA) for CZTSSe TFSC direct deposited from ink/slurry of non-CZTS particles in toxic hydrazine.
- For vacuum-deposited TFSCs, the highest efficiency attained is 9.7% for CZTSe by IMEC/Solliance (Europe).
- In India, our group (Tiwari et al. [72]) has made 6.17% efficient CZTS TFSCs by a unique ion-exchange solution technique. This is a record for all solution-processed CZTS solar cells.
- CZTS films deposited by simple, non-vacuum, direct-write and solution-based techniques, like spin coating and doctor blading, have yielded the TFSCs with relatively higher efficiencies of 8–12.7%.

5.10 Concluding Remarks and Future Prospects

The microwave process is a simple and solution-based method for obtaining solar quality kesterite CZTS absorbers. High-quality CZTS nanoparticles have been achieved using such technique without using either capping or tedious sulpherization process. CZTS ink is found to be suitable for coating the films. Films with different structures, including micro and nano grains, have been coated from inks. CZTS films coated from nanoparticle ink seems to be promising and shows better electronics properties compared to those of microparticle ink. Since the ink is found to be suitable for solar cells, it is now desirable to fabricate CZTS/CZTSSe solar cells from such ink in substrate and superstrate structure. Optimization of each layer with respect to the structure, composition and processing must be done to compare the results with other conventional and well-studied semiconductor such as CIGS and CdTe.

Further, it has been observed in the literature that the extra addition of Na plays a significant role in improving the structural, morphological and electrical properties of the resulting absorber layers (CIGS, CIS and CZTS). Hence, CZTS solar cells should also be fabricated by incorporating appropriate Na either in precursor solution or in finalized films.

Acknowledgments The authors are grateful to the President and Provost of Charotar University of Science and Technology, Changa, Anand, Gujarat, India, for providing research facilities. Helpful discussion from Dr. Maykel Courel, National Autonomous University of Mexico (UNAM), Mexico, is highly appreciated.

References

1. H. Azimi, Y. Hou, C.J. Brabec, Energy Environ. Sci. **7**, 1829 (2014)
2. K. Ito, *Copper zinc tin sulfide-based thin-film solar cells* (Wiley, Chichester, 2015)
3. R.H. Bube, *Photovoltaic materials, series on properties of semiconductor materials*, vol 1 (Imperial College Press, London, 1998)
4. S. Ji, C. Ye, Rev. Adv. Sci. Eng. **1**, 42 (2012)
5. http://www.semiconductor-today.com/news_items/2013/NOV/ZSW_261113.shtml
6. W. Wang, M.T. Winkler, O. Gunawan, T. Gokmen, T.K. Todorov, Y. Zhu, D.B. Mitzi Adv, Energy Mater. **4**, 1301465 (2014)
7. J. Kim, H. Hiroi, T.K. Todorov, O. Gunawan, M. Kuwahara, T. Gokmen, D. Nair, M. Hopstaken, B. Shin, Y.S. Lee, W. Wang, H. Sugimoto, D.B. Mitzi Adv, Adv Mater **26**, 7427 (2014)
8. B. Flynn, W. Wang, C.-H. Chang, G.S. Herman, Phys. Status Solidi (a) **209**, 2186 (2012)
9. S. Riha, B. Parkinson, A. Prieto, J. Am. Chem. Soc. **131**, 12054 (2009)
10. Q. Guo, H. Hillhouse, R. Agrawal, J.Am. Chem. Soc. **131**, 11672 (2009)
11. Y. Liu, J. Xu, Z. Ni, G. Fang, W. Tao, J. Alloys Compd. **630**, 23 (2015)
12. M. Cao, Y. Shen, J. Cryst. Growth **318**, 1117 (2011)
13. R. AdhiWibowo, E. Soo Lee, B. Munir, K.H. Kim, Phys. Status Solidi (a) **204**, 3373 (2007)
14. N. Mirbagheri, S. Engberg, A. Crovetto, S.B. Simonsen, O. Hansen, Y.M. Lam, J. Schou, Nanotechnology **27**, 185603 (2016)
15. S. Engberg, Z. Li, J. Yan Lek, Y. Ming Lamb, J. Schoua, RSC Adv. **5**, 96593 (2015)
16. C. Steinhagen, M.G. Panthani, V. Akhavan, B. Goodfellow, B. Koo, B.A. Korgel, J. Am. Chem. Soc. **131**, 12554 (2009)
17. T. Kameyama, T. Osaki, K.-I. Okazaki, T. Sb, A. Kudo, S. de Kuwabata, T. Torimoto, J. Mater. Chem. **20**, 5319 (2010)
18. Y.-L. Zhou, W.-H. Zhou, Y.-F. Du, M. Li, S.-X. Wu, Mater. Lett. **65**, 1535 (2011)
19. O. Zaberca, F. Oftinger, J.Y. Chane-Ching, L. Datas, A. Lafond, P. Puech, A. Balocchi, D. Lagarde, X. Marie, Nanotechnology **23**, 18540 (2012)
20. X. Yang, J. Xu, L. Xi, Y. Yao, Q. Yang, C.Y. Chung, C. Lee, J. Nanopart. Res. **14**, 931 (2012)
21. R. Kumar, B. Ryu, S. Chandramohan, J. Seol, S. Lee, C. Hong Mater. Lett. **86**, 174 (2012)
22. S. Shin, J. Han, C. Park, A. Moholkar, J. Lee, J. Kim, J. Alloys, Compd. **516**, 96 (2012)
23. W. Wang, H. Shen, X. He, Mater. Res. Bull. **48**, 3140 (2013)
24. P. Sarswat, M. Free, J. Cryst. Growth **372**, 87 (2013)
25. G. Wang, P. Chen, C. Tseng, Cryst. Eng. Comm **15**, 9863 (2013)
26. T. Knustson, P. Hanson, E. Aydil, R. Penn, Chem. Commun. **50**, 5902 (2014)
27. Y. Zhao, W. Tao, J. Liu, A. Wei, Mater Lett **148**, 63 (2015)
28. W. Wang, H. Shen, H. Yao, J. Li, J. Jiao, J. Mater, Sci. Mater. Electron **26**, 1449 (2015)
29. Y.-H. Lin, S. Das, C.-Y. Yang, J.-C. Sung, C.-H. Lu, J. Alloys Compd. **632**, 354 (2015)
30. T. Martini, C. Chubilleau, O. Poncelet, A. Ricaud, A. Blayo, C. Martin, K. Tarasova, Sol. Energy Mater. Sol. Cells **144**, 657 (2016)
31. H.W. Hillhouse, M.C. Beard, Curr Opin, Colloid Interface Sci **14**, 245–249 (2009)
32. R. Kumar, B. Ryu, S. Chandramohan, J. Seol, S. Lee, C. Hong, Mater. Lett. **86**, 174 (2012)
33. S. Shin, J. Han, C. Park, A. Moholkar, J. Lee, J. Kim, J. Alloys Compd. **516**, 96 (2012)
34. C.O. Kappe Angew, Chem. Int. Ed **43**, 6250 (2004)
35. B.J. Hayes, *Microwave synthesis: chemistry at the speed of light* (CEM Publications, Matthews, NC, 2002)
36. T.K. Chaudhuri, D. Tiwari, Sol. Energy Mater. Sol. Cells **101**, 46 (2012)
37. Jardine, F. H. in Emeleus, H. J. and Sharpe, A. G. (Ed.), Advances in Inorganic chemistry and Radiochemistry, 17 (1975) 133, Academic Press, USA
38. P.R. Ghediya, T.K. Chaudhuri, D. Vankhade, J. Alloys Compd. **685**, 498 (2015)
39. P.R. Ghediya, T.K. Chaudhuri, J.R. Ray, AIP Conf. Proc. **1728**, 020020 (2016)
40. P.R. Ghediya, T.K. Chaudhuri, J. Phys. D. Appl. Phys. **48**, 455109 (2015)

41. R. Wagner, H.D. Wiemhöfer, J. Phys. Chem. Solids **44**, 801 (1983)
42. C. Malerba, Cu_2ZnSnS_4 thin films and solar cells: material and device characterization, an investigation into the stoichiometry effect on CZTS microstructure and optoelectronic properties, Ph.D. Thesis, University of Trento, Italy, 2014
43. T. Tanaka, T. Nagatomo, D. Kawasaki, M. Nishio, Q. Guo, A. Wakahara, A. Yoshida, H. Ogawa, J. Phys. Chem. Solids **66**, 1978 (2005)
44. K. Wang, B. Shin, K.B. Reuter, T. Todorov, D.B. Mitzi, S. Guha, Appl. Phys. Lett. **98**, 051912 (2011)
45. D.B. Mitzi, O. Gunawan, T.K. Todorov, K. Wang, S. Guha, Sol. Energy Mater. Sol. Cells **95**, 1421 (2011)
46. A. Walsh, S. Chen, S.-H. Wei, X.-G. Gong, Adv. Energy Mater. **2**, 400 (2012)
47. P.A. Fernandes, P.M.P. Salome, A.F. da Cunha, Thin Solid Films **517**, 2519 (2009)
48. X. Fontane, L. Calvo-Barrio, V. Izquierdo-Roca, E. Saucedo, A. Perez-Rodriguez, J.R. Morante, D.M. Berg, P.J. Dale, S. Siebentritt, Appl. Phys. Lett **98**, 181905 (2011)
49. A.-J. Cheng, M. Manno, A. Khare, C. Leighton, S.A. Campbell, E.S. Aydil, J. Vac. Sci. Technol. A **29**, 051203 (2011)
50. M. Himmrich, H. Haeuseler, Spectrochim. Acta A Mol. Biomol. Spectrosc. **47**, 933 (1991)
51. M. Guc, S. Levcenko, V. Izquierdo-Roca, X. Fontane, L.V. Volkova, E. Arushanov, A. Pérez-Rodríguez, Sci. Rep **6**, 19414 (2016)
52. M.I. Khalil, O. Atici, A. Lucotti, S. Binetti, A. Le Donne, L. Magagnin, Appl. Surf. Sci. **379**, 91 (2016)
53. Y. Xi, Z. Chen, Z. Zhang, X. Fang, G. Liang Nanoscale, Res. Lett. **9**, 208 (2014)
54. B. Flynn, I. Braly, P.A. Glover, R.P. Oleksak, C. Durgan, G.S. Herman, Mater. Lett. **107**, 214 (2013)
55. G. Altamur, J. Vidal, Chem. Mater. **28**, 3540 (2016)
56. S.Y. Chen, A. Walsh, X.G. Gong, S.H. Wei, Adv. Mater. **25**, 1522 (2013)
57. S. Chen, J.H. Yang, X.G. Gong, A. Walsh, S.H. Wei, Phys. Rev. **B81**, 245204 (2010)
58. A. Nagoya, R. Asahi, R. Wahl, G. Kresse, Phys. Rev. B **81**, 113202 (2010)
59. S. Das, S.K. Chaudhuri, R.N. Bhattacharya, K.C. Mandal, Appl. Phys. Lett. **104**, 192106 (2014)
60. S. Chen, L. Wang, A. Walsh, X.G. Gong, S.H. Wei, Appl. Phys. Lett. **101**, 223901 (2012)
61. M. Kumar, A. Dubey, N. Adhikari, S. Venkatesan, Q. Qiao, Energy Environ. Sci. **8**, 3134 (2015)
62. Y. Gang Zou, J. Liu, X. Zhang, Y. Jiang, J.S. Hu, L.-J. Wan, Sci. China Chem. **57**, 1552 (2014)
63. A.E. Morales, E.S. Mora, U. Pal, Rev. Mex. Fis. **53**, 18 (2007)
64. S. Abermann, Sol. Energy **94**, 37 (2013)
65. S. Tombolato, CZTS(e) thin films grown by chemical methods for PV application, Ph.D. Thesis, University of Milano-Bicocca, Bicocca, Italy, 2015
66. P.R. Ghediya, T.K. Chaudhury, J. Mater. Sci. Mater. Electron. **26**, 1908 (2015)
67. P. Kush, S.K. Ujjain, N.C. Mehra, P. Jha, R.K. Sharma, S. Deka, ChemPhysChem **14**, 2793 (2013)
68. P.A. Fernandes, P.M.P. Salome, A.F. Cunha, J. Alloys Compd. **509**, 7600 (2011)
69. D. Dumcenco, Y.-S. Huang, Opt. Mater. **35**, 419 (2013)
70. J. Tauc, R. Grigorovici, A. Vancu, Phys. Status Solidi (b) **15**, 627 (1966)
71. P.R. Ghediya, T.K. Chaudhuri, AIP Conf. Proc. **1665**, 120032 (2015)
72. D. Tiwari, T.K. Chaudhuri, A. Ray, K.D. Tiwari, Thin Solid Films **551**, 42 (2014)
73. V. Kosyak, N.B. Mortazavi Amiri, A.V. Postnikov, M.A. Scarpulla, J. Appl. Phys. **114**, 124501 (2013)
74. X. Lin, J. Kavalakkatt, M.C. Lux-Steiner, A. Ennaoui, Adv. Sci. **2**, 1500028 (2015)
75. F. Jiang, S. Ikeda, T. Harada, M. Matsumura, Adv. Energy Mater. **4**, 1301381 (2014)
76. T.P. Dhakal, C.-Y. Peng, R. Reid Tobias, R. Dasharathy, C.R. Westgate, Sol. Energy **100**, 23 (2014)

77. Z. Su, K. Sun, Z. Han, H. Cui, F. Liu, Y. Lai, J. Li, X. Hao, Y. Liu, M.A. Green, J. Mater. Chem. A **2**, 500 (2014)
78. W. Wu, Y. Cao, J.V. Caspar, Q. Guo, L.K. Johnson, I. Malajovich, H. David Rosenfeld, K.R. Choudhury, J. Mater. Chem. C **2**, 3777 (2014)
79. H. Xin, J.K. Katahara, I.L. Braly, H.W. Hillhouse, Adv. Energy Mater. **4**, 1301823 (2014)
80. G. Larramona, S. Bourdais, A. Jacob, C. Choné, T. Muto, Y. Cuccaro, B. Delatouche, C. Moisan, D. Péré, G. Dennler, J. Phys. Chem. Lett. **5**, 3763 (2014)
81. C.K. Miskin, W.-C. Yang, C.J. Hages, N.J. Carter, C.S. Joglekar, E.A. Stach, R. Agrawal, Prog. Photovolt. Res. Appl. **23**, 654 (2015)
82. G. Brammertz, M. Buffière, S. Oueslati, H. ElAnzeery, K. Ben Messaoud, S. Sahayaraj, C. Köble, M. Meuris, J. Poortmans, Appl. Phys. Lett. **103**, 163904 (2013)
83. B. Shin, Y. Zhu, N. Bojarczuk, S.J. Chey, S. Guha, Appl. Phys. Lett. **101**, 053903 (2012)
84. I. Repins, C. Beall, N. Vora, C. DeHart, D. Kuciauskas, P. Dippo, B. To, J. Mann, W.C. Hsu, A. Goodrich, R. Noufi, Sol. Energy Mater. Sol. Cells **101**, 154 (2012)
85. W. Yang, H.-S. Duan, B. Bob, H. Zhou, B. Lei, C.-H. Chung, S.-H. Li, W.W. Hou, Y. Yang, Adv. Mater. **24**, 6323 (2012)

Chapter 6
Solid Oxide Fuel Cell Materials

Tae Ho Shin, Jong-Jin Choi, and Hyung-Tae Lim

6.1 Introduction

Solid oxide fuel cells (SOFCs) are promising power generation systems that electrochemically convert chemical energy into electrical energy with little or no emission of pollutants [1–3]. Moreover, a high-temperature fuel cell has many advantages such as a high efficiency and fuel flexibility in comparison with a low-temperature fuel cell. For these reasons, a considerable amount of attention has been paid to SOFCs in recent years for application to medium- to large-scale power generation and combined heat and power (CHP).

An SOFC stack comprises two components, namely (a) porous electrodes in a dense electrolyte and (b) separators that connect the cells electrically and mechanically and prevent any direct contact between the fuel and air. Each cell component requires different electrical properties and microstructures. Thus, it is important to optimize the choice of cell material and process technique. Figure 6.1 illustrates a typical anode-supported SOFC electrode and electrolyte microstructure. As shown in Fig. 6.1, the electrolyte should have a dense structure to prevent gas crossover. Moreover, the electrolyte must possess a high oxygen ion conductivity and very high electronic resistivity. The anode and cathode should be porous in order to

T.H. Shin
Energy Materials Center, Korea Institute of Ceramic Engineering and Technology, Jinju, South Korea

J.-J. Choi
Functional Ceramics Department, Korea Institute of Materials Science, Changwon, South Korea

H.-T. Lim (✉)
School of Materials Science and Engineering, Changwon National University, Changwon, South Korea
e-mail: htaelim@changwon.ac.kr

J. Zhang, Y.-G. Jung (eds.), *Advanced Ceramic and Metallic Coating and Thin Film Materials for Energy and Environmental Applications*,
DOI 10.1007/978-3-319-59906-9_6

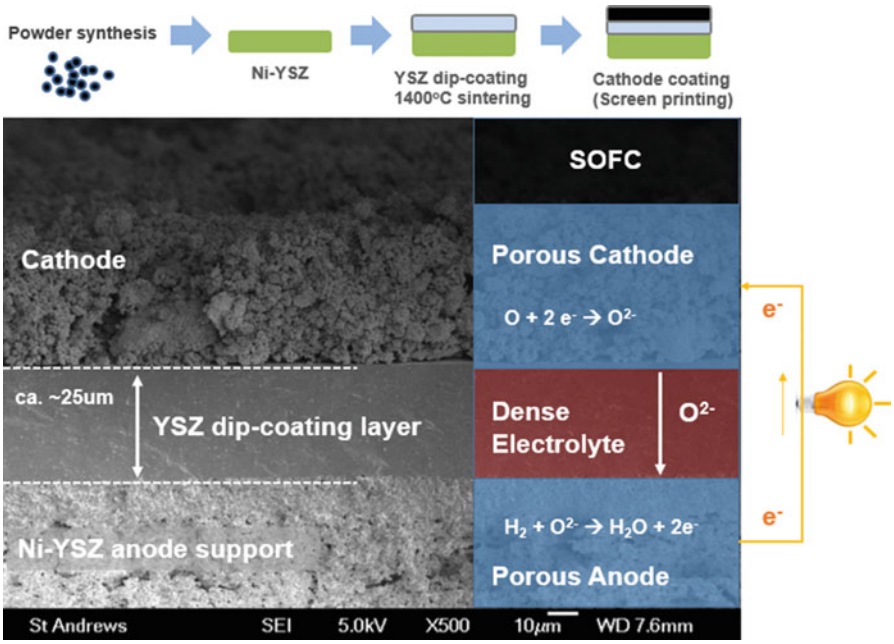

Fig. 6.1 Microstructure of a sandwich geometric solid oxide fuel cell (SOFC) by the dip-coating process

allow the fuel gas and oxygen to diffuse into them and have high electronic conductivities. In addition to these structural and electrical properties, the thermal expansion coefficients of the component materials must be identical to those of the other components in the cell in order to ensure stability against thermal cycling. Furthermore, there should be no chemical reaction or diffusion among the SOFC stack components to ensure long-term stability. Yttria-stabilized zirconia (YSZ), La(Sr)MnO_3 (LSM), and Ni–YSZ cermet are widely employed as the electrolyte, cathode, and anode, respectively, for SOFCs. These conventional SOFC materials are stable under SOFC operating conditions and can be fabricated in many forms using present ceramic manufacturing processes and thin-film technologies [4–7].

There are various types of SOFCs with respect to cell designs: electrolyte support (ES), anode support (AS), cathode support (CS), metal support (MS), etc. Each design has its own advantages and disadvantages with respect to the cell performance, durability, and production cost [2, 8–10]. Among them, the AS is the most popular for commercial and research purposes because the cell resistance can be significantly reduced with a thin electrolyte. However, anode (fuel) gas transport in and water vapor transport out are limited through the thick AS, increasing the resistance related to the gas diffusion and conversion in the cell. With this design, the AS, anode functional layer, and electrolyte layer are successively deposited (coated); then, these layers are cofired to a high temperature at which the electrolyte layer can be densified. The ES is also widely used in industry and laboratories

because of its fabrication simplicity. With this design, the electrolyte layer is first sintered at the highest temperature for the fabrication process of the entire cell; then, the electrodes are coated at a relatively lower temperature. Consequently, undesired chemical reactions between the electrolyte and the electrode can be avoided. However, the cell resistance is high with the thick electrolyte layer because the electrolyte has the largest contribution to the cell resistance. The CS design has some advantages with respect to the system size; however, this design has received less attention because of its high manufacturing cost. The MS is a new concept that provides many advantages for improving the mechanical properties and reducing the manufacturing cost in the near future.

Various cell fabrication techniques are involved in the fabrication of SOFCs [1, 2, 11–17]. Conventional ceramic processing such as slurry drop coating, dip coating, tape casting, and screen printing is commonly used for most of the commercial cells in the market because of its cost-effectiveness. Among them, tape casting is commonly used for planar SOFCs, and this method is most appropriate for large-area cells and mass production. Slurries are prepared for each layer (electrolyte and electrodes); then, layers with slits can be created using a doctor blade. The dried layers (green sheet) are now laminated by sequentially casting one layer on top of another. Slurry coating and dip coating are easy and low-cost methods but not suitable for mass production because they are time consuming. Screen printing can also be feasibly scaled-up, but in some cases, densification of the electrolyte cannot be easily achieved. These wet ceramic processing approaches usually are carried out at elevated temperatures, which may cause problems such as undesirable interfacial reactions, warping of the large plate anodes, and grain growth of the Ni anode [3, 18, 19]. Other advanced deposition techniques such as aerosol deposition (AD), sputtering, pulsed-laser deposition (PLD), electron-beam physical vapor deposition (EB-PVD), and electrophoretic deposition (EPD) have been extensively studied to enhance the electrochemical properties at low temperatures and to prevent undesired chemical reactions between cell components. Automation, nanostructures, and miniaturized SOFCs are feasible with the PLD method. However, these deposition techniques have a high cost and also limit the cell area [20–25].

In this chapter, conventional and novel SOFC materials (anode, cathode, and electrolyte) for SOFCs are introduced, and a low-temperature ceramic coating process (such as AD) is applied to fabricate the SOFC electrode and electrolyte layers. In addition, the effects of the electrolyte configuration (single layer or multiple layers) on the durability and performance of the cell will be discussed.

6.2 Electrode

The durability and reliability of an SOFC are important issues in addition to others for commercialization in the energy market. The most critical issue for current SOFC technology is the low reliability in the presence of reoxidation and carbon

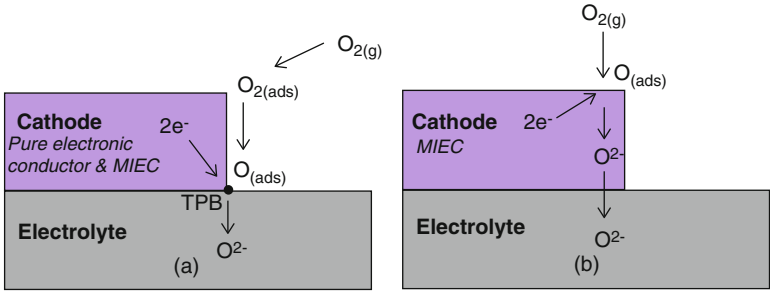

Fig. 6.2. Oxygen pathways on the cathode surface for an MIEC [26]

coke deposition. In addition, the operating temperature of an SOFC is high (1073–1273 K); therefore, all of the materials used in SOFC construction should be durable at high temperatures, dimensionally stable, and resistant to sintering. Owing to the high operating temperature of SOFCs, some noble metals and a mixed ionic–electronic conductor (MIEC) can be restrictively allowed as electrode materials. A high electrochemical activity on the cathode surface is required for efficient oxygen transport performance, the oxygen reduction reaction (ORR), surface exchange, and diffusion. To understand cathode materials and their manufacture, the oxygen pathway should be predicted by the ion-conducting portion of the cathode materials [26]. Pure electronic conducting materials only enable reaction on the surface path or the so-called triple phase boundary (TPB), where oxygen, the cathode, and the electrolyte meet. As shown in Fig. 6.2, the ORR occurs at the TPB and within the cathode itself, where ions are transferred through the bulk surface of the cathodes because of the ionic conductivity in MIEC [26]. Therefore, the cathode materials strongly depend on the oxygen self-diffusion coefficient (D^*) and surface exchange rate (k^*) [27]. Although many types of simple perovskite structures, LSM, La(Sr)Co(Fe)O_3, Ba(Sr)Co(Fe)O_3, and Sr(Sm)CoO_3, have been studied as a new cathode for decades [28–34], significant effort has recently focused on the understanding of the atomic-scale processes governing the cathode performance with 3D stacking materials such as those of the Ruddlesden–Popper (RP) series or double-layered perovskites for enhancing the oxygen mobility at the lattice scale [35–43]. The electrochemical properties of conventional and 3D cathode materials are listed in Table 6.1. Many studies are still needed to verify the potential of these advanced materials.

Electrons are released at the anode, which is obviously crucial for high-performance fuel cells. The main function of the anode is to provide reaction sites for electrochemical oxidation of the fuel. Thus, the anode materials should be stable in a reducing atmosphere and have a sufficient electronic conductivity and catalytic activity for the fuel gas reaction. It is necessary to have a high catalytic activity to provide electrochemical sites and a high electrical conductivity. Therefore, an increase in the electrochemical reaction is important to improve the power generation properties. It has been asserted that a system that connects the reactant transport, the product, the ion transport, and the electrochemical conversion of the

Table 6.1 Summary of the electrochemical properties for different SOFC cathodes [27, 44]

	D^*/cm^2 s^{-1} $T = 500$ °C	E_A^D/eV	k^*/cm s^{-1} $T = 500$ °C	E_A^K/eV	σ/S cm^{-1} $T = 500$–750 °C
$La_{0.8}Sr_{0.2}MnO_{3-\delta}$	4.5×10^{-20}	2.80	3.1×10^{-11}	1.30	120–130
$La_{0.8}Sr_{0.2}CoO_{3-\delta}$	9.0×10^{-14}	2.22	2.8×10^{-9}	1.32	1500–1600
$La_{0.5}Sr_{0.5}CoO_{3-\delta}$	1.5×10^{-10}	1.41	3.9×10^{-7}	0.81	1300–1800
$La_{0.6}Sr_{0.4}Co_{0.2}$ $Fe_{0.8}O_{3-\delta}$/ $Ce_{0.8}Gd_{0.2}O_{2-\delta}$	1.2×10^{-10}	1.39	3.3×10^{-9}	1.60	250–300
$Ba_{0.5}Sr_{0.5}Co_{0.8}Fe_{0.2}O_{3-\delta}$	1.2×10^{-7}	0.50	1.1×10^{-6}	1.76	10–55
$La_2NiO_{4+\delta}$[a]	3.3×10^{-9}	0.56	7.0×10^{-9}	0.60	55–65
$La_2CoO_{4+\delta}$[a]	2.5×10^{-8}	0.12	3.2×10^{-6}	0.03	1–5
$GdBaCo_2O_{5+\delta}$[a]	2.8×10^{-10}	0.60	7.5×10^{-8}	0.81	550–925
$PrBaCo_2O_{5+\delta}$[a]	3.6×10^{-7}	0.48	6.9×10^{-5}	0.67	400–700
$Ba_{0.5}Sr_{0.5}Co_{0.8}Fe_{0.2}O_{3-\delta}$	1.2×10^{-7}	0.50	1.1×10^{-6}	1.76	10–55

[a]Layered mixed ionic–electronic conductors

ionic current at the TPB should be considered for a description of the anode reaction [45]. There are more complicated phenomena such as the multistage characteristics of the reactions and the adsorption–desorption steps of gas molecules, which are shown in Fig. 6.3 [45–51]. The exact nature of the reaction kinetics is still not established. Holtappels et al. considered the hydrogen oxidation reaction as a multistep electrochemical reaction mechanism, which involves atomically adsorbed hydrogen in the charge transfer reaction [52, 53]. Mogensen et al. suggested that the dissociative adsorption or surface diffusion of Ni is not limiting in Ni–YSZ cermet commercial anodes. Their study was based on the fundamental results from surface science that show that the Ni surface is covered with a large degree of H_{ad} (Adsorbed hydrogen molecular in Fig. 6.3) and that H_{ad} have a high mobility under SOFC operating conditions. Further, Mogensen et al.'s logic is that a rate-limiting process may take place in the TPB or adjacent YSZ surface [46, 48, 50, 51]. Considering the above kinetic model and other researchers' results, an analogical interpretation is possible when studying the anodic performance to search for new suitable electrodes for SOFCs. It is certain that one of the above steps can be rate-determining for the anodic reaction. In particular, the key requirements for the anode are listed below [54–62].

- Catalytic activity: the anode must have a high catalytic activity for oxidation of the fuel gas.
- Stability: the anode must be chemically, morphologically, and dimensionally stable at the operating temperature in the fuel gas environment; it must also be tolerant towards contaminants.
- Conductivity: a maximum electrical conductivity under a large variety of operating conditions is desired to minimize ohmic losses.
- Compatibility: the anode must be chemically, thermally, and mechanically compatible with the other fuel cell components during fabrication and operation.

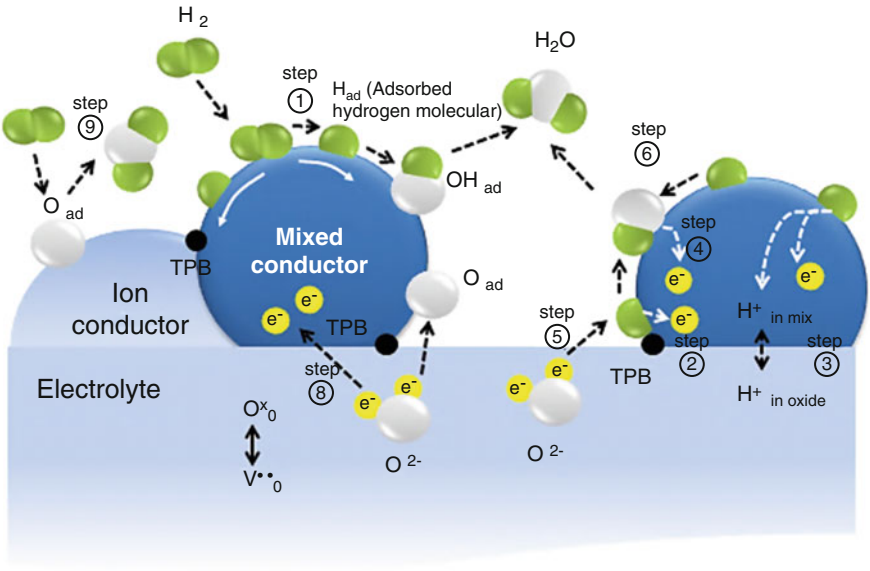

Fig. 6.3 Possible electrochemical reactions of gaseous hydrogen and water at the TPB in the anode

- Porosity: the porosity of the anode must be tailored with regard to mass transport considerations and the mechanical strength.

A mixture of a metal such as Ni and ion-conducting oxide materials such as cermet is widely used. Despite the fact that Ni is an excellent catalyst for the dissociation of hydrogen and an excellent electronic conductor, it has a significant thermal expansion mismatch to stabilized zirconia, and at high temperatures, the metal aggregates by grain growth, resulting in a reduced porosity for the anode and blocking of the TPBs required for cell operation [63–67]. Furthermore, the conventional Ni-based anode is known to react with the LSGM ($La(Sr)Ga(Mg)O_3$) electrolyte, causing NiO diffusion through the LSGM [67], and to exhibit poor reoxidation stability during cycling of the fuel cell [64, 68].

Currently, metal Ni-based cermets containing an oxide ion conductor such as YSZ or GDC are widely used for the anode; however, to improve the reliability, there are several issues to overcome, i.e., a high tolerance against the coke deposition and reoxidation and a high mechanical strength. Namely, the Ni-based anode also exhibits some disadvantages such as a low tolerance to sulfur and carbon deposition when it is directly exposed to hydrocarbons [67–69]. To overcome some of the disadvantages of Ni-based anode materials, some research groups have reported alternative anode materials. Gorte et al. reported that ceria-based ceramic anodes with small amounts of metal additives such as Cu or Pd perform reliably with hydrocarbon fuels, and Cu–ceria seems better suited for hydrocarbon fuels

with a good carbon coke tolerance [70, 71]. Cu particles, however, have a relatively low melting point and are thus not compatible with many standards in high-temperature SOFC processing [72–74]. They also have a poor catalytic activity for direct hydrocarbon oxidation. Consequently, the redox stability and reversibility have recently been emphasized as important requirements for the anode material in SOFCs. For advanced materials in durable SOFC/SOEC systems, various MIEC oxides have been evaluated. Thus far, several conductive perovskite oxides have been considered as potential oxide anode materials in SOFCs, which may also be useful as cathode materials in SOECs. In particular, researchers have mainly demonstrated that La(Sr)MO_3 (M = Cr, Mn, Fe, Ti) perovskite oxides can, in principle, be good fuel electrode materials with a sufficient electronic conductivity [75–77]. Furthermore, several groups have reported that $SrTiO_3$-based oxides can be used reliably as SOFC anodes [64, 71, 78–82]. Tao et al. reported that reasonably high power densities could be achieved with $La_{0.75}Sr_{0.25}Cr_{0.5}Mn_{0.5}O_3$ perovskite oxide [64, 66, 82]. Moreover, they showed fairly good stability under redox cycling because of the nature of the oxide. However, further improvement in the anodic performance in still necessary for adaptable oxide anodes for SOFCs. Mn- and Fe-based perovskites and doped ceria could be used as catalysts in redox reactions such as the electrochemical oxidation of a hydrocarbon such as propane, although the catalytic properties are strongly dependent on the composition of the perovskite [83, 84]. Shin et al. found that a relatively high power density and an excellent redox tolerance can be achieved using an oxide composite anode composed of Ce(Mn, Fe)O_2–La(Sr)Fe(Mn)O_3 [85, 86]. Recently, a particular class of double-layered perovskites, $LnBaMn_2O_{5+\delta}$ (Ln = Pr, Nd, Gd, Sr) and $Sr_2Mg(Mo)O_6$, in which the A-site cations are ordered in alternating layers, has received considerable attention as electrode materials for SOFCs/SOECs [87–89]. Moreover, Dragos et al. reported the design of an A-site-deficient perovskite capable of exsolving catalytically active metal particles in situ for application at the SOFC anode, which is subsequently discussed in the following Sects. 6.2.2–6.2.4.

Despite these reports of oxides as alternative electrodes for SOFCs, the development of active oxide electrodes is a rather difficult subject, and further improvement in the anodic performance is yet to be achieved because of their insufficient electrical conductivity and surface activity. Even so, oxide electrodes can be expected to overcome some of the limitations of other electrode materials used for SOFCs. Detailed representative results of the new, advanced, layered, 3D stacked perovskites are given in the following Sects. 6.2.1–6.2.4.

6.2.1 *K_2NiF_4-Type Layered Perovskites with a High Oxygen Mobility*

The general formula of the Ruddlesden Popper (RP) series of materials can be written as $A_{n+1}B_nO_{3n+1}$ and consists of an $n$$ABO_3$ perovskite of layered intergrown

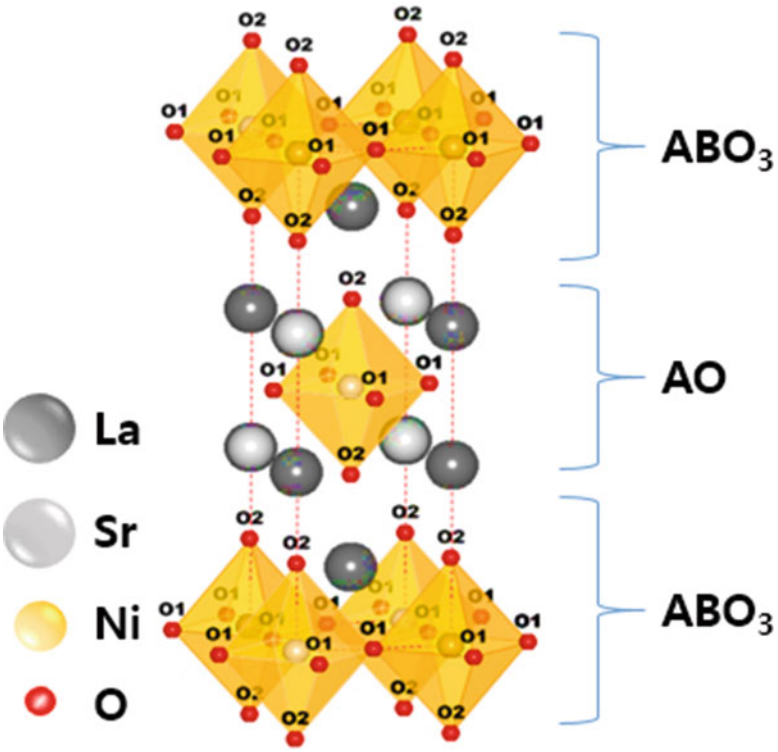

Fig. 6.4 Crystal structure of a representative K_2NiF_4-type cathode material, $La(Sr)_2NiO_{4+\delta}$

oxides, $[ABO_3][AO][ABO_3]$, as shown in Fig. 6.4. This RP phase has been commonly indicated with a simple tetragonal structure (*I4*/*mmm*); thus, they structurally have anisotropic properties for oxygen diffusion and transport, resulting in lower activation energies and sufficient oxygen surface exchange with a higher oxygen mobility. These fast oxygen transport properties are related to their ability to accommodate hyperstoichiometric oxygen at the interstitial positions in the rock-salt layers. The activity of a perovskite electrode is closely related to its material composition, lattice structure, physicochemical properties, and morphological structure. To design a novel optimized composition with an improved RP-type MIEC for SOFC cathodes, it is very important to identify the oxygen diffusion mechanisms at the lattice or atomic-surface scale precisely, which involve three types of oxygen in a low-dimensional lattice, leading to highly anisotropic diffusion properties [90]. Several groups have attempted to model the oxygen diffusion mechanisms in $Ln_2(Ni, Co, Fe, Cu)O_{4+\delta}$ (Ln = Nd, La, or Pr) by theoretical calculations. M. Burriel et al. unequivocally showed that Ni is not present in the outermost atomic layer in the $La(Sr)_2NiO_{4+\delta}$ structure through a combination of surface-sensitive techniques such as low-energy ion scattering (LEIS), crystal truncation rods (CTRs), and angle-resolved X-ray photoelectron spectroscopy

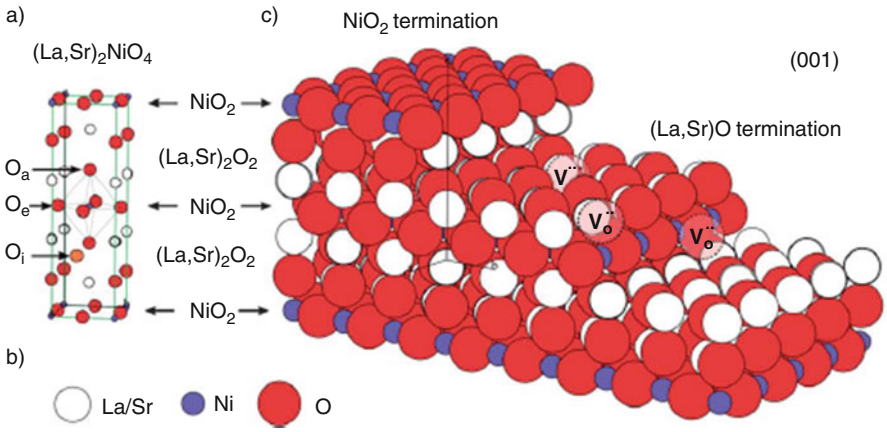

Fig. 6.5 3D view of the $La(Sr)_2NiO_{4+\delta}$ crystal, highlighting two possible ideal terminations for the (001) face (*top* surface): a step edge and possible oxygen vacancy positions [36]

(AR-XPS) [36]. Figure 6.5 shows a 3D view of the $La(Sr)_2NiO_{4+\delta}$ crystal, highlighting two possible ideal terminations for the (001) top surface.

Although nickelates, e.g., Ln_2NiO_4, have been extensively studied as potential cathodes, little attention has been paid to cuprate-based materials, e.g., $Ln_2CuO_{4+\delta}$ (Ln = Nd, La, Pr); only a few studies have been carried out for the practical cathode performance in the case of SOFCs, which were concerned with single crystals or doped superconducting materials such as $La(Sr)_2CuO_{4+\delta}$. Although promising cathode performance would be expected for doped $Ln_2CuO_{4+\delta}$ considering the positive effects of the A- and B-site dopants towards improving the conductivity and ORR catalytic activity, research on the electrochemical performance of practical SOFCs with cuprate cathodes is rarely reported [91–93]. Recently, Xiubing et al. reported dramatically high power densities for a cell using the nanostructured $La_2CuO_{4+\delta}$ series, specifically, hierarchically nanostructured $La_{1.7}Ca_{0.3}Ni_xCu_{1-x}O_{4-\delta}$ ($0 \leq x \leq 0.75$) cathode materials [94]. The maximum power densities (MPDs) of their cells were 1.5 ($La_{1.7}Ca_{0.3}CuO_{4+\delta}$) and 1.3 W/cm^2 ($La_{1.7}Ca_{0.3}Ni_{0.75}Cu_{0.25}O_{4+\delta}$) at 850 °C, as shown in Fig. 6.6.

6.2.2 *Double-Layered Perovskite with High Reversible Phase Switching*

Recently Sengodan et al. have succeeded in synthesizing an oxygen-deficient layered phase, $PrBaMn_2O_{5+\delta}$, in a reducing atmosphere [88]. Although polycrystalline samples sintered in air adopt the cubic ABO_3 perovskite structure, the A-site-ordered layered perovskite $PrBaMn_2O_{5+\delta}$ can be grown under reducing conditions. The disordered cubic perovskite $Pr_{0.5}Ba_{0.5}MnO_3$ was prepared by a

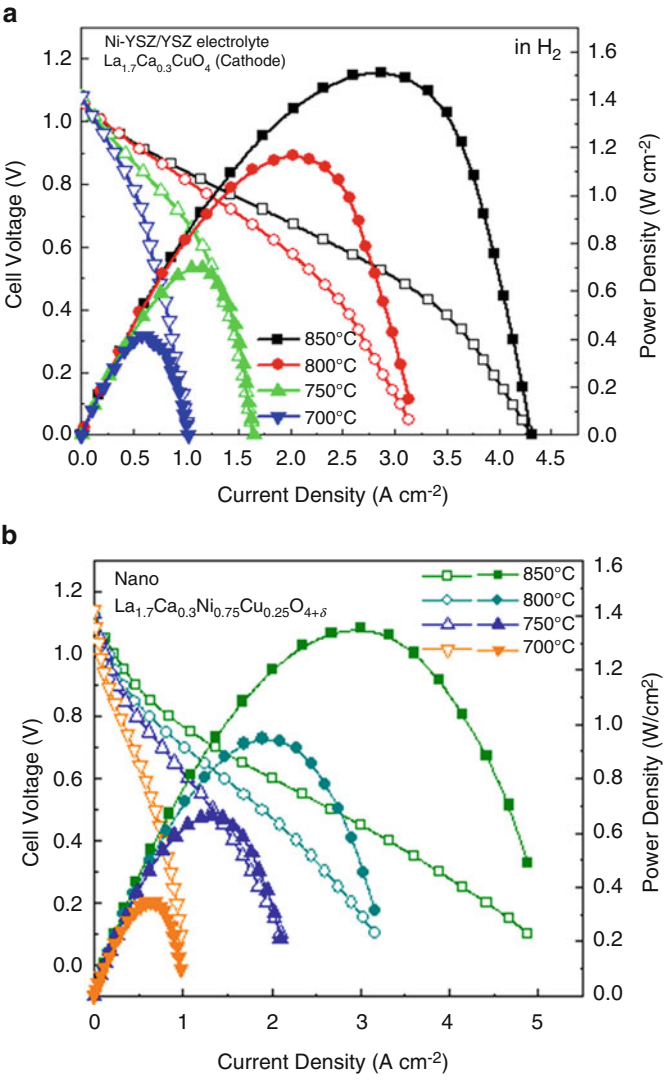

Fig. 6.6 Single cell performance of a cell with (**a**) $La_{1.7}Ca_{0.3}CuO_{4+\delta}$ and (**b**) nano-$La_{1.7}Ca_{0.3}Ni_{0.75}Cu_{0.25}O_{4+\delta}$ on a YSZlNi–YSZ anode-supported electrolyte [94]

typical solid-state reaction. The A-site ordering in the layered manganite perovskite would be partially hindered by the formation of the related hexagonal perovskite $BaMnO_3$. The reducing conditions lead to A-site ordering and hence doubling of the unit cell, giving a layered phase with a tetragonal symmetry, as shown in Fig. 6.7.

To fully understand the phase changes and A-site ordering of the double-layered perovskite during redox cycling, Shin et al. investigated the phase transition from the disordered cubic $Pr_{0.5}Ba_{0.5}MnO_3$ phase (O3) to the oxygen-deficient layered

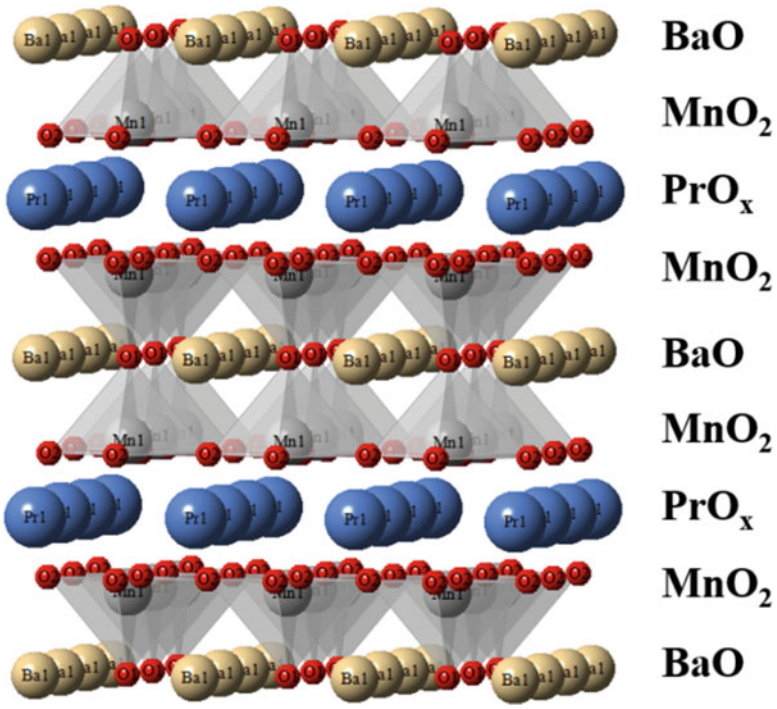

Fig. 6.7 Schematic of a crystal structure model for A-site-ordered layered $PrBaMn_2O_{5+\delta}$ (O5) and oxygen vacancies [89]

$PrBaMn_2O_{5+\delta}$ (O5) phase by in situ variable-temperature/atmospheric X-ray diffraction (Mo Kα1/Kα2) while performing reduction–oxidation cycles [89]. Figure 6.8 shows the Rietveld refinement profiles of the $Pr_{0.5}Ba_{0.5}MnO_3$ (O3), $PrBaMn_2O_{5+\delta}$ (O5), and $PrBaMn_2O_{6-}$ (O6) phases from the in situ XRD data at 800 °C in various atmospheres. According to the literature, the A-site-ordered O5 phase emerges with tetragonal symmetry, causing a relative shrinkage of the *c*-axis compared to the *a*-axis in a reducing atmosphere. Refinement is successful using the *P4*/*mmm* space group, as shown in Fig. 6.8. Subsequent reoxidation of the A-site-ordered O5 phase at 800 °C results in the emergence of the double perovskite $PrBaMn_2O_{6-\delta}$ (O6) phase. This O6 phase also has tetragonal symmetry with the space group *P4*/*mmm* (Fig. 6.9).

Furthermore, the double structure $LnBaMn_2O_{5+\delta}$ (Ln = Nd, Pr) could be beneficial for oxygen intercalation/deintercalation, which underpins the phase stability during redox cycling and in a wet atmosphere in high-temperature electrochemical devices [95]. The fully oxygen-charged $LnBaMn_2O_{5+\delta}$ (O6) phase has been reduced in 5% H_2 at elevated temperatures up to 800 °C, cooled to room temperature (2.5 °C/min), and reoxidized to 700 °C in air. Figure 6.8 shows the thermogravimetric analysis (TGA), in which a weight gain ca. 3.58 wt% was observed for both reduction and reoxidation, corresponding to a loss/uptake of

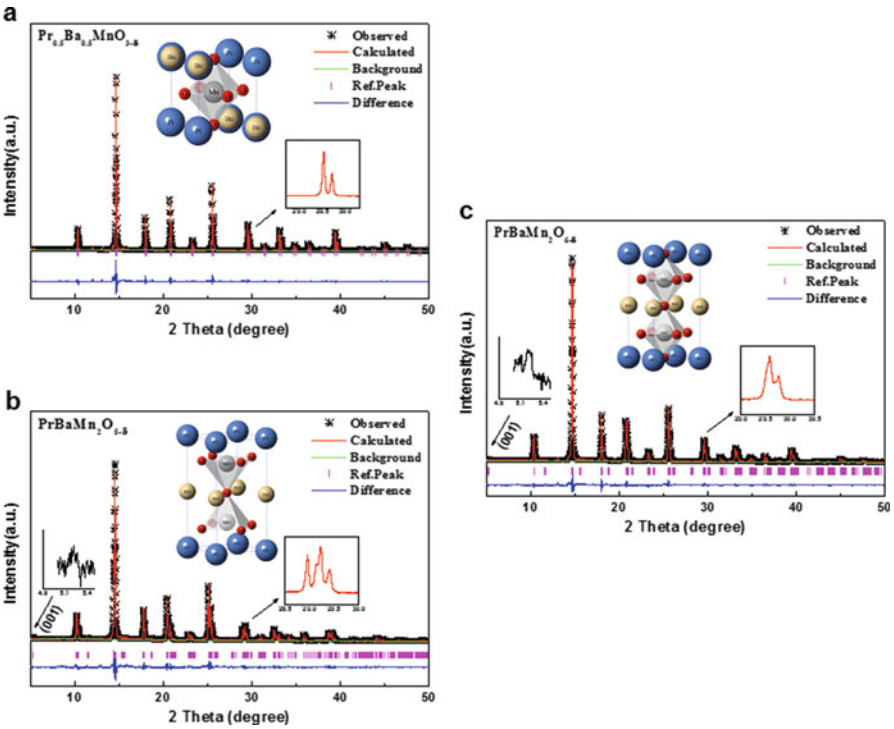

Fig. 6.8 Rietveld-refined XRD profiles of (**a**) $Pr_{0.5}Ba_{0.5}MnO_3$ (O3), (**b**) $PrBaMn_2O_{5+\delta}$ (O5), and (**c**) $PrBaMn_2O_{6-\delta}$ (O6) obtained by simultaneous fitting of the in situ high-temperature XRD data at 800 °C in air, 5% H_2, and air, respectively (Mo Kα1, Kα2 radiation) [89]

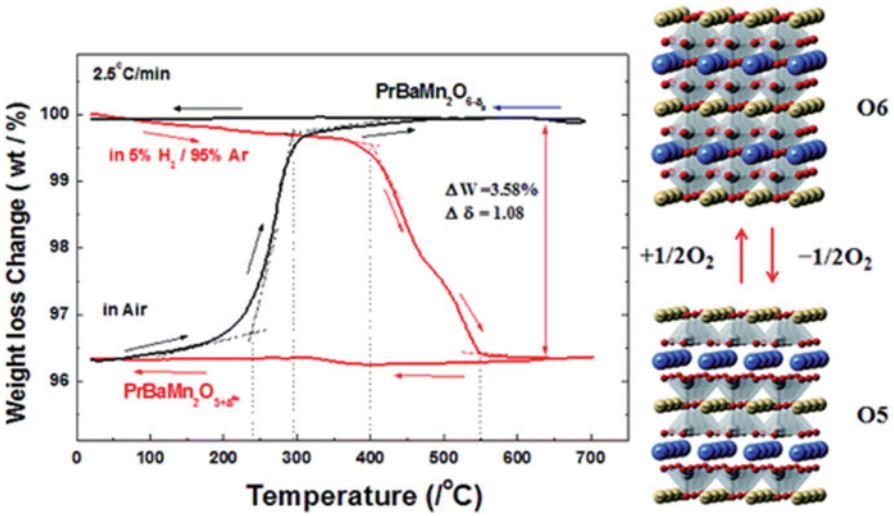

Fig. 6.9 TGA curves of $PrBaMn_2O_{5+\delta}$ in 5% H_2/Ar from room temperature to 700 °C and back to room temperature during a reoxidation cycle [89]

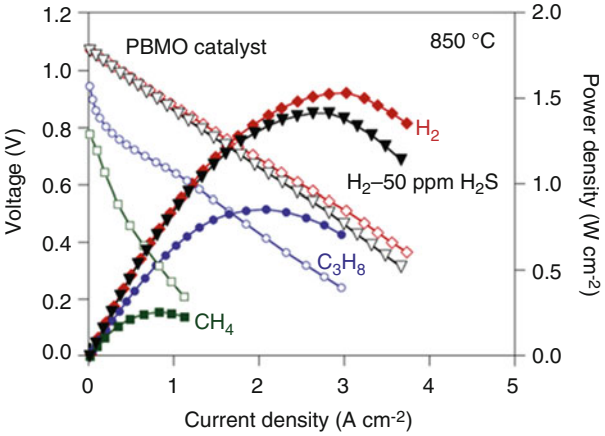

Fig. 6.10 Single cell performance of a cell with $PrBaMn_2O_{5+\delta}$ on an LSGM| $NdBa_{0.5}Sr_{0.5}Co_{1.5}Fe_{0.5}O_{5+\delta}$–$Ce_{0.9}Gd_{0.1}O_{2-\delta}$-supported electrolyte [88]

1 formula unit of oxygen ($\delta = 1$). This symmetry between the reduction and oxidation cycles suggests excellent reversibility, which is in agreement with the dilatometry data reported by Sengodan et al. [88]. A-site-ordered double-layered perovskite–manganese oxide demonstrates good SOFC anode performance and stability for various fuels; the power density of layered $PrBaMn_2O_{5+\delta}$ on an LSGM electrolyte support was 1.42 W/cm^2 at 850 °C, as shown in Fig. 6.10.

6.2.3 *Intelligent Switching Electrode*

Recently, the addition of cost-effective amounts of precious metals to perovskites has been shown to effectively improve their catalytic activity. However, precious metals with a small particle size were easily aggregated at high temperatures such as those in SOFC operating conditions, resulting in a degradation in their catalytic performance. One of the possible solutions is to periodically redissolve the small metal catalysts into the oxide phase and then reprecipitate them in their small and highly active state. Tanaka et al. prepared Pd-doped perovskite catalysts having a self-regenerative function, so-called "intelligent catalysts," for automotive applications [96]. Barnet et al. also reported that Pd-substituted (La, Sr)CrO_3-based oxide anodes show self-recovery performance in the redox cycle of SOFCs [97]. Shin and Ishihara et al. also showed improved anodic performance with Pd exsolving La(Sr)Fe(Mn)O_3 (LSFMP), as shown in Fig. 6.11 [98].

To confirm the regeneration of Pd nanoparticles in the redox cycles of $LaFeO_3$, the morphology of the $LaFeO_3$ catalyst was analyzed by TEM and XPS, as shown in Fig. 6.12. Pd nanoparticles ca. 10 nm in diameter appear to be repeatedly formed in the oxidation and reduction cycles, which is a phenomenon similar to that reported

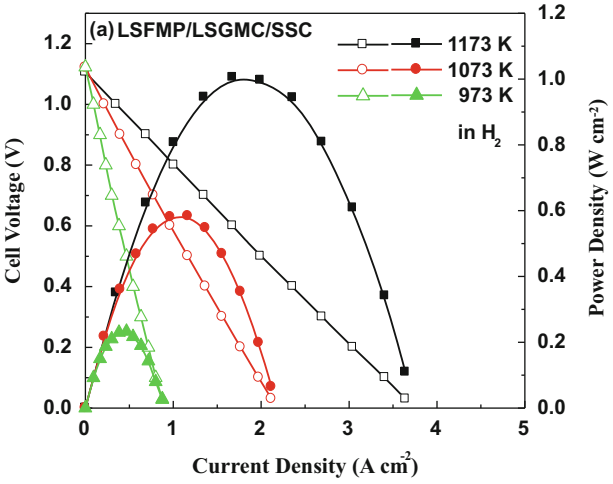

Fig. 6.11 Single cell performance of a cell with Pd-nanoparticle exsolved La(Sr)Fe(Mn,Pd)O_3 on an LSGM|SSC-supported electrolyte [98]

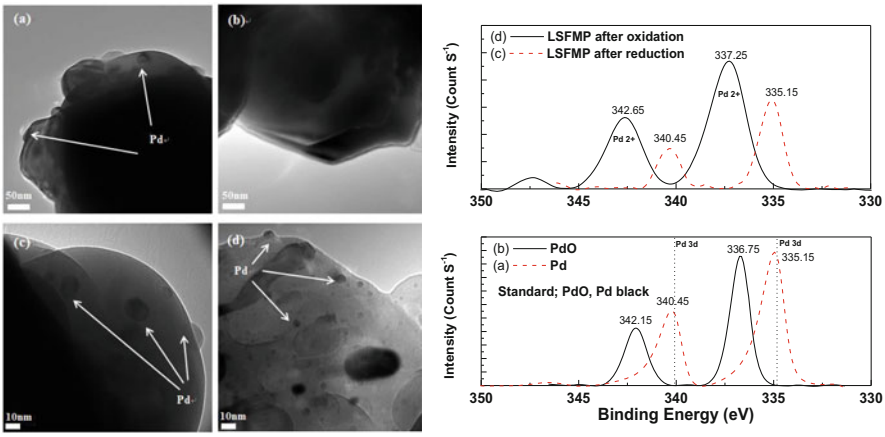

Fig. 6.12 TEM images of LSFMP during reduction in (**a**) H_2 for 2 h at 800 °C and (**b**) a reoxidation atmosphere and (**c**), (**d**) at high magnification after a reduction treatment with H_2 for 2 h at 800 °C. XPS Pd 3d spectra of LSFMP powder after reduction in H_2 for 10 h at 1073 K, and LSFMP powder after oxidation in air at 800 °C [98]

for intelligent three-way catalysts [96]. Pd may easily exist on the LSFMP surface as Pd^{0+} and Pd nanoparticles resulting from reduction by H_2. On the other hand, the oxidation state of Pd in LSFMP was considered to be Pd^{2+} in air at 800 °C because Pd redissolved in the lattice.

The reversibility of the anode performance recovery upon exposure to air was further studied. Figure 6.13 shows the self-regeneration performance of the Pd

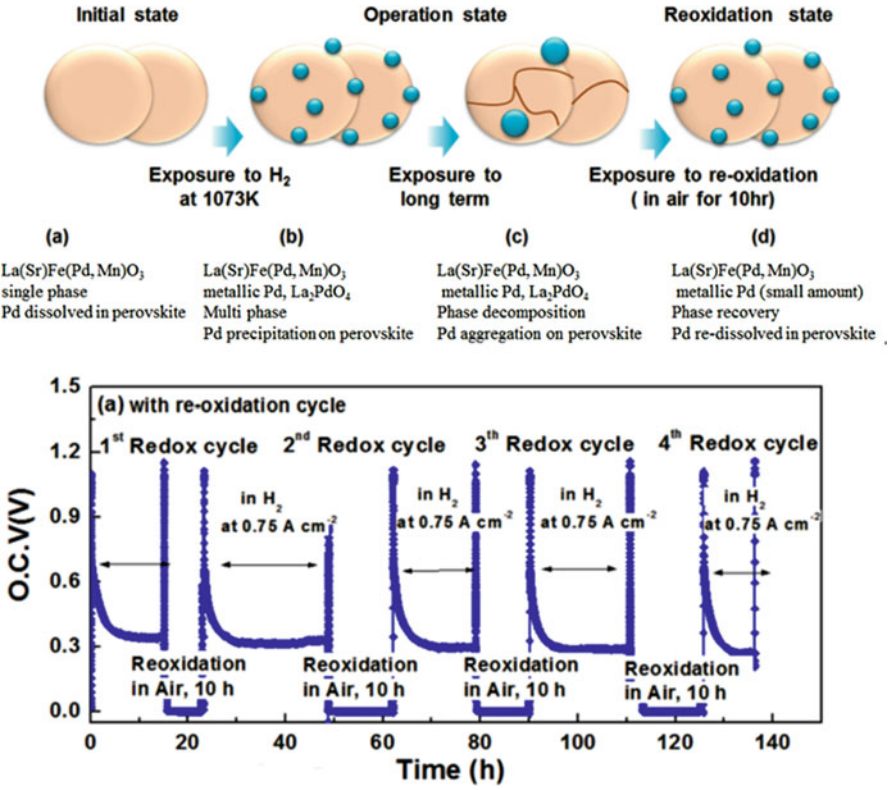

Fig. 6.13. Self-regeneration of the Pd exsolved anode during redox cycling performance

exsolved switching electrode during a long-term redox cycle of a cell using LSFMP. For a longer time after the redox cycle, the terminal voltage stabilized and immediately became almost equal to that observed for cells operating in the initial state after each redox cycle. Since the Pd nanoparticles are recovered during the reoxidation and reduction cycles, the power density can be also recovered through the redox cycle. Thus, the Pd exsolved La(Sr)Fe(Mn)O_3 is highly reversible, and fine Pd particles can be maintained by using a redox treatment.

6.2.4 Exsolution in the Perovskite

Recently, an in situ exsolution method for various perovskites has received considerable attention as alternative for fabricating electrodes for SOFCs and SOECs. Neagu et al. have shown that perovskite lattice defects, in particular, the built-in A-site vacancies (e.g., $A_{1-\alpha}BO_3$), are instrumental for tailoring several aspects related to exsolution, including particle nucleation, size, and dispersion, and can

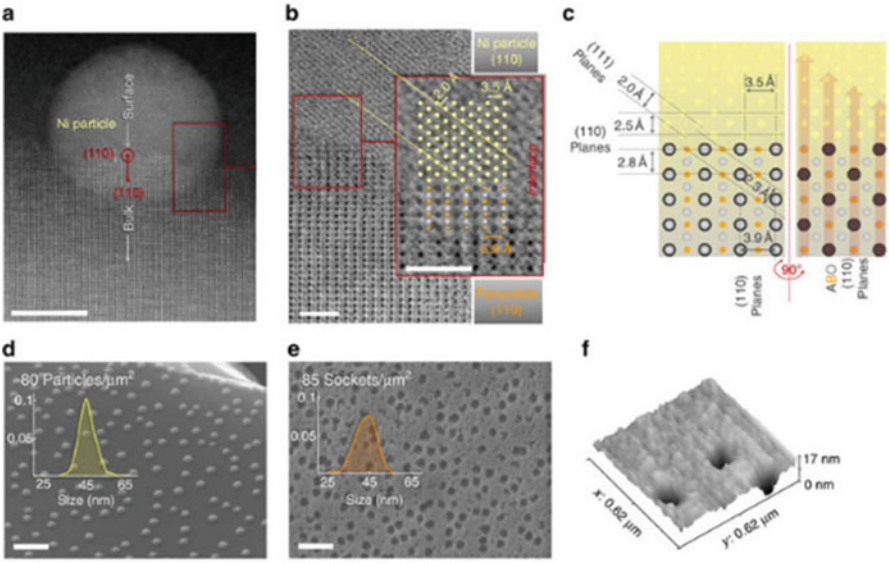

Fig. 6.14 Anchorage of exsolved particles in relation to their redox stability: (**a**, **b**) TEM images of nanosocketed Ni particles after exsolution; (**c**) schematic of exsolution and anchorage; (**d**) overview of the exsolved particles with a small size; (**e**) the sample in (**d**) after etching in HNO_3, showing that particles are socketed in shallow pits; and (**f**) 3D AFM image of the sockets [99]

also enable a wider range of species to be exsolved more reliably, including Ni, as shown in Fig. 6.14 [99, 100]. This simplifies the overall procedure of decorating porous scaffolds with active nanoparticles and provides an opportunity to control where particles grow in devices with intricate architectures by adjusting the initial composition at the locations of interest.

Perovskite oxides can accommodate defects having various natures including different sizes of the constituents through tilting or deformation of octahedra; a different charge through nonstoichiometry, i.e., a deficiency (predominantly at the A and/or O sites) by the creation of vacancies, while preserving corner-sharing of the octahedra; or excess (primarily at the A and/or O sites) through intergrowths, which locally interrupt the corner-sharing octahedra chains. When a stoichiometric perovskite ABO_3 is used, exsolution from the B sites is generally accompanied by corresponding amounts of A oxides (e.g., AO) and observed experimentally [101, 102]. In the case of exsolved Pd for stoichiometric perovskites [103], it was observed that Pd easily migrated to the surface and agglomerated on the host surface during high-temperature sintering processing, even without a reducing atmosphere.

These electrode structures perform well as both fuel cells and electrolysis cells; for example, at 900 °C, they deliver 2 W/cm^2 of power in humidified hydrogen gas and a current of 2.75 A/cm^2 at 1.3 V in 50% water/nitrogen gas, as shown in Fig. 6.15 [104].

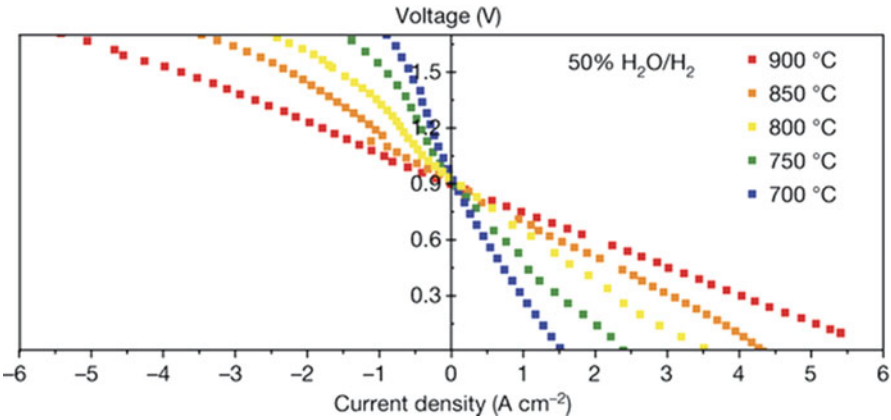

Fig. 6.15 Single cell electrochemical performance in the reversible-cell mode in 50% H_2O/H_2. The cell was based on an 80-μm-thick electrolyte (Sc-stabilized ZrO_2) [104]

6.2.5 *Development of Porous Cathode Coating Using an Aerosol Deposition Process*

Oxygen molecules adsorbed on the surface of the cathode migrate to the three-phase interface of the electrode and electrolyte either by dissociation or surface diffusion, and upon gaining electrons, they are transformed into oxygen ions. Then, these ions are transferred to the anode through the electrolyte. The cathode should be a porous membrane with a high ionic and electron conductivity ($\geq$50 s cm^{-1}), stable in an oxidizing atmosphere, inert to chemical reactions and interdiffusion with other components, and have a thermal expansion coefficient similar to other components. The cathode of an SOFC is generally regarded as an important component in determining the overall performance of the cell, primarily because its overpotential is the largest among the other components of the cell.

One of the important factors in the cathode manufacturing process is the compatibility with electrolytes. Particularly, if a reaction with an electrolyte occurs during the cathode manufacturing process, the performance of the entire cell is significantly deteriorated. For example, in the case of a $La_{0.6}Sr_{0.4}Co_{0.2}Fe_{0.8}O_{3-\delta}$ (LSCF) cathode, although it is known to have excellent performance due to its high ionic and electronic conductivity, the performance of the cell is greatly degraded by the formation of a secondary phase due to a reaction with the YSZ electrolyte at its heat-treatment temperature of 1100 °C. Furthermore, when a cell using a metal support is manufactured, the process temperature is limited during the production of the cathode owing to the decomposition problem in the reduction atmosphere. Therefore, it is expected that a technique for preparing a cathode at a low temperature would be very useful, and the aerosol deposition (AD) process can be successfully applied to solve these problems. Since the AD process is essentially a process technology applied to fabricate dense films, in order to prepare porous

films, the coating needs to include a polymer material that is decomposed at a high temperature to form pores [105, 106] (Fig. 6.16).

Figure 6.17 shows the surface and cross-sectional microstructures of the LSCF anode formed on an LSGM electrolyte and the Ni–GDC anode structure [106]. Polyvinylidene fluoride (PVDF) is used as a macromolecular material for pore formation. The porosity of the electrode changes according to the changes in the PVDF content, and similarly, the bonding strength between the cathode and the electrolyte is also changed. This relationship suggests that optimization of the PVDF content is required.

The cathode material of an SOFC has been extensively studied by many researchers since it is an important component that determines the overall cell performance. Recently reported MIEC materials with high electron and ionic

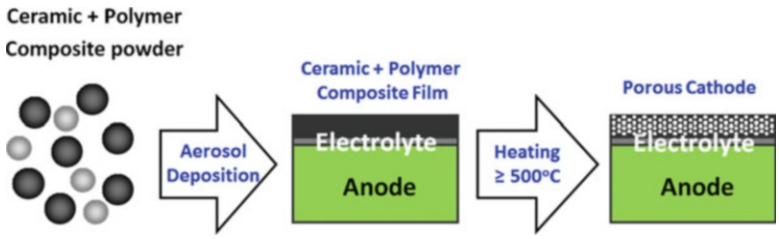

Fig. 6.16 Porous cathode manufacturing process using the AD process [101, 102]

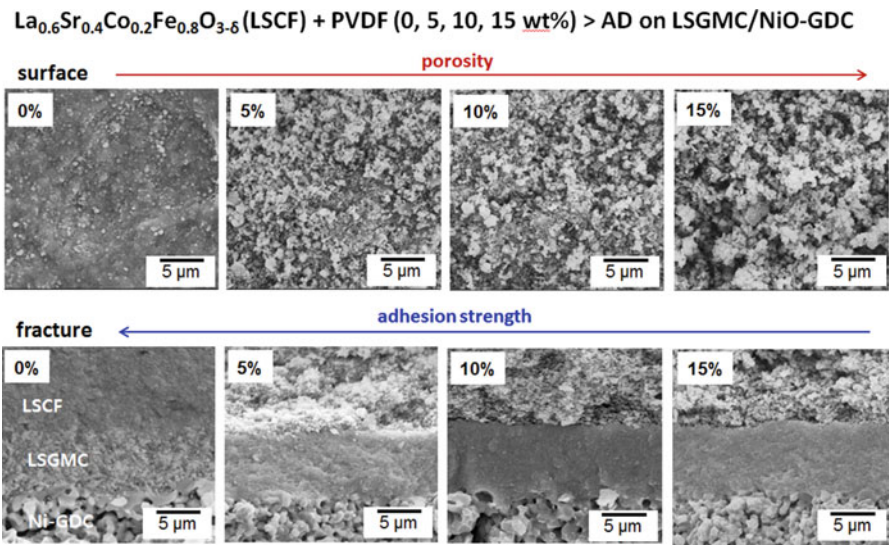

Fig. 6.17 Changes on an LSCF cathode surface and in the cross-sectional microstructure due to the changes in the PVDF content [106]

conductivities include $La_{0.6}Sr_{0.4}Co_{0.2}Fe_{0.8}O_3$, $Sm_{0.2}Sr_{0.8}CoO_3$, $Gd_{0.2}Sr_{0.8}CoO_3$, $Nd_{0.2}Sr_{0.8}CoO_3$, and $Ba_{0.5}Sr_{0.5}Co_{0.8}Fe_{0.2}O_{3-\delta}$. These materials react with the electrolyte material and have high thermal expansion coefficients; moreover, their physical properties deteriorate owing to the change in their microstructure upon prolonged use. Therefore, the use of these materials would also require low-temperature cathode formation techniques such as AD.

6.2.6 *Antioxidant Coating for Metallic Interconnect Using the AD Process*

An interconnect is a key material for manufacturing SOFC stacks. Since this material separates fuel and air and prevents them from crossing in the cell, it is also called a separator. Essentially, it electrically connects the anode of a cell to the cathode of the adjacent cell (interconnect) and physically blocks the air supplied to the cathode and the fuel gas supplied to the anode (separator). The interconnect used in SOFCs must have a high electrical conductivity ($\geq$1 s cm^{-1}) for electrical connection, chemical stability in the cathode and anode environments, and a similar thermal expansion coefficient as all other SOFC cell components. It must also have sufficient mechanical strength to support the stack and be relatively easy to process and cost-effective.

In general, $LaCrO_3$-based ceramic interconnect materials have been used to prevent stability problems at high temperatures. In recent years, efforts have been made to lower the operating temperature of SOFCs and to attain an excellent electrical conductivity and mechanical strength and easy processing. Moreover, metallic interconnects are preferred over ceramic interconnects owing to their cost. The use of a metallic interconnect at a high temperature results in the formation of oxide scales on the surface of the interconnects in the atmosphere of the SOFC cathode. This causes a rapid increase in the contact resistance and contamination of the electrode due to chemical instability and thus results in a degradation in the activity of the cathode. Examples of alloys used include Hitachi Metals' ZMG232, ThyssenKrupp's Crofer22APU, and Plansee's Cr-5Fe1Y2O3. Nevertheless, the metal interconnects still have a large reduction in the contact resistance due to oxide growth over long-term use. In the case of an alloy containing Cr, volatile Cr (VI) is formed in the SOFC operating environment and transformed into Cr_2O_3 at the air electrode/electrolyte interface. This hinders the oxidation–reduction reaction, and further reactions with the cathode material are known to reduce the electrode activity [107].

The concept of coating conductive ceramics on the surface of metal interconnects has also been actively investigated. This coating method was developed to increase the electrical and chemical stability at high temperatures while maintaining the excellent thermal and mechanical properties, processability, and cost-effectiveness of the metal interconnects. Perovskite-structured $La_{0.8}Sr_{0.2}MnO_3$

(LSM), $La_{0.6}Sr_{0.4}CoO_3$ (LSC), and $La_{0.6}Sr_{0.4}Co_{0.2}Fe_{0.8}O_3$ (LSCF), which are conventionally cathode materials, have been widely used as coating materials. More recently, spinel-based $(Mn,Co)_3O_4$ materials have been actively developed for this purpose [108]. The conductive ceramic coating technique greatly increases the electrical and chemical stability compared to the use of the metal interconnect by itself. Since a relatively dense and thick ceramic film is coated onto the metal, the manufacturing costs of the SOFC increase owing to the costs for coating. In addition, the electrode resistance increases owing to the formation of oxides at the interface as a result of the reaction between the coating layer and the metal interconnect as well as internal oxidation through the coating layer. The main coating techniques include spray pyrolysis, physical vapor deposition (PVD), plasma spray, slurry coating, and EPD. Studies describing the use of the AD coating technique, which can deposit dense ceramic layers without causing a thermal degradation in the metal interconnects at room temperature, have also been reported [109–112]. After depositing various conductive ceramics (e.g., $La_{0.8}Sr_{0.2}MnO_3$, $La_{0.6}Sr_{0.4}Co_{0.2}Fe_{0.8}O_3$, $(Mn,Co)_3O_4$, and $LaNiO_3$) onto inexpensive ferritic stainless steel (STS 400 series), the coating layer showed almost no defects such as cracks or voids. In addition, interfacial bonding with ferrite-based stainless steel was found to be in a good state before and after an oxidation test. Figure 6.18 shows a specimen of $La_{0.8}Sr_{0.2}MnO_3$ coated on a separator and collector mesh. From an analysis of its cross section, it is evident that a dense film was formed on the stainless steel, which remained structurally intact, even after heat treatment at 800 °C for 1000 h in air. The electrical resistance of stainless steel increased rapidly in a short period of time while the specimens coated with conductive ceramics showed a surface Cr concentration of 1 mol% or less and an area specific resistance (ASR) of 5 mΩ cm^2, even after being exposed at 800 °C for 1000 h. These results confirmed that AD can be successfully used as a coating technique for an interconnect [112].

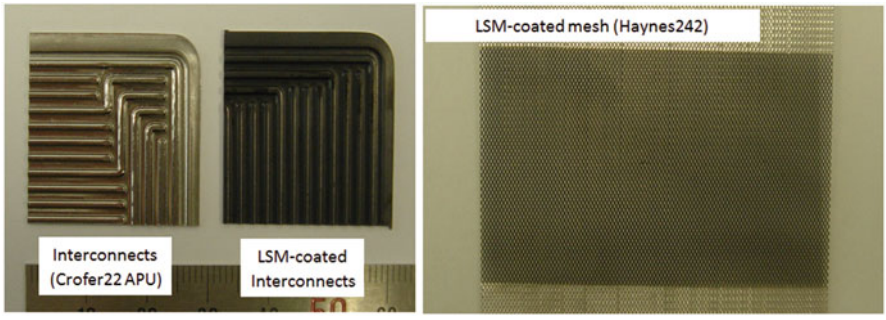

Fig. 6.18 Photographs of the interconnect and collector specimens of conducting ceramics (LSM) coated using an AD process

6.3 Electrolyte

6.3.1 Development of an Electrolyte Coating Using the Aerosol Deposition Process

AD is very useful method for producing large-area ceramic films at a high speed. This technique was first developed at the National Institute of Advanced Industrial Science and Technology (AIST) and has received widespread attention since it is possible to obtain thin films with a thickness of 1 μm or less as well as dense and thick films (hundreds of micrometers or more in thickness) in a very short time [113–115]. This process uses an engineering grade ceramic powder as a starting material, and the film is deposited by spraying accelerated powder particles at a supersonic speed (~500 m s^{-1}) through a nozzle onto a substrate. Other methods that also use the particle colliding mechanism include thermal spray coating and cold-gas spray coating. The thermal spray coating method requires heating the material to be deposited to its melting point. The cold-gas spray coating method also requires heating of the material to its softening point, which is usually lower than the melting point. On the other hand, the most distinctive feature of the AD process is that a dense film coating can be obtained at room temperature. Thus, no interfacial reaction occurs between the substrate and the film during coating, and various materials including polymers and metals may be used as substrates. Since there is no change in the composition of the material in the two states, i.e., from a coating powder to the deposited film, it is possible to produce a film for a compound having a complicated composition. Deposition and patterning of the film are also possible by inserting an appropriately designed mask between the nozzle and the substrate. Figure 6.19 shows a schematic of a typical AD instrument.

At present, several research institutions around the world, including material research institutes in Korea and the Akedo group of AIST, are performing research on manufacturing thick films using the AD process. Specifically, in Korea, this technique was introduced for the first time at the Korea Institute of Materials Science (KIMS). Using the equipment developed at the institute, a variety of functional films have been successfully manufactured during the development of functional ceramic thick films, piezoelectric devices, biocoatings, and photocatalytic coating technologies [116–122]. The characteristics of the AD coating process are summarized as follows:

- High-speed coating (Coating speed: 30 μm/min).
- Formation of a dense, crack-free, coating layer at room temperature.
- Capability of forming a porous thick film by introducing pore formers.
- Coating with a wide range of thicknesses (less than a micrometer to several hundred micrometers).
- Easy control of the composition and stoichiometry of the coating layer.
- Fabrication of dense ceramic coatings with crystal gains within several tens of nanometers.

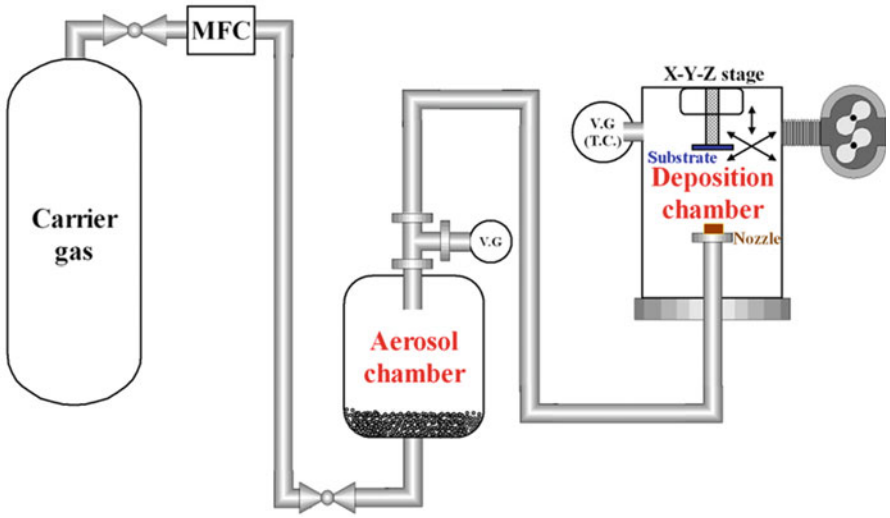

Fig. 6.19 Schematic of aerosol deposition equipment [116]

- Utilization of different substrates including metals, ceramics, and hard polymers.
- Coating of various ceramic materials.

The AD process can easily fabricate a dense film with a thickness ca. 10 μm at room temperature. A dense, crack-free, electrolyte film is difficult to manufacture using conventional ceramic thin-film deposition technology without a high-temperature process. Figure 6.20 compares the requirements for the electrolyte and the ionic conductivity of an SOFC. When the electrolyte is manufactured by the AD process, a thin and dense film with low enough gas permeability can be deposited at a room temperature without reaction during the process. Figure 6.20 also shows photographs of electrolyte films fabricated on transparent substrates by the AD process. As illustrated, it is possible to form a semitransparent dense film in which the backside of the coating film is visible [123, 124].

Figure 6.21 compares the microstructures of the electrolyte prepared by the AD process and that of the powder used in the coating. The electrical conductivity measured by the DC four-probe method for each electrolyte is also given [123–129].

Figure 6.21 shows that a very dense film of 5 μm or less was formed by using particles with an initial size of 1–2 μm. The electrical conductivity was in the range of 7–66 ms cm^{-1} depending on the material at 750 °C. Although this range of conductivities is lower than that of the bulk material sintered at a high temperature, it is sufficient for a thin-film-type electrolyte of a cathode-supported fuel cell. When the cell structure is designed by utilizing this room-temperature dense film formation technique, high-performance cells can be manufactured by minimizing the reaction of the interfacial reactions during cell fabrication [123, 125, 126].

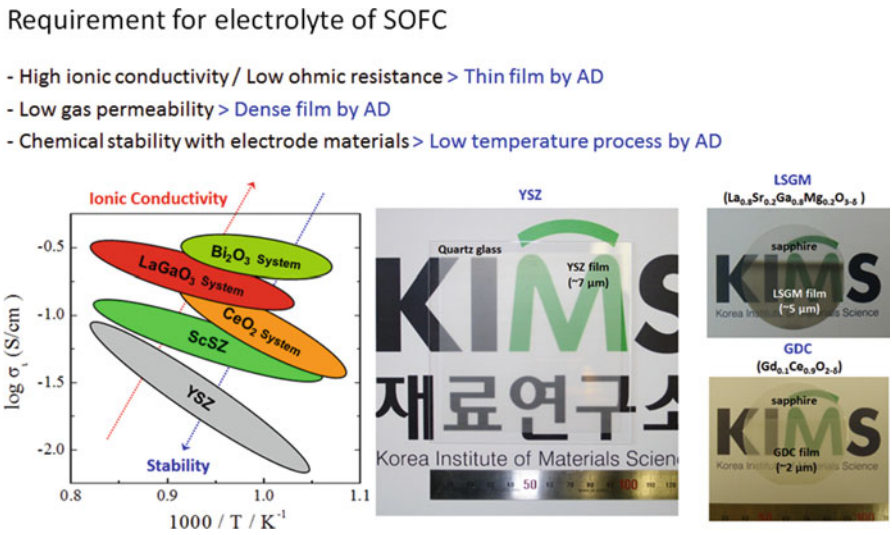

Fig. 6.20 Requirements for an SOFC electrolyte, comparison of the ionic conductivity, and electrolyte films fabricated by the AD process [123, 124]

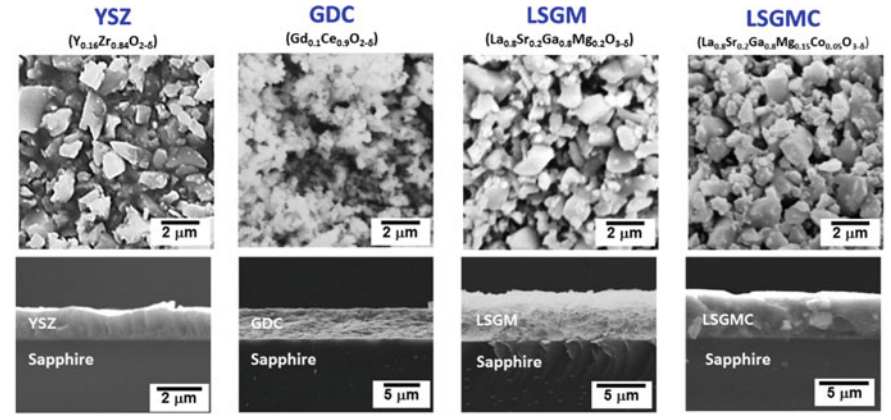

Electrolyte (as dep.)	YSZ		GDC		LSGM		LSGMC	
Temperature [°C]	@650	@750	@650	@750	@650	@750	@650	@750
Conductivity* [mS/cm]	1.7	6.9	12.6	31.6	8.2	30.0	29.6	66.5

Fig. 6.21 SOFC electrolyte requirements and ionic conductivity comparison for electrolyte films fabricated by the AD process

6.3.2 $Zr_{1-x}M_xO_{2-\delta}$ ($M = Y, Sc$) Electrolyte Films via EB-PVD Coating

The most important consideration thus far for a solid electrolyte is the decrease in the ohmic resistance by controlling the microstructure in addition to the material composition. For this purpose, a reliable thin electrolyte film on a durable support is required. During the past decades, various thin-film technologies, e.g., plasma spraying, electrochemical vapor deposition (EVD), and sputtering techniques, have been applied to YSZ electrolytes [130–133]. Among them, much attention has been paid to vapor deposition methods including sputtering and PVD due to its strict control of the microstructure, porosity, and stoichiometry of the film and the growth rate during deposition [134–136]. Ishihara et al. reported that a cell using a thin LSGM electrolyte prepared by pulsed laser deposition (PLD) shows excellent cell power generation properties at an intermediate temperature [137]. Despite the positive results reported, the use of some vacuum deposition processes in industrial manufacturing has been still limited owing to the small deposition area of the coating and the low reproducibility.

EB-PVD has been widely used to fabricate the thermal barrier ceramic coating (TBC) in the engineering industry. Another advantage of the conventional process of EB-PVD is the continuous deposition of different components and different microstructural layers such as porous electrodes and dense electrolytes. Shin et al. fabricated highly conducting and dense $Zr_{1-x}M_xO_{2-\delta}$ (M = Y, Sc) thin films via commercial 10-kW-level EB-PVD [15]. The coating films were prepared by EB-PVD using an 8 mol% YSZ powder (TZ-8YS, Tosoh Co., Japan) as an evaporation source material on a NiO–YSZ cermet substrate. The deposition time and average deposition rate were 25 min and 0.5 μm/min, respectively. Detailed information about the deposition conditions are listed in Table 6.2.

Overall, thin films fabricated via EB-PVD show pure ionic conducting behavior and a fairly good conductivity was achieved for films prepared at substrate temperature of 950 °C having large columnar grains; the ScSZ and YSZ films had conductivities of 0.23 and 0.11 s/cm, respectively, at 900 °C in air, as shown in Fig. 6.22.

Table 6.2 EB-PVD conditions [6.6]

Target source	8 YSZ (8 mol% Yttrium)
Vacuum	10^{-4}–10^{-5} Torr
Substrate temp.	600–950 °C
Deposition time	25 min
Generation power of electron beam	3.5 kW
Substrate	NiO–YSZ sintered @ 1400 °C
	Average roughness of surface: 0.132 μm
	Porosity ca. 20% (before reducing): EB-PVD
	Porosity ca. 35% (after reducing)

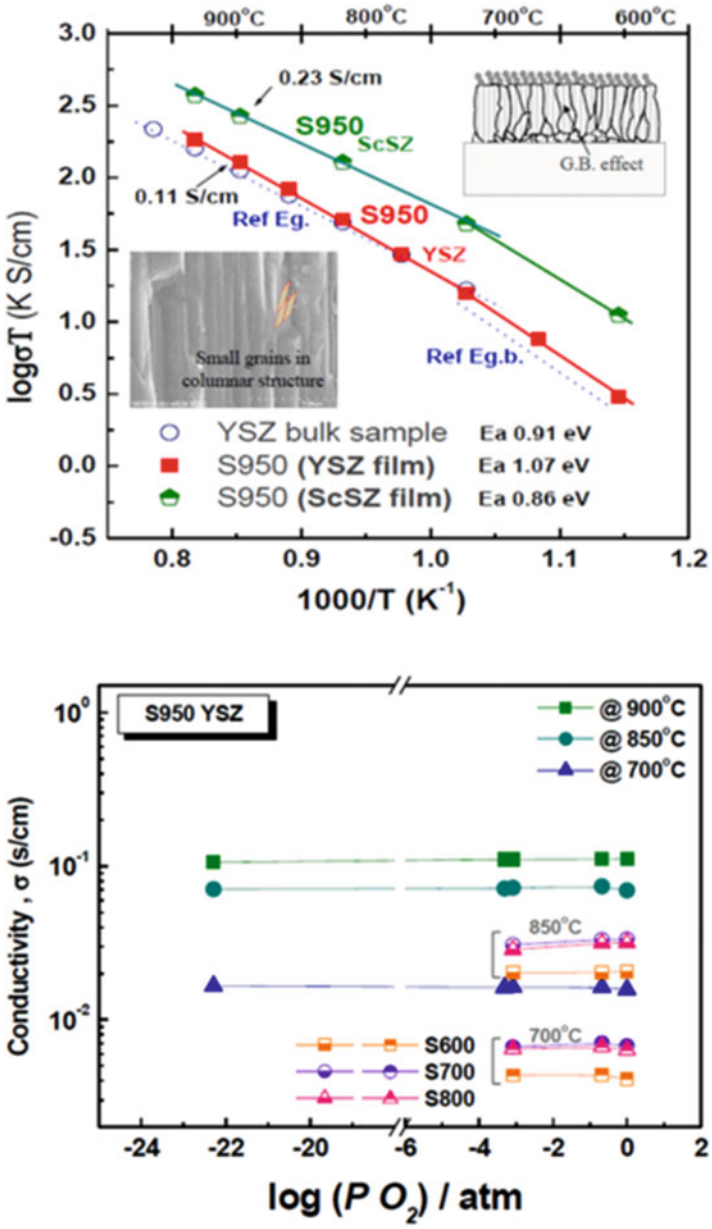

Fig. 6.22 Electrical conductivity of YSZ films prepared at a substrate temperature of 950 °C and the PO_2 dependence of the electrical conductivity [6]

In the case of the ScSZ film deposited via EB-PVD, the O.C.V.s of the cell at 700, 800, and 900 °C were 1.15, 114, and 1.12 V, which are close to the theoretical value, suggesting that the ScSZ film has significant gas tightness for an SOFC application. Moreover, a high power density (>0.8 W/cm^2) was achieved, and a power density ca. 1 W/cm^2 at voltages less than 0.75 V was achieved in H_2 at 900 °C [6]. Consequently, this study reveals that EB-PVD is an attractive option for thin-film SOFCs with conventional vacuum processing, and reasonably high-power performance is achieved with ScSZ films deposited by EB-PVD (Fig. 6.23).

6.3.3 Bilayer Electrolyte Fabrication and Performance

The electromotive force of a fuel cell is at most ~1 V per unit cell, and to obtain a higher output, it is necessary to stack multiple cells in series. The most important consideration when configuring a stack is minimization of the performance variation among the cells connected in series. Its importance can be illustrated by the following example. When batteries with different capacities are mixed, the efficiency of the entire battery pack is reduced. This phenomenon occurs because a battery with a relatively low capacity has a high resistance. Another problem is that a battery with a relatively low capacity can be overcharged and overdischarged, potentially leading to failure of the entire battery pack [138, 139]. Thus, if one cell in a fuel cell stack exhibits a large performance difference, the cell with a low performance operates at a negative (−) voltage at the same current density at which the other cells are operating normally, leading to physical failure due to rapid degradation [139]. This is a common phenomenon for electrochemical devices connected in series. In order to stabilize and commercialize cells, it is important to understand and solve the cell imbalance in stacks and minimize the performance variation among cells.

The most widely used electrolyte for solid oxide fuel cells nowadays is zirconia doped with 8 mol% yttria (YSZ). YSZ has a predominant oxygen-ion conductivity due to the oxygen vacancies generated by the addition of yttria. It has advantages such as electron conductivity that is almost zero and a chemical stability that is unaffected by oxidizing or reducing atmospheres [9]. From a performance point of view, the predominant oxygen-ion conductivity offers the advantage of a high open-circuit voltage and high power density. However, from a durability point of view, the predominant oxygen-ion conductivity becomes a disadvantage. Operation at the abovementioned negative (−) voltage can cause an abnormally high oxygen chemical potential inside the solid electrolyte and eventually lead to delamination of the electrode–electrolyte interface. This can be explained by considering the directions of the oxygen-ion and electron flows under the assumption of local equilibrium [138–140] as follows:

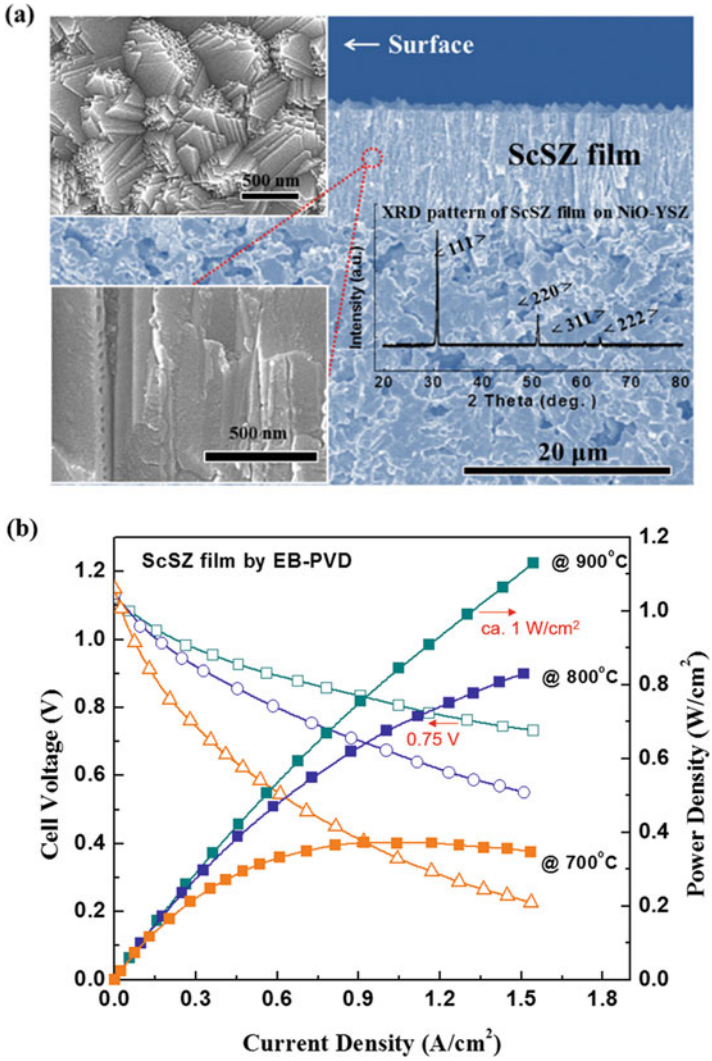

Fig. 6.23 (**a**) SEM images of an ScSZ film prepared at a NiO–YSZ anode substrate temperature of 950 °C and an XRD pattern. (**b**) Single cell performance of a cell using an ScSZ film prepared at a substrate temperature of 950 °C with a NiO–YSZ cermet anode and LSM cathode in H_2 and air atmospheres [6]

$$\frac{1}{2}O_2 + 2e' \rightarrow O^{2-} \tag{6.1}$$

Local equilibrium assumes that one oxygen ion inside the electrolyte is in equilibrium with one half of an oxygen molecule and two electrons, as shown in

Eq. (6.1). The relationship in Eq. (6.1) can be written in terms of the electrochemical and chemical potentials as follows:

$$\frac{1}{2}\mu_{O_2} + 2\tilde{\mu}_{e} = \tilde{\mu}_{O^{2-}} \tag{6.2}$$

where μ_{O_2} denotes the chemical potential of oxygen, and $\tilde{\mu}_{e}$ and $\tilde{\mu}_{O^{2-}}$ denote the electrochemical potentials of an electron and oxygen ion, respectively.

Equations (6.3) and (6.4) show the current densities of oxygen ions and electrons in terms of the electrical conductivity and electrochemical potential gradient, which can be transformed into Eqs. (6.5) and (6.6) using the local equilibrium assumption in Eq. (6.2). Equations (6.5) and (6.6) include the ASRs of an oxygen ion and electron denoted by $r_{O^{2-}}$ and r_e, respectively.

$$I_{O^{2-}} = \frac{\sigma_{O^{2-}}}{2e}\nabla\tilde{\mu}_{O^{2-}} = \frac{\sigma_{O^{2-}}}{2e}\nabla\left(\frac{1}{2}\mu_{O_2} + 2\tilde{\mu}_{e}\right) = \sigma_{O^{2-}}\nabla\left(\frac{1}{4e}\mu_{O_2} - \varphi\right) \tag{6.3}$$

$$I_{e} = \frac{\sigma_{e}}{e}\nabla\tilde{\mu}_{e} = -\sigma_{e}\nabla\varphi \tag{6.4}$$

$$I_{O^{2-}} = \frac{1}{4e}\frac{\triangle\mu_{O_2}}{r_{O^{2-}}} - \frac{\triangle\varphi}{r_{O^{2-}}} \tag{6.5}$$

$$I_{e} = -\frac{\triangle\varphi}{r_{e}} \tag{6.6}$$

In the above equations, the variation in the oxygen ions and the variation in φ $\left(\frac{\tilde{\mu}_{e}}{e}\right)$ can be written as follows:

$$\mu_{O_2}{}^{c} = \mu_{O_2}{}^{I} + 4e(r_{O^{2-}}{}^{c} I_{O^{2-}} - r_{e}{}^{c} I_{e}) \tag{6.7}$$

$$\mu_{O_2}{}^{a} = \mu_{O_2}{}^{II} + 4e(r_{O^{2-}}{}^{a} I_{O^{2-}} - r_{e}{}^{a} I_{e}) \tag{6.8}$$

where $\mu_{O_2}{}^{I}$ and $\mu_{O_2}{}^{II}$ denote μ_{O_2} of the porous cathode and anode, respectively; $\mu_{O_2}{}^{c}$ and $\mu_{O_2}{}^{a}$ denote μ_{O_2} inside the electrolyte at the cathode–electrolyte interface (inside the electrolyte just below the cathode) and μ_{O_2} inside the electrolyte at the anode–electrolyte interface (inside the electrolyte just below the anode), respectively; $r_{O^{2-}}{}^{c}$ and $r_e{}^{c}$ represent the ASRs for an oxygen ion and electron, respectively, at the cathode–electrolyte interface; and $r_{O^{2-}}{}^{a}$ and $r_e{}^{a}$ denote the ASRs for an oxygen ion and electron, respectively, at the anode–electrolyte interface.

Under normal operating conditions, oxygen ions are transported through the electrolyte at a positive (+) voltage from the cathode to the anode. Thus, the sign of the ionic current density is $I_i < 0$. Furthermore, because the cathode is at a higher

electric potential φ than the anode, electrons are transported through the electrolyte from the anode to the cathode, and the sign of the electron current density is $I_e > 0$. This is reflected in Eqs. (6.7) and (6.8), which can be used to obtain the following relationship:

$$\mu_{O_2}{}^{I} \geq \mu_{O_2}{}^{c} \rangle \ \mu_{O_2}{}^{a} \geq \mu_{O_2}{}^{II} \tag{6.9}$$

This means that the chemical potential of the oxygen inside the electrolyte is within the ranges of the oxygen chemical potential of the two electrodes (porous).

In the case where the cells operate at a negative (−) voltage, the oxygen ions are transported through the electrolyte from the cathode to the anode (as with the positive voltage), and the sign of the ion current density is $I_i < 0$. However, for the transport of electrons, a high electric potential φ is formed at the anode owing to the negative (−) voltage. Thus, the sign of the electron current density is also $I_e < 0$. In other words, the direction of the current for electrons becomes identical to that of the ions. If this is described using Eq. (6.7), the following relationship is established:

$$\mu_{O_2}{}^{I} >=< \mu_{O_2}{}^{c}, \ \mu_{O_2}{}^{a} >=< \mu_{O_2}{}^{II} \tag{6.10}$$

As I_i and I_e are currents in the same direction, the chemical potential inside the electrolyte can be outside of the ranges of the oxygen chemical potential of the two electrodes. In other words, an abnormally large or small μ_{O_2} can form inside the electrolyte, and the oxygen chemical potential becomes unpredictable.

An experiment was conducted to simulate the degradation due to a negative (−) voltage occurring in a stack composed of cells using the original YSZ electrolyte [139]. During negative (−) voltage operation, decreases in both the power density and open-circuit voltage were observed. Furthermore, delamination at the interface between the anode and the electrolyte was also observed during a post-analysis using a scanning electron microscope. Therefore, the high oxygen partial pressure inside the electrolyte during operation at a negative (−) voltage causes delamination (degradation).

However, in the case of YSZ that is doped to enhance the electron conduction, the occurrence of a high oxygen partial pressure at the cathode/electrolyte interface at negative (−) voltages is mitigated owing to the electron conduction; therefore, the interface does not show delamination (degradation) [140]. This can be explained by the following equations:

$$\frac{1}{2}\triangle\mu_{O_2} = \triangle\tilde{\mu}_{O^{2-}} + 2e\triangle\varphi \tag{6.11}$$

$$\frac{1}{2}\left(\mu_{O_2}{}^{a} - \mu_{O_2}{}^{II}\right) = \left(\tilde{\mu}_{O^{2-}}{}^{a} - \tilde{\mu}_{O^{2-}}{}^{II}\right) + 2e\left(\varphi^{a} - \varphi^{II}\right) \tag{6.12}$$

Equations (6.11) and (6.12) represent the variation in the potential inside the electrolyte. At a negative (−) voltage, the variation in φ ($\varphi^{a} - \varphi^{II}$) becomes smaller owing to the electron conduction, and this decreases the variation in the oxygen chemical potential (oxygen partial pressure) in the corresponding region [140]. In other words, the electron conductivity inside the electrolyte can relieve the abnormal oxygen chemical potential at the electron–electrolyte interface at a negative (−) voltage, thus preventing physical degradation (delamination). However, an electrolyte with a higher electron conduction has a disadvantage because it can decrease basic performance metrics such as the open-circuit voltage of the fuel cell. In other words, YSZ with pure ionic conductivity is preferred from a performance point of view, and doped YSZ with an increased electron conduction is preferred from a stack degradation point of view. Therefore, to achieve both high stability and performance for SOFCs, a bilayered electrolyte was devised by arranging doped YSZ for enhanced electron conduction at the anode/electrolyte interface (where delamination can occur owing to the formation of a high oxygen partial pressure during operation at a negative (−) voltage) with YSZ with a predominant ionic conduction placed at the cathode/electrolyte interface [141].

To apply this electrolyte with a new structure, planar-type anode-supported cells with a size of 25 cm^2 (5 cm × 5 cm) were fabricated and subjected to degradation rate/durability tests at a negative (−) voltage [142]. The solid oxide fuel cell typically consists of six layers, as shown in Fig. 6.24. The AS (Ni + YSZ) and anode functional layer (AFL, Ni + YSZ) can be prepared through the tape casting method, which is advantageous in terms of the productivity and cost. The electrolyte layer is fabricated by the drop coating method. For the bilayered electrolyte, an 8 mol% ceria-doped YSZ (8CYSZ) layer is deposited onto the anode (AFL, Ni + YSZ) through a thermal treatment process for 1 h at 1050 °C, followed by depositing a YSZ layer onto the 8CYSZ layer. Then, it is sintered for 4 h at 1400–1450 °C. The total thickness of the electrolyte is ~15 μm. The cathode functional layer (CFL) and cathode current collector (CC) are screen-printed onto the surface of the sintered electrolyte and heat-treated at 1170 and 1160 °C,

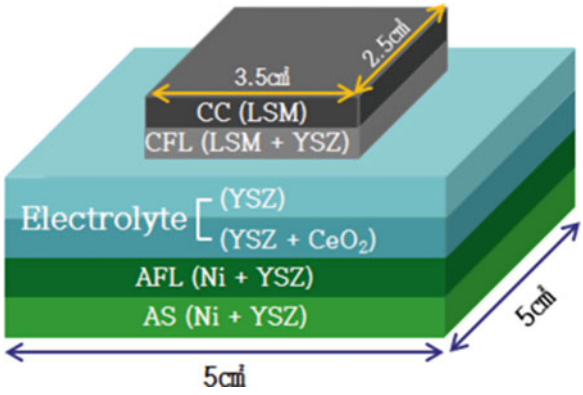

Fig. 6.24 Schematic of an anode-supported cell including a bilayered electrolyte [142]

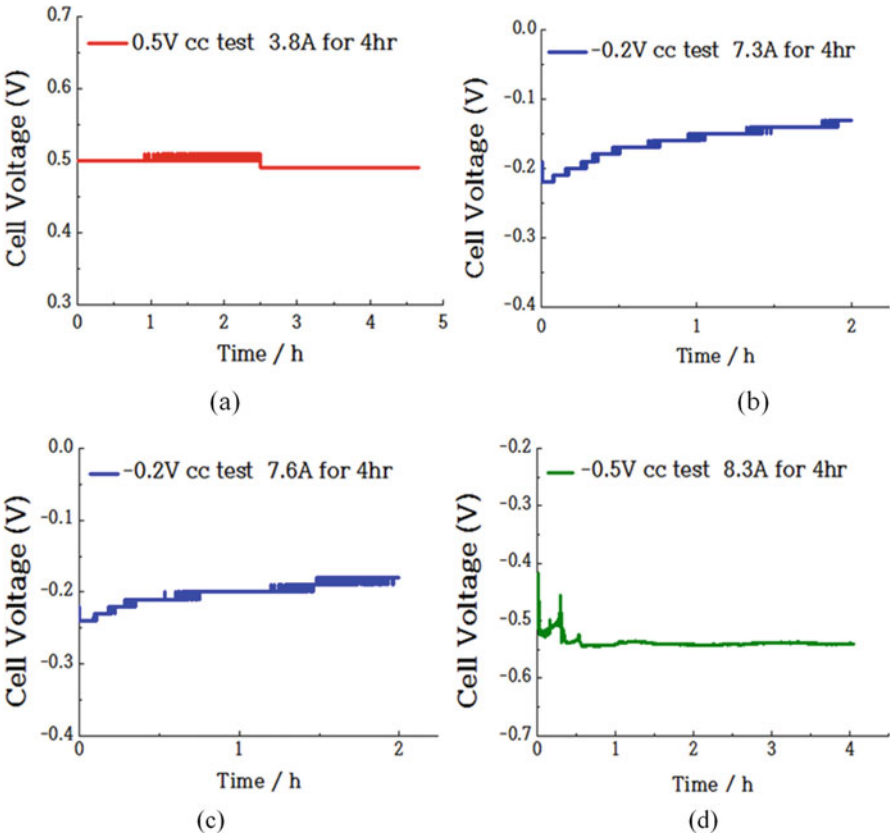

Fig. 6.25 Plots of the cell voltage versus time (**a**) at ~3.8 A (0.5 V) for 4 h, (**b**) at ~7.3 A (−0.2 V) for 2 h, (**c**) at ~7.6 A (−0.2 V) for 2 h, and (**d**) at ~8.3 A (−0.5 V) for 4 h [142]

respectively. La–Sr–Mn oxide (LSM) is commonly used for the cathode in SOFCs. The cell area is 25 cm^2 (5 cm × 5 cm), and the cathode active area is 8.75 cm^2 (2.5 cm × 3.5 cm), as shown in Fig. 6.24.

Figure 6.25a shows a graph of the voltage changes during a test at a constant current for the abovementioned bilayered cell; the test continued for 5 h at 3.8 A (~0.5 V), and no voltage drop was observed. Figure 6.25b, c shows the cell voltage versus time at a negative (−) voltage for approximately 4 h at 7.3–7.6 A (−0.2 V). For the first 2 h, the voltage increased from −0.21 V to −0.13 V, as shown in Fig. 6.25b. For the next 2 h, the test was conducted around 7.6 A, and the voltage changed from −0.22 V to −0.18 V, as shown in Fig. 6.25c. This suggests that even during abnormal (negative voltage) operation, the performance did not decrease (performance increased slightly). Figure 6.25d shows a test at a higher constant current for 4 h at 8.3 A (−0.5 V); the voltage increased from −0.508 V to −0.54 V. Figure 6.26 shows a graph comparing the power density after the test at a constant

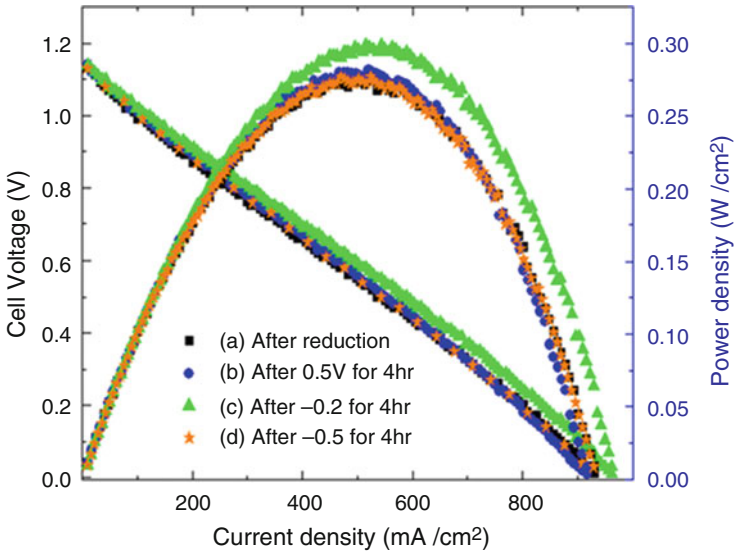

Fig. 6.26 Voltage versus the current density and power density for the planar-type cell corresponding to (**a**) the initial test, (**b**) after operation at ~0.5 V for 4 h, (**c**) after operation at approximately −0.2 V for 4 h, and (**d**) after operation under approximately −0.5 V for 4 h [142]

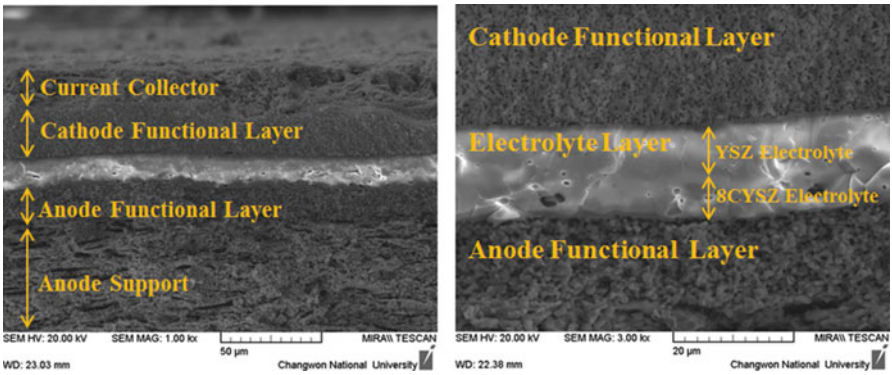

Fig. 6.27 SEM micrographs of the cross section of a planar-type cell after operation at a negative voltage, showing that the anode is bound to the electrolyte well [142]

current with the positive and negative (−) voltages immediately after NiO reduction. It is noted that the bilayered cell showed high open-circuit voltages (>1 V) due to the YSZ electron-blocking layer. No reduction in the power density was observed in long-term negative (−) voltage tests at −0.2 V (4 h) and −0.5 V (4 h); in particular, the performance increased slightly after operation at −0.2 V. This seems to be an effect of the current treatment of the cathode. Figure 6.27 shows the results of an SEM analysis after the tests; no delamination between the electrode and the

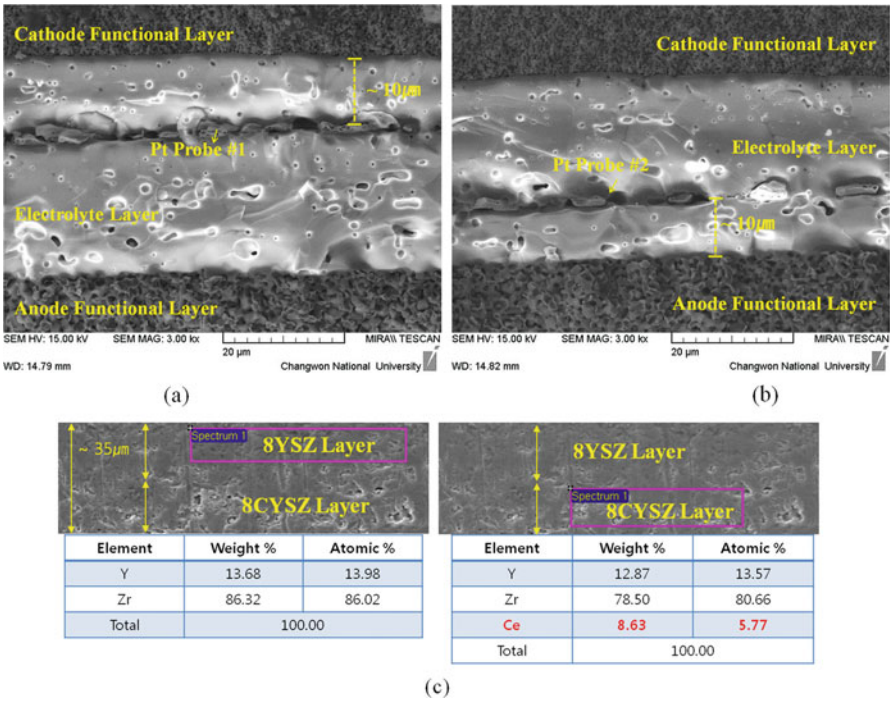

Fig. 6.28 SEM images of the cross section of a bilayered electrolyte: (**a**) Pt probe #1 embedded in the YSZ electrolyte ~10 μm from the cathode interface, (**b**) Pt probe #2 embedded in 8CYSZ ~10 μm from the anode interface, and (**c**) the boundary between the YSZ layer (17–18 μm) and the 8CYSZ layer (17–18 μm) with the EDS analysis results [141]

electrolyte of the cell was observed after the negative (−) voltage test, i.e., no degradation (delamination) occurred owing to the increase in the oxygen partial pressure inside the electrolyte in the bilayered cells, even under abnormal operation at a negative (−) voltage.

The reduction in the oxygen partial pressure inside the electrolyte can be explained using quantitative oxygen partial pressure measurements conducted by inserting a reference electrode into the electrolyte. Figure 6.28 shows Pt reference electrodes embedded in the bilayered cell [141]. In the open-circuit condition, the change in the electrochemical potential of the oxygen ions is equal to zero; thus, the equation relating the variation in φ to the variation in μ_{O_2} can be written as $\nabla\varphi = \frac{1}{4e}\nabla\mu_{O_2}$. Therefore, the variation in the chemical potential of the oxygen inside the electrolyte can be calculated as follows:

$$\Delta\varphi = \left(\varphi^{\mathrm{Ref}} - \varphi^{\mathrm{Anode}}\right) = \frac{\left(\mu_{O_2}{}^{\mathrm{Ref}} - \mu_{O_2}{}^{\mathrm{Anode}}\right)}{4e} = \frac{kT}{4e}\ln\left(\frac{P_{O_2}{}^{\mathrm{Ref}}}{P_{O_2}{}^{\mathrm{Anode}}}\right) \qquad (6.13)$$

where $\triangle\varphi = (\varphi^{\mathrm{Ref}} - \varphi^{\mathrm{Anode}})$ indicates the voltage change from a point inside the electrolyte to the anode, which can be measured experimentally using a reference electrode. As a result of measuring the oxygen partial pressure of the pure YSZ electrolyte, the oxygen partial pressure of the electrolyte about 10 μm away from the anode was determined to be approximately 1.00×10^{-5} atm. For the 8CYSZ electrolyte, however, the oxygen partial pressure in the electrolyte about 10 μm away from the cathode was approximately 8.19×10^{-17} atm, which is lower by ~10^{12} compared to YSZ with no ceria [141]. This difference was caused by the electron conduction developed by the reduction of ceria in 8CYSZ. Consequently, the bilayered electrolyte with a locally increased electron conduction was effective in preventing delamination due to degradation while maintaining the basic performance of the cells. Furthermore, because this bilayered structure is applicable to all electrochemical cells connected in series and SOFCs, it can prevent degradation due to cell imbalance.

6.4 Conclusion

SOFCs can provide up to 70% efficiency in combined power generation systems. In order to meet the demand for sustainable energy sources and to secure competitive prices for the commercialization of SOFC systems, low-temperature SOFC technology is necessary. This requires the development of novel electrolyte/electrode materials that display both high performance and long-term durability, and accordingly, the appropriate process technologies should be developed for these materials. Using room-temperature film deposition technology, both dense and porous membranes of different thicknesses can be achieved with acceptable electrochemical performance. Moreover, the cell configuration and material composition play important roles in the lifetime of the SOFC stack, and a new concept for the cell configuration can be realized with different coating technologies.

References

1. J. Fergus, R. Hui, X. Li, D.P. Wilkinson, J.J. Zhang, *Solid Oxide Fuel Cells: Materials Properties and Performance* (CRC Press, London, 2009)
2. S.C. Singhal, K. Kendall, *High Temperature Solid Oxide Fuel Cells: Fundamentals, design and applications* (Elsevier Ltd, Amsterdam, 2003)
3. D.K. Lim, J.G. Guk, H.S. Choi, S.J. Song, Measurement of partial conductivity of 8YSZ by Hebb-Wagner polarization method. J. Kor. Ceram. Soc. **52**, 299–303 (2015)
4. I.Y. Jung, D.H. Lee, S.O. Lee, D.H. Kim, J.S. Kim, S.H. Hyun, J.H. Moon, LSCM-YSZ nanocomposites for a high performance SOFC anode. Ceram. Int. **39**, 9753–9758 (2013)
5. M. Toshiaki, M. Yuichi, M. Hiroki, E. Koichi, Influence of (La,Sr)$MnO_{3+\delta}$ cathode composition on cathode/electrolyte interfacial structure during long-term operation of solid oxide fuel cells. J. Power Sources **242**, 790–796 (2013)

6. T.H. Shin, M. Shin, G.W. Park, S. Lee, S.K. Woo, J. Yu, Fabrication and characterization of oxide ion conducting films, $Zr_{1-x}M_xO_{2-\delta}$ (M=Y, Sc) on porous SOFC anodes, prepared by electron beam physical vapor deposition. Sustain. Energy Fuels **1**, 103–111 (2017)
7. H.Z. Wang, Z. Gao, S.A. Barnett, Anode-supported solid oxide fuel cells fabricated by single step reduced-temperature co-firing. J. Electrochem. Soc. **163**, 196–201 (2016)
8. B. Timurkutluk, C. Timurkutluk, M.D. Mat, Y. Kaplan, Development of high-performance anode supported solid oxide fuel cell. Int. J. Energy Res. **36**, 1383–1387 (2012)
9. S.P.S. Badwal, K. Foger, Solid oxide electrolyte fuel cell review. Ceram. Int. **22**, 257–265 (1996)
10. K. Huang, S.C. Singhal, Cathode-supported tubular solid oxide fuel cell technology. A critical review. J. Power Sources **237**, 84–97 (2013)
11. D. Stolten, B. Emonts, P. Heidebrecht, S. Piewek, K. Sundmacher, *Fuel Cell Science and Engineering: Materials, Processes, systems and technology* (Wiley-VCH, Weinheim, 2012)
12. Z. Lu, X.D. Zhou, D. Fisher, J. Templeton, J. Stevenson, N. Wu, A. Ignatiev, Enhanced performance of an anode-supported YSZ thin electrolyte fuel cell with a laser-deposited $Sm_{0.2}$ $Ce_{0.8}$ $O_{1.9}$ interlayer. Electrochem. Commun. **12**, 179–182 (2010)
13. EG & G Technical Services, *Fuel Cell Handbook*, 5th edn. (Parsons, Inc, Morgan, 2000)
14. D. Perednis, L.J. Gauckler, Solid oxide fuel cells with electrolytes prepared via spray pyrolysis. Solid State Ionics **166**, 229–239 (2004)
15. M.J. Santillán, A. Caneiro, N. Quaranta, A.R. Boccaccini, Electrophoretic deposition of $La_{0.6}Sr_{0.4}Co_{0.8}Fe_{0.2}O_{3-\delta}$ cathodes on $Ce_{0.9}Gd_{0.1}O_{1.95}$ substrates for intermediate temperature solid oxide fuel cell (IT-SOFC). J. Eur. Ceram. Soc. **29**, 1125–1132 (2009)
16. M. Matsuda, T. Hosomia, K. Murata, T. Fukui, M. Miyake, Fabrication of bilayered YSZ/SDC electrolyte film by electrophoretic deposition for reduced-temperature operating anode-supported SOFC. J. Power Sources **165**, 102–107 (2007)
17. I. Muneeb, S. Khurram, R. Rizwan, A. Anwar, T. Pankaj, Z. Bin, R. Asia, A. Amjad, K.U. Muhammad, U. Arslan, A brief description of high temperature solid oxide fuel cell's operation, materials, design, fabrication technologies and performance. Appl. Sci. **6**, 75 (2016)
18. Y.J. Leng, S.H. Chan, K.A. Khor, S.P. Jiang, P. Cheang, Effect of characteristics of Y_2O_3/ZrO_2 powders on fabrication of anode-supported solid oxide fuel cells. J. Power Sources **117**, 26–34 (2003)
19. W. Li, K. Hasinska, M. Seabaugh, S. Swartz, J. Lannutti, Curvature in solid oxide fuel cells. J. Power Sources **138**, 145–155 (2004)
20. M.F. Carolan, J.N. Michaels, Growth rates and mechanism of electrochemical vapor deposited yttria-stabilized zirconia films. Solid State Ionics **37**, 189–196 (1990)
21. H.Y. Jung, K.S. Hong, H. Kim, J.K. Park, J.W. Son, J. Kim, H.W. Lee, J.H. Lee, Characterization of thinfilm YSZ deposited via EB-PVD technique in anode-supported SOFCs. J. Electrochem. Soc. **153**, 961–966 (2006)
22. T. Ishihara, K. Sato, Y. Takita, Electrophoretic deposition of Y_2O_3-stabilized ZrO_2 electrolyte films in solid oxide fuel cells. J. Am. Ceram. Soc. **79**, 913–919 (1996)
23. T. Setoguchi, M. Sawano, K. Eguchi, H. Arai, Application of the stabilized zirconia thin film prepared by spray pyrolysis method to SOFC. Solid State Ionics **40-41**, 502–505 (1990)
24. M. Gaudon, C.L. Robert, F. Ansart, P. Stevens, Thick YSZ films prepared via a modified sol-gel route: thickness control (8~80 mm). J. Eur. Ceram. Soc. **26**, 3153–3160 (2006)
25. G. Schiller, R.H. Henne, M. Lang, R. Ruckdaeschel, S. Schaper, Development of vacuum plasma sprayed thinfilm SOFC for reduced operating temperature. Fuel Cells Bulletin **21**, 7–12 (2000)
26. N.A. Baharuddin, A. Muchtar, M.R. Somalu, Short review on cobalt-free cathodes for solid oxide fuel cells. Int. J. Hydrog. Energy **42**, 9149–9155 (2017)
27. A. Tarancón, M. Burriel, J. Santiso, S.J. Skinner, J.A. Kilner, Advances in layered oxide cathodes for intermediate temperature solid oxide fuel cells. J. Mater. Chem. **20**, 3799–3813 (2010)

28. F.S. Baumann, J. Fleig, H.U. Habermeier, J. Maier, $Ba_{0.5}Sr_{0.5}Co_{0.8}Fe_{0.2}O_{3-\delta}$ thin film microelectrodes investigated by impedance spectroscopy. Solid State Ionics **177**, 3187–3191 (2006)
29. F.S. Baumann, J. Maier, J. Fleig, The polarization resistance of mixed conducting SOFC cathodes: A comparative study using thin film model electrodes. Solid State Ionics **179**, 1198–1204 (2008)
30. A. Bieberle-Hütter, M. Søgaard, H.L. Tuller, Electrical and electrochemical characterization of microstructured thin film $La_{1-x}Sr_xCoO_3$ electrodes. Solid State Ionics **177**, 1969–1975 (2006)
31. A. Bieberle-Hütter, H.L. Tuller, Fabrication and structural characterization of interdigitated thin film $La_1 - X\ Sr_xCoO_3$ (LSCO) electrodes. J. Electroceram. **16**, 151–157 (2006)
32. N. Grunbaum, L. Mogni, F. Prado, Phase equilibrium and electrical conductivity of $SrCo_{0.8}Fe_{0.2}O_{3-\delta}$. J. Solid State Chem. **177**, 2350–2357 (2004)
33. J.A. Lane, S.J. Benson, D. Waller, J.A. Kilner, Oxygen transport in $La_{0.6}Sr_{0.4}Co_{0.2}Fe_{0.8}O_{3-\delta}$. Solid State Ionics **121**, 201–208 (1999)
34. F. Prado, T. Armstrong, A. Caneiro, A. Manthiram, Structural stability and oxygen permeation properties of $Sr_{3-x}La_xFe_{2-y}Co_yO_{7-\delta}$ ($0 \leq x \leq 0.3$ and $0 \leq y \leq 1.0$). J. Electrochem. Soc. **148**, J7–J14 (2001)
35. J.A. Kilner, C.K.M. Shaw, Mass transport in $La_2Ni_{1-x}Co_xO_{4+\delta}$ oxides with the K_2NiF_4 structure. Solid State Ionics **154-155**, 523–527 (2002)
36. M. Burriel, S. Wilkins, J.P. Hill, M.A. Munoz-Marquez, H.H. Brongersma, J.A. Kilner, M.P. Ryana, S.J. Skinner, Absence of Ni on the outer surface of Sr doped La_2NiO_4 single crystals. Energy Environ. Sci. **7**, 311–316 (2014)
37. G. Kim, S. Wang, A.J. Jacobson, Z. Yuan, W. Donner, C.L. Chen, L. Reimus, P. Brodersen, C.A. Mims, Oxygen exchange kinetics of epitaxial $PrBaCo_2O_{5+\delta}$ thin films. Appl. Phys. Lett. **88**, 1–3 (2006)
38. J.H. Kim, A. Manthiram, $LnBaCo_2O_{5+\delta}$ oxides as cathodes for intermediate-temperature solid oxide fuel cells. J. Electrochem. Soc. **155**, B385–B390 (2008)
39. J.H. Kim, F. Prado, A. Manthiram, Characterization of $GdBa_{1-x}Sr_xCo_2O_{5+\delta}$ ($0 \leq x \leq 1.0$) double perovskites as cathodes for solid oxide fuel cells. J. Electrochem. Soc. **155**, B1023–B1028 (2008)
40. F. Mauvy, C. Lalanne, J.M. Bassat, J.C. Grenier, H. Zhao, L. Huo, P. Stevens, Electrode properties of $Ln_2NiO_{4+\delta}$ (Ln=La, Nd, Pr): AC impedance and DC polarization studies. J. Electrochem. Soc. **153**, A1547–A1553 (2006)
41. S.J. Skinner, Recent advances in perovskite-type materials for solid oxide fuel cell cathodes. Int. J. Inorg. Mater. **3**, 113–121 (2001)
42. S.J. Skinner, J.A. Kilner, Oxygen diffusion and surface exchange in $La_{2-x}Sr_xNiO_{4+\delta}$. Solid State Ionics **135**, 709–712 (2000)
43. Q. Zhou, T. He, Y. Ji, $SmBaCo_2O_{5+x}$ double-perovskite structure cathode material for intermediate-temperature solid-oxide fuel cells. J. Power Sources **185**, 754–758 (2008)
44. A. Tarancón, S.J. Skinner, R.J. Chater, F.H. Ramírez, J.A. Kilner, Layered perovskites as promising cathodes for intermediate temperature solid oxide fuel cells. J. Mater. Chem. **17**, 3175–3181 (2007)
45. T. Horita, H. Kishimoto, K. Yamaji, Y. Xiong, N. Sakai, M.E. Brito, H. Yokokawa, Materials and reaction mechanisms at anode/electrolyte interfaces for SOFCs. Solid State Ionics **177**, 1941–1948 (2006)
46. M. Mogensen, S. Skaarup, Kinetic and geometric aspects of solid oxide fuel cell electrodes. Solid State Ionics **86-88**, 1151–1160 (1996)
47. P. Holtappels, F.W. Poulsen, M. Mogensen, Electrical conductivities and chemical stabilities of mixed conducting pyrochlores for SOFC applications. Solid State Ionics **135**, 675–679 (2000)
48. M. Mogensen, K.V. Jensen, M.J. Jørgensen, S. Primdahl, Progress in understanding SOFC electrodes. Solid State Ionics **150**, 123–129 (2002)

49. M. Mogensen, N.M. Sammes, G.A. Tompsett, Physical, chemical and electrochemical properties of pure and doped ceria. Solid State Ionics **129**, 63–94 (2000)
50. S. Primdahl, B.F. Sørensen, M. Mogensen, Effect of nickel oxide/yttria-stabilized zirconia anode precursor sintering temperature on the properties of solid oxide fuel cells. J. Am. Ceram. Soc. **83**, 489–494 (2000)
51. S. Primdahl, M. Mogensen, Mixed conductor anodes: Ni as electrocatalyst for hydrogen conversion. Solid State Ionics **152-153**, 597–608 (2002)
52. P. Holtappels, L.G.J. De Haart, U. Stimming, Reaction of hydrogen/water mixtures on nickel-zirconia cermet electrodes I. DC polarization characteristics. J. Electrochem. Soc. **146**, 1620–1625 (1999)
53. P. Holtappels, I.C. Vinke, L.G.J. De Haart, U. Stimming, Reaction of hydrogen/water mixtures on nickel-zirconia cermet electrodes II. AC polarization characteristics. J. Electrochem. Soc. **146**, 2976–2982 (1999)
54. D. Simwonis, F. Tietz, D. Stöver, Nickel coarsening in annealed Ni/8YSZ anode substrates for solid oxide fuel cells. Solid State Ionics **132**, 241–251 (2000)
55. S.J. Tao, T.S. Irvine, Synthesis and characterization of $(La_{0.75}Sr_{0.25})Cr_{0.5}Mn_{0.5}O_{3-\delta}$, a redox-stable, efficient perovskite anode for SOFCs. J. Electrochem. Soc. **151**, A252–A259 (2004)
56. A.V. Virkar, J. Chen, C.W. Tanner, J.W. Kim, The role of electrode microstructure on activation and concentration polarizations in solid oxide fuel cells. Solid State Ionics **131**, 189–198 (2000)
57. W.Z. Zhu, S.C. Deevi, A review on the status of anode materials for solid oxide fuel cells. Mater. Sci. Eng. A **362**, 228–239 (2003)
58. O.A. Marina, C. Bagger, S. Primdahl, M. Mogensen, A solid oxide fuel cell with a gadolinia-doped ceria anode: preparation and performance. Solid State Ionics **123**, 199–208 (1999)
59. A. Atkinson, B. Sun, Residual stress and thermal cycling of planar solid oxide fuel cells. Mater. Sci. Technol. **23**, 1135–1143 (2007)
60. Q.X. Fu, F. Tietz, Ceramic-based anode materials for improved redox cycling of solid oxide fuel cells. Fuel Cells **8**, 283–293 (2008)
61. L.J. Gauckler, D. Beckel, B.E. Buergler, J. Eva, U.P. Muecke, M. Prestat, J.L.M. Rupp, R. Jörg, Solid oxide fuel cells: systems and materials. CHIMIA Int. J. Chem. **58**, 837–850 (2004)
62. N.H. Menzler, F. Tietz, S. Uhlenbruck, H.P. Buchkremer, D. Stöver, Materials and manufacturing technologies for solid oxide fuel cells. J. Mater. Sci. **45**, 3109–3135 (2010)
63. B.C.H. Steele, I. Kelly, H. Middleton, R. Rudkin, Oxidation of methane in solid state electrochemical reactors. Solid State Ionics **28-30**, 1547–1552 (1988)
64. S. Tao, J.T.S. Irvine, J.A. Kilner, An efficient solid oxide fuel cell based upon single-phase perovskites. Adv. Mater. **17**, 1734–1737 (2005)
65. A. Atkinson, S. Barnett, R.J. Gorte, J.T.S. Irvine, A.J. McEvoy, M. Mogensen, S.C. Singhal, J. Vohs, Advanced anodes for high-temperature fuel cells. Nat. Mater. **3**, 17–27 (2004)
66. S. Tao, J.T.S. Irvine, Discovery and characterization of novel oxide anodes for solid oxide fuel cells. Chem. Rec. **4**, 83–95 (2004)
67. P. Huang, A. Horky, A. Petric, Interfacial reaction between nickel oxide and lanthanum gallate during sintering and its effect on conductivity. J. Am. Ceram. Soc. **82**, 2402–2406 (1999)
68. B.C.H. Steele, I. Kelly, H. Middleton, R. Rudkin, Oxidation of methane in solid-state electrochemical reactors. Solid State Ionics **28**, 1547–1552 (1988)
69. E.P. Murray, T. Tsai, S.A. Barnett, A direct-methane fuel cell with a ceria-based anode. Nature **400**, 649–651 (1999)
70. G. Kim, S. Lee, J.Y. Shin, G. Corre, J.T.S. Irvine, J.M. Vohs, R.J. Gort, Investigation of the structural and catalytic requirements for high-performance SOFC anodes formed by infiltration of LSCM. Electrochem. Solid-State Lett. **12**, B48–B52 (2009)
71. M.D. Gross, J.M. Vohs, R.J. Gorte, Recent progress in SOFC anodes for direct utilization of hydrocarbons. J. Mater. Chem. **17**, 3071–3077 (2007)

72. R.J. Gorte, S. Park, J.M. Vohs, C. Wang, Anodes for direct oxidation of dry hydrocarbons in a solid-oxide fuel cell. Adv. Mater. **12**, 1465–1469 (2000)
73. S. Park, R.J. Gorte, J.M. Vohs, Applications of heterogeneous catalysis in the direct oxidation of hydrocarbons in a solid-oxide fuel cell. Appl. Catal. A Gen. **200**, 55–61 (2000)
74. S. Park, J.M. Vohs, R.J. Gorte, Direct oxidation of hydrocarbons in a solid-oxide fuel cell. Nature **404**, 265–267 (2000)
75. X.L. Yue, J.T.S. Irvine, Alternative cathode material for CO_2 reduction by high temperature solid oxide electrolysis cells. J. Electrochem. Soc. **159**, F442–F448 (2012)
76. S. Wang, H. Tsuruta, M. Asanuma, T. Ishihara, Ni–Fe–La(Sr)Fe(Mn)O_3 as a new active cermet cathode for intermediate-temperature CO_2 electrolysis using a $LaGaO_3$-based electrolyte. Adv. Energy Mater. **5**, 2 (2015)
77. Y. Li, J. Zhou, D. Dong, Y. Wang, J. Jiang, H. Xia, K. Xie, Composite fuel electrode $La_{0.2}Sr_{0.8}TiO_{3-\delta}$–$Ce_{0.8}Sm_{0.2}O_{2-\delta}$ for electrolysis of CO_2 in an oxygen-ion conducting solid oxide electrolyser. Phys. Chem. Chem. Phys. **14**, 15547–15553 (2012)
78. S.W. Lee, G.T. Kim, J.M. Vohsa, R.J. Gortea, SOFC anodes based on infiltration of $La_{0.3}Sr_{0.7}TiO_3$. J. Electrochem. Soc. **155**, B1179–B1183 (2008)
79. S. McIntosh, J.M. Vohs, R. Gorte, J. Electrochim, An examination of lanthanide additives on the performance of Cu–YSZ cermet anodes. Electrochim. Acta **47**, 3815 (2002)
80. S. McIntosh, J.M. Vohs, R.J. Gorte, Effect of precious-metal dopants on SOFC anodes for direct utilization of hydrocarbons. Solid-State Lett. **6**, A240 (2003)
81. S. McIntosha, S.B. Adlerb, J.M. Vohs, R.J. Gortea, Effect of polarization on and implications for characterization of LSM-YSZ composite cathodes J. Electrochem. Solid-State Lett. **7**, A111 (2004)
82. S. Tao, J.T.S. Irvine, A redox-stable efficient anode for solid-oxide fuel cells. Nat. Mater. **2**, 320–323 (2003)
83. J. Beckers, R. Drost, I.V. Zandvoort, P.F. Collignon, G. Rothenberg, Selective hydrogen oxidation in the presence of C_3 hydrocarbons using perovskite oxygen reservoirs. ChemPhysChem **9**, 1062–1068 (2008)
84. K. Kammer, E.M. Skou, LSFM perovskites as cathodes for the electrochemical reduction of NO. Solid State Ionics **176**, 915–920 (2005)
85. T.H. Shin, P. Vanalabhpatana, T. Ishihara, Oxide composite of Ce(Mn,Fe)O_2 and La(Sr)Fe(Mn)O_3 for anode of intermediate temperature solid oxide fuel cells using $LaGaO_3$ electrolyte. J. Electrochem. Soc. **157**, B1896–B1901 (2010)
86. T.H. Shin, S. Ida, T. Ishihara, Doped CeO_2–$LaFeO_3$ composite oxide as an active anode for direct hydrocarbon-type solid oxide fuel cells. J. Am. Chem. Soc. **133**, 19399–19407 (2011)
87. Y.H. Huang, R.I. Dass, Z.L. Xing, J.B. Goodenough, Double perovskites as anode materials for solid-oxide fuel cells. Science **312**, 254–257 (2006)
88. S. Sengodan, S. Choi, A. Jun, T.H. Shin, Y.W. Ju, H.Y. Jeong, J.Y. Shin, J.T.S. Irvine, G.T. Kim, Layered oxygen-deficient double perovskite as an efficient and stable anode for direct hydrocarbon solid oxide fuel cells. Nat. Mater. **14**, 205–209 (2015)
89. T.H. Shin, J.H. Myung, M. Verbraeken, G.T. Kim, J.T.S. Irvine, Oxygen deficient layered double perovskite as an active cathode for CO_2 electrolysis using a solid oxide conductor. Faraday Discuss. **182**, 227–239 (2015)
90. M. Burriel, H. Tellez, R.J. Chater, R. Castaing, P. Veber, M. Zaghrioui, T. Ishihara, J.A. Kilner, J.M. Bassat, Influence of crystal orientation and annealing on the oxygen diffusion and surface exchange of $La_2NiO_{4+\delta}$. J. Phys. Chem. C **120**, 17927–17938 (2016)
91. K. Zheng, A. Gorzkowska-Sobaś, K. Świerczek, Evaluation of Ln_2CuO_4 (Ln: La, Pr, Nd) oxides as cathode materials for IT-SOFCs. Mater. Res. Bull. **47**, 4089–4095 (2012)
92. Y.N. Kim, Y.N.A. Manthiram, $La_{1.85}Sr_{1.15}Cu_{2-x}Co_xO_{6+\delta}$ intergrowth oxides as cathodes for intermediate temperature solid oxide fuel cells. Electrochim. Acta **70**, 375–381 (2012)
93. E. Boehm, J.M. Bassat, M.C. Steil, P. Dordor, F. Mauvy, J.C. Grenier, Oxygen transport properties of $La_2Ni_{1-x}Cu_xO_{4+\delta}$ mixed conducting oxides. Solid State Sci. **5**, 973–981 (2003)

94. X. Huang, T.H. Shin, J. Zhoua, J.T.S. Irvine, Hierarchically nanoporous $La_{1.7}Ca_{0.3}CuO_{4-\delta}$ and $La_{1.7}Ca_{0.3}Ni_xCu_{1-x}O_{4-\delta}$ ($0.25 \leq x \leq 0.75$) as potential cathode materials for IT-SOFCs. J. Mater. Chem. A **3**, 13468–13475 (2015)
95. F. Tonus, M. Bahout, V. Dorcet, G.H. Gauthier, S. Paofai, R.I. Smithd, S.J. Skinner, Redox behavior of the SOFC electrode candidate $NdBaMn_2O_{5+}$ d investigated by high-temperature in situ neutron diffraction: first characterisation in real time of an $LnBaMn_2O_{5.5}$ intermediate phase. J. Mater. Chem. A **4**, 11635–11647 (2016)
96. I. Hamada, A. Uozumi, Y. Morikawa, A. Yanase, H.K. Yoshida, A density functiona2l theory study of self-regenerating catalysts $LaFe_{1-x}M_xO_{3-y}$ (M = Pd, Rh, Pt). J. Am. Chem. Soc. **133**, 18506–18509 (2011)
97. D.M. Bierschenk, E. Potter-Nelson, C. Hoelb, Y. Liao, L. Marks, K.R. Poeppelmeier, S.A. Barnett, Pd-substituted (La,Sr)$CrO_{3-\delta}$-$Ce_{0.9}Gd_{0.1}O_{2-\delta}$ solid oxide fuel cell anodes exhibiting regenerative behavior. J. Power Sources **196**, 3089–3094 (2011)
98. T.H. Shin, Y. Okamoto, S. Ida, T. Ishihara, Self-recovery of Pd nanoparticles that were dispersed over La(Sr)Fe(Mn)O_3 for intelligent oxide anodes of solid-oxide fuel cells. Chem. Eur. J. **18**, 11695 (2012)
99. D. Neagu, T.S. Oh, D.N. Miller, H. Ménard, S.M. Bukhari, S.R. Gamble, R.J. Gorte, J.M. Vohs, J.T.S. Irvine, Nano-socketed nickel particles with enhanced coking resistance grown in situ by redox exsolution. Nat. Commun. **6**, 8120 (2015)
100. D. Neagu, G. Tsekouras, D.N. Miller, H. Ménard, J.T.S. Irvine, In situ growth of nanoparticles through control of non-stoichiometry. Nat. Chem. **5**, 916–923 (2013)
101. Y. Nishihata, J. Mizuki, T. Akao, H. Tanaka, M. Uenishi, M. Kimura, T. Okamoto, N. Hamada, Self-regeneration of a Pd-perovskite catalyst for automotive emissions control. Nature **418**, 164–167 (2002)
102. H. Tanaka, M. Uenishi, M. Taniguchi, I. Tan, K. Narita, M. Kimura, K. Kaneko, Y. Nishihata, J.H. Mizuki, The intelligent catalyst having the self-regenerative function of Pd, Rh and Pt for automotive emissions control. Catal. Today **117**, 321–328 (2006)
103. T.H. Shin, Y. Okamoto, S. Ida, T. Ishihara, Self-recovery of pd nanoparticles that were dispersed over La(Sr)Fe(Mn)O_3 for intelligent oxide anodes of solid-oxide fuel cells. Chemistry **18**, 11695–11702 (2012)
104. J.H. Myung, D. Neagu, D.N. Miller, J.T.S. Irvine, Switching on electrocatalytic activity in solid oxide cells. Nature **537**, 528–531 (2016)
105. J.J. Choi, S.H. Oha, H.S. Nohb, H.R. Kimb, J.W. Sonb, D.S. Parka, J.H. Choi, J.H. Ryua, B.D. Hahna, W.H. Yoon, H.W. Lee, Low temperature fabrication of nano-structured porous LSM–YSZ composite cathode film by aerosol deposition. J. Alloys Compd. **509**, 2627–2630 (2011)
106. J.J. Choi, J.H. Choi, J.H. Ryu, B.D. Hahn, J.W. Kim, C.W. Ahn, W.H. Yoon, D.S. Park, Low-temperature fabrication of nano-structured porous (La,Sr)(Co,Fe)$O_{3-\delta}$ cathodes by aerosol deposition. J. Alloys Compd. **545**, 186–189 (2012)
107. H. Tu, U. Stimming, Advances, aging mechanisms and lifetime in solid-oxide fuel cells. J. Power Sources **127**, 284 (2004)
108. Z. Yang, G. Xia, Z. Templeton, J. Nie, J.W. Stevenson, Ce-Modified $(Mn, Co)_3O_4$ spinel coatings on ferritic stainless steels for SOFC interconnect applications. Electrochem. Solid-State Lett. **11**, B140 (2008)
109. J.J. Choi, J.H. Lee, D.S. Park, B.D. Hahn, W.H. Yoon, H.T. Lim, Oxidation resistance coating of LSM and LSCF on SOFC metallic interconnects by the aerosol deposition process. J. Am. Ceram. Soc. **90**, 1926–1929 (2007)
110. J.J. Choi, D.S. Park, B.D. Hahn, J.H. Ryu, W.H. Yoon, Oxidation behavior of ferritic steel alloy coated with highly dense conducting ceramics by aerosol deposition. J. Am. Ceram. Soc. **91**, 2601–2606 (2008)
111. J.J. Choi, J.H. Ryu, B.D. Hahn, W.H. Yoon, B.K. Lee, D.S. Park, Dense spinel $MnCo_2O_4$ film coating by aerosol deposition on ferritic steel alloy for protection of chromic evaporation and low-conductivity scale formation. J. Mater. Sci. **44**, 843–848 (2009)

112. J.J. Choi, J.H. Ryu, B.D. Hahn, W.H. Yoon, B.K. Lee, J.H. Choi, D.S. Park, Ni-containing conducting ceramic as an oxidation protective coating on metallic interconnects by aerosol deposition. J. Am. Ceram. Soc. **93**, 1614–1618 (2010)
113. J. Akedo, M. Lebedev, U.S. Patent. Pub. No. US2005/0181208 A1 (2005)
114. D.S. Park, B.D. Hahn, J.J. Choi, W.H. Yoon, J. Ryu, Ceramics coating process technology by aerosol deposition. Machin. Mater. **18**, 6–20 (2006)
115. J. Choi, B. Han, D. Park, Machin. Mater. **18**, 21–38 (2006)
116. J.J. Choi, B.D. Hahn, J.H. Ryu, W.H. Yoon, D.S. Park, Effects of $Pb(Zn_{1/3}Nb_{2/3})O_3Pb(Zn_{1/3}Nb_{2/3})O_3$ addition and postannealing temperature on the electrical properties of $Pb(Zr_xTi_{1-x})O_3Pb(Zr_xTi_{1-x})O_3$ thick films prepared by aerosol deposition method. J. Appl. Phys. **102**, 044101 (2007)
117. J.J. Choi, J.H. Jang, B.D. Hahn, D.S. Park, W.H. Yoon, J.H. Ryu, C. Park, Preparation of highly dense PZN–PZT thick films by the aerosol deposition method using excess-PbO powder. J. Am. Ceram. Soc. **90**, 3389–3394 (2007)
118. J.H. Ryu, J.J. Choi, B.D. Hahn, D.S. Park, W.H. Yoon, K.H. Kim, Fabrication and ferroelectric properties of highly dense lead-free piezoelectric $(K_{0.5}Na_{0.5})NbO_3(K_{0.5}Na_{0.5})NbO_3$ thick films by aerosol deposition. Appl. Phys. Lett. **90**, 152901 (2007)
119. B.D. Hahn, J.M. Lee, D.S. Park, J.J. Choi, J.H. Ryu, W.H. Yoon, B.K. Lee, D.S. Shin, H.E. Kim, Mechanical and in vitro biological performances of hydroxyapatite–carbon nanotube composite coatings deposited on Ti by aerosol deposition. Acta Biomater. **5**, 3205–3214 (2009)
120. B.D. Hahn, D.S. Park, J.J. Choi, J.H. Ryu, W.H. Yoon, K.H. Kim, C. Park, H.E. Kim, Dense nanostructured hydroxyapatite coating on titanium by aerosol deposition. J. Am. Ceram. Soc. **92**, 683–687 (2009)
121. B.D. Hahn, D.S. Park, J.J. Choi, J.H. Ryu, W.H. Yoon, K.H. Kim, C. Park, H.E. Kim, Photocatalytic TiO2 thin films by aerosol-deposition: from micron-sized particles to nanograined thin film at room temperature. Appl. Catal. B Environ. **83**, 1–7 (2008)
122. J.H. Ryu, K.Y. Kim, B.D. Hahn, J.J. Choi, W.H. Yoon, B.K. Lee, D.S. Park, C. Park, Photocatalytic nanocomposite thin films of $TiO_{2-\beta}$-calcium phosphate by aerosol-deposition. Catal. Commun. **10**, 596–599 (2009)
123. J.J. Choi, K.S. Cho, J.H. Choi, J.H. Ryu, B.D. Hahn, W.H. Yoon, J.W. Kim, C.W. Ahn, J.D. Yun, D.S. Park, Low temperature preparation and characterization of LSGMC based IT-SOFC cell by aerosol deposition. J. Eur. Ceram. Soc. **32**, 115–121 (2012)
124. J.J. Choi, J.H. Choi, J.H. Ryu, B.D. Hahn, J.W. Kim, C.W. Ahn, W.H. Yoon, D.S. Park, Microstructural evolution of YSZ electrolyte aerosol-deposited on porous NiO-YSZ. J. Eur. Ceram. Soc. **32**, 3249–3254 (2012)
125. J.J. Choi, K.S. Cho, J.H. Choi, J.H. Ryu, B.D. Hahn, W.H. Yoon, J.W. Kim, C.W. Ahn, D.S. Park, J.D. Yun, Electrochemical effects of cobalt doping on $(La,Sr)(Ga,Mg)O_{3-\delta}$ electrolyte prepared by aerosol deposition. Int. J. Hydrog. Energy **37**, 6830–6835 (2012)
126. J.J. Choi, K.S. Cho, J.H. Choi, J. Ryu, B.D. Hahn, J.W. Kim, C.W. Ahn, W.H. Yoon, J. Yun, D.S. Park, Effects of annealing temperature on solid oxide fuel cells containing $(La,Sr)(Ga,Mg,Co)O_{3-\delta}$ electrolyte prepared by aerosol deposition. Mater. Lett. **70**, 44–47 (2012)
127. S.F. Wang, Y.F. Hsu, C.H. Wang, C.T. Yeh, Solid oxide fuel cells with $Sm_{0.2}Ce_{0.8}O_{2-\delta}$ electrolyte film deposited by novel aerosol deposition method. J. Power Sources **196**, 5064–5069 (2011)
128. J.J. Choi, D.S. Park, B.G. Seong, H.Y. Bae, Low-temperature preparation of dense $(Gd,Ce)O_{2-\delta}$–Gd_2O_3 composite buffer layer by aerosol deposition for YSZ electrolyte-based SOFC. Int. J. Hydrog. Energy **37**, 9809–9815 (2012)
129. H. Bae, J. Choi, G.M. Choi, Electrical conductivity of Gd-doped ceria film fabricated by aerosol deposition method. Solid State Ionics **236**, 16–21 (2013)
130. C.J. Li, C.X. Li, Y.Z. Xing, M. Gao, G.J. Yang, Influence of YSZ electrolyte thickness on the characteristics of plasma-sprayed cermet supported tubular SOFC. Solid State Ionics **177**, 2065–2069 (2006)

131. Y. Jiang, H. Song, J. Gao, G. Meng, Formation and rate processes of Y_2O_3 stabilized ZrO_2 thin films from $Zr(DPM)_4$ and $Y(DPM)_3$ by cold-wall aerosol-assisted MOCVD. J. Electrochem. Soc. **152**, C498–C503 (2005)
132. M. Liu, J. Gao, D. Dong, X. Liu, G. Meng, Comparative study on the performance of tubular and button cells with YSZ membrane fabricated by a refined particle suspension coating technique. Int. J. Hydrog. Energy **35**, 10489–10494 (2010)
133. M.V.F. Schlupp, M. Prestat, J. Martynczuk, J.L.M. Rupp, A. Bieberle-Hütter, L.J. Gauckler, Thin film growth of yttria stabilized zirconia by aerosol assisted chemical vapor deposition. J. Power Sources **202**, 47–55 (2012)
134. M. Haydn, K. Ortner, T. Franco, S. Uhlenbruck, N.H. Menzler, D. Stöver, G. Bräuer, A. Venskutonis, L.S. Sigl, H.P. Buchkremer, R. Vaßen, Multi-layer thin-film electrolytes for metal supported solid oxide fuel cells. J. Power Sources **256**, 52–60 (2014)
135. A.C. Johnson, A. Baclig, D.V. Harburg, B.K. Lai, S. Ramanathan, Fabrication and electrochemical performance of thin-film solid oxide fuel cells with large area nanostructured membranes. J. Power Sources **195**, 1149–1155 (2010)
136. K. Kerman, B.K. Lai, S. Ramanathan, Nanoscale compositionally graded thin-film electrolyte membranes for low-temperature solid oxide fuel cells. Adv. Energy Mater. **2**, 656–661 (2012)
137. J. Yanz, H. Matsumoto, M. Enoki, T. Ishihara, High-power SOFC using $La_{0.9}Sr_{0.1}Ga_{0.8}Mg_{0.2}O_{3-\delta}/Ce_{0.8}Sm_{0.2}O_{2-\delta}$ composite film. Electrochem. Solid-State Lett. **8**, A389–A391 (2005)
138. D. Berndt, U. Teutsch, Float charging of valve-regulated lead-acid batteries: a balancing act between secondary reactions. J. Electrochem. Soc. **143**, 790–798 (1996)
139. H.-T. Lim, A.V. Virkar, A study of solid oxide fuel cell stack failure by inducing abnormal behavior in a single cell test. J. Power Sources **185**, 790–800 (2008)
140. H.-T. Lim, A.V. Virkar, Electrochemical degradation of fuel cell: effect of electrolyte composition. ECS Trans. **25**, 447–456 (2009)
141. M.Y. Park, Y.G. Jung, H.-T. Lim, Delamination-resistant bi-layer electrolyte for anode-supported solid oxide fuel cells. Solid State Ionics **262**, 438–443 (2014)
142. M.Y. Park, H. Bae, H.-T. Lim, Bi-layer electrolyte for preventing solid oxide fuel cell stack degradation. J. Kor. Ceram. Soc. **51**, 289–294 (2014)

Chapter 7
Metallic Coatings in Solid-Phase Microextraction: Environmental Applications

Idaira Pacheco-Fernández, Adrián Gutiérrez-Serpa, Ana M. Afonso, and Verónica Pino

7.1 Introduction

Solid-phase microextraction (SPME) is a miniaturized extraction technique developed by Arthur and Pawliszyn in 1990 [1]. The first step of the microextraction procedure is based on the sorption of analytes onto the surface of a coated fiber when exposed to a sample. The extraction is followed by the later desorption of the trapped analytes to perform their analytical determination. Desorption can be carried out (1) by a thermal step: normally placing the SPME fiber in the hot injection port of a gas chromatograph (GC) or (2) by exposing the fiber to a small volume of organic solvent where analytes dissolve: normally when combining SPME with high-performance liquid chromatography (HPLC) or capillary electrophoresis (CE). Independently on the desorption step, the coating material of the SPME fiber is able to maintain its integrity and thus it can be reused in a high number of analyses. Figure 7.1 shows a scheme of the general procedure to carry out SPME analysis.

SPME is considered an environmental-friendly technique due to the reduction of organic solvents employed during the sample preparation, being even a solvent-free approach when combined with GC [2]. The procedure is also accompanied by high enrichment factors, with a maximum preconcentration easily estimated by the ratio sample volume/SPME coating volume (commonly 10–20 mL/0.5 μL). Thus, the technique is highly sensitive, simple, fast, portable, and can be automated. All these characteristics make SPME an attractive and potential technique compared to

I. Pacheco-Fernández • A. Gutiérrez-Serpa • A.M. Afonso • V. Pino (✉)
Departamento de Química, Unidad Departamental de Química Analítica, Universidad de La Laguna (ULL), La Laguna, Tenerife 38206, Spain
e-mail: veropino@ull.edu.es

J. Zhang, Y.-G. Jung (eds.), *Advanced Ceramic and Metallic Coating and Thin Film Materials for Energy and Environmental Applications*,
DOI 10.1007/978-3-319-59906-9_7

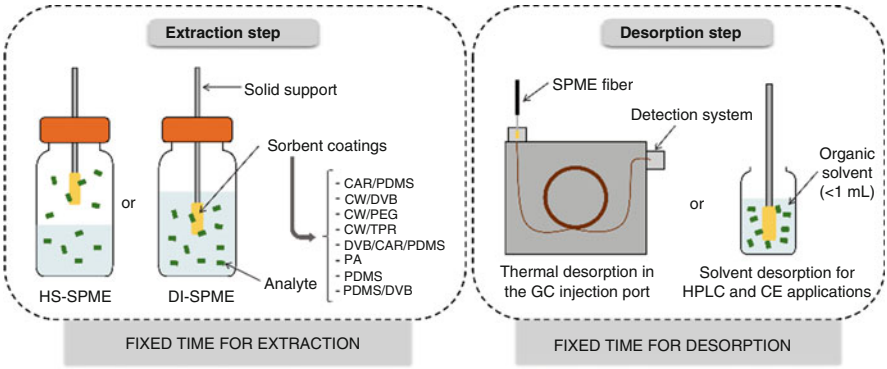

Fig. 7.1 General scheme for the extraction and desorption steps in the SPME analysis

conventional liquid-liquid extraction or other solid-phase extraction methods, conventionally used in sample preparation.

There are two main modes of operation in SPME: direct immersion (DI), in which the fiber is directly immersed into the aqueous sample; and headspace (HS), in which the fiber is exposed to the gas phase present between the sample (with solid or liquid nature) and the top of the vial [3], as shown in Fig. 7.1. The selection of each mode depends on the nature of the analytes to be determined and also on the type of sample. The DI-SPME mode is commonly used for semi-volatile and nonvolatile compounds present in aqueous samples, while the HS-SPME mode is employed for volatile compounds, which can be present in samples of high complexity. The versatility of this technique has made possible its introduction into several fields such as sampling and analysis of environmental [4], food [5], and biological samples [6], with successful results.

Environmental analysis is one of the most demanding areas in terms of sensitivity requirements, given the trace levels at which several contaminants are normally present. Traditional sample preparation methods for the analysis of this kind of samples are tedious, imply several steps and require large quantities of sample and toxic organic solvents. It results indeed paradoxical to utilize large amounts of organic solvents in environmental monitoring. In addition, the complexity of environmental samples and the presence of countless interferences in the matrix make their analysis quite challenging. The introduction of SPME has been an important breakthrough within the pretreatment of complex samples in analytical chemistry [7]. This technique has substantially reduced the errors associated to common sample preparation strategies due to the reduction of steps in the entire process. Furthermore, SPME allows sampling, extraction, and preconcentration of the compounds in a unique step, and even automatically. Its miniaturized size and design ensure portability, and thus SPME permits on-site analysis, driving out errors associated to sample transportation and conservation [4].

Main interactions between target compounds and SPME coatings are due to absorption or adsorption partitioning, highly dependent on the nature of the fiber

coating. In any case, the extraction efficiency not only depends on the strength of the partitioning analyte-coating, but also on the coating thickness of the SPME fiber, and on the extraction time. Clearly, thicker coatings are beneficial, but they require longer times to achieve equilibration, which is not always adequate for routine analysis. A compromise solution is normally required regarding extraction time. In any case, reproducible SPME measurements can be achieved as long as the extraction time is carefully controlled and kept constant for samples and standards.

Currently, eight different commercial SPME coatings are available in the market: polydimethylsiloxane (PDMS), polydimethylsiloxane/divinylbenzene (PDMS/DVB), carboxen/polydimethylsiloxane (CAR/PDMS), divinylbenzene/carboxen/polydimethylsiloxane (DVB/CAR/PDMS), polyacrylate (PA), carbowax/divinylbenzene (CW/DVB), carbowax/polyethylene glycol (CW/PEG), and carbowax/templated resin (CW/TPR). All commercial fibers have 1 cm length (to adequately fit in common GC liners), and thicknesses varying from 7 to 100 μm. Commercial fibers have the main advantage of providing comprehensive information regarding their sensitivity, accuracy, and repeatability because they have been subjected to a variety of interlaboratory validations and evaluation processes. Therefore, they are suitable for routine analysis [8]. However, commercial fibers also have some drawbacks: they are not selective, they present important carryover effects (particularly in HPLC and CE applications), and they present relatively low mechanical and thermal stability. The operating temperatures for most of the commercial fibers range from 240 to 280 °C, which is not enough to ensure the complete desorption of several heavy, nonvolatile compounds.

For all abovementioned reasons, efforts in last years have been shifted to the development of novel SPME sorbents, characterized for being chemically and thermally stable, mechanically robust, selective, low cost (if possible), and of easily preparation and processing [9–11]. Among them, it is important to highlight ionic liquids and polymeric ionic liquids [12], carbon nanotubes [13], graphene [14], molecularly-imprinted polymers [15], metal-organic frameworks [16], metal and metal oxides, and other nanomaterials, such as nanoporous silica [17] and nanostructured conducting polymers [18].

This chapter focuses on the description of the preparation, characterization, and performance of metal-based SPME coatings devoted to environmental analysis applications.

7.2 Synthesis and Development of Metallic SPME Coatings

A wide range of metal-based sorbents has been employed as coatings in SPME. These new type of stationary phases can be classified attending to their chemical nature in: metallic nanoparticles (NPs) coatings [19–29]; metal oxides coatings [30–43]; and hybrid coatings, composed by (i) metal NPs (or metal oxides) and other materials, or (ii) mixtures of different metallic materials [44–57]. The preparation of these new SPME fibers based on metallic coatings follows a general

procedure: first, the solid support is selected, then, its surface is cleaned-up and pretreated, afterwards, the sorbent is coated on the supporting substrate, and finally the resulting fiber is activated at high temperatures or by its immersion in an organic solvent.

The selection of an adequate solid support to prepare the SPME fiber has an important effect in the mechanical stability of the final coating [58]. Fused-silica (FS) has been the most common support employed to develop new SPME coatings due to its ease of functionalization, permitting a simple preparation of sorbents coatings chemically bonded to the solid support. However, FS fibers are fragile and their lifetime is short. In this sense, metallic supports such as silver wires (AgW), nitinol alloys (NiTi), and titanium wires (TiW) comprise a group of robust solid supports suitable for SPME applications. Nevertheless, as these materials are very expensive, stainless steel (SS) has become the most popular solid substrate for the preparation of SPME fibers in the recent years. Thus, the fabrication of metal-based SPME fibers for environmental applications includes as supports: SS [19, 22–24, 26–29, 33, 34, 42, 47–49, 51, 52, 56], NiTi wires [40, 44, 45, 55], TiW [35, 36, 41, 57], platinum wires (PtW) [31–33], FS [21, 37, 38], and copper wires (CuW) [20, 43, 53]. Aluminum wires (AlW) [30, 50], zinc wire (ZnW) [39], and Ag-Cu wires (Ag-CuW) [25] have also been employed but with a lower number of applications.

The clean-up procedure of the solid support prior to the coating process removes the passivated film present on the surface. In some cases, it also generates a porous surface, which increases the contact area between the support and the materials to be deposited. This clean-up step is described weakly in the literature despite its importance. In general, three different types of pretreatments or clean-up procedures have been reported so far for metallic supports: soft, mild, and strong. The purpose of the soft pretreatments is to remove any possible pollutant. This process involves washing the fiber with diluted detergent and deionized water [30, 39], or sonicating the support material into water, acetone, and/or ethanol [19, 29, 34, 56]. A mild pretreatment is the most common approach employed. It consists on etching the solid support using acids (HNO_3 or HCl) or alkali solutions (NaOH). This procedure generates a rough surface and few activated points along the support [24, 37, 49, 55]. Strong clean-up procedures imply etching the solid support with strong acids (like HF), mixtures of acids (HNO_3:H_2SO_4 or HF:HNO_3:H_2O), or both. This strong clean-up is very aggressive and a decrease on the support size is clearly observed [28, 57]. Once mild or strong pretreatment of the surface is accomplished, the solid support is washed according to the soft pretreatments. For FS supports, this kind of approaches cannot be used due to its inherent fragility. In this case, it is important to remove the polyimide protective layer, which can be accomplished by washing the fiber with acetone or burning it in a flame [21, 33, 37, 38]. Afterwards, the FS fiber is immersed in a NaOH solution to expose the silanol groups all over the surface, and improve the linkage of the sorbent material.

Immobilization strategies to generate metallic (1), metal oxide (2), and hybrid coatings (3) cover a broad range of techniques such as dipping, chemical deposition, sol-gel, and electrodeposition methods [59, 60], depending on the nature of the sorbent material and the type of attachment. Table 7.1 summarizes the metal-based

Table 7.1 Summary of metal-based SPME fibers reported up to date, including the nature of the solid support used, their composition, the coating procedure followed, and several physical characteristics

Support	Metallic material	Additive	Fiber type	Fiber coating procedure	Coating length (cm)/thickness (μm)	Max.T (°C)	Solvents in which fibers are stable	Refs.
1. *Metal NPs*								
SS	Au	–	SS/Au	Layer-by-layer	2/–	350	– HCl (0.01 M) – NaOH (0.01 M)	[19]
CuW	Cu	3MPTS[a]	CW/Cu-3MPTS[a]	Electrodeposition	3/5	400	–	[20]
FS	Au	–	FS/Au	Chemical deposition	1/–	500	–	[21]
SS	Au	OT[b]	SS/Au-OT[b]	Electrodeposition	1.5/–	–	– Methanol – Dimethylsulfoxide – Tetrahydrofuran – Chloroform	[22]
SS	Au	–	SS/Au	Chemical deposition	1.5/–	–	– HCl (0.01 M) – NaOH (0.1 M)	[23]
SS	Cu	–	SS/Cu	Electroless plating	–/–	300	– Acetone	[24]
Ag-CuW	Ag	PTH[c]	Ag-CuW/Ag-PTH[c]	Layer-by-layer	–/6	–	–	[25]
SS	Au	–	SS/Au	Chemical deposition	–/–	–	– HCl (0.01 M) – NaOH (0.01 M)	[26]
SS	Au	–	SS/Au	Chemical deposition	1.5/–	–	– HCl (0.01 M) – NaOH (0.1 M) – Methanol – Acetonitrile – Chloroform	[27]
SS	Au	MUO[d]	SS/Au-MUO[d]	Chemical deposition	1.5/–	–	– Methanol – Dimethylsulfoxide – Tetrahydrofuran – Chloroform	[28]
SS	Au	–	SS/Au	Layer-by-layer	–/3	–	–	[29]

(continued)

Table 7.1 (continued)

Support	Metallic material	Additive	Fiber type	Fiber coating procedure	Coating length (cm)/thickness (μm)	Max.T (°C)	Solvents in which fibers are stable	Refs.
2. *Metal oxides*								
AlW	Al_2O_3	–	AlW/Al_2O_3	Anodization	1/20	300	–	[30]
PtW	Co_3O_4	–	PtW/Co_3O_4	Hydrothermal growth	1/20	320	–	[31]
PtW	PbO_2	–	PtW/PbO_2	Anodization	2/70	300	–	[32]
SS	TiO_2	–	SS/TiO_2	Electrophoretic deposition	1/80	400	– HCl (0.01 M) – NaOH (0.01 M)	[33]
SS	TiO_2	–	SS/TiO_2	Hydrothermal synthesis of TiO_2 and attachment with silicon glue	–/17	300	– Methanol	[34]
TiW	TiO_2	–	TiW/TiO_2	Oxidation with H_2O_2	1/1.2	220	–	[35]
TiW	TiO_2	–	TiW/TiO_2	Anodization	–/–	350	– HCl (0.001 M) – NaOH (0.01 M)	[36]
FS	ZnO	–	FS/ZnO	Hydrothermal growth	–/–	320	–	[37]
FS	ZnO	–	FS/ZnO	Hydrothermal growth	1.5/–	300	–	[38]
ZnW	ZnO	–	ZnW/ZnO	Anodization	1/–	300	Stable in presence of humidity (100%)	[39]
NiTi	ZrO_2	–	NiTi/ZrO_2	Cathodic electrodeposition	–/1.35	270	Stable in presence of humidity (40–60%)	[40]
TiW	TiO_2-Phenyl	–	TiW/TiO_2-Phenyl	Anodization and immersion in trichlorophenylsilane solution	–/2	–	–	[41]
SS	CdS	–	SS/CdS	Deposition by evaporation of the solvent	2/30	400	–	[42]
CuW	CuCl	–	CuW/CuCl	Anodization	–/–	350	–	[43]
3. *Hybrid materials*								
NiTi	ZrO_2	PEG[e]	NiTi/ZrO_2@PEG[e]	Electrodeposition of ZrO_2 and sol-gel method	2/17	320	–	[44]

NiTi	ZrO_2	PDMS[f]	NiTi/ZrO_2@PDMS[f]	Electrodeposition of ZrO_2 and sol-gel method	2/25	320	–	[45]
FS	ZnO	PDMS[f]	FS/ZnO@PDMS[f]	Dip-coating of ZnO NPs, hydrothermal growth of ZnO nanorods and sol-gel method	–/2	250	–	[46]
SS	NiO	PBT[g]	SS/NiO@PBT[g]	Electrospinning	1.5/–	280	– Water – Methanol – Dichloromethane – Acetonitrile	[47]
SS	SiO_2	PET[h]	SS/SiO_2@PET[h]	Electrospinning	1.5/60	300	– Water – Methanol – Dichloromethane – Acetonitrile	[48]
SS	Au NPs	PEDOT[i]	SS/PEDOT[i] @AuNPs	*in situ* electropolymerization	–/40	330	–	[49]
AlW	Al_2O_3	TBOT[j]/ PEG[e]	AlW/ Al_2O_3@TBOT[j]/ PEG[e]	Anodization and sol-gel forming TBOT[j]/PEG[e]/TEA[k]	1/25	300	–	[50]
SS	Ag NPs	GO[l]	SS/GO[l]@AgNPs	Treatment with APTES[m], immersion into GO[l], treatment with MPTES[n] and -dip-coating with Au NPs	2/–	300	–	[51]
SS	Au NPs	GO[l]	SS/GO[l]@AuNPs	Addition of Si layer, treatment with APTES[m], immersion into GO[l], treatment with MPTMS[o] and dip-coating with Au NPs	–/4	320	– Ethanol – *n*-hexane – HCl (0.1 M) – NaOH (0.1 M)	[52]
CuW	Cu NPs	CC[p]	CuW/CC[p]@CuNP	Sol-gel method	–/–	–	–	[53]
SS	ZrO_2	mpC[q]	SS/ZrO_2@mpC[q]	Direct carbonization of a Zr-based metal-organic framework and attachment with silicon glue	1.5/14	250	–	[54]

(continued)

Table 7.1 (continued)

Support	Metallic material	Additive	Fiber type	Fiber coating procedure	Coating length (cm)/thickness (μm)	Max.T (°C)	Solvents in which fibers are stable	Refs.
NiTi	TiO_2-NiO	Au NPs	NiTi/TiO_2-NiO@AuNP	Hydrothermal growth of TiO_2 and NiO, and electrodeposition of Au NPs	1.5/–	–	– Methanol – Tetrahydrofuran – Chloroform – Dimethylsulfoxide – HCl (0.01 M) – NaOH (0.01 M)	[55]
SS	ZnO	Au NPs	SS/ZnO@AuNP	Dip-coating of ZnO seeds, hydrothermal growth of ZnO nanorods and sputtering of Au NPs	1/3.5	–	–	[56]
TiW	TiO_2	ZrO_2	TiW/TiO_2@ZrO_2	Oxidation with H_2O_2 solution to obtain TiO_2 and electrodeposition of ZrO_2	1/4.5	–	–	[57]

[a]3-(trimethoxysilyl)propylmethacrylate
[b]1,8-octanedithiol
[c]Propanethiol
[d]Mercaptoundecanol
[e]Polyethylene glycol
[f]Polydimethylsiloxane
[g]Polybutylene terephthalate
[h]Polyethylene terephthalate
[i]Poly-3,4-ethylenedioxythiophene
[j]Tetrabutyl orthotitanate
[k]Triethanolamine
[l]Graphene oxide
[m]3-aminopropyltriethoxysilane
[n]3-mercaptopropyl triethoxysilane
[o]3-mercaptopropyl trimethoxysilane
[p]Carbon ceramic
[q]mesoporous carbon

SPME fibers reported up to date, including the solid support used, their composition, the coating procedure followed, and several physical characteristics.

7.2.1 Metal Nanoparticles-Based SPME Coatings

Metal NPs have emerged as useful tools for SPME as a consequence of their high thermal, mechanical and chemical stability, and a feasible functionalization. Among metallic NPs, gold NPs, silver NPs, and copper NPs have been the main focus of recent research.

The majority of metallic NPs coated fibers have been deposited or generated over stainless steel (SS) supports, because SS brings to the fibers a high chemical stability and robustness.

The procedure mostly employed for gold nanoparticle coatings (SS/Au) is chemical deposition. The method implies immersion of the cleaned SS support into a solution of $HAuCl_4$ (0.05–0.06% w/w), at least for 3 h [23, 27]. Then, gold NPs are generated and immobilized onto the surface of the SS support due to the following redox reaction (reaction 7.1):

$$Fe + [AuCl_4]^- \leftrightarrow Fe^{3+} + Au + 4Cl^- \qquad \text{(reaction 7.1)}$$

This first coating of gold NPs generated by chemical deposition can be used as the basis for the construction of bigger thickness coatings via layer-by-layer deposition (LBL). This approach is based on the use of linker substances that contain thiol groups, such as 1,8-octanedithiol (SS/Au-OT) or 11-mercapto-1-undecanol (SS/Au-MUO), that form a well-organized self-assembled monolayer (SAM) of dithiol. Once the SAM is formed over the surface, it is exposed to gold NPs solutions, and the process is repeated for several times [19, 29]. Taking advantage on the interaction of thiol groups and gold, SS/Au fibers have been functionalized with SAM, thus improving their selectivity [26, 28].

Electrodeposition is another approach widely used for the generation of metallic NPs coatings on SS supports. Deposition of gold NPs can be performed by cyclic voltammetry (CV) in an electrolytic solution of $HAuCl_4$ with a three-electrode system, using the etched SS wire as the working electrode. The potential is normally applied from −0.2 to −0.5 V for 20 CV cycles at a scan rate of 20 mV s^{-1}. Once the electrodeposition process ends up, the fiber can be also functionalized with a SAM of 1,8-octanedithiol (SS/Au-OT) [22].

Silver NPs coatings have been also prepared using chemical deposition followed by the LBL approach using an Ag-Cu alloy (Ag-CuW/Ag) [25].

Copper coatings have been prepared by electrodeposition onto CuW by applying −500 mV for 5 min, using an electrochemical cell containing 10% (v/v) H_2SO_4, 5% (w/v) $CuSO_4$, with CuW as the cathode and another CuW acting as the anode. Afterwards, the fiber can be functionalized with SAM, being reported the use of 3-(trimethoxysilyl)propylmethacrylate (CuW/Cu-3MPTS) [20]. Another way

to elaborate copper NPs coatings is the utilization of a plating process over SS (SS/Cu). Briefly, the solid support is immersed directly into a plating solution of $CuSO_4 \cdot 5H_2O$ (10 g L^{-1}), $NaKC_4H_4O_6$ (40 g L^{-1}), NaOH (8 g L^{-1}), Na_2CO_3 (2 g L^{-1}), $NiCl_2 \cdot 6H_2O$ (1 g L^{-1}), HCHO (20 mL L^{-1}), and sodium dodecyl benzene sulfonate (0.2 g L^{-1}) at 40 °C during 5 min [24].

FS/Au fibers have been also described as supports for metallic NPs for SPME, but their chemical stability is not as good as SS-coated supports. In this case, the reduction of Au NPs cannot be performed directly over the support, and thus the FS needs previous functionalization with 3-aminopropyltriethoxysilane (APTES). This functionalization allows immobilization of Au NPs over the surface of the fiber given the interactions of the amino groups onto silica with gold [21].

A summary of metallic NPs coatings used in SPME is included in Table 7.1.

7.2.2 Metal Oxides Nanoparticles-Based SPME Coatings

The immobilization of metal oxide NPs onto the surface of different solid supports provides robust and porous coatings that increase the effective area for the extraction of the compounds. The fabrication of these SPME sorbents results quite simple, in general, using methods based on electrodeposition approaches, where the solid support of the final fiber acts as one of the electrodes in the electrochemical system. Thus, Al W/Al_2O_3 [30], Pt W/PbO_2 [32], Ti W/TiO_2 [36, 41], Zn W/ZnO [39], and Ni Ti/ZrO_2 [40] SPME fibers have been developed using this coating method. The further functionalization of the metal oxide layer formed has also been accomplished for a Ti W/TiO_2 coating [41]. After the anodization of the support, the fiber was immersed in NaOH solution to increase the number of titanol groups. This treatment enhanced the functionalization of the fiber with phenyl groups by the reaction between the activated fiber and trichlorophenylsilane, thus obtaining the final Ti W/TiO_2-Phenyl SPME fiber.

In these electrodeposition methods, the electrolyte solution can be composed by an acidic solution [30] or by an alkali solution [36, 39, 41], together with different stabilizers in the cases where the metallic support has the same nature as the metal oxide coating. For the Pt W/PbO_2 [32] and Ni Ti/ZrO_2 [40] SPME fibers, solutions of $Pb(NO_3)_2$ and $ZrOCl_2$ were used as electrolytes, respectively.

It is interesting to mention the development of a SPME fiber where TiO_2 was electrophoretically deposited on a SS wire (SS/TiO_2) [33]. In this case, the TiO_2 NPs were previously prepared and dispersed in an aqueous solution. Then, the SS support was immersed in the solution and used as the cathode, with a Pt wire acting as anode. Once the voltage was applied, the suspended TiO_2 NPs migrated under the influence of the electric field to be finally deposited onto the SS wire.

Potentials around 20 V were those normally utilized in these methods, with electrodeposition times ranging between 15 min [40] and 60 min [30], except for the SS/TiO_2 fiber prepared by electrophoretic deposition [33], for which 60 s were enough to obtain an adequate thickness. It should be highlighted that the final

thickness of the fiber strongly depends on the voltage and on the time of voltage application. Therefore, thicker coatings are obtained when longer times and higher voltages are used. However, the thicker the coating, the longer the extraction times required, and also the mechanical stability of the SPME fiber decreases [30, 32, 33, 39].

The utilization of a hydrothermal growth has been described for ZnO-based SPME fibers [37, 38]. Basically, FS supports were vertically kept in a solution containing $Zn(NO_3)_2$ and hexamethylenetetramine as stabilizer for 4 h at temperatures between 80 and 90 °C, and FS/ZnO SPME fibers were obtained. This chemical deposition method was also used to prepare Co_3O_4-coated Pt wires (PtW/Co_3O_4) [31]. Cobalt acetate was used as Co source, while PEG and ammonia were added to the solution to stabilize and adjust the pH of the media, respectively. The Pt support was placed into the solution, and kept during 2 h at 80 °C. Mesoporous TiO_2 NPs have also been prepared by a hydrothermal method by reacting TiF_4 and SiO_2 at 130 °C for 12 h [34]. However, its immobilization on the SS support was carried out using silicon glue. The SS wire was dipped in a solution containing the dispersed sealant, and subsequently it was rotated in the powder of the as synthetized TiO_2 NPs. The coating was then cured at 150 °C for 15 min before repeating the coating process until three layers were obtained.

The direct oxidation of a metallic wire yields a layer of metal oxide on its surface. This quite simple procedure has been employed for the preparation of a TiW/TiO_2 SPME fiber [35]. Thus, Ti wires were soaked in H_2O_2 solution at 80 °C during 24 h to form a porous, uniform, and stable TiO_2 layer.

The preparation of SPME fibers based on binary compounds with metallic elements can be included within this group. In this sense, CuCl has been deposited onto a Cu wire (CuW/CuCl) by anodization [43]. Sodium chloride was used in the electrolyte solution, and after applying a constant potential of 12 V, CuCl was formed on the surface of the Cu wire used as anode. CdS has also been coated onto SS wires (SS/CdS) by evaporation of the solvent from a dispersion of the sulfide [42]. Briefly, CdS NPs were dispersed in an aqueous solution containing the surfactant polyvinylpyrrolidone as stabilizer. The SS support was immersed in the dispersion, the solvent was evaporated in an oven, and a thin layer of CdS was formed on its surface. This procedure was repeated several times to obtain a uniform coating.

A summary of metal oxide coatings used in SPME is included in Table 7.1.

7.2.3 Hybrid-based SPME Coatings

One of the most interesting trends within the development of new SPME coatings is the preparation of composite-based stationary phases. This way, the resulting coating presents enhanced analytical performance, which is attributed to the properties of each component of the hybrid sorbent. In this sense, metallic coatings have

been combined with other materials, such as polymers [44–50], carbon-based nanomaterials [51–54], and even other metallic compounds [55–57].

ZrO_2-coated fibers have been combined with PEG (NiTi/ZrO_2@PEG) [44] and PDMS (NiTi/ZrO_2@PDMS) [45] to obtain thermally stable SPME fibers incorporating these polymers. The coating process consists on the electrodeposition of ZrO_2 onto nitinol wires followed by the sol-gel coating with PEG or PDMS. The sol-gel procedure was repeated three to five times in order to obtain the desired SPME thickness. Prior to the sol-gel process, the surface of the ZrO_2-coated fiber was activated by immersion in a NaOH solution. This way, the linkage between both materials composing the hybrid sorbent was improved, and therefore the stability of the resulting SPME fiber.

A similar approach has been used to the development of a FS/ZnO@PDMS SPME fiber [46]. In this case, the metal oxide coating was prepared in two steps: first, the bare FS fiber was dip-coated using a solution containing the required reagents to prepare ZnO NPs, this step was repeated five times to obtain a uniform coating. Afterwards, ZnO nanorods were deposited on the modified FS fiber by hydrothermal growth. As in the abovementioned studies, the PDMS was incorporated by a sol-gel method, which was performed in triplicate to get a thin PDMS layer covering the ZnO nanorods.

Nanocomposites based on different metal oxide NPs and polyethylene terephthalate (PET) or polybutylene terephthalate (PBT) have been prepared and immobilized onto SS fibers by a electrospinning coating method [47, 48]. Briefly, the solution containing the corresponding polymer and NPs was placed in a syringe connected to a high voltage power supply system together with the solid support. The SPME device was also attached to an electrical motor so that the wire could be rotated while the voltage was applied, thus ensuring a uniform formation of the nanofibers onto its surface. This preparation method provides sorbent coatings with enhanced surface area and high porosity, which leads to an increase in the extraction efficiency of the resulting SS/NiO@PBT [47] and SS/SiO_2@PET [48] SPME fibers.

Au NPs have been combined with poly-3,4-ethylenedioxythiophene (PEDOT) to develop a new highly hydrophobic SPME coating (SS/PEDOT@AuNPs) [49]. The Au NPs were prepared by the conventional reduction of $HAuCl_4$. Then they were put in contact with the monomer and the electropolymerization was accomplished *in situ* on the surface of the solid support by cyclic voltammetry. Twenty-five cycles performed during 20 min were sufficient to obtain the hybrid black coating.

An alumina-coated fiber has been combined with an inorganic polymer based on tetrabutyl orthotitanate (TBOT) and PEG to obtain a new homogeneous and stable SPME coating [50]. The Al wire was previously anodized to form a layer of Al_2O_3, which provides a porous surface that improved the attachment of the polymeric coating to the solid support. Then, the anodized fiber was immersed in the sol-gel solution containing TBOT, PEG, and triethanolamine as stabilizer to prepare the final Al/Al_2O_3@TBOT/PEG SPME coating. This method was repeated several times until the desired SPME thickness was obtained.

Graphene oxide (GO) decorated with metal NPs composites has been also reported as efficient SPME coatings [51, 52]. In these studies, several functionalization steps of the solid support have been required in order to improve the linkage between the SS wire and the sorbent. For the SS/GO@AgNPs fiber [51], the etched SS wire was functionalized with APTES prior to its immersion in the GO dispersion, to ensure the GO bonds to the SS fiber. The incorporation of Ag NPs to the sorbent coating involved the functionalization of the SS/GO fiber with 3-mercaptopropyl triethoxysilane (MPTES). This pretreatment provided the thiol groups, necessary to attach the Ag NPs to the coating once the functionalized fiber was immersed into the NPs aqueous solution. In the case of SS/GO@AuNPs [52], a Si layer was incorporated using a medium frequency unbalanced magnetron sputtering method in a multifunctional deposition system [61], and hydroxyl groups were exposed by dipping the fiber in a solution of sulfuric acid and hydrogen peroxide. Afterwards, the coating procedure was similar to that of the SS/GO@AgNPs fiber. The silanized support was functionalized with APTES and immersed into a GO solution. Thereafter, the SS/GO fiber was treated with 3-mercaptopropyl trimethoxysilane (MPTMS) and then dipped in a solution containing the Au NPs prepared by reduction of $HAuCl_4$.

In another interesting application, a copper wire has been used as a support for the development of a carbon ceramic (CC) and Cu NPs composite-based SPME fiber (CuW/CC@CuNP) [53]. Both components of the hybrid sorbent were synthetized separately. The CC was prepared by mixing graphite powder and methyltrimethoxysilane in an acidic solution, whereas the Cu NPs were obtained by the reduction of $CuSO_4$ with ascorbic acid. The SPME coating was prepared following a sol-gel procedure using a mixture of both individual constituents. This step was repeated several times until the desired SPME thickness was obtained.

Recently, a simple procedure based on the direct carbonization of a metal-organic framework was used to prepare a mesoporous carbon (mpC) and ZrO_2 composite [54]. With this method, the same precursor provided both the metallic and carbonaceous materials composing the sorbent, which results in an inexpensive and simple approach. In this case, the composite was attached to the SS wire using silicon glue. The solid support was first vertically dipped in the glue, and then immersed in the composite powder to obtain the SS/ZrO2@mpC SPME fiber.

This section also covers the preparation of SPME fibers based on the combination of diverse metallic materials. The sorbent coating of $TiW/TiO_2@ZrO_2$ fiber consists on a mixture of different metal oxides [57]. The Ti wire was immersed in a solution of H_2O_2 to form a TiO_2 layer on its surface by the oxidation reaction. Next, the modified fiber was treated with a NaOH solution to activate its surface prior to the electrodeposition of ZrO_2 NPs by cyclic voltammetry. This step was crucial in the development of a uniform coating since more than 10 cycles of cyclic voltammetry led to the formation of significant cracking in the coating.

Au NPs-decorated metal oxide coatings have been reported [55, 56]. These hybrid coatings take advantages of the properties of both metallic materials to obtain sorbents with high active surface area. Thus, $NiTi/TiO_2$-NiO@AuNP SPME fiber [55] was prepared employing a hydrothermal growth method based

on the immersion of the nitinol wire in a NaOH solution. Afterwards, the Au NPs were electrodeposited on the modified support using a $HAuCl_4$ solution. The fabrication of the SS/ZnO@AuNP fiber [56] required a more complex procedure. The metal oxide layer was prepared in two steps. First, the SS fiber was coated with ZnO seeds by annealing the fiber at 350 °C after dipping the wire in a solution of zinc acetate dehydrate. Then, ZnO nanorods were hydrothermally grown onto the surface of the modified SS fiber. Finally, the Au NPs were integrated in the sorbent coating by sputtering.

7.3 Characterization of Coatings

The main technique used to characterize these new metal-based SPME sorbents is scanning electron microscopy (SEM), which provides relevant information regarding the morphology, homogeneity, and robustness of the resulting coating. Figure 7.2 includes examples of SEM images obtained for the three types of metal-based SPME coatings [27, 38, 55]. Figure 7.2a shows the surface of the SS/Au fiber at different magnifications as a representative example of a metallic NPs-based SPME fiber [27]. It can be observed the uniformity of the resulting coating together with the cedar leaves-like morphology of the deposited Au NPs. This morphology has also been observed for the SS/Au-MUO [28] and CuW/Cu-3MPTS [20] SPME fibers. However, the most common shape observed for deposited metallic NPs is spherical NPs forming aggregates [19,21–24,26].

A representative example of a SPME fiber for a metal oxide-based coating is included in Fig. 7.2b. In this case, the surface of the FS/ZnO SPME fiber exhibited a layer of ordered ZnO nanorods [38], which has also been observed for the FS/ZnO SPME fiber developed by Ghasemi and Sillanpää using the same coating method [37]. Other nanostructures such as perfectly aligned TiO_2 nanotubes for the Ti/TiO_2 fiber [36], PbO_2 cornflower-like structures in the Pt/PbO_2 fiber [32], and agglomerations of spherical metal oxide NPs for the remaining SPME fibers [31, 33, 34, 41, 42] have been reported.

The coating surface of NiTi/TiO_2-NiO@AuNP SPME fiber is shown in Fig. 7.2c as a representative example of hybrid stationary phases [55]. In the SEM micrographs, it can be clearly observed both individual materials composing the hybrid sorbent: the TiO_2-NiO nanosheets and the spherical Au NPs formed at the edge of the nanosheets. Similar surface morphologies have been obtained for all those hybrid materials composed by metallic NPs combined with GO [51, 52] and metal oxides [56]. In the case of SPME sorbents based on composites created with metal oxides and polymers, uniform and smooth surfaces are obtained [44–46]. It is interesting to highlight the morphology of the fibers prepared with the NiO@PBT [47] and SiO_2@PET [48] composites obtained by the electrospinning method. The SEM images clearly showed the formation of nanofibers with high surface area. In these studies, Fourier transform infrared spectroscopy (FTIR) technique was employed to evaluate the presence and integrity of the individual

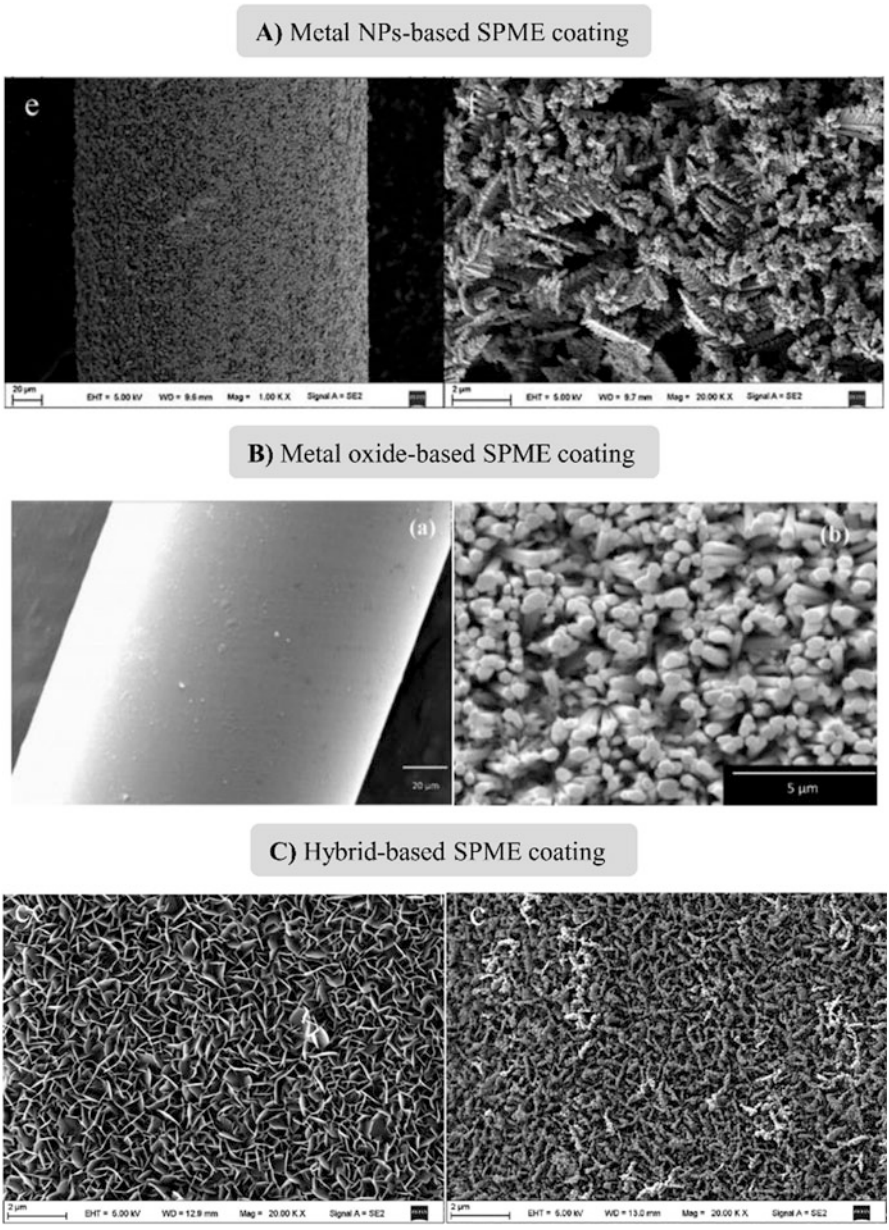

Fig. 7.2 SEM micrographs obtained for (**a**) metal NP-based SS/Au SPME fiber (adapted from [27], with permission from Elsevier), (**b**) metal oxide-based FS/ZnO SPME fiber (adapted from [38], with permission from Elsevier), and (**c**) hybrid-based NiTi/TiO_2-NiO@AuNP SPME fiber (adapted from [55], with permission of The Royal Society of Chemistry)

components of the resulting composite after the application of the coating procedure.

SEM images of the cross sections of the developed SPME fibers are useful for the determination of the thickness of the resulting coating. The amount (length × thickness) of the sorbent material plays an important role in the final efficiency of the SPME fiber. Several studies did not include this information; however, proper estimation of the thickness should be accomplished in order to evaluate their further analytical performance and adequate comparison with commercial fibers. Table 7.1 includes the size of the prepared metal-based SPME sorbents. Lengths ranged between 1 and 3 cm within the three kinds of metallic fibers. In general, thinner coatings were obtained for the metallic NPs-based stationary phases, varying from 3 μm [29] to 6 μm [25]. Larger coatings with thicknesses around 20 μm are reported when metal oxide or hybrid materials are used. The metal oxide SS/TiO_2 fiber prepared by electrophoretic deposition [33] presented the thicker coating (80 μm), while the TiW/TiO_2 fiber obtained by direct oxidation of the solid support exhibited the lowest (1.2 μm) [35]. It is important to mention that there is no relation between the coating method employed to fabricate the SPME fiber and the thickness obtained. As a general trend, authors performed several coatings steps to obtain thicker coatings.

SEM characterization has been commonly combined with energy dispersive X-ray spectroscopy (EDXS) [22, 26–28, 40, 41, 44, 45, 49, 56, 57] or X-ray photoelectron spectroscopy (XPS) [25, 36, 51]. These microanalysis techniques allow determining the chemical composition of the sorbent material employed to fabricate the SPME fiber. In some cases, transmission electron microscopy (TEM) resulted quite useful to stablish the morphology of the synthetized nanomaterials [34] as well as to ensure the presence of all components in hybrid materials [49, 54].

It results also quite important to determine the thermal stability of SPME coatings, particularly if they are intended for environmental applications combined with GC. Clearly, SPME coatings must be stable when desorbing trapped analytes in a GC injector. Furthermore, all SPME fiber coatings are conditioned before their first use by heating during a certain timing. This activation temperature also depends on the thermal stability of the coating, which needs to be evaluated [19–21, 24, 29–31, 33–40, 42–54]. The maximum temperatures achieved by the reported metal-based SPME fibers are around 300 °C, as shown in Table 7.1, thus being totally compatible with the further desorption of the analytes in the GC system. Common desorption temperatures in the GC injector for compounds of environmental interest varied from 220 to 300 °C.

When the SPME approach is carried out in combination with HPLC, it is essential to evaluate the stability of the coatings in the presence of several organic solvents. It must be prevented the bleeding of the metallic coating in this desorption step for HPLC applications. In this sense, the stabilities of the metal-based fibers SS/Au-OT [22], SS/Au [27], SS/Au_MUO [28], SS/NiO@PBT [47], SS/SiO_2@PET [48], and NiTi/TiO_2-NiO@AuNP [55] have been assessed in presence of different solvents such as methanol, acetonitrile, chloroform, or dichloromethane.

If focusing the attention of the performance of the metal-based coatings in the SPME extraction step, the HS- mode hardly presents any problem. However, in the DI- mode it is certainly important to assess the integrity of the sorbent coatings when directly exposed to the aqueous medium: testing the influence of high ionic strengths, presence of acidic or alkali samples. The main advantage of these metal-based SPME coatings is their elevated chemical stability in aggressive media, which has been correctly evaluated for the SS/Au [23, 26, 27], SS/TiO_2 [33], TiW/TiO_2 [36], SS/GO@AuNPs [52], and NiTi/TiO_2-NiO@AuNPs [55] fibers in HCl and NaOH solutions at different concentrations. This robustness permits a wider applicability in a variety of environmental samples.

7.4 Environmental Applications

Djozan et al. were the first to report the utilization of metallic coatings in SPME for environmental applications in 2001 [30]. Authors fabricated an AlW/Al_2O_3 SPME fiber of low cost, with high-temperature resistance, firmness, and long durability. The novel coating was employed for the determination of alcohols in gaseous samples. Since then, these novel SPME fibers have been successfully used for trace analysis in environmental samples due to their improved selectivity and robustness over commercial coatings. Table 7.2 summarizes main environmental applications carried out with metal-based SPME coatings. The main analytes determined with these fibers have been hydrophobic compounds, such as polycyclic aromatic hydrocarbons (PAHs), benzene, toluene, ethylbenzene and xylene (BTEX), UV filters, phthalate esters (PAEs), and pesticides, as it is shown in Fig. 7.3a. The selection of these compounds lies in the enhanced selectivity found with metallic sorbents due to hydrophobic interactions and the electron-transfer effect between the π-donor analyte and the metal-containing coating [19, 28]. Regarding the environmental samples studied with metallic SPME fibers, waters from different sources (rain, river, lake, sea, tap, and sewage waters, among others) have been analyzed [19–29, 31–38, 41, 42, 51, 52, 54–57], as it is summarized in Fig. 7.3b. Other matrix samples have been analyzed, including soil samples [19, 37, 53], ambient air [43], and gaseous fuel samples [39]. In this sense, these novel metallic nanomaterials employed as SPME sorbent coatings have emerged as a potential tool for multiple environmental applications, being possible their use for different kind of samples (solid, liquid, or gas) and analytes.

It is interesting to mention that the high mechanical and chemical stability that these metallic SPME fibers exhibit has made possible their utilization in both DI [19, 22–29, 33, 34, 36, 41, 44, 52, 53, 55–57] and HS mode [20, 21, 30–32, 35, 37–40, 42–51, 54]. The optimum extraction times reported for these coatings are around 30 min, independently of the thickness and nature of the coating, and totally agrees with the times required in SPME applications with commercial fibers. Extraction temperatures between 30 and 80 °C have been employed, depending on the volatility of the analytes. Some extractions have been accomplished even at

Table 7.2 Main features of environmental applications using metal-based SPME fibers

SPME fiber	Sample (amount)	Analytes (number)	Extraction conditions	Desorption conditions	Analytical technique	Lifetime[a]	LOD[b] (ng L^{-1})	RSD[c] (%)	Refs.
1. *Metal NPs*									
SS/Au	Rain water (20 mL) and soil (335 g)	PAHs[d] (5), HOCs[e] (3)	50 min at 60 °C	6 min at 300 °C	DI-SPME-GC-FID[f]	–	12–250	4.3–26.4	[19]
CW/Cu-3MPTS	River water (6 mL)	PAHs[d] (5)	15 min at 30 °C	250 °C	HS-SPME-GC-MS[g]	–	5–10	10.8–15.2	[20]
FS/Au	Sea water (50 mL)	PAHs[d] (6)	50 min at 60 °C	6 min at 300 °C	HS-SPME-GC-FID[f]	65	10,000–200,000	8.5–13.6	[21]
SS/Au-OT	Wastewater, river and rain water (15 mL)	PAEs[h] (3), PCBs[i] (4), CPs[j] (3), UV filters (4), PAHs[d] (6), anilines (2)	40 min at 35 °C	On-line for 6 min	DI-SPME-HPLC-UV	200	25–56	6.4–9.4	[22]
SS/Au	Wastewater, tap, lake, river and rain water (10 mL)	PAHs[d] (5)	50 min at 45 °C	On-line for 3 min	DI-SPME-HPLC-UV	150	16–220	1.88–9.09[k]	[23]
SS/Cu	Bottled mineral water	Estrogens (2)	40 min at 30 °C	3 min at 280 °C	DI-SPME-GC-FID[f]	80	10	7.4–10	[24]
Ag-CuA/Ag-PTH	Water (25 mL)	PAHs[d] (3)	180 min at 25 °C	–	DI-SPME-SERS[l]	16	–	2.97–5.66[k]	[25]
SS/Au	Wastewater, river and rain water (15 mL)	UV filters (4)	40 min at 55 °C	On-line for 3 min	DI-SPME-HPLC-UV	200	0.4–500	1.9–4.2[k]	[26]
SS/Au	Wastewater and river water (15 mL)	UV filters (4), PAEs[h] (5), PAHs[d] (5)	20 min at 50 °C	On-line for 5 min	DI-SPME-HPLC-UV	200	8–37	5.15–6.87	[27]
SS/Au-MUO	Wastewater, river and snow water (10 mL)	UV filters (2), PAHs[d] (5), PAEs[h] (7)	40 min at 35 °C	On-line for 7 min	DI-SPME-HPLC-UV	180	10–44	5.15–6.52	[28]

SS/Au	Tap, pond and well water (15 mL)	OCPs[m] (7)	60 min at RT[n]	3 min at 260 °C	DI-SPME-GC-ECD[o]	100	130–200	8.67–21.3	[29]
2. *Metal oxides*									
AlW/Al_2O_3	Gaseous samples (35 mL)	Alcohols (6)	15 min at RT[n]	1 min at 250 °C	HS-SPME-GC-FID[f]	–	30–300	4.3–8.1	[30]
PtW/Co_3O_4	River and sewage water (15 mL)	BTEX[p] (4)	14 min at 59 °C	3 min at 250 °C	HS-SPME-GC-MS[g]	50	1000–11,000	7.9–11.2	[31]
PtW/PbO_2	Well water (7 mL)	BTEX[p] (5)	40 min at 80 °C	3 min at 250 °C	HS-SPME-GC-FID[f]	50	12–54	9.1–12.5	[32]
SS/TiO_2	Bottled mineral water (9 mL)	PAEs[h] (4)	75 min at 30 °C	5 min at 285 °C	DI-SPME-GC-MS[g]	60	50–120	8.9–10.2	[33]
SS/TiO_2	Rain and lake water (10 mL)	OCPs[m] (6)	50 min at 50 °C	5 min at 270 °C	DI-SPME-GC-MS[g]	100	0.08–0.6	3.7–15.7	[34]
TiW/TiO_2	River and well water (10 mL)	DDT[q] derivatives (4)	40 min at 55 °C	2 min at 220 °C	HS-SPME-GC-μECD[o]	150	0.2–1	28	[35]
TiW/TiO_2	River water	Alkanes (5) PAHs[d] (4)	60 min at 50 °C	5 min at 300 °C	DI-SPME-GC-FID[f]	–	10–100	–	[36]
FS/ZnO	Wastewater, well, river, tap, and seawater (10 mL), soil (2 g)	Chlorobenzenes (6)	30 min at 50 °C	4 min	HS-SPME-GC-MS[g]	150	0.01–0.1	3.6–4.6	[37]
FS/ZnO	Seawater	HOCs[e] (3)	30 min at 60 °C	4 min at 270 °C	HS-SPME-GC-MS[g]	100	0.001–10	11.5	[38]
ZnW/ZnO	Gaseous fuel samples (35 mL)	Thiophenol	5 min at RT[n]	1 min at 300 °C	HS-SPME-GC-FID[f]	–	7	3.77	[39]
NiTi/ZrO_2	Gaseous samples	Alcohols (6) BTEX[p] (4) THMs[r] (4)	20 min at 35 °C for alcohols and BTEX[p], 20 min at 25 °C for THMs[r]	270 °C	HS-SPME-GC-FID[f]	300	20–28,100	11.9	[40]
TiW/TiO_2-Phenyl	Rain and river water (8 mL)	UV filters (4)	25 min at 35 °C	On-line for 4 min	DI-SPME-HPLC-UV	350	0.1–50	5.5–9.1	[41]

(continued)

Table 7.2 (continued)

SPME fiber	Sample (amount)	Analytes (number)	Extraction conditions	Desorption conditions	Analytical technique	Lifetime[a]	LOD[b] (ng L^{-1})	RSD[c] (%)	Refs.
SS/CdS	River water	PAHs[d] (6)	50 min at 70 °C	3 min at 300 °C	HS-SPME-GC-FID[f]	50	5–15	8.3–12.6	[42]
CuW/CuCl	Ambient air	Amines (5)	15 min at 10 °C	5 min at 300 °C	HS-SPME-GC-FID[f]	–	350–700	4.3–8.1	[43]
3. *Hybrid materials*									
NiTi/ZrO_2@PEG	Water (20 mL for halophenols and 25 mL for PAEs[e])	Halophenols (2), PAEs[h] (4)	40 min at 48 °C for halophenols 30 min at 50 °C for PAEs[h]	3 min at 300 °C	HS-SPME-GC-ECD[o] for halophenols DI-SPME-GC-FID[f] for PAEs[h]	300	1.2–700	12	[44]
NiTi/ZrO_2@PDMS	Water (20 mL)	BTEX[p] (4)	16 min at 6 °C	3 min at 300 °C	HS-SPME-GC-FID[f]	250	600–1600	3.9–6.7	[45]
FS/ZnO@PDMS	Water	BTEX[p] (3)	20 min at 43 °C	250 °C	HS-SPME-GC-MS[g]	–	2–5	5.6–10.8	[46]
SS/NiO@PBT	Water (4 mL)	VOCs[s] (4)	10 min at 30 °C	3 min at 240 °C	HS-SPME-GC-MS[g]	115	1–5	3.1–9[k]	[47]
SS/SiO_2@PET	Water (4 mL)	BTEX[p] (5)	10 min at 50 °C	3 min at 240 °C	HS-SPME-GC-MS[g]	125	0.7–0.9	5–11	[48]
SS/PEDOT@AuNPs	Water (10 mL)	PAHs[d] (5)	40 min at 20 °C	4 min at 280 °C	HS-SPME-GC-FID[f]	160	2.5–25	5.8–9.9	[49]
AlW/Al_2O_3@TBOT/PEG	Water (20 mL)	BTEX[p] (4)	20 min at 60 °C	12 s at 180 °C	HS-SPME-GC-FID[f]	30	5400–14,800	13.5	[50]
SS/GO@AgNPs	Tap and rain water	PAHs[d] (8)	50 min at 70 °C	5 min at 300 °C	HS-SPME-GC-FID[f]	120	2–10	8.6–17.5	[51]

SS/GO@AuNPs	Tap and snow water (22 mL)	Aromatic HOCs[e] (10)	40 min at 40 °C	5 min at 300 °C	DI-SPME-GC-FID[f]	–	5–60	6.7–16.9	[52]
CuW/CC@CuNPs	Soil samples (1 g + 10 mL water)	Nitro explosives (5)	45 min	8 min at 200 °C	DI-SPME-GC-FID[f]	100	0.6–2.6[t]	7.7–9.6	[53]
SS/ZrO_2@mpC	Wastewater and river water (10 mL)	BTEX[p] (4)	15 min at 30 °C	3 min at 250 °C	HS-SPME-GC-FID[f]	–	50–560	7.4–9.1	[54]
NiTi/TiO_2-NiO@AuNPs	Wastewater, river and rain water (15 mL)	PAHs[d] (4)	30 min at 45 °C	On-line for 5 min	DI-SPME-HPLC-UV	200	12–53	5.2–7.2	[55]
SS/ZnO@AuNPs	Aquaculture water	Crystal violet	120 min	Acquisition during 2 s	DI-SPME-SERS[l]	–	$1.03 \cdot 10^{-10}$[u]	8.9[k]	[56]
TiW/TiO_2@ZrO_2	Wastewater and river water (15 mL)	UV filters (4)	30 min at 35 °C	On-line for 4 min	DI-SPME-HPLC-UV	250	32–82	4.3–11	[57]

[a] Number of extraction/desorption cycles
[b] Limits of detection
[c] Relative standard deviation for interfiber studies
[d] Polycyclic aromatic hydrocarbons
[e] Hydrophobic organic compounds
[f] Flame ionization detection
[g] Mass spectrometry
[h] Phthalate esters
[i] Polychlorinated biphenyls
[j] Chlorophenols
[k] Relative standard deviation for intraday studies
[l] Surface enhanced Raman spectroscopy
[m] Organochlorine pesticides
[n] Room temperature
[o] Electron capture detection
[p] Benzene, toluene, ethylbenzene, and xylene
[q] Dichlorodiphenyltrichloroethane
[r] Trihalomethanes
[s] Volatile organic compounds
[t] Limits of detection in μg g^{-1}
[u] Limits of detection in mol L^{-1}

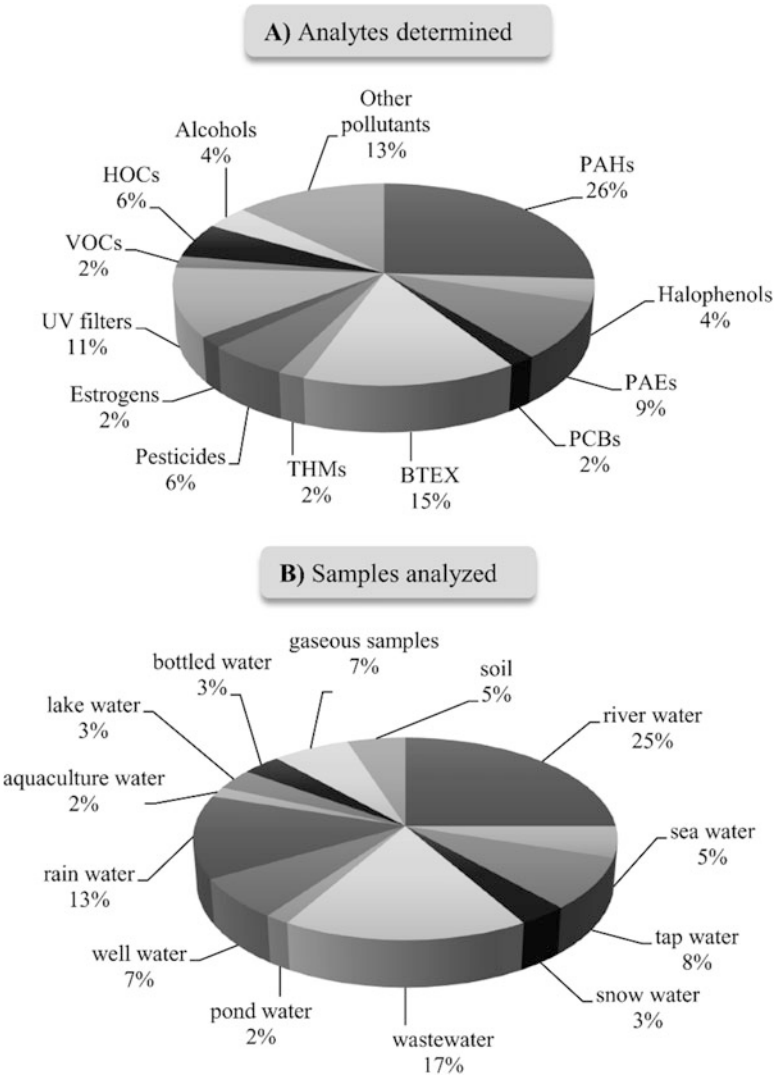

Fig. 7.3 (**a**) Summary of analytes determined using metal-based SPME fibers in environmental applications and (**b**) summary of environmental samples subjected to analysis using metal-based SPME fibers

room temperature (RT) for highly volatile analytes, such as organochlorine pesticides (OCPs) [29], alcohols [30], and thiophenol [39].

Main environmental applications of metal-containing SPME fiber have been performed in combination with GC and with different detectors such as flame ionization detection (FID) [19, 21, 24, 30, 32, 36, 39, 40, 42–45, 49–54], mass spectrometry (MS) [20, 31, 33, 34, 37, 38, 46–48], and electron capture detection

(ECD) [29, 44]. In these cases, the desorption of the analytes was performed in the inlet of the GC system at temperatures around 250–300 °C, which takes good notice of the thermal stability of the developed coatings.

Regarding the sensitivity achieved with these fibers, the lowest limits of detection (LODs) were obtained with the FS/ZnO fiber for the determination of hydrophobic organic compounds (HOCs) from seawater, varying between 0.001 and 10 ng L^{-1} [38], and the SS/TiO_2 fiber for the extraction of OCPs from river and lake water, ranging between 0.08 and 0.6 ng L^{-1} [34]. In both works, MS was used as detection system.

Due to the chemical stability in presence of organic solvents, SPME applications with metal-based coatings have been widely coupled with HPLC, mainly for the determination of UV filters [26–28, 41, 57], PAHs [23, 27, 28, 55], and PAEs [27, 28]. In this case, the desorption of the analytes was performed in a SPME interface coupled to the HPLC injector, to ensure on-line performance. Despite UV detection is the most extensively used in these SPME-HPLC applications, quite low LODs have been reached for UV filters, around 0.1 ng L^{-1} for the TiW/TiO_2-Phenyl fiber [41] and around 0.4 ng L^{-1} for the SS/Au fiber [26].

It is also interesting to point out the combination of the Ag-Cu/Ag-PTH [25] and SS/ZnO@AuNPs fibers [56] with surface enhanced Raman spectroscopy (SERS) for the determination of PAHs and dye crystal violet, respectively. The metallic nature of the developed SPME fiber allows their coupling with this technique, which provides enhanced sensitivity and selectivity.

Many authors performed interfiber studies, which provide information regarding the reproducibility of the coating approach employed. Thus, the reproducibility (as relative standard deviation, RSD) of the entire method is evaluated by testing different fibers prepared in the same way. The RSD reported was, in general, lower than 17%, as shown in Table 7.2, supporting both the effectiveness of the coating method and the extraction performance of the fibers. The metal NPs-based SPME fibers presented the lowest interfiber RSD values. Thus, the SS/Au fiber synthetized by chemical deposition exhibited interfiber RSD values ranging from 1.8 to 9.0% [23], whereas RSDs between 3.0 and 5.7% were obtained for the Ag-Cu/Ag-PTH SPME fiber prepared using a layer-by-layer approach [25].

The lifetime of the fiber refers to the number of extraction/desorption cycles without significant loss in the extraction efficiency. It strongly depends on the SPME mode (DI or HS) and the separation system employed. Average lifetimes of 110 cycles have been reported for the metal-containing SPME fibers when they are used in GC applications, being the hybrid NiTi/ZrO_2@PDMS fiber the most robust, with a lifetime of 300 cycles in both DI and HS mode for the extraction of halophenols and PAEs [44]. It should be highlighted that the fibers used in combination with HPLC present higher lifetimes than those used in GC applications, being reusable for more than 200 cycles. Indeed, the metal oxide-based SPME fiber TiW/TiO_2-Phenyl could be used during 350 cycles in DI-SPME mode for the determination of UV filters [41].

A few of the developed metal-based SPME fibers have been properly compared with the commercially available SPME fibers to demonstrate their improved

characteristics. Thus, the metal NPs-based SS/Au-OT SPME fiber provided much higher peak areas than the commercial PA and PDMS fibers for UV filters in river waters [22]. The SS/TiO_2 fibers, prepared by electrophoretic deposition [33] and attachment with silicon glue [34], also exhibited better analytical performance for the extraction of PAEs and OCPs, respectively, when compared to PDMS [33], PA and PDMS/DVB [34] commercial fibers. It must be highlighted the performance of the FS/ZnO fiber, which presented LODs from 100 to 100,000 times lower than those obtained with the commercial PDMS fiber for the determination of HOCs [38]. It has been reported the use of the normalized peak area (peak area/coating thickness or volume) as a tool to compare the extraction efficiency among SPME fibers, taking into the account that the thickness of the developed coatings are thinner than those of the commercially available SPME fibers. This type of comparison assessment suggests that if these metallic coatings are prepared with thicker thicknesses, the analytical performance will be significantly better than that of commercial fibers.

7.5 Concluding Remarks

Metallic coatings, including metal NPs, metal oxide NPs, and hybrid sorbents, constitute a promising alternative to commercially available SPME fibers due to their high chemical and thermal stability, together with their ease of synthesis and outstanding selectivity and sensitivity towards hydrophobic compounds. Therefore, the utilization of metal-based sorbents in environmental applications for the analysis of different matrix samples comprises an interesting research field within recent improvements in sample preparation.

References

1. C.L. Arthur, J. Pawliszyn, Solid phase microextraction with thermal desorption using fused silica optical fiber. Anal. Chem. **62**, 2145–2148 (1990)
2. A. Spietelun, Ł. Marcinkowski, M. de la Guardia, et al., Recent developments and future trends in solid phase microextraction techniques towards green analytical chemistry. J. Chromatogr. A **1321**, 1–13 (2013)
3. J. Pawliszyn, Theory of solid-phase microextraction. J. Chromatogr. Sci. **38**, 270–278 (2000)
4. É.A. Souza-Silva, R. Jiang, A. Rodríguez-Lafuente, et al., A critical review of the state of the art of solid-phase microextraction of complex matrices I. Environmental analysis. Trac-Trends Anal Chem **71**, 224–235 (2015)
5. É.A. Souza-Silva, E. Gionfriddo, J. Pawliszyn, A critical review of the state of the art of solid-phase microextraction of complex matrices II. Food analysis. Trac-Trends Anal Chem **71**, 236–248 (2015)
6. É.A. Souza-Silva, N. Reyes-Garcés, G.A. Gómez-Ríos, et al., A critical review of the state of the art of solid-phase microextraction of complex matrices III. Biological and clinical applications. Trac-Trends Anal Chem **71**, 249–264 (2015)

7. J. Li, Y.-B. Wang, K.-Y. Li, et al., Advances in different configurations of solid-phase microextraction and their applications in food and environmental analysis. Trac-Trends Anal Chem **72**, 141–152 (2015)
8. H. Piri-Moghadam, F. Ahmadi, J. Pawliszyn, A critical review of solid phase microextraction for analysis of water samples. Trac-Trends Anal Chem **85**, 133–143 (2016)
9. A. Mehdinia, M.O. Aziz-Zanjani, Recent advances in nanomaterials utilized in fiber coatings for solid-phase microextraction. Trac-Trends Anal Chem **42**, 205–215 (2013)
10. J. Tian, J. Xu, F. Zhu, et al., Application of nanomaterials in sample preparation. J. Chromatogr. A **1300**, 2–16 (2013)
11. B.H. Fumes, M.R. Silva, F.N. Andrade, et al., Recent advances and future trends in new materials for sample preparation. Trac-Trends Anal Chem **71**, 9–25 (2015)
12. H. Yu, T.D. Ho, J.L. Anderson, Ionic liquid and polymeric ionic liquid coatings in solid-phase microextraction. Trac-Trends Anal Chem **45**, 219–232 (2013)
13. X.-Y. Song, J. Chen, Y.-P. Shi, Different configurations of carbon nanotubes reinforced solid-phase microextraction techniques and their applications in the environmental analysis. Trac-Trends Anal Chem **86**, 263–275 (2017)
14. R. Sitko, B. Zawisza, E. Malicka, Graphene as a new sorbent in analytical chemistry. Trac-Trends Anal Chem **51**, 33–43 (2013)
15. D.-L. Deng, J.-Y. Zhang, C. Chen, et al., Monolithic molecular imprinted polymer fiber for recognition and solid phase microextraction of ephedrine and pseudoephedrine in biological samples prior to capillary electrophoresis analysis. J. Chromatogr. A **1219**, 195–200 (2012)
16. P. Rocío-Bautista, I. Pacheco-Fernández, J. Pasán, et al., Are metal-organic frameworks able to provide a new generation of solid-phase microextraction coatings?—a review. Anal. Chim. Acta **939**, 26–41 (2016)
17. M.B. Gholivand, M.M. Abolghasemi, P. Fattahpour, A hexagonally ordered nanoporous silica-based fiber coating for SPME of polycyclic aromatic hydrocarbons from water followed by GC–MS. Chromatographia **74**, 807–815 (2011)
18. P. Olszowy, M. Szultka, T. Ligor, et al., Fibers with polypyrrole and polythiophene phases for isolation and determination of adrenolytic drugs from human plasma by SPME-HPLC. J. Chromatogr. B **878**, 2226–2234 (2010)
19. J. Feng, M. Sun, H. Liu, et al., Au nanoparticles as a novel coating for solid-phase microextraction. J. Chromatogr. A **1217**, 8079–8086 (2010)
20. P.A. Azar, M.S. Tehrani, S. Mohammadiazar, et al., A novel strategy to increase performance of solid-phase microextraction fibers: electrodeposition of sol-gel films on highly porous substrate. J. Sep. Sci. **35**, 3354–3360 (2012)
21. M. Karimi, F. Aboufazeli, H.R.L.Z. Zhad, et al., Determination of polycyclic aromatic hydrocarbons in Persian Gulf and Caspian Sea: gold nanoparticles fiber for a head space solid phase micro extraction. Bull. Environ. Contam. Toxicol. **90**, 291–295 (2013)
22. Y. Yang, Y. Li, H. Liu, et al., Electrodeposition of gold nanoparticles onto an etched stainless steel wire followed by a self-assembled monolayer of octanedithiol as a fiber coating for selective solid-phase microextraction. J. Chromatogr. A **1372**, 25–33 (2014)
23. H. Liu, L. Liu, X. Wang, et al., Preparation of a robust and sensitive gold-coated fiber for solid-phase microextraction of polycyclic aromatic hydrocarbons in environmental waters. Anal. Lett. **47**, 1759–1771 (2014)
24. J. Feng, M. Sun, Y. Bu, et al., Nanostructured copper-coated solid-phase microextraction fiber for gas chromatographic analysis of dibutyl phthalate and diethylhexyl phthalate environmental estrogens. J. Sep. Sci. **38**, 128–133 (2015)
25. C. Liu, X. Zhang, L. Li, et al., Silver nanoparticle aggregates on metal fibers for solid phase microextraction–surface enhanced Raman spectroscopy detection of polycyclic aromatic hydrocarbons. Analyst **140**, 4668–4675 (2015)
26. L. Hai-Xia, Y. Yao-Xia, M. Ming-Guang, et al., Self-assembled gold nanoparticles coating for solid-phase microextraction of ultraviolet filters in environmental water. Chin. J. Anal. Chem. **43**, 207–211 (2015)

27. Y. Zhang, Y. Yang, Y. Li, et al., Growth of cedar-like Au nanoparticles coating on an etched stainless steel wire and its application for selective solid-phase microextraction. Anal. Chim. Acta **876**, 55–62 (2015)
28. Y. Zhang, W. Song, Y. Yang, et al., Self-assembly of mercaptoundecanol on cedar-like Au nanoparticle coated stainless steel fiber for selective solid-phase microextraction. Anal. Methods **7**, 7680–7689 (2015)
29. A. Gutiérrez-Serpa, P. Rocío-Bautista, V. Pino, et al., Gold-nanoparticles-based solid-phase microextraction coatings for determining organochlorine pesticides in aqueous environmental samples. J. Sep. Sci. **40**(9), 2009–2021 (2017)
30. D. Djozan, Y. Assadi, S.H. Haddadi, Anodized aluminum wire as a solid-phase microextraction fiber. Anal. Chem. **73**, 4054–4058 (2001)
31. M.B. Gholivand, M. Shamsipur, M. Shamizadeh, et al., Cobalt oxide nanoparticles as a novel high-efficiency fiber coating for solid phase microextraction of benzene, toluene, ethylbenzene and xylene from aqueous solutions. Anal. Chim. Acta **822**, 30–36 (2014)
32. A. Mehdinia, M.F. Mousavi, M. Shamsipur, Nano-structured lead dioxide as a novel stationary phase for solid-phase microextraction. J. Chromatogr. A **1134**, 24–31 (2006)
33. M.H. Banitaba, S.S.H. Davarani, A. Pourahadi, Solid-phase microextraction of phthalate esters from aqueous media by electrophoretically deposited TiO2 nanoparticles on a stainless steel fiber. J. Chromatogr. A **1283**, 1–8 (2013)
34. S. Liu, L. Xie, J. Zheng, et al., Mesoporous TiO2 nanoparticles for highly sensitive solid-phase microextraction of organochlorine pesticides. Anal. Chim. Acta **878**, 109–117 (2015)
35. D. Cao, J. Lü, J. Liu, et al., In situ fabrication of nanostructured titania coating on the surface of titanium wire: a new approach for preparation of solid-phase microextraction fiber. Anal. Chim. Acta **611**, 56–61 (2008)
36. H. Liu, D. Wang, L. Ji, et al., A novel TiO2 nanotube array/Ti wire incorporated solid-phase microextraction fiber with high strength, efficiency and selectivity. J. Chromatogr. A **1217**, 1898–1903 (2010)
37. E. Ghasemi, M. Sillanpää, Optimization of headspace solid phase microextraction based on nano-structured ZnO combined with gas chromatography–mass spectrometry for preconcentration and determination of ultra-traces of chloro benzenes in environmental samples. Talanta **130**, 322–327 (2014)
38. R. Alizadeh, N.M. Najafi, S. Kharrazi, A new solid phase micro extraction for simultaneous head space extraction of ultra traces of polar and non-polar compounds. Anal. Chim. Acta **689**, 117–121 (2011)
39. D. Djozan, L. Abdollahi, Anodized zinc wire as a solid-phase microextraction fiber. Chromatographia **57**, 799–804 (2003)
40. D. Budziak, E. Martendal, E. Carasek, Preparation and application of NiTi alloy coated with ZrO2 as a new fiber for solid-phase microextraction. J. Chromatogr. A **1164**, 18–24 (2007)
41. L. Li, R. Guo, Y. Li, et al., In situ growth and phenyl functionalization of titania nanoparticles coating for solid-phase microextraction of ultraviolet filters in environmental water samples followed by high performance liquid chromatography–UV detection. Anal. Chim. Acta **867**, 38–46 (2015)
42. L. Wang, S. Tang, S. Wang, et al., Cadmium sulfide nanoparticles as a novel coating for solid-phase microextraction. J. Sep. Sci. **38**, 1326–1333 (2015)
43. M.A. Farajzadeh, N.A. Rahmani, Electrolytically produced copper(I) chloride on the copper wire as an excellent sorbent for some amines. Talanta **65**, 700–704 (2005)
44. D. Budziak, E. Martendal, E. Carasek, New poly(ethylene glycol) solid-phase microextraction fiber employing zirconium oxide electrolytically deposited onto a NiTi alloy as substrate for sol–gel reactions. J. Chromatogr. A **1198–1199**, 54–58 (2008)
45. D. Budziak, E. Martendal, E. Carasek, Preparation and characterization of new solid-phase microextraction fibers obtained by sol–gel technology and zirconium oxide electrodeposited on NiTi alloy. J. Chromatogr. A **1187**, 34–39 (2008)

46. D. Wang, Q. Wang, Z. Zhang, et al., ZnO nanorod array polydimethylsiloxane composite solid phase micro-extraction fiber coating: fabrication and extraction capability. Analyst **137**, 476–480 (2012)
47. H. Bagheri, A. Roostaie, Polybutylene terephthalate-nickel oxide nanocomposite as a fiber coating. Anal. Chim. Acta **863**, 20–28 (2015)
48. H. Bagheri, A. Roostaie, Roles of inorganic oxide nanoparticles on extraction efficiency of electrospun polyethylene terephthalate nanocomposite as an unbreakable fiber coating. J. Chromatogr. A **1375**, 8–16 (2015)
49. L. Yang, J. Zhang, F. Zhao, et al., Electrodeposition of self-assembled poly(3,4-ethylenedioxythiophene)@gold nanoparticles on stainless steel wires for the headspace solid-phase microextraction and gas chromatographic determination of several polycyclic aromatic hydrocarbons. J. Chromatogr. A **1471**, 80–86 (2016)
50. K. Farhadi, R. Tahmasebi, R. Maleki, Preparation and application of the titania sol–gel coated anodized aluminum fibers for headspace solid phase microextraction of aromatic hydrocarbons from water samples. Talanta **77**, 1285–1289 (2009)
51. L. Wang, X. Hou, J. Li, et al., Graphene oxide decorated with silver nanoparticles as a coating on a stainless-steel fiber for solid-phase microextraction. J. Sep. Sci. **38**, 2439–2446 (2015)
52. L. Xu, H. Suo, X. Liang, et al., Au nanoparticle decorated graphene oxide as a novel coating for solid-phase microextraction. RSC Adv. **5**, 41536–41543 (2015)
53. K. Farhadi, S. Bochani, M. Hatami, et al., Gas chromatographic detection of some nitro explosive compounds in soil samples after solid-phase microextraction with carbon ceramic copper nanoparticle fibers. J. Sep. Sci. **37**, 1578–1584 (2014)
54. M. Saraji, N. Mehrafza, Mesoporous carbon–zirconium oxide nanocomposite derived from carbonized metal organic framework: a coating for solid-phase microextraction. J. Chromatogr. A **1460**, 33–39 (2016)
55. H. Wang, Y. Zhang, M. Zhang, et al., Gold nanoparticle modified NiTi composite nanosheet coating for efficient and selective solid phase microextraction of polycyclic aromatic hydrocarbons. Anal. Methods **8**, 6064–6073 (2016)
56. B. Li, Y. Shi, J. Cui, et al., Au-coated ZnO nanorods on stainless steel fiber for self-cleaning solid phase microextraction-surface enhanced Raman spectroscopy. Anal. Chim. Acta **923**, 66–73 (2016)
57. Y. Li, Y. Yang, H. Liu, et al., Fabrication of a novel Ti–TiO2–ZrO2 fiber for solidphase microextraction followed by highperformance liquid chromatography for sensitive determination of UV filters in environmental water samples. Anal. Methods **6**, 8519–8525 (2014)
58. J. Feng, H. Qiu, X. Liu, et al., The development of solid-phase microextraction fibers with metal wires as supporting substrates. Trac-Trends Anal Chem **46**, 44–58 (2013)
59. M.O. Aziz-Zanjani, A. Mehdinia, A review on procedures for the preparation of coatings for solid phase microextraction. Microchim. Acta **181**, 1169–1190 (2014)
60. F. Pena-Pereira, R.M.B.O. Duarte, A.C. Duarte, Immobilization strategies and analytical applications for metallic and metal-oxide nanomaterials on surfaces. Trac-Trends Anal Chem **40**, 90–105 (2012)
61. H. Liu, L. Ji, J. Li, et al., Magnetron sputtering Si interlayer: A protocol to prepare solid phase microextraction coatings on metal-based fiber. J. Chromatogr. A **1218**, 2835–2840 (2011)

Chapter 8
Different Approaches for Thin Film Solar Cell Simulation

Maykel Courel and Osvaldo Vigil-Galán

8.1 Introduction

Over the last decades, thin film technology has become more and more attractive as it allows the manufacturing of devices at lower cost while keeping the required fundamental physical properties for a good device performance. One of the greatest successes of thin film technology has certainly been the solar cell field. While traditional silicon solar cell technology entails device widths of about 500 μm, the application of thin films to solar cells has shown reduced widths of only few microns with efficiencies comparable to the ones reported for Si technology. The use of thin films to solar cell processing has been widely named as the second generation of solar cells. In fact, the application of thin film materials such as CdTe and $Cu(In,Ga)(S,Se)_2$ as absorber layers in solar cells has demonstrated conversion efficiencies higher than 20% [1]. However, the toxicity of cadmium and the low abundance of indium are the main drawbacks when it comes to a massive panel production. Nowadays, some semiconductor materials such as SnS, Sb_2S_3, and kesterite family (Cu_2ZnSnS_4, $Cu_2ZnSnSe_4$, $Cu_2ZnSn(S,Se)_4$, $Cu_2Zn(Sn,Ge)(S,Se)_4$, etc.) which have adequate physical properties for solar cell applications have emerged as promising absorbers to replace CdTe and $Cu(In,Ga)(S,Se)_2$ technology [2–18]. Most of the research on these materials are still undergoing. So far, a

ORCID: http://orcid.org/0000-0001-9149-3506

M. Courel (✉)
Instituto de Energías Renovables, Universidad Nacional Autónoma de México, Temixco, Morelos 62580, Mexico
e-mail: maykelcourel@gmail.com

O. Vigil-Galán
Escuela Superior de Física y Matemáticas-Instituto Politécnico Nacional (IPN), C.P. 07738, México DF, Mexico

J. Zhang, Y.-G. Jung (eds.), *Advanced Ceramic and Metallic Coating and Thin Film Materials for Energy and Environmental Applications*,
DOI 10.1007/978-3-319-59906-9_8

record efficiency of 12.6% has been reported for kesterite solar cells which is far below than the ones reported for CdTe and $Cu(In,Ga)(S,Se)_2$ technology [1, 19]. The efficiency results are even lower for SnS thin film solar cells demonstrating that all of these thin film technologies are just in its beginnings [4, 20].

Different deposition techniques have been used to deposit semiconductor thin films for solar cells. In particular, magnetron sputtering [21, 22], thermal evaporation [23], sol gel [24], screen printed [25], electrodeposition [26], photochemical deposition [27], co-evaporation [28], and spray pyrolysis [15, 17, 18, 22, 29–31] are among the most used ones. These techniques offer an easy and cheap route for thin film processing. Each deposition technique has its own advantages and disadvantages. For example, chemical routes do not often require a level of vacuum making the cost of deposition cheaper but at the same time the absence of a controlled atmosphere might involve the incorporation of unwanted atoms introducing defects [32]. Conversely, physical routes such as sputtering and thermal evaporation allow thin film deposition with good crystalline quality but production cost is higher. However, even under these conditions, processing cost is quite lower than the ones of silicon technology making thin film technology one attractive route for replacing silicon-based panel production.

Among the different proposed materials for thin film solar cell processing, $Cu_2Zn(Sn, Ge)(S,Se)_4$ compound is currently one of the most promising due to its *p*-type conductivity, high absorption coefficient, direct band gap transitions, and a band gap near to the optimal one required for solar cell applications [14–19]. Besides, its physical properties can be tailored by changing Sn and Ge composition as well as S and Se composition [33–36]. Despite this compound has recently received a great deal of attention from scientific community, its efficiency is not able to overcome the barrier of 13%. A high open-circuit voltage (V_{oc}) deficit has been widely identified as the main issue that dooms solar cell efficiency [9–12]. Many factors have been proposed to explain V_{oc} deficit such as non-adequate band alignment, a high density of defects at absorber and buffer/kesterite interface, and kesterite internal disorder. [11, 37]. In order to overcome CdS buffer layer issue, routes focused on replacing CdS by other buffer layers as well as the using of a bilayer have been proposed [38–41]. In spite of the fact that an improvement in solar cell properties has been reported with respect to the baseline cell, none of these works have obtained efficiency values higher than the record one [19]. Therefore, further studies are needed to deeply understand the main limiting factors concerning kesterite technology as well as finding adequate routes to promote it.

Solar cell modeling and simulation always offer an easy way to understand the effect of microscopic phenomena on device macroscopic parameters. While experimental routes entail investment of materials and time to survey a possible solar cell parameters trend with some experimental conditions modification, simulation tool provides an easier route to study the effect of such experimental modifications on device performance guaranteeing then a reduction of material utilization along with time. In this way, simulation tool and experimental routes should always go side by side. Of course, the quality of simulation results depends on physical considerations. That is, each microscopic transport mechanism has a unique impact on solar

cell parameters. The better understanding of microscopic phenomena provides the higher reliability of results. Beside this, a good selection of input parameters for simulation should be done as well.

Different approaches to study the performance of $Cu_2ZnSn(S,Se)_4$ solar cells have been proposed [42–53]. The simplest but often accurate ones consider the fit of J–V and external quantum efficiency (EQE) curves as well as the dependence of solar cell parameters with temperature to extract information on device transport mechanisms and then to set possible paths to promote solar cell performance [42, 44, 47, 52]. Other methods entail the calculation of device parameters starting from some experimental inputs and assuming different transport mechanisms [43, 45, 46, 48–51, 53]. In the latter case, the viability of the calculations will depend mainly on the assumed transport mechanisms governing the solar cell properties as well as the adequate selection of the input parameters during the modeling. Commonly, different existing programs for thin film solar cell modeling such as AMPS, SCAPS, and Sentaurus are used for that purpose.

This chapter aims at summarizing the state-of-the-art literature on kesterite solar cell modeling. Firstly, different approaches proposed for modeling kesterite solar cells will be presented and discussed. Details on each modeling route will be presented. As an important part, the impact of different transport mechanisms on kesterite solar cell behavior will be introduced.

8.2 Routes for Modeling $Cu_2ZnSn(S,Se)_4$ Solar Cells

8.2.1 Fitting Method

As mentioned before, the easier route to study kesterite solar cells is by fitting some experimental curves (J–V, EQE, $V_{oc}(T)$, $n(T)$) of processed thin film solar cells. For example, from J–V curve, information on reverse dark current density (J_0), diode ideality factor (n), series resistance (Rs), and shunt resistance (Rsh) can be extracted while from EQE curve minority carrier lifetime can be estimated. The dependence of V_{oc} and n parameters with temperature is also an important part for finding out transport mechanisms that better describe the solar cell operation [54]. Once knowing these properties, the efficiency limitation in solar cells can be found.

C. J. Hages et al. studied the J–V behavior of the measured kesterite thin film solar cells by the single-exponential diode equation [42]:

$$J(V) = J_0(T)\,\mathrm{Exp}\left(\frac{q(\mathrm{V}-\mathrm{JRs})}{n(T)kT}\right) - \frac{\mathrm{V}-\mathrm{JRs}}{\mathrm{Rsh}} - J_{\mathrm{PH}} \tag{8.1}$$

where J_{PH} is the photocurrent density, k is the Boltzmann constant, and T is the absolute temperature. To better estimate transport mechanisms that determine solar cell behavior, J–V measurements at lower temperatures were carried out by authors

to obtain $J_0(T)$ and $n(T)$ curves profile. For a thermally activated transport mechanism with activation energy (E_A), the following dependence for J_0 is found:

$$J_0 = J_{00}\,\mathrm{Exp}\left(\frac{-E_A}{n(T)kT}\right) \tag{8.2}$$

where J_{00} is a weakly temperature dependent current density prefactor which is correlated to the dominant recombination mechanism in the device. Theoretical analysis of J_{00} can be considered for various dominant recombination mechanisms as discussed by Hages [42]:

– Recombination dominated in the neutral zone of the absorber yields:

$$J_{00} = \frac{qD_nN_VN_C}{N_AL_D} \tag{8.3}$$

where D_n is the electron diffusion constant, N_C and N_v are the effective density of states in the conduction band and valence band, respectively, N_A is the acceptor density, and L_D is the minority carrier diffusion length.

– Recombination dominated in the space charge region (SCR) yields:

$$J_{00} = \frac{kTD_n\pi\sqrt{N_CN_V}}{F_mL_D^2} \tag{8.4}$$

where F_m is the electric field at the position of maximum recombination.

– Recombination dominated at the heterojunction interface yields

$$J_{00} = qS_pN_V \tag{8.5}$$

where S_p is the recombination velocity at the absorber interface. However, authors demonstrated that these theoretical analyses along with traditional characterization of J_0 data (described above) are insufficient to analyze CZTSSe devices due to a large J_{00} value. As a result, further characterizations of the dependence of activation energy, reverse saturation current density, and diode ideality factor on temperature are proposed to better estimate transport mechanisms. It is important to mention that authors were also able to propose an expression for V_{oc} which considered among its terms potential fluctuations, explaining in this way high V_{oc} deficit.

8.2.2 wxAMPS Software

wxAMPS is a solar cell simulation program derived from AMPS, being the latter developed at the Pennsylvania State University [55]. A comprehensive review of wxAMPS applications for solar cell modeling was presented by Liu et al. [56]. Taking a glance into wxAMPS program, it is a solar cell simulator for modeling one-dimensional devices composed of various materials. It accepts the same input parameters as AMPS, conforms to similar physical principles and numerical descriptions of defects and recombination, and adds the effects of tunneling currents based on two different tunneling models [56]. In wxAMPS, there is no limit to the number of layers allowed; hence, it is feasible to design a device with parameters consistent with an arbitrary depth profile, which is appropriate for modeling graded alloy composition solar cells. The wxAMPS program includes tunneling effects; in particular, there are two tunneling models incorporated into wxAMPS: trap-assisted tunneling and the intra-band tunneling [56]. The trap-assisted tunneling model is necessary when high electric fields exist at junctions. In the trap-assisted tunneling model, the expression for recombination rate is changed from the typical Shockley–Read–Hall model [57] to a new form which depends on the applied electric field [58]. The intra-band tunneling model is implemented by adding a thermionic emission boundary condition at any layer interface, including the primary junction.

The wxAMPS software has been used for modeling CZTSSe solar cells. In particular, a device model to understand hydrazine-processed CZTSSe solar cell with world record efficiency of 12.6% was proposed by Gokmen et al. [44]. The proposed model was able to reproduce experimental observations, including V_{OC}, J_{SC}, FF, and efficiency under normal operating conditions, and temperature vs. V_{OC}, sun intensity vs. V_{OC}, and quantum efficiency. Also, as an interesting point, the model does not assume any interface defects/states, suggesting that all the experimentally observed features can be accounted for by the bulk properties of CZTSSe. As a result, a good interface kesterite/buffer is required to make valid Gokmen's model. On the other hand, in this model authors proposed band tailing due to the presence of electrostatic potential fluctuations as the main V_{oc} limiting factor for champion CZTSSe solar cells, which points to the bulk of the CZTSSe as being the primary origin of the V_{oc} deficit. The role of band tailing in CZTSSe solar cell performance was also considered by other authors [59, 60]. Due to a spike-like band alignment at CdS/CZTSSe heterojunction, there is no need to introduce the effect of an interface recombination. However, under other conditions, interface losses are expected to have a major impact on solar cell parameters and authors' model could be no longer valid.

8.2.3 SCAPS Software

SCAPS-1D is a one-dimensional solar cell simulation software developed at the Department of Electronics and Information Systems of Gent University, Belgium [61]. It is generally developed for polycrystalline thin film devices. SCAPS estimates the steady state band diagram, recombination profile, and carrier transport in 1-dimension using the Poisson's equation and continuity equations for electrons and holes. The Shockley–Read–Hall (SRH) model is implemented to describe the deep recombination levels and their occupation.

SCAPS software has been used for modeling CZTS solar cells. Patel et al. have discussed the enhancement of CZTS solar cell performance in terms of back contact metal work function, absorber thickness, and acceptor concentration [50]. A comparative study on the performance of CZTS, CZTSe, and CZTSSe thin film solar cells was presented by Simya et al. [51]. In this work, the optimization of layer thicknesses, back contact work function, series resistance, and different kinds of band-to-band recombination mechanisms (radiative and Auger) were studied. Frisk et al. suggested a device model for CZTS solar cells using SCAPS [47] where they have incorporated band gap narrowing, short minority carrier diffusion length and interface recombination into this model. Other works focused on optimizing CZTS solar cells have been presented by Zhao et al. and Meher et al. [43, 49] by using AMPS-1D simulator. The main concern of these approaches could be that transport mechanisms that are often assumed such as radiative, auger, and diffusion are only valid under ideal conditions for solar cells.

8.2.4 Sentaurus Software

Other software that has been used for modeling kesterite solar cells is Sentaurus [62]. The software package solves Poisson and continuity equations. Kanevcen et al. carried out a study on the impact of bulk properties and local secondary phases on the $Cu_2(Zn,Sn)Se_4$ solar cells open-circuit voltage [53]. Authors collected a set of parameters from experimental data and theory, created a model for CZTSe solar cells, and compared the model with experiment. They demonstrated that although carrier lifetime and interface recombination are the strongest sources for the V_{oc} deficit, local secondary phases can also contribute and explain the losses in V_{oc}. The magnitude of their impact depends on their size, band gap, and location. In particular, authors found that secondary phases are strong contributor to V_{oc} losses when located at the heterointerface, and they can increase the impact of interface recombination. As the lower band gap phases move away from the heterointerface, their impact on V_{oc} decreases. Besides, with the inclusion of secondary phases, 2D models could reproduce experimental J–V parameters, which was not possible for the 1D model with reasonable limits of parameter variation.

8.2.5 *Tunneling Enhanced Recombination and Kesterite/Buffer Interface Recombination as Possible Causes of High Open-Circuit Voltage Deficit*

So far, the greatest problem of kesterite thin film solar cells is low open-circuit voltage values. This problem is mainly associated to band tailing as mentioned before. At the same time, other authors such as Kanevcen have demonstrated that such low behavior could be also due to the presence of secondary phases. Secondary phases are still a remaining point to be solved in kesterite technology as pure-kesterite compound is only formed at a narrow region of the phase diagram. However, it has been observed that secondary phases impact can be reduced at kesterite optimal compositional ratios [63]. On the other hand, one important disadvantage of most theoretical works that have been proposed is the consideration of transport mechanisms such as diffusion, radiative recombination, and Auger recombination as dominant, though it is understood that such mechanisms are only valid under ideal circumstances, and consequently not reliable [45, 46, 50]. Kesterite compounds have been characterized by a high density of bulk defects which could contribute to carrier losses [32]. Bulk defects contribute to reduce minority carrier lifetime. Furthermore, under a relatively high electric field—p–n junction—, losses can be assisted by a tunneling process. On the other hand, recombination at buffer/kesterite interface is another important mechanism to be considered when it comes to kesterite solar cells. As a result, a more adequate approach to survey the route towards an improvement in kesterite solar cell efficiency should entail transport mechanisms such as kesterite/buffer interface recombination and kesterite tunneling enhanced recombination. Unfortunately, scant information on this subject can be found along the existing literature.

8.2.5.1 From MQWSC to KestTFSC Software

KestTFSC (Kesterite Thin Film Solar Cells) is a software program derived from MQWSC (Multiple Quantum Well Solar Cells) program developed at Havana University by Rimada [64–66]. MQWSC software consists of a package developed at Wolfram Mathematics (version 5.2) to model AlGaAs/GaAs quantum well solar cells containing all required physical constants as well as equations that describe physical phenomena in quantum well solar cells. In short, by using Rimada's package, the impact of several semiconductor parameters such as minority carrier lifetime, minority carrier diffusion length, interface, front and back contact recombination speeds, minority carrier mobility values, material widths, majority carrier concentrations, band offsets, carrier effective mass, absorption coefficient as a function of wavelength, surface reflectivity, etc. on solar cell performance can be evaluated. As an important feature, Rimada demonstrated that his proposed model was able to reproduce experimental data of quantum well solar cells from Imperial College of London [65] validating in this way his approach and in turn his software.

Later, after few modifications, this package was used for modeling AlGaAs/GaAs and GaInNAs/GaAs superlattice solar cells by Courel [67–69] under Wolfram Mathematics version 6.0. In order to study quantum well and superlattice solar cells behavior, the J–V characteristics were described by two diodes involving diffusion, radiative and non-radiative recombinations and interface recombination as the main transport mechanisms. In particular, photocurrent density is calculated from external quantum efficiency (EQE) measurements. AM1.5 data were considered for calculating photocurrent density. As a result, this program allows obtaining EQE data as a function of wavelength. Once J–V characteristics for quantum well and superlattice solar cells are known, different solar cell parameters such as efficiency, short-circuit current density, and open-circuit voltage can be evaluated as well as their dependence on parameters such as minority carrier lifetime, minority carrier diffusion length, interface recombination, and materials width.

Recently, MQWSC package was further modified by Courel to model kesterite thin film solar cells (KestTFSC). Due to the differences in nature between quantum well solar cells and thin film solar cells, software was changed almost throughout. Material constants and physical equations were all replaced. Other transport mechanisms which were not previously included such as thermionic emission, buffer/absorber interface recombination, and tunneling enhanced recombination were implemented. Besides, under this new version, series and shunt resistance influence on solar cells can be calculated.

8.2.5.2 KestTFSC Software for Modeling Kesterite Solar Cells

The current density–voltage relation of a kesterite-based solar cell can be described by [70–73]:

$$J = J_{01}\left[\exp\left(\frac{q(V - JR_S)}{kT}\right) - 1\right] + J_{02}\left[\exp\left(\frac{q(V - JR_S)}{2kT}\right) - 1\right] + \frac{V - JR_S}{R_{Sh}} - J_{PH} \tag{8.6}$$

where q is the electron charge, R_s is the series resistance, R_{sh} is the shunt resistance, V is the applied voltage, kT is the thermal energy, and J_{PH} is the photocurrent. The J_{01} and J_{02} reverse saturation current terms contain transport mechanism contributions to dark current. The photocurrent density can be calculated by the following integration:

$$J_{PH} = q\int_{\lambda_1}^{\lambda_2} F(\lambda)\mathrm{EQE}_T(\lambda)d\lambda \tag{8.7}$$

where λ_1 and λ_2 are limits of the taken solar spectrum, $F(\lambda)$ is the solar spectrum AM1.5, and $\mathrm{EQE}_T(\lambda)$ is the total external quantum efficiency of the cell. The EQE_T

is obtained from the superposition of depletion zone ($EQE_{DZ}(\lambda)$), p and n quasi-neutral zone ($EQE_P(\lambda)$, $EQE_N(\lambda)$) contributions as follows:

$$EQE_T(\lambda) = EQE_P(\lambda) + EQE_{N\text{-}CdS}(\lambda) + EQE_{N\text{-}ZnO}(\lambda) + EQE_{N\text{-}TCO}(\lambda) + EQE_{DZ}(\lambda) \tag{8.8}$$

It is important to point out that ZnO and ZnO:Al or ITO (TCO) contributions to n quasi-neutral zone EQE are considered along with the CdS one as presented in Eq. (8.8). The *p* and *n* quasi-neutral zone EQE contributions are evaluated by solving the carrier transport equations at room temperature within the minority carrier and depletion approximations. Such contributions can be represented by:

$$EQE_P(\lambda) = \frac{\alpha_{Abs}(\lambda)L_n[1-R(\lambda)](1-G)\exp\{-\Sigma\alpha_i(\lambda)z_i\}}{\alpha_{Abs}^2(\lambda)L_n^2 - 1} \times \left\{ \alpha_{Abs}(\lambda)L_n - \frac{\frac{S_nL_n}{D_n}\left[\mathrm{Cos}\,h\left(\frac{d_{Abs}}{L_n}\right) - \exp(-\alpha_{Abs}(\lambda)d_{Abs})\right] + \mathrm{Sin}\,h\left(\frac{d_{Abs}}{L_n}\right) + \alpha_{Abs}(\lambda)L_n\exp(-\alpha_{Abs}(\lambda)d_{Abs})}{\frac{S_nL_n}{D_n}\mathrm{Sin}\,h\left(\frac{d_{Abs}}{L_n}\right) + \mathrm{Cos}\,h\left(\frac{d_{Abs}}{L_n}\right)} \right\} \tag{8.9}$$

and

$$EQE_N(\lambda) = \frac{\alpha_n(\lambda)L_p[1-R(\lambda)](1-G)\exp\{-\Sigma\alpha_i(\lambda)z_i\}}{\alpha_n^2(\lambda)L_p^2 - 1} \times \left\{ \frac{\frac{S_pL_p}{D_p} + \alpha_n(\lambda)L_p - \exp(-\alpha_n(\lambda)d_n) - \left[\frac{S_pL_p}{D_p}\mathrm{Cos}\,h\left(\frac{d_n}{L_p}\right) + \mathrm{Sin}\,h\left(\frac{d_n}{L_p}\right)\right]}{\frac{S_pL_p}{D_p}\mathrm{Sin}\,h\left(\frac{d_n}{L_p}\right) + \mathrm{Cos}\,h\left(\frac{d_n}{L_p}\right)} - \alpha_n(\lambda)L_p\exp(-\alpha_n(\lambda)d_n) \right\} \tag{8.10}$$

where G is shading from grid, $R(\lambda)$ is the surface reflectivity spectrum, the first exponential factor is due to the attenuation of light in the precedent layers (ITO, ZnO, etc.), $a_i(\lambda)$ and z_i are the absorption coefficient and the width of the precedent layers, respectively, the $a_{Abs}(\lambda)$ and $a_n(\lambda)$ terms are the absorption coefficients of the absorber and *n*-type materials (CdS, ZnO, ITO), respectively. The d_n and d_{Abs}

terms are quasi-neutral zone widths corresponding to *n*-type materials and absorber, respectively. Besides, L_n and L_p are diffusion length values for minority carriers in *p*- and *n*-type semiconductors, respectively, while D_n and D_p are diffusion coefficients for minority carriers and S_n and S_p are surface recombination velocity values for minority carriers. It is important to remark that Eq. (8.10) is used to calculate CdS, ZnO, and TCO quasi-neutral zone EQE contributions ($EQE_{N\text{-}CdS}$, $EQE_{N\text{-}ZnO}$, $EQE_{N\text{-}TCO}$)—separately—as functions of wavelength. On the other hand, the contribution of photo-generated carriers in the depletion zone ($EQE_{DZ}(\lambda)$) is calculated by the expression:

$$EQE_{DZ}(\lambda) = [1 - R(\lambda)][1 - G]\exp\{-\Sigma\alpha_i(\lambda)z_i\} \times [1 - \exp(-\alpha_{CdS}(\lambda)x_{CdS} - \alpha_{Abs}(\lambda)x_{Abs})] \quad (8.11)$$

where $a_{Abs}(\lambda)$ and $a_{CdS}(\lambda)$ are the absorption coefficients of absorber (CZTS, CZTSe) and CdS materials, respectively, while x_{Abs} and x_{CdS} are their depletion zone widths, respectively. The first exponential factor is also due to the attenuation of light in the precedent layers (ITO or ZnO:Al, ZnO and CdS quasi-neutral zones). The absorption coefficient as a function of wavelength for direct band gap transitions for each thin film was evaluated from a well-known expression for unpolarized light [74]:

$$\alpha(E) = \frac{\sqrt{2}q^2E_g\left[m_h^* \times m_e^*/\left(m_h^* + m_e^*\right)\right]}{3\pi nc\varepsilon_0 m_e^*\hbar^2} \times \frac{\sqrt{E - E_g}}{E} \quad (8.12)$$

where q is the electron charge, E_g is the semiconductor band gap, m_h^* and m_e^* are hole and electron effective masses, respectively. The term E is the photon energy, c the speed of light, ε_0 the vacuum dielectric permittivity, and $\hbar$ the reduced Planck constant. To match accurately with experimental data in the long wavelength region—energy values lower than CZTS and CZTSe band gap—, experimental CZTS and CZTSe absorption coefficient data were considered [75]. The well-known Poisson's equation is used to find depletion region characteristics—potential barrier, electric fields, and depletion region widths. The surface reflectivity data provided for CZTSe solar cell with the record efficiency is used [7] while for CZTS solar cell, the Fresnel equations and the antireflection coating theory are used.

From Eqs. (8.9)–(8.11), EQE contribution of each zone as a function of wavelength can be evaluated. Then, the solar cell photocurrent density can be calculated by Eq. (8.7). In order to validate this approach, experimental EQE data provided for CZTS and CZTSe solar cells were considered.

Different Loss Mechanisms

The most important loss mechanisms that can take place in kesterite-based solar cells are majority carrier diffusion and/or thermionic emission, minority carrier

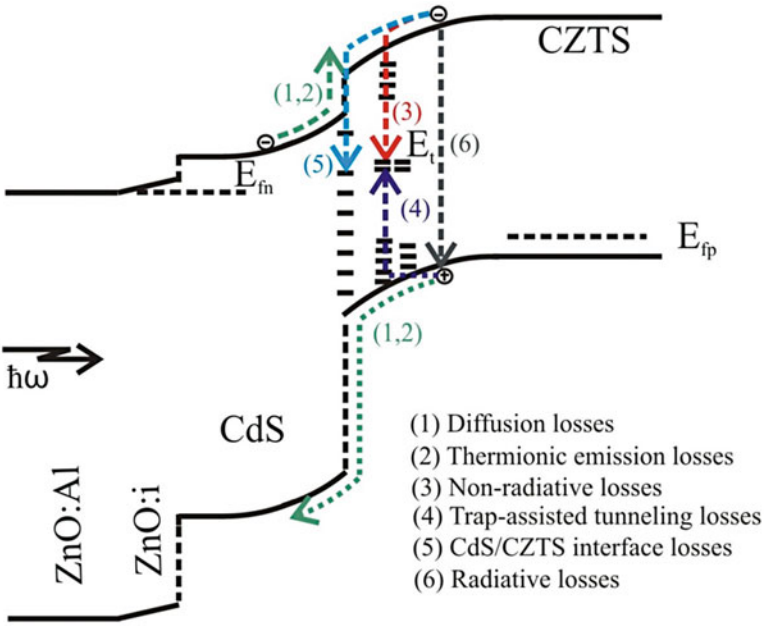

Fig. 8.1 Main transport mechanisms presented at CdS/kesterite heterojunction

radiative and non-radiative recombinations, CdS/kesterite interface recombination, and trap-assisted tunneling recombination. Each loss mechanism is schematized in Fig. 8.1 considering band diagram for CZTS compound. A detailed study of each one is presented below.

Diffusion

The diffusion theory consists of electrons injected from the n-side over the potential barrier into the p-side, where they diffuse away from the junction and eventually recombine either in the bulk or at a surface. The current component also consists of an analogous current due to holes injected from the *p*-side into the *n*-side. The behavior of these minority carriers is governed by the continuity equations. Under the diffusion mechanism, current density–voltage dependence is less sensitive to temperature compared with the thermionic emission. In a heterojunction, current density–voltage characteristic is expected to be reduced even further by the appropriate energy discontinuity in the valence (valence band offset). This energy barrier largely impedes holes from being injected into CdS material. The current density–voltage dependence for diffusion mechanism has been previously published [76]. This has been the most common mechanisms assumed for modeling CZTS solar cells [45, 46, 50].

Thermionic Emission

The thermionic emission mechanism assumes that there is a probability for majority carriers, which is proportional to temperature to overcome the potential barrier. In particular, for type-II heterojunction (CdS/CZTS), majority carrier must overcome not only built-in potential barrier but also the corresponding band offsets as shown in Fig. 8.1. The current density–voltage dependence for thermionic emission mechanism has been also published [77].

Radiative Recombination

Radiative (band-to-band) recombination is simply the inverse of the optical generation process and is much more efficient in direct band gap semiconductors than in indirect band gap semiconductors. The radiative recombination rate in each semiconductor can be described by:

$$R = B\left(np - n_{\mathrm{i}}^2\right) \tag{8.13}$$

where n and p are nonequilibrium carrier concentrations, n_{i} is the intrinsic carrier concentration, and B is the radiative recombination coefficient. The total contribution of radiative recombination losses to J_{01} at the depletion region can be expressed by [71–73]:

$$J_{01-\mathrm{rad}} = q\left(x_{\mathrm{n}} B_{\mathrm{n}} n_{\mathrm{i-CdS}}^2 + x_{\mathrm{p}} B_{\mathrm{p}} n_{\mathrm{i-Abs}}^2\right) \tag{8.14}$$

where x_{n} and x_{p} are the depletion region widths corresponding to CdS and CZTS (CZTSe) semiconductors, respectively. Assuming a quasi-Fermi level separation constant and equal to the applied voltage V, hence, according to the detailed balance theory, the radiative recombination coefficient is given by:

$$B = \frac{8\pi n_{\mathrm{r}}^2}{c^2 h^3 n_{\mathrm{i}}^2} \int_{E_{\mathrm{g}}}^{\infty} \frac{\alpha E^2 dE}{\exp\left(\frac{E}{kT}\right) - 1} \tag{8.15}$$

where c is the speed of light, h is the Planck constant, α is the absorption coefficient, n_{r} is the refraction index, and k is the Boltzmann constant.

Non-radiative Recombination

Assuming the Shockley–Read–Hall (SRH) recombination theory (trap levels located near the middle of the forbidden gap), a constant recombination rate within the depletion region for each material and a point at which carrier concentrations are equal—which corresponds to the maximum recombination rate—, the non-radiative final contribution to J_{02} in the depletion region is given by [70–73]:

$$J_{02-\text{non}-\text{rad}} = q\left(\frac{x_n n_{i-\text{CdS}}}{\tau_n} + \frac{x_p n_{i-\text{CZTSe}}}{\tau_p}\right) \tag{8.16}$$

where τ is the non-radiative minority carrier lifetime. For kesterite material, defects such as Cu_{Sn} and Sn_{Zn} are expected to be formed near the middle of forbidden gap [78] while defects associated with Cd vacancies are predicted near the middle of CdS forbidden gap [79]. As a result, recombination via such centers could have a significant impact on solar cell performance.

Trap-Assisted Tunneling Recombination

Heterojunctions are very often dominated by tunneling, a result of the many energy states that can be introduced within the band gaps. Particularly, for kesterite semiconductor, centers due to defects such as Cu_{Zn}, V_{Cu}, Zn_{Sn}, and V_{Zn} with energy values in the range of 20–200 meV above the valence band maximum are expected to be formed which may allow tunneling [78]. On the other hand, for CdS material, shallow donor states such as Cd_i and Cd_S defects with energy values about 150 meV and 200 meV, respectively, could favor tunneling [79]. The fundamental theory of generation-recombination statistics in semiconductors, known as the SRH theory, has been successfully used for understanding fundamental semiconductor device physics and for analysis of the electrical characteristics of semiconductor devices. However, under large electric fields as in depletion regions, the quantum tunneling of charge carriers from energy bands to traps and the reverse process are very likely. A recombination model which took into account trap-assisted tunneling in both forward and reverse bias was proposed by Hurkx et al. [80, 81] where contributions from not only shallow states but also deep states were considered. The tunneling contribution was found to be a function of center energy and electric field values. In particular, for forward-biased junctions (solar cells), it is established that tunneling contribution in the depletion layer could only occur at an energy level between the local valence band maximum and the valence band maximum at the neutral *p*-type zone (V_{VB})—because for higher energies there are no states available from (and into) which a hole can tunnel [80, 81]. Obviously, the same reasoning holds for the tunneling of electrons in CdS material (V_{CB}). As an interesting result, authors pointed out that tunneling contribution Γ is independent of trap depth (ΔE_p) for not too large values of the electric field—condition given by expression (8.17). Conversely, for higher electric field (F) values, tunneling contribution depends on trap depth.

$$F < \frac{2kT\sqrt{2m^*\Delta E_p}}{q\hbar} \tag{8.17}$$

Taking into account that the highest electric field obtained for CZTS and CZTSe kesterite solar cell with record efficiency is about 1.3×10^4 V/cm, it is found that all shallow centers associated to kesterite and CdS materials—Cu_{Zn}, V_{Cu}, Zn_{Sn},V_{Zn},

Cd_i, and Cd_S—fulfill condition presented by expression (8.17). Furthermore, these centers also fulfill the previously mentioned requirement for tunneling. Consequently, these centers could play an important role in tunneling process. For lower electric field values, only centers that fulfill previously mentioned condition for tunneling will be involved in that mechanism. Then, under these conditions, Hurkx model establishes that the net recombination rate via traps (R_t) can be expressed by [81]:

$$R_t = (1 + \Gamma)R_{SRH} \tag{8.18}$$

where the Γ term which accounts for the effects of tunneling on both the density of captured carriers by a trap and the emission rate of carriers from a trap mainly depends on the built-in field (F) and is given by:

$$\Gamma = 2\sqrt{3\pi}\frac{Fq\hbar}{\sqrt{24m^*(kT)^3}}\mathrm{Exp}\left(\frac{Fq\hbar}{\sqrt{24m^*(kT)^3}}\right)^2 \tag{8.19}$$

It is important to notice that R_t (Eq. 8.18) contains not only the conventional SRH mechanism but also tunneling via traps. Therefore, under trap-assisted tunneling recombination model, majority carriers in CZTS(e)/(CdS) semiconductor are able to tunnel to bulk states in CZTSe/(CdS) depletion zone and then are captured by deep levels where the SRH recombination is completed when minority carriers are also captured, as displayed in Fig. 8.1. So, trap-assisted tunneling recombination only entails bulk states from either CZTS(e) or CdS material. The total contribution of this loss mechanism to J_{02} is obtained by integrating the net recombination rate via traps over the depletion region and is expressed by [70–73]:

$$J_{02-\mathrm{trap-assisted}} = q\left(\frac{x_n n_{i-\mathrm{CdS}}(1 + \Gamma_{\mathrm{CdS}})}{\tau_n} + \frac{x_p n_{i-\mathrm{CZTSe}}(1 + \Gamma_{\mathrm{kest}})}{\tau_p}\right) \tag{8.20}$$

This last equation involves both tunneling contributions from CZTS(e) and CdS bulk materials. Under a weak electric field (i.e., lowly doped junctions), the model reduces to the conventional SRH expression for recombination via traps (Eq. (8.16)).

CdS/Kesterite Interface Recombination

Another important route of carrier losses could be CdS/CZTS(e) interface—a result of defects formation caused by the lattice and thermal expansion mismatches—as shown in Fig. 8.1. These defects could play a fundamental role in solar cell performance. Taking into account that the interface recombination depends on interface recombination speed and minority carrier concentrations; the interface recombination losses contribution to J_{02} is given by [70–73]:

$$J_{02-\text{Interface}} = qSn_{\text{i-CZTSe}}\left(1 + \gamma_{\text{DOS}} e^{-(\Delta E_C + \Delta E_V)/2kT}\right) \tag{8.21}$$

where S is the interface recombination speed, $\gamma_{\text{DOS}} = g_{\text{CdS}}/g_{\text{kest}}$ is the density of states enhancement factor, with g_{CdS} and g_{kest} as the effective densities of states for CdS and kesterite materials, respectively, and finally, ΔE_c and ΔE_v are the conduction band offset and the valence band offset, respectively. From this equation, the influence of the band offsets on minority carrier recombination is demonstrated. In particular, for type-II ("cliff-like") heterojunction ($\Delta E_c < 0$), the interface recombination is expected to be greater than for type-I ("spike-like") heterojunction ($\Delta E_c > 0$). Therefore, since CdS/CZTSe is characterized by a spike-like heterojunction, the interface losses are expected to be lower than that for heterojunctions with cliff-like configuration such as CdS/CZTS.

Once the expressions for the dark current density, the absorption coefficient, and photocurrent density are found for kesterite/CdS solar cell, it is possible to evaluate the J–V characteristic (Eq. (8.6)). Then, the conversion efficiency is found. Therefore, a study on the impact of loss mechanisms can be carried out. That is, reverse saturation current density from each loss mechanism can be evaluated to calculate solar cell parameters (V_{oc}, J_{sc}, FF, and η) once the photocurrent density is known.

Model Parameters

An adequate selection of input parameters is an important part of solar cell simulation. Solar cells with Mo/CZTS/CdS/ZnO/ZnO:Al and Mo/CZTSe/CdS/ZnO/ITO configurations are modeled. ITO, ZnO, ZnO:Al, and CdS semiconductor parameters used in this model are well known and are presented in Table 8.1. It is important to note that these parameters were selected based on experimental values reported on literature and theory [50, 71–73].

Table 8.1 Simulation parameters for ZnO:Al, ZnO, ITO, and CdS films

Parameters	ZnO:Al	ZnO	ITO	CdS
Relative dielectric permittivity (ε_r)	9	9	2	9
Hole mobility, μ_p (cm^2/V s)	25	25	75	50
Donor concentration, N_D (cm^{-3})	10^{20}	10^{18}	10^{20}	10^{17}
Band Gap (eV)	3.3	3.3	3.6	2.4
Conduction band effective density of states, N_c (cm^{-3})	2.2×10^{18}	2.2×10^{18}	2×10^{20}	1.8×10^{19}
Valence band effective density of states, N_v (cm^{-3})	1.8×10^{19}	1.8×10^{19}	1.8×10^{19}	2.4×10^{18}
Defect density (cm^{-3})	10^{17}	10^{17}	10^{17}	10^{17}
Hole capture cross section (cm^2)	10^{-15}	10^{-15}	10^{-15}	10^{-13}
Hole thermal velocity (m/s)	10^7	10^7	10^7	10^7
Electron effective mass, m_e^*/m_0	0.275	0.275	0.3	0.25
Hole effective mass, m_h^*/m_0	0.59	0.59	0.6	0.7

In order to study CZTS and CZTSe performance, two comprehensive experimental reports of solar cells—which are among the highest efficiencies reported for kesterite compounds—were considered [7, 82]. One of the main reasons why these works were chosen for kesterite solar cell modeling is that authors provided details on important parameters such as minority carrier lifetime, minority carrier diffusion length, and acceptor concentration. As a result, a better estimation of kesterite solar cell behavior is expected. Values for CZTS and CZTSe parameters are shown in Table 8.2. Besides, film widths, series and shunt resistance values reported for these solar cells are also tabulated in Table 8.2. On top of this, other important parameters such as electron and hole effective masses, conduction band-offset values, relative dielectric permittivity values, and kesterite/CdS interface recombination were added to Table 8.2 [71–73]. The effective density of states of the conduction band (N_c) and the valence band (N_v) were calculated from CZTS and CZTSe electron and hole effective masses, respectively.

In order to calculate $EQE_T(\lambda)$, some other parameters such as surface reflectivity spectrum, front and back surface recombination velocities, minority carrier diffusion length, and minority carrier diffusion coefficient values are required. With the aim of obtaining ZnO:Al/ZnO/CdS/CZTS surface reflectivity, experimental spectral dependences of the refractive index (n) and the extinction coefficient (κ) for ZnO [83, 84], CdS [85], and CZTS [86] were used. It is important to note that these

Table 8.2 Reported parameters for CZTS- and CZTSe-based solar cells

Parameters	CZTS solar cell ($\eta = 8.27\%$) [82]	CZTSe solar cell ($\eta = 11.6\%$) [7]
ARC width (nm)	100	110
TCO width (nm)	450 (ZnO:Al)	50 (ITO)
ZnO width (nm)	80	10
CdS width (nm)	91	25
CZTS (CZTSe) width (nm)	720	2200
Series resistance (Ω cm^2)	5.8	0.32
Shunt resistance (Ω cm^2)	2.2×10^4	2.2×10^4
Absorber minority carrier lifetime (ns)	1.7	2
Absorber minority carrier mobility (cm^2/V s)	6.2	690
Absorber acceptor concentration (cm^{-3})	10^{16}	2×10^{15}
Absorber Band Gap (eV)	1.51	1.0
Shading from grid (%)	4	4
Absorber electron effective mass	0.18 m_0	0.08 m_0
Absorber hole effective mass	0.71 m_0	0.33 m_0
Conduction band offset (ΔE_c): eV	−0.24	0.48
Relative dielectric permittivity	10	8.5
Interface recombination speed (cm/s)	10^4	10^3

n and κ spectral dependences for ZnO and CdS materials have been also considered for modeling CIGS solar cells [87]. A front and back surface recombination velocity value of 10^5 cm/s for CdS and CZTS (CZTSe) minority carriers was taken into account as previously considered by Patel et al. [50]. On the other hand, the minority carrier diffusion coefficient and diffusion length for ZnO, ITO, and CdS materials are obtained from hole mobility, defect density, hole capture cross section, and hole thermal velocity. Conversely, from CZTS and CZTSe minority carrier lifetime and mobility values reported for solar cells, the minority carrier diffusion coefficient and diffusion length values are calculated. Relative dielectric permittivity values for CdS and CZTS(e), CZTS(e) acceptor concentration and CdS donor concentration values are used to calculate depletion zone characteristics (built-in voltage, CdS and CZTS(e) depletion zone widths, and electric field) by means of the Poisson's equation. The solar radiation AM 1.5 ($300 < \lambda < 1300$ nm) was adopted as the illuminating source with a power density of 100 mW/cm^2.

Comparing Model Outcomes with Experimental Data

EQE Data

The EQE contributions for *p*-, *n*-, and depletion zone as functions of wavelength were firstly calculated for CZTS and CZTSe solar cells using previously presented parameters. The results of each zone, total, and experimental data [7, 82] are shown in Fig. 8.2. The ZnO, ZnO:Al, and ITO contributions to n quasi-neutral zone EQE values were considered. The comparison of the simulation results to the measured EQE values shows that the presented model is able to reproduce with good agreements the experimental observations. For wavelength values higher than 553 nm, EQE_T is characterized by CZTS(e) contribution while for wavelength

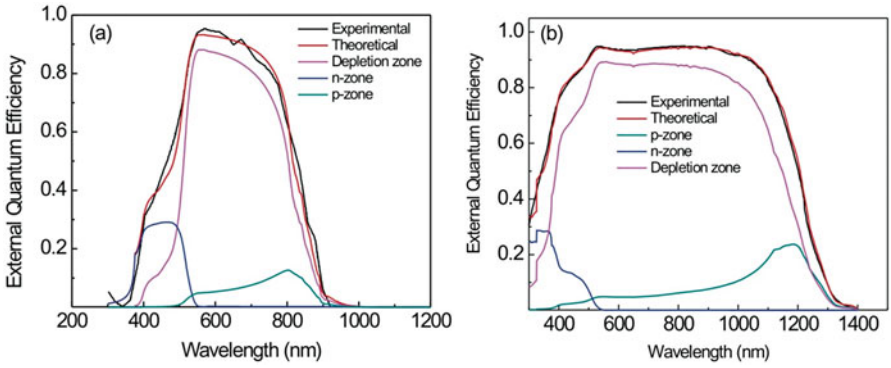

Fig. 8.2 EQE theoretical and experimental data for CZTS (**a**) and CZTSe (**b**) solar cells with efficiencies of 8.27% and 11.6%, respectively. The contribution of each zone was also added

values lower than 553 nm CdS contribution becomes important as shown in Fig. 8.2a, b. In particular, ZnO:Al and ZnO contributions ($\lambda < 375$ nm) are almost negligible. Besides, the results show that depletion zone contributions to EQE_T in both solar cells are the most important. Since most photons are absorbed in the depletion zone, the contribution of the p quasi-neutral zone to EQE_T is small. Conversely, the results suggest that the n quasi-neutral zone contribution is not negligible for CZTS solar cell. In fact, a further improvement in EQE_T values could be reached by decreasing n quasi-neutral zone contribution by using thinner CdS layers (~40 nm) since it would allow a higher ultraviolet photon absorption in the absorber depletion region increasing short-circuit current density [70].

Study of Loss Mechanisms Impact on Solar Cell Performance

A study of each loss mechanism effect on CZTS/CdS and CZTSe/CdS solar cells behavior was carried out and results are presented in Table 8.3 along with experimental reports [7, 82]. It is important to note that each loss mechanism has a direct impact on V_{oc} values as displayed in Table 8.3. If the main transport mechanisms were diffusion, thermionic, or radiative recombination, high V_{oc} (>906 mV for CZTS and >733 mV for CZTSe) and efficiency values higher than 15% would be expected. As a result, such loss mechanisms are not able to explain the experimentally reported data for CZTS and CZTSe solar cells. On the other hand, among the different loss mechanisms, non-radiative recombination, CdS/CZTS interface

Table 8.3 Loss mechanisms: diffusion (*Diff*), thermionic emission (*TE*), radiative recombination (*RR*), non-radiative recombination (*NRR*), interface recombination (*IR*), and trap-assisted tunneling recombination (*TATR*) influence on CZTS- and CZTSe-based solar cell performance. The experimental data for solar cells are also added for comparison

	Mechanisms	η (%)	J_{sc} (mA/cm^2)	V_{oc} (mV)	FF (%)
CZTS solar cell	Diff	15.4	20.3	961	78.7
	TE	15.0	20.3	950	77.7
	RR	14.5	20.3	917	78.0
	Diff +TE + RR	14.3	20.3	906	77.6
	NRR	9.3	20.3	709	64.5
	IR	10.4	20.3	772	66.5
	TATR	8.5	20.3	667	62.9
	NRR + IR	9.0	20.3	696	63.9
	TATR +IR	8.4	20.3	661	62.7
	Experimental	*8.4*	*19.5*	*661*	*65.8*
CZTSe solar cell	Diff	24.4	22.4	782	76.2
	TE	23.0	40.9	745	75.6
	RR	22.6	40.9	733	75.4
	NRR	12.5	40.9	457	66.9
	IR	21.9	40.9	713	75.2
	TATR	11.5	40.9	426	66.2
	Experimental	*11.6*	*40.6*	*423*	*67.3*

recombination, and trap-assisted tunneling recombination have a major influence on V_{oc} values for CZTS solar cells while trap-assisted tunneling recombination is the dominant transport mechanism for CZTSe solar cell.

In particular, the comparison of experimental results to the model outcomes shows that both solar cells are mainly dominated by trap-assisted tunneling recombination (TATR). For CZTS solar cell, despite a high CdS/CZTS interface recombination velocity value was assumed for calculations, efficiency values higher than 10.4% were obtained under interface recombination (IR) contribution and the experimental data were not described—differences of 23.8% in efficiency, 16.8% in V_{oc}, and 1.1% in FF between the IR mechanism and experimental results are observed. However, if IR contribution is considered along with the TATR one, a better fit to experimental data is reached as shown in Table 8.3. Conversely, IR influence on CZTSe solar cell is negligible, which is a result of a spike-like band alignment. Therefore, for donor and acceptor concentrations of the solar cells with high efficiencies, trap-assisted tunneling recombination has a major impact on solar cell performance. As a result, defects in depletion zone play a fundamental role in kesterite solar cell performance. This fact is due to electric field at junction is high enough to favor tunneling of carriers via traps and therefore its contribution should not be considered negligible. Despite most reports consider SRH recombination as one of the most important loss mechanisms, this result suggests that tunneling losses are significant and offer a better fit to experimental data. This fact can be explained taking into account that kesterite material is characterized by a high defect density which favors trap-assisted tunneling recombination under a high electric field present at CdS/kesterite heterojunction. Therefore, trap-assisted tunneling recombination is introduced as the dominant loss mechanism in kesterite-based solar cells. Consequently, for a further solar cell efficiency improvement, an enhancement in kesterite crystalline quality is required. This would guarantee higher minority carrier lifetimes and diffusion lengths. Table 8.3 shows another aspect of interest, for a low non-radiative recombination contribution, CZTS solar cell could reach efficiency values close to 10%. Such value is mainly limited by interface recombination and is still lower than those reached by CZTSSe compounds (12.4%) [19]. Therefore, after reaching a CZTS crystalline quality improvement, a study focused on the CdS material replacement is highly required for boosting open-circuit voltage values and thus solar cell efficiency. Therefore, further studies should be focused on improving CZTS crystalline quality along with replacing CdS material with another that fulfill adequate physical properties for photovoltaic applications. On the other hand, for CZTSe solar cell, it is important to remark that for a high CZTSe crystalline quality—a low density of defects—, efficiency values about 21.9% and V_{oc} values close to 713 mV are estimated. It is interesting to notice that experimental reports on CZTGSSe, CdTe, and CIGS solar cells with efficiency values lower than 12% have also introduced TATR as the dominant loss mechanism [88–90]. Consequently, this transport mechanism could be playing an important role in open-circuit voltage deficit.

The Path Towards a Further Kesterite Solar Cell Efficiency Improvement

CZTS Solar Cell

In order to optimize solar cell efficiency, CZTS and CdS widths were varied and results are displayed in Fig. 8.3. It is demonstrated that a further efficiency improvement (~9.8%) can be reached for thinner CdS and thicker CZTS layers. A thinner CdS layer would allow a higher ultraviolet photon absorption in the depletion region of the absorber increasing short-circuit current density, while thicker CZTS layers will guarantee major photon absorption. On the other hand, Fig. 8.3 shows that a CZTS width of 1.5 μm is suitable to ensure the complete absorption of photons. Furthermore, it was found that under the CdS/CZTS interface recombination limit (low non-radiative recombination contribution), the efficiency value can be further improved to 12.4% (for ~40 nm CdS and 1.5 μm CZTS widths), which is comparable to the record efficiency reached for CZTSSe kesterite compounds [19].

In order to further optimize solar cell efficiency, CZTS acceptor concentration and CdS donor concentration were varied. Optimized CZTS and CdS widths of 1.5 μm and 40 nm, respectively, were taken into account as previously demonstrated. Since trap-assisted tunneling recombination along with CdS/CZTS interface recombination well described experimental CZTS solar cell performances, their contributions were considered in J–V characteristics. Figure 8.4 shows contour plots for efficiency, short-circuit current density, and open-circuit voltage as a function of CZTS acceptor concentration (N_a) and CdS donor concentration (N_d). CdS donor concentration values in the range of 10^{16}–10^{17} cm^{-3} were considered as experimentally reported for CdS thin films grown by chemical bath deposition,

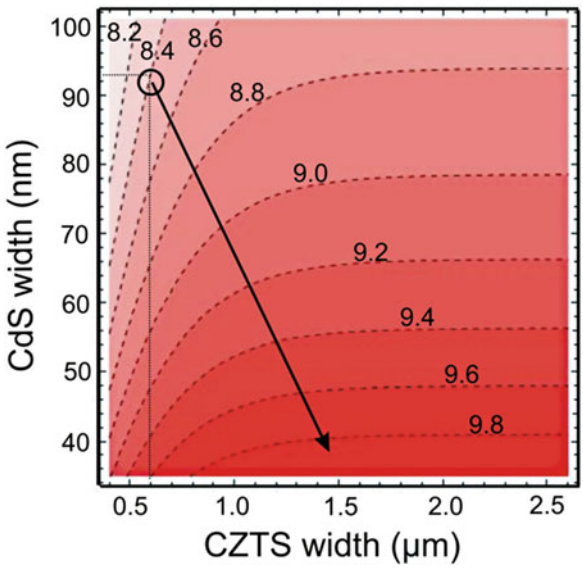

Fig. 8.3 Contour plot of CdS/CZTS efficiency as a function of the CdS and CZTS widths

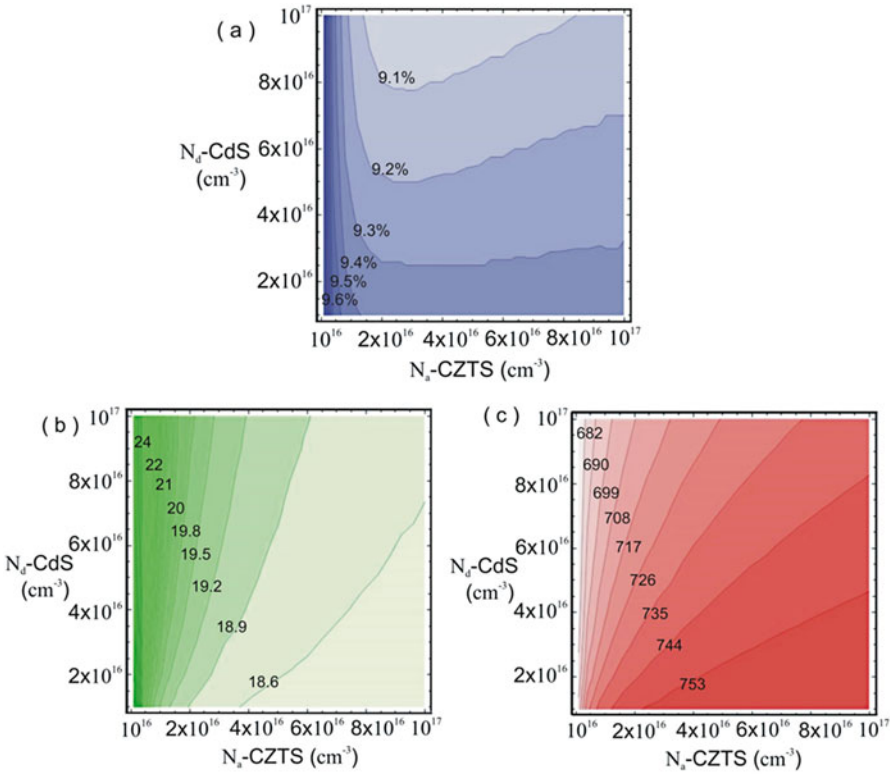

Fig. 8.4 Contour plot of CdS/CZTS efficiency (**a**), short-circuit current density (mA/cm^2) (**b**), and open-circuit voltage (mV) (**c**) as a function of the CdS donor concentration (N_d) and CZTS acceptor concentration (N_a)

while CZTS acceptor concentrations in the range of 10^{16}–10^{17} cm^{-3} were taken into consideration.

The first thing to highlight from Fig. 8.4a is CZTS solar cell efficiency decrease with N_a increase for a constant N_d value. Bigger N_a values would reduce absorber depletion region width, implying a lower contribution to short-circuit current density as shown in Fig. 8.4b, as less photo-generated carriers will achieve the depletion region. On the other hand, an attractive result is obtained when N_d is decreased. A solar cell efficiency improvement is observed when N_d is diminished. It is interesting to note that a similar performance was obtained for CdS/CZTSe-based solar cell [91]. Authors showed that when CdS is doped with Cu, which implies a CdS donor concentration decrease, despite short-circuit current density value was decreased, open-circuit voltage and thus efficiency were enlarged. This performance was assumed to be related with the MIS theory. For CZTS-based solar cell, a similar result is theoretically found. This performance is explained taking into account that when trap-assisted tunneling recombination is the main transport mechanism, there is a trade-off between short-circuit current density and open-

circuit voltage. For lower N_d values, short-circuit current density is decreased (Fig. 8.4b) since absorber depletion region width is reduced but open-circuit voltage is increased (Fig. 8.4c) due to electric field in depletion zone is decreased and thus trap-assisted tunneling contribution. Therefore, a path to increase CZTS solar cell efficiency could be related to reduce CdS donor concentration by means of its doping with Cu as reported for CZTSe-based solar cells [91]. In the cited work, it was assumed that CdS:Cu with a thickness about 30 nm suggests the CdS/CZTSe solar cell behaviors as a MIS structure. In this work, it is demonstrated that CdS donor concentration decrease (for 40 nm CdS width) could be seen as a confirmation of previously assumed.Under this approach, a new record in open-circuit voltage about 710 mV (under trap-assisted tunneling recombination losses) could be achieved for relatively low N_a values as illustrated in Fig. 8.4c.

A study of the most important loss mechanisms effect on dark current density as a function of N_d (for $N_a = 10^{16}$ cm^{-3}) was carried out and results are presented in Fig. 8.5. For $N_d \sim 10^{17}$ cm^{-3}, which corresponds to value reported for the CZTS solar cell, the trap-assisted tunneling contribution to dark current is important and bigger than SRH contribution. When N_d is decreased, SRH and trap-assisted tunneling contributions are decreased as well. This behavior for dark current density explains the open-circuit voltage improvement shown in Fig. 8.4c when N_d is decreased. For a CdS donor concentration lower than 10^{14} cm^{-3}, electric field in depletion region is small and trap-assisted tunneling recombination turns into SRH mechanism. Besides, both mechanisms approach to CdS/CZTS interface

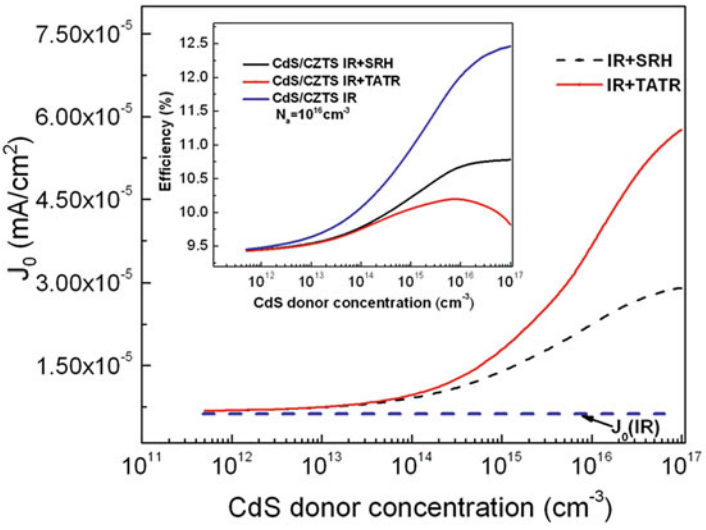

Fig. 8.5 Dark current density for CdS/CZTS solar cell as a function of CdS donor concentration. The possible contribution of the most important loss mechanisms: non-radiative recombination (*SRH*), trap-assisted tunneling recombination (*TATR*), and interface recombination (*IR*) were taken into account. The inset shows solar cell efficiency behavior under each loss mechanism as a function of CdS donor concentration

recombination, meaning that interface recombination becomes the most important loss mechanism for low N_d values.

An interesting trend is observed for the conversion efficiency by decreasing N_d values in the inset of Fig. 8.5 as functions of transport mechanisms. The efficiency performance is directly a result of the trade-off between short-circuit current density and open-circuit voltage. Under trap-assisted tunneling recombination and CdS/CZTS interface recombination as the dominant loss mechanisms, if N_d value is decreased until ~5×10^{15} cm^{-3}, the efficiency will increase from 9.7 to 10.2%. However, for lower N_d ($<5 \times 10^{15}$ cm^{-3}) values, the open-circuit voltage increase cannot compensate short-circuit current density drop, implying a solar cell efficiency fall. Therefore, these loss mechanisms set a limit for CZTS-based solar cell efficiency. As a result, an optimized efficiency value of 10.2% can be only achieved for $N_d \sim 5 \times 10^{15}$ cm^{-3}, $N_a \sim 10^{16}$ cm^{-3}, 40 nm CdS and 1.5 μm CZTS widths. Nevertheless, this new value is still quite low. On the other hand, inset of Fig. 8.5 also displays that under the CdS/CZTS interface recombination limit (low non-radiative recombination contribution), the efficiency value can be further improved to 12.4%. Furthermore, under CdS/CZTS interface recombination limit and ideal series and shunt resistance values ($R_s = 0$, $R_{sh} = \infty$), an efficiency value of 14.7% was achieved; therefore, further studies should be focused on improving CZTS crystalline quality and replacing Mo which is mostly used as back contact. Nevertheless, even under these conditions, CdS/CZTS solar cell efficiency is still relatively low, therefore another approach to high efficiency could be to replace CdS with an adequate buffer material with a high band gap value and that forms a spike-like configuration with CZTS material. This fact could improve CZTS solar cell efficiency to 20.9%, being diffusion or radiative recombination the most important loss mechanisms. Only then, CZTS solar cell technology would be able to replace CdTe- and CIGS-based technology.

On the other hand, one important parameter having a great impact on trap-assisted tunneling recombination (TATR) and consequently on solar cell behavior is minority carrier lifetime. So far, poor information on kesterite minority carrier lifetime role in solar cell performance is found. A study of CZTS solar cell parameters as functions of minority carrier lifetime in the range of 10^{-11}–10^{-6} s was carried out and results are presented in Fig. 8.6a–d. By increasing CZTS minority carrier lifetime to 10^{-6} s, an improvement in solar cell efficiency near to 11% is obtained. It is important to mention that this result was obtained under non-optimized CdS and CZTS widths (Table 8.2). However, even under optimized CdS and CZTS conditions, a 12.4% is expected as previously shown. These results demonstrate that not only high-quality CZTS material is required for high efficiencies but also a good CZTS/CdS interface quality as such efficiency values are the same that were found for CZTS solar cells under IR mechanism as previously shown. As a result, it is demonstrated that IR is the dominant mechanism for CZTS solar cell under good CZTS crystalline quality. This is a direct consequence of the high CdS/CZTS interface recombination speed (10^4 cm/s) that describes such heterojunction. Besides, it was found that further improvements to 22.7 mA/cm^2 in J_{sc}, 770 mV in V_{oc}, and 63% in fill factor are expected with increasing CZTS

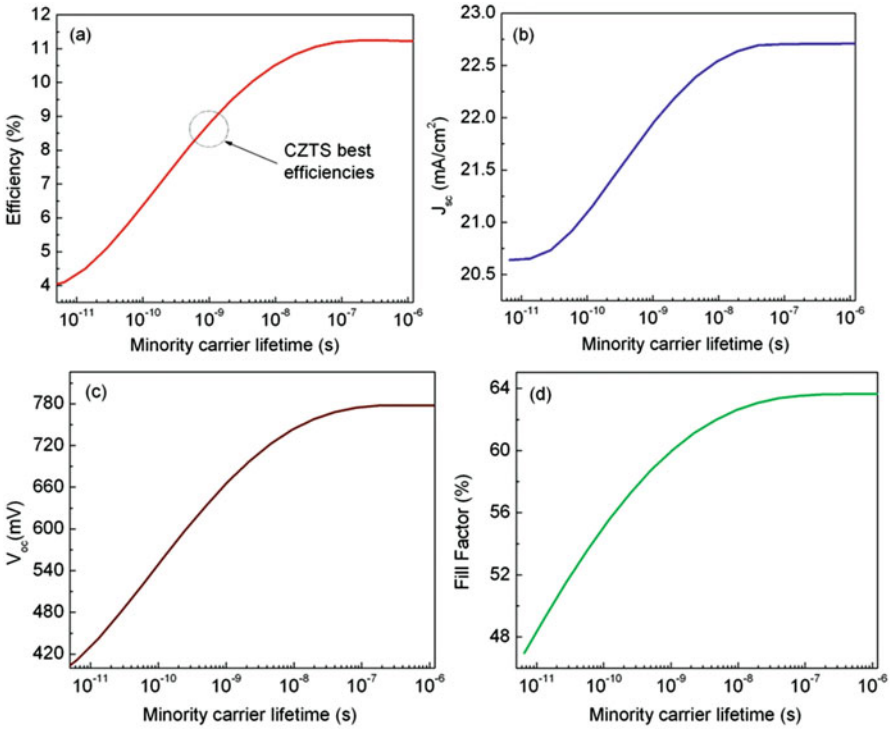

Fig. 8.6 Impact of CZTS minority carrier lifetime on: (**a**) solar cell efficiency, (**b**) short-circuit current density, (**c**) open-circuit voltage, and (**d**) fill factor

crystalline quality. These values are still quite poor; therefore, it is demonstrated that after reaching good crystalline quality, a second task for higher solar cell efficiencies will be improving CdS/CZTS interface quality. Otherwise, a low solar cell efficiency of 11% (12.4%) is expected from this heterojunction under non-optimized (optimized) CdS and CZTS widths.

Despite CdS/kesterite interface recombination speed values in the range of 10^3–10^4 cm/s are commonly assumed, a more comprehensive impact of interface recombination speed was considered in this work (1–10^6 cm/s). Results for efficiency and V_{oc} values as functions of CZTS minority carrier lifetime and interface recombination speed are presented in Fig. 8.7a, b, respectively. It is elucidated that interface recombination speed values as low as 1 and 10 cm/s have a negligible impact on V_{oc} and efficiency values. In fact, a solar cell efficiency of 16% (with about 1.0 V of V_{oc}) is expected for good CZTS crystalline quality under such conditions. For an interface recombination speed of 10^2 cm/s, V_{oc} and efficiency are slightly reduced to about 15% and 950 mV, respectively. However, for higher CdS/CZTS interface recombination speed values, solar cell efficiency and V_{oc} are dropped. Another interesting feature is observed from Fig. 8.7. For low minority carrier lifetime values ($<10^{-9}$ s) and CdS/CZTS interface recombination speed

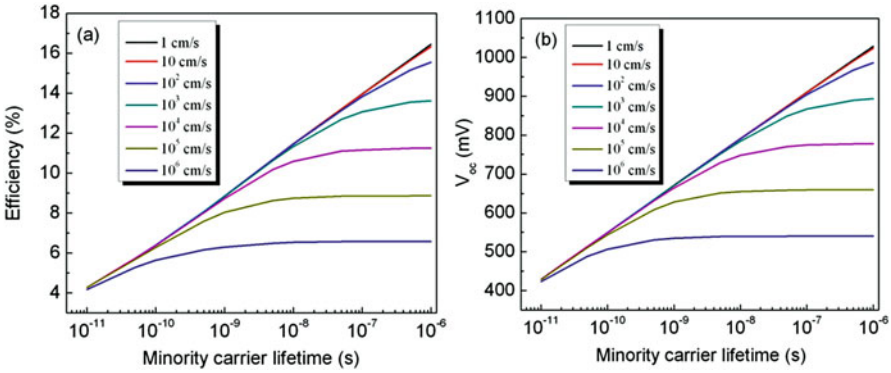

Fig. 8.7 Effect of CZTS minority carrier lifetime and CdS/CZTS interface recombination speed on: (**a**) solar cell efficiency and (**b**) open-circuit voltage

values lower than 10^4 cm/s, TATR is the dominant mechanism since the impact of CdS/CZTS interface recombination is almost the same regardless the interface recombination speed. Assuming CdS/CZTS interface recombination speed values in the range of 10^3–10^4 cm/s, and only few nanoseconds of minority carrier lifetime—as reported elsewhere—, the impact of interface recombination is almost negligible in comparison to the TATR one; this result is in correspondence with the one obtained for CZTS solar cell as previously shown. On the other hand, a trade-off is clearly observed between IR and TATR. The higher the IR speed, the lower improvement in V_{oc} and efficiency with CZTS minority carrier lifetime enhancement while lower IR speed values lead to higher V_{oc} and efficiency values with CZTS minority carrier lifetime increasing. As a result, better CdS/CZTS interface quality and better CZTS bulk quality are important conditions to promote CZTS solar cell outcomes.

Improvements in V_{oc} with increasing CZTS minority carrier lifetime can be explained by the reduction in carrier losses due to TATR mechanism. The impact of minority carrier lifetime on EQE values is shown in Fig. 8.8a, b for relatively low and high values, respectively. Since a higher minority carrier lifetime contributes to reduce carrier losses, more carriers from p quasi-neural region will be able to reach depletion zone as illustrated in Fig. 8.8b in comparison with Fig. 8.8a.

In order to better understand the impact of IR and TATR depending on CZTS minority carrier lifetime and interface recombination speed, reverse dark current density of these mechanisms (J_{IR} and J_{TATR}) were evaluated and results are illustrated in Fig. 8.9a, b. It is observed that for low minority carrier lifetime values, TATR is the dominant loss mechanism while IR contribution is negligible as previously demonstrated from Fig. 8.7. For higher CZTS minority carrier lifetime, lower reverse dark current density values are achieved which is a result of carrier loss reduction. Once again, for CZTS minority carrier lifetime of 2 ns, IR losses are almost negligible while for higher values IR becomes the dominant loss mechanism. In particular for 10^{-8} s of CZTS minority carrier lifetime as reported by

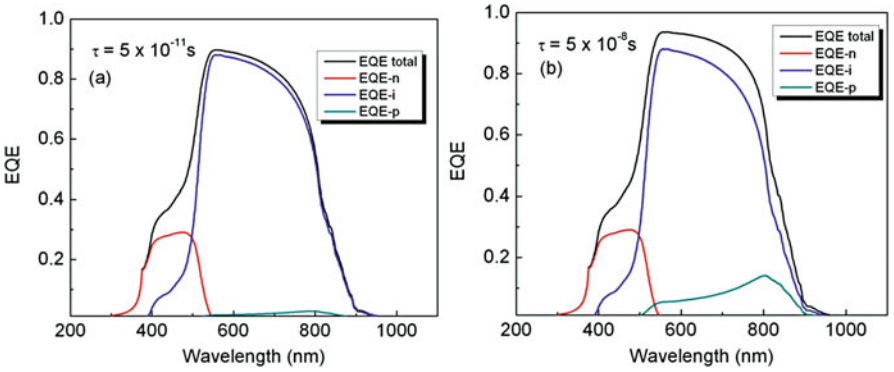

Fig. 8.8 Theoretical data for external quantum efficiency of *p* quasi-neutral zone, *n* quasi-neutral zone, depletion zone and total for CZTS solar cell under different minority carrier lifetimes: (**a**) 5×10^{-11} s and (**b**) 5×10^{-8} s

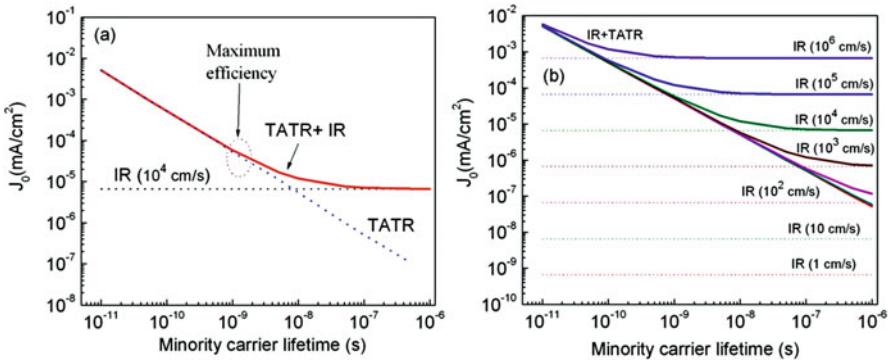

Fig. 8.9 Reverse dark current density as a function of CZTS minority carrier lifetime: (**a**) under an interface recombination speed of 10^4 cm/s and (**b**) under interface recombination speed values in the range of 1–10^6 cm/s. Trap-assisted tunneling recombination and interface recombination are considered as the dominant loss mechanisms

F. Liu et al. [92], a higher attention should be given to CdS/CZTS interface quality for further promoting solar cell efficiency. Therefore, this result is also consistent with the experimental one reported by F. Liu et al. Figure 8.9b shows similar trends for reverse dark current density as a function of CZTS minority carrier lifetime and IR speed. For the lowest CZTS minority carrier lifetime values, IR speed impact on reverse dark current density is almost negligible. A correlation between IR and TATR is also observed for reverse dark current density results. Consequently, it is demonstrated that such mechanisms have a direct impact on V_{oc} and efficiency values. Under a CZTS minority carrier lifetime of 10^{-9} s, the impact of IR is almost negligible. Nevertheless, a further improvement in minority carrier lifetime to

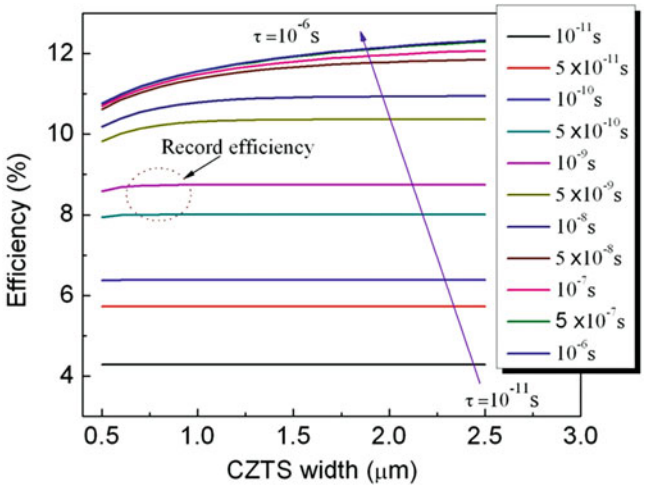

Fig. 8.10 CZTS efficiency as a function of CZTS width and minority carrier lifetime considering an interface recombination speed of 10^4 cm/s

higher efficiency values also requires a reduced IR speed for promoting solar cell efficiency over 11%.

With the purpose of optimizing CZTS width, solar cell efficiency as a function of CZTS width and CZTS minority carrier lifetime was found; results are presented in Fig. 8.10. Unlike previous shown results, where only one value for minority carrier lifetime was considered, now the effect of different minority carrier lifetime values is evaluated. An interface recombination speed of 10^4 cm/s is considered. For low CZTS minority carrier lifetime (lower than 10^{-10} s), solar cell efficiency is independent of CZTS width. This result is a consequence of the poor contribution of photo-generated carriers at p quasi-neutral zone—most electron–hole pairs recombined before reaching the depletion zone. It is clearly observed that CZTS semiconductor with minority carrier lifetime of few nanoseconds only requires of about 750 nm width. For higher widths, carriers created at p quasi-neutral zone at a bigger position are not able to reach the depletion region and hence solar cell efficiency does not change. This result is in correspondence with those reported in the literature—CZTS width of only about 800 nm is required for solar cell applications [82]. Better CZTS solar cell performances are found for minority carrier lifetimes higher than 5×10^{-8} s. In fact, under such condition the higher CZTS width the bigger CZTS solar cell efficiency as more electron–hole pairs created at p quasi-neutral zone are able to reach the depletion zone. Consequently, in order to use a higher CZTS width in solar cells, it is firstly required to guarantee a higher CZTS minority carrier lifetime. From this figure, it is also observed the impact of CZTS minority carrier lifetime on solar cell efficiency. For the lowest CZTS minority carrier lifetime, only a 4% is obtained while a tendency to 12% is observed for the highest value with CZTS width increasing. This last efficiency value is mainly limited by the interface recombination as previously mentioned.

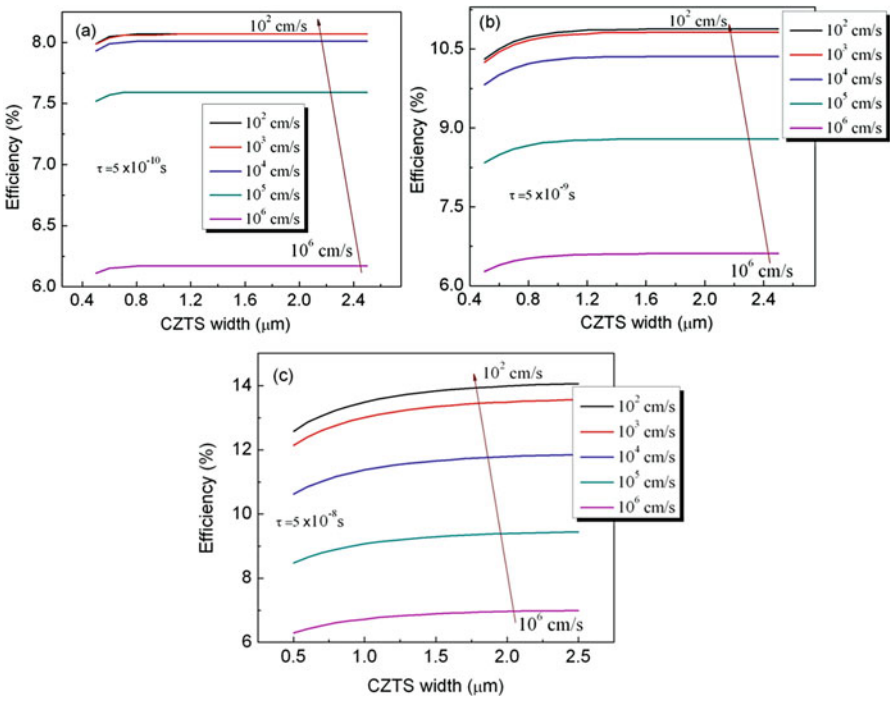

Fig. 8.11 CZTS efficiency as a function of CZTS width and interface recombination speed for CZTS minority carrier lifetime of: (**a**) 5×10^{-10} s, (**b**) 5×10^{-9} s, and (**c**) 5×10^{-8} s

Results for CZTS solar cell efficiency as a function of CZTS width for different minority carrier lifetimes and CdS/CZTS interface recombination speeds are presented in Fig. 8.11a–c. The lowest CZTS efficiency is attained for the highest interface recombination speed and the lowest minority carrier lifetime. By considering a CZTS minority carrier lifetime of 5×10^{-8} s and an IR speed of 10^2 cm/s, CZTS solar cell efficiency can be promoted to about 14% using a CZTS with of 2.5 μm.

One important parameter to be optimized is CdS width as previously mentioned. The impact of CdS width and CZTS/CdS interface recombination on solar cell efficiency is illustrated in Fig. 8.12a while the effect of CdS width and CZTS minority carrier lifetime on solar cell efficiency is presented in Fig. 8.12b. The lower CdS width the higher solar cell efficiency since more photons are absorbed in the CZTS material. Besides, it is demonstrated that the impact of CdS width highly depend on CZTS minority carrier lifetime and IR speed. Particularly, for CZTS minority carrier lifetime of about 10^{-8} s, a variation from 10.7 to 12% is expected with CdS decreasing for an IR speed of 10^4 cm/s. A 9% could be obtained for CdS width lower than 50 nm and keeping IR speed lower than 5×10^4 cm/s for a CZTS minority carrier lifetime of 1.7 ns. However, keeping the same IR speed with CdS width reduction is sometimes quite challenging as thinner CdS layers entail a major

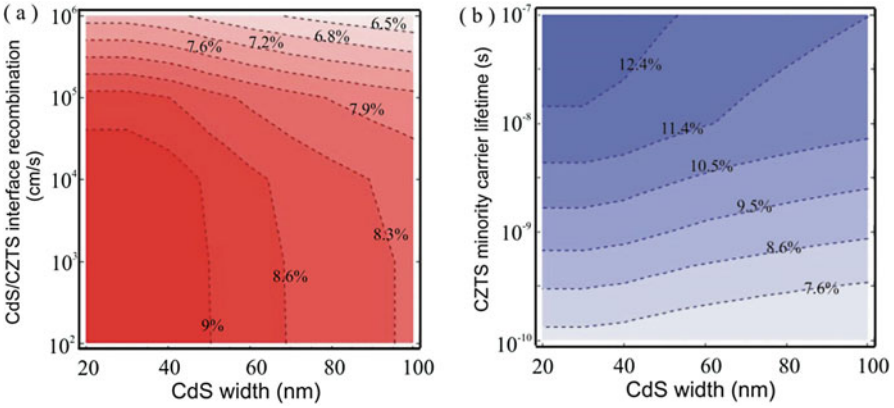

Fig. 8.12 Contour plot of CZTS solar cell efficiency as a function of: (**a**) CdS/CZTS interface recombination speed and CdS width considering a CZTS minority carrier lifetime of 1.7 ns and (**b**) CZTS minority carrier lifetime and CdS width considering an interface recombination speed of 10^4 cm/s

pinhole formation and thus a major recombination contribution. From Fig. 8.12a, b, it is also noticed that higher efficiencies are reached for thinner CdS widths by increasing CZTS minority carrier lifetime than reducing IR speed. This result is a consequence of the low interface recombination impact for CZTS minority carrier lifetime of few nanoseconds. However, it is important to remark that for higher minority carrier lifetime values, interface recombination becomes dominant as previously shown. For obtaining efficiency values higher than 12.4%, a particular attention should be given to improve CdS/CZTS interface quality—IR speed lower than 10^4 cm/s is needed—as previously demonstrated.

Finally, the influence of IR speed and minority carrier lifetime on solar cell efficiency and open-circuit voltage for optimized CdS and CZTS widths is presented in Fig. 8.13a, b. A 30 nm CdS width and 2.5 μm CZTS width were considered. A solar cell efficiency enhancement from 10 to 18% is expected depending on CZTS minority carrier lifetime and IR speed. The better efficiency values are observed for the lowest IR speed and the highest minority carrier lifetime. Under such conditions, open-circuit voltage value can be improved to 918 mV making this result attractive to replace CdTe and CIGS technology. Consequently, further experimental research should be focused on improving CZTS crystalline quality along with CdS/CZTS interface quality. Otherwise, CZTS solar cell efficiency will remain at about 9% as previously demonstrated in this work.

CZTSe Solar Cells

Once the experimental data for CZTSe solar cell with the record efficiency were reproduced with good agreements, the path towards a further CZTSe solar cell

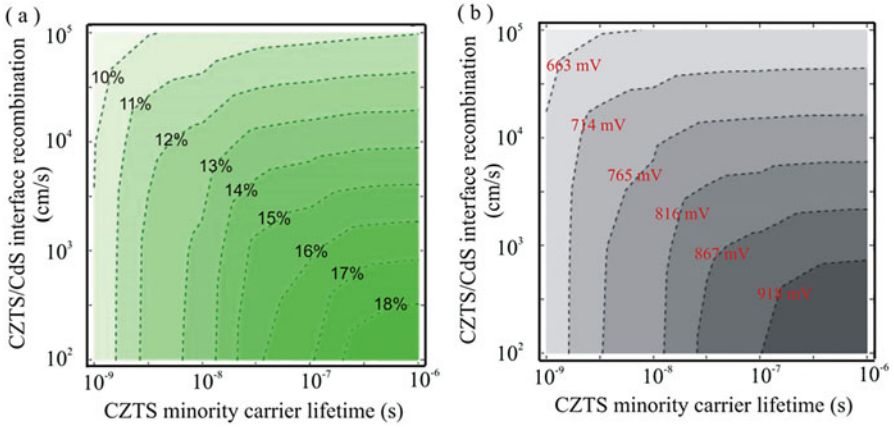

Fig. 8.13 Contour plot of CZTS solar cell efficiency (**a**) and open-circuit voltage (**b**) as functions of CdS/CZTS interface recombination speed and CZTS minority carrier lifetime. Optimized CdS and CZTS widths were considered

efficiency improvement is presented. Taking into account CZTSe depletion width (0.23 μm), CZTSe minority carrier diffusion length (2.1 μm), and an average CZTSe absorption coefficient of 10^4 cm^{-1}, a CZTSe width of 2.2 μm is suitable to ensure the complete absorption of photons with a high contribution to the photocurrent density. On the other hand, to obtain a CdS width lower than 25 nm without pinholes formation is perhaps one of the greatest challenges in CdS technology. Therefore, CZTSe solar cell with the record efficiency was based on optimized CdS and CZTSe widths. In order to further optimize solar cell efficiency, CdS donor concentration (N_d) and CZTSe acceptor concentration (N_a) were varied in a commonly reported range; results are presented in Fig. 8.14. Since trap-assisted tunneling recombination (TATR) well described the experimental data, its contribution to J–V characteristics was considered. A particular behavior in solar cell efficiency (Fig. 8.14a) for N_a and N_d concentrations variation is found which is associated with the trade-off between short-circuit current density (J_{sc}) (Fig. 8.14b) and open-circuit voltage (V_{oc}) (Fig. 8.14c) values. A slight increase in CZTSe solar cell efficiency is obtained when N_a is increased, for $N_d \sim 10^{17}$ cm^{-3} (as reported for the solar cell with the record efficiency). In this way, better performances are reached for more conductive CZTSe layers since V_{oc} increase compensates J_{sc} losses. On the other hand, a slight solar cell efficiency improvement is observed when N_d is decreased. It is interesting to note that a similar trend was previously found for CZTS.

In order to study if better performances can be reached, CdS donor concentrations lower than 10^{16} cm^{-3} were considered and efficiency results are displayed in Fig. 8.15.

Similar behaviors to CZTS solar cells are found for J_{sc} and V_{oc} values in CZTSe solar cells as shown in the inset of Fig. 8.15. When trap-assisted tunneling recombination is the dominant transport mechanism, there is a trade-off between short-

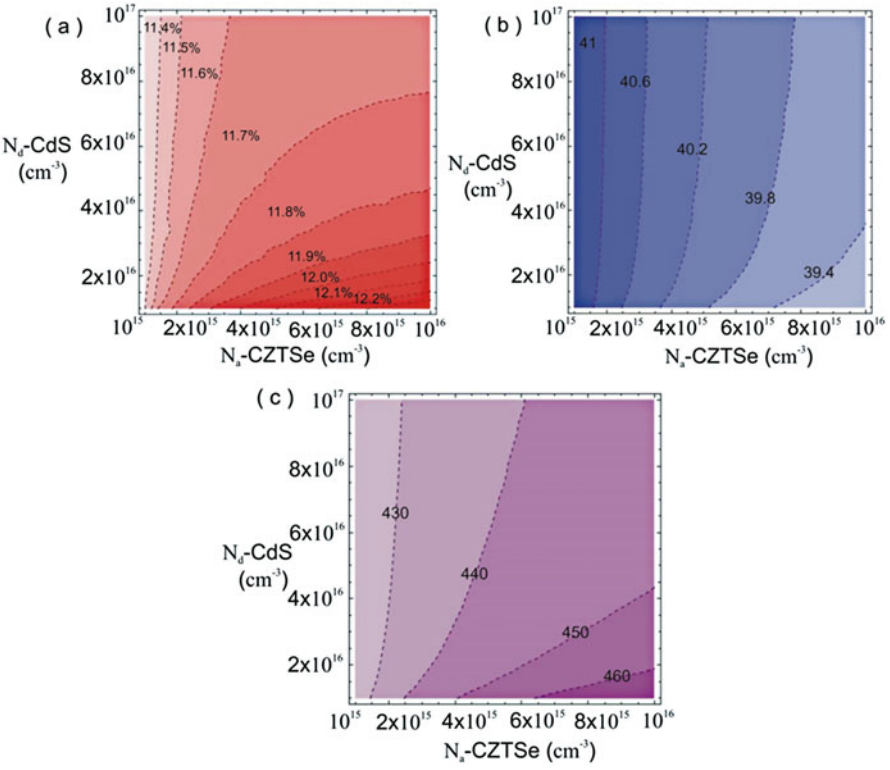

Fig. 8.14 Contour plot of CdS/CZTSe efficiency (**a**), short-circuit current density (mA/cm^2) (**b**), and open-circuit voltage (mV) (**c**) as a function of the CdS donor concentration (N_d) and CZTSe acceptor concentration (N_a)

circuit current density and open-circuit voltage. For lower N_d values, short-circuit current density is decreased since absorber depletion region width is reduced. But, open-circuit voltage is increased because electric field in depletion zone is decreased and thus trap-assisted tunneling contribution as well. That is, when the donor density in CdS is high, more band bending occurs at the interface of CdS/CZTSe, which allows more tunneling to occur. Thus, the lower donor density in CdS, the less tunneling contribution in depletion layers and consequently V_{oc} increases. Therefore, a path to increase CZTSe solar cell efficiency is associated with achieving more resistive CBD-CdS thin films (CdS:Cu could be a method). Under this approach, a new efficiency record of about 19.4% with an open-circuit voltage close to 708 mV could be achieved. For higher CdS resistivity values, better insulators are obtained. Therefore, taking into account that TCO and CZTSe behave like a metal and as a semiconductor, respectively, a more resistive and thinner CdS layer makes device to operate in a similar way to a MIS structure instead of a p–n junction. This theory is also supported by results reported for the most efficient CZTSe solar cell with a buffer layer thickness of 25 nm. A thinner CdS layer for

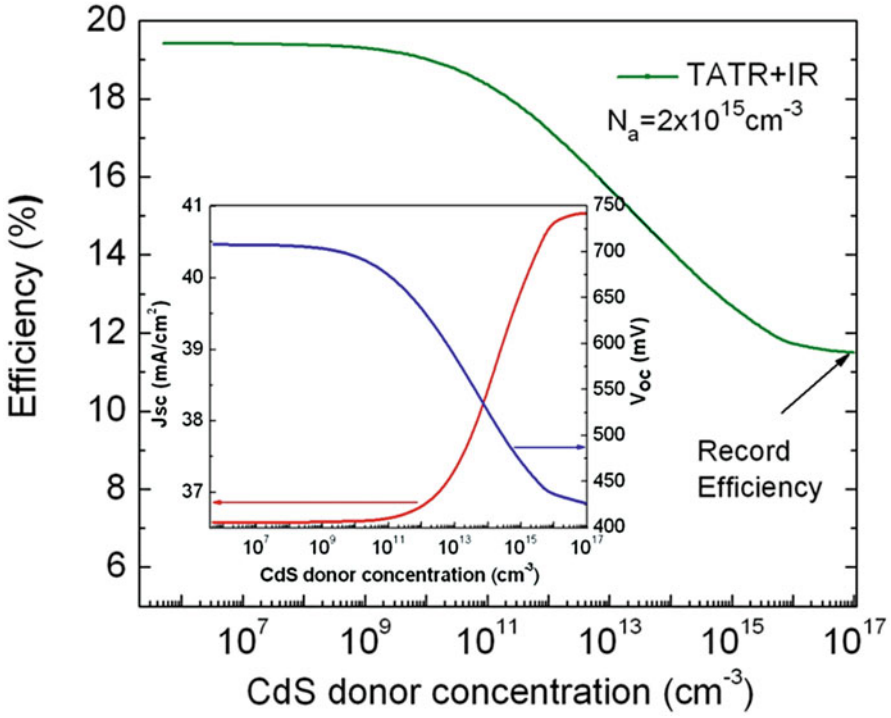

Fig. 8.15 CdS/CZTSe efficiency as a function of CdS donor concentration (N_d) taking into consideration trap-assisted tunneling recombination (TATR) and interface recombination (IR) transport mechanisms. The inset shows V_{oc} and J_{sc} dependence on N_d values

enhanced efficiency was also suggested by Winkler et al., reaching an improvement in solar cell performance [93]. Nevertheless, since reduced CdS thickness can adversely impact device open-circuit voltage and fill factor, a more adequate strategy—for solar cells dominated by TATR—involves not only lower CdS widths but also more resistive CdS layers. In this way, by using thinner and more resistive CdS layers, improvements in the spectral response at short wavelength region as well as in V_{oc} value are expected. As a result, a MIS behavior could be a potential choice to solve one of the most important limiting factors of this technology. It is worth mentioning that this result is directly a consequence of TATR as the dominant loss mechanism. In other words, strategies to improve thin film solar cell efficiency are associated with dominant loss mechanisms. Therefore, for thin film solar cells with TATR as the dominant loss mechanism, better performances will be only obtained by reducing either absorber density of defects or electric field in depletion layer. Reducing kesterite density of defects is currently a challenge to scientific community while decreasing CdS donor concentration seems to be a more adequate choice. By increasing sulfur salt concentration in CBD-CdS, more stoichiometric CdS layers were obtained—which implies more resistive CdS layers—with enhanced CdTe solar cell efficiency [94]. Other approaches have involved

CdS:O and CdS:Cu for more resistive CdS layers obtaining more efficient CdTe solar cells [95, 96]. The main feature in all of these approaches is the V_{oc} improvement for more resistive CdS layers. Therefore, these results also confirm a possible MIS performance in CdTe solar cells. In fact, based on these evidences, a MIS performance was previously proposed by Karpov et al. for CdTe solar cells [97]. In that paper, authors also suggest that mechanism of MIS junction can be common between the CdTe and CIGS PV. As a matter of fact, a MIS strategy could be also applied to CIGS solar cells dominated by TATR mechanism to reach better performances. As a result, this potential strategy is quite attractive for thin film solar cells characterized by low V_{oc} values and dominated by TATR as shown for CZTGSSe, CdTe, and CIGS [42, 88–90]. On the other hand, despite resistive CdS layers with low widths are good candidates for MIS configuration due to less optical losses, it is important to consider that for thicknesses lower than 25 nm, the formation of pinholes is very likely along with the increase of shunt conductance, lowering fill factor and solar cell efficiency values.

A study on SRH, TATR, and IR loss mechanisms impact on solar cell efficiency as a function of CdS donor concentration was also carried out and results are shown in Fig. 8.16a. For the record solar cell, TATR mechanism has a major impact on solar cell performance than the SRH one. As a result, these N_a and N_d values are high enough to allow tunneling of majority carriers via traps. Furthermore, solar cell efficiency is improved for more resistive CdS layers because reverse saturation current density (J_0) is reduced as illustrated in Fig. 8.16b. As an interesting result, from the comparison between TATR and SRH mechanism outcomes, it is demonstrated that tunneling contribution is significant for N_d values higher than 10^{13} cm^{-3} as shown in Fig. 8.16a, b. Conversely, for N_d values lower than 10^{13} cm^{-3}, TATR turns into SRH mechanism as displayed in Fig. 8.16b, since electric field at depletion zone is reduced. Moreover, for CdS donor concentration in the range of 10^{17}–10^{16} cm^{-3}, the solar cell efficiency slightly increases since reverse saturation current density (J_0) variation is quite small as displayed by Fig. 8.16a, b. Besides, from Fig. 8.16b, it is also observed that CdS/CZTSe interface recombination influence on solar cell efficiency is negligible for N_d values higher than 10^{13} cm^{-3}.

Taking into account that researchers can usually deposit CdS layers about 50 nm without pinholes formations, results on solar cell efficiency as a function of N_d for different CdS widths—50 nm and 75 nm—were presented in Fig. 8.17. It is interesting to notice that CdS width plays a significant role in solar cell efficiency. The lower the CdS width, the higher the CZTSe solar cell efficiency. This result is mainly due to J_{sc} improvements, a consequence of a major photon absorption in CZTSe absorber material. As an important result, it is demonstrated that more resistive CdS layers generate improvements in solar cell efficiency for CdS widths in the range of 25–75 nm. Therefore, better performances are obtained for more resistive and thinner CdS layers. These results support the MIS performance of CZTSe solar cells. In particular, efficiency values in the range of 17.5–19.4% could be reached for very resistive CdS layers with thicknesses in the range of 25–75 nm. More resistive CdS films could be obtained by either increasing S/Cd ratio in CBD

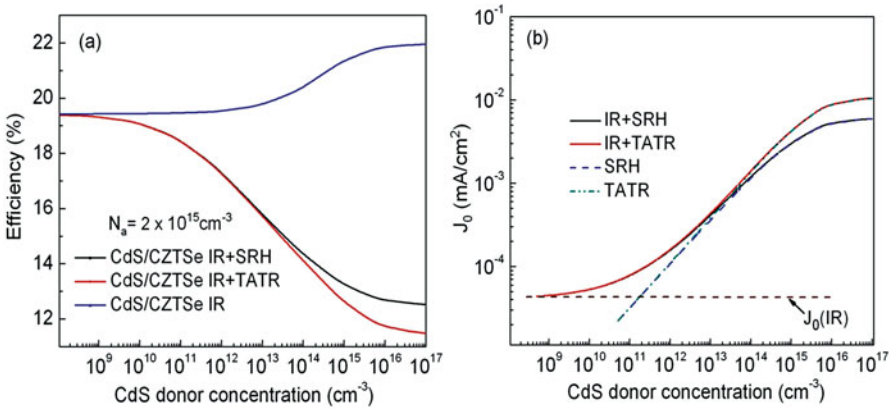

Fig. 8.16 CZTSe solar cell efficiency as a function of CdS donor concentration under IR, SRH, and TATR mechanisms (**a**). Reverse saturation current density as a function of CdS donor concentration under IR, SRH, and TATR mechanisms (**b**)

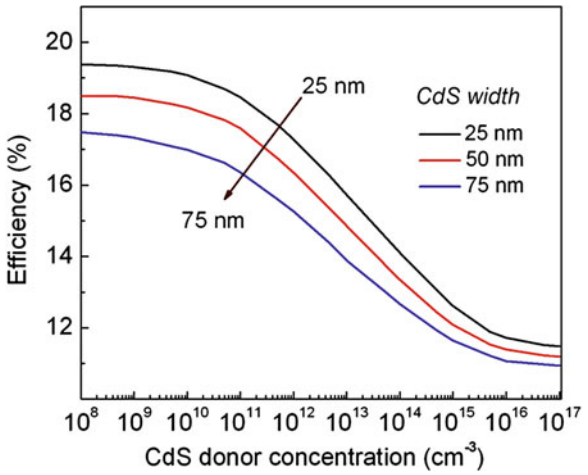

Fig. 8.17 CdS/CZTSe solar cell efficiency as a function of CdS donor concentration for different CdS widths

solution or doping CdS with Cu or O as mentioned before. Despite it is actually a challenge to obtain CdS films with too low donor concentrations, this study elucidates that the more resistive CdS obtained, the higher efficiency achieved.

One important potential limit of the present approach is the fact that a small constant CdS/CZTSe interfacial recombination speed was assumed for calculations. It is often very challenging to make a good quality interface with low doping and thin CdS layer. Therefore, it is very likely that thinner and more resistive CdS layers entail higher interface recombination. Under such situation, solar cell performance will depend on the dominant loss mechanism. If TATR is still the dominant one, then higher efficiencies will be achieved for thinner and more resistive CdS layers;

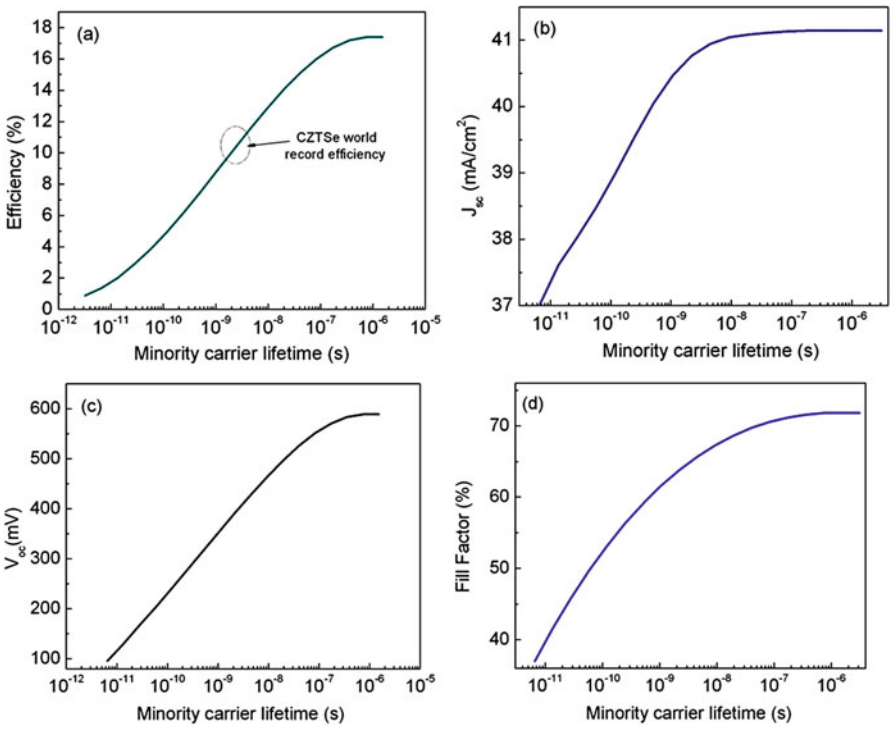

Fig. 8.18 Impact of CZTSe minority carrier lifetime on: (**a**) solar cell efficiency, (**b**) short-circuit current density, (**c**) open-circuit voltage, and (**d**) fill factor

however, these new values are expected to be lower than 19.4% depending on CdS/CZTSe interfacial quality due to a major IR contribution. Conversely, if CdS/CZTSe interfacial quality is quite poor (a high interfacial recombination speed) so that IR becomes the dominant loss mechanism, this approach to promote solar cell efficiency would be no longer valid as displayed in Fig. 8.16a, being this then one of the potential limits of this approach. Otherwise, this approach is quite attractive to solve one of the most important limiting factors in kesterite technology as experimentally shown in CZTSe solar cells and by other authors in CdTe solar cells as mentioned before.

The influence of CZTSe minority carrier lifetime on solar cell outcomes was found and results are presented in Fig. 8.18a–d. The contribution of IR is considered along with the TATR one. It is important to keep in mind that unlike CZTS/CdS heterojunction, IR losses are negligible for CZTSe/CdS solar cells. Consequently, TATR is the dominant transport mechanism and a further solar cell efficiency improvement to 17% can be attained by only increasing CZTSe minority carrier lifetime. Besides, by increasing minority carrier lifetime to 10^{-8} s, a further J_{sc} enhancement to 41 mA/cm^2 is expected. On the other hand, open-circuit voltage can be promoted to 600 mV by increasing CZTSe minority carrier lifetime. To

achieve higher V_{oc} values, once again a particular attention should be given to the CdS/CZTSe interface quality. However, by only focusing on CZTSe crystalline quality, a 17% could be acquired. Besides, a fill factor improvement to about 70% could be also obtained with CZTSe minority carrier lifetime increasing, which is desirable in solar cells. As previously demonstrated, by using thinner and resistive CdS layers, a 19.4% is expected from a MIS structure formation in CZTSe solar cells. However, to achieve highly resistive CdS layers of about 25 nm without pinhole formations is sometimes quite challenging. On top of this, it is also quite difficult to guarantee a good CdS/CZTSe interface quality with thinner and very resistive CdS layers. As a result, increasing CZTSe crystalline quality could be a more appropriate choice to achieve CZTSe efficiency values of 17%. Nevertheless, both routes should be experimentally evaluated to elucidate the best choice.

Since for CZTSe solar cell with record efficiency, optimized CdS and CZTSe widths were used, a study of the influence of IR speed and CZTSe minority carrier lifetime on solar cell efficiency and V_{oc} under optimal conditions for CdS and CZTSe are illustrated in Fig. 8.19a, b. A similar trend obtained for the CZTS solar cell is displayed for CZTSe solar cell. However, unlike CZTS case, highly performing CZTSe solar cell can be obtained by the CZTSe minority carrier lifetime increasing. Therefore, this result supports CZTSe compound as a better candidate for thin film solar cell applications.

Finally, the dependence of reverse saturation current density on minority carrier lifetime was evaluated for CZTSe solar cell. Results are presented in Fig. 8.20a. The contribution of IR is considered along with the TATR one. For CZTSe minority carrier lifetime values lower than 10^{-8} s, IR seems to be negligible. This result is consistent with the previous finding. For higher minority carrier lifetime values, IR becomes an important mechanism; however, only for a minority carrier lifetime higher than 10^{-7} s, IR is presented as the dominant loss mechanism in this solar

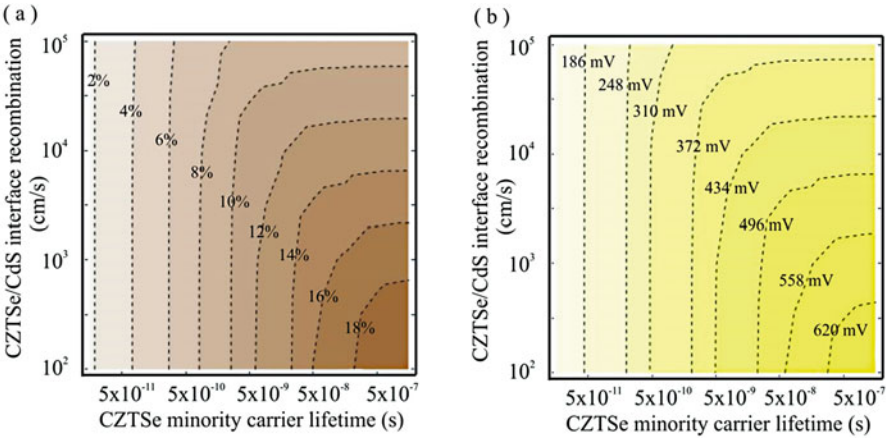

Fig. 8.19 Contour plot of CZTSe solar cell efficiency (**a**) and open-circuit voltage (**b**) as functions of CdS/CZTSe interface recombination speed and CZTSe minority carrier lifetime

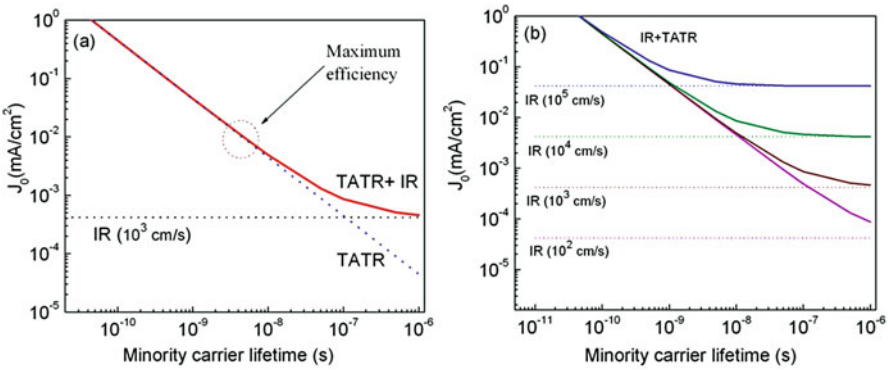

Fig. 8.20 Reverse dark current density as a function of CZTSe minority carrier lifetime: (**a**) under an interface recombination speed of 10^3 cm/s and (**b**) under interface recombination speed values in the range of 10^2–10^5 cm/s. Trap-assisted tunneling recombination and interface recombination are considered as the dominant loss mechanisms

cell. Nevertheless, an efficiency of 17% can be obtained under such conditions without paying any attention to the IR, as mentioned before. The impact of different IR speeds along with the CZTSe minority carrier lifetimes was also taken into account and results are presented in Fig. 8.20b. For minority carrier lifetime values lower than 10^{-9} s, J_0 is independent of interface recombination speed within the range of 10^2–10^4 cm/s. As a result, IR impact on CZTSe solar cell under such range is negligible. For CZTSe minority carrier lifetime values higher than 10^{-8} s, better interface quality is required to further promote CZTSe solar cell efficiency.

In short, KestTFSC software has been implemented in Wolfram Mathematica for modeling CZTS and CZTSe solar cells. In particular, the role of different transport mechanisms on these solar cells operation was implemented. As an advantage of this program, the possible effect of different microscopic and macroscopic parameters on solar cell behavior can be evaluated.

8.3 Summary

Modeling and simulation is a powerful tool to understand main limiting factors concerning thin film solar cell technology and propose routes to promote solar cell performance. However, in order to have accurate results, a good understanding of physical phenomena as well as adequate input parameters is required. Kesterite thin films are among the most promising materials for solar cell applications; nevertheless, only few theoretical works have been proposed to understand high Voc deficit. In particular, most of these consider transport mechanisms such as diffusion, radiative and non-radiative recombinations which are not able to explain experimental data reported for solar cells with the highest efficiencies. These transport

mechanisms are dominant under almost ideal conditions. Commonly, CdTe, CIGS, and kesterite thin film solar cells have been described by tunneling mechanisms by J–V measurements of solar cells at low temperatures. This result is a consequence of defect formation related with thin film processing route. Therefore, when it comes to thin film solar cells modeling, tunneling mechanisms should not be neglected. In this chapter, up-to-date approaches for modeling kesterite solar cells have been considered. So far, only two approaches have been able to reproduce experimental data accurately, one is by considering the effect of potential fluctuations and the other is by means of tunneling mechanisms assisted by defects along with losses at kesterite/buffer interface. One possible concern of the former is the absence of interface recombination which may play a fundamental role in kesterite solar cell technology. By assuming trap-assisted tunneling and kesterite/buffer interface recombination as the dominant mechanisms, it is demonstrated that despite the former better explains V_{oc} losses, interface losses do not allow efficiency improvements higher than 13% for CZTS thin film solar cells. Conversely, for CZTSe thin film solar cells, losses at interface are almost negligible. As a result, CZTSe solar cells could be a more adequate option for replacing CdTe and CIGS current technology. Two strategies are proposed to promote CZTSe solar cells to about 20%, the first is by means of a MIS structure while the second is by enhancing CZTSe crystallite quality. Both strategies are quite challenging so in order to estimate the better approach they need to be evaluated.

References

1. M.A. Green, K. Emery, Y. Hishikawa, W. Warta, E.D. Dunlop, Prog. Photovolt. Res. Appl. **24**, 905–913 (2016)
2. J.A. Andrade-Arvizu, M.F. García-Sánchez, M. Courel-Piedrahita, J. Santoyo-Morales, D. Jiménez-Olarte, M. Albor-Aguilera, O. Vigil-Galán, Mater. Des. **110**, 878–887 (2016)
3. J.A. Andrade-Arvizu, M.F. García-Sánchez, M. Courel-Piedrahita, F. Pulgarín-Agudelo, E. -Santiago-Jaimes, E. Valencia-Resendiz, A. Arce-Plaza, O. Vigil-Galán, J. Anal. Appl. Pyrolysis **121**, 347–359 (2016)
4. J.A. Andrade-Arvizu, M. Courel-Piedrahita, O. Vigil-Galán, J. Mater. Sci. Mater. Electron. **26**, 4541–4556 (2015)
5. A.M. Salem, M. Soliman Selim, J. Phys. D. Appl. Phys. **34**, 12–17 (2001)
6. G. Brammertz, M. Buffiere, S. Oueslati, H. ElAnzeery, K.B. Messaoud, S. Sahayaraj, C. Köble, M. Meuris, J. Poortmans, Appl. Phys. Lett. **103**, 163904 (2013)
7. Y.S. Lee, T. Gershon, O. Gunawan, T.K. Todorov, T. Gokmen, Y. Virgus, S. Guha, Adv. Energy Mater. **5**, 1401372 (2015). doi:10.1002/aenm.201401372
8. O. Gunawan, T.K. Todorov, D.B. Mitzi, Appl. Phys. Lett. **97**, 233506 (2010)
9. S. Siebentritt, Thin Solid Films **535**, 1 (2013)
10. T. Gokmen, O. Gunawan, T.K. Todorov, D.B. Mitzi, Appl. Phys. Lett. **103**, 103506 (2013)
11. A. Polizzotti, I.L. Repins, R. Noufi, S. Huai Wei, D.B. Mitzi, Energy Environ. Sci. **6**, 3171–3182 (2013)
12. O. Vigil Galán, M. Courel, J.A. Andrade-Arvizu, Y. Sánchez, M. Espíndola Rodríguez, E. Saucedo, D. Seuret-Jiménez, M. Titsworth, J. Mater. Sci. Mater. Electron. **26**, 5562–5573 (2015). doi:10.1007/s10854-014-2196-4

13. C.J. Hages, S. Levcenco, C.K. Miskin, J.H. Alsmeier, D. Abou-Ras, R.G. Wilks, M. Bär, T. Unold, R. Agrawal, Prog. Photovolt. Res. Appl. (2013). doi:10.1002/pip.2442
14. O. Vigil-Galán, M. Courel, M. Espindola-Rodriguez, D. Jiménez-Olarte, M. Aguilar-Frutis, E. Saucedo, Sol. Energy Mater. Sol. Cells **132**, 557–562 (2015)
15. M. Courel, E. Valencia-Resendiz, F.A. Pulgarín-Agudelo, O. Vigil-Galán, Solid State Electron. **118**, 1–3 (2016)
16. O. Vigil-Galán, F.A. Pulgarín, F. Cruz-Gandarilla, M. Courel, G. Villarreal-Ruiz, Y. Sánchez, D. Jiménez-Olarte, E. Saucedo, Mater. Des. **99**, 254–261 (2016)
17. M. Courel, E. Valencia-Resendiz, J.A. Andrade-Arvizu, E. Saucedo, O. Vigil-Galán, Sol. Energy Mater. Sol. Cells **159**, 151–158 (2017)
18. M. Courel, J.A. Andrade-Arvizu, A. Guillén-Cervantes, M.M. Nicolás-Marín, F.A. Pulgarín-Agudelo, O. Vigil-Galán, Mater. Des. **114**, 515–520 (2017)
19. W. Wang, M.T. Winkler, O. Gunawan, T. Gokmen, T.K. Todorov, Z. Yu, D.B. Mitzi, Adv. Energy Mater. **4**, 1301465 (2014)
20. P. Sinsermsuksakul, L. Sun, S.W. Lee, H.H. Park, S.B. Kim, C. Yang, R.G. Gordon, Adv. Energy Mater. **4**, 1400496 (2014)
21. A. Fairbrother, X. Fontané, V. Izquierdo-Roca, M. Espindola-Rodriguez, S. López Marino, M. Placidi, J. López-García, A. Pérez-Rodríguez, E. Saucedo, Chem. Phys. Chem. **9**, 1836–1843 (2013)
22. H. Katagiri, K. Jimbo, W.I.N. Shwe Maw, K. Oishi, M. Yamazaki, H. Araki, A. Takeuchi, Thin Solid Films **517**, 2455–2460 (2009)
23. T. Tanaka, D. Kawasaki, M. Nishio, Q. Guo, H. Ogawa, Phys. Status Solidi C **3**, 2844–2847 (2006)
24. N. Moritake, Y. Fukui, M. Oonuki, K. Tanaka, H. Uchiki, Phys. Status Solidi C **6**, 1233–1236 (2009)
25. Z. Zhou, Y. Wang, D. Xu, Y. Zhang, Sol. Energ. Mater. Sol. C **94**, 2042–2045 (2010)
26. J.J. Scragg, P.J. Dale, L.M. Peter, G. Zoppi, I.A.N. Forbes, Phys. Status Solidi B **245**, 1772–1778 (2008)
27. K. Moriya, J. Watabe, K. Tanaka, H. Uchiki, Phys. Status Solidi C **3**, 2848–2852 (2006)
28. G. Suresh Babu, Y.B. Kishore Kumar, P. Uday Bhaskar, S.R. Vanjari, Sol. Energ. Mater. Sol. C **94**, 221–226 (2010)
29. N. Nakayama, K. Ito, Appl. Surf. Sci. **92**, 171–175 (1996)
30. N. Kamoun, H. Bouzouita, Thin Solid Films **515**, 5949–5952 (2007)
31. J. Madarász, P. Bombicz, M. Okuya, S. Kaneko, Solid State Ionics **141–142**, 439–446 (2001)
32. M. Courel, O. Vigil-Galan, D. Jimenez-Olarte, M. Espındola-Rodrıguez, E. Saucedo, J. Appl. Phys. **116**, 134503 (2014)
33. F. Li, Z. Xia, Q. Liu, J. Phys. Chem. C **120**, 16969–16976 (2016)
34. M. Singh, T.R. Rana, J.H. Kim, J. Alloys Compd. **675**, 370–376 (2016)
35. J. Chen, W. Li, C. Yan, S. Huang, X. Hao, J. Alloys Compd. **621**, 154–161 (2015)
36. E. Garcia-Llamas, M. Guc, I.V. Bodnar, X. Fontané, R. Caballero, J.M. Merino, M. León, V. Izquierdo-Roc, J. Alloys Compd. **692**, 249–256 (2017)
37. S. Bourdais, C. Choné, B. Delatouche, A. Jacob, G. Larramona, C. Moisan, A. Lafond, F. Donatini, G. Rey, S. Siebentritt, A. Walsh, G. Dennler, Adv. Energy Mater. **6**, 1502276 (2016)
38. J. Kim, H. Hiroi, T.K. Todorov, O. Gunawan, M. Kuwahara, T. Gokmen, D. Nair, M. Hopstaken, B. Shin, Y.S. Lee, W. Wang, H. Sugimoto, D.B. Mitzi, Adv. Mater. **26**, 7427–7431 (2014)
39. H. Hiroi, N. Sakai, T. Kato, H. Sugimoto, High Voltage Cu2ZnSnS4 Submodules by Hybrid Buffer Layer, in *39th IEEE Photovoltaic Specialists Conference*, Tampa, FL, vol. 863–866 (2013)
40. H. Hiroi, J. Kim, M. Kuwahara, T.K. Todorov, D. Nair, M. Hopstaken, Y. Zhu, O. Gunawan, D.B. Mitzi, H. Sugimoto, Over 12% efficiency Cu2ZnSn(SeS)4 solar cell via hybrid buffer

layer, in *40th IEEE Photovoltaic Specialists Conference*, Denver, CO, vol. 30–32 (2014). Doi:10.1109/PVSC.2014.6925044
41. M. Neuschitzer, K. Lienau, M. Guc, L.C. Barrio, S. Haass, J.M. Prieto, Y. Sanchez, M. - Espindola-Rodriguez, Y. Romanyuk, A. Perez-Rodriguez, V. Izquierdo-Roca, E. Saucedo, J. Phys. D. Appl. Phys. **49**, 125602 (2016)
42. C.J. Hages, N.J. Carter, R. Agrawal, T. Unold, J. Appl. Phys. **115**, 234504 (2014)
43. W. Zhao, W. Zhou, X. Miao, Numerical Simulation of CZTS Thin Film Solar Cell, in *2012 7th IEEE International Conference on Nano/Micro Engineered and Molecular Systems (NEMS)* (2012), pp. 502–505. Doi:10.1109/NEMS.2012.6196826
44. T. Gokmen, O. Gunawan, D.B. Mitzi, Appl. Phys. Lett. **105**, 033903 (2014)
45. P. Lin, L. Lin, J. Yu, S. Cheng, P. Lu, Q. Zheng, J. Appl. Sci. Eng. **17**, 383–390 (2014). doi:10.6180/jase.2014.17.4.05
46. M. Djinkwi Wanda, S. Ouédraogo, F. Tchoffo, F. Zougmoré, J.M.B. Ndjaka, Int. J. Photoenergy **2016**, 9 (2016). doi:10.1155/2016/2152018
47. C. Frisk, T. Ericson, S.-Y. Li, P. Szaniawski, J. Olsson, C. Platzer-Björkman, Sol. Energy Mater. Sol. Cells **144**, 364–370 (2016)
48. D. Hironiwa, M. Murata, N. Ashida, Z. Tang, T. Minemoto, Jpn. J. Appl. Phys. **53**, 071201 (2014)
49. S.R. Meher, L. Balakrishnan, Z.C. Alex, Superlattice. Microst. (2016). doi:10.1016/j.spmi.2016.10.028
50. M. Patel, A. Ray, Physica B **407**, 4391–4397 (2012)
51. O.K. Simya, A. Mahaboobbatcha, K. Balachander, Superlattice. Microst. **82**, 248–261 (2015). doi:10.1016/j.spmi.2015.02.020
52. P. Aobo, F. Ma, C. Yan, J. Huang, K. Sun, M. Green, X. Hao, Sol. Energy Mater. Sol. Cells **160**, 372–381 (2017)
53. A. Kanevcen, I. Repins, S.-H. Wei, Sol. Energy Mater. Sol. Cells **133**, 119–125 (2015)
54. U. Rau, H.W. Schock, Electronic properties of Cu(In,Ga)Se2 heterojunction solar cells-recent achievements, current understanding, and future challenges. Appl. Phys. A Mater. Sci. Process. **69**(2), 131–147 (1999)
55. H. Zhu, A.K. Kalkan, J.Y. Hou, and S.J. Fonash, Applications of AMPS-I D for solar cell simulation, in *Aip Conference Proceedings*. pp. 309–314
56. Y. Liu, Y. Sun, A. Rockett, Sol. Energy Mater. Sol. Cells **98**, 124–128 (2012)
57. W. Shockley, W.T. Read, Statistics of the Recombinations of holes and electrons. Phys. Rev. **87**, 835–842 (1952)
58. J.A. Willemen, M. Zeman, J.W. Metselaar, Computer modeling of amorphous silicon tandem cells, in *Conference Record of the Twenty Fourth IEEE Photovoltaic Specialists Conference, 1994 and the First World Conference on Photovoltaic Energy Conversion*, vol. 1, (1994), pp. 599–602
59. J.E. Moore, C.J. Hages, R. Agrawal, M.S. Lundstrom, J.L. Gray, Appl. Phys. Lett. **109**, 021102 (2016). doi:10.1063/1.4955402
60. C.J. Hages, N.J. Carter, R. Agrawal, J. Appl. Phys. **119**, 014505 (2016). doi:10.1063/1.4939487
61. M. Burgelman, P. Nollet, S. Degrave, Modeling polycrystalline semiconductor solar cells. Thin Solid Films **361–362**, 527–532 (2000). doi:10.1016/S0040-6090(99)00825-1
62. Synopsys, TCAD SDEVICE Manual, Release H-2013.03, Zurich, Switzerland, www.synopsys.com
63. O. Vigil-Galán, M. Espíndola-Rodríguez, M. Courel, X. Fontané, D. Sylla, V. Izquierdo-Roca, A. Fairbrother, E. Saucedo, A. Pérez-Rodríguez, Sol. Energy Mater. Sol. Cells **117**, 246–250 (2013)
64. J.C. Rimada, L. Hernandez, Microelectron. J. **32**, 719–723 (2001)
65. J.C. Rimada, L. Hernandez, J.P. Connolly, K.W.J. Barnham, Phys. Status Solidi B **242**, 1842–1845 (2005)

66. J.C. Rimada, L. Hernández, J.P. Connolly, K.W.J. Barnham, Microelectron. J. **38**, 513–518 (2007)
67. M. Courel, J.C. Rimada, L. Hernández, Appl. Phys. Lett. **100**, 073508 (2012)
68. M. Courel, J.C. Rimada, L. Hernández, J. Appl. Phys. **112**, 054511 (2012)
69. M. Courel, J.C. Rimada, L. Hernández, Prog. Photovolt. Res. Appl. **21**, 276–282 (2013)
70. M. Courel, J.A. Andrade-Arvizu, O. Vigil-Galán, Appl. Phys. Lett. **105**, 233501 (2014)
71. M. Courel, J.A. Andrade-Arvizu, O. Vigil-Galán, Solid State Electron. **111**, 243–250 (2015). doi:10.1016/j.sse.2015.05.038
72. M. Courel, F.A. Pulgarín-Agudelo, J.A. Andrade-Arvizu, O. Vigil-Galán, Sol. Energy Mater. Sol. Cells **149**, 204–212 (2016)
73. M. Courel, J.A. Andrade-Arvizu, O. Vigil-Galán, Mater. Res. Express **3**, 095501 (2016)
74. J. Singh, *Electronic and Optoelectronic Properties of Semiconductor Structures* (Cambridge University Press, Cambridge, 2003), pp. 359–360
75. K. Ito (ed.), *Copper zinc tin sulfide-based thin film solar cells Physical Properties: Compiled Experimental Data* (Wiley, Chichester, 2015), Ch. 7, p. 172
76. H.J. Hovel, Solar cells, in *Semiconductors and Semimetals*, ed. by R. K. Willardson (Ed), vol. 11, (Academic, 1975)
77. S.M. Sze, *Physics of Semiconductor Devices*, 2nd edn. (Wiley, New York, 1981)
78. S. Chen, A. Walsh, X. Gong, S.-H. Wei, Adv. Mater. **25**, 1522–1539 (2013)
79. J.B. Varley, V. Lordi, Appl. Phys. Lett. **103**, 102103 (2013). doi:10.1063/1.4819492
80. G.A.M. Hurkx, D.B.M. Klaassen, M.P.G. Knuvers, A new recombination model for device simulation including tunneling. IEEE Trans. Electron Devices **39**, 331–338 (Feb. 1992)
81. G.A.M. Hurkx, H.C. de Graaff, W.J. Kloosterman, M.P.G. Knuvers, A new analytical diode model including tunneling and avalanche breakdown. IEEE Trans. Electron Devices **39**, 2090–2098 (1992)
82. T. Gershon, B. Shin, N. Bojarczuk, T. Gokmen, S. Lu, S. Guha, J. Appl. Phys. **114**, 154905 (2013)
83. W.N. Shafarman, S. Siebentritt, L. Stolt, *Handbook of Photovoltaic Science and Engineering*, 2nd edn. (Wiley, West Sussex, UK, 2011), pp. 546–599
84. Z.-H. Dai, R.-J. Zhang, J. Shao, Y.-M. Chen, Y.-X. Zheng, J.-D. Wu, L.-Y. Chen, J. Korean Phys. Soc. **55**, 1227–1232 (2009)
85. S. Ninomiya, S. Adachi, J. Appl. Phys. **78**, 1183–1190 (1995)
86. S. Levcenko, G. Gurieva, M. Guc, A. Nateprov, Moldavian J. Phys. Sci. **8**(N2), 173–177 (2009)
87. L.A. Kosyachenko, X. Mathew, P.D. Paulson, V.Y. Lytvynenko, O.L. Maslyanchuk, Sol. Energy Mater. Sol. Cells **130**, 291–302 (2014)
88. H. Bayhan, A.S. Kavasoglu, Solid State Electron. **49**, 991–996 (2005)
89. U. Rau, A. Jasenek, H.W. Schock, F. Engelhardt, T. Meyer, Thin Solid Films **361–362**, 298–302 (2000)
90. U. Rau, Appl. Phys. Lett. **74**, 111–113 (1999)
91. Y. Sanchez, M. Neuschitzer, M. Dimitrievska, M. Espindola-Rodriguez, J. Lopez-Garcia, V. Izquierdo Roca, O. Vigil-Galán, E. Saucedo, High VOC Cu2ZnSnSe4/CdS:Cu based solar cell: Evidences of a metal-insulator-semiconductor (MIS) type hetero-junction, in *Photovoltaic Specialist Conference (PVSC), 2014 I.E. 40th*, pp. 0417–0420
92. F. Liu, C. Yan, J. Huang, K. Sun, F. Zhou, J.A. Stride, M.A. Green, X. Hao, Adv. Energy Mater. **6**, 1600706 (2016)
93. M.T. Winkler, W. Wang, O. Gunawan, H.J. Hovel, T.K. Todorov, D.B. Mitzi, Energy Environ. Sci. **7**, 1029–1036 (2014)
94. O. Vigil-Galán, A. Arias-Carbajal, R. Mendoza-Pérez, G. Santana-Rodríguez, J. Sastre-Hernández, J.C. Alonso, E. Moreno-García, G. Contreras-Puente, A. Morales-Acevedo, Semicond. Sci. Technol. **20**(8), 819–822 (2005)
95. T.R. Ohno, E. Sutter, J. Kestner, A.S. Gilmore, V. Kaydanov, C.A. Wolden, P.V. Meyers, L. Woods, M.J. Romero, M.M. Al-Jassim, S. Johnston, Microscopic characterization of

polycrystalline APCVD CdTe thin film PV devices. Mat. Res. Symp. Proc. **668**, H6.5 (2001). doi:10.1557/PROC-668-H6.5
96. X. Wu, Y. Yan, R.G. Dhere, Y. Zhang, J. Zhou, C. Perkins, B. To, Phys. Status Solidi C **1**, 1062–1066 (2004)
97. V.G. Karpov, D. Shvydka, Y. Roussillon, Physics of CdTe photovoltaics: from front to back. Mater. Res. Soc. Symp. Proc. **865**, F10.1.1–F10.1.12 (2005)